JP0050614

JAERI-Conf
2000-005

INDC(JPN)-185/U

PROCEEDINGS OF THE 1999 SYMPOSIUM ON NUCLEAR DATA NOVEMBER 18-19, 1999, JAERI, TOKAI, JAPAN

March 2000

(Eds.) Naoki YAMANO* and Tokio FUKAHORI

日本原子力研究所
Japan Atomic Energy Research Institute

本レポートは、日本原子力研究所が不定期に公刊している研究報告書です。
入手の問合わせは、日本原子力研究所研究情報部研究情報課（〒319-1195　茨城県那珂郡東海村）あて、お申し越し下さい。なお、このほかに財団法人原子力弘済会資料センター（〒319-1195　茨城県那珂郡東海村日本原子力研究所内）で複写による実費頒布を行っております。

This report is issued irregularly.
Inquiries about availability of the reports should be addressed to Research Information Division, Department of Intellectual Resources, Japan Atomic Energy Research Institute, Tokai-mura, Naka-gun, Ibaraki-ken 〒319-1195, Japan.

編集兼発行　日本原子力研究所

JAERI−Conf 2000−005 INDC(JPN)-185/U

Proceedings of the 1999 Symposium on Nuclear Data November 18-19, 1999, JAERI, Tokai, Japan

(Eds.) Naoki YAMANO* and Tokio FUKAHORI

Japanese Nuclear Data Committee
Tokai Research Establishment
Japan Atomic Energy Research Institute
Tokai-mura, Naka-gun, Ibaraki-ken

(Received February 4, 2000)

The 1999 Symposium on Nuclear Data was held at Tokai Research Establishment, Japan Atomic Energy Research Institute (JAERI), on 18th and 19th of November 1999. Japanese Nuclear Data Committee and Nuclear Data Center, JAERI organized this symposium. In the oral sessions, presented were 18 papers on keynote address, nuclear data measurement for long-lived RI and in medium energy region, status of JENDL, international session and other topics. In the poster session, presented were 46 papers concerning experiments, evaluations, benchmark tests and on-line database on nuclear data. Those presented papers are compiled in the proceedings.

Keywords: Nuclear Data, Symposium, Proceedings, Nuclear Reaction, JENDL, Experiment, Evaluation, Benchmark Test, Cross Section.

*Sumitomo Atomic Energy Industries, Ltd.

1999年核データ研究会報文集
1999年11月18日～19日，東海研究所，東海村

日本原子力研究所東海研究所
シグマ研究委員会
（編）山野　直樹*・深堀　智生

(2000年2月4日受理)

1999年核データ研究会が、1999年11月18日と19日の両日、日本原子力研究所東海研究所において開催された。この研究会は、日本原子力研究所のシグマ研究委員会と核データセンターが主催して開いたものである。口頭発表では、基調講演、長寿命放射性核種及び中高エネルギー核データ測定、JENDLの進捗、国際セッション、その他のトピックスについての18件の報告があった。ポスター発表では、46件の発表があり、それらは、核データの測定、評価や評価済核データのベンチマークテスト、オンラインデータベース等に関するものであった。本報文集は、それらの論文をまとめたものである。

東海研究所：〒319-1195 茨城県那珂郡東海村白方白根2-4
* 住友原子力工業㈱

Program Committee

Naoki YAMANO(Chairman)	Sumitomo Atomic Energy Industries, Ltd.
Takeo ARUGA	Japan Atomic Energy Research Institute
Tokio FUKAHORI	Japan Atomic Energy Research Institute
Hidero HARADA	Japan Nuclear Cycle Development Institute
Masayuki IGASHIRA	Tokyo Institute of Technology
Jun-ichi KATAKURA	Japan Atomic Energy Research Institute
Norio KISHIDA	Japan Atomic Energy Research Institute
Takaaki OHSAWA	Kinki University
Kazuhiro OYAMATSU	Nagoya University
Makoto SASAKI	Mitsubishi Heavy Industries, Ltd.
Teiko TAKADA	Japan Atomic Energy Research Institute
Tadashi YOSHIDA	Musashi Institute of Technology
Atsushi ZUKERAN	Hitachi, Ltd.

プログラム委員会

山野　直樹（委員長）	住友原子力工業（株）
有賀　武夫	日本原子力研究所
深堀　智生	日本原子力研究所
原田　秀郎	核燃料サイクル開発機構
井頭　政之	東京工業大学
片倉　純一	日本原子力研究所
岸田　則生	日本原子力研究所
大澤　孝明	近畿大学
親松　和浩	名古屋大学
佐々木　誠	三菱重工業（株）
高田　禎子	日本原子力研究所
吉田　正	武蔵工業大学
瑞慶覧　篤	（株）日立製作所

This is a blank page.

Contents

目　次

This is a blank page.

1. Introduction

The 1999 symposium on nuclear data was held at Tokai Research Establishment, Japan Atomic Energy Research Institute (JAERI), on 18th and 19th of November 1999, with about 150 participants. Japanese Nuclear Data Committee and Nuclear Data Center, JAERI organized the symposium.

The program of the symposium is listed below. In the oral sessions, total 18 papers were presented on keynote address, nuclear data measurement for long-lived RI and in medium energy region, status of JENDL, international session and other topics. In the poster session, presented were 46 papers concerning nuclear data experiments, evaluations, benchmark tests, on-line database on nuclear data, etc. Those papers are compiled in the proceedings.

Program

Oral Presentation [Talk + Discussion (min.)]

Nov. 18 (Thu.)

9:50-10:00 Session 1: Opening Address — M. Nakagawa (JAERI)

10:00-11:00 Session 2: Keynote Address — Chairman: M. Nakazawa (U. of Tokyo)

2.1 Requirement and Prospect of Nuclear Data Activities for Nuclear Safety [30+10]
I. Kimura (Inst. of Nucl. Safety System. Inc.)

2.2 Review of Nuclear Data Needs for Fusion Energy Development [15+5]
E.T. Cheng (TSI)

11:00-12:00 Session 3: Nuclear Data Measurement for Long-lived RI
-- for Radioactive Waste Transmutation --
Chairman: M. Igashira (TIT)

3.1 Precise Measurements of Neutron Capture Cross Sections for FP [25+5]
S. Nakamura (JNC)

3.2 MA Nuclear Data Measurements with Lead Slowing-down Spectrometer [25+5]
K. Kobayashi (KUR)

12:00-14:00 Poster Session 1 (Odd Number) ＋ Lunch

14:00-15:30 Session 4: Nuclear Data Measurement in Intermediate Energy Region
-- for Usage of Medium Energy Quanta --
Chairman: K. Kawade (Nagoya U.)

4.1 Nuclear Data Measurements for 40~90 MeV Neutrons at TIARA[25+5]
M. Baba (Tohoku U.)

4.2 Status of the AGS Experiment for Mercury Spallation Target Development [25+5]
Y. Ikeda (JAERI)

4.3 High Resolution Measurement of Total Photonuclear Cross Sections [25+5]
H. Harada (JNC)

15:30-16:00 Coffee Break

16:00-18:05 Session 5: International Session Chairman: A. Hasegawa (JAERI)

5.1 Recent Nuclear Data Measurement, Evaluation and Calculation in China [20+5]
Y. Zhuang (CIAE)

5.2 Nuclear Data Project in Korea (and Resonance Parameter Evaluation of Fission Products) [20+5] J. Chang (KAERI)

5.3 Study on Nuclear Power Introduction into Vietnam [20+5]
Vuong Huu Tan (VAEC)

5.4 Customization of ENDF/B-VI and JENDL3.2 Basic Data for MCNP Calculation and Measurements of Neutron Cross Section at INST, AERE, Savar [20+5]
N.I. Molla (AERE)

5.5 Empirical Systematics for Selection of Threshold Reaction Excitation Functions [20+5]
V. Manokhin (IPPE)

18:20- RECEPTION at Akogi-ga-ura Club

Nov. 19 (Fri.)

9:30-10:50 Session 6: Topics Chairman: K. Oyamatsu (Aichi Shukutoku U.)

6.1 RI Beam Factory Project at RIKEN [30+10] H. Sakurai (RIKEN)

6.2 Synthesis of Superheavy Nuclei using Heavy-ion Fusion Reactions [30+10]
H. Ikezoe (JAERI)

10:50-11:10 Coffee Break

11:10-11:50 Session 6: Topics (Cont.)

6.3 Present Status of International Criticality Safety Benchmark Evaluation Project (ICSBEP) [30+10] Y. Miyoshi (JAERI)

12:00-14:00 Poster Session 2 (Even Number) ＋ Lunch

14:00-15:40 Session 7: High Energy Nuclear Data Calculation & Status of JENDL
Chairman: Y. Watanabe (Kyushu U.)

7.1 High Energy Nuclear Reaction Code JAM [30+10]	K. Niita (RIST)
7.2 Revision of Heavy Nuclei Data of JENDL-3.2 [25+5]	T. Kawano (Kyushu U.)
7.3 Present Status of JENDL FP Decay Data File [25+5]	J. Katakura (JAERI)

15:40-15:45 Session 8: Poster Award N. Yamano (SAE)

16:00-16:20 Session 9: Summary Talk A. Zukeran (Hitachi)

Poster Session

Nov. 18 (Thu.) 12:00-14:00 (Odd Number), and

Nov. 19 (Fri.) 12:00-14:00 (Even Number)

P1. Capture Cross Section Measurement of Np-237 below 1 keV with Lead Slowing-down Spectrometer — Hyun-Je Cho (KUR)

P2. Measurement of Neutron Total Cross-Sections of Dy and Hf in the Energy Region from 0.002 eV to 100 keV — Hyun-Je Cho (KUR)

P3. Measurement of keV-Neutron Capture Cross Sections and Capture Gamma-Ray Spectra of Er Isotopes — Harun-Ar-Rashid A.K.M. (TIT)

P4. Measurements of Fast Neutron-Induced Fission Spectra for ^{233}U, ^{238}U, ^{232}Th — T. Miura (Tohoku U.)

P5. Effect of Anisotropic Scattering for MOX fuel Analysis — D. Sato (Osaka U.)

P6. Development of JOYO MK-II Core Characteristics Database — S. Tabuchi (JNC)

P7. Properties of Fission-Product Decay Heat from Minor-Actinide Fissioning Systems — K. Oyamatsu (Aichi Shukutoku U.)

P8. A $\beta-\gamma$ Coincidence Measurement System for Precise Determination of γ -ray Emission Probabilities of Short-Lived FP Nuclides — K. Furutaka (JNC)

P9. Measurements of $^{9}Be(d,x)$ and $^{9}Be(p,x)$ Cross Sections at Low Energy — K. Ishii (Osaka U.)

P10. Measurement of Leakage Neutron Spectra from Advanced Blanket Materials and Structural Materials Induced by D-T Neutrons — T. Nishio (Osaka U.)

P11. Measurement of Double Differential Cross Sections of Charged Particle Emission Reactions by Incident DT Neutrons —Correction for Energy Loss of Charged Particle in Sample Materials— — H. Takagi (Osaka U.)

P12. Measurement of Secondary Gamma-ray Production Cross Sections of Structural Materials for Fusion Reactor -- Extraction of Discrete and Continuum Components -- — T. Kondo (Osaka U.)

This is a blank page.

2. Papers Presented at Oral Session

This is a blank page.

2.1 Requirement and Prospect of Nuclear Data Activities for Nuclear Safety

Itsuro KIMURA
Professor Emeritus, Kyoto University
Director, Institute of Nuclear Technology, Institute of Nuclear Safety System, Inc., Mihama, Fukui 919-1205
e-mail : kimura@inss.co.jp

Owing to continuous efforts by the members of JNDC (Japanese Nuclear Data Committee) and Nuclear Data Center in JAERI (Japan Atomic Energy Research Institute), several superb evaluated nuclear data files, such as JENDL, FP (fission product) yields and decay heat, have been compiled in Japan and opened to the world. However, they are seldom adopted in safety design and safety evaluation of light water reactors and are hardly found in related safety regulatory guidelines and standards except the decay heat. In this report, shown are a few examples of presently used nuclear data in the safety design and the safety evaluation of PWRs (pressurized water reactors) and so forth. And then, several procedures are recommended in order to enhance more utilization of Japanese evaluated nuclear data files for nuclear safety.

1. Introduction

At present, 51 light water reactors produce about 1/3 of electricity in Japan, and a new fuel reprocessing plant is now being constructed in Rokkasho-mura. However, successively occurred accidents, particularly the most recent one at a fuel conversion plant of JCO, Inc. in Tokai-mura, must have increased anxiety on nuclear energy in many people's mind. Japanese nuclear energy is at a crisis. We ought to overcome this situation by making efforts for improvement in nuclear safety and for recovery of reliability on nuclear energy. It seems quite difficult to do this, yet nuclear energy itself is essentially important not only for national prosperity, but also for reservation of global environment in the 21st Century.

The activities in nuclear science and engineering in Japan have reached the top level in the world, but many scientists and engineers are now inclined to too specialized by losing common sense and curiosity to other fields. Most of plant engineers and workers in nuclear industries hardly try to get new informations in nuclear science and engineering. The JCO accident was occurred in the very same village where beautiful transient experiments were carried out for simulating criticality accidents of aqueous fuel solution using TRACY of the NUCEF facility at JAERI. It is regrettable that there is estrangement between research institutes and manufacturing plants in Japanese nuclear energy.

Similar tendency can be seen in the field of nuclear data in Japan. Owing to continuous

efforts by the member of JNDC and Nuclear Data Center in JAERI, several superb evaluated nuclear data files, such as JENDL, FP yields and decay heat, have been compiled. However, these evaluated nuclear data are seldom adopted in safety design and safety evaluation of light water reactors even now. They are hardly found in related safety regulatory guidelines and standards except the decay heat. Very recently, the staff of JAERI didn't use the FP yields data of JNDC, but German ones for the measurement of the FP densities in the precipitation tank at the conversion plant of JCO. In this report, shown are a few examples of presently used nuclear data in the safety design and safety evaluation of PWRs and so forth. Thereafter, several procedures are recommended in order to enhance more utilization of Japanese evaluated nuclear data files for nuclear safety.

2. Legal Regulations for Safety of Power Reactors and Nuclear Facilities

By the Law Concerning Regulation of Nuclear Raw Material Substances, Nuclear Fuel Substances and Nuclear Reactors, establishment of a nuclear reactor and enterprise of a nuclear fuel facility must be permitted by Japanese Government. The procedure from site selection to commencement of operation for a nuclear power reactor is depicted in Fig.1[1]. In the procedure the safety examination organization of nuclear facilities is shown in Fig.2[1]. In the attachments of the application for permission of the establishment of a nuclear reactor, nuclear data are required in the following 3 articles:

(1) Explanation about the safety design of reactor facilities (Attachment No.8),
(2) Explanation about the control of exposed radiation doses caused by nuclear fuel and by substances contaminated by it, and about the disposal of radioactive wastes (Attachment No.9)
(3) Explanation about the type, the degree, the influence etc. of reactor incidents and accidents assumed to occur by misoperations, faults of machines and instruments, earthquake, fire and so forth (Attachment No.10, safety evaluation).

For the safety examination of a light water reactor, Nuclear Safety Commission have decided several safety regulatory guidelines and reports of related rules. Among them the following 2 items include nuclear data:

(1) Regulatory guideline for the evaluation of an emergency core cooling system (ECCS),
(2) Energies of radiations for the calculation of exposed doses.

In the first one, the recommended values of the decay heat by JNDC is adopted as a heat source, but their newly evaluated nuclear decay data are not found in the second one.

After getting the permission of the establishment of a reactor, the enterpriser has to apply for the sanction of its construction plan to the Government. In this application, nuclear data are required in the following 5 items:

(1) Thermal power calculation,
(2) Control capability calculation,
(3) Explanation about nuclear fuel substances not reaching criticality in new fuel racks,
(4) Explanation about nuclear fuel substances not reaching criticality in spent fuel racks,

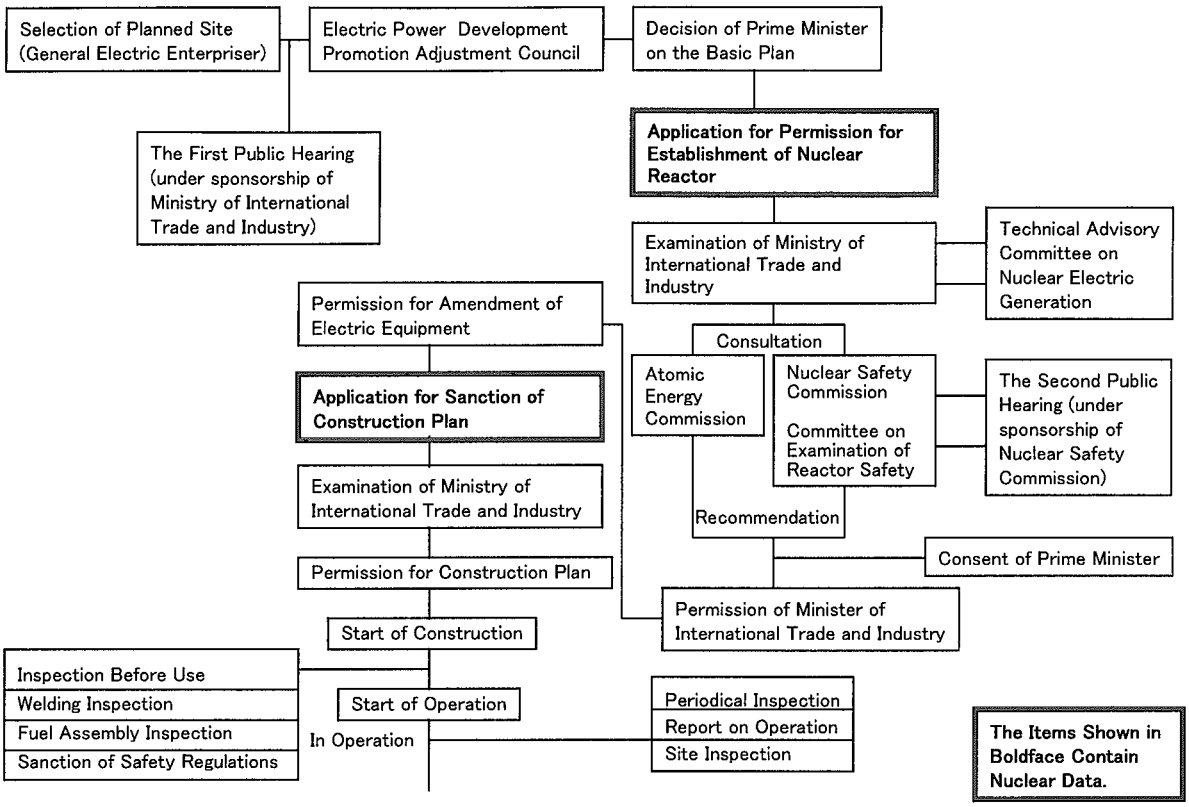

Fig.1 Procedure from site selection to commencement of operation for a nuclear power reactor

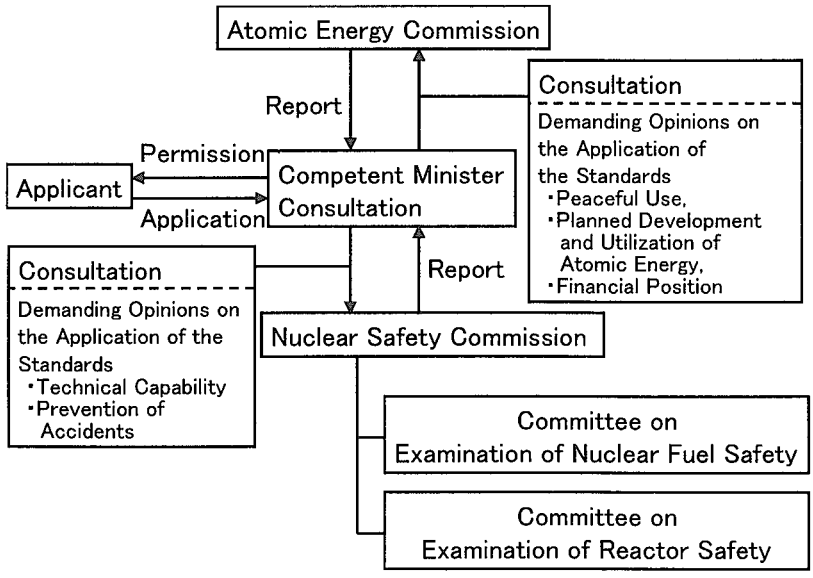

Fig.2 Safety examination organization of nuclear facilities

(5)Calculation of radiation shielding and heat removal of biological shields.

Three regulatory guidelines have been determined for the safety examination of nuclear fuel facilities as follows:

(1) Basic regulatory guideline,

(2) Regulatory guideline for fabrication facilities of nuclear fuel,

(3) Regulatory guideline for reprocessing plant of spent fuel.

In these guidelines, no nuclear data are given explicitly.

3. Some Examples of Recent Nuclear Data Utilization in Safety Examination of Nuclear Facilities

In Table 1, shown are the nuclear data recently used in safety design and safety evaluation of PWRs. It is seen that a few American nuclear data in commercial calculation codes are mainly used except the recommended values of the decay heat by JNDC. Relatively old evaluated nuclear data, ENDF/B IV, is still used for radiation shielding calculation.

As the FP yields, not JNDC data but those by Meek and Rider in 1974 are used for the safety evaluation of a full mixed oxide (MOX) core of advanced boiling water reactors (ABWRs).

In the attachment of the application for the permission of enterprise of the conversion plant in JCO, they adopted the Hansen-Roach 16 group constants in KENO IV for the calculation of subcriticality. Very recently, the staff of JAERI didn't use the FP yields data of JNDC, but those in Chart of Nuclides by Seelmann et al. for the measurement of the FP densities in the precipitation tank at the conversion plant in JCO.

Evaluated nuclear data are similar to commercial goods, and hence they must be utilized by customers. Lack of "business activities" to promote their more uses is strongly pointed out for nuclear safety, although this review is not very thorough but only showing a few examples.

4. Recommendation to Enhance More Utilization of Japanese Evaluated Nuclear Data for Nuclear Safety

In order to enhance more utilization of Japanese evaluated nuclear data for nuclear safety, the following procedures may be recommended:

(1) Careful survey of nuclear data "market" in the fields of nuclear safety, especially for light water reactors and nuclear fuel facilities.

(2) Making efforts for Japanese evaluated nuclear data to be adopted in safety design and safety evaluation of light water reactors and nuclear fuel facilities. More active works, such as execution of these calculations using JENDL by themselves, are required, otherwise no change can be expected.

(3) Making efforts for Japanese evaluated nuclear data to be adopted in safety regulatory guidelines which are used for the safety examination of nuclear facilities, as the case of the decay heat.

(4) Making efforts for Japanese evaluated nuclear data to be adopted in technical standards of Atomic Energy Society of Japan (AESJ) etc. as well as those of ANSI, ASTM and so forth.

Table 1 Nuclear data recently used in safety design and safety evaluation of PWRs

Item	Required Nuclear Data	Analytical Codes ／ Method	Nuclear Data	Necessity of Nuclear Data Improvement	Remarks
Core Design Reactor Establishment Application *1, Att.8 [Core Nuclear Design]	Neutron Cross Sections (σ_{tr}、σ_a、σ_f、σ_s) κ、ν Decay Constant Fission Spectrum Fission Yield Branching Ratio	・PHENIX-P ・ANC	ENDF/B-V	・Present data are sufficient in the practical use for safety design and evaluation. ・In general, improvement of data is preferable.	
Sub-Criticality Calculation for Spent Fuel Pit Reactor Establishment Application *1, Att.8 [Sub-criticality design]	Neutron Cross Sections (σ_{tr}、σ_a、σ_f、σ_s) ν Decay Constant Fission Spectrum	・PHOENIX-P ・HIDRA	ENDF/B-V		
Decay Heat Evaluation for Spent Fuel Pit Reactor Establishment Application *1, Att.8 [SFP Cooling System Design]	Decay Energy Decay Constant Fission Yield Branching Ratio	・AESJ Recommended data (Decay Heat from FP) ・ORIGEN2 (Decay Heat from Actinides)	・JNDC-V2 ・ORIGEN Library	・Ditto ・Use of the same library is preferable in both FP and actinides decay heat evaluations.	The use of AESJ's decay heat data is approved in the NSC's regulatory guide for ECCS evaluation.
Evaluation of Radioactivities in Reactor Coolant Reactor Establishment Application *1, Att.9,10 [Dose Evaluation during Normal Operation] [Dose Evaluation during Accident]	Decay Constant Fission Yield Neutron Absorption Cross Section σ_a (Xe-135)	Equations in the NSC's regulatory guide for dose evaluation during Normal Operation	・Data shown in NSC's Report ・2.65×10^6 barn	・Present data are sufficient in the practical use for safety design and evaluation. ・In general, improvement of data is preferable.	
Safety Analysis (Kinetic Calculation) Reactor Establishment Application *1, Att.10 [Safety Evaluation]	Effective Delayed Neutron Fraction Prompt Neutron Lifetime	Transient Analysis Codes (MARVEL, etc)	Keepin's Data(β) (ENDF/B-V)	・Present data are sufficient in the practical use for safety design and evaluation. ・In general, improvement of data is preferable.	Core average values are calculated by PHENIX-P／ANC using ENDF/B-V and Keepin's data., and used as input for kinetic calculations by transient codes.
Core Decay Heat Evaluation Reactor Establishment Application ＊1, Att.10 [Safety Evaluation]	Decay Energy Decay Constant Fission Yield Branching Ratio	・AESJ Recommended data (Decay Heat from FP) ・ORIGEN2 (Decay Heat from Actinides)	・JNDC-V2 ・ORIGEN Library	・Ditto ・Use of the same library is preferable in both FP and actinides decay heat evaluations.	The use of AESJ's decay heat data is approved in the NSC's regulatory guide for ECCS evaluation.
FP Inventory Calculation Reactor Establishment Application*1, Att.10 [Dose Evaluation During Accidents]	Fission Yield Decay Constant Branching Ratio	・Equation shown in the application Report(simple production-decay balance equation)	・Data shown in NSC's Report ・TABLE OF ISOTOPES, 6th edition	・Present data are sufficient in the practical use for safety design and evaluation. ・In general, improvement of data is preferable.	
Radiation Transportation Calculation Construction Plan Application *2 [Radiation Shield Design]	Neutron Cross Sections (σ_{tr}、σ_a、σ_f) Secondary γ-ray Production Cross Section Neutron Spectrum γ-ray Spectrum	・Point Attenuation Kernel Codes ・Transportation Calculation Codes	ENDF/B-IV		

＊1: Formally called "Application for Permission for Establishment of Nuclear Reactor"
＊2: Formally called "Application for Sanction for Construction Plan"
(NSC: Nuclear Safety Commission、AESJ: Atomic Energy Society of Japan)

(5) Publication of handbooks, tables and charts of Japanese evaluated nuclear data, and their wide distribution by the Internet.
(6) Survey of nuclear data used in essential textbooks on reactor physics, radiation protection and shielding and nuclear safety. If these data seem to be insufficient or imprecise, make contact with the authors or the translators and ask them to revise these data.
(7) Publication of a new textbook on neutron cross sections and evaluated nuclear data for safety design and safety evaluation of nuclear facilities by themselves.

Acknowledgements

The author is very grateful to Mr. N. Nunogane for his survey of recent nuclear data utilization in safety examination of nuclear facilities. He is also thankful to Mr. C. Yanagi and Ms. R. Yamaguchi for their help in the preparation of this manuscript.

Reference

[1] Nuclear Safety Commission: "1991 Annual Report on Nuclear Safety in Japan" (1992).

2.2 Review of Nuclear Data Needs for Fusion Energy Development

E.T. Cheng
TSI Research, Inc.
225 Stevens Avenue
Solana Beach, California U.S.A. 92075
E-mail: etcheng@cts.com

Nuclear data is essential for the development of environmentally attractive fusion power plants. A long-term approach has been taken for the development of fusion nuclear data. Remarkable progress has been made that established an internationally available nuclear data library. Review of nuclear data needs is continuing and deficiencies are identified based on recent trends in fusion energy development. Benchmark testing and experimental verification activities have been continuing to improve the evaluated nuclear data library.

Introduction

A common goal of fusion energy development is to secure an inexhaustible energy source that is economically competitive and environmentally attractive. Low cost electricity generation with fusion can only be achieved by adopting the development path that eventually leads to a smaller fusion core and higher thermal power density. The resulting high neutron wall loading and surface heat flux will require the development of exotic blankets and plasma facing components such as the liquid wall using lithium, lithium-lead, lithium-tin, and flibe.[1-2] Reduction of long-lived radwaste volume is a very important objective of the development of environmentally attractive fusion power plants. Recycle and reuse of fusion reactor materials can be a very attractive strategy that can allow fusion energy to achieve the environmental objective.[3]

Nuclear data, however, is essential for providing the necessary parameters of the anticipated fusion power plants. Tritium breeding, which is necessary in a deuterium-tritium (D-T) fueled fusion plasma, can be predicted only when reliable nuclear data is available. Nuclear heating rate, which includes total thermal power output and localized power density, is essential for the assessment of high power density blankets. Activation of reactor materials is fundamental for the assessment of radioactive safety and long-term waste issues. Both nuclear heating and activation can only be predicted when the available nuclear data is complete and reliable.

Fusion Nuclear Data Development

Nuclear data needed include at least the following for the candidate fusion reactor materials:[4]

Double-differential cross sections,
Gamma production cross sections,
Neutron multiplication reactions namely Li-7(n,n'α), Be(n,2n), and Pb(n,2n), and
Activation cross sections.

The fusion nuclear data base has been evolved by first adopting the large volume of data base already or being developed for the fission reactor technology and then improving it through measurements and evaluations of data at 14 MeV. International interest in fusion energy development has promoted the cooperation in fusion nuclear data development. The measurement of basic nuclear data has been progressed worldwide through the review of nuclear data status and compilation of nuclear data requests lists maintained by the IAEA and

the OECD/NEA. The nuclear data measurement and evaluation activities have also been encouraged by the internationally cooperative interests in nuclear physics, as well as in the development of fusion nuclear technologies for energy applications. These efforts have led to the compilation, under the coordination of the IAEA Nuclear Data Section, a complete set of fusion evaluated nuclear data libraries, FENDL, for fusion power plant development.[5] In addition to the evaluated libraries, FENDL also consists of processed working libraries for neutron transport and activation calculations.

The evaluated libraries include the general-purpose library (FENDL/E), activation library (FENDL/A), dosimetry library (FENDL/DS), decay data library (FENDL/D), and incident charged-particle reaction data library (FENDL/C). The processed working libraries are the continuous energy cross section library for Monte-Carlo transport calculations (FENDL/MC), the multi-group cross section library for discrete-ordinates transport calculations (FENDL/MG), and the uncertainty library (FENDL/U).

The first version of the incident charged-particle reaction data library (FENDL/C-1.0) consists of major fusion reactions from ENDF/B-VI, namely H-2(d,n)He-3, H-2(d,p)H-3, H-3(d,n)He-4, He-3(d,p)He-4, and H-3(t,2n)He-4. A processed working data library, containing Maxwellian-averaged reaction rates, is also available from the Livermore Thermonuclear Data File (TDF). The general-purpose library, FENDL/E-1, consists of neutron and photon interaction cross sections. The neutron interaction cross sections are selected from:

ENDF/B-VI -- H-1, H-3, Li-6, Li-7, Be-9, B-10, B-11, C-12, O-16, F-19, P, S, Cl, K, V-51, Cr-50, Cr-52, Cr-53, Cr-54, Mn-55, Fe-54, Fe-56, Fe-57, Fe-58, Co-59, Ni-58, Ni-60, Ni-61, Ni-62, Ni-64, Cu-63, Cu-65, Ba-134, Ba-135, Ba-136, Ba-137, Ba-138, W-182, W-183, W-184, W-186, Pb-206, Pb-207, and Pb-208;

JENLD-3.1 -- Na-23, Mg, Al-27, Ca, Ti, Mn-55, Mo, Ta-181, and Bi-209;

BROND-2) -- H-2, N-14, N-15, Si, Zr-90, Zr-91, Zr-92, Zr-94, Zr-96, Nb-93, and Sn.

The photon interaction cross sections are from:

ENDF/B-VI -- H, Li, Be, B, C, N, O, F, Na, Mg, Al, Si, P, S, Cl, K, Ca, Ti, V, Cr, Mn, Fe, Co, Ni, Cu, Zr, Nb, Mo, Sn, Ba, Ta, W, Pb, and Bi.

Several new or improved evaluations have been proposed for the updated version, FENDL/E-2.0. The criteria established for the selection of these evaluations are that the candidate evaluations have to include the following information:

Gamma ray production cross section,

Neutron and charged-particle emission data in File 6 format,

File 1 descriptive information,

Recoil distributions in File 6 format for major structural materials, and

Energy balance must be better than 2% for all energies.

The selected FENDL/E-2.0 evaluations that meet the above criteria include:[5]

ENDF/B-VI -- Si-28, Si-29, and Si-30;

JENDL-FF -- Be-9, C-12, N-14, O-16, V-51, Zr, Nb-93, Mo, and W;

BROND-2 -- H-2 and Sn; and

EFF-3 -- Al-27 and Fe-56.

The decay data library, FENDL/D-1.0, consists of approximately 2900 nuclides, which are extracted from ENDF/B-VI and ENSDF, and contains the basic information needed for activation analysis, namely isotope, half-life, decay mode, daughter nuclide and branching ratio, and decay gamma intensity and energy spectrum. The activation data library, FENDL/A-2.0, is a version evolved from merging important reactions and the basic library recommended by an IAEA/NDS expert panel. The important reactions include 404 reactions selected from JENDL-3.2/A, EAF-4.1, ADL-3, IAEA/CRP for long-lived activation cross sections [6], and the first version FENDL/A-1.0. It is noted that the IAEA/CRP activity (1988-96) has measured and evaluated a number of important reactions leading to the

generation of long-lived radionuclides. These include Al-27(n,2n)Al-26, Ni-62(n,γ)Ni-63, Cu-63(n,p)Ni-63, Mo-94(n,p)Nb-94, Mo-98(n,γ)Mo-99(Tc-99), Ag-109(n,2n)Ag108m, Eu-151(n,2n)Eu-150, Eu-153(n,2n)Eu152, Dy-158(n,p)Tb-158, Tb-159(n,2n)Tb-158, Ho-165(n,γ)Ho-166m, Hf-179(n,2n)Hf-178n, W-182(n,n'α)Hf-178n, Re-187(n,2n)Re-186m, Ir-191(n,γ)Ir-192n, and Ir-193(n,2n)Ir-192n. The basic library includes 12,972 reactions mainly from EAF-4.1. Due to the concern for consistent identification of daughter nuclides, the EAF-4.1 decay data library is also used as FENDL/D-2.0.

Status of Fusion Nuclear Data

Due to the recent emphasis of fusion science research, especially in the U.S., the urgency of nuclear data needs for power reactor development is also subjected to adjustment. Accordingly, the priority in the nuclear data requests list submitted to the OECD/NEANSC has been degraded from the high priority to a lower second or third priority. However, new requests have been added. These are primarily for the differential data and activation reaction data for Sn isotopes. Review and evaluation of nuclear data for Sn isotopes for neutron transport and activation calculations are needed for the assessment of using Sn-Li bimetallic material in the fusion power plants. Table 1 lists these recent requests.

Assessment of low activation materials can be reliable only when the nuclear data library used in the calculation is complete and accurate. One of the important issues of using SiC-SiC composites as low activation structural material in a fusion blanket is the production of long-lived radionuclide, Al-26 (half-life 740,000 y), from Si via the two step reactions: Si-28(n,n'p)Al-27 and Al-27(n,2n)Al-26. Using the recently updated evaluations for Si-28(n,n'p)Al-27 cross section, it shows a significantly low production rate of Al-27. Experimental verification of the evaluated reaction cross section is still needed.

Recycle and/or reuse of fusion reactor materials is a very unique strategy to reduce the long-term radioactive waste to be generated in the future D-T fueled fusion power plants. The concentration (and thus the activity) of long-lived radionuclides after many cycles of reusing the reactor materials depends not only the production cross sections, but also the removal cross sections. There is a need to review the removal cross sections for the important fusion specific long-lived radionuclides such as Nb-94, Tc-99, Ag-108m, Al-26, and so on.

Benchmark data testing and experimental data verification are essential for the validation of the evaluated nuclear data. They are required to assess the quality of the evaluated nuclear data library, a necessary procedure to maintain the high quality of the FENDL and other libraries for fusion applications. Under the coordination of the IAEA/NDS, benchmark experiments, which include integral neutronics and activation experiments, have been compiled and used for data validation purposes.[6-8] Table 2 shows the list of these benchmark experiments. Data testing using these benchmark experiments has been applied for the selection of the FENDL/E-2.0 and FENDL/A-2.0 libraries. A new initiative to establish benchmark problems for Sn, however, appears to be needed since no such experiment exists, as shown in Table 2.

Conclusions

Nuclear data is essential for the development of environmentally attractive fusion power plants. A long-term approach has been taken for the development of fusion nuclear data and has achieved significant progress. An international nuclear data library, FENDL, has been established and used in various national and international fusion research projects. Review of nuclear data needs is constantly performed based on the current trends in fusion energy development and deficiencies are identified accordingly. Benchmark data testing and data verification experiments have been important processes to improve the completeness and to control the quality of available nuclear data for fusion energy development.

Table 1. Nuclear Data Requests for Fusion Submitted to OECD/NEANSC

Type of Reactions/Nuclides/Comments
I. Double-differential cross sections at energies - 6, 8, 10, 12, and 14 MeV; accuracy - 10%. O, Si, V, Fe, W, Pb, Li-6, Li-7, Be, B-10, B-11, C, Cr, Mn, Ni, Sn
II. Neutron multiplication reactions: 3% from threshold to 15 MeV. Li-7(n,n'p), Pb(n,2n), Be(n,2n)
III. Activation cross sections: 20% accuracy unless otherwise specified; threshold reaction - threshold to 15 MeV; n,γ reactions: - thermal to 1 MeV; dosimetry cross section – 5 to 15 MeV (5%). Waste disposal concern: N-14(n,p)C-14; Ti-48(n,α)Ca-45(n,α)Ar-42; Fe-58(n,γ)Fe-59; Ni-63(n,α)Fe-60; Ni-64(n,2n)Ni-63; Cu-65(n,t)Ni-63; Mo-94(n,p)Nb-94; W-182(n,n'α)Hf178m2; W-186(n,n'α)Hf-182; Ca-45(n,α)Ar-42; Sn-120(n,γ)Sn-121m; Sn-125(n,γ)Sn-126; Sn122(n,2n)Sn121m; Sn112(n,n'α)Cd108 Materials recycling concern: V-50(n,2n)V-49 Dosimetry cross section: Zn-64(n,p)Cu-64 Decay heat and radiological hazard concerns: Pb-204(n,p)Tl-204; Pb-204(n,t)Tl-202; Sn122(n,γ)Sn123; Sb121(n,γ)Sb122; Sn120(n,p)In120m; Sn119(n,p)In119; Sn118(n,p)In118m; Sn117(n,p)In117m; Sn116(n,p)In116m; Sn115(n,p)In115m; Sn114(n,2n)Sn113; Sn112(n,2n)Sn111; Sn112(n,γ)Sn113, Al-27(n,n'α)Na-23; Si-29(n,t)Al-27 Inconsistency in experiment and evaluation: V-51(n,n'α)Sc-47 Neutron absorption in Sn: Sn(n,γ) from thermal to 15 MeV; Natural element and isotopic n,γ cross sections.
IV. Near-term (e.g., ITER) and very low activation power reactors Nuclear heating in the super-conducting TF magnet 1. Cu(n,xn): Double-differtial cross sections at 6, 8, 10, 10, 12, and 14 MeV; 10% accuracy. 2. Cu-63(n,γ)and Cu-65(n,γ): 10% accuracy at energies from thermal - 1 MeV. 3. Ta-181(n,γ)Ta-182: 10% accuracy from thermal - 1 keV; resonance region is important to determine the self-shielding effect. Decay heat in 316SS and Inconel alloy 4. Mn-55(n,γ)Mn-56: 10% accuracy at energies from thermal - 1 MeV. 5. Ta-181(n,γ)Ta-182: 10% accuracy at energies from thermal to 1 keV. See IV-3. Waste management for reactor components (316SS and Inconel structures) 6. Ni(n,x)Co-60: Threshold - 15 MeV; 20% accuracy; principal reactions needed: Ni-60(n,p) and Ni-61(n,n'p). Waste disposal issue for SiC 7. Si(n,x)Al-27: Threshold - 15 MeV; 20% accuracy; primarily Si-28(n,n'p); recommended measurements: Si-28(n,xp) at 14 MeV.
V. Alpha slowing-down dosimetry reactions (20% accuracy) 1. O16(n,2n)O15: from threshold to 20 MeV. 2. O16(γ,n)O15: from 17 MeV to 20 MeV. 3. Be9(n,d)Li8: from threshold to 20 MeV. 4. Be9(n,p)Li9: from threshold to 16 MeV. 5. Ne20(n,2n)Ne19: from threshold to 20 MeV. 6. Ne20(γ,n)Ne19: above 17 MeV. 7. Ne22(n,α)O19: from threshold to 16 MeV. 8. Ne20(n,t)F18: from threshold to 20 MeV. 9. Mg24(n,t)Na22: from threshold to 20 MeV. 10. Si30(n,He-3)Mg28: from threshold to 20 MeV. 11. Si28(n,t)Al26: from threshold to 20 MeV. 12. T-He4 scattering cross sections: He-4 energy is from 1 to 3.5 MeV; high priority is given at 3.5 MeV; more precise energy transfer data is needed.

References used for Table 1:
1. The most recent U.S. data requests list compiled by ORNL.
2. ECN report, EAF-Doc-004, March 1994
3. Personal communication with R. Fisher, General Atomics, regarding nuclear data needs for Tokamak diagnostics, June 1994.
4. Personal communication with Don Smith, ANL, and Yujiro Ikeda, JAERI, March 1996.

Table 2. Experimental Benchmarks for FENDL Data Testing

Material	Geometry	Measured Quantity	Facility
◦ Integral Neutronics Experiments			
Li2O, Be, C, Liquid O, Liquid N, Fe, Pb	Cylinder Slab	Angular neutron spectra, 30 keV - 15 MeV	JAERI (FNS)
Li2O, Be, C, Fe, Cu, W, V	Cylinder Slab	Neutron and gamma spectra, reaction rate, heating rate	JAERI (FNS)
SS316L	Slab	Neutron spectra, Reaction Rates, gamma heating	JAERI, ENEA, CEA
Be, Be-Li, Fe, Ni	Sphere	Neutron leakage spectra	Osaka U. (OKTAVIAN)
Li, Pb-Li, Pb-Li-C, Be-Li, Be-Li-C	Sphere	Tritium production rate	Osaka U. (OKTAVIAN)
Be, Al, Fe, Ni, Pb, V	Sphere	Neutron leakage spectra	IPPE
Be (Sphere), Fe	Slab	Reaction rates	KIAE
Be	Sphere	Neutron Reaction Rates	INEL
Fe (Slab), Pb, V	Sphere	Neutron and gamma spectra	TUD
Be, Fe, Pb, V	Sphere	Neutron Reaction Rates	SWINPC
Be	Sphere	Total neutron leakage	FZK
◦ Induced Radioactivity Measurements			
Al, Co, Cr, Cu, Fe, Mo, Mn, Nb, Ni, Si, Ta, Ti, V, W, Zr	Small Samples	Induced radioactivity and Heating Rates	JAERI, ENEA, FZK, TUD, KIAE

Acknowledgments

This work was supported by the USDOE, Office of Fusion Energy Science, under Research Grant No.: DE-FG03-92ER54137. Invitation from the program committee of this Symposium is appreciated very much.

References

[1] Moir, R.W.: "Liquid First Wall for Magnetic Fusion Energy Configurations," Nuclear Fusion, Vol. 37, 557 (1997).
[2] Abdou, M.A., The APEX Team: "Exploring Novel High Power Density Concepts for Attractive Fusion Systems," Fusion Engineering and Design, Vol. 45, 145 (1999).
[3] Cheng, E.T., et al.: "Waste Management Aspects of Low Activation Materials," Fusion Technology, Vol. 34, 721 (1998).
[4] Cheng, E.T., et al., "Overview of Recent Nuclear Data Development for Fusion Reactor Technology," Fusion Technology, Vol. 30, 1183 (1996).
[5] Pashchenko, et al.: "FENDL-2: An Improved Nuclear Data Library for Fusion Applications," Proceedings of International Conference on Nuclear Data for Science and Technology, May 19-24, Trieste, Italy, p. 1150 (1997 Italian Society of Physic, Vol. 59).
[6] Ikeda, Y., et al.: "Experiments on Induced Radioactivity Characteristics of Vanadium Alloy," Fusion Technology, Vol. 30, 715 (1998).
[7] Maekawa, F., et al.: "Benchmark Experiment on Vanadium-Alloy Assembly with D-T Neutrons, In-situ Measurement," ibid, 1019.
[8] Fischer, U., et al.: "Neutronics and Nuclear Data: Achievements in Computational Simulations and Experiments in Support of Fusion Reactor Design," Proc. International Symposium on Fusion Technology, September 1999, Rome, Italy (to be published).

2.3 Precise Measurements of Neutron Capture Cross Sections for FP

Shoji NAKAMURA[1], Hideo HARADA[1], Toshio KATOH[1,2]

1 Japan Nuclear Cycle Development Institute, Tokai Works, Tokai-mura, Naka-gun, 319-1194
2 Visiting staff at Gifu College of Medical Technology, Ichihiraga, Seki, 501-3892
E-mail : rgm@tokai.jnc.go.jp

The thermal neutron capture cross sections (σ_0) and the resonance integrals (I_0) of some fission products (FP), such as ^{137}Cs, ^{90}Sr, ^{99}Tc, ^{129}I and ^{135}Cs, were measured by the activation and γ-ray spectroscopic methods. Moreover, the cross section measurements were done for other FP elements, such as ^{127}I, ^{133}Cs and ^{134}Cs. This paper provides the summary of the FP cross section measurements, which have been performed by authors.

1. Introduction

In nuclear waste management, the major 29 fission product (FP) nuclides shown in **Table 1** are important nuclides as the objective nuclides for transmutation. For the study of transmutation by using reactor neutrons, the accurate data are needed on the neutron capture cross sections (σ_0) and the resonance integrals (I_0) in order to estimate the accurate reaction rates of those FP nuclides. However, there are few cross section data on those FP nuclides. If any, most of the data have large errors. By using the recently developed measuring equipments and the accurate γ-ray emission probability (I_γ) data, one could obtain more accurate cross section data than that measured previously. Accordingly, we had started to measure the cross sections of FP nuclides to obtain the accurate ones. In the beginning five nuclides, ^{137}Cs[1], ^{90}Sr[2], ^{99}Tc[3], ^{129}I[4] and ^{135}Cs[5], were chosen from the nuclides listed in Table 1 because of their large fission yields and long half-lives, and then the cross sections of these nuclides were measured by the activation and γ-ray spectroscopic methods.

The nuclear waste sometimes contains a large amount of stable nuclei having the same atomic number as that of long-lived FP. These stable nuclei absorb thermal neutrons during the neutron irradiation of the nuclear waste and affect the neutron economics; the reaction rate of the target nuclei is reduced. Moreover, some of these stable nuclei breed more radioactive nuclei by the neutron capture process.. It is also necessary for the transmutation study to accurately estimate these influences caused by stable nuclei involved in the FP targets. Consequently, the cross sections of the stable nuclei, such as ^{127}I[6], ^{133}Cs[7], were measured.

2. Brief Outline of Analysis

Since the details of Westcott's convention[8] that we used to determine the cross sections and neutron fluxes were described elsewhere[1], here we present only a brief outline of the analysis. Equations based on Westcott's convention can be rewritten by using simplified flux notation[1] as follows:

$$R/\sigma_0 = \phi_1 + \phi_2 s_0 , \qquad (1)$$

for irradiation without a Cd shield capsule,

$$R'/\sigma_0 = \phi_1' + \phi_2' s_0 , \quad (2)$$

for irradiation with a Cd shield capsule. Here, the R (or R') is the reaction rate and σ_0 the thermal neutron (2,200m/s neutron) capture cross section; ϕ_1 and ϕ_1' are neutron flux components in the thermal energy region, and ϕ_2 and ϕ_2' are those in the epithermal energy region. The s_0 is the parameter defined by

$$s_0 = \frac{2}{\sqrt{\pi}} \frac{I_0'}{\sigma_0}, \quad (3)$$

where I_0' is the reduced resonance integral, i.e. the resonance integral after subtracting the $1/\upsilon$ components. The resonance integral I_0 is calculated as follows:

$$I_0 = I_0' + 0.45\sigma_0 , \quad (4)$$

where $0.45\sigma_0$ is the $1/\upsilon$ contribution given by assuming the Cd cut-off energy to be 0.5eV.

Eqs.(1) and (2) give the relation,

$$s_0 = -\frac{\phi_1 - \phi_1'(R/R')}{\phi_2 - \phi_2'(R/R')} , \quad (5)$$

so that the value of s_0 is obtained from R/R' value of each irradiated target. The σ_0 is derived by substituting the s_0 into Eq.(1), and then the values of I_0' and I_0 are calculated from Eqs.(3) and (4).

3. Experiment

The cross section measurements were performed by the activation and γ-ray spectroscopic methods. The information of each experiment is summarized in **Table 2**.

The wires of 0.112wt% Au/Al alloy (0.510mm in diameter) and 0.46wt% Co/Al alloy (0.381mm in diameter) were used as activation detectors to monitor the neutron flux (two foil method[9]) at the irradiation position. The method of measuring the neutron flux was the same as that for the cross section measurements. Using the well-known data of both the cross sections σ_0 and the parameter s_0 for cobalt and gold, the values of the flux terms, i.e. $\phi_{1,2}$ and $\phi'_{1,2}$, were determined by solving the simultaneous equations for cobalt and gold from Eqs. (1) and (2) in **Sec.2**. For example, **Table 3** summarizes the experimental results of the neutron fluxes in the case of Rikkyo Reactor together with the R and R' values of the flux monitors.

The yields of γ-rays emitted from the irradiated targets were measured by a high purity Ge detector with a 90% relative efficiency to a 7.6cm×7.6cmϕ(NaI) detector and an energy resolution of 2.1keV FWHM at 1.33MeV of ^{60}Co. The details of the data taking system were described elsewhere[4]. An example of the gamma-ray spectrum is shown in **Figure 1**. As can be seen in Figure 1, the two γ-rays originated from ^{100}Tc, 540 and 591keV γ-rays, were clearly measured. The cross sections of ^{99}Tc were deduced from the measured γ-ray intensities according to the Westcott's convention.

4. Results and Discussion

The results of the cross sections obtained in this work are summarized in **Tables 4**[10-18] together with the previously reported data. The brief discussion for each target is made as follows:

Cesium-137 Our result of σ_0 was about twice larger than the previous one[10] and the I_0 was obtained for the first time.

Strontium-90 Our result of σ_0 was in agreement with the value obtained by McVey et al. [11], but not agreement with the value by Zeisel [12]. The I_0 of ^{90}Sr was also measured in this work. However, the upper limit value of the I_0 ($I_0 \leqq 0.16$ b) was obtained. That remains to be re-measured in the future.

Technetium-99 The cross section σ_0 was almost equal to the previous data, but the resonance integral was about twice of that by Lucas et al.[13]. The possible reasons were that Lucas et al. used the huge amount of target, therefore the self-shielding effect influenced their results.

Iodine-129 Our data of σ_0 was 12% larger than the previously reported one[14]. This discrepancy was probably caused by the lack of the contribution of the isomeric state ^{130m}I because the existence of the isomeric state was not known.

Cesium-135 The value of σ_0 obtained in this experiment was almost the same as that reported by Baerg et al.[15]. On the other hand, the value of I_0 was about 2/3 of that by Berg et al. They used only one kind of flux monitor, i.e. Co/Al alloy wire, therefore they did not take the contribution of the epithermal component into consideration sufficiently.

Iodine-127 and Cesium-133 There are some discrepancies between our results and reported data[16,17]. There may be still some problems in cross section data of not only FP nuclides but also stable FP elements. It seems that the cross sections of other stable nuclides have to be re-measured.

5. Conclusions

The thermal neutron capture cross sections and the resonance integrals of some FP nuclides were measured by the activation and γ-ray spectroscopic methods.

Some future plans, which aim for the more precise measurements of the cross sections, are shown below:

(1) the measurement of the isomer production ratio of ^{138m}Cs to ^{138g}Cs in the ^{137}Cs(n, γ) ^{138}Cs reaction;
(2) the measurement of the emission probability (I_γ) of γ-ray from ^{100}Tc by β-γ coincidence technique [19];
(3) the measurement of the resonance integral of the ^{90}Sr(n,γ)^{91}Sr reaction;
(4) the measurements of the cross sections for long-lived FPs, such as ^{79}Se(6.5×10^5 y), ^{126}Sn($\sim1\times10^5$ y), ^{107}Pd(6.5×10^6 y), ^{93}Zr(1.53×10^6 y), ^{166m}Ho(1200 y).

The plans of (1),(2) and (3) are now in progress at the Research Reactor Institute, Kyoto University under join-research.

Acknowledgments

The authors wish to acknowledge their indebtedness to the crew of both the Rikkyo Research Reactor and JRR-3, 4 reactor at JAERI for their cooperation.

This work was supported by JNC and Inter-University Program for the Joint Use of Rikkyo University Reactor, and by the Grant-in-Aid for Scientific Research of the Ministry of Education, Science and Culture.

References

[1] Sekine, T. et al.: J. Nucl. Sci. Technol., **Vol.30**, No.11, 1099 (1993).
[2] Harada, H. et al.: J. Nucl. Sci. Technol., **Vol. 31**, No.3, 173 (1994).
[3] Harada, H. et al.: J. Nucl. Sci. Technol., **Vol.32**, No.5, 395 (1995).
[4] Nakamura, S. et al.: J. Nucl. Sci. Technol., **Vol.33**, No.4, 283 (1996).
[5] T. Katoh et al.: J. Nucl. Sci. Technol., **Vol.34**, No.5, 431 (1997).
[6] Katoh, T. et al.: J. Nucl. Sci. Technol., **Vol.36**, No.3, 223 (1999).
[7] Nakamura, S. et al.: J. Nucl. Sci. Technol., **Vol.36**, No.10 (1999).
[8] Beckurts, K.H. and Wirtz, K.: "*Neutron Physics*", Springer-Verlang, New York, (1964).
[9] Westcott, C.H. et al.: "*Proc. 2nd Int. Conf. Peaceful Uses of Atomic Energy, Geneva*", United Nations, New York, **Vol.16**, 70(1958).
[10] Stupegia, D.C.: J. Nucl. Energy, **A12**, 16 (1960).
[11] McVey, L.A. et al.: J. Radio. Chem., **76**, 131 (1983).
[12] Zeisel, G.: Acta. Phys. Austr., **23**, 5223 (1966).
[13] Lucas, M. et al.: *IAEA-TC-119/14*, 407 (1977).
[14] Eastwood, T.A. et al.: "*Proc. 2nd Int. Conf. Peaceful Uses of Atomic Energy, Geneva*", United Nations, New York, **Vol.16**, 54 (1958).
[15] Baerg, A.P. et al.: Can. J. Phys., **36**, 863 (1958).
[16] Friedmann, L. et al.: Radiochemica Acta, **33**, 182 (1983).
[17] Baerg, A.P. et al.: Can. J. Phys., **38**, 2528 (1960).
[18] Bayly, J.G. et al.: Inorg. Nucl. Chem., **5**, 259 (1958).
[19] Furutaka, K. et al.: Proc. of 1999Symposium on Nucl. Data, JAERI Tokai, Nov.18-19,1999.

Table 1 Major 29 fission product nuclides for the nuclear waste management

Nuclide	Half-Life (year)	Nuclide	Half-Life (year)	Nuclide	Half-Life (year)
^{129}I	1.57×10^{7}	^{108m}Ag	418	^{155}Eu	4.7611
^{107}Pd	6.5×10^{6}	^{151}Sm	90	^{102}Rh	2.9
^{135}Cs	2.3×10^{6}	^{121m}Sn	55	^{125}Sb	2.7582
^{93}Zr	1.53×10^{6}	^{137}Cs	30.07	^{147}Pm	2.6234
^{99}Tc	2.1×10^{5}	^{90}Sr	28.78	^{134}Cs	2.062
^{126}Sn	1×10^{5}	^{113m}Cd	14.1	^{171}Tm	1.92
^{79}Se	6.5×10^{4}	^{152}Eu	13.542	^{109}Cd	1.270
^{94}Nb	2.03×10^{4}	^{93m}Nb	16.13	^{106}Ru	1.007
^{166m}Ho	1200	^{85}Kr	10.756	(^{14}C	5730)
^{158}Tb	180	^{154}Eu	8.593		
		^{146}Pm	5.53		

Table 2 Target preparation and neutron irradiation for each experiment

Nuclide	Irradiation	Method to determine the number of target nuclei	Target amount
^{137}Cs	JRR-4 at JAERI (4×10^{13}n/cm^{2}s)	Comparison of γ-ray intensities of the target (^{137}Cs) and the product nuclei (^{138}Cs) (an isotope ratio method; **IRM**)	CsCl containing about 0.4MBq of ^{137}Cs
^{90}Sr	JRR-4 at JAERI (4×10^{13}n/cm^{2}s)	Same method as ^{137}Cs by using ^{85}Sr as a tracer of strontium. (**IRM**)	$SrCl_2$ containing about 2MBq of ^{90}Sr
^{99}Tc 370kBq	Rikkyo Reactor (5×10^{11}n/cm^{2}s)	Liquid scintillation counting of β-rays (an efficiency tracing method; **ETM**)	The standardized solution containing about of ^{99}Tc
^{129}I	Rikkyo Reactor (5×10^{11}n/cm^{2}s)	Liquid scintillation counting of β-rays (**ETM** + coin.-anticoin. Counting)	About 60ml solution containing about 2600Bq of ^{129}I for the irradiation within a Cd capsule, about 260Bq of ^{129}I for the irradiation without it.
^{135}Cs ^{135}Cs	JRR-3 at JAERI (1×10^{14}n/cm^{2}s)	Mass analysis with a quadrupole mass spectrometer and IRM (**IRM** + mass analysis)	About 0.37MBq of ^{137}Cs which contains
^{133}Cs	Rikkyo Reactor (5×10^{11}n/cm^{2}s)	weight measurement	About 12mg of the high purity(99.99%) ^{nat}CsCl
^{127}I	Rikkyo Reactor (5×10^{11}n/cm^{2}s)	The amount of ^{127}I in the KI target was used as the reference to determine the amount of ^{127}I in the ^{127}I-^{129}I target	^{127}I as a contamination contained in the ^{129}I solution

Table 3 Results of the neutron flux measurements in RSR of Rikkyo Reactor

Irradiation Type	Irradiation period	Reaction rates of the flux monitors ^{60}Co	^{198}Au (10^{-11}/s)	ϕ_1 or ϕ_1' (10^{11} n/cm^{2}sec)	ϕ_2 or ϕ_2'
bare	10min	1.76 ±0.04	7.31±0.15	4.42 ±0.09	0.173±0.004
with Cd	25min	0.155±0.003	3.20±0.06	0.099±0.004	0.183±0.004
Cadmium ratio		11.3 ±0.3	2.28±0.07		

Table 4. Summary of thermal neutron capture cross sections (σ_0) and resonance integrals (I_0) of important fission product nuclides for transmutation studies

Nuclide	Half-Life	Previous Data (Author and reported year)	Data of JNC
^{137}Cs	30 years	σ_{eff}=0.11±0.03 b (Stupegia '60[10])	σ_0= 0.25±0.02 b I_0= 0.36±0.07 b ('93)
^{90}Sr	29 years	σ_0=0.0140±0.0024 b (McVey '83[11]) σ_{eff}=0.8±0.5 b (Zeisel '66[12])	σ_0= 15.3$\pm^{1.3}_{4.2}$ mb $I_0 \leqq$0.16 b ('94)
^{99}Tc	2.1×10^5 years	σ_0= 20±2 b I_0'= 186±16 b (Lucas '77[13])	σ_0= 22.9±1.3 b I_0= 398±38 b ('95)
^{129}I	1.6×10^7 years	σ_0= 27±2 b I_0= 36±4 b (Eastwood '58[14])	σ_0= 30.3±1.2 b I_0= 33.8±1.4 b ('96)
^{127}I	(stable)	σ_0= 4.7±0.2 b I_0= 109±5 b (Friedmann '83[16])	σ_0= 6.40±0.29 b I_0= 162±8 b ('99)
^{135}Cs	3×10^6 years	σ_0= 8.7±0.5 b I_0= 61.7±2.3 b (Baerg '58[15])	σ_0= 8.3±0.3 b I_0= 38.1±2.6 b ('97)
^{134}Cs	2 years	σ_{eff}=134±12 b (Bayly '58[18])	σ_{eff}=141±9 b ('99)
^{133}Cs	(stable)	σ_0= 30.4±0.8 b I_0= 461±25 b (Baerg '60[17])	σ_0= 29.0±1.0 b I_0= 298±16 b ('99)

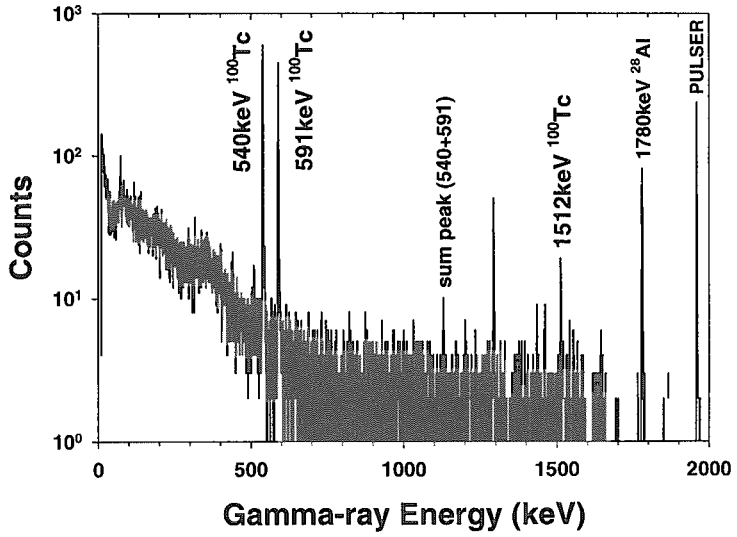

Figure 1 Gamma-ray spectrum of an irradiated ^{99}Tc sample target

2.4 MA Nuclear Data Measurement with Lead Slowing-down Spectrometers

Katsuhei Kobayashi
Research Reactor Institute, Kyoto University
Kumatori-cho, Sennan-gun, Osaka 590-0494
e-mail: koba@rri.kyoto-u.ac.jp

This paper reviews the minor actinide (MA) nuclear data measured with lead slowing-down spectrometers. The Kyoto University Lead Slowing-down Spectrometer (KULS) at the Research Reactor Institute, Kyoto University has been applied to the measurements of (1) the fission cross sections of Np-237, Am-241, Am-242m and Am-243 in the energy range from 0.1 eV to 10 keV and (2) the capture cross section of Np-237 at energies between 0.01 eV and 1 keV. The results are compared with the existing experimental and the evaluated nuclear data (ENDF/B-VI, JENDL-3.2 and JEF-2.2).

The recent MA nuclear data, which were measured with the Rensselaer Intense Neutron Spectrometer (RINS) at the Resselaer Polytechnic Institute and the spectrometer at the Kurchatov Institute, are also introduced.

1. Introduction

Neptunium (Np), americium (Am) and curium (Cm) are burdensome minor actinides (MA), which are abundantly produced in power reactors[1,2]. The nuclear data are of great importance for the design of reactors with MOX or Pu fuels and the system design of spent fuel reprocessing. From a standpoint of the disposal of radioactive waste, the fission/capture cross sections are of interest for their transmutation.

Up to now, numerous cross section measurements for MA nuclides have been made[3]. However, there still exist discrepancies among the measured and the evaluated data, such as ENDF/B-VI[4], JENDL-3.2[5] and JEF-2.2[6]. The difficulties to measure the fission/capture cross sections for the MA isotopes have been caused by strong alpha-particle activities or pile up pulses, or due to their short half-lives. Another problem for the cross section measurement is often due to lack of pure isotope samples. In addtion, some of the cross sections are lower than about 1 b in the low/resonance energy region.

A lead slowing-down spectrometer is a powerful tool and is often used for this kinds of fission/capture cross section measurements because of about 10^4 incerase in neutron flux comparing to the conventional time-of-flight (TOF) experiment at a 5 m flight path[7], although the energy resolution of the spectrometer is about 30 to 40 % full width at half maximum (FWHM).

In this report, first a survey of lead slowing-down spectrometers, Kyoto University Lead slowing-down Spectrometer (KULS)[8], Rensselaer Intense Neutron Spectrometer (RINS)[7] and a spectrometer at the Kurchatov Institute[9], is provided. Then the MA nuclear data measured with these spectrometers are presented.

2. Lead Slowing-down Spectrometers

2.1. Kyoto University Lead Slowing-down Spectrometer

The Kyoto University Lead slowing-down Spectrometer (KULS) has been installed in coupling to the 46 MeV linac at KURRI[8]. The KULS is composed of 1600 lead blocks (each size : 10 x 10 x 20 cm^3, purity : 99.9 %) and the blocks are piled up to make a cube of 1.5 x 1.5 x 1.5 m^3 (about 40 tons in weight) without any structural materials. At the center of the KULS, an air-cooled photoneutron target of Ta is set to generate pulsed fast neutrons.

The slowing-down constant K in the relation of $E=K/t^2$ was experimentally determined to be 190 ± 2 for the Bi hole in the KULS[8] using the measured relation between the neutron slowing-down time t in μs and the average neutron energy E in keV[8]. The energy resolution was also deduced to be about 40 %(FWHM) at energies between a few electron-volts and about 500 eV and was worse than that below a few electron-volts and above about 500 eV[8]. The characteristics of the KULS were also verified by Monte Carlo calculations[8].

2.2. Rensselaer Intense Neutron Spectrometer

The Rensselaer Intense Neutron Spectrometer (RINS) is coupled to the 100 MeV electron linac at the Rensselaer Polytechnic Institute (RPI) Gaerttner Laboratory[7]. The RINS is a cube, 1.8 m on edge and is stacked containing 75 tons of 99.99 % purity lead. The photoneutron target is constructed of tantalum plates and cooled by recirculated helium.

The neutron behavior in the RINS between the average neutron energy E in keV and the slowing-down time t in μs is represented by the expression; $E=K/(t+t_o)^2$, where $t_o=\sim0.3\,\mu$s and $K=165\pm3$ for the RINS. The energy resolution of the RINS was ~35 % (FWHM) from 1 eV to 1 keV[7].

2.3. Spectrometer at Kurchatov Institute

The lead slowing-down spectrometer is driven by the high current electron linac "Fakel" at Kurchatov Institute[9,10]. The size of the spectrometer is 1.6 x 1.8 m^2 and 1.6 m depth and is built with many pieces of lead blocks (20x10x5 cm^3 ; 99.99%). The total weight of the spectrometer is 50 tons. The neutron target is assembled of the tungsten (W) disks of 40 mm in diameter and 40 mm in thickness and is cooled by air.

The relation between the slowing-down time t in μs and the neutron energy E in keV was derived as $E=K/(t+t_o)^2$, where K=181.5 and t_o=0.9 were experimentally determined. The energy resolution was equal to be 30 %[9,10].

3. Measured Results and Discussion

3.1 Measurements with the KULS

^{237}Np(n,f) cross section[11]

The first measurement using the KULS was the ^{237}Np(n,f) cross section from ~1 eV to ~5 keV[11], as seen in Fig. 1. The data by Plattard et al. and in ENDF/B-VI and JENDL-3.1 are lower by a factor of three[11]. Just after Yamanaka et al. published the result[11], Carlson et al. measured the cross section by the neutron TOF method[12] and reported that their data were in good agreement with the data by Yamanaka et al. These new

measurements were taken into account in the evaluation of JENDL-3.2. The data measured by Hoffman et al. are in general agreement with those by Yamanaka et al. in the relevant energy region[11].

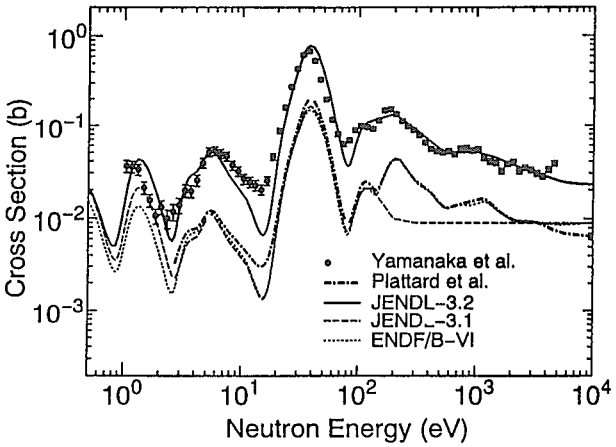

Fig. 1 Fission cross section of Np-237.

^{241}Am(n,f), ^{242m}Am(n,f) and ^{243}Am(n,f) cross sections[13,14,15]

The fission cross section of Am-241 measured by Dabbs et al. are in good agreement with those by Yamamoto et al[13]. Some of the experimental data are in disagreement, and some other data are close to the Yamamoto's. As shown in Fig. 2, good agreement can be seen in general shape and absolute values between the data by Yamamoto et al. and the evaluated data in ENDF/B-VI and JENDL-3.2, which are energy broadened with the resolution function of the KULS. The JENDL-3.2 data between 22 and 140 eV are underestimated by 1.2 to 2.3 times, while the ENDF/B-VI data are in good agreement with the measurement.

The evaluated data in ENDF/B-VI and JENDL-3.2 for the ^{242m}Am(n,f) reaction seem to be a little higher below about 0.3 eV and lower in the range from 0.6 to 3 eV than the measurement by Kai et al.[14], as displayed in Fig. 3. Above 3 eV, the JENDL-3.2 data are close to the measurement in general, while the ENDF/B-VI data are obviously high.

The ^{243}Am(n,f) cross sections measured by Wisshak et al. and Knitter et al. show good agreement with those by Kobayashi et al.[15], while the result by Seeger is considerably higher above hundreds of electron-volts. Kobayashi et al. measured the fission cross section for the first time in the lower/resonance energy region. Figure 4 shows that the ENDF/B-VI data are in general agreement except for the region above 300 eV and lower at energies between 15 and 60 eV. The JENDL-3.2 data seem to be lower than the Kobayashi's in general above 100 eV.

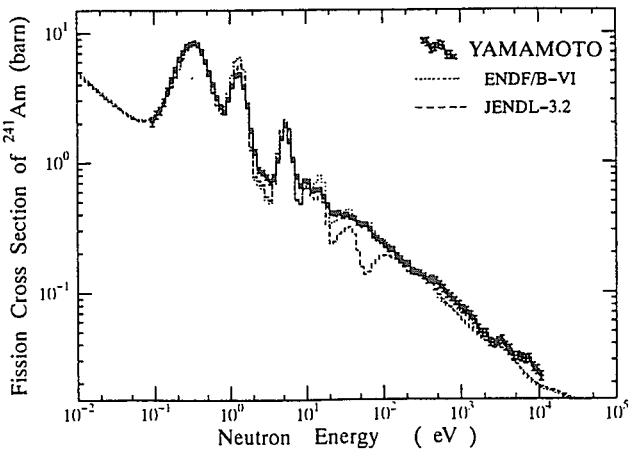

Fig. 2 Fission cross section of Am-241.

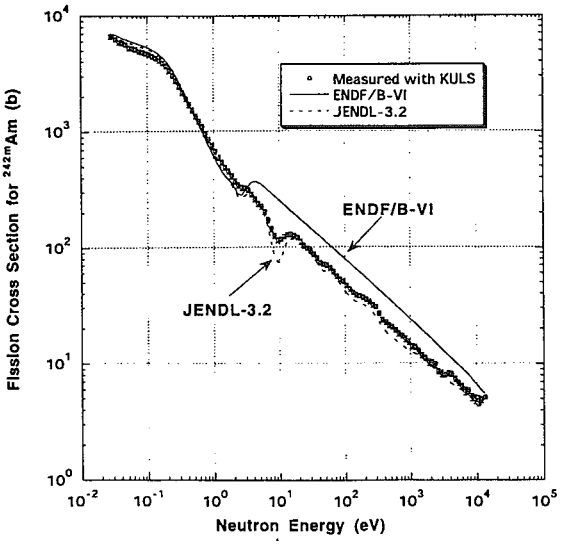

Fig. 3 Fission cross section of Am-242m.

In contrast to this, the evaluation shows a tendency to be higher below 0.3 eV. The JEF-2.2 data are obviously low except for the big resonance region.

^{237}Np(n, γ)^{238}Np cross section[16]

Figure 5 shows the measured and the existing experimental/evaluated data which are broadened by the resolution function of the KULS. The data by Weston et al. are in good agreement with those by Kobayashi et al.[16]. However the data by Hoffman et al. are markedly lower. The evaluated data in ENDF/B-VI and JENDL-3.2 agree well with the Kobayashi's.

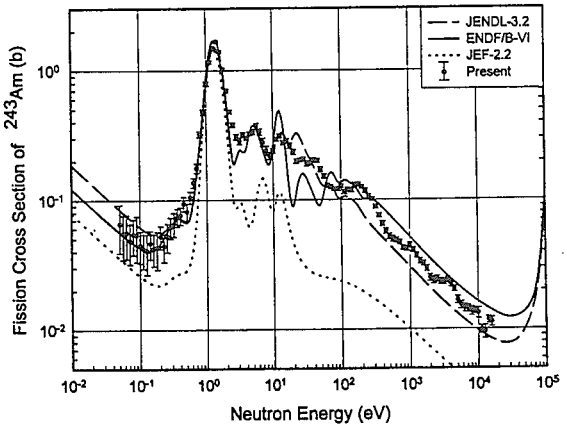

Fig. 4 Fission cross section of Am-243.

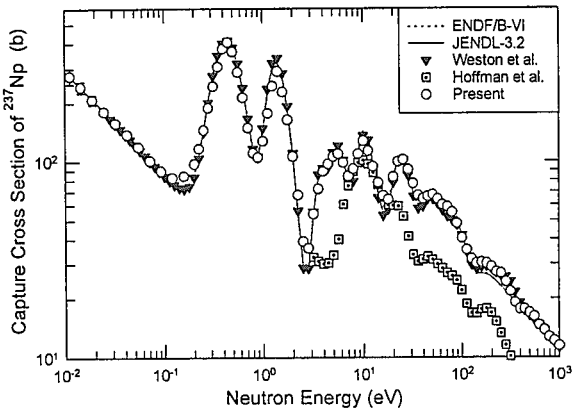

Fig. 5 Capture cross section of Np-237.

3.2. Measurements with the RINS

^{238}U(n,f) and ^{238}Pu(n,f) cross sections[7,17]

Making use of the RINS, the ^{238}U(n,f) cross section was measured relative to the ^{235}U(n,f) cross section from 3 eV to ～100 keV with 2.2 cm diam. cylindrical ionization chamber coated with highly enriched U-238[7]. Fission in the lowest energy U-238 resonance was clearly resolved for the first time. The fission cross section of Pu-238 was measured in the 0.1 eV to 100 keV[17], which was the second reported measurement below ～2 eV. The ENDF/B-VI data are generally in poor agreement with the measurement in the resonance structure region[17].

^{242}Cm(n,f), ^{244}Cm(n,f), ^{246}Cm(n,f), ^{247}Cm(n,f) and ^{248}Cm(n,f) cross sections[17-19]

Alam et al. made the first fission cross section measurement of Cm-242 from 0.1 eV to 100 keV[17]. Maguire,Jr et al. measured the fission cross sections of Cm-244, Cm-246 and Cm-248[18]. These data were the first measurements between 0.1 and 20 eV. Figure 6 shows the ^{246}Cm(n,f) cross section comparing with the ENDF/B-V data[18]. The evaluated data for these even curium isotopes are generally in poor agreement with the measurement. Danon et al. measured the ^{247}Cm(n,f) cross section from 0.1 eV to 80 keV[19], and this was the first measurement at the energy range of 0.1 to 20 eV. In the energy range from 20 eV to 100 keV, the shape of the cross section agrees with the fission cross section measured by Moor and Keyworth, but higher by about 30 % above 150 eV[19].

^{250}Cf(n,f) and ^{254}Es(n,f) cross sections[19]

These cross sections were first measured in the energy range of 0.1 eV to 80 keV. The Cf-250 cross section has only one resonance at 0.53 eV and has an average cross section of the order of ～4 b in the 17 to 76 eV energy range[19]. Es-254 showed only very little structure possibly because of wide fission widths and small level spacing[19].

3.3. Measurements with the Kurchatov Spectrometer

^{237}Np(n,f), ^{236,239,241}Pu(n,f), ^{241,242m}Am(n,f), ^{245}Cm(n,f) and ^{249}Cf(n,f) cross sections[9,10]

Making the correction procedure for the resolution function with the Kurchatov spectrometer, the MA fission cross sections were obtained. For Np-236, Pu-236, Pu-239, Pu-241, Am-242m and Cm-245 isotopes, the results were published elsewhere[20,21]. The data for the Np-236 and Pu-236 so far remain the unique experimental evaluations of the fission cross section in the over-thermal neutron energy region. The fission cross section of Np-237 measured by Gerasimov et al.[10] seems to be close to that by Yamanaka et al.[11] although a little discrepancy are seen in the peak or valley structure region due to the different energy resolution between the spectrometers. For the Pu-239 measurement, good agreement is seen between the results using the RINS and the Kurchatov spectrometer. The Kurchatov data of the ^{241}Am(n,f) and ^{242m}Am(n,f) reactions are in very good agreement with the measurements with the KULS[13,14], respectively. Figure 7 show the ^{245}Cm(n,f) cross section measured by Gerasimov et al.[9]. RPI group has not measured this cross section, although the group has measured some other Cm fission cross sections with the RINS.

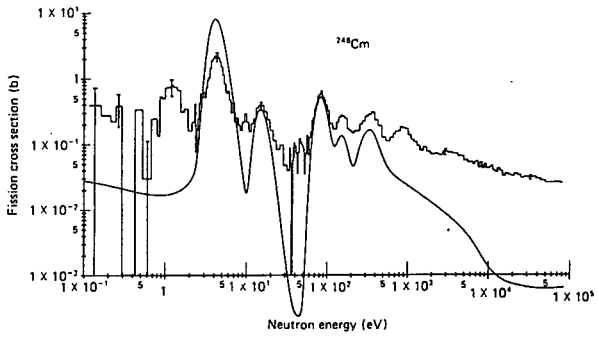

Fig. 6 Fission cross section of Cm-246.

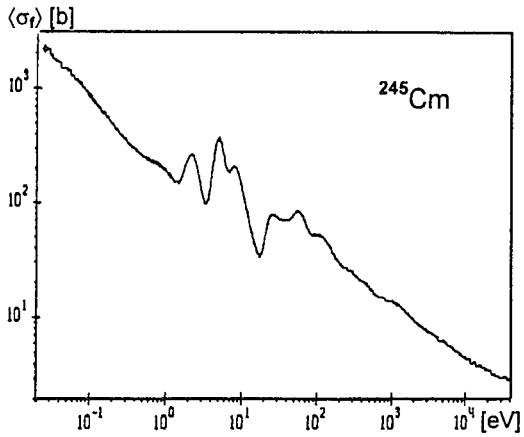

Fig. 7 Fission cross section of Cm-245.

4. Summary

The present review of the recent MA nuclear data measurements are summarized as follows:

(1) Making use of the KULS, the fission cross sections of Np-237, Am241, -242m and -243 and the capture cross section of Np-237 have been measured in the energy range of about ～0.1 eV to 10 keV.

(2) The RINS has been used to measure fission cross sections of U-238, Pu-238, -239, Cm-242, -244, 246, -247, -248, Cf-250 and Es-254 between about 0.1 eV and ～100 keV.

(3) With the Kurchatov spectrometer, the fission cross section of Pu-236, -238, -239 -241, Np-

237, Am-241, -242m, Cm-245 and Cf-249 have been measured below 40 keV. The fission cross section of Pu-238 has been measured with the RINS and the Kurchatov spectrometer, and those of Np-237, Am-241 and Am-242m have been measured with the KULS and the Kurchatov spectrometer. It is said that the MA nuclear data measured with these Spectrometers are in general agreement with each other. However, discrepancies can be still seen between the evaluation and measurement or among the measurements for some MA nuclear data. It is expected in future that more experimental studies with MA nuclides are carried out with the pure sample.

References

[1] Lancaster, D.: *Proc. Int. Conf. and Technol. Exposition on Future Nucl. system: Global '93*, Seattle, 1993, ANS, La Grange Park, Illinois, p.609 (1993).
[2] Mukaiyama, T. *et al.*: *J. At. Energy Soc. Jpn*, 37(3), 159 (1995).
[3] MaLane, V. *et al.*: "*Neutron Cross Sections*", Vol.2, Neutron Cross Section Curves, Academic Press (1988).
[4] Rose, R. F.(Ed.): ENDF/B-201, ENDF/B-VI Summary Documentation, *BNL-NCS*17541, 4th Ed.(ENDF/B-VI) (1991), and ENDF/B-VI Mod.2 Evaluation, by P.G.Young (1996).
[5] Shibata, K. and Narita, T.(Eds.): *JAERI-Data/Code* 98-006 (part II) (1998).
[6] Nordbor, C. and Salvatores, M.: *Proc. Int. Conf. Nucl. Data Science and Technol.*, Gatlinberg, Tenn. 1994, ANS, Vol.2, p.680 (1994).
[7] Slovacek, R. E. *et al.*: *Nucl. Sci. Eng.*, 62, 455 (1977).
[8] Kobayashi, K. *et al.*: *Nucl. Instrum. Methods Phys. Res. A*, 385, 145 (1997).
[9] Gerasimov, V. F. *et al.*: *Proc. V Int. Seminar on Interaction of Neutrons with Nuclei, ISINN-5*, Dubna, p.361 (1997).
[10] Gerasimov, V. F. *et al.*: *ibid.*, p.348 (1997).
[11] Yamanaka, A. *et al.*: *J. Nucl. Sci. Technol.*, 30(9), 863 (1993).
[12] Carlson, A. D. *et al.*: *Proc. Int. Conf. Nucl. Data Science and Technol.*, Gatlinberg, Tenn. 1994, ANS, Vol.1, p.40 (1994).
[13] Yamamoto, S. *et al.*: *Nucl. Sci. Eng.*, 126, 201 (1997).
[14] Kai, T. *et al.*: *JAERI-Conf*98-003, p.225 (1998).
[15] Kobayashi, K. *et al.*: *J. Nucl. Sci. Technol.*, 36(1), 20 (1999).
[16] Kobayashi, K. *et al.*: To be published in this Symposium.
[17] Alam, B. *et al.*: *Nucl. Sci. Eng.*, 99, 267 (1988).
[18] Maguire, Jr., H. T. *et al.*: *Nucl. Sci. Eng.*, 89, 293 (1985).
[19] Danon, Y. *et al.*: *Nucl. Sci. Eng.*, 109, 341 (1991).
[20] Gerasimov, V. F. *et al.*: *Proc. Int. Conf. on Neutron Phys.*, Kiev, Vol.3, p.87 (1988).
[21] Gromova, E. A. *et al.*: *Atomnaja Energija*, Vol.68, p.193 (1989).

2.5 Nuclear Data Measurements for 40-90 MeV Neutrons at TIARA*

M.Baba
Cyclotron and Radioisotope Center, Tohoku University
980-8578, Sendai Japan
e-mail: babam@cyric.tohoku.ac.jp

Experimental activities at the ^{7}Li neutron source of TIARA, Japan Atomic Energy Research Institute, Takasaki Establishment are reviewed briefly. Experiments on 1)double-differential charged particle production cross sections for 40-90 MeV neutrons and protons, and 2)neutron elastic scattering and non-elastic cross sections are described as well as the frame of the research.

1.Introduction

Nuclear data for intermediate energy region are required for the development of large and intense accelerator facilities, and dosimetery for high energy particles in acceleartor facilities and cosmic space. To reply the requirement, a ^{7}Li(p,n) quasi-monoenergetic neutron source for 40-90 MeV region was installed at TIARA of Takasaki Establishment, Japan Atomic Energy Research Institute (JAERI) using a K=110 AVF cyclotron [1].

Using the source, experiments on "Basic data for accelerator shielding" have been conducted since 1992 by the members of universities and JAERI under the framework of "Universities-JAERI Joint Research Project" [2]. Experiments were carried out on nuclear data, neutron detector calibration as well as shielding benchmark experiment. Thick target neutron yields were measured too for energetic light and heavy ion beams provided by the cyclotron.

In 1997, the 2-nd phase research program "Particle production by the nuclear reaction of neutrons and charged particles" has started as a three-years-projects [2].

Under the program, four research works have been carried out:

1)Particle production by neutron reactions,

2)Particle production by charged-particle reactions,

3)Development and characterization of neutron detectors, and

4)Particle transport in media and human-bodies.

The subjects 1) and 2) aim at the microscopic nuclear data studies, and measurements have been carried out on differential particle-production cross sections by neutrons and protons to validate the nuclear reaction codes and models, and to find systematic behavior of cross sections which will be useful for nuclear data evaluation. The subjects 3) and 4) are for integral measurements and benchmark experiments. These data are indispensable to evaluate particle transport and the radiation effect in accelerator systems.

In the subject 1, two experiments for neutron-induced reactions have been undertaken for 55, 65 and 75 MeV neutrons; a)double-differential cross sections of light charged-particle emission (n,xz) reactions, and b)elastic-scattering and non-elastic cross sections. In the subject 2), double-differential cross sections for proton-induced light charged-particle emission (p,xz) reactions have been measured for 68 MeV and 42 MeV protons. Data for proton induced reactions are of interest because they

* Takasaki Ion Accelerators for advanced Radiation Application

provide information on nucleon induced reactions and useful to derive model parameters for neutron induced reactions which are more difficult to study with high energy resolution and statistical accuracy. Therefore, measurements of (n,xz) and (p,xz) reactions were done for common elements to enable data comparison. Further, in (n,xz) and (p,xz) experiments, charged-particle spectrometers were designed to have large pulse-height dynamic range to measure almost all light charged particles up to α-particles. It is important to study emission cross sections and the reaction mechanism.

This report describes the outline and typical results of the experiments 1) and 2). Details of each experiment and results have been described separately in Refs. 3-11.

2. Experiments of Neutron Induced Reactions

The experiments for neutron induced reactions are done at the LC-0 course of the TIARA cyclotron facility shown in Fig.1. Details of the neutron source is described in Ref.1. A clean neutron beam is provided in the Light Ion Room 3 through a clearing magnet and a ≅3m thick collimator between the ^{7}Li target and the experimental room, where experimental apparatus are setup. Figure 2 illustrates the experimental setup for neutron induced reactions. As shown in the figure, the charged-particle spectrometer and neutron scattering apparatus are setup in tandem along the neutron beam for efficient utilization of the neutron beam.

2.1 (n,xz) Experiment [3-5]

Up to now, measurements have been carried out for (n,xp), (n,xd), (n,xt) and (n,xα) reactions of C, Al, Fe, Ni at 55, 65 and 75 MeV. First experiment for C, Al at 65, and 75 MeV was done using conventional spectrometers [3], but recently measurements employ a three sets of three-elements counter telescope to achieve a wide dynamic range. Each telescope consists of a BaF_2 scintillator, PIPS Si detector and a low-pressure proportional counter for wide dynamic-range operation. Using the system and applying energy loss correction, particles of several MeV can be detected while further study is required for reliable energy loss correction [4,5].

Typical results are shown in Fig.4 together with the recently released LA-150 data library [12]. No other experimental data are available for comparison. The library seems to reproduce experimental data fairly well while there are rooms for improvement. Systematic comparison with proton induced data will be done.

2.2 Elastic scattering and non-elastic-scattering cross section

As shown in Fig.2, measurements were done using five NE213 detectors. A TOF method was used to select events caused by peak neutrons in the ^{7}Li(p,n) source. However, events due to inelastic process and still remaining non-peak components of the source neutrons have to be eliminated. Both were done with the help of calculation using the LA-150 library [8,9]. Up to now, data were obtained for C, Si, Fe, Zr and Pb at 55, 65 and 75 MeV. Non-elastic cross sections were obtained with different setup employing a transmission geometry [6].

Figure 5 shows typical results for differential elastic-scattering cross sections together with LA-150. The present data cover much wider angular ranges with better angular resolution than those by the UC-Davis group [7,8]. This was enabled by taking advantage of wide experimental room at TIARA. LA-150 shows good agreement with the present data while it underestimates at very forward angles for Pb and Fe. This argument is consistent with the results of non-elastic cross section measurement. The present data indicated that nucleon scattering cross section data in the cascade codes and the HILO libraries are greatly different from the experiment [7,8]. The present data, therefore, will be useful for refinement of the data base and optical model potential parameters.

3. (p,xz) measurement

The experiment is carried out at HB 1 course (Fig.1) using the setup in Fig.3. The detector consists of two Si-SSDs (30μm and 500 μm thick), and a CsI scintillator with Photo-diode read out to cover a wide particle energy. Care was taken to reduce the backgrounds due to slit scattering in forward angles. Measurements were done for (p,xp), (p,xd), (p,xt) and (p,xα) reactions of C, Al , Ni at 42 and 68 MeV, and are planned for Zr and Bi.

In Fig.6, (p,xd) data for C and Al at 68 MeV are shown, compared with LA-150 and the data by Bertrand & Peelle [13]. There is good agreement between the experiments if the difference in incident energy is considered but LA-150 are in large difference; it tends to overemphasize the high energy part in particular at forward angles. Similar trend was observed for neutron induced reactions [3-5], which should be traced further though comparison of (p,xz) and (n,xz) data.

4. Summary and Future Plan

The project research on "Particle production by the nuclear reaction of neutrons and charged particles" will finish this year. Until now, as described above, many experimental data were obtained under the project and will contribute to establish data bases and models or computer codes. Further, experimental techniques developed will also contribute to extend experimental activities.

Following the present subjects, a new project on dosimetry of high energy particles will start next year in which experiments and analysis related to radiation effects of high energy particles will be undertaken. The wide range charged-particle spectrometers developed in the project research will be useful also in the new projects.

A plan for neutron experiments is in progress too at Cyclotron and Radio Isotope Center of Tohoku University. A K=130 AVF cyclotron under construction will be used for production of neutrons up to ten's of MeV and applied to neutron physics and nuclear data studies. High current operation enabled by negative ion extraction will achieve intense neutron beams useful for the studies. A beam swinger system and a long flight path with a bright neutron detector system will also contribute to high resolution data for spectroscopy of secondary neutrons and neutron scattering.

By combining activities of facilities, further activities are expected on high energy nuclear data.

Acknowledgement:

The experiments above described were undertaken by the members below.
M.Ibaraki, T.Miura, Y.Nauchi, Y.Hirasawa, T.Hiroishi, T.Aoki (Tohoku Univ.), Y.Watanabe, M.Harada, A.Yamamoto, Y.Tanaka, Sun Weil (Kyushu Univ.), K.Shin (Kyoto Univ), H.Nakashima, S.Meigo, H.Takada, O.Iwamoto, S.Chiba, T.Fukahori, T.Sasa (JAERI Tokai), Su.Tanaka (JAERI Takasaki).
The author appreciates the oprating crew of the TIARA cyclotron for their cooperation. He is also indebted to Drs.Y.Sakamoto, H.Yasuda and Prof. Nakamura for their kind arrangements.

References

[1] Baba, M : *JAERI-Conf* 98-003 (1998) pp.107
[2] Baba, M. et al: *Nucl. Instrum. Methods* A428 454 (1999)
[3] Nauchi,Y et al.: *J.Nucl.Sci.Technol.*: 36(2) 143 (1999)
[4] Baba, M. et al: *Int. Conf. Reactor Dosimetry* (1999, Osaka) to be published
[5] Hirasawa, Y. et al.: *This proceedings* No. P20
[6] Ibaraki, M et al.: *This proceedings* No. P22
[7] Ibaraki, M.: *Proc. International Conf. on Radiation Shielding* (Tsukuba 1999), to be published,
[8] Ibaraki, M. et al.: *JAERI-Conf* 99-002 pp.153

[9] Ibaraki, M. et al: *Nucl. Instrum. Methods,* to be published
[10] Harada, M.: *Proc. 1998 Nuclear Data Symposium, JAERI-Conf* 99-002 pp.268
[11]Harada, M.et al: *Proc. International Conf. on Radiation Shielding* (Tsukuba 1999), to be published
[12] Chadwick,M. et al. : *Nucl. Sci. Eng.,* 131 (1999) 293
[13] Bertrald F.E., Peelle, R.W.: *Phys. Rev.*, C8 1045 (1973); ORNL-4799 (1973),

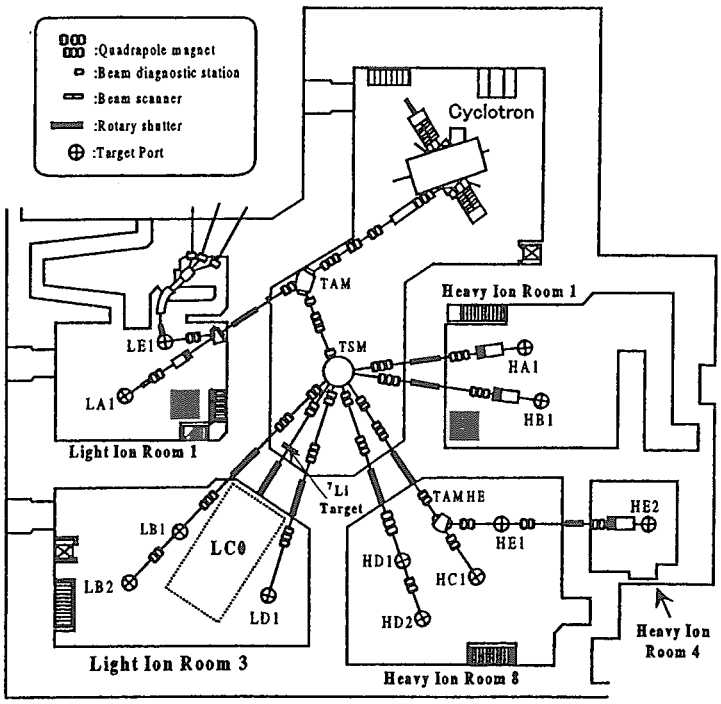

Fig.1 The layout of TIARA cyclotron facility

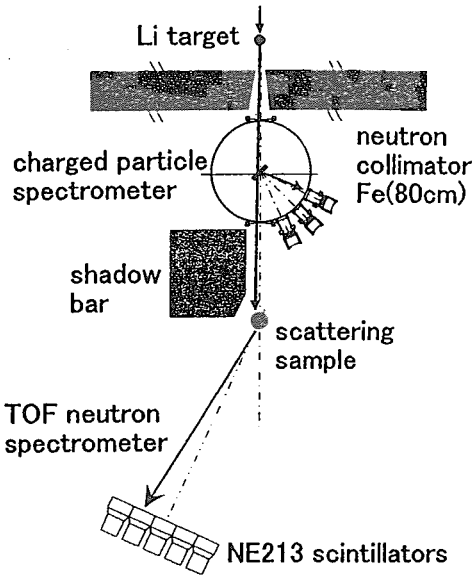

Fig.2 The experimental setup for neutron induced reactions.

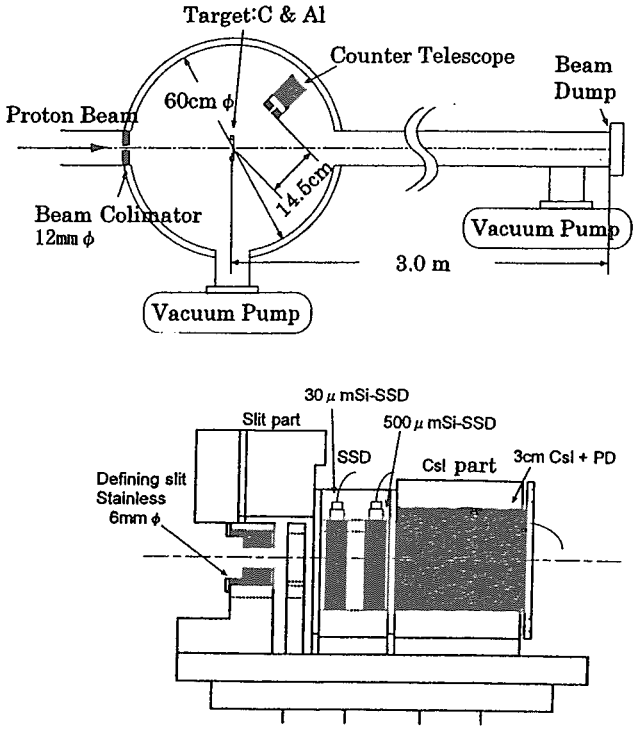

Fig.3 The experimental setup (upper) and charged particle spectrometer (below) for (p,xz) experiment.

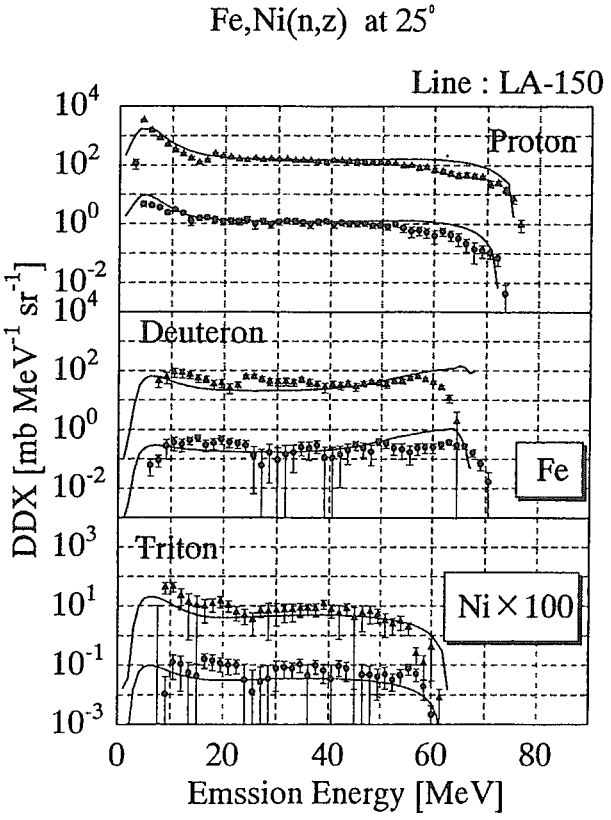

Fig.4 P, d, t emission spectra of Fe, Ni for 75 MeV neutrons.

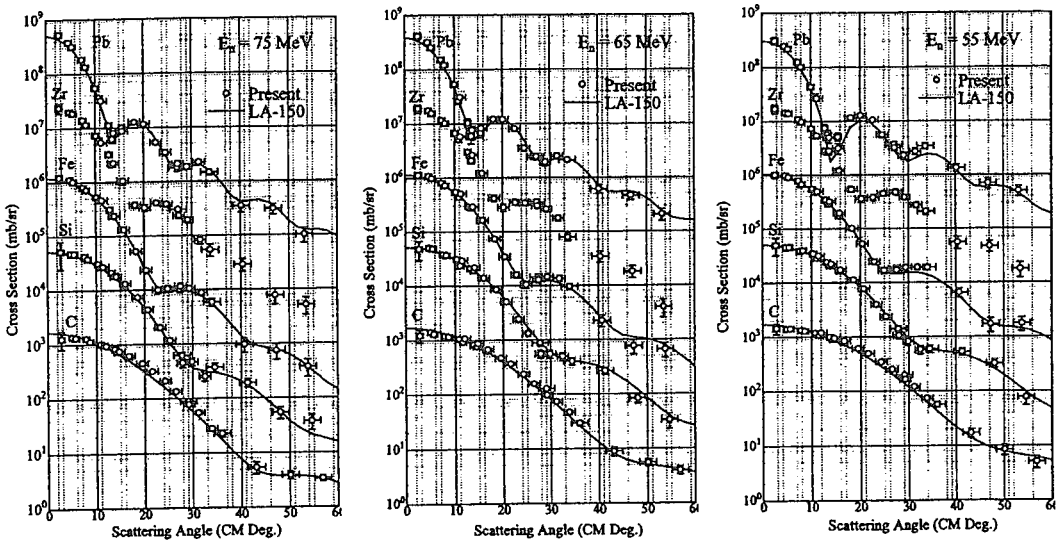

Fig.5 Neutron elastic-scattering cross sections for 75, 65 and 55 MeV neutrons.

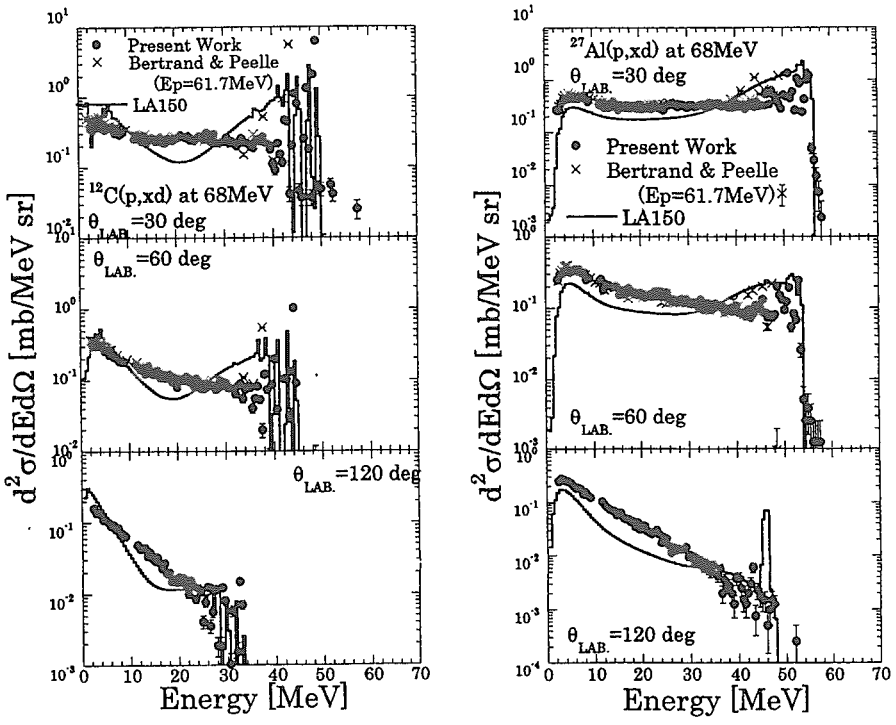

Fig.6 Double-differential (p, xd) cross sections at 68 MeV.

2.6 Status of the AGS Experiment for Mercury Spallation Target Development

Y. Ikeda[1] and ASTE Collaboration Team[2]

1 Japan Atomic Energy Research Institute, Tokai-mura, Naka-gun, Ibaraki-ken 319-1195
2 International collaboration for AGS Spallation Target Experiment (ASTE) from Japan (JAERI and KEK), EU (FZJ, PSI) and US (BNL, ORNL)
e-mail: ikeda@fnshp.tokai.jaeri.go.jp

Abstract

An experimental endeavor for exploitation of a MW class spallation target has been conducted using the AGS accelerator at BN on the neutron production along with the shock wave characteristics in the target, which are induced by a high intensity proton incident. This paper reviews the experiments, which has been carried out since 1997 in an international collaborative framework, namely the ASTE (AGS Spallation Target Experiment) collaboration with an emphasis on neutronics measurement, and gives the current status of the results provided through the experiment.

1. Introduction

A strong need of an intense pulse neutron source has been requested from the neutron scattering research. For the development of a MW class accelerator driven spallation neutron source, mercury was identified as a unique choice for the target material from a thermal dynamics point of view. There was, however, a serious concern of a shock wave associated with the high intensity proton beam incident, and an experimental validation was addressed. AGS, an intense proton accelerator at Brookhaven National Laboratory in USA, was identified as a potential source , which is eligible for the all requirements in terms of proton energy and intensity for yielding a shock wave. As the issues was so critical that an international collaborative framework, namely the ASTE (AGS Spallation Target Experiment) collaboration was established with participation from EU, US and JA, who are fully involved in their own national projects for the spallation source, e.g., SNS (USA)[1], ESS (Europe)[2] and NSP (Japan)[3]. The primary missions of the AGS experiment were set to provide experimental validation of analytical codes for neutronics, mechanical and thermal-hydraulics quantities associated with GeV proton induced spallation reactions in a mercury target. Since then, experiments have been planned and conducted as maximizing the opportunity and resources as possible This paper gives the current status of the results provided through the experiment with an emphasis on neutronics measurement.

2. Primary Objectives of ASTE

It has been recognized an important step that provides experimental validation of analytical codes for physical, mechanical and thermal-hydraulics quantities associated with GeV proton induced spallation reactions in a mercury target; quantification of all technical responses are strongly requested from the intense spallation pulse neutron source (target, moderator, reflector) development. Issues relevant to the ASTE collaboration are schematically illustrated in Fig. 1.

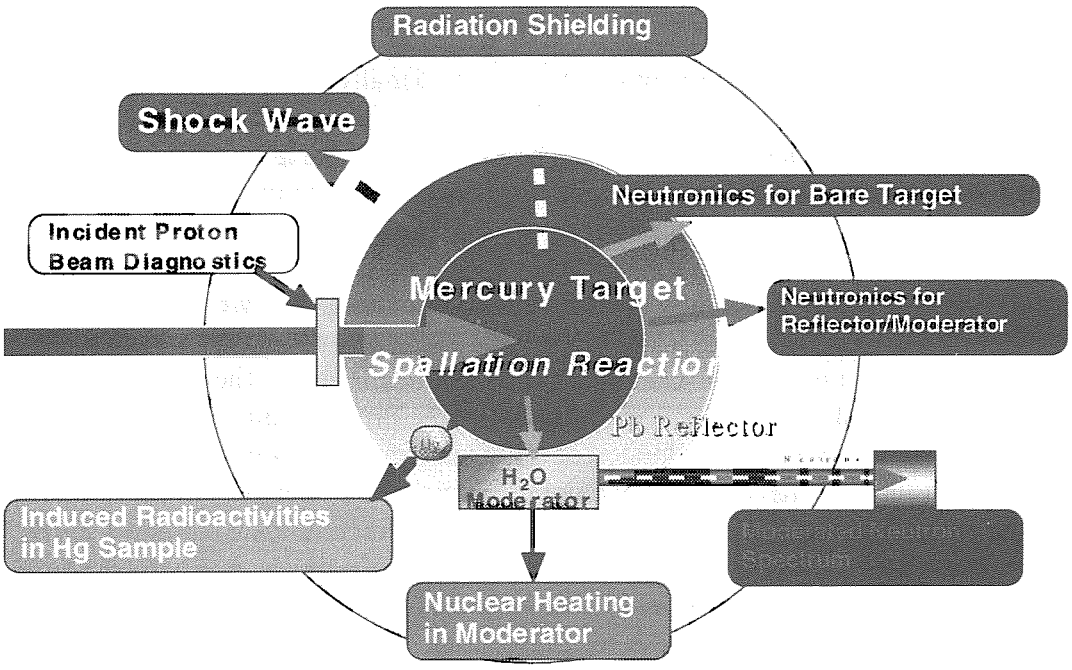

Fig. 1 Schematic view of the relation of the various nuclear issues associated with the proton induced spallation reaction with the mercury target.

The experimental items were discussed and selected as follows:

1) Measurement of the pressure wave associated with a high intensity proton beam in the mercury target.
2) Measurements of the neutronics characteristics in terms of the spallation neutron production profile along the mercury target, induced radio-activities in mercury samples, neutron leakage spectrum from a light water moderator which is placed adjacent to the target, nuclear heating in the moderator.
3) Development and establishment of measurement techniques for both the numbers of incident protons and the profile of the proton beam on the target.
4) Radiation shielding with a thick iron and concrete for high energy neutron and secondary particles.

3. Overviews of the experimental runs

3.1 The first run

At the first experiment with a bare Hg target, we were in successful, for the first time, in detection of the shock wave in the mercury target associated with the proton incident.[4] Neutronics measurements in terms of reaction-rate distribution along the mercury target were carried with proton beams of 1.5, 7, and 24 GeV. We have also tested all available proton beam diagnostics in terms of intensity, profile and mean position employing the imaging plate with aluminum activation foils. As a result, the ASTE team established the experimental environment at AGS/BNL and demonstrated the technical capability pertinent to the target development.

3.2 The second run

For the second run, the bare target experiment was repeated in November, 1998, providing final neutronics experimental data on Hg. Finally we have obtained a full set of experimental data for the bare Hg target, at 1.6, 12 and 24 GeV.[5] It should be noted that along with those neutronics data, radio-activities induced in Hg samples that were placed nearby the Hg target were measured. The pressure wave was also measured.

3.3 The third run

According to the initial missions of the ASTE collaboration, we have done the third experiment with a moderator assembly in which a light water moderator with a Pb reflector was placed in the Hg target. The schematic cross sectional view of the target, moderator, and reflector assembly is shown in Fig. 2 with respect to the proton beam. The main focus for that experiment was to measure the moderated neutron spectrum intensity from the moderator. We have applied a newly developed technique, namely the current mode Time-of-Flight (CTOF),[6] for the neutron spectrum measurement. Experimental measurements of the nuclear heating in the moderator were newly tested using thermistors as the thermal sensor. Also, neutronics effect from the new assembly with reflector was examined with respect to the bare target configuration. Along with these, we have done again the pressure wave measurement without reflector.

In the nest section, topics of results are to be given.

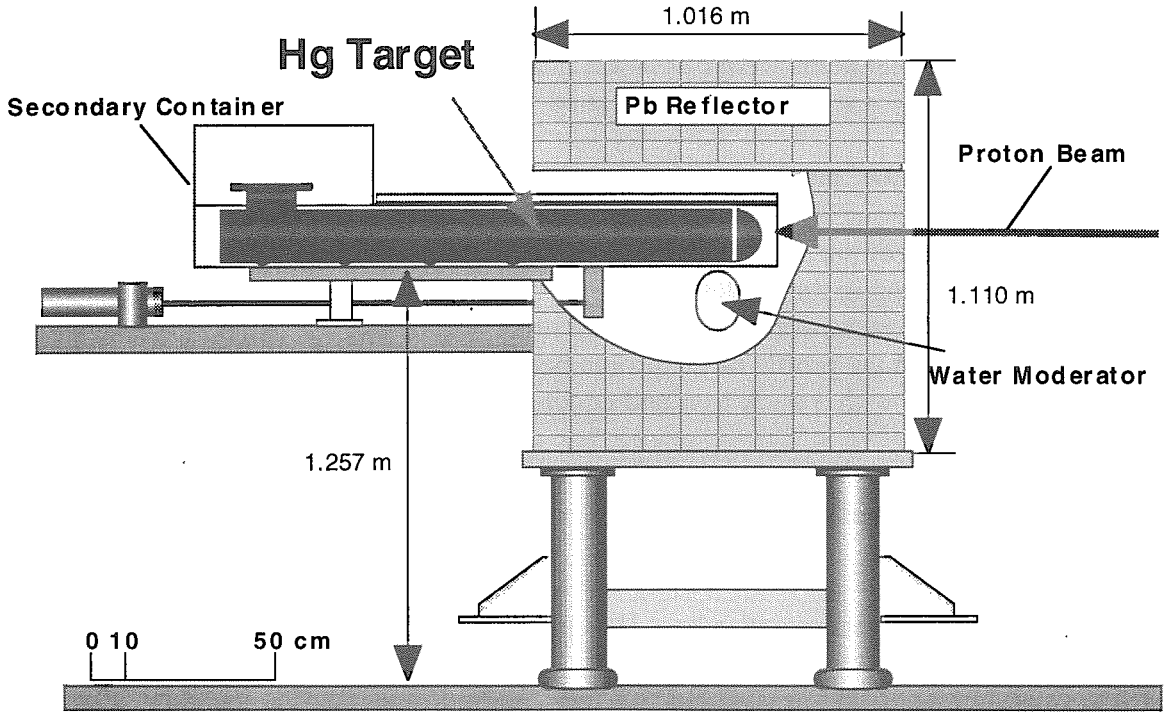

Fig. 2. The schematic cross sectional view of the target, moderator, and reflector assembly with respect to the proton beam.

4. Topical results on neutronics experiments

4.1 Measurements of proton beam intensity and profile

The proton incident beams were monitored with a current transformer (CT) for the total beam current, a wire ionization chamber (CHIDORI named by KEK) for a beam profile (X-Y), the Cu activation foil for the total incident proton number using $^{Nat}Cu(n,x)^{24}Na$, the imaging plate (IP) with a aluminum foil which is exposed in the proton beam. Data provided by these monitors were consistent each other and provided important base data for analyzing the measurements of interest. In Fig.3 shows the proton beam profiles obtained with IP for the protons of 1.6, 12 and 24 GeV used in the neutronics experiments with the foil activation measurement. The profiles are of importance in defining the proton beam distribution and positions with respect to the mercury target. With these profiles, the precise experimental analysis can be accomplished. It is notable that the profiles are consistent with the difference in the reaction rates around the target which is to be described in the next sub-section.

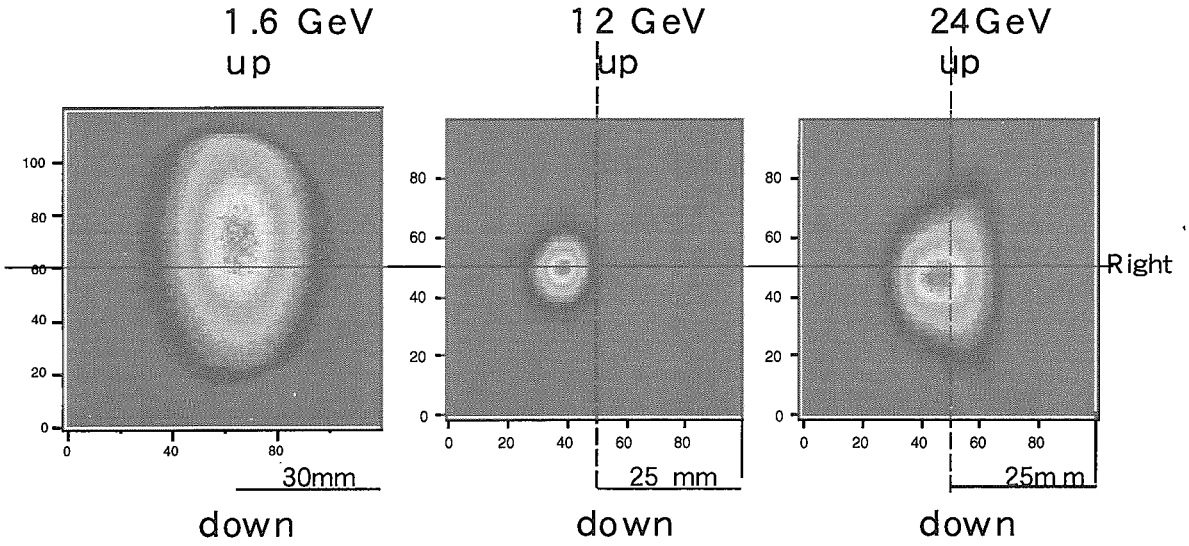

Fig. 3. Incident proton profiles measured by the imaging plates using Al foils, which were exposed to the proton beams of 1.6, 12 and 24 GeV at the second experimental run.

4.2 Reaction rate measurements

The first measurement of the neutron production distribution along thebear mercurytargetwas done in 1997. In order to finalize the data, the measurement was repeatedly carried out in 1998 for the incident proton energies of 1.6, 12 and 24 GeV. The measurement was performed with the activation technique and the data are documented in a technical report.[5] Experimental errors ranges form ± 5 % to several tens % depending on the activation counting statistics. Note that almost all experimental errors fall within ± 10 %. Thus, substantial experimental analysis can be made very effectively in terms of comparisons of the simulation codes with these experimental data.

In the mean time, various simulation codes that treat the high energy particle reactions and their transports have been widely developed for the nuclear design of thespallation target system.[7,8] A code named by NMTC/JAM[9] has been recently developed at JAERI in order to improve the simulation The code is an updated version of NMTC/JAERI97[7] in terms of extension of the proton energy and improving the nuclear cross sections. The experimental analysis for the AGS experiment was performed with the NMTC-/JAM, resulted in demonstration of the code validity as shown in Fig.4, which shows a good agreement between the calculation and the measurement of reaction-rate distributions

of the $^{209}Bi(n,4n)^{206}Bi$ and $^{209}Bi(n,5n)^{205}Bi$ reactions at the 24 GeV proton run. For the other reactions at other proton energies, there are reasonable agreements between the calculations and measurements. It is one of direct contribution of the AGS experiments to the code validations needed in the spallation nuclear system development.

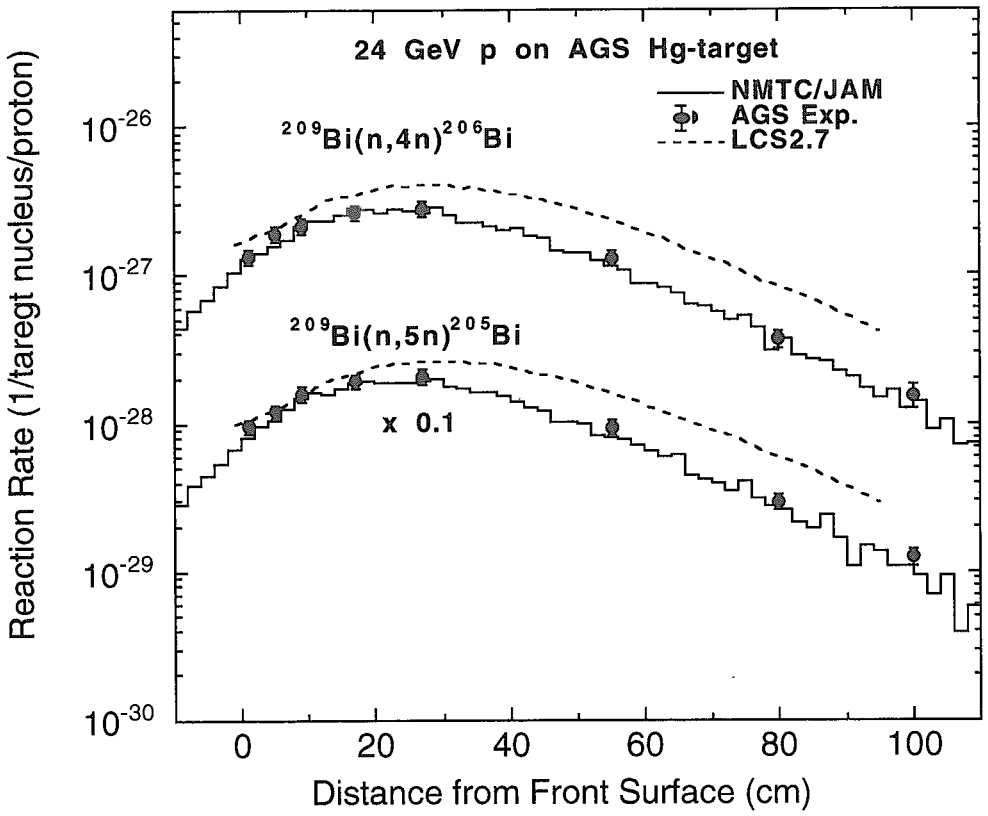

Fig. 4 Comparison of the reaction rates of the $^{209}Bi(n,4n)^{206}Bi$ and $^{209}Bi(n,5n)^{205}Bi$ reactions between NMTC/JAM calculations and measurements. The calculations with LCS-2.7 are shown for comparison.

4.3 Nuclear heating in the light water moderator

In the experiment with the water moderator and the lead reflector, an attempt to measure nuclear heating rates in the moderator was made applying a micro-calorimetric method*). Signals of temperature rises in the moderator corresponded to the proton beam injection. The result indicated that precise nuclear heating rates can be measured with an accuracy of ± 10 % even the number of proton pulses is limited.

4.4 Neutron spectrum from the moderator

The neutron spectrum leaked from the moderator was measured with a current mode Time of Flight (CTOF) technique.[6] CTOF was newly developed for this ASTE experiment at AGS, in which number of proton pulses are limited as low as possible from the radiation safety point of view. For this reason, the normal TOF with high frequency pulses could not be applied. CTOF solved this problem and enabled to obtain a neutron spectrum with a single pulse. In Fig. 5, the measured neutron spectrum moderated in the moderator is shown for the

24 GeV proton run.

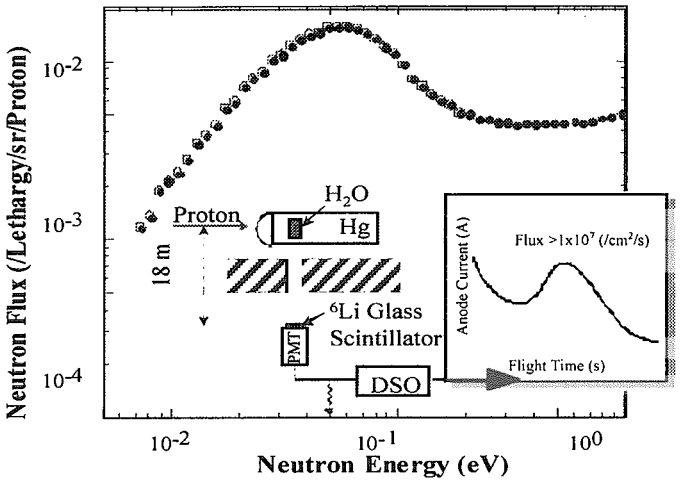

Fig. 5 The measured neutron spectrum from the Water moderator with the detector arrangement.

5. Summary

Experimental analysis is extensively underway for all measurements. The ASTE collaboration demonstrated being effective and efficient for the spallation target development. Utilizing the unique resource which became available, it is strongly requested to continue the endeavor to arrive at the goal of the ASTE collaboration.

Acknowledgements

The experimental work at BNL was supported by the U.S. Department of Energy (DOE) under the contract DE-AC02-98-CH10996 with Brookhaven Science Associates.

References

1. B. A. Appleton, "A Progress Report on the Spallation Neutron Source", Proc. ICANS-XIV, Jun 14-18 1998 Utica, IL, USA.
2. ESS, "A Next Generation Neutron Source for Europe Vol. III –The Technical Study", ISBN 090 237 6 659, (1997)..
3. S, Nagamiya, "JAERI-KEK Joint Project on High Intensity Proton Accelerator," to be published in Proc. Intl. Conf. On Radiation Shielding, ICRS-9, Oct. 17-22, Tsukuba, Japan (1999).
4. M. Futakawa, at al., Nucl. Instrum. Meth. A 439, (2000) 1-7.
5. H. Takada, et al., "Measurements of Activation Reaction Rate Distributions on a Mercury Target Bombarded with High-Energy Protons at AGS," to be published as JAERI-Research (2000).
6. S. Meigo, "Development of Current Mode Time-of –Flight Technique for Measurement of Thermal Neutron Spectrum," to be published in Proc. Intl. Conf. On Radiation Shielding, ICRS-9, Oct. 17-22, Tsukuba, Japan (1999).
7. H. Takada, et al., JAERI-Data/Code 98-005 (1998).
8. R. R. Prael and H. Lichtensyein, "User Guide to LCS: LAHET Code System," LA-UR-89-3014, LANL (1989).
9. H. Takada, "Recent Progress on Nucleon-meson Transport Code Development at JAERI," Proc. Mathmatics ad Computation, Reactor Physics and Environmental Analysis in Nuclear Applications, Sept. 1999, Madrid, Spain.

2.7 HIGH RESOLUTION MEASUREMENT OF TOTAL PHOTONUCLEAR CROSS SECTIONS

Hideo HARADA, Kazuyoshi FURUTAKA
Japan Nuclear Cycle Development Institute, Tokai-mura, Ibaraki-ken 319-1194
e-mail: harada@tokai.jnc.go.jp

Hideaki OHGAKI and Hiroyuki TOYOKAWA
Electrotechnical Laboratory, Umezono, Ibaraki-ken 305-8568

A high-resolution photo-absorption spectroscopic method has been developed in order to investigate the fine structures in photonuclear reactions. To achieve an energy resolution of about 0.1% for high-energy photons (10-30 MeV), a new type of a photon spectrometer has been developed. To enhance a quality of data, the beam of laser Compton photon has been utilized. Recent progress of this new spectroscopic method is reviewed.

1. Introduction

Fine structures in photonuclear reactions are important quantities for the investigation of the innovative applications of photonuclear reactions because the photonuclear cross sections of some special states are expected to have huge values that are comparable to the photo-atomic cross sections. However, very little is known about the fine structures neither experimentally nor theoretically.

Nuclear photoabsorption (NPA) spectroscopic method is an ideal tool to investigate photonuclear reactions. The measurement gives the cross section of the total photonuclear reaction that is the sum of all the γ-induced reaction channels. The NaI scintillation spectrometer, LD_2/TOF spectrometer or the magnetic spectrometer has been applied for the photon absorption measurements.[1,2,3] However, the energy resolving power of these spectrometers were about a few percent, and were not enough to investigate fine structures in photonuclear reactions.

Recent progress on Ge detector fabrication technologies makes it possible to develop a high-resolution high-energy photon spectrometer (HHS)[4] with an excellent energy resolution of about 0.1% for high-energy photons, typically 10-30 MeV, with which NPA method can achieve a high resolution. As a result the fine structure in photonuclear reaction can be studied up to about 30 MeV.

The beam of laser Compton photon (LCP)[5] is now strong enough to be used in NPA experiments. The use of LCP overcomes the inherent disadvantage of the use of bremsstrahlung, that is, its high background, especially at the low energy side. The low energy tail of the LCP beam is cut off with a collimator since the energy of LCP is

determined by LCP's scattering angle.

The experimental technique of NPA using HHS and LCP has been developed for several years,[6] and recently the energy resolving power of 0.1% has been successfully demonstrated.[7] The progress of the new spectroscopic method is briefly reviewed.

2. Experiments

2.1 Principle of a new NPA spectroscopic method

In principle, the developed measurement method is similar to earlier NPA experiments[1,2,3], but in the present measurements two powerful devices, HHS and LCP, have been incorporated.

The total photo nuclear cross section is given by

$$\sigma_{tot}(E) = \frac{1}{\rho \ell}\log\left(\frac{cU_0(E)}{U(E)}\right) - \sigma_{atom}(E), \qquad (1)$$

where ρ and l mean the atomic density and the length of the target. The E is the photon energy. The U and U_0 are transmitted LCP spectra obtained by unfolding the observed LCP spectra Y(target) and Y(reference), respectively, with the response functions of the HHS. The c in eq. (1) is a normalization constant. The $\sigma_{atom}(E)$ is the photo-atomic cross section that is tabulated in ref. (8).

2.2 Development of the super high-resolution photon spectrometer, HHS

The HHS was designed to detect high-energy photons in the energy range of 10-30 MeV with the energy resolution of about 0.1%. The HHS (Fig. 1) consists of two large N-type Ge detectors and thick BGO detectors. The energy resolution of the HHS is more than 10 times superior to the previously developed high-energy photon spectrometers[1,2,3]. This is the key device that enables it to obtain super high-resolution data of photo-absorption cross sections. The HHS is a new type of a super high-resolution photon spectrometer that enables the high-energy photon spectroscopy with the energy resolution of 0.1 %.

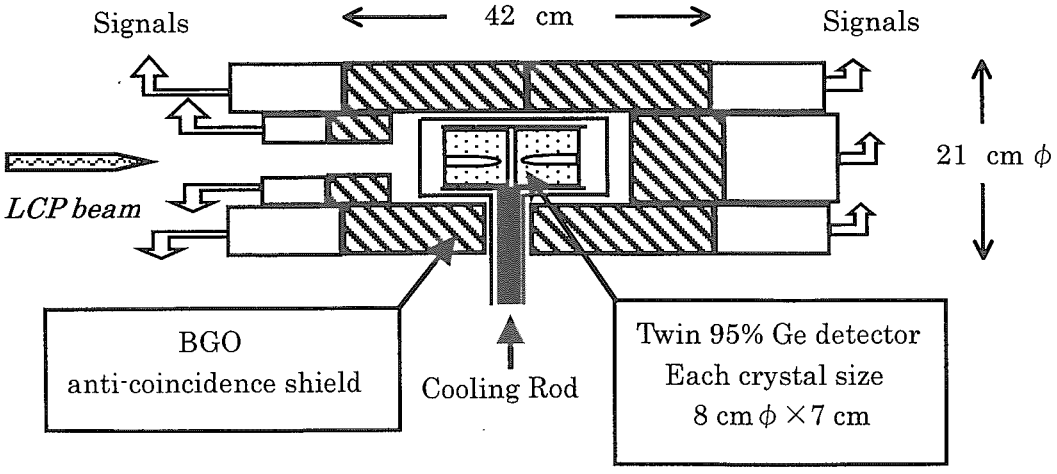

Fig. 1 A schematic representation of the HHS

2.3 Impact of LCP on NPA spectroscopy

The kinematics of the LCP is expressed by the next equation

$$E_{LCP}(\theta) \cong \frac{E_{max}}{1+a(\gamma\theta)^2}, \quad \theta \ll 1, \qquad (2)$$

where $E_{max} = 4\gamma^2\omega a$, $a = 1/(1+4\gamma\omega/m)$, and $\gamma = E_e/m$. The E_e, m, and ω mean electron energy, electron mass, and laser (one photon) energy, respectively. For example, E_{max} is 13.23 MeV in the case of E_e = 613 MeV and ω = 2.35 eV (= 527 nm). The LCP energy at scattering angle of 0.01° is decreased to 12.67 MeV in this case. Therefore, the low energy tail of the LCP photon flux is eliminated with a collimator. The elimination of needless photons helps to reduce the counting rate of the photon spectrometer. The energy width of the LCP beam is also variable by changing the diameter of the hole in the collimator. These characteristics of the LCP make the NPA spectroscopy very powerful spectroscopic method compared to that using bremsstrahlung beam that has been traditionally used.

2.4 Setup

The experimental setup is shown in Fig. 2. A laser beam enters the window of a vacuum chamber of the electron storage ring TERAS[9] after being reflected by a mirror and passing through a lens (f = 2 m), and then interacted with the stored electron beam at the straight section. The lead collimator is placed along the LCP beam axis to cut off the low energy tail of the LCP beam. The distance between the centers of the interacting region and the collimator is 5.2 m.

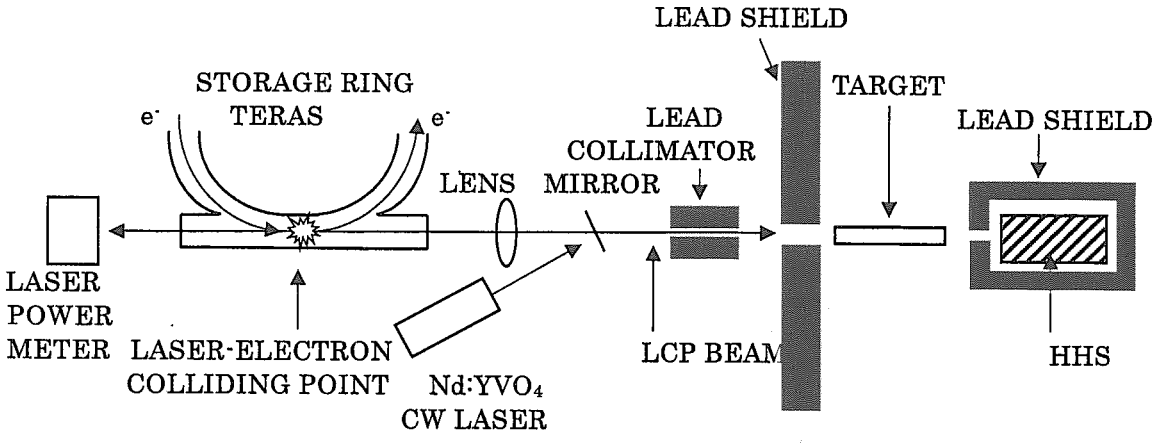

Fig.2 Schematic overview of the NPA experimental area at the LCP facility

3. Results

Solid line and dashed line in Figure 3(a) show the transmitted LCP spectra observed by HHS for a water target enriched to 98 % in ^{18}O and a natural water target, respectively. Figure 3(b) shows the difference of the transmitted spectra, Y(^{16}O) –

Y(^{18}O). The previous data reported the only four resonances at 9.1, 10.3, 11.4, and 13.1 MeV for ^{18}O(γ, abs) reaction in the observed energy region. The present data resolves the four resonances into nine resonances. The details of the analysis and the deduced cross sections are described in ref. 6.

Figure 4 shows the transmitted LCP spectra observed by HHS, Y(●) and Y(○), for a ^{13}C target and a blank target, respectively. A significant sharp dip is shown at 15.11 MeV in the spectrum for ^{13}C. The intrinsic width of the resonance at 15.11 MeV in ^{13}C was known to be 5.5 keV from the ^{9}Be+ α reaction.[10] Assuming the intrinsic width to be 5.5 keV, the energy resolution of HHS is 12 keV for 15.11 MeV photon energy, that is, 0.08 %. This resolution is 20 times superior to that of July's state of art of present day photo-neutron measurement.[11]

4. Conclusions

New measurement method using HHS and LCP has been developed to investigate fine structures in photo-nuclear reactions. The energy resolution has been demonstrated to reach 0.1% by measuring the first T=3/2 resonance peak at 15.11 MeV in ^{13}C. Fine structure peaks in the ^{18}O(γ, abs) reaction have been observed for the first time by utilizing this method. It is required to obtain systematic data of high-resolution photoabsorption cross sections to shed light on the fine structures in photonuclear reactions.

Acknowledgments

Contributions of T. Noguchi and Y. Shigetome during the early stage of the experiments are acknowledged. The experimental success would have been impossible without the cooperative effort of ETL accelerator group. This work has been supported by Japan Nuclear Cycle Development Institute and Electrotechnical Laboratory.

References

[1] Ahrens, J. et al., *Nucl. Phys.* **A251** (1975) 479.
[2] Gurevich, G.M. et al., *Nucl. Phys.* **A338** (1980) 97.
[3] Sherman, N.K. et al., *Phys. Rev.* **C21** (1980) 2328.
[4] Harada, H and Shigetome, Y., *J. Nucl. Sci. Technol.* **32** (1995) 1189.
[5] Ohgaki, H. et al., *Nucl. Instrum. Methods* **A353** (1994) 384.
[6] Harada, H. et al., *Phys. Rev. Lett.* **80** (1998) 33.
[7] Harada, H. et al., *J. Nucl. Sci. Technol.* **35** (1998) 733.
[8] Hubbell, J.H., Seltzer, S.M., *NIST Rep.*, **NISTIR 5632** (1995).
[9] Tomimasu, T. et al., *IEEE Trans. Nucl. Sci.* **30** (1983) 3133.
[10] Hinterberger, F. et al., *ibid.* **A308** (1978) 61.
[11] July, J.W. et al., *Phys. Rev.* **C19** (1979) 1684.

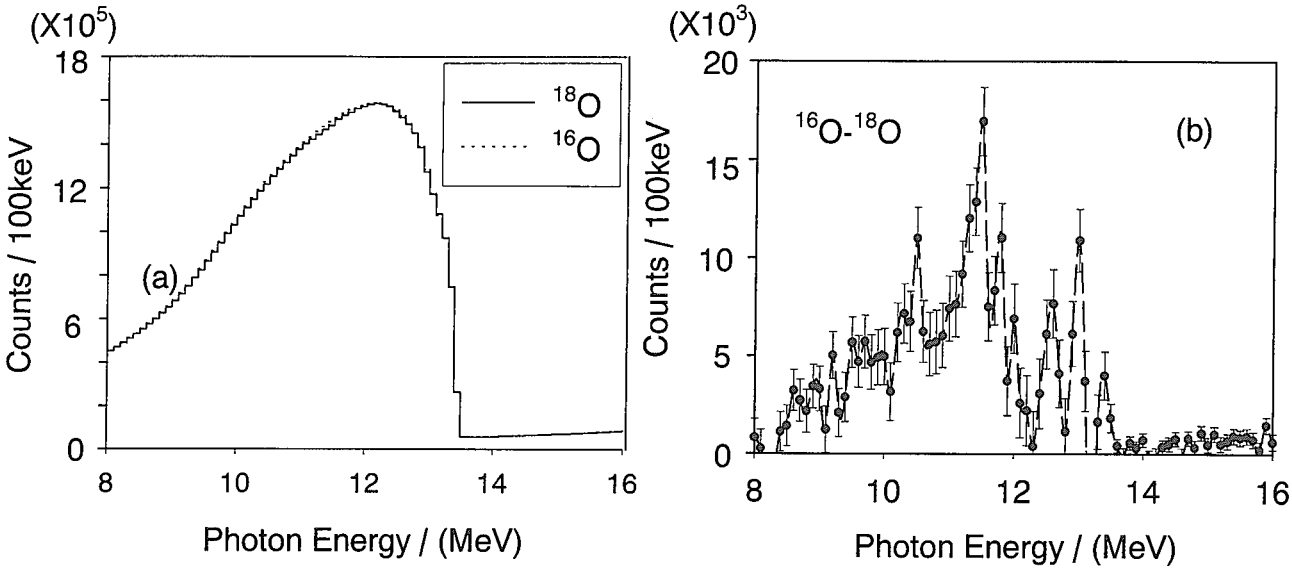

Fig. 3 (a) Transmitted LCP spectra observed by HHS for ^{18}O and ^{16}O targets
(b) Difference of the LCP spectra, Y(^{16}O) - Y(^{18}O)

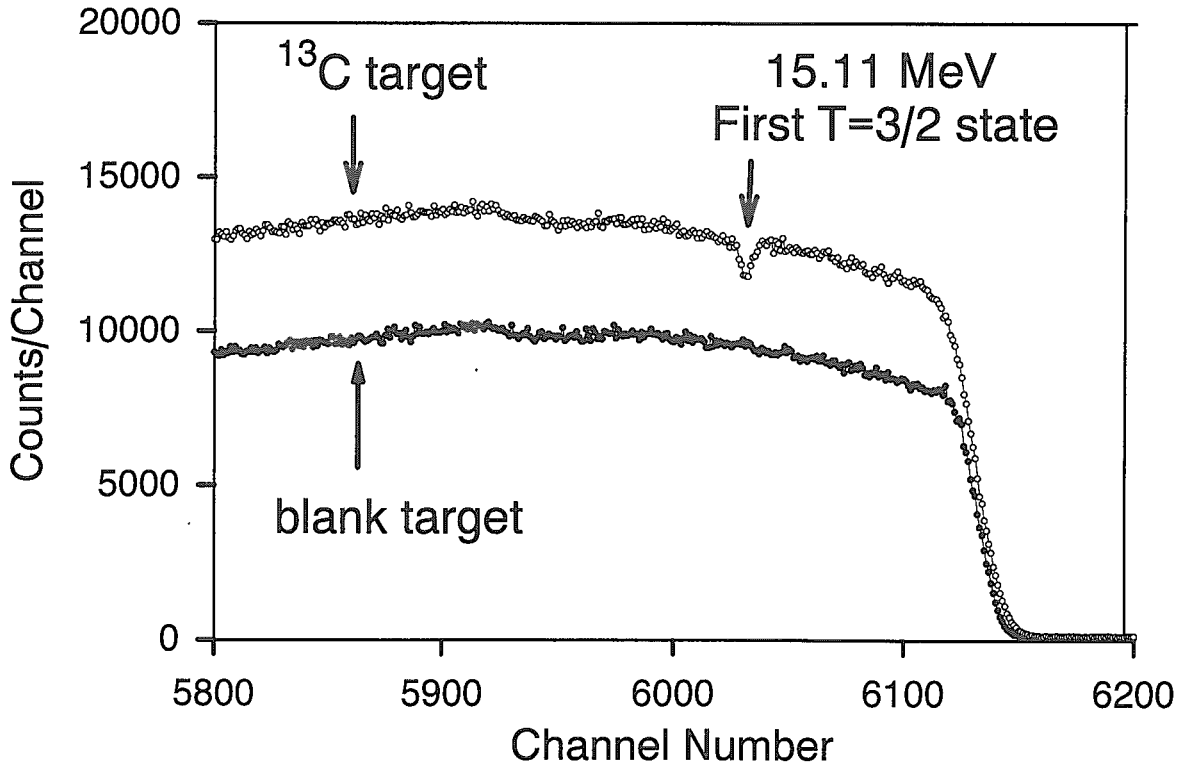

Fig. 4 Transmitted LCP spectra observed by HHS for ^{13}C and blank targets

2.8 Recent Nuclear Data Measurement, Evaluation and Calculation in China

Zhuang Youxiang Zhou Zuying Zhang Jingshang
(China Institute of Atomic Energy)

Recent nuclear data measurement, evaluation and calculation in China related to CENDL-3 are summarized. They include the measurements of secondary neutron and charged particle DDXs, activation CS, fission yields, neutron spectra and radiative capture gamma-rays; the evaluation and calculation.

I. Nuclear Data Measurement

1. Neutron Double Differential Cross Section (DDX)

The DDX are continuously measured at CIAE at 10 MeV incident neutron energy with Tandem by means of both normal and abnormal TOF spectrometers. The D(d,n) neutron source was used and the abnormal TOF spectrometer was used to separate the d-d breakup continuous neutron for measuring low energy part of the secondary neutron spectrum. The measurements for ^{6,7}Li are in progress.

The DDX of ^{9}Be(n,n emission) were measured at incident neutron energy 5.9 and 6.4 MeV at Peking University with Van de Graaf accelerator by using time of flight method at 10 angles between 25 and 150 degree for En=5.9 MeV and 11 angles between 15 and 150 degree for En=6.4 MeV. The energy resolution is about 5%, and the error of data is about 10%.

2. Charged-particle Double Differential Cross Section(CDDX)

The DDX of (n,x emission) were measured at Peking University with 4.5 MV Van de Graaff accelerator by means of gridded ionization chamber(GIC). The D(d,n) reaction was used as neutron source with a deuteron gas target. The DDX of ^{39}K(n,α) at 4.41, 5.46, 6.52 MeV and the differential cross section of ^{6}Li(n,t) at 3.67, 4.42 MeV were completed in last year. In addition, the DDX of ^{40}Ca(n,α) at 5.0, 6.0 MeV and ^{40}Ca(n,p) at 4.41 MeV were improved, which were measured in 1998.

3. Activation Cross Section

The excitation functions have been measured in China by several groups with activation method, such as CIAE, Peking University, Lanzhou University. The influence of the low energy neutrons was carefully paid attention and deducted by irradiating samples in the conditions of gas in and gas out, selecting a monitor with nearly same threshold and similar shape of excitation function as investigated or a group of monitors with different threshold.

4. Fission Product Yield

The fission product yield has been measured at CIAE by means of direct gamma spectrum method. Two HPGe gamma spectrometers with volume 110 cm^3 and 120 cm^3 were used. In last year, the chain yields of 8 products at light peak, 10 at heavy peak and 1 at valley were measured at incident neutron energy 5.5 MeV with HI-13 Tandem and 14.9 MeV with Cockcroft-Walton accelerator.

II. Nuclear Data Evaluation

1.General Purpose File

CENDL-3 was started in 1996 and will be accomplished by the end of 2000. It contains about 200 nuclides. Among them, the data of following nuclides will be newly or reevaluated: fissile nuclides 15, structure materials 18, light nuclides 5, fission products 91. It will contain consistent data between natural elements and their isotopes for structure material, newly evaluated data for fission products, much improved secondary neutron spectra for light nuclides and more gamma-production data(Files 12 ~ 15), double differential cross section(File 6).

1.1 Fissile Nuclides

The evaluation of ^{238}U complete data was completed at Peking University based on the available new experimental data and theory alculation by using codes APOM(automatically adjusting parameter optical model program), FMT(Hauser-Feshbach theory, exiton model), DWUCK and coupled channel optical model. The cross section of inelastic scattering was evaluated and calculated by using coupled channel optical code for first two levels and DWUCK for other higher levels,

the result is consistent with the newly measured data. The neutron double differential cross sections(File 6) were calculated and good agreement with the data measured by M.Baba and Shen was got by adjusting the parameters of FMT and DWUCK based on above experimental data.

The theoretical calculations have been completed for ^{239}Pu and the evaluation is under way. The results have been compared with the data from ENDF/B-6 and JENDL-3.2. The calculation and experimental data collecting are in progress for other Uranium and Plutonium isotopes.

1.2 Structure Material

The evaluation of complete data for natural Ni and its isotopes ^{58,60,61,62}Ni have been completed and improved. Due to the new experimental data are available in last years, the evaluated data have been considerably improved, especially the (n,p), (n,n'p), (n,α), (n,d), and inelastic scattering cross sections. The cross sections between natural Ni and its isotopes are consistent with each other, which was achieved by adjusting them with code CABEI. The energy balance was tested and the energy taken by outgoing particles and the available from the reaction are in balance within several percent.

Also the complete data have been completed for ^{63}Cu, and primary completed for ^{65}Cu. For natural Zr and its isotopes ^{90,91,92,94,96}Zr, the experimental data have been evaluated and the calculations are under way. For natural Fe and its isotopes ^{54,56,57,58}Fe, the calculations have been improved and the evaluations of the experimental data are in progress.

1.3 Light Nuclides

A new model for neutron induced reaction on light nucleus and corresponding code LUNF were developed. The key point of the model is the description of the particle emissions from discrete level to discrete levels in pre-equilibrium states. In the whole reaction processes the angular momentum and parity are conserved and the energy balance is taken into account. The level broadening effect and energy resolution are considered to fit experimental data. Using the code, the calculations for ^{9}Be and ^{12}C have been completed. The calculations for other light nuclei are under way.

1.4 Fission Product Nuclides

According to the plan, the files 1-5 will be included in CENDL-3 for 91 fission product nuclides. So far the evaluations have been completed for 40 nuclides, including theoretical calculation, experimental data evaluation, comprehensive adjusting and checking. The theoretical calculations have been completed for more than 80 nuclides.

2. Special Purpose File

According to the plan, also the special files for fission yield, activation cross section and photonuclear reaction data are being developed.

2.1 Fission Yield

The reference fission yield were continuously evaluated. The evalu-ations have been completed in last year for 15 product nuclides of ^{235}U fission and 25 nuclides of ^{238}U fission. They are as follows:

^{235}U fission: ^{85}As, $^{88,89,90,91}Br$, ^{92}Sr, ^{97}Mo, $^{115g,115m}Cd$, ^{135}Sb, $^{135,137}I$, ^{136}Cs, $^{147,152}Sm$;

^{238}U fission: $^{88,89}Br$, $^{85g,85m,87,88}Kr$, ^{91g}Y, ^{95}Zr, ^{99}Mo, ^{106}Ru, ^{105g}Rh, ^{111g}Ag, ^{115m}Cd, ^{125}Sb, $^{131,137}I$, $^{133g,134g}Xe$, ^{140}Ba, ^{144}Ce, $^{147,148}Nd$, ^{151}Sm, ^{156}Eu, ^{161}Tb.

Taking into account of the special features of the retrieval and processing for fission yield data, a fission yield data evaluation system FYDES have been developed. The system includes data retrieval, data table standardization, data correction and data processing(average with weight, simultaneous evaluation and curve fitting etc.). The system has been used for above reference and other yield data evaluations.

2.2 Activation Cross Section

The activation cross sections were continuously evaluated for about 40 reaction channels to supplement and improve Chinese Evaluated Nuclear Data File CENDL-ACF. The evaluations were combined with experimental measurements closely, and the recommended data were determined with new measured data at CIAE or other laboratories in China, when the discrepancies were faced in the evaluations.

2.3 Photonuclear Reaction Data

The complete data of photonuclear reaction up to 30 MeV, including cross section, double differential cross section, gamma production data of all possible reactions, have been continuously evaluated and calculated by using code GUNF as the task of IAEA CRP. In last year, the evaluations have been completed for nuclides ^{54,56}Fe, ^{209}Bi, ^{63,65}Cu. The evaluations are in progress for nuclides ^{27}Al, ^{9}Be and Cr.

III. Theoretical Calculation

1. General Situation on Model Developing

To fit the needs to set up neutron files UNF program system has been established. This code system includes

- "UNF" code for neutron induced reactions on structure material below 20 MeV including file-6;
- "SUNF" code for neutron induced reactions on fission production below 20 MeV including file-5, which is the simplified edition of UNF code;
- "NUNF" code for neutron induced reactions on natural element below 20 MeV including file-6;
- "CUNF" code for charged particle induced reactions on structure material below 30 MeV;
- "FUNF" code for neutron induced reactions on fissile material below 20 MeV including file-6 or file-5;
- "GUNF" code for gamma-ray induced reactions on structure material below 30 MeV including file-6;

Beside the codes of nuclear reaction calculation some auxiliary codes are also established. "APMN" and "APFO" codes for adjusting optical model parameters of structure materials and fissile materials, respectively. The codes for retrieving experimental data, the codes for plotting and "DWUCK", "ECIS" for calculating direct reaction data have been developed.

To coordinate with the theoretical model calculations the input parameter data files have been established. The evaluated nuclear parameter library (CENPL) includes six sub-library. They are

- "MCC": the atomic masses and characteristic constants of the nuclear ground states;
- "GDP": the giant dipole resonance parameters for gamma-ray strength function;

- "FBP": the fission barrier parameters;
- "DLS": the discrete level schemes and gamma branching ratios;
- "NLD": the nuclear level density parameters;
- "OMP": the optical model parameters.

With the useful tools mentioned above the nuclides calculated for CENDL-3 are about 150.

China Nuclear Data Center joined the CRP on Compilation and Evaluation of Photonuclear Data for Applications, and the relevant data of some structure material and ^{9}Be have been calculated with GUNF and GLUNF codes.

2. Characteristic on Theoretical Model

In the theoretical model the nuclear structure effect is taken into account for multi-particle emission processes. The calculated data included the discrete levels not only for the neutron emission but also for the charged particle emission. The gamma production data can also be calculated. Since the recoil effect is taken into account exactly to maintain the energy balance both in C.M.S. and L.S. in the model, so the energy balance is fully satisfied in the output files. The recoil effect can expanse the spectra of the outgoing secondary particles. If the recoil effect were not taken into account, the spectra would have unseasonable shapes.

Since the method of the double differential cross sections have been developed, so that the file-6 data for all of kinds composed particle emissions can be obtained.

An new model has been developed for calculating all kinds of reaction cross sections and double differential cross sections for neutron induced reactions of light nuclei. Therefore the file-6 can given in CENDL-3. The LUNF code is developed, in which the reaction mechanisms of sequential two-body reaction, two body separation processes and three-body break-up processes are involved. Because the Legendre expansion can be employed in C.M.S. for the file-6 outputting. In this way it will reduce the size of file-6 obviously. Since the emission of the first particle has definite energy, while the secondary particle emissions have ringg-type spectra in C.M.S. So the histogram form is the suitable format to record the file-6.

2.9 Nuclear Data Project in Korea and Resonance Parameter Evaluation of Fission Products

Jonghwa Chang and Soo-Youl Oh
Korea Atomic Energy Research Institute
P.O. Box 105, Yusong, Taejon, Korea 305-600
e-mail: jhchang@kaeri.re.kr, syoh@kaeri.re.kr

Nuclear data activities in the fields of evaluation, processing, measurement, and service in Korea are presented in this paper. As one of the current activities, the neutron resonance parameters for stable or long-lived nineteen fission products have been evaluated and the results are presented here.

1. Introduction

Until mid-nineties, nuclear data relevant activity in Korea Atomic Energy Research Institute (KAERI) had been limited to the generation of the multi-group constant libraries for reactor physics codes to support the design of a research reactor and the localization of nuclear fuel and of power plant design technology. In 1997, the Nuclear Data Evaluation Laboratory (NDEL) was established in KAERI. Korea Ministry of Science and Technology has included the nuclear data project in the long-term nuclear research and development program. The nuclear data services, evaluations, and measurements have been included as a part of the work scopes of nuclear data project. KAERI/NDEL is now leading the nuclear data project in Korea with 12 staffs including 4 temporal staffs. The Pohang Accelerator Laboratory, Seoul National University, Korea Institute of Geology, Mining and Materials, and others are participating in the project.

Current activities are briefly introduced in the next section. As one of the activities, we have evaluated resonance parameters in both resolved and unresolved resonance energy regions for selected 19 stable or long-lived fission products. The next release of ENDF/B-VI will include this new evaluation. The results are presented in Section 3.

2. Nuclear Data Activities in Korea

The KAERI/NDEL has generated and benchmarked the multi-group libraries for lattice physics codes such as WIMS/D, CASMO-3, and HELIOS based on up-to-date evaluated libraries such as JENDL-3 and ENDF/B-VI. Those libraries are used for the design of the research reactor HANARO, advanced fuels for an advanced PWR, and the fast reactor KALIMER. In addition, the libraries for the neutron transport codes such as DANTSYS, DOORS, and MCNP have been generated and benchmarked for the reactor shielding and PWR pressure vessel surveillance.

The evaluation activity has rather short history. The current issue is the burnup credit problem of the spent fuel storage. Among many of related directions, KAERI/NDEL is collaborating on the neutron data of the long-lived fission product nuclides. This work is undergoing together with the Brookhaven National Laboratory as one of the international collaborations. We have completed the evaluation of individual resonance parameters. This work will be presented in the next section. For the higher energy applications such as the transmutation of radwaste, KAERI/NDEL is working on the model calculation for the neutron and proton reaction data at the intermediate energy region. This work is underway as the collaboration with JAERI/NDC. In addition, the photo-nuclear data evaluation up to 140 MeV is under progress as an IAEA CRP to provide data for the electron linac-based isotope production. The evaluation for more than 130 nuclides has been completed. The charged particle nuclear data up to 60 MeV is also under progress. These data are useful for the medical isotope production for PET and SPECT using a cyclotron and also useful for the thin layer activation analysis of metallic materials.

Current objective of the nuclear data experiments is to develop capability and manpower for nuclear data measurements in Korea. The Pohang Accelerator Laboratory is leading the activities. One of them is to construct a pulsed neutron source using a 100 MeV electron linac. The other activity is to obtain and develop measurement skills by participating in the experiments at foreign facilities such as KURRI's. Domestic efforts are the proton scattering experiment using a cyclotron at KAERI hospital by the physics department of Seoul National University and the fast neutron generation using a Van de Graaff at the Korea Institute of Geology, Mining and Materials.

The nuclear data service is provided through internet for domestic and foreign users. The target of the internet web service is to provide data to novice users in the area of nuclear data. The web service consists of a table of nuclide, a cross section plotter, decay schemes, and a capture cross section plotter. Based on the IP address, the number of users who have retrieved the data at least once is 25,817 in the year 1998. Among them, about 1,000 are the frequent users; they have retrieved 7.6 times on the average.

3. Resonance Parameter Evaluation of Fission Products

In many engineering fields dealing with spent nuclear fuels such as storage of spent fuels and transmutation of long-lived isotopes as well as in basic research fields such as astrophysics, the neutron data for fission products are very important especially in the viewpoint of neutron absorption. However, even in the latest release of ENDF/B-VI, most of resonance data for major fission products are those based on old measurements, about 20 years old or more. Although rather recent libraries such as JENDL-3.2 and JEF-2.2 had adopted some recent measurements, still the source for many isotopes was the Mughabghab's BNL compilations published in 1981 and 1984[1,2] as those were. Therefore a need for new evaluations incorporating new measurements has arisen. For selected 19 fission products that largely contribute to the total neutron absorption in a system, we have evaluated resonance parameters in both resolved and unresolved resonance energy regions. In the evaluation, we reviewed all available measured data not only new but also old.

In the resolved resonance region, we adopted the multi-level Breit-Wigner formula. The resonance energy, orbital angular momentum of incident neutron (l), resonance spin (J), neutron scattering width, and radiative width are the parameters to be provided for each resonance. The BNL compilations[1,2] were adopted as the primary sources of resolved resonance parameters and thermal cross sections at 0.0253 eV. Then values recommended in the compilations were revised and/or supplemented by taking into account recent measurements. The old measurements were also revisited: the old ones were corrected, re-normalized, or revived according to relevant new measurements or evaluator's decision, if necessary. In the next step, the bound level resonances were invoked, if necessary, to reproduce reference thermal cross sections and scattering lengths. For a resonance with unknown l value, the Bayesian approach[1] was applied to the calculation of probability that the resonance is due to p-wave neutron. Then l was assigned as either 0 or 1 from the probability. Resonance spins were randomly assigned to resonances for which the spins were unknown. After the assignment of l values for all resonances of an isotope, the distribution of reduced neutron widths was analyzed in terms of the Porter-Thomas distribution. The fit of distribution of measured widths to the theoretical distribution results in the average level spacing and neutron strength function, especially, of s-wave resonances.

The unresolved resonance region was set to cover an energy range up to the first excited level for inelastic scattering, 50~200 keV for most fission products under consideration. The present evaluation provides average resonance parameters for s-, p- and d-wave resonances. In principle, we adopted the average parameters that had been obtained from the analyses of resolved resonances. The level spacing varies with neutron energy according to the Bethe's level density formula,

$$1/D(U,\mathrm{J}) \propto \frac{(2\mathrm{J}+1)}{U^{5/4}} e^{2\sqrt{aU}}\ e^{-(\mathrm{J}+1/2)^2/2\sigma^2},$$

where U is the effective excitation energy that depends on the incident neutron energy, a the level density parameter, and σ the spin cutoff factor. Values of a and parameters for calculating U were

adopted from Refs. 3 and 4. The proportional constant was determined from the s-wave level spacing D_0, which had been obtained from the analysis of resolved resonances. Concerning the d-wave strength functions, as well as p-wave functions for some isotopes, we adopted values from mass-dependent systematics[1,2] for lack of measurements of resolved high l-value resonances. The average gamma widths for p- and d-wave resonances were assumed to be equal to the width for s-wave that had been obtained by averaging known widths of resolved resonances. In some cases, however, the average width for p-wave was adopted from systematics[2] or directly from the measurement (^{95}Mo case). Finally, the average parameters for high l-value resonances, if necessary, were adjusted to reproduce measured capture cross sections in the unresolved energy region.

Table 1 summarizes the sources of evaluation. The old sources before the BNL compilations are not listed except ones that are used for the revision of data in the BNL compilations. In the unresolved region, the capture cross section reproduced using present average parameters show good agreement with the measurements listed in the table. Tables 2 and 3 show the 2200 m/s capture cross sections and capture resonance integrals, respectively. There are significant differences between present evaluation and ENDF/B-VI in capture cross sections of ^{145}Nd and ^{147}Sm as well as in resonance integrals of ^{99}Tc, ^{131}Xe, ^{133}Cs, ^{149}Sm, and ^{153}Eu. However, present resonance integrals of above nuclides are rather close to those from the JENDL-3.2. The other quantities such as the s-wave strength functions and level spacing, the average capture cross sections weighted with Maxwellian spectrum at 30 keV, and so on will be found in a more detailed report. Improvements in Maxwellian-average as well as energy-dependent capture cross sections in the unresolved region are observed in most cases.

We took all available measured data into account for the new evaluation of resonance parameters of major fission products. Therefore, generally speaking, present resonance parameters are more reliable than those in existing libraries are. In addition, the evaluation methods and physics models developed or adopted during this work may be used as standard ones for future evaluations. We have proposed to the Cross Section Evaluation Working Group to substitute newly evaluated resonance parameters for those in current release of the ENDF/B-VI.

4. Concluding Remarks

KAERI/NDEL is working on the evaluation and the processing of the nuclear data and supporting the activities to buildup the capability for the nuclear data measurements in Korea. KAERI/NDEL is also providing an internet service for novice users.

We will continue the nuclear data activity to support the research and development of nuclear energy and radiation applications. In addition to the effort for concentrating domestic capabilities, it is necessary to extend and strengthen the international collaborations, especially with Japan, to meet the needs effectively from various R&D fields.

References

1. Mughabghab, S.F. *et al.*, *Neutron Cross Sections*, Vol.1, Part A, Academic Press (1981).
2. Mughabghab, S.F., *Neutron Cross Sections*, Vol.1, Part B, Academic Press (1984).
3. Mughabghab, S.F. and Dunford, C.L., "New Approach for the Determination of the Nuclear Level Density Parameters," *Proc. Int'l Conf. on Phys. of Nucl. Sci. Technol.*, p. 784, Long Island, U.S.A., Oct. 5-8, 1998.
4. Mughabghab, S.F. and Dunford, C.L., Phys. Rev. Lett. **81**, 4083 (1998).
5. Allen, B.J. *et al.*, Nucl. Sci. Eng. **82**, 230 (1982).
6. Macklin, R.L. and Winters, R.R., Nucl. Sci. Eng. **78**, 110 (1981).
7. Holden, N.E., "Neutron Scattering and Absortion Properties," *CRC Handbook of Chemistry and Physics*, 78th ed., CRC Press (1998).
8. Abagyan, L.P., "The LIPAR-5 Resonance Parameter Library," INDC(CCP)-406 (1997).

Table 1. Sources of Evaluation [a]

Isotope	Thermal Characteristics [b]	Resolved Resonance Parameters	Capture Cross Section in Unresolved Resonance Region [c]
42-Mo-95	87 Koester	68 Wynchank, 76 Musgrove	76 Musgrove, 64 Kapchigashev
43-Tc-99	-	97 Gunsing, 97 Raepsaet	82 Macklin
44-Ru-101	-	85 Anufriev	80 Macklin
45-Rh-103	91 Koester, 70 Ribon	80 Macklin	90 Wisshak, 85 Bokhovko
46-Pd-105	87 Glaettli, 82 Buyl, 80 Antonov	-	82 Cornelis, 79 Macklin
47-Ag-109	-	97 Corvi, 97 Lowie, 83 Mizumoto, 82 Macklin	87 Bokhovko, 83 Mizumoto, 82 Macklin
54-Xe-131	-	96 Skoy, 69 Ribon	-
55-Cs-133	91 Koester, 79 Glaettli	90 Nakajima, 82 Macklin, 81 Popov	91 Bokhovko, 83 Yamamuro, 82 Macklin
59-Pr-141	91 Knopf, 76 Akopian	82 Alfimenkov, 79 Taylor, 69 Morgenstern	79 Taylor, 71 Zaikin, 64 Konks
60-Nd-143	-	77 Musgrove	98 Wisshak
60-Nd-145	-	77 Musgrove, 71 Rohr	98 Wisshak, 85 Bokhovko
62-Sm-147	67 Fenner	93 Georgiev	93 Wisshak, 86 Macklin, 85 Bokhovko
62-Sm-149	82 Word	92 Georgiev	93 Wisshak, 86 Macklin
62-Sm-150	74 Eiland, 62 Halperin, 61 Aitken	-	93 Wisshak, 86 Winters, 63 Macklin
62-Sm-151	-	-	-
62-Sm-152	-	-	94 Luo, 93 Wisshak, 85 Bokhovko
63-Eu-153	-	-	94 Xia, 93 Yu, 87 Macklin, 85 Bokhovko
64-Gd-155	-	90 Belyaev	95 Wisshak, 89 Nakajima, 88 Beer
64-Gd-157	-	90 Belyaev	95 Wisshak, 89 Nakajima, 88 Beer

a: BNL compilations are included in all cases.
b: Capture and elastic scattering cross sections, scattering lengths.
c: ORNL data were corrected according to Refs. 5 and 6.

Table 2. Capture Cross Sections at 0.0253 eV (barn)

Isotope	BNL Compilation	98CRC[7]	ENDF/B-VI [a]	JEF-2.2 [a]	JENDL-3.2 [b]	LIPAR-5[8]	Present [c]	Relative Diff. (%) [d]
42-Mo-95	14.0±0.5	13.4±0.3	14.6	14.0	14.0	–	13.6	−7.4
43-Tc-99	20±1	23±2	19.6	19.1	19.6	–	20.0	2.0
44-Ru-101	3.4±0.9	5±1	3.43	3.42	3.36	–	3.45	0.6
45-Rh-103	145±2	145	147	146	147	–	145	−1.4
46-Pd-105	20.0±3.0	22±2	20.1	21.8	20.3	–	20.9	3.8
47-Ag-109	91.0±1.0	91.2	91.0	90.8	90.5	90.7	90.8	−0.2
54-Xe-131	85±10	90±10	90.6	85.1	85.0	–	90.0	−0.7
55-Cs-133	29.0±1.5	30.4	29.7	29.1	29.0	–	29.0	−2.4
59-Pr-141	11.5±0.3	11.5	11.5	11.5	11.5	–	11.5	0.0
60-Nd-143	325±10	330±10	325	323	330	319	325	0.0
60-Nd-145	42±2	47±6	42.1	41.9	43.8	41.9	49.8	15.5
62-Sm-147	57±3	56±4	57.5	57.2	58.0	56.7	50.0	−15.0
62-Sm-149	40140±600	40100±600	39730	40480	40150	39420	40530	2.0
62-Sm-150	104±4	102±5	104	103	109	108.2	100	−3.9
62-Sm-151	15200±300	15200±300	15250	15190	15160	15160	15170	−0.5
62-Sm-152	206±6	206±15	207	206	206	202	206	−0.5
63-Eu-153	312±7	300±20	313	300	313	312	312	0.0
64-Gd-155	60900±500	61000±1000	61100	60790	60890	60710	60730	−0.6
64-Gd-157	254000±815	254000±3000	255800	253400	254100	253500	253700	−0.8

a: From JEF Report 14, OECD/NEA, Paris (1994).
b: From General Description (MF=1) of JENDL-3.2
c: Calculated using LINEAR–RECENT–SIGMA1–INTER codes
d: Relative Difference = $(1 - \sigma_\gamma^{\text{ENDF/B-VI}} / \sigma_\gamma^{\text{Present}}) \times 100$

Table 3. Capture Resonance Integrals (barn)

Isotope	BNL Compilation	98CRC	ENDF/B-VI [a]	JEF-2.2 [a]	JENDL-3.2 [b]	LIPAR-5 [c]	Present [d]	Relative Diff. (%) [e]
42-Mo-95	109±5	109±5	113	110	119	–	111	−2.2
43-Tc-99	340±20	–	350	304	312	–	312	−12.2
44-Ru-101	100±20	110±30	111	111	100	–	111	0.1
45-Rh-103	1100±50	1180	1035	1035	1040	–	1036	0.1
46-Pd-105	62.2	60±20	111	93.1	96.8	–	95.2	−16.6
47-Ag-109	1400±48	1480	1471	1473	1470	1467	1476	0.4
54-Xe-131	900±100	900±100	1016	890	900	–	882	−15.2
55-Cs-133	437±26	422	383	439	396	–	421	9.0
59-Pr-141	17.4±2.0	14±3	19.0	17.9	18.4	–	17.6	−7.7
60-Nd-143	128±30	128±30	130	130	130	127	130	0.7
60-Nd-145	240±35	260±40	231	231	204	228	245	5.7
62-Sm-147	–	710±50	789	794	781	721	777	−1.4
62-Sm-149	3390	3100±500	3258	3484	3490	3355	3482	6.4
62-Sm-150	358±50	290±30	338	339	325	334	334	−1.2
62-Sm-151	3520±160	3520±60	3449	3465	3410	3397	3430	−0.6
62-Sm-152	2970±100	3000±300	2981	2977	2770	2958	2976	−0.2
63-Eu-153	1420±100	1800±400	1499	1448	1410	1305	1408	−6.5
64-Gd-155	1447±100	1540±100	1555	1543	1540	1437	1537	−1.2
64-Gd-157	700±20	800±100	759	762	763	711	754	−0.7

a: From JEF Report 14, OECD/NEA, Paris (1994) b: From General Description (MF=1) of JENDL-3.2

c: Integrated from 0.5 eV to the upper energy of resolved resonance region

d: Integrated from 0.5 eV to 100 keV with 1/E spectrum e: Relative Difference = $(1 - I_\gamma^{\text{ENDF/B-VI}} / I_\gamma^{\text{Present}}) \times 100$

2.10 Study on Nuclear Power Introduction into Vietnam

Vuong Huu Tan
Vietnam Atomic Energy Commission
59 Ly Thuong Kiet, Hanoi
Vietnam
Tel: (84 4) 8 256 647
Fax: (84 4) 8 266 133
E-mail: vuonghuutan@hotmail.com

The report presents main results of the study on nuclear power introduction into Vietnam which have been carried out at Vietnam Atomic Energy Commission in collaboration with Ministry of Industry of Vietnam and other countries like Japan, Canada and Korea. The study covers all topics related to the nuclear power introduction into Vietnam such as electricity demands and supply, economics, finance, technology, safety, manpower, site selection etc.

I. Introduction

In the year 1986, the Government of Vietnam began launching an economic reform with the aim of shifting centrally planned economy to socialist-oriented market one with regulation of the State. As a result of the reform, the Vietnamese economy developed significantly in the period of 1989-1997 (see Table 1).

Since the year 1997, however, because of financial crisis in Asia the Vietnamese economy has been facing many difficulties, especially in foreign direct investment and export sectors. GDP growth rate in the year 1998 reduced to below the planned targets. The Government of Vietnam has reviewed and adjusted some targets of economic development in the period of 1999-2020.

Table 1: GDP Growth Rate in Vietnam in the Period of 1989-2000

Year	89-90	91-94	95	96	97	98	99-2000*
GDP growth rate (%)	6.8	8.5	9.5	9.6	8.2	5.8	5-6

* estimated

The population of Vietnam is now about 76.3 million, of which around 80% is in the rural area and the remaining 20% in the urban area. The annual population

growth rare, now, is 1.7% against 2.2% in the beginning of this decade.

During recent years, Vietnam has been conducting a national development strategy of industrialization and modernization with the aim of creating a quantum leap in the economy, at the same time strengthening potential of the country. Together with economic growth, energy and electricity production have been increased remarkably (see Table 2).

Table 2: Energy Production in Vietnam in the Period of 1995-2000

Type	Unit	1995	1996	1997	1998	1999*	2000*
Coal	MT	8.35	9.80	11.40	10.70	11-12	11-12
Crude oil	MT	7.60	8.80	10.91	12.60	14.50	16-18
Natural gas	Gm^3	0.22	0.30	0.53	1.10	1.50	2.5-3.0
Electricity	TWh	14.64	16.96	19.15	21.65	23 - 25	25 - 27

* estimated

Main targets in the policy of electricity development in Vietnam are:

- Increasing effectiveness of electricity use;
- Conducting rural electrification;
- Constructing a sound policy on electricity price;
- Encouraging private investment;
- Diversifying electricity production sources;
- Minimizing environmental impacts caused by electricity production sector;
- Studying possibilities of the introduction of nuclear power into Vietnam;
- Ensuring energy supply security.

For the time being, two chief duties of the electricity production sector in Vietnam are:

1) To concentrate very effort on upgrading and enlarging some existing hydropower, coal-, oil- and gas-fired power plants, in the meantime on building new ones in order to meet increasing electricity demand and to reduce hydropower percentage in the sources structure to below 50% after the year 2003.

2) To conduct long-term planning of electricity supply sources development up to the year 2020, in which possibilities of the introduction of nuclear power into Vietnam need to be thoroughly considered.

Realizing the important role of the energy, especially, electricity in the

national economy, although the economy is facing many difficulties, the Government continues to give high priority in investment for renovating and upgrading some existing power plants, as well as for building new ones. The Government has also formulated a national energy programme "*Strategy and Policy of Sustainable Energy Development (1996-1999)*" aimed to define an energy policy in the future.

In order to evaluate the role of nuclear power in the national electricity supply structure, the Government has assigned the Ministry of Industry (MOI) and Vietnam Atomic Energy Commission (VAEC) to jointly conduct the project "*Overview Study on Possibilities of the Introduction of Nuclear Power into Vietnam (1996-1999)*". In the meantime the International Atomic Energy Agency (IAEA) supported the VAEC in carrying out the technical co-operation project "*Pre-feasibility Study on the Introduction of Nuclear Power into Vietnam (1996-1999)*".

II. Existing Status of Electricity Production in Vietnam

Electricity supply structure in Vietnam, now, is composed of hydropower, coal-, oil- and gas-fired power, in which hydropower and coal-fired power plants are mainly located in the North, and oil- and gas-fired power ones are chiefly situated in the South. In the year 1994, a North-South 500 kV high voltage line with a length of 1500 Km was established and brought into operation, which has contributed to better dispatching of electricity supply in the country.

Total installed capacity, so far, is 5,559 MW (of which IPP plants is 425 MW), available capacity is 5,130 MW, of which hydropower accounts for a biggest portion of 55%, coal-fired power 24% and diesel & gas turbine 21%.

In the year 1998, total amount of electricity production is 21,654 GWh, of which the shares of hydropower, coal-fired and diesel & gas turbine power are 51%, 26%, and 23%, respectively.

Annual growth rates of capacity demand and total electricity production in the period of 1990-1998 are given in Table 3.

Table 3: Historical Development of the Power System (1990-1998)

Year	1990	1991	1992	1993	1994	1995	1996	1997	1998
Capacity Demand (MW)	1,660	1,850	2,005	2,141	2,408	2,774	3,177	3,582	3,875
Total Electricity Production (GWh)	8,678	9,152	9,654	10,665	12,248	14,636	16,960	19,151	21,654
Growth rate (%)	-	5.5	5.5	10.5	15.2	19.1	15.9	12.9	13.1

From the Table 3, we see that the annual average growth rate of electricity production in the period 1990-1998 is 12.2%, meanwhile annual average growth rate of GDP is 8.2%, so that the elasticity on electricity is 1.5.

Projection on electricity demand of the period 1995-2020 is conducted according to the elasticity approach on electricity demand and GDP growths. Relative to the economics development scenarios, three electricity demand scenarios are forecasted as shown in Table 4.

Table 4: Projection on Electricity Production (1995-2020)

Unit: GWh

Year	1995	2000	2005	2010	2015	2020	Annual average growth rate
Low Scenario	14,636	26,000	42,409	64,553	96,906	142,113	9,5 %
Base Scenario	14,636	26,000	44,230	70,437	109,439	167,002	10.2 %
High Scenario	14,436	26,000	46,554	78,466	126,949	201,367	11.0 %

III. Electricity Generating System Expansion Planning in the period of 1995-2020

3.1. Projection on the capacity of the indigenous fuel resource for electricity production.

Resulting from the studies on reserves and capacity of exploiting the indigenous primary energy resources in the period 2015-2020, forecasted amounts of the primary energy productions per year are estimated as follows:

1. Coal: 15 MT (6, 7 MT used for electricity production)
2. Crude oil: 20 – 25 MT
3. Natural gas: 15 bill. m^3 (12 bill. m^3 used for electricity production)
4. Hydro power: 50 – 60 bill. kWh
5. Geothermal: 200 MW
6. Uranium: reserve 200,000 Tonne of low content, of which 50% is the economically feasible

3.2. Electricity generating system expansion planning up to 2020

According to energy experts, after the year 2015, the electricity yield produced from the indigenous fuel sources would not be able to meet the electricity consumption demand, and around the year 2020, the Vietnam would be short of from 30 to 90 billion kWh every year.

In order to solve that problem, Vietnam would have to import electricity from neighbor countries and fuel to produce electricity. Vietnam already concluded with Laos an agreement, under which after the year 2003 Vietnam will be able to import from Laos about 10 billion kWh every year. Another possibility of importing electricity from China about 10 billion kWh every year is also taken into account.

Possibility of importing oil and liquefied natural gas (LNG) to produce electricity is not considered because of high cost, hence not economic competitiveness.

Supposing coal import is considered as the sole solution to the anticipated shortage of electricity, after the year 2020 Vietnam would import from 5 to 25 million tonnes of coal every year. It would not be feasible for Vietnam to import a huge amount of coal due to the problems related to poor technical infrastructure, the environment protection and energy supply security.

Despite the fact that nuclear power cost is slightly higher than that of conventional electricity production type, nuclear power would be well acceptable if strategic aspects such as diversification of energy, energy supply security, the environment protection, and development of national potential of science and technology are taken into consideration. Furthermore, nuclear power can well compete with imported coal-fired power economically.

With that approach, the projects related to possibility study on the introduction of nuclear power into Vietnam have agreed and come to a conclusion that nuclear power need be considered as an option in the future. If the Government approves the project on NPP construction in Vietnam, the first nuclear power plant would be brought into commercial operation in the year 2017. The total installed capacity of nuclear power would be able to reach from 1200 MW, accounting for 3.6% (according to Base Scenario) to 4000 MW, accounting for 10.4% (according to High Scenario), in the year 2020. Following that direction, after the year 2020 Vietnam would continue building some more new nuclear power plants.

In parallel with the long-term electricity planning studies, the site survey for NPP has been conducted. The VAEC in cooperation with IE has carried out preliminary survey and selection of 6 sites for NPP construction. These sites are mainly located in the South of Central Region of Vietnam. They are listed below (in priority order).

1. Commune VINH HAI, district NINH HAI, province NINH THUAN
2. Commune HOA THANG, district BAC BINH, province BINH THUAN
3. HON LA, commune QUAN DONG, district QUANG TRACH, province QUANG BINH
4. Commune HON ROM, PHAN THIET, province BINH THUAN
5. Commune PHUOC DINH, district NINH PHUOC, province NINH THUAN
6. Commune HOA TAN, TUY HOA, province PHU YEN

IV. The major activities related to nuclear power development in Vietnam

On August 1999, the Ministry of Science, Technology and Environment (MOSTE) in colaboration with the Ministry of Industry (MOI) submitted to the Government the *Nuclear Power Development Plan in Vietnam (period 1998-2020)* on the basic of the research done by Vietnam Atomic Energy Commission and Institute of Energy. We suggested the Government to formulate a *Long Term Programme on Study of Nuclear Power Development in Vietnam* and to establish a *Committee for Preparation of Nuclear Power Project* belonged to the Government.

From recent years, the cooperative relation between Vietnam and several countries in carrying out the possibility study of the introduction of nuclear power into Vietnam has been developing. Japan is playing an active role in helping Vietnam in this field. The organizations, institutions and companies of Japan including STA, JAIF, JAERI, JNC, JCI, JAPC, MITSUBISHI, TOSHBA have taken part in jointly conducting site survey, workshops, seminars, and offered Vietnam the material and NPP models necessary to project activities. Several Vietnamese high rank delegations were invited to attend the conferences and forums on nuclear power organized in Japan. Every year, many Vietnamese researchers and experts have been sent to Japan to train and study in the fields relating to nuclear power. We do hope that the cooperation between two countries will be strengthened and developed continuously.

In current unfavorable economic situation, the introduction of nuclear power into Vietnam is facing with many challenges. First, it needs to be approved by the Government, ratified by the National Assembly, and accepted by the public. Then, it has to be proven to be acceptable in terms of economics, and it has to be gained strong and reliable commitment of finance arrangement. After that, it requires a necessary infrastructure together with respective capable and qualified manpower.

However, if the Asian economy, in general, and the Vietnamese economy, in particular, are soon restored, if the Vietnamese economic growth rate increases, if energy supply security and diversification of electricity supply sources are taken into consideration, and, especially, Clean Development Mechanism (CDM) is accepted and implemented worldwide, we do hope that Nuclear Power would be introduced into Vietnam in the near future.

References

1. Report of the Government Project on *Overview Study on Possibilities of the Introduction of Nuclear Power into Vietnam (1996-1999).*
2. Report of the IAEA TC Project on *Pre-feasibility Study on the Introduction of Nuclear Power into Vietnam (1996-1999).*
3. Report of the National Energy Programme on *Strategy and Policy of Sustainable Energy Development (1996-1999).*

2.11

Customization of ENDF/B-VI and JENDL3.2 Basic Data for MCNP Calculation and Measurements of Neutron Cross Section at INST, AERE, SAVAR

S.I. Bhuiyan, N.I. Molla, T.K. Chakrobortty, M.Q. Huda, M.A.W. Mondal
Institute of Nuclear Science & Technology (INST), Atomic Energy Research Establishment (AERE), Savar, P.O. Box 3787, Dhaka- 1000, BANGLADESH
e-mail: aere@bangla.net

The NJOY94.10^{+}, a version of NJOY, has been installed in a VAX computer under Open VMS operating system. ENDF/B-VI, latest release of ENDF data, has been also implemented in the same system. A data library has been processed using the modules RECONR, BROADR and ACER of NJOY code. MCNP4B2 computer code has been used to validate the prepared data library for some benchmark experiments. The results obtained have been found to be in good agreement with the experimental results. Excitation function have been measured for ^{81}Br(n,alpha)^{78}As, ^{79}Br(n,alpha)^{76}As, ^{73}Ge(n,p)^{73}Ga, ^{72}Ge(n,p)^{72}Ga, ^{64}Zn(n,p)^{64}Cu, ^{68}Zn(n,alpha)^{65}Ni, and ^{70}Zn(n,2n)^{69m}Zn reactions in the neutron energy range 13.57-14.71 MeV via Activation technique.

1. Introduction

The NJOY [1] nuclear data processing system is a comprehensive computer code for producing pointwise and multigroup nuclear cross sections and related quantities from evaluated nuclear data in the ENDF format. The latest version, ENDF/B-VI [2], of the release 3 has been used to generate cross section for some benchmark problems and TRIGA reactor calculations.

2. Generation of Cross Section Library for MCNP4B2

For the MCNP continuous- energy neutron- photon Monte Carlo code, the ACER module prepares libraries in ACE (a compact ENDF) format. One of the design goals for MCNP has been to use the most detailed presentation of the physics of a problem that is practical. Therefore, the ACE format has evolved to include all the details of the ENDF representations for neutron and photon data. However, for sake of efficiency, the representation of data in ACE format is quite different from that in ENDF.

The following benchmarks demonstrate and test the preparation of ACE - format libraries for the MCNP code. The materials selected for processing were H-1, O-16, AL-27, U-234, U-235, U-238, Pu-239, Pu-240, Er-166, Er-167.

3. Comparison with benchmark problems

This study was undertaken to benchmark the generated continuous energy neutron cross sections for the Monte Carlo code MCNP4B2 against a set of critical experiments performed at room temperature to establish the basic data processing capability developed at INST, AERE, Savar. To determine the validity of the generated neutron cross section from ENDF/B-VI and JENDL3.2 for MCNP4B2 (latest version of MCNP) five experimental critical assemblies were analyzed. Each system was modeled and the simulation results were compared with the experimental data.

(i) **GODIVA :** The specifications used to define a bare uranium sphere were taken from the data of G.E. Hansen and H.C. Paxton [3] which was originally generated at Los Alamos National Laboratory, USA and then revised there in 1969. Lady GODIVA, as the setup was called, is an example of a fast neutron critical system. It was a simple geometry, consisting of a 52.42kg sphere of U (93.71)-93.71% ^{235}U enriched. The density of the system was measured and found to be 18.74 gm/cc. These data correspond to a sphere of radius equal to 8.741 cm.

(ii) **JEZEBEL at 95.5% ^{239}Pu Enrichment:** Jezebel was similar to the Godiva experiment and was reevaluted by G.E. Hansen and H.C. Paxton [3] at LANL in 1969. This system consisted of a bare plutonium sphere. Two different isotopic combinations of ^{240}Pu and ^{239}Pu were analyzed - a ^{239}Pu composition of 95.5% and one of 80%. In both instances, the remaining material was ^{240}Pu. These are "fast" critical assemblies with a relatively hard spectrum. The 95.5% ^{239}Pu system was a 17.02 kg sphere with a density of 15.61 gm/cc and a radius of 6.385 cm.

(iii) **JEZEBEL at 80% ^{239}Pu Enrichment:** The 80% enriched system had a critical mass of 19.46 kg, a density of 15.73 gm/cc and a radius of 6.660 cm.

(iv) - (v) **TRX-1 and TRX-2 Experiments:** This pair of experiments [4] are parts of the CSEWG thermal benchmarks and consisted of cylindrical aluminum clad metallic fuel rods in water. The pitch was triangular and the system was modeled as an infinite medium. Published leakage factors were then [5] used to obtain the effective multiplication factor as well as other integral quantities. The experiments were conducted at room temperature. The pitches for TRX-1 and TRX-2 are 1.806 cm and 2.174 cm respectively. The parameters of the experiments are as follows.

Material	Outer radius (cm)	Isotope	Atom/Density (atom/barn-cm)
Fuel	0.4915	U-235 U-238	6.2530e-4 4.7205e-2
Void	0.5042	----	-----
Clad	0.5753	Al-27	6.0250e-2
Moderator	-----	H-1 O-16	6.67060e-2 63.3380e-2

4. Monte Carlo Simulation and Results

All MCNP simulations were performed on a 133 MHz Pentium PC under Windows95 operating system. The required cross section sets used as the various temperatures were generated in our laboratory at Institute of Nuclear Science & Technology (INST) from both the ENDF/B-VI and JENDL3.2 data using the NJOY94.10^{+} cross section generation code which constructs, broadens and formats the data into the appropriate form for MCNP. Another two cross section sets were also used which were derived from ENDF/B-VI data processed at Los Alamos National Laboratory, USA and JENDL3.2 data processed at Japan Atomic Energy Research Institute (JAERI), Japan, in order to compare our processed data with those processed in advanced laboratories in the world.. Full S(α,β) treatment [6] was used for thermal scattering of hydrogen in the water and this was obtained from the standard set that accompanied the MCNP4B2 code. The computation for all the cases were run using 500 cycles containing 3000 particles each, with 100 settle cycles to give a total of 1,200,000 histories. However, for TRX-1 & 2, 150 cycles were run containing 3000 particles each with 25 settle cycles to give a total of 375,000 histories. The code generates k_{eff} information using

the track length, collision and absorption estimators, as well as various combinations of these, to give a total of eleven estimates for the k_{eff} value. The combined average of the absorption /collision/track-length estimator is quoted as the k_{eff} value in MCNP. In addition to the eigenvalue comparisons, local integral quantities like fission density comparisons were included for some of the experiments. The experimental uncertainty in the eigenvalues for TRX 1-2 experiments have been reported as about 0.2%. A relative error of 0.003 was assumed to be an acceptable fluctuation in the MCNP tally. The results from the GODIVA and JEZEBEL simulations are presented in Table I and for TRX-1 and TRX-2 in Table II.

Table I. Results from the simulation of the GODIVA and JEZEBEL experiment

Experiment	k_{eff}				
	Experimental result with (relative error)	MCNP4B2 result with (relative error)			
		ENDF/B-VI		JENDL3.2	
		LANL	INST	JAERI	INST
GODIVA	1.00000 (0.00300)	0.99546 (0.00053)	0.99681 (0.00051)	1.00156 (0.00056)	1.00035 (0.00058)
JEZEBEL (95.5%)	1.00000 (0.00300)	1.00194 (0.00051)	1.00334 (0.00057)	1.00284 (0.00053)	1.00289 (0.00055)
JEZEBEL (80%)	1.00000 (0.00300)	1.00847 (0.00053)	1.00765 (0.00055)	1.01042 (0.00054)	1.01010 (0.00056)

Table II. Result from the simulation of the TRX-1 and TRX-2 experiment

Parameter	Experiment Studied	Experimental result with (relative error)	MCNP4B2 result with (relative error)			
			ENDF/B-VI		JENDL3.2	
			LANL	INST	JEARI	INST
k_{inf}	TRX-1	1.17932 (0.00200)	1.17777 (0.00067)	1.18221 (0.00076)	1.18322 (0.00079)	1.18332 (0.00069)
	TRX-2	1.16645 (0.00200)	1.16441 (0.00063)	1.16825 (0.00063)	1.16896 (0.00068)	1.16968 (0.00059)
k_{eff}	TRX-1	1.00000 (0.00200)	0.99863 (0.00067)	1.00239 (0.00076)	1.00325 (0.00079)	1.00333 (0.00069)
	TRX-2	1.00000 (0.00200)	0.99625 (0.00063)	1.00154 (0.00063)	1.00215 (0.00068)	1.00277 (0.00059)
δ^{28}	TRX-1	0.09460 (0.00410)	0.09885 (0.00195)	0.09780 (0.00165)	0.09498 (0.00210)	0.09544 (0.00180)
	TRX-2	0.06988 (0.00350)	0.06988 (0.00185)	0.06924 (0.00200)	0.06737 (0.00188)	0.06777 (0.00195)

The eigenvalue estimates of MCNP using our processed data from ENDF/B-VI and JENDL3.2, as shown in Table I, compare very well with the GODIVA and JEZEBEL experiments and the relative errors are also much lower than the acceptable limit for MCNP. In some instances MCNP calculation using our processed data shows relatively better agreement than those with processed data of LANL and JAERI laboratories and this is due to the fact that we used less fractional tolerance the neutron cross section using the NJOY data processing code.

In case of the TRX-1 & 2 experiments, in addition to the k_{eff} and k_{inf} values, the ^{238}U to ^{235}U total fission reaction ratio, δ^{28}, has also been studied. This factor is used to convert infinite medium simulation results to the actual finite critical experiment results. Table II shows that the eigenvalue predicted by MCNP using our processed data from ENDF/B-VI and JENDL3.2 is found to be in excellent agreement with experimental results and the relative error is also very much within the acceptance limit.

5. Conclusion

The set of critical experiments studied in this report have different fuel types, temperatures and fuel-to-moderator ratios. Thus a study of these experiments provides a rigorous test of the performance of any processed cross section for MCNP code. The results for different critical experiments obtained with our processed data are found to be in very good agreement with the experimental values. The deviation from the mean is well within the acceptance limit for MCNP. In some instances MCNP calculation using our processed data shows relatively better agreement than those obtained with data processed in LANL and JAERI laboratories, as because we used less fractional tolerance to generate the neutron cross section using the NJOY data processing code. It is also clear that the MCNP code coupled with the processed cross section from ENDF/B-VI and JENDL3.2 data is accurate enough to serve as a benchmark to compare with the experimental results. This study has also provided an independent validation of the ENDF/B-VI and JENDL3.2 data and the NJOY cross section processing code for reactor criticality calculations at different temperatures. The results demonstrates that the data processed at INST can be used with confidence for our reactor calculations. Therefore, the Er-166 and Er-167 cross sections processed in INST were used to support MCNP calculations for our TRIGA reactor which yielded very good agreement with experimental results.

6. 14 MeV Neutron Nuclear Data Measurements

6.1 Introduction

Extensive measurements of fast neutron induced reactions cross sections on structural materials of fission and fusion reactors have been carried out during the last decades at several laboratories over the neutron energy range from threshold upto 15.0 MeV. Excitation function of some reactions on the isotopes of Zn, Ge and Br in the neutron energy range 13.74 to 14.71 MeV have been measured. The measured cross section data together with nuclear model calculations using statistical code EXIFON are reported here in some cases.

6.2 Experimental

High purity target materials of Zinc, Germanium and Bromine pellets each sandwiched between aluminium foils were irradiated at 0^0, 30^0, 40^0, 60^0, 70^0, 80^0, 90^0, 110^0, 120^0 and 166^0 in a ring geometry arrangement over a period of 1-3 hours. Neutrons were produced at J-25

neutron generator via dt reaction with 110 keV deuterons and 300 μA beam. The effective neutron energy at each angular position was determined by measuring the ratio of the ^{89}Zr to ^{92m}Nb specific activities induced in Zr and Nb foils by (n,2n) reactions [7]. ^{27}Al(n,alpha)^{24}Na served as monitor reaction. Cross section data for this reaction was taken fron Vonach [8]. The radioactivity of the reaction products was measured by using a high resolution HPGe detector. The detector was calibrated with a set of standard gamma ray sources. Canberra S-100 MCA master board package based personal computer system was used for the data acquisition. Gamma software GANAAS has been used for the analysis of gamma ray spectra. The count rates were corrected for dead time loss, coincidence effect, detector efficiency and gamma transition intensities.

6.3 Results and Discussions

This work literature data [9-24] and values obtained via nuclear model calculations with the statistical code EXIFON [25], based on model of statistical multistep direct and multistep compound reactions, are shown in figs. 1-6 as a function of neutron energy. The uncertainty in the cross section values represents both systematic and statistical errors.

Acknowledgement

The authors thank the Chairman Bangladesh Atomic Energy Commission for supporting the work. One of the authors (N.I. Molla) gratefully acknowledge the financial support and invitation from JAERI and the Organizing Committee of the Symposium.

References

[1] MacFarlane R.E. and Muir D.W.: "The NJOY Nuclear Data Processing System 91," LANL-12740-M, October (1994).
[2] ENDF/B-VI - The U.S. Evaluated Nuclear Data Library for Neutron Reaction Data, the US National Nuclear Data Center, BNL, New York, USA, June (1993).
[3] Hansen G.E. and Paxton H.C.: "Reevaluated Critical Specifications of Some Los Alamos Fast-Neutron Systems," LA-4208, LANL, USA, (1969).
[4] Hardy J. et. al.: "A Study of Physics Parameters in Several Water Moderated Lattices of Slightly Enriched and Natural Uranium," WAPD-TM-931, Bettis Atomic Power Laboratory, USA, (1969).
[5] Hardy J. et. al.: "A study of Physics Parameters in Several H_2O-Moderated Lattices of Slightly Enriched and Natural Uranium," Nucl. Sci. & Eng., 40, p 101-115, (1970).
[6] MCNPXS- Standard Neutron, Photon, and Electron Data Libraries for MCNP4B, DLC-189, LANL, USA, January (1998).
[7] Csikai J.: Handbook of fast Neutron Generators, Vol. 1, CRC Press Inc. Boca Raton, Florida, 3 (1987).
[8] Vonach H.: Nucl. Data Standards, Technical Report Series 227, IAEA, Vienna, 59 (1983).
[9] Bormann M.: Nucl. Phys. 65, 257 (1965).
[10] Konno C., Ikeda Y., Oishi K., Kawade K., Yamamoto H. and Maekawa H.: JAERI Report, 1392 (1993).
[11] Pai H.L., Clarke R.L. and Cross W.G.: Nucl. Phys. A164, 526 (1971).
[12] Press I.L. and Pink K.W.: "Activation Cross Section of Nickel, Cobalt and Zinc for 14.8 MeV neutrons" NP. 15, 326 (1960).

[13] Allan D.L.: "An experimental test of the statistical theory of nuclear reactions", NP 24, 274 (1961).
[14] Donald G. Gardner and Yu-wenyu, " The (n,α) reaction induced by 14.5 MeV neutrons for elements in the range 6 ≤Z ≤30", NP60,49 (1964).
[15] Ranakumar N., Kondaiah E. and Fink R.W.: "Neutron Activation Cross Section at 14.4 MeV for Si and Zn isotopes", NP. A122, 679 (1968).
[16] Bramlitt E.T. and Fink R.W.: "Rare Nuclear Reactions Induced by 14.7 MeV neutrons", PR 131, 2449-2658 (1963).
[17] Molla N.I. and Qaim S.M.,: "A systematic study of (n,p) reactions at 14.7 MeV", NP. 283, 269 (1977).
[18] Molla N.I.: "A study of some (n,p) and (p,γ) reactions" Ph.D. Thesis, Dhaka University, (1981).
[19] Paul E.B. and Clarke R.L.: Can. J. Phys., 31, 264, (1953).
[20] Demichelis F., Guidetti ., Miraldi E. and Oldano C.: Nuovocim, B58, 177 (1968).
[21] Wood R.E., Cook W.S., Goodgame J.R. and Fink R.W.: Phys. Rev. 154, 1108 (1967).
[22] Rieppo R., Keunanen J.K. and Valkonen M.: J. Inorg. Nucl. Chem. 38, 1927 (1976).
[23] Levekovskij V.N.: Sov. Physics-JETP, 18, 213 (1964).
[24] Khurana C.S.: GOVIL, I.M. Nucl. Phys. 69, 153 (1965).
[25] Kalka H.: "EXIFON-A Statistical Multistep Reaction Code", NEA DATA BANK, Saclay, France (1991).

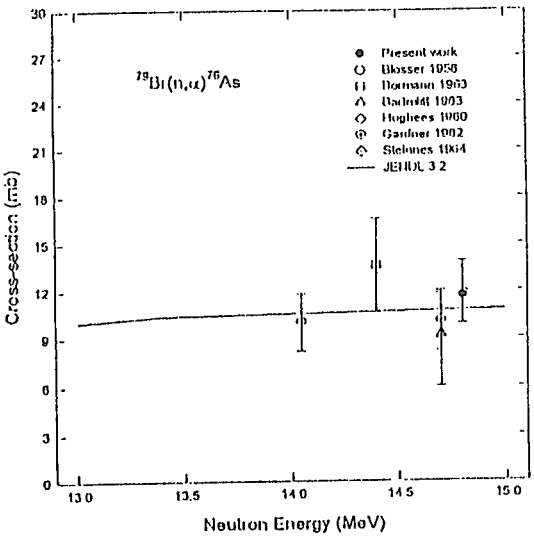

Figure 1: Excitation function of ^{79}Br(n,α)^{76}As reaction in 13 - 15 MeV neutron energy region

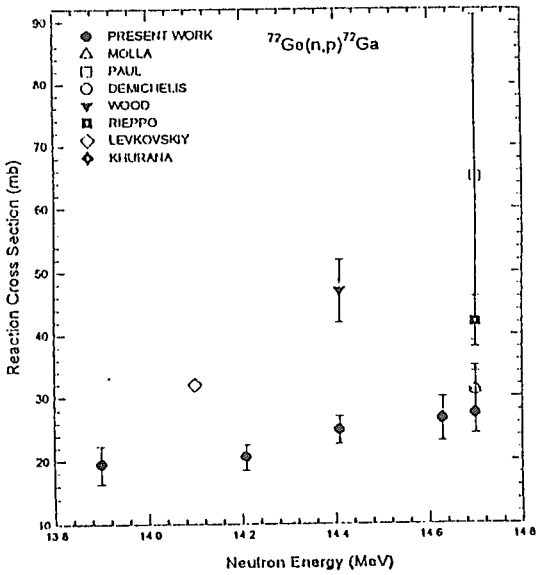

FIG. 2. THE EXCITATION FUNCTION OF ^{72}Ge(n,p)^{72}Ga REACTION IN THE ENERGY RANGE 13.90-14.70 MeV.

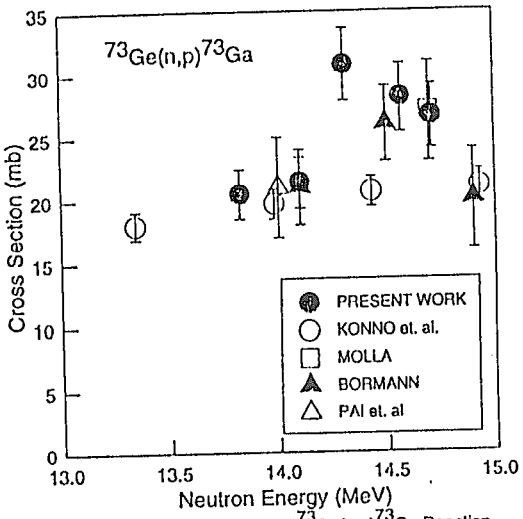

Fig.3. Excitation Function of ^{73}Ge(n,p)^{73}Ga Reaction.

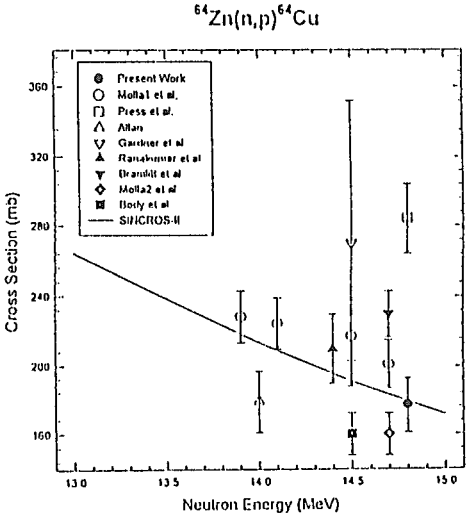

Fig. 4 Excitation Function of ^{64}Zn(n,p)^{64}Cu Reaction

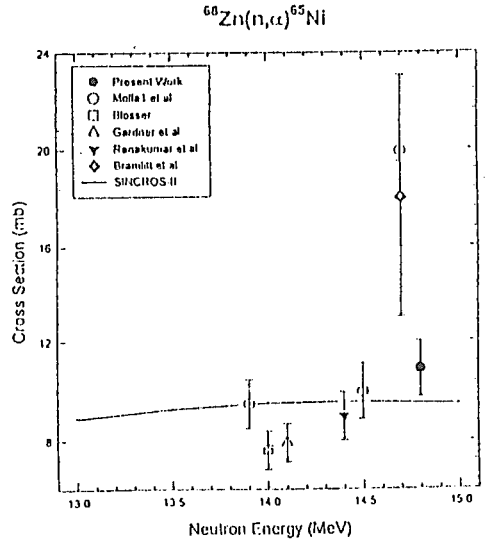

Fig 5 Excitation Function of ^{68}Zn(nα)^{65}Ni Reaction

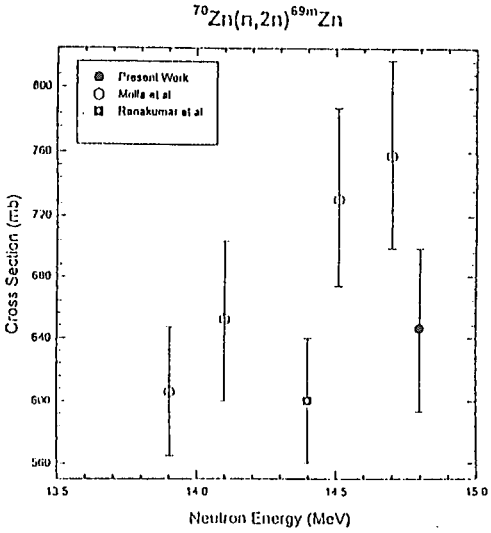

Fig. 6. Excitation Function of ^{70}Zn(n,2n)^{69m}Zn Reaction

2.12 EMPIRICAL SYSTEMATICS FOR SELECTION OF THRESHOLD REACTION EXCITATION FUNCTIONS.

V.N.Manokhin, A.I.Blokhin

Institute of Physics and Power Engineering, Obninsk, Russia
E-mail: manokhin@ippe.rssi.ru
blokhin@ippe.rssi.ru

Abstract

This report is devoted to empirical excitation functions systematics of threshold reactions (n,p), (n,α), (n,2n) and (n,3n). The shapes and maximum cross sections of excitation functions were analysed as functions of neutron excess (N-Z) and mass number A. Some systematical trends are shown for the fission and (n,2n) cross sections of fissile isotopes.

Introduction

At the present time in the world there are several national and international evaluated data libraries of general purpose and some specialised libraries. The data of these libraries are evaluated mainly on the basis of theoretical calculations and essentially discrepant very often. In this connection the problem appears to select more reliable evaluated data.

To solve the problem different systematics are developed on the basis of available experimental data and using in some cases nuclear reaction theory models as well. There are many systematics of neutron cross sections in the incident neutron energy of 14-15 MeV. These systematics play important role in nuclear data evaluation, however their predictions does not solve the problem of data discrepancies in the energy range above 15 MeV, particular for reactions with high energy thresholds. Usually the value (N-Z)/A is used as a parameter in those systematics.

However, some works were made to analyse shapes of excitation functions and cross sections at its maxim. The important results have been obtained by H.Vonach et al in the work /1/ for (n,2n) reaction. The similarity of (n,2n) excitation function shapes for heavy nuclei (A>100) was shown and universal excitation function and systematics of the peak cross sections were proposed. In the works /2,3/ Yu.Trofimov proposed relations for evaluation of (n,p) reaction cross sections at the maximum of the excitation functions and for determination of the neutron energy corresponding to the maxim.

Independently in the works /4-7/ the systematics were developed on the basis of comparison of excitation functions by shapes and cross sections in particular points of excitation functions (in maximum for threshold reactions and in maximum and minima for fission reactions).

The following values were considered as parameters of nuclear reaction excitation functions: reaction threshold, difference of thresholds of the main and competing reactions (for example, (n,p) and (n,np)), cross section at the maximum of excitation function and position of the maximum on neutron energy scale.

The systematics mentioned above are empirical generalisation and to some extent are hypothesis needed in further investigation from point of view of limits their applicability and dependence on the leading parameters.

In the present paper some systematics and systematical trends for parameters, which characterise the threshold reaction excitation functions, are described. These empirical systematics were published earlier and used by authors in evaluation of nuclear data and for selection of neutron data for Russian library BROND-3 and for international library of fusion interest.

Systematics of (n,p) and (n,α) reaction excitation functions.

Analysis shows that the neutron excess (N-Z) and mass number A are main parameters, which determine the characteristics of the (n,p) and (n,α) reaction excitation functions. Because it is reasonable to arrange isotopes as table in dependence on (N-Z) and Z and compare excitation functions for isotopes with the same (N-Z) and Z. Below as an example the part of such table is given for A = 17-30.

Z / N-Z	18	19	20	21	22	23	24	25	26	27	28	29	30
0	^{36}Ar		^{40}Ca										
1		^{39}K											
2	^{38}Ar		^{42}Ca		^{46}Ti		^{50}Cr		^{54}Fe		^{58}Ni		
3		^{41}K	^{43}Ca	^{45}Sc	^{47}Ti								
4	^{40}Ar		^{44}Ca		^{48}Ti	^{50}V	^{52}Cr		^{56}Fe		^{60}Ni		^{64}Zn
5					^{49}Ti	^{51}V	^{53}Cr	^{55}Mn	^{57}Fe	^{59}Co	^{61}Ni	^{63}Cu	
6			^{46}Ca		^{50}Ti		^{54}Cr		^{58}Fe		^{62}Ni		^{66}Zn
7												^{65}Cu	^{67}Zn
8			^{48}Ca								^{64}Ni		^{68}Zn
9													
10													^{70}Zn

As a result of comparison of available experimental data the following systematical trends were observed in dependence on (N-Z) and A:

1. The maximum of (n,p) reaction cross sections for the isotopes of a given element in semilogarithmic scale decreases linearly within experimental uncertainties (Fig.1). For the different elements these linear dependencies are practically parallel and equidistant (this was pointed by D.Gardner in 1962 for 14.5 MeV neutrons /8/).

. The maximum of (n,p) reaction cross sections in semilogarithmic scale increases also practically linearly within experimental uncertainties as a function of Z for the isotopes with the same (N-Z). These both dependencies for different elements seem to be almost parallel and equidistant (Fig.1).

The spread of cross sections around averaged linear dependencies is determined by the value $\Delta Q=(Q_{nnp}-Q_{np})$. At bigger $\Delta Q=(Q_{nnp}-Q_{np})$ the cross sections lie higher, but at less $\Delta Q=(Q_{nnp}-Q_{np})$ bellow. There are some indications that with the increase of A the influence of $\Delta Q=(Q_{nnp}-Q_{np})$ on this spread relative to averaged dependence decreases.

With increasing of the (N-Z) values the slopes of linear dependencies decreases. However, there are no enough experimental data to prove this argument.

2. For the isotopes with the same (N-Z) value the shapes of excitation functions are similar. In any case this takes place for reactions in mean mass numbers and for isotopes with

close values of $\Delta Q=(Q_{nnp}-Q_{np.})$. Influence of $\Delta Q=(Q_{nnp}-Q_{np.})$ on the shape did not investigated because of little amount of experimental data.

In Fig.2 the normalised experimental (n,p) reaction excitation functions for isotopes ^{48}Ti, ^{52}Cr, ^{56}Fe, ^{64}Zn, having the same values (N-Z) = 4. The functions are normalised to $^{48}Ti(n,p)$ reaction excitation function. The spread of curves are within experimental uncertainties.

All the mentioned systematical trends are supported by theoretical calculations based on the present day understanding of nuclear reaction mechanism.

As an example of application of these systematics let us compare excitation functions for ^{56}Fe and ^{58}Ni. Large spread of experimental data did not permit to describe reliably the $^{58}Ni(n, \alpha)$ reaction excitation function (Fig.3). However the $^{56}Fe(n, \alpha)$ reaction excitation function (Fig.4) is determined reliably enough. As far as the $\Delta Q=(Q_{nnp}-Q_{np.})$ for both reactions are practically equal one can propose that positions of maximum of both excitation functions relative to threshold are the same. Shifting the $^{56}Fe(n, \alpha)$ reaction threshold to that for ^{58}Ni and having in mind the systematics dependence of cross section at maximum of excitation function one can obtain the $^{58}Ni(n, \alpha)$ reaction excitation function given in Fig.3. This curve is supported by recent experimental data.

3. For (n, α) reaction excitation functions the similar dependencies are observed. However the slope of linear dependencies in semilogarithmic scale are noticeably less than for (n,p) reactions.

Those systematics for (n,p) and (n, α) reactions are observed for the mass numbers from 10 to 100 and for (N-Z) = 0 -15.

As far as a position of the maximum of the (n,p) reaction excitation functions above $E_{th}+Q_C$ (where Q_C is Coulomb barrier) is proportionally to the value of $(Q_{nnp}-Q_{np})$, where Q_{nnp}-and Q_{np} are reaction energies of (n,np) and (n,p) reactions, respectively, it is useful to compare these values for different isotopes in the process of selection and evaluation of the (n,p) reaction excitation functions.

The systematics of (n,2n), (n,3n) and (n,np) - reactions.

The value of cross section in the maximum of (n,2n) reaction excitation function depends essentially on interrelation of (n,2n) and (n,np) reaction energies ($Q_{n,2n}$ and $Q_{n,np}$, respectively). Let us consider two cases: $Q_{n,2n} \leq Q_{n,np}$ and $Q_{n,2n} > Q_{n,np}$.

1. $Q_{n,2n} \leq Q_{n,np}$. In this case (n,2n) dominates and the maximum (top) cross sections of the (n,2n)-reaction excitation functions are determined by the following equation /5/: $\sigma_{top} = 65.4\ A^{2/3}$ mb, where A is atomic mass number. Experimental data support this relation for A = 50-210. However theoretical calculations permit to suppose that this relation is suitable for mass numbers in the range of 10-50.

2. The (n,2n)-reaction excitation functions in the neutron energy region from the threshold to the maximum of excitation functions are similar and can be described by the $\sigma = \sigma_{max} (\Delta E/\Delta E_m)^{1.35} \exp[1.4(1-\Delta E/\Delta E_m])$, where σ_{max} - cross section at the maximum, $\Delta E=E-E_{th}$, E_{th} - threshold energy, $\Delta E_{max} = E_{max} - E$, E - neutron energy, E_{max} - neutron energy at the maximum of excitation function and corresponds to (n,3n) reaction threshold.

This relation gives a reasonable result but the normalised function (Table 1) is better adjusted to experimental data (especially near threshold) and recommended for the use instead of the relation.

Table 1. Normalised excitation function of (n,2n)-reaction

$\Delta E/\Delta E_{max}$	σ/σ_{max}	$\Delta E/\Delta E_{max}$	σ/σ_{max}	$\Delta E/\Delta E_{max}$	σ/σ_{max}
0.05	0.03	0.35	0.60	0.65	0.91
0.10	0.09	0.40	0.68	0.70	0.93
0.15	0.18	0.45	0.75	0.75	0.95
0.20	0.30	0.50	0.81	0.80	0.97
0.25	0.42	0.55	0.85	0.85	0.98
0.30	0.53	0.60	0.88	0.90	0.99

The influence of difference ($Q_{n,3n}$ - $Q_{n,2n}$) on excitation function shape was not investigated, however there are grounds to suppose that such influence can be noticeable as far as this difference is within 5-12 MeV and normalised function for isotopes with different ($Q_{n,3n}$ - $Q_{n,2n}$) can be no exact similar and differ from averaged normalised function.

3. $Q_{n,2n}>Q_{n,np} + Q_C$. In this case the (n,2n) cross section in the maximum of the excitation function is below the values, calculated from the equation mentioned above, and the difference is determined by contribution of the (n,np) reaction cross section at the same neutron energy. At this condition the maximum of both reaction excitation functions are near 20 MeV and the sum of the (n,2n) reaction cross section and the (n,np) reaction cross section is approximately equal to $\sigma_{top} \approx \sigma_{n,2n} + \sigma_{n,np}$.

If $Q_{n,2n}>Q_{n,np}$, then σ_{max} is determined from experimental data or from other considerations however the shape of excitation function is described by the same normalised function.

In the Fig. 5 one can see the (n,2n), (n,p), (n,np) and (n,xp) reaction excitation functions of ^{58}Ni evaluated on the base of experimental data.

The values of (n,2n) and (n,np) reaction cross sections at the maximum of its excitation functions can be evaluated as 80 and 870 mb, respectively. In the sum it gives 950 mb that is close to 978 mb, predicted by equation for σ_{top}.

The ^{58}Ni (n,np) reaction excitation function, plotted in Fig.5, in the energy range above Coulomb barrier can be approximated by the normalised function, which almost similar that for (n,2n) reaction.

The sum of (n,np) and (n,p) reaction excitation functions (Fig.5) gives the (n,xp) reaction excitation function. As one can see there is a reasonable agreement with the experimental (n,xp) reaction cross sections measured by S.Grimes et al. and S.Saraf et al. The (n,p) reaction excitation function was evaluated on the base of reliable experimental data.

The shapes of the (n,3n) reaction excitation functions are similar in the neutron energy region from the threshold up to the neutron energy at the maximum of the excitation function (at 10-11 MeV above the threshold) and can be approximated by the equation:

$$\sigma = \sigma_{max} (\Delta E/\Delta E_m)^{3.3} \cdot \exp[3.3(1-\Delta E/\Delta E_m]),$$

where ΔE and ΔE_m are counted from the (n,3n) reaction threshold, σ_{max} is determined by the equation: $\sigma_{max} \approx 10$ A mb, where A is atomic mass number.

Systematics of fission and (n,2n) reaction cross section of fissile isotopes.

Analysis of available experimental data on fission cross sections for the isotopes in the region from thorium up to curium shows that for all isotopes the energy dependence of fission cross sections in the incident neutron energy of 1-20 MeV have similar structures: maximum

in the energy intervals of 1-3 and 8-9 MeV and minima in the energy intervals of 5-6 and 11-13 MeV.

Because these maximum and minima are situated practically in the same neutron energy intervals for all isotopes it is possible to compare fission cross sections in these intervals in dependence on A and Z. It should be noted that in the 5-6 MeV interval there is (n,nf) reaction threshold, in the 11-13 MeV there are (n,2nf) reaction threshold, the maximum of (n,2n) reaction excitation function and (n,3n) reaction threshold. From theoretical model calculations one can see that at 11-13 MeV the inelastic scattering cross section is small (about 50 mb) and main contribution to nonelastic process cross section in this energy range gives the fission and (n,2n) reactions.

In Fig. 6 all available experimental data and calculated by STAPRE code /10/ are given. As it is seen the straight lines can approximate the fission cross sections of a given element. in some region.

In Fig. 7 the experimental and calculated (n,2n) reaction cross sections in the maximum of excitation function are presented. As one can see that there is linear dependence of this cross section as a function of atomic mass number A.

In Table 2 the sums of fission and (n,2n) reaction cross sections are given in the incident energy interval of 11-13 MeV. The sum changes weakly against Z and A and in the first approximation can be considered as constant in all range of isotopes from Th up to Am and equal to 2580+−50 mb. The theoretical calculations /10/ shows that for Cf and Bk the sum of fission and (n,2n) reaction cross sections lies within the same limits.

Table 2. The fission and (n,2n) reaction cross sections for 12 MeV.

Isotope	Fission cross section, mb	(n,2n) reaction cross section, mb	Sum of fission and (n,2n) reaction cross sections, mb
Th-232	350±30	2200±50	2550
U-235	1750±50	870±30	2550
U-238	1000±50	1500±100	2550
Np-237	2100±50	530±30	2630
Pu-239	2200±50	400±50	2600
Am-241	2350	250±20	2600

The normalised excitation function for (n,2n) reaction describes quite well the shape of the (n,2n) reaction cross sections from the threshold up to the maximum of the cross section for fissile isotopes ^{232}Th, ^{238}U, ^{237}Np.

Conclusion.

These systematical trends give good possibility of selection of more reliable and physically based excitation functions or at least to show confidence interval of values and exclude the excitation functions with considerable deviations in shapes and wrong absolute values.

References.

1. H.Vonach, In: Proc. the 19th Int. Symp. on Nuclear Physics (Report ZfK-733), Gaussig, Germany, 1989, p.109.
2. Yu.Trofimov, In: Neutron Physics (Proc. of 4th All-Union Conf. on Neutron Physics, Kiev), Moscow, 1977, v.2, p.140 (in Russian).
3. Yu.Trofimov, In: Voprosy Atomnoi Nauki I Tekhniki, ser. Yadernye Konstanty, issue 2(33), 1979, p.47.
4. V.N.Manokhin, Report INDC(CCP)-397, Vienna, 1996.
5. V.N.Manokhin, Report INDC(CCP)-398, Vienna, 1996.
6. V.N.Manokhin, A.I.Blokhin, Proc.Int.Conf. on Nuclear Data for Science and Technology, Trieste, Italy, 1997, v.1, p.871.
7. V.N.Manokhin, A.I.Blokhin, In: Voprosy Atomnoi Nauki I Tekhniki, ser. Yadernye Konstanty, issue 2, 1998, p.30.
8. D.G.Gardner. Nucl. Phys. (1962), v.29, p.373.
9. V.N.Manokhin, In: Voprosy Atomnoi Nauki I Tekhniki, ser. Yadernye Konstanty, issue 1, 1999, p.39.
10. V.A.Konshin, JAERI Research Report 95-010, Japan, 1995.

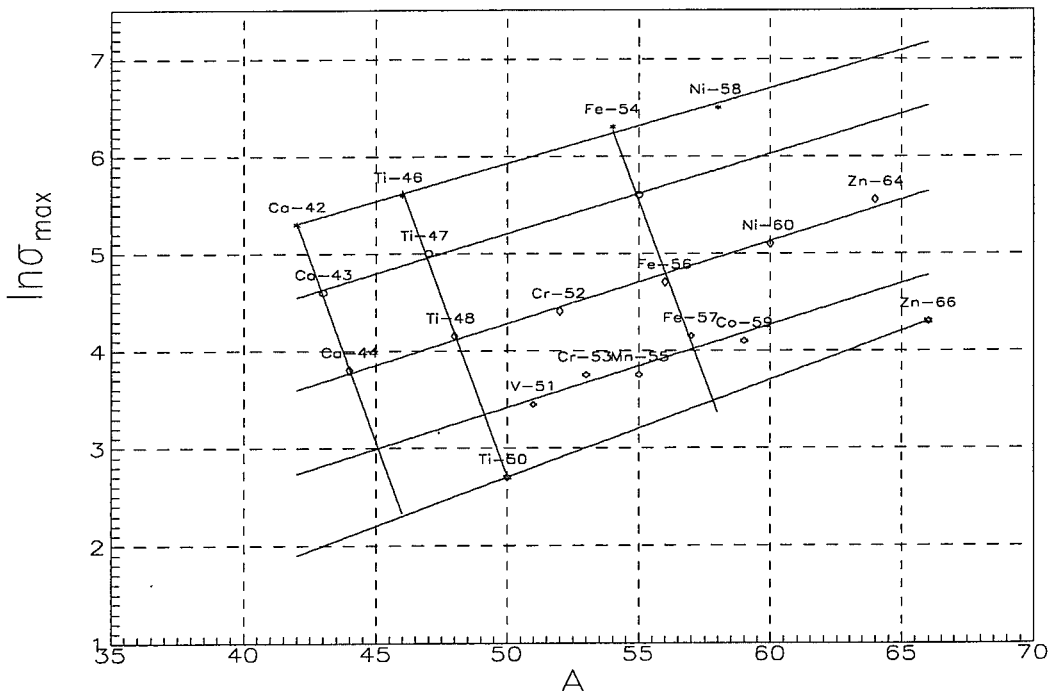

Fig.1. The (n,p) reaction cross sections at the maximum of the excitation functions against mass number A.

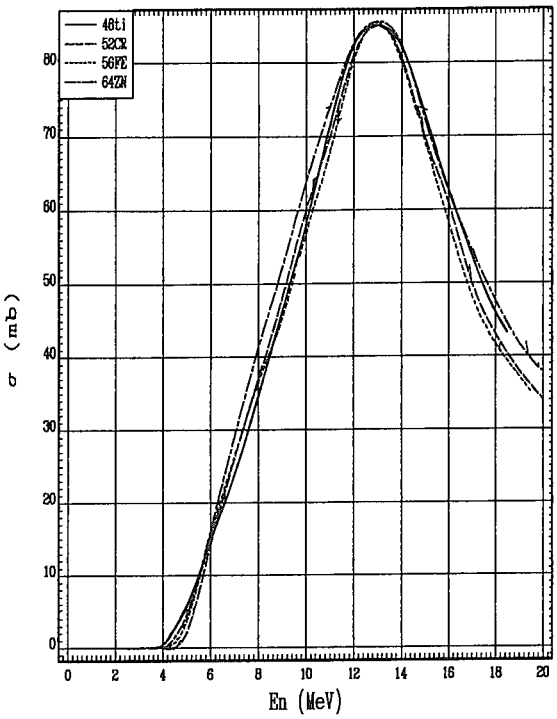

Fig.2. The normalised (n,p) reaction excitation functions for isotopes with (N-Z)=4.

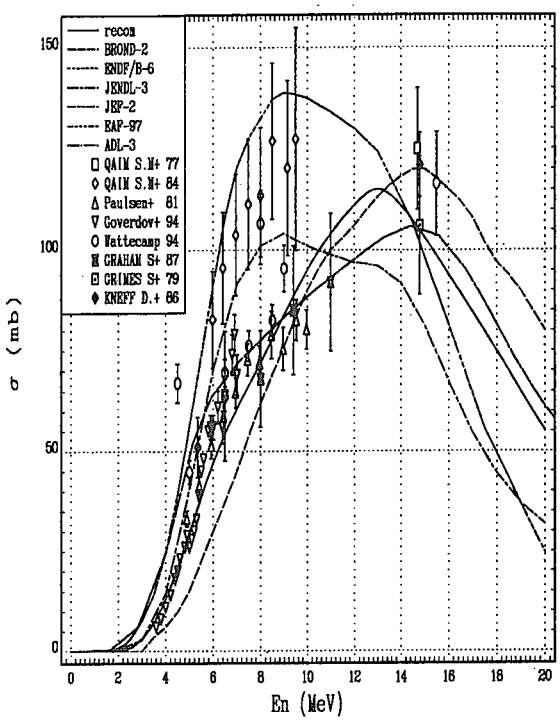

Fig.3. Cross section of ^{58}Ni(n,α)^{55}Fe reaction.

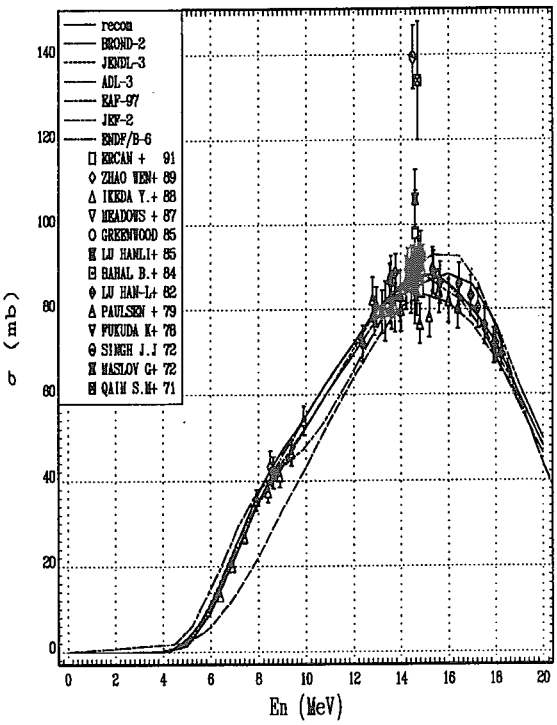

Fig.4. The experimental and evaluated data for ^{54}Fe(n,α)^{51}Cr.

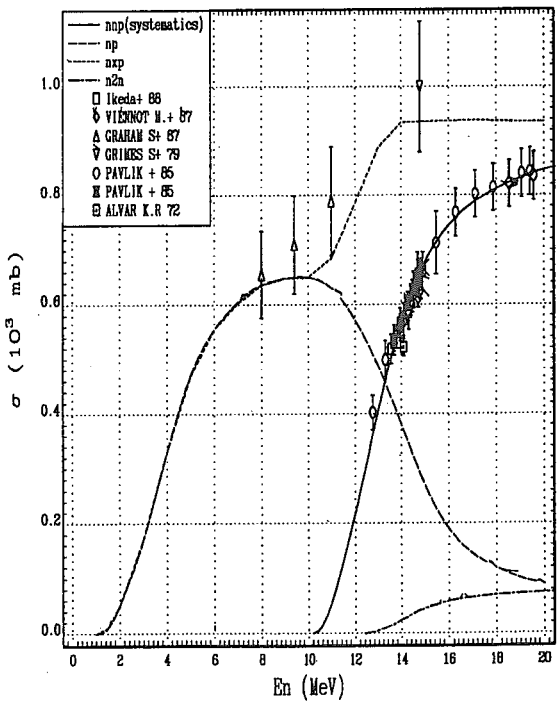

Fig.5. The (n,2n), (n,p), (n,np) and (n,xp) reactions on ^{58}Ni.

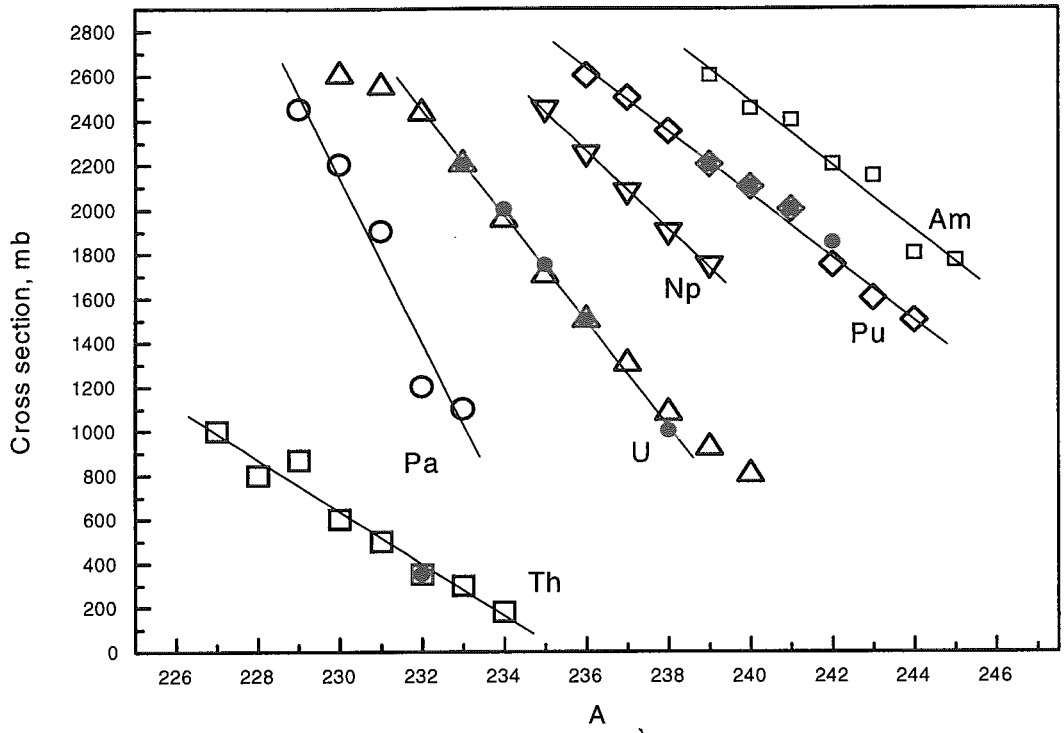

Fig.6. Fission cross section as a function of À at 12-13 MeV. Dark symbols - experiment, open symbols - calculation /10/.

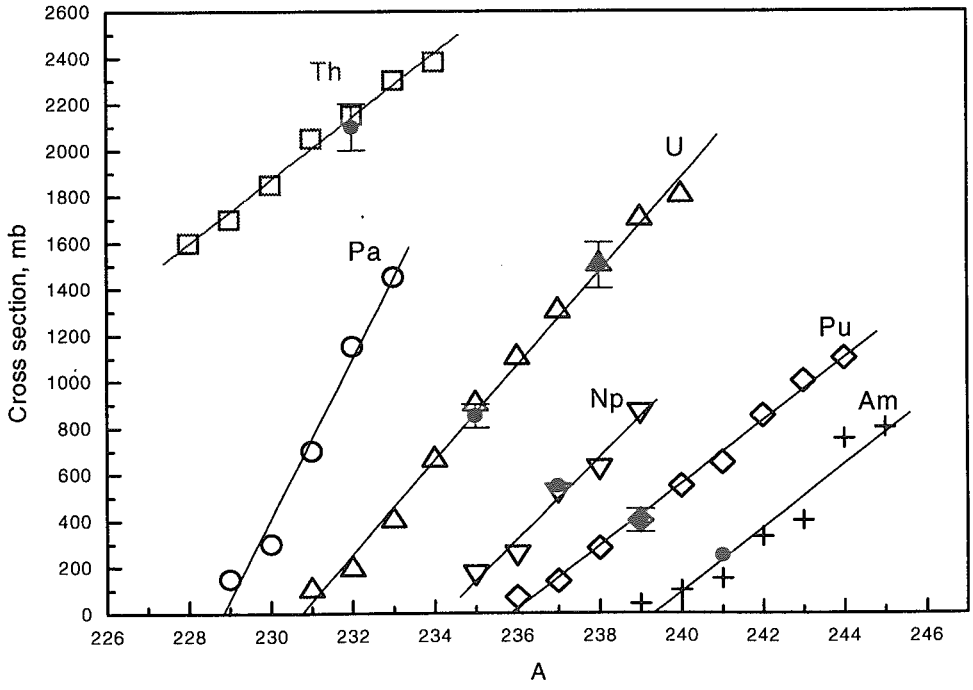

Fig.7. The (n,2n) reaction cross section at 12-13 MeV. Dark symbols - experiment, open symbols - calculation /10/.

2.13 RI Beam Factory Project at RIKEN

Hiroyoshi SAKURAI
Radiation Laboratory, RIKEN
2-1 Hirosawa, Wako, Saitama, 351-0198
e-mail:sakurai@rikaxp.riken.go.jp

The RI Beam Factory at RIKEN is introduced in connection with the present research activities with RI beams.

1 Introduction

Radioactive isotope (RI) beams providing a high isospin degree of freedom have given a great opportunity to investigate nuclei far from stability and to reveal out new phenomena in extreme conditions of isospin asymmetry [1]. To enforce the advantage of RI beams, the RI Beam Factory (RIBF) project at RIKEN aims to expand the range of radioactive nuclei, and to open up a new era for nuclear physics [2].

The RIBF project was proposed to further promote research fields by utilizing RI beams which are now being provided at the RIKEN accelerator research facility (RARF). We first introduce the present research-activities with RI beams at RIKEN, where many experimental programs undergoing are shown as examples for the future programs. Then, the accelerator complex and experimental devices at this project will be described.

2 Research activities at RARF

High-energy ($\sim$100 A MeV) and high-intensity ($<$500 pnA) primary beams of light-atomic mass ($A<60$), obtained from a ring cyclotron (RRC) at RARF, are converted into RI beams via the projectile fragmentation reaction. The RI beam intensity obtained there is the world-highest level, which has been made possible by the combination of the powerful primary beams and the RIKEN projectile fragment separator (RIPS) [3].

RIPS has large momentum and angular acceptances as well as a sizable maximum magnetic rigidity, hence has a high collecting power of projectile fragments. These features were adopted in taking into account energy dependences of RI beam intensity as well as kinematical broadening of projectile fragments. Another feature to be pointed out is that at the upstream of production target a beam swinger system is equipped to produce polarized RI beams. Such a high capability of RI beam production has stimulated nuclear experimentalists to discover new phenomena and new properties, especially for very neutron-rich nuclei.

Resent experimental results have been reported in variety of studies. The global characteristics of nuclei have been investigated toward the drip-line. Information on particle stability and instability has been obtained in the experiments searching for new neutron-rich isotopes [4]. One of the recent highlights is the experimental evidence for particle

stability of ^{31}F and instability of ^{28}O. The decay properties ($T_{1/2}$ and P_n) of neutron drip-line nuclei in the B, C and N isotopes have been measured [5]. Formation of a halo structure has been deduced from the total cross section measurements at intermediate energies, where tail parts of nuclear matter distributions become sensitive to the cross sections [6]. By using the polarized RI beams, nuclear moments (μ- and Q-moments) for many isotopes have been obtained via the β-NMR method [7].

High yield rates of RI beams have allowed to research the nuclear structure in details. Especially, the magicity loss at neutron rich nuclei at N=8 and 20 has been intensively studied. The light neutron-rich isotopes around N=8 (e.g. ^{11}Be, ^{11}Li) have called attentions with respect to the formation of neutron-halo system and the problem of single-particle level ($1p_{1/2}$ and $2s_{1/2}$) inversion. The neutron-rich isotopes at $N\sim$20 (e.g. ^{32}Mg) have manifested the large deformation in spite of the magic number of 20.

β-spectroscopy in double- or triple coincidences of β-rays and delayed-neutron or γ-rays [8] has been possible due to the high intensity of RI beams available at RIPS. Several direct reactions in inverse kinematics have been widely used to deduce spectroscopic informations for the nuclear structure and to study dynamical response of exotic nuclear matters; elastic and inelastic scattering for very neutron-rich nuclei [9], electromagnetic dissociation for halo nuclei [10], the charge exchange reaction for isobaric analog states of halo nuclei [11], Coulomb excitation for nuclei in the deformation region [12], quasi-free nucleon-nucleon scattering for single-hole information [13].

Applications of RI beams for nuclear astrophysics are ones of the major activities at RIPS. The electromagnetic dissociation reaction has been applied for astrophysical cross section determination in an indirect method [14], where the cross sections at a few 100 keV are deduced by using the intermediate energy beams. Direct cross section measurements with RI beams at astrophysical energies have been performed [15], too.

Isospin-dependences in reactions have been investigated. Fusion cross sections at the sub-Coulomb barrier energy ($\sim 5A$ MeV) have been measured with low energy Be-isotope beams in a variety of isospin [16]. The fusion reaction was once applied to observe correlations of two valence neutrons in a halo nucleus of ^{11}Li [17].

It should be noted that most of the above reaction experiments have been based on newly developed spectroscopy methods; the missing mass method with exit channel determinations [9], the invariant mass spectroscopy [10, 11, 14], in-beam γ-spectroscopy with high energy beams [12], and in-beam α-spectroscopy with a multi-target system [16].

3 RIBF project

According to the performances of primary beams at the present RARF, the efficient productions for RI beams are now in the relatively light nuclear region, Z<20. In the region with higher Z, interesting subjects in extremely high-isospin asymmetry conditions are waiting for nuclear physicists investigating; the nuclear structure at the magic numbers as well as the collectivity [18], the dynamical aspects of nuclear matters in terms of the neutron skin formation [19], and the nuclear astrophysics, especially for the r-process path [20]. The RIBF project aims to proceed to such new domains of the nuclear chart.

To realize the wide dynamic-range of available RI beams over the nuclear chart needs more powerful primary beam than at the present facility, of which energies may be more than $100A$ MeV upto Uranium, and of which intensities be as high as possible. To achieve

such high performances in heavy ion beams, two new ring cyclotrons, IRC and SRC, are to be built as post accelerators of the existing ring cyclotron RRC, as shown in Fig. 1 [2]. The cascade operation of these cyclotrons boosts energies of heavy ion beams up to 400 A MeV for light heavy ions like Oxygen, 300 A MeV for Kr ions, 200 A MeV for Xe ions and 150 A MeV for U ions. The expected beam intensity is as high as 1 pμA.

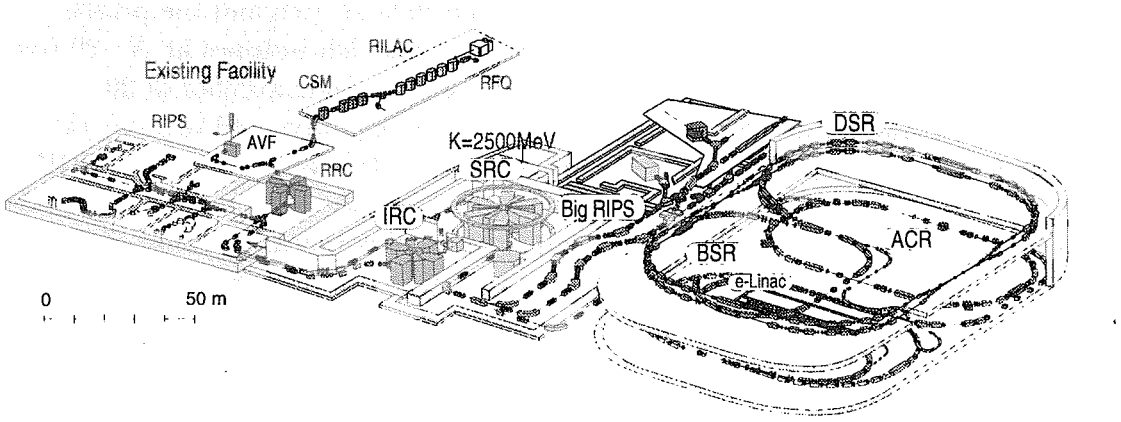

Figure 1: Bird's eye view of RI Beam Factory layout.

The heavy-ion beams accelerated at SRC are to be used for RI beam productions via not only the projectile fragmentation reaction but also the fission reaction of Uranium beams. Fragments of interest are collected and separated at fragment separators, called "Big-RIPS". We will have two types of Big-RIPS's; one is dedicated to the experiments by using stoppers or fixed targets, as described in the previous section, another is for the MUSES facility. The MUSES facility consists of four rings as shown in Fig. 1. Detail descriptions are not shown here, but found in Ref. [21].

The first Big-RIPS system aims for the high isospin frontier. The choice of the fission reaction with ^{238}U is essential for RI productions around ^{78}Ni (a double magic nucleus with N=50) and $^{\sim 104}$Zr (a largely deformed nucleus) region, since the production cross sections of such neutron-rich fission fragments are a few orders of magnitude higher than in the case of the projectile fragmentation [22]. The momentum and angular acceptances of Big-RIPS must be determined according to the kinematical broadening of fission fragments.

We here emphasize two experimental points with RI beams. One of them is that a purity of a RI of interest in RI beams is not 100%. Thus, in general, particle identification to determine Z and A of RI beams particle-by-particle is essential to deduce reliable results. At RIPS, the mass region of intense RI beams is A<60, thus the particle identification does not require nice resolutions in the Z and A determination. However, in the RIBF project, experimentalists will treat more heavier isotopes. In this sense, to achieve nice resolutions for particle identification is essential and the first priority in designing

the experimental facility.

Another point is energies of RI beams especially for reaction experiments. The research based on nuclear reactions needs appropriate energies of beams according to the reaction type. For instance, transfer reactions are efficient at a few 10 A MeV, and quasi-free nucleon-nucleon scattering demands ~200 A MeV RI beams which allow us to assume one step reaction inside a nucleus and to deduce reliable spectroscopic information. Thus, the dynamic range of beam energy is one of important aspects of RI beams.

Taking into account such requirements for experimental programs at RIBF, we are now proposing a cascade configuration of two fragment separator. The first separator could be dedicated to the RI production and separation only. The second one which also has a momentum dispersive focal plane provides a several functions for the requirements. High-resolution particle identification can be realized on the basis of accurate determination of fragment momenta. More efficient decrease of RI beam energies may be possible with an achromatic energy-degrader to be placed at the focal plane, compared with in the case of a flat-shaped degrader.

Experimental devices will come to the end of the cascade separator system. Relatively large devices proposed so far are, for instance, a large dipole magnetic spectrometer with a high acceptance for particles decayed from particle-unbound excited states, a forward spectrometer with a high resolution for particle identification of ejectiles, some γ-ray detectors based on Ge- and CsI-crystals for particle bound excited states. Such devices are being designed for high energy and/or heavy RI beams.

4 Summary

The RIBF project aims to open a new era of nuclear physics in the next century. The construction of the part including SRC and Big-RIPS will start soon, and the RI beams at RIBF will be ready a few years later.

References

[1] C. Detraz and D.J. Vieira, Annu. Rev. Nucl. Part. Sci. 39, 407 (1989); A.C. Mueller and B.M. Sherrill, Annu. Rev. Nucl. Part. Sci. 43, 529 (1993).

[2] I. Tanihata, *ENAM98: Exotic Nuclei and Atomic Masses*, Jun. 23–27, 1998, Michigan, USA, ed. B.M. Sheririll, D.J. Morrissey, and C.N. Davids (AIP CP455) p.943 (1998).

[3] T. Kubo *et al.*, Nucl.Instr. and Methods, B**70**, 309 (1992).

[4] H. Sakurai *et al.*, Phys. Rev. C 54, R2802 (1996); Nucl. Phys. A616, 311c (1997); Phys. Lett. B448, 180 (1999).

[5] K. Yoneda *et al.*, J. Phys. (London) G24, 1395 (1998).

[6] M. Fukuda *et al.*, Nucl. Phys. A656, 209 (1999).

[7] K. Matsuta *et al.*, Hyperfine Interactions 97/98, 519 (1996); H. Izumi *et al.*, Phys. Lett. B366, 51 (1996); T. Minamisono *et al.*, Phys. Lett. B420, 31 (1998); H. Ogawa *et al.*, Phys. Lett. B415, 11 (1999).

[8] N. Aoi *et al.*, Nucl. Phys. A616, 181c (1997); A. Ozawa *et al.*, J. Phys.(London) G24, 143 (1998).

[9] A.A. Korsheninnikov *et al.*, Phys. Rev. Lett. 78, 2317 (1997); Phys. Rev. Lett. 82, 3581 (1999).

[10] T. Nakamura *et al.*, Phys. Rev. Lett. 83, 1112 (1999).

[11] T. Teranishi *et al.*, Phys. Lett. B407, 110 (1997).

[12] T. Motobayashi *et al.*, Phys. Lett. B346, 9 (1995); T. Nakamura *et al.*, Phys. Lett. B366, 51 (1996).

[13] T. Kobayashi *et al.*, Nucl. Phys. A616, 223c (1997).

[14] , T. Kikuchi *et al.*, Phys. Lett. B391, 261 (1997); Eur. Phys. J. A3, 213 (1998).

[15] R.N. Boyd *et al.*, Phys. Rev. Lett. 68, 1283 (1992).

[16] A. Yoshida *et al.*, Phys. Lett. B389, 457 (1996).

[17] M. Petrascu *et al.*, Phys. Lett. B405, 224 (1997).

[18] W. Nazarewicz, Nucl. Phys. A654, 195c (1999).

[19] I. Tanihata, Nucl. Phys. A654, 235c (1999).

[20] K.-L. Kratz *et al.*, Nucl. Phys. A630, 352c (1998).

[21] I. Tanihata, Nucl. Phys. A616, 56c (1997); I. Tanihata, Nucl. Instr. and Mthods B126, 224 (1997).

[22] Ch. Engelmann *et al.*, Z. Phys. A352, 351 (1995).

2.14 Synthesis of Superheavy Nuclei using Heavy-ion Fusion Reactions.

Hiroshi IKEZOE, Shin-ichi MITSUOKA, Katsuhisa NISHIO, Jun LU and Ken-ichiro SATO
Advanced Science Research Center, JAERI, Tokai, Ibaraki, 319-1195, Japan
e-mail: Ikezoe@popsvr.tokai.jaeri.go.jp

The present status related to the synthesis of the superheavy elements is briefly reported. The fusion between deformed nuclei, the gentle fusion or the hugging fusion, has been theoretically proposed as a new type of fusion reaction. In order to investigate this type of reaction, we measured the dependence of the fusion probability on the orientation of deformed nucleus with respect to the beam axis in the fusion reactions of ^{60}Ni with ^{154}Sm and ^{76}Ge with ^{150}Nd. We found that the fusion probability strongly depends on the orientation of the nuclear deformation. When the projectiles collide at the tip of the deformed nuclei, the fusion probability is considerably reduced. On the other hand, when the projectiles collide at the side of the deformed nuclei, the fusion occurs without any hindrance. This phenomenon was understood qualitatively by comparing the distance between the mass centers of two colliding nuclei at the touching configuration with the position of the saddle point of the compound nucleus.

1. Introduction

The study of the superheavy element is the one of new frontier in nuclear physics. The superheavy element (Z=114, N=184) was predicted more than 30 years to be a doubly closed shell nucleus beyond ^{208}Pb. Experimentally, many authors tried to synthesize this element by the bombardment of existing heavy element with energetic ion beams or to search it in materials of the earth and the moon. Up to the present time, there is no definite evidence for the discovery of the superheavy element. The GSI group [1] has synthesized the heavy elements up to Z=112 step by step using the lead based fusion reaction. Recently, the Dubna group [2] reported one α decay chain which is a good candidate for originating from the decay of the parent nucleus ^{289}114. The fusion reaction of ^{48}Ca with ^{244}Pu was used and the production cross section in the 3n-evaporation channel was about 1 pb. The Berkeley group [3] also reported three decay chains in the reaction of ^{86}Kr with ^{208}Pb, each consisting of an implanted heavy atom and six subsequent α decay. These decay chains are consistent with the formation of ^{293}118 and its decay by sequential α-particle emission. The reported α-decay sequences are shown in Fig.1 together with the experimental result of the Dubna group and the known isotopes up to now. The production cross section of the reaction of ^{86}Kr with ^{208}Pb, 2.2 pb, is considerably larger compared with the production systematics [1] of the lead based fusion reaction. This experiment was performed following a prediction by Smolanczuk [4]. He calculated the evaporation residue cross section in the 1n-evaporation channel for the lead based reaction and gave a large production cross section, 670 pb, for the reaction of ^{86}Kr with ^{208}Pb. This large production cross section mainly comes from a large negative Q-value of this fusion reaction and a large fission barrier height of the compound nucleus. These factors result in a small excitation energy at fusion

barrier and a large survival probability of a compound nucleus in the de-excitation process.

In order to make a fully equilibrated compound nucleus in the heavy-ion fusion reaction, a projectile must have an enough kinetic energy to surmount one-dimensional barrier (fusion barrier) between projectile and target nuclei. Furthermore, when the product of the atomic numbers of projectile and target, Z_1Z_2, is larger than about 1800, an extra kinetic energy is needed to surmount a saddle point of the compound nucleus. This energy is called as an *extra-extra push energy*. This is because the saddle point locates inside compared with a contact point of two colliding nuclei in the case of heavy reaction system. The compact configuration at touching is more favorable for fusion. The most compact configuration may be realized in the collision between deformed nuclei as pointed out by [5,6], where the gentle fusion [5] and the hugging fusion [6] between well-deformed nuclei have been theoretically proposed. When the symmetry axes of the deformed nuclei are orthogonal to each other at the contact configuration, the two deformed nuclei can take the most compact configuration and then proceeds to the formation of the compound nucleus. Furthermore, it is expected that this touching configuration makes the fusion path far from the competing axial-symmetric fission path. In order to investigate this theoretical prediction experimentally, we have measured the fusion cross sections of the reaction of ^{60}Ni + ^{154}Sm, ^{32}S + ^{182}W, ^{76}Ge + ^{150}Nd and ^{28}Si + ^{198}Pt, where the former two reactions and the latter two reactions make the same compound nucleus ^{214}Th and ^{226}U, respectively. The nuclear deformations β_2 of ^{150}Nd, ^{154}Sm, ^{182}W and ^{198}Pt are 0.36, 0.32, 0.28 and –0.11, respectively.

2. Experiments and results

The experiments were carried out at the tandem-booster facility of Japan Atomic Energy Research Institute (JAERI). The fusion residues emitted from targets to the beam direction were separated in-flight from the primary beam and various products of background reactions by the JAERI recoil mass separator. The experimental details are shown in [7]. The evaporation residue cross sections measured in the reaction of ^{32}S with ^{182}W are shown Fig. 2, where the cross section of each residue is shown as a function of the center-of-mass kinetic energy. These cross sections were compared with the calculation, where the fusion cross section was calculated by the coupled channel code CCDEF [8] by taking account of the target deformation and the coupling of the inelastic channel to the fusion process. The evaporation residue cross sections were calculated by the statistical model code HIVAP [9]. As shown in Fig. 2, the evaporation residue cross sections in the reaction of ^{32}S with ^{182}W were well reproduced by the calculation (the solid curves). This indicates that the deformation of ^{182}W, as well as the inelastic couplings of target and projectile to the fusion process, makes an enhancement of the fusion cross section at subbarrier energy region. On the other hand, the measured evaporation residue cross sections in the reaction of ^{60}Ni with ^{154}Sm shown in Fig. 3 were well below the calculated cross section (the dashed curves) at the subbarrier energy (E_{cm}<190 MeV), while the cross sections measured above E_{cm}>200 MeV were consistent with the calculation. It is noted that the Coulomb barrier height depends on the collision angle of ^{60}Ni with respect to the symmetry axis of the deformed nucleus ^{154}Sm. For example, the barrier height for the collision at the tip of the ^{154}Sm is 174 MeV, while it for the collision at the side of the ^{154}Sm is 198 MeV. The present result indicates that the collision at the

tip of the deformed ^{154}Sm nucleus does not proceed to the formation of the compound nucleus, even if the barrier at the tip is surmounted. On the other hand, the collision at the side of the ^{154}Sm nucleus forms the compound nucleus without any hindrance. This tendency was also observed in the reaction of ^{76}Ge with ^{150}Nd, where we observed a strong hindrance of the evaporation residue cross section at the subbarrier energy region as compared with the calculation taking account of the nuclear deformation of ^{150}Nd, while the measured evaporation cross section were consistent with the same calculation at the above-barrier energy region.

The present result is qualitatively explained by considering relative positions of the saddle point and the distance between the mass centers of two colliding nuclei at touching point. According to the liquid drop model calculation of [10], the saddle point of ^{214}Th is located at $1.5R_0$, where R_0 is the radius of ^{214}Th. In the reaction of ^{60}Ni with ^{154}Sm, the longest distance between the mass centers at the touching point is $1.7R_0$ and the shortest distance is $1.4R_0$. That is, the touching configuration at the tip is elongated more than the saddle point and thus even if the Coulomb barrier at this point is surmounted, the reaction system does not automatically proceed to form the compound nucleus. On the other hand, in the reaction of ^{32}S with ^{182}W, the longest distance at the touching configuration is $1.5R_0$, approximately the same position as the saddle point. Therefore we expect that the reaction system automatically fuse when the Coulomb barrier is surmounted in this reaction. The same argument can be applied in the reaction of ^{76}Ge with ^{150}Nd, where the saddle point is located at 1.4 times of the radius of the ^{226}U. This location of the saddle point is approximately close to the distance between the mass centers at the side collision. This explains the strong hindrance of the fusion cross section and thus the measured evaporation residue cross sections considerably smaller than the calculation at subbarrier energy.

The present experimental result is consistent with the idea of the proposed hugging fusion or the gentle fusion between deformed nuclei. In order to convince the present consideration, further experimental studies of fusion between deformed nuclei is needed.

References

[1] S. Hofmann, Rep. Prog. Phys. 61, 639 (1998).
[2] Yu. Ts. Oganessian et al., Phys. Rev. C 83, 3154 (1999).
[3] V. Ninov et al., Phys. Rev. Lett. 83, 1104 (1999).
[4] R. Smolanczuk, Phys. Rev. C 59, 2634 (1999).
[5] W. Nörenberg, Proc. Int. Workshop on Heavy-Ion Fusion, Padva, Italy (1994).
[6] A. Iwamoto et al., Nucl. Phys. A596, 329 (1997).
[7] S. Mitsuoka et al., Proc. 1st Int. Conf. On the Chemistry and Physics of the Transactinide Elements, Sep. 26-30, 1999, Seeheim, Germany and submitted to Phys. Rev. C
[8] J. Fernandez-Niello et al., Comput. Phys. Commun. 54, 409 (1989).
[9] W. Reisdorf and M. Schädel, Z. Phys. A343, 47 (1992).
[10]P. möller and J.R. Nix, Nucl. Phys. A272, 502 (1976).

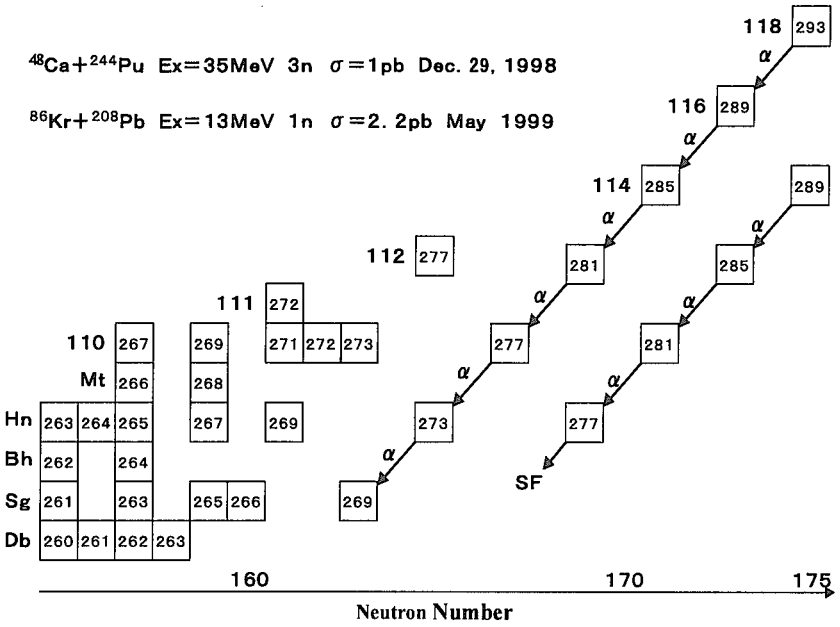

Fig. 1 α decay chains observed in the reactions of ^{48}Ca with ^{244}Pu [2] and ^{86}Kr with ^{208}Pb [3], together with the known heavy isotopes above Z=105.

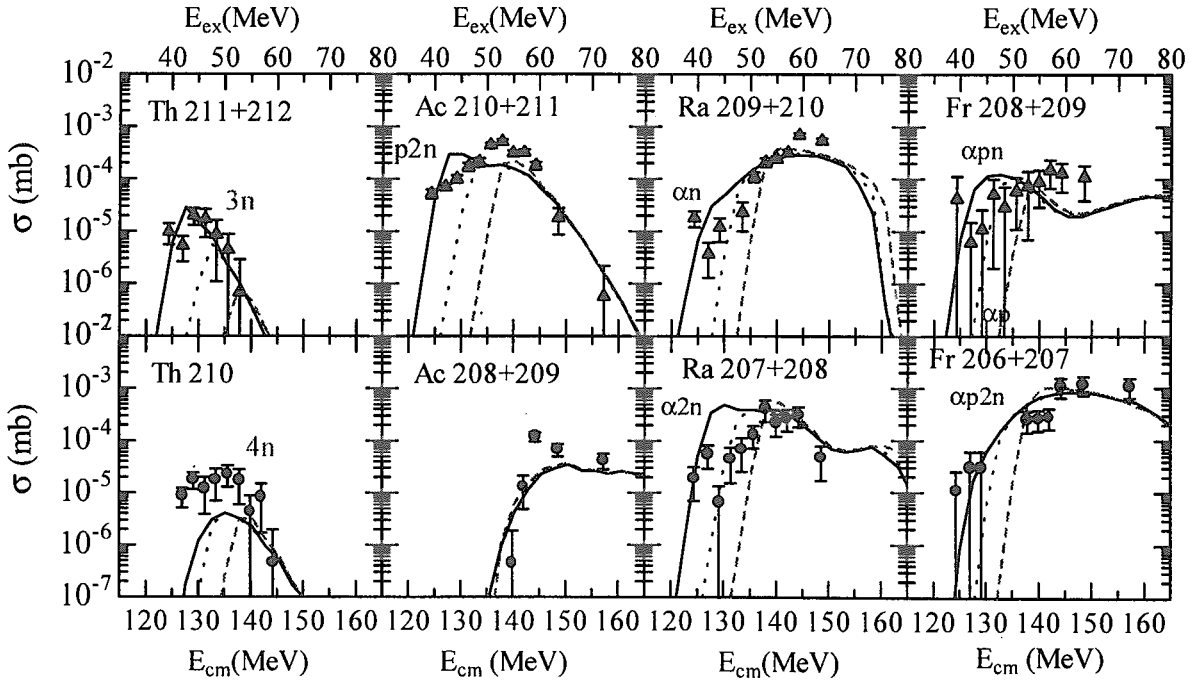

Fig. 2 Evaporation residue cross sections measured in the reaction of ^{32}S with ^{182}W as a function of the center-of-mass energy. The excitation energy E_{ex} of the compound nucleus is also shown. The Solid curves show the calculation including the deformation of ^{154}Sm and the inelastic couplings of ^{182}W and ^{32}S. The long dashed curves show the calculation without the deformation and the inelastic couplings. The short dashed curves show the calculation including the deformation only.

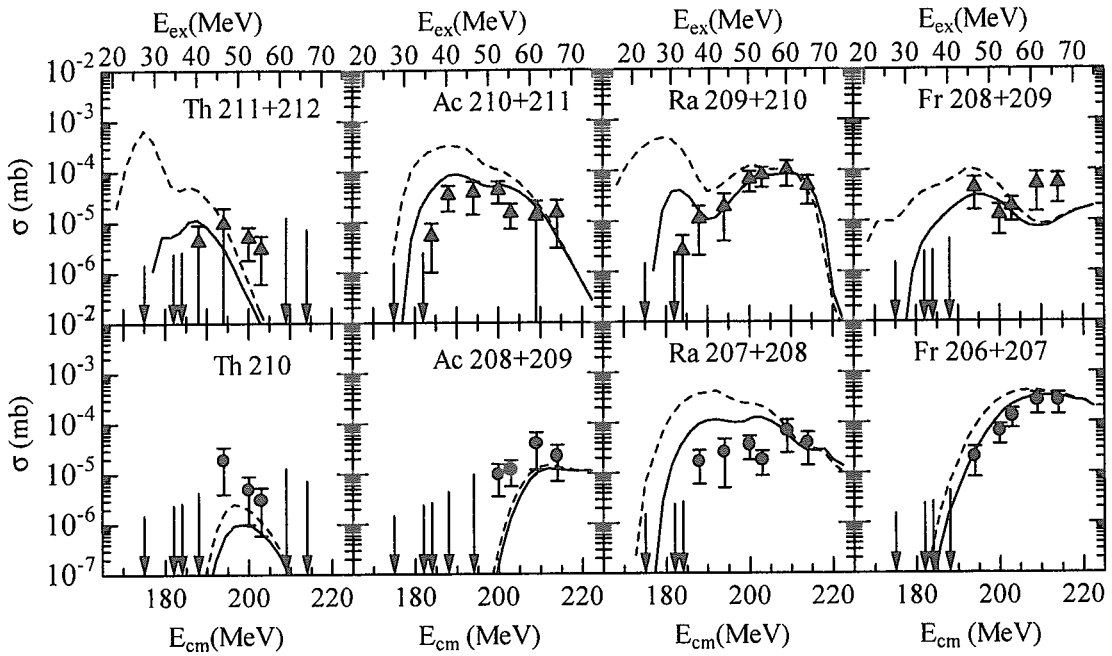

Fig. 3 Evaporation residue cross sections measured in the reaction of ^{60}Ni with ^{154}Sm. The dashed curves show the calculation taking account of the deformation of ^{154}Sm. The solid curves show the calculation including an extra-extra push energy in addition to the deformation.

2.15

Present Status of International Criticality Safety Benchmark Evaluation Project (ICSBEP)

Yoshinori MIYOSHI

Criticality Safety Laboratory, Japan Atomic Energy Research Institute
Tokai-mura, Naka-gun, Ibaraki-ken 319-1195
e-mail: miyoshi@melody.tokai.jaeri.go jp

The International Criticality Safety Evaluation Project, ICSBEP was designed to identify and evaluate a comprehensive set of critical experiment benchmark data. Compilation of the data into a standardized format are made by reviewing original and subsequently revised documentation for calculating each experiment with standard criticality safety codes. Five handbooks of evaluated criticality safety benchmark experiments have been published since 1995.

1. Introduction

The International Criticality Safety Evaluation Project, ICSBEP is an official activity of the Organization for Economic Cooperation and Development- Nuclear Energy Agency, OECD-NEA. This activity was initiated as the Criticality Safety Evaluation Project ,CSBEP in October of 1992 by the United States Department of Energy, DOE. Main countries contributing to this project are United Kingdom, Japan, Russia, France, Republic of Korea and USA as shown in Figure 1. ICSBEP has evaluated a large number of criticality experiments performed at various nuclear facilities all over the world. The detail specifications of the critical conditions are intended to validate the criticality calculation codes and nuclear data libraries. Criticality safety personnel in 39 different countries are now using the international handbook of evaluated criticality safety benchmark experiments[1].

2. Classification of Critical Experiments

Criticality safety benchmark experiments are classified into seven different types of fissile materials; (Ⅰ) Plutonium System, (Ⅱ) Highly Enriched Uranium Systems (wt.%^{235}U ≥ 60), (Ⅲ) Intermediate and Mixed Enrichment Uranium Systems (10 < wt.% ^{235}U < 60), (Ⅳ) Low Enriched Uranium Systems (wt.%^{235} U ≤ 10), (Ⅴ) Uranium-233 Systems, (Ⅵ) Mixed Plutonium - Uranium Systems, and (Ⅶ) Special Isotope Systems. Each of these seven systems are divided into four physical form of the fissile material such as metal, compound, solution and miscellaneous systems. In this handbook, fast, intermediate and thermal systems are defined as systems in which over 50% of the

fissions occur at energies over 100 keV, from 0.625 eV to 100 keV, and less than 0.625eV, respectively. The fruit of this project is a benchmark data handbook consisting of seven volumes representing above different systems for the criticality safety computer codes. The number of evaluations and configurations contained in the five handbooks are listed in Table 1.

3. Main Critical Experiment Facilities

In United States, BNWL, LANL, and ORNL are main research organization producing the critical data. BNWL were specially concerning to plutonium and uranium nitrate solution for fast reactor fuel cycle. LANL has accumulated many critical data on high enriched uranium and plutonium metal using critical assemblies such as GODIVA, BIG TEN and FLATTOP. In France, Valduc research center of IPSN has performed various type of experiments for fuel rod lattices with fixed absorber and high enriched uranyl nitrate solution. Experiments on multiple units of tank array containing plutonium solution were also performed. In Russia Federation, IPPE supplied with high enriched uranyl nitrate solution in cylindrical and annular geometry. Reactivity effects of soluble poison such as gadolinium were also measured. In Japan, JAERI has submitted some evaluations of STACY experiments on single unit containing 10 % enriched uranyl nitrate solution and TCA experiments on low enriched uranium oxide fuel rod arrays.

4. Sample Evaluation for Uranyl Nitrate Solution[2]

Sample evaluations about uranyl nitrate solution in the benchmark handbook are listed in Table 2.

1) HEU-sol-therm-021

The experiments consisted of cubic arrays of 8, 27, 64, or 125 cylindrical units with height-to-diameter ratios near unity. Each unit of the array contains 5-liter uranyl nitrate solution at concentrations of 415, 279, or 63.3 g/L. The ^{235}U enrichment was 92.6 w/o. The array was either bare or reflected by paraffin and/or Plexiglas with thickness between 1.27 and 15.24 cm.

2) HEU-sol-therm-006

The highly enriched uranyl nitrate poisoned with enriched boron in boric acid were contained in a cylindrical tank surrounded by two annular regions, in which various radial reflector existed. The inner annular region contained either air or a thick nickel sleeve. The outer annular region contained air, water, or borated water. Critical configurations had height to diameter ratios in the range from 0.19 to 1.04. Uranium concentration was varied between 293.4 and 297.8 g/L. The boron in the uranyl nitrate solution was enriched to 50.55 w/o ^{10}B, and concentration was changed within 2.64 gB/L.

3) HEU-sol-therm-014～019

Each experiment involving a single water-reflected tank of highly enriched uranyl nitrate solution (U=70 ～ 400g/liter) were performed in IPPE (Russia). These experiments were performed with the concentration of gadolinium within 2.0 g/L. The diameter of the cores was 40

cm or 25 cm. Cores were surrounded by thick water reflectors on the bottom and side.

4) LEU-sol-therm-004, 007～010

Using STACY, critical solution levels were systematically measured for a cylindrical tank of 60 cm in diameter using 9.97 w/o ^{235}U enriched uranyl nitrate solution. The core tank was reflected with structural material such as ordinary concrete, borated concrete and polyethylene. The main parameters were the thickness of the reflector and boron concentration. Reactivity effects of these material were also measured. For unreflected and water reflected core, the uranium concentration was changed from 225 to 313 gU/L at free nitric acid of 2 mol/L. Core configurations of experiments on uranium solution system are shown in Figure 2.

5. Calculation for Uranyl Nitrate Solution

Critical calculations were made to study the bias of neutron multiplication factor when using Japanese nuclear data library JENDL 3.2. Histogram of calculated neutron multiplication for each experiment is shown in Figure 3. A Continuous energy Monte Carlo code MCNP 4A or 4B was used in order to compare between JENDL 3.2 and ENDF/B-V. For both high enriched and low enreiched uranyl solution system, it should be noted that the calculated keff with JENDL3.2 are about 0.5% Δ k larger than that with ENDF/B-V for uranyl nitrate solution system. The experimental uncertainties in the neutron multiplication factor due to geometry and composition of fuel and structural region, which were evaluated by sensitivity analyses, are less than 0.2% Δ k.

6. Summary

Critical configurations described in the ICSBEP handbook are helpful to verify the reliability of the criticality calculation code system including nuclear data library. As typical input data for reference calculation are also attached in the evaluation, it is easy for users to make calculations with their own code systems. In addition to critical data, ICSBEP has established a subcritical working group which evaluate the subcritical condition including primary data in similar format to make the comprehensive database for criticality safety evaluation.

References

1) J.B.Briggs et al., ICNC'99 in France (1999)

2)NEA/NSC/DOC(95), NEA NUCLEAR SCIENCE COMMITTEE, International Handbook of Evaluated Criticality Safety Benchmark Experiments, September 1999 Edition

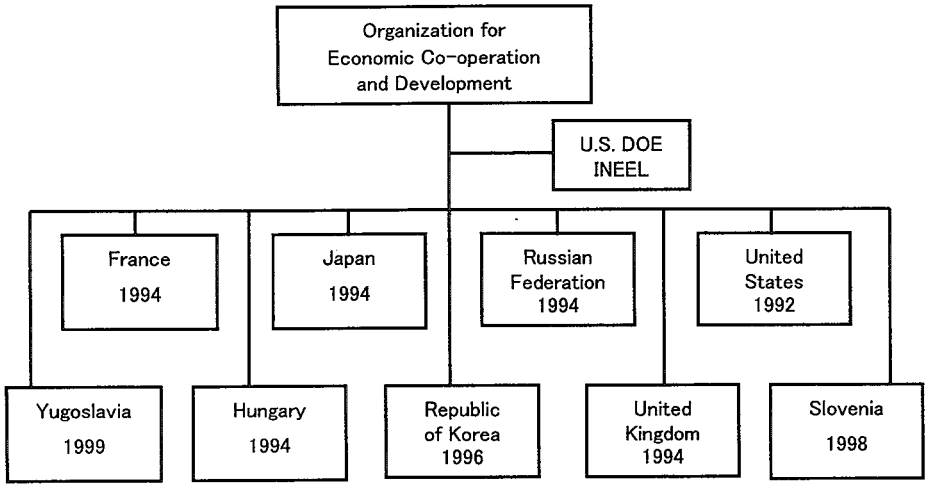

Figure 1 International Criticality Safety Benchmark Evaluation Project

Table 1.1 Distribution of Critical Configurations

System		Thermal Energy<0.625eV	Intermediate 0.625eV≦Energy≦100keV	Fast Energy>100KeV	Mixed
Pu	Metal	–	–	74	–
	Solution	347	–	–	–
	Compound	21	1	6	7
HEU	Metal	29	1	161	6
	Solution	334	2	–	–
	Compound	115	17	–	17
IEU	Metal	–	–	13	–
	Solution	4	–	–	–
	Compound	37	–	–	–

Table 1.2 Distribution of Critical Configurations

System		Thermal Energy<0.625eV	Intermediate 0.625eV≦Energy≦100keV	Fast Energy>100KeV	Mixed
LEU	Metal	13	–	–	–
	Solution	44	–	–	–
	Compound	643	–	–	–
U233	Metal	–	–	10	–
	Solution	31	–	–	–
	Compound	–	–	–	–
MIX	Meta	–	2	38	1
	Solution	42	–	–	–
	Compound	125	–	–	–
SPEC	Metal	–	–	10	–
	Solution	–	–	–	–
	Compound	–	–	–	–

Table 2 International Criticality Safety Benchmark Experiment Evaluation

Evaluation	Case	System	Geometry	Refrector	Poison	U conc. (gU/liter)	U enrichment (wt. %)
HEU-sol-therm-021	8	Homogeneous/Array (N×N×N, N=2.3.4)	Cylinder	paraffin, plexigias	–	415	92.6
HEU-sol-therm-006	17	Homogeneous	Cylinder	air, water, nickel, borated water	B	293.4～297.8	93.06
HEU-sol-therm-014～019	35	Homogeneous	Cylinder	water	Gd	70～400	89.04
LEU-sol-therm-004	7	Homogeneous	Cylinder	water	–	225.3～310.1	9.97
LEU-sol-therm-007	5	Homogeneous	Cylinder	bare	–	241.9～313.0	9.97
LEU-sol-therm-008	4	Homogeneous	Cylinder	concrete	–	239.8～241.1	9.97
LEU-sol-therm-009	3	Homogeneous	Cylinder	borated concrete	–	244.7～245.2	9.97
LEU-sol-therm-010	4	Homogeneous	Cylinder	polyethylene	–	242.1～243.3	9.97

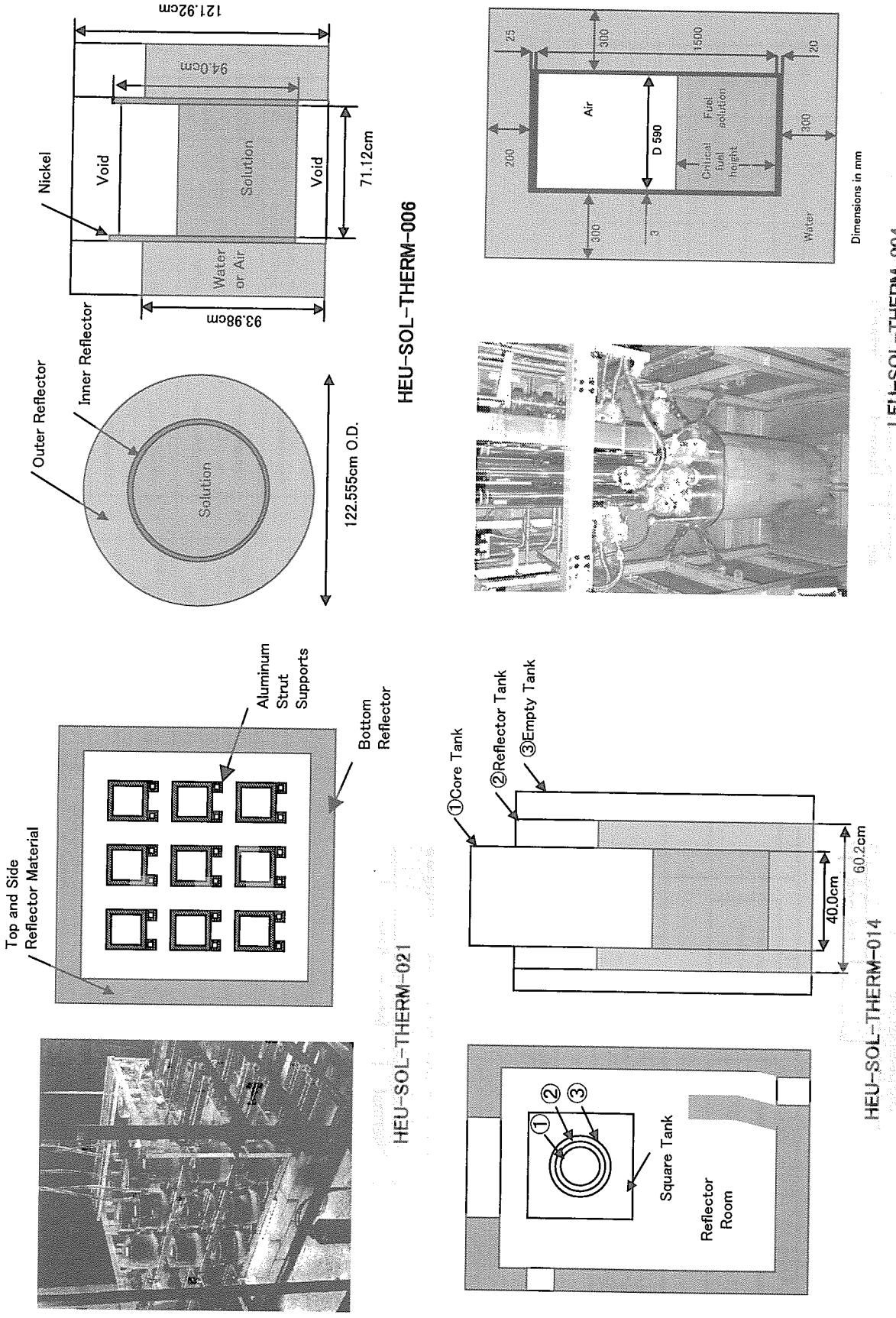

Figure 2 Core Configuration

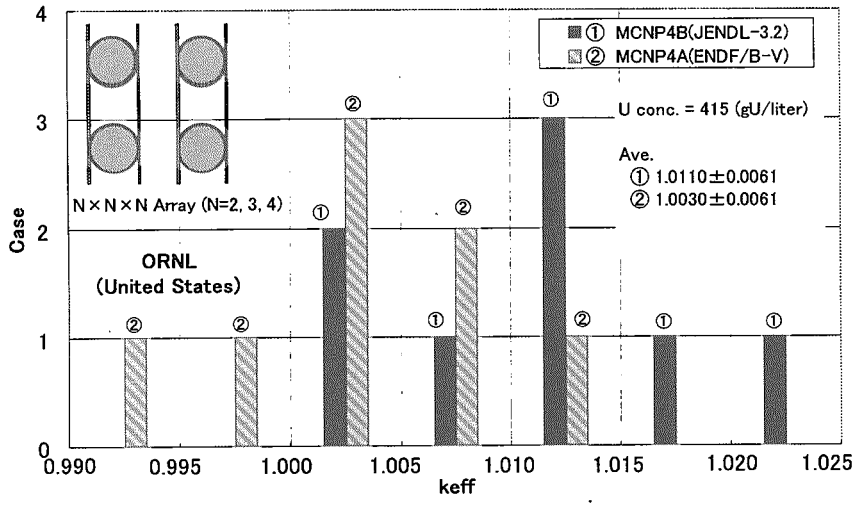

HEU-sol-therm-021

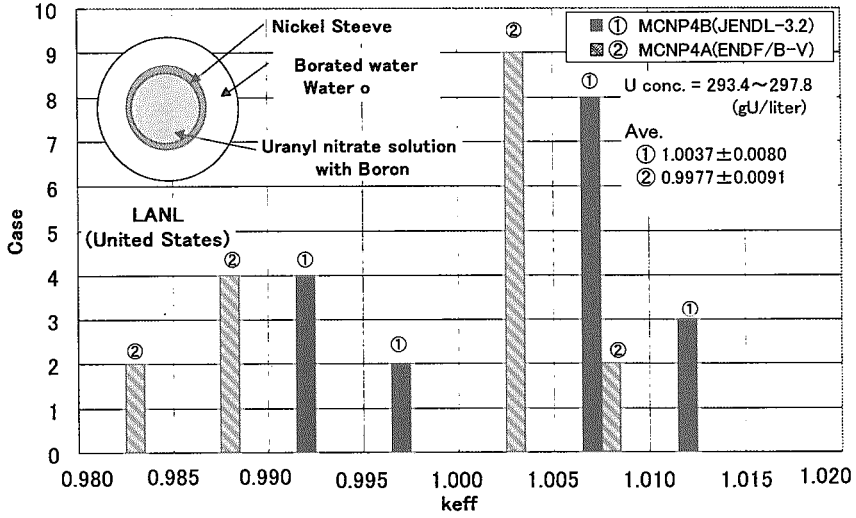

HEU-sol-therm-006

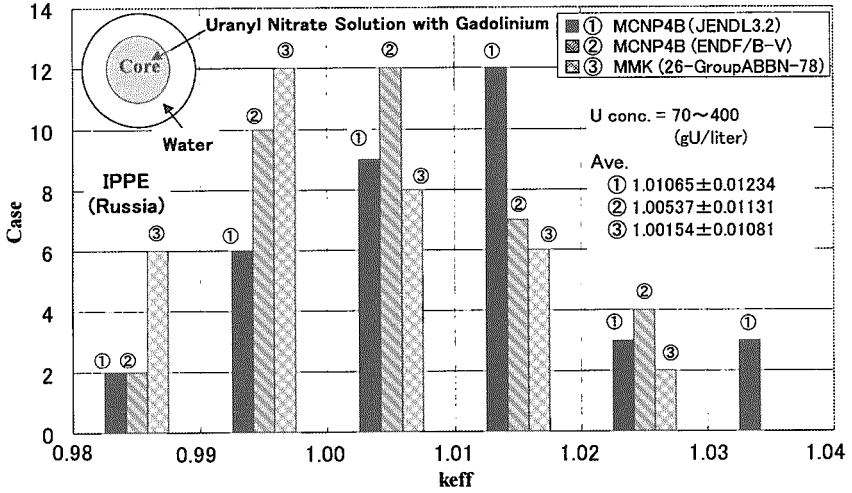

HEU-sol-therm-014 ～019

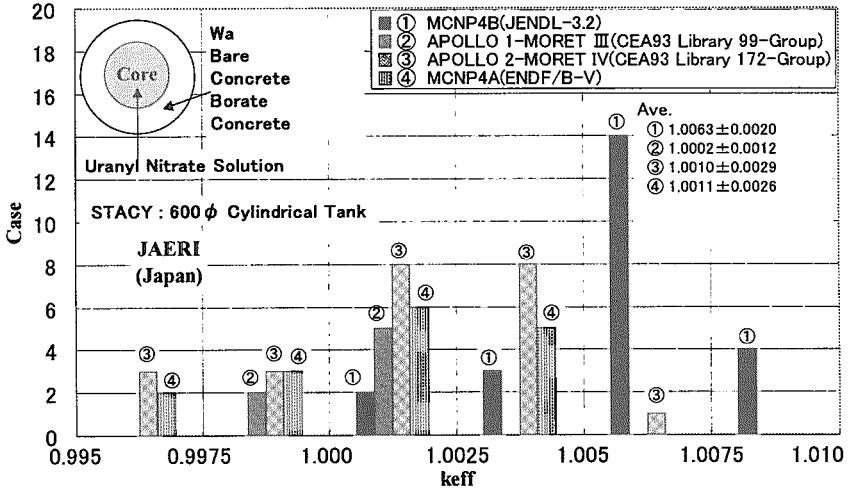

LEU-sol-therm-004, 007～010

Figure 3 Histogram of Calculation Results

2.16 High Energy Nuclear Reaction Code JAM

Koji Niita

RIST (Research Organization for Information Science & Technology)
Tokai-mura, Naka-gun, Ibaraki-ken 319-1106
e-mail: niita@hadron02.tokai.jaeri.go.jp

We have developed a nucleon-meson transport code NMTC/JAM, which is an upgrade version of NMTC/JAERI97. The available energy range of NMTC/JAM is extended to 200 GeV for nucleons and pions, since NMTC/JAM implements the high energy nuclear reaction code JAM for the intra-nuclear cascade part. We compare the calculations by NMTC/JAM code with the experimental data of thin and thick targets for proton induced reactions up to several 10 GeV. The results of NMTC/JAM code show excellent agreement with the experimental data.

1. Introduction

NMTC/JAERI97 [1] has been used in combination with MCNP4A [2] as a standard code system at JAERI in the neutronics design study for the spallation neutron source. For the validation of NMTC/JAERI97, we used the experimental data, which have been provided from the ASTE [3] (AGS Spallation Target Experiment) using a mercury target bombarded with protons at incident energies ranging from 1.5 to 24 GeV. Since NMTC/JAERI97 cannot treat the nuclear reactions above 3.5 GeV, it is required to extend the available energy range to higher region. Thus we have introduced the high energy nuclear reaction code JAM [4] into the intra-nuclear cascade part of NMTC/JAERI97 and we have named this new code system NMTC/JAM. In NMTC/JAM code, we have also upgraded the nucleon-nucleus nonelastic, elastic and differential elastic cross section data above 100 MeV by employing new systematics. In this paper, we describe the main feature of JAM and the upgrading work for the cross section data. The comparisons with the experimental data are shown with respect to the thin and thick target systems.

2. JAM

JAM (Jet AA Microscopic Transport Model) [4] is a hadronic cascade model, which explicitly treats all established hadronic states including resonances with explicit spin and isospin as well as their anti-particles. We have parametrized all hadron-hadron cross sections based on the resonance model and string model by fitting the available experimental data. Below c.m. energy $\sqrt{s} < 4$ GeV, the inelastic hadron-hadron collisions are described by the resonance formations and their decays, and at higher energies , string formation and their fragmentation into hadrons are assumed. Inelastic cross sections are assumed to be filled up with the resonance formations up to $\sqrt{s} = 3 \sim 4$ GeV. At higher energies, the difference between experimental inelastic cross section and resonance formation cross sections are assigned to the string formation.

We have parametrized the resonance formation cross sections in terms of the extended Breit-Wigner form and used the established data [5] for its decay channels and probabilities. At an

energy range above $\sqrt{s} > 4 \sim 5$ GeV, the (isolated) resonance picture breaks down because width of the resonance becomes wider and the discrete levels get closer. The hadronic interactions at the energy range $4 \sim 5 < \sqrt{s} < 10 \sim 100$ GeV where it is characterized by the small transverse momentum transfer is called "soft process", and string phenomenological models are known to describe the data for such soft interaction well. The hadron-hadron collision leads to a string like excitation longitudinally. In actual description of the string formation, we follow the prescription adopted in the HIJING model [6]. The strings are assumed to hadronize via quark-antiquark or diquark-antidiquark creation. As for the fragmentation of the strings, we adopted Lund fragmentation model PYTHIA6.1 [7].

3. Elementary Cross Sections of Hadron-Hadron

For the validation of above prescription of JAM, we compared the results of JAM for the elementary cross sections of hadron-hadron with the experimental data. In Fig. 1. we show the calculated rapidity distributions and the transverse momentum distributions of protons, positive and negative pions for proton-proton collisions at 12GeV/c and also the data from Ref. [8]. The proton stopping behavior and the pion yields are well described by the present model. Within our model, fast protons come from resonance decays and mid-rapidity protons from string fragmentation.

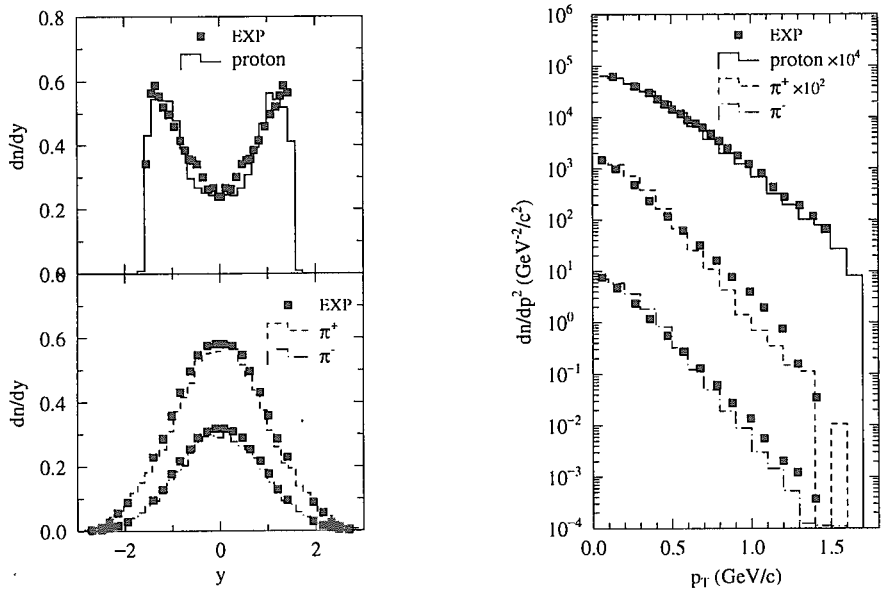

Fig. 1. The rapidity distributions (left panel) and the transverse momentum distributions (right panel) of proton, π^+ and π^- in pp collisions at 12 GeV/c.

Fig. 2. shows the energy dependence of the exclusive pion production cross sections in pp reactions. We compare the results obtained from our simulation with the data [9]. Overall agreement is achieved in these exclusive pion productions. Smooth transition from the resonance picture to the string picture at $E_{cm} = 3 \sim 4$ is achieved since no irregularity of the energy dependence is present in the calculated results.

As for the other elementary cross sections of hadron-hadron, the results of JAM have shown good agreement [4] with the experimental data.

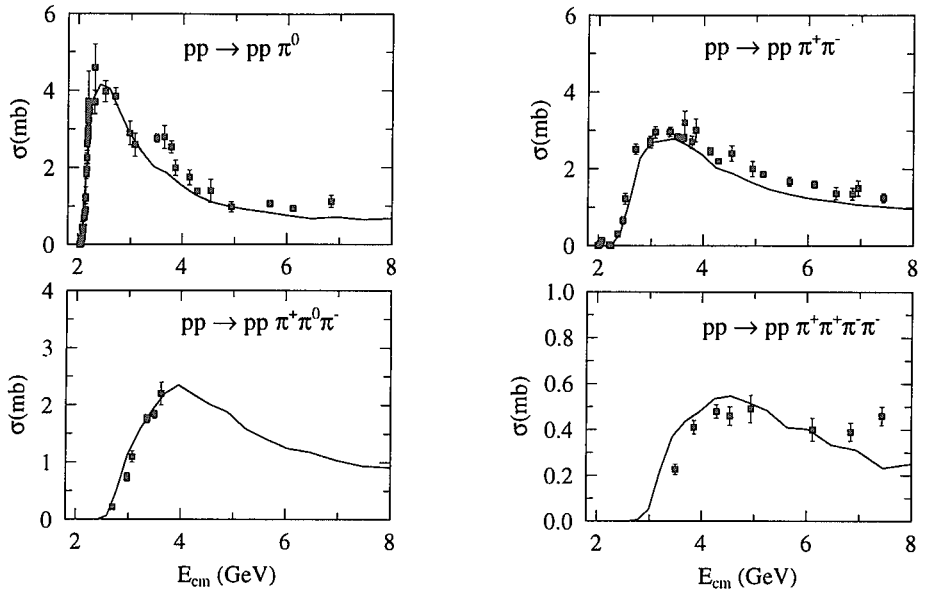

Fig. 2. The energy dependence of the exclusive pion production cross sections for proton-proton as a function of c.m. energy.

4. DDX from Thin Target

By making use of these elementary cross sections, we have calculated the DDX of produced particles from proton induced reactions on thin targets. In Fig. 3, we plot the invariant transverse mass distribution of proton (left panel), π^- (middle panel), and K^+ (right panel) from proton on thin Au target reaction at 13.7 GeV. The results of JAM (histograms) and data [10] are plotted for each rapidity bin quoted in the figure. For all ejectiles, the results of JAM agree well with the experimental data [10]. The agreements are also shown in the other targets of Be, Al, and Cu in Ref. [4]

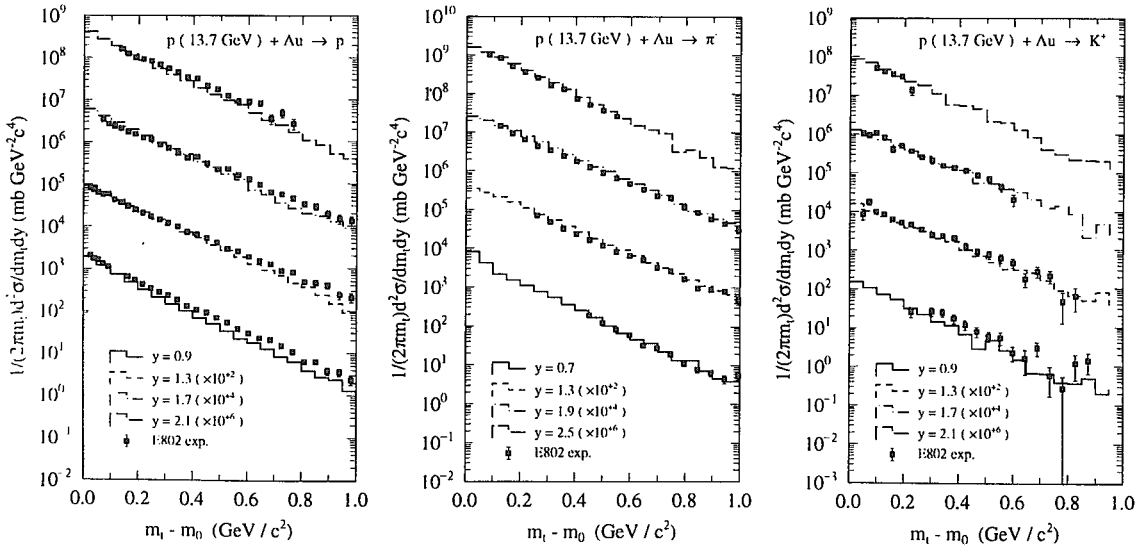

Fig. 3. Invariant transverse mass distribution of proton (left panel), π^- (middle panel), and K^+ (right panel) from proton on thin Au target reaction at 13.7 GeV.

5. Upgrade of the Nucleon-Nucleus Cross Sections

We have included the above JAM code into the intra-nuclear cascade part of NMTC/JAERI97. For this purpose, it is important to use reliable cross section data of nucleon-nucleus for simulating nucleon and meson transport in medium. In NMTC/JAERI97, Pearlstein's systematic [11] is used for non-elastic and elastic cross sections of neutron-nucleus reactions, while for proton-nucleus reactions, elastic collision is not considered, and non-elastic cross section is determined by Bertini model [12] (which is the intra-nucleus cascade model used in NMTC/JAERI97). We have then made new systematics based on Pearlstein's for proton as well as neutron nucleus cross sections.

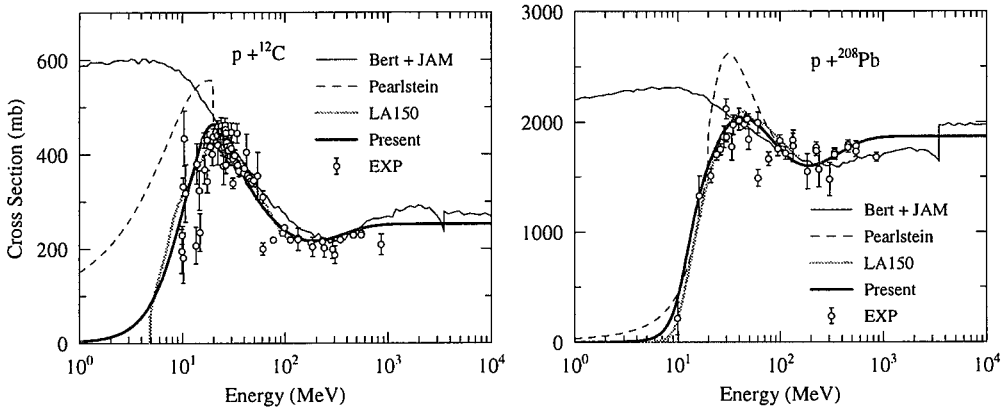

Fig. 4. Non-elastic cross section of p+C (left panel) and p+Pb (right panel).

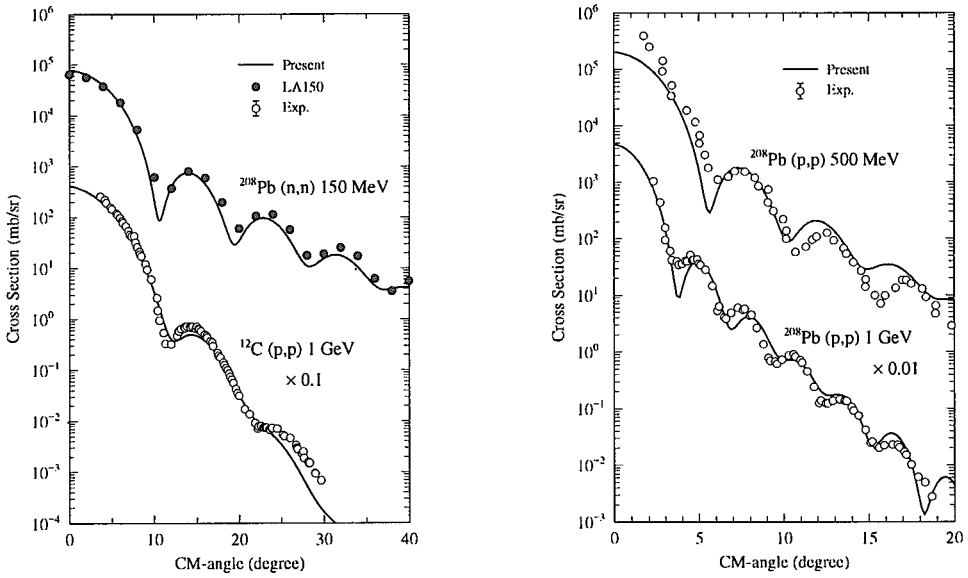

Fig. 5. Angular distribution of the elastic cross sections.

In Fig. 4., we plot the results of new systematic (bold solid lines) for the non-elastic cross section of p+C and p+Pb. In the same figure, we also show the results of LA150 [13] (gray lines), the original Pearlstein's systematics (dashed lines), and the simulation results of Bertini model (solid lines up to 3.5 GeV) and JAM code (solid line above 3.5 GeV). The present results well

follow the experimental data and also LA150 data, while the results of the original Pearlstein's systematics overestimates the data below 100 MeV. The connection of the simulation results between Bertini and JAM is not smooth and in the low energy region, the results of Bertini are too high. This is one of the reason to create present new systematics.

We have also created the new systematics based on the Pearlstein systematics for nucleon-nucleus elastic angular distributions. Fig. 5. shows the results of the new systematics of the angular distribution of the elastic cross sections. We compare the present results with the experimental data and LA150. The present results well reproduce the experimental data for all over the incident energies.

6. Analysis of High Energy Proton on Thick Target System

We have applied NMTC/JAM to thick target analysis. Fig. 6. shows the distribution of the ^{117}In(n,n')^{115m}In (left panel), ^{209}Bi(n,4n)^{206}Bi and ^{209}Bi(n,5n)^{205}Bi (right panel) reaction rates along the cylindrical surface of 20 cm diameter and 130 cm long mercury target bombarded with 24 GeV protons at AGS [3]. In this figures, the solid histograms denote the results of JAM, while the dashed lines show the results of LCS2.7 [14], respectively. The results of JAM reproduce the experimental distribution quite well for all position. In the actual calculations, we have used the Bertini model for the intra-nuclear cascade part below 3.5 GeV, and JAM above 3.5 GeV and used the in-medium nucleon-nucleon cross sections [1] in Bertini model. This connection between Bertini and JAM models is due to the reduction of the calculation time. The cpu time of JAM calculation is about ten times longer than that of Bertini model, and the results of the cross sections calculated by both models are almost the same below 3.5 GeV. The results of LCS2.7, however, overestimate the reaction rate at deeper position. LCS2.7 also uses Bertini model for intra-nuclear cascade part. Then LCS2.7 employs the scaling low in order to extend the upper limit of the energy of Bertini model. This figure shows that this scaling low is not adequate above 10 GeV (this overestimate is also observed at 12 GeV).

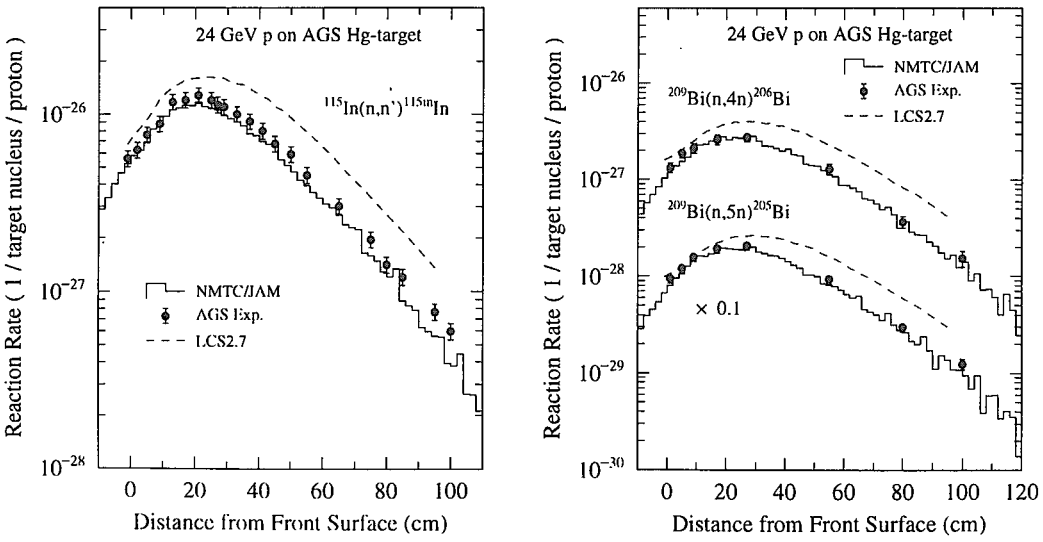

Fig. 6. Longitudinal distribution of the reaction rates along the cylindrical surface of mercury target bombarded with 24 GeV protons at AGS.

7. Summary

We have developed a nucleon-meson transport code NMTC/JAM, which is an upgrade version of NMTC/JAERI97. The available energy range of NMTC/JAM is extended to 200 GeV for nucleons and pions. JAM is a hadronic cascade model, in which we have parametrized all hadron-hadron cross sections based on the resonance model and string model by fitting the available experimental data. For the transport part of NMTC/JAM, we have upgraded the nucleon-nucleus non-elastic and elastic cross sections by employing the new systematics. We have compared the calculations by NMTC/JAM code with the experimental data of thin and thick targets for proton induced reactions up to several 10 GeV. The results of NMTC/JAM code show excellent agreement with the experimental data. From these code validation, NMTC/JAM will enable us to carry out reliable neutronics optimization study of the high intense spallation neutron utilization facility.

References

[1] Takada H. et al.: NMTC/JAERI97, JAERI-Data/Code 98-005, (1998).

[2] Breismaister J. F. (Ed.): MCNP A General Monte Carlo N-Particle Transport Code, Version 4A, LA-12625 (1993).

[3] Takada H. et al.: Proc. of the 14th Mtg. of the Int. Collaboration on Advanced Neutron Sources , June 14-19, 1998.

[4] Y. Nara, et al.: Phys, Rev. C, in press
http://hadron31.tokai.jaeri.go.jp/jam/.

[5] Particle-Data-Group: Phys. Rev. D54, (1996).

[6] Wang X. N. and Gyulassy M.: Phys. Rev. D44, 3501 (1991); Wang X. N.: Phys. Rep. 280, 287 (1997); Wang X. N. and Gyulassy M.: Comp. Phys. Comm. 83, 307 (1994);
http://www-nsdth.lbl.gov/~xnwang/hijing/.

[7] SjöstrandC T.: Comp. Phys. Comm. 82, 74 (1994); PYTHIA 5.7 and JETSET 7.4 Physics and Manual. *http://thep.lu.se/tf2/staff/torbjorn/Welcome.html.*

[8] Bonn-Hamburg-München Collaboration, Blobel V. et al.: Nucl. Phys. B69, 454 (1974).

[9] Total Cross-Sections for Reactions of High Energy Particles vol. 12a and vol. 12b edited by Baldni A., Flaminio V., Moorhead W. G. and Morrison D. R. O. (Springer-Verlag Berlin 1988).

[10] E802 Collaboration, Abbott T., et al.: Phys. Rev. D45 3906 (1992); Compilation of Relativistic Heavy-Ion Data, *http://www.nndc.bnl.gov/~hi_data/rhid.html.*

[11] Pearlstein S.: Nucl. Sci. Eng., 49, 162 (1972); Nucl. Sci. Eng., 95, 116 (1987).

[12] Bertini H. W.: Monte Carlo Calculation on Intranuclear Cascade, ORNL-3833, (1963).

[13] Chadwick M. B., et al.: Nucl. Sci. Eng. 131, 293 (1999).

[14] Prael R. E., Lichtenstein H.: User Guide to LCS: The LAHET Code System, LA-UR-89-3014 (1989).

2.17 Revision of Heavy Nuclei Data in JENDL-3.2

KAWANO Toshihiko†
and
Heavy Nuclear Data Evaluation Working Group[1]
†*Advanced Energy Engineering Science, Kyushu University*
6-1 Kasuga-kouen, Kasuga 816-8580, Japan
e-mail: kawano@aees.kyushu-u.ac.jp

In order to deal with problems concerning the data of heavy nuclides in JENDL-3.2, a working group was organized to update the evaluated nuclear data of Uranium, Plutonium, and Thorium isotopes. The current status of the working group is reviewed, and some results about resonance parameters, secondary neutron energy spectra, fission cross sections, and direct/semidirect capture process are shown.

1. Introduction

After the release of JENDL-3.2, several problems concerning the data of heavy nuclides have been reported. The quantities with problems of great importance are as follows :

- ^{235}U resonance parameter
- Secondary neutron energy spectrum
- Fission cross sections in the smooth region
- Direct/semi-direct capture process

A working group on evaluation of nuclear data of heavy nuclides was organized in 1997 to update the evaluated nuclear data of Uranium, Plutonium, and Thorium isotopes in JENDL-3.2. The objectives of the working group are to investigate the problems and to re-evaluate the nuclear data for the next revision of JENDL — JENDL-3.3. We have investigated these problems for a couple of years, and adopted outcomes of the discussions in the new evaluations. The current status of the working group is reviewed, and some results are reported.

2. Resonance Parameters

In JENDL-3.1, resonance parameters of the single-level Breit-Wigner formula was adopted for ^{235}U in the energy range up to 100 eV. These parameters were replaced with the data of ENDF/B-VI which were based on a Reich-Moore R-matrix analysis of Leal, de Saussure, and Perez[1] at the release of JENDL-3.2. Several problems concerning cross sections in the resolved resonance region have been reported since then. The major problems are an underestimation of capture cross sections and an overestimation of k_{eff} for thermal reactors. Note that Leal

[1]M. Baba, O. Iwamoto, M. Kawai, T. Kawano, H. Matsunobu, T. Murata, T. Nakagawa, Y. Nakajima, T. Ohsawa, K. Shibata, T. Yoshida, and A. Zukeran

Table 1: Fission and capture cross sections at the thermal energy calculated with the ^{235}U resonance parameters.

		Fission		Capture		Ref.
	formula	2200 m/s [b]	Res. Integ. [b]	2200 m/s [b]	Res. Integ. [b]	
JENDL-3.1	SLBW	584.0	275	96.0	152	
JENDL-3.2	R-M	584.4	279	98.81	134	[1]
JENDL-3.3	R-M	584.88	276.04	98.66	140.49	[2]

et al. gave the resonance parameters up to 2.25 keV, however the upper limit of the resolved resonance region for ^{235}U in JENDL-3.2 was 500 eV.

In 1997, Leal, Derrien, Larson, and Wright carried out a new R-matrix analysis[2] of ^{235}U resonance parameters up to 2.25 keV. We decided to adopt this resonance parameter set for JENDL-3.3. Thermal cross sections and resonance integral calculated with those parameters are shown in Table 1.

A preliminary benchmark test with the resonance parameters of Leal *et al.*[2] was carried out, and it was reported that the overestimation of k_{eff} was improved to some extent, but it is insufficient. To improve the predictivity of k_{eff}, re-evaluation of other quantities such as a prompt neutron fission spectrum is needed. The fission spectrum is under investigation by Ohsawa with a multimodal fission analysis[3].

Recently an R-matrix analysis for ^{240}Pu was also carried out[4]. The resonance parameters obtained by Bouland *et al.* will be adopted in JENDL-3.3.

3. Secondary Neutron Energy Spectrum

Secondary neutron energy spectra for the (n, n'), $(n, 2n)$, and $(n, 3n)$ reactions compiled in JENDL-3.2 have been criticized for a long time. There exists three reasons for this problem. The first one is an adoption of the evaporation formula for neutron energy spectra above a threshold energy of $(n, 2n)$ reaction. This problem arises for several minor actinodes. The second one is a special case for ^{238}U. The energy spectra of ^{238}U were calculated with the GNASH code[5], and the crude output was stored into JENDL-3.2 without any post-processing procedures. However one had to employ a processing code such as GAMFIL[6] to convert into the ENDF format. The third one is not crucial. In JENDL-3.2, energy spectra for many important nuclei were calculated with the PEGASUS code[7]. This is an evaporation model calculation code and generates an appropriate spectrum in the ENDF format, although use of the GNASH code may be preferable in view of more accurate evaluation.

In the present revision work, we adopted the GNASH code to calculate the energy spectra. Results of the GNASH calculations were processed with the GAMFIL code. Figure 1 shows an example of the calculated spectrum, which is a spectrum of neutrons from ^{238}U at $E_n = 18$ MeV. The total neutron spectrum is compared with the experimental data[8] in Fig. 1.

4. Simultaneous Evaluation of Fission Cross Sections

A simultaneous evaluation method[9, 10] was adopted to evaluate the fission cross sections of ^{235}U, ^{238}U, ^{239}Pu, ^{240}Pu, and ^{241}Pu for JENDL-3, and the results were slightly modified and compiled into JENDL-3.2. After the release of JENDL-3.2, some new measurements of the fission cross sections of these nuclides have been published. These experimental data should be

added to the database of the simultaneous evaluation in order to update the evaluated cross sections in JENDL-3.2. We investigated new experimental data which were not included in the previous evaluation, and developed a new simultaneous evaluation code SOK — Simultaneous evaluation On KALMAN — which is based on the model parameter estimation code KALMAN[11].

In the previous simultaneous evaluation, the capture cross sections of ^{238}U and ^{197}Au were incorporated into the experimental database. These reactions were, however, omitted in the present evaluation, because the evaluation of ^{238}U capture cross section was made independently[12] of the fission cross sections, and no data will be given for ^{197}Au in JENDL-3.3. Instead of these reactions we included the fission cross sections of ^{233}U in the present evaluation. A comparison of the evaluated fission cross sections of ^{233}U with the evaluated values in JENDL-3.2 and ENDF/B-VI, as well as the experimental data is shown in Fig. 2. Figure 3 shows a comparison of the fission cross section ratios of ^{233}U to ^{235}U. Since there are so many data points and they are indistinguishable, all experimental data are represented by the same symbol.

5. Direct/Semidirect Capture Process

The radiative capture process above about 5 MeV is explained by the Direct/Semidirect (DSD) radiative capture theory[13, 14]. However this process was not considered for many nuclei in JENDL-3.2. To overcome this problem, we made a computer program DSD. This code is based on the theory of Kitazawa *et al.*[15], which is the DSD theory for deformed nuclei. The maximum values of capture cross sections calculated with the DSD theory are in the order of 1 mb. Such a small cross section is not so important for practical applications. We made several approximations to make the calculation easy.

Comparisons of the calculated capture cross sections with the experimental data[16, 17] are shown in Fig. 4. The dot-dashed line is calculated with the Hauser-Feshbach theory which predicts almost negligible cross sections above 5 MeV. A summation of the Hauser-Feshbach and DSD calculations gives the final evaluated cross sections in this energy region. The dotted line in Fig. 4 shows the cross sections in JENDL-3.2, which were evaluated empirically.

6. Concluding Remarks

We briefly described some major revisions of the data of heavy nuclei — the resonance parameters of ^{235}U and ^{240}Pu, the secondary neutron energy spectra, the fission cross sections in the smooth region, and the direct/semidirect capture process. However there exists many other revisions which are not mentioned above, such as angular distributions for elastic/inelastic scattering, ν_p, ν_d, $(n, 2n)$ and $(n, 3n)$ reactions, and so forth. We have almost completed the re-evaluation of the cross sections and the other quantities described above. These nuclear data will be finalized after several benchmark tests. In addition, the working group will be active for an evaluation of covariance data.

References

[1] Leal, L.C., de Saussure, G., Perez, R.B. : *Nucl. Sci. Eng.*, **109**, 1 (1991).

[2] Leal, L.C., Derrien, H., Larson, N.M., Wright, R.Q. : *ORNL/TM-13516* (1997), *Nucl. Sci. Eng.*, **131**, 230 (1999).

[3] Ohsawa, T., Horiguchi, T., Hayashi, H. : *Nucl. Phys. A*, **653**, 17 (1999).

[4] Bouland, O., Derrien, H., Larson, N.M., Leal, L.C. : *Nucl. Sci. Eng.*, **127**, 105 (1997).

[5] Young, P.G., Arthur, E.D. : "GNASH, A Pre-equilibrium, Statistical Nuclear-Model Code for Calculation of Cross Section and Emission Spectra," LA-6947 (1977).

[6] Hida, K. : "GAMFIL : A Computer Program for Generating Photon Production Nuclear Data File," JAERI-M 86-150 (1986), in Japanese.

[7] Nakagawa, T., Iijima, S., Sugi, T., Nishigori, T. : "PEGASUS : A Preequilibrium and Multi-step Evaporation Code for Neutron Cross Section Calculation," JAERI-Data/Code 99-031, (1999).

[8] Baba, M., Wakabayashi, H., Ito, N., Maeda, K., Hirakawa, N. : *J. Nucl. Sci. Technol.*, **27**, 601 (1990).

[9] Uenohara, Y., Kanda, Y. : *J. Nucl. Sci. Technol.*, **20**, 967 (1983).

[10] Kanda, Y., Uenohara, Y., Murata, T., Kawai, M., Matsunobu, H., Nakagawa, T., Kikuchi, Y., Nakajima, Y. : "Simultaneous Evaluation of Fission and Capture Cross Sections and Their Covariances for Heavy Nuclei," *Proc. Int. Conf. Nuclear Data for Basic and Applied Science,* Santa Fe, New Mexico, 13–17 May 1985, p.1567 (1986).

[11] Kawano, T., Shibata, K. : "Covariance Evaluation System," *JAERI-Data/Code* 97-037 (1997), in Japanese.

[12] Kanda, Y., Kikuchi, Y., Nakajima, Y., Sowerby, M.G., Moxon, M.C., Fröhner, F.H., Poenitz, W.P., Weston, L.W. : "A Report on Evaluated ^{238}U(n,γ) Cross Section," *Proc. Int. Conf. Nuclear Data for Science and Technology,* Jülich, Germany, 13–17 May 1991, p.851 (1992).

[13] Brown, G.E. : *Nucl. Phys.*, **57**, 339 (1964).

[14] Clement, C.F., Lane, A.M., Rook, J.R. : *Nucl. Phys.*, **66**, 273,293 (1965).

[15] Kitazawa, H., Hayase, T., Yamamuro, N. : *Nucl. Phys. A*, **301**, 1 (1978).

[16] McDaniels, D.K., Varghese, P., Drake, D.M., Arthur, E., Lindholm, A., Bergqvist, I., Krumlinde, J. : *Nucl. Phys. A*, **384**, 88 (1982).

[17] Drake, D., Bergqvist, I., McDaniels, D.K. : *Phys. Lett.*, **36B**, 557 (1971).

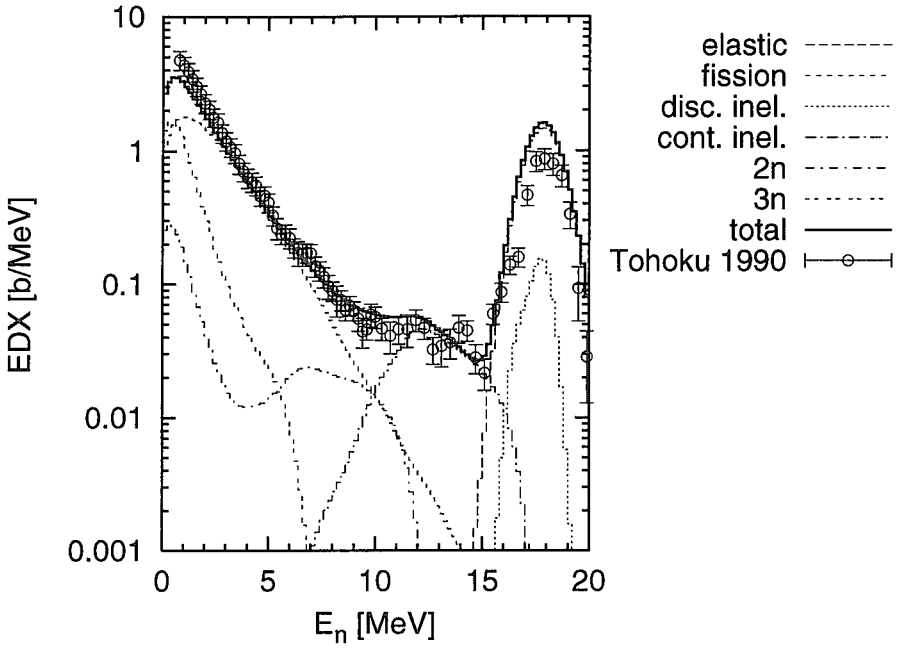

Figure 1: Secondary neutron energy spectrum of ^{238}U at the incident energy of 18 MeV. The total spectrum is decomposed into contributions of various processes.

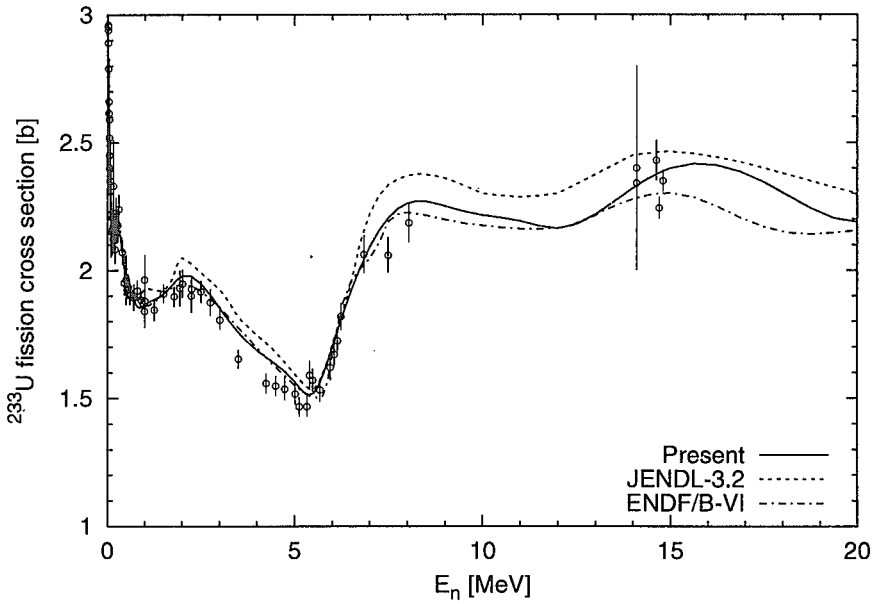

Figure 2: Comparison of the fission cross sections of ^{233}U with the experimental data and the evaluated cross sections in JENDL-3.2 and ENDF/B-VI.

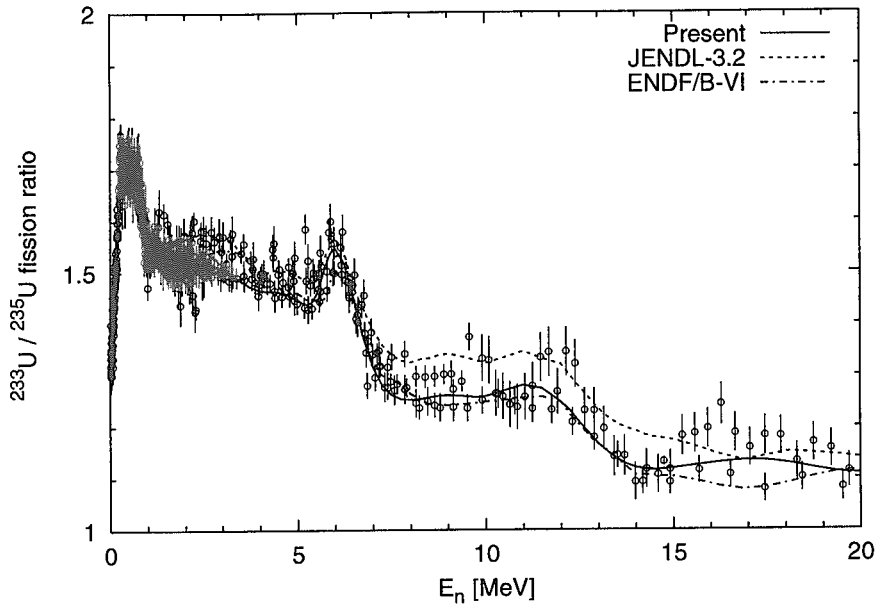

Figure 3: Comparison of the fission cross section ratios of ^{233}U to ^{235}U with the experimental data, and with the evaluated values of JENDL-3.2 and ENDF/B-VI.

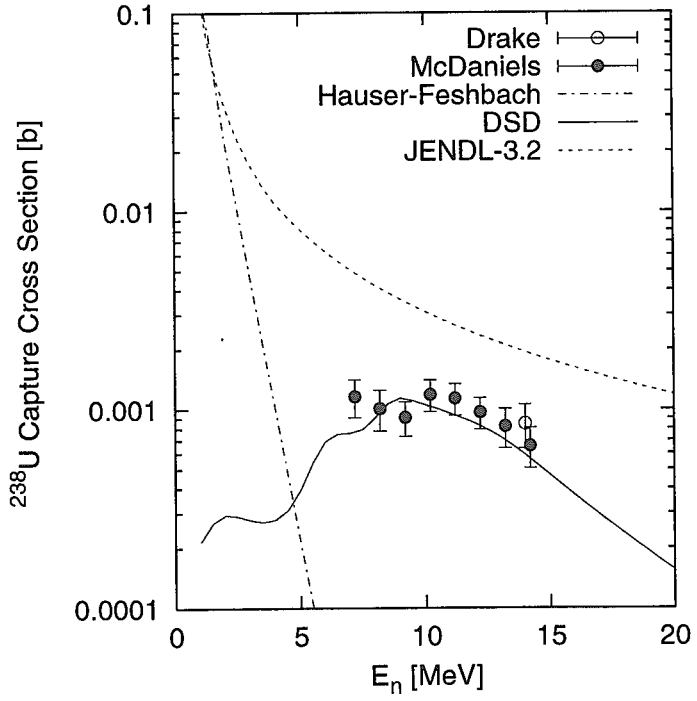

Figure 4: Comparison of the radiative capture cross sections of ^{233}U, and with the evaluated cross sections in JENDL-3.2. The solid line is calculated with the DSD code, the dot-dashed line is calculated with the Hauser-Feshbach theory.

JAERI−Conf 2000−005

2.18 Present Status of JENDL FP Decay Data File

J. Katakura
Nuclear Data Center
Japan Atomic Energy Research Institute
e-mail: katakura@ndc.tokai.jaeri.go.jp

JENDL FP Decay Data File is now being prepared for the use of such application fields as decay heat analysis of nuclear reactor, inventory analysis, radiation source estimation of nuclear fuel and so on. The primary file of the file has been compiled and is under quality test. After the test the file will be released until the end of next March. In the present report the present status of the JENDL Decay Data File is presented.

1 Introduction

The JENDL FP Decay Data File was planed to be compiled as a special purpose file of JENDL (Japanese Evaluated Nuclear Data Library) libraries. The libraries are expected to be used for application fields in nuclear technology. As for the decay data file for application use JNDC library [1] has been compiled in Japan for decay heat analysis. The file has been successfully applied to decay heat estimation of nuclear reactor. The file, however, has not JENDL (ENDF) format [2] and is not a JENDL library. This situation sometimes cause confusion among nuclear data community. In order to remove such confusion, the compilation of JENDL FP Decay Data File has been started. The decay data included in the JNDC library are those collected almost 10 years ago. The new measured data are reported after the compilation of JNDC library. These newly measured data are also included in JENDL FP Decay Data File. The spectrum data which are not included in the JNDC library are also included in the new file. In this report the outline of the JENDL FP Decay Data File and the some tests performed by now are presented.

2 Outline of Proposed FP Decay Data File

The FP Decay Data File is one of the JENDL Special Purpose Files; that means the file has JENDL format which is the same as ENDF one. The file is expected to include such data as half-life, decay modes, branching ratios, Q values, average decay energy values of emitted radiations (gamma rays, beta rays, alpha particles, internal conversion electrons, X rays), and their spectrum data of all fission product nuclides. The primary source of these data are measured ones. The measured data are taken from the compilation of ENSDF (Evaluated Nuclear Structure Data File) [3] which is compiled with international cooperation and is revised continuously. The primary purpose of the file is to be used for such application fields as decay heat evaluation, nuclear waste management, radiation shielding, nuclide concentration in a reactor and so on. The data contained in the file, therefore, should be "complete" and "consistent". The measured data, however, are often "incomplete", that is missing of gamma rays or beta rays are occurred. In such a case the average gamma energy values are underestimated and the average beta energy values are overestimated. The theoretical model calculation is needed to compensate the missing radiations. The model calculation is applied to the nuclides with no measured data and "incomplete" ones of beta and/or gamma rays. The number of nuclides to be contained is summarized in Table 1.

As shown in Table 1, the nuclides with spectrum data are 1085 out of total 1229 fission product nuclides. However, all of the nuclides do not always have complete measured spectrum data of beta and gamma rays. Most of the short-lived nuclides often lack complete measured spectrum. For these nuclides model calculation is also needed for beta and gamma ray spectrum for compensating the incomplete spectrum. The present primary file of the JENDL FP Decay Data includes the model calculated spectrum for beta and gamma rays.

Table 1: Number of nuclides contained in JENDL FP Decay Data File

• Total Nuclides :	1229	• γ ray spectrum	
○ Stable :	142	○ Measured :	629
○ Isomer :	179	○ Calculated :	543
○ Second Isomer :	8	○ Both :	121
• With Spectrum :	1085	• β ray spectrum	
○ γ ray :	1051	○ Measured :	472
○ β ray :	896	○ Calculated :	521
○ α ray :	5	○ Both :	97
○ X ray :	507		
○ ICE :	454		

There are about 100 nuclides which have both measured and calculated spectra of beta and gamma rays. The measured data of these nuclides are "incomplete" and are compensated by the theoretical model calculation. The adoption of the model calculated spectrum are first performed for ENDF/B-VI FP Decay Data File [4]. Using the model calculated spectrum the ENDF file can reproduce the measured aggregate spectra of beta and gamma rays after fission of variety of fissioning nuclides. The JENDL FP Decay Data File is also expected to be good agreement with the measured spectra.

3 Adoption of Model Calculation

In the decay heat evaluation, the average energy values of nuclides with incomplete measured decay data and no measured ones were calculated by "Gross Theory of Beta Decay" [5] developed by Waseda University Group. Using these calculated energy values the decay heat values of various fissioning nuclides are well reproduced. The brief description of the model is presented here. In beta decay process, the decay constant and average beta and gamma values are described as follows:

$$\begin{aligned}
\lambda &= \sum_{i=0}^{n} \lambda^{(i)}, \\
&= \frac{1}{2\pi^3} \sum_{i=0}^{n} \sum_{\Omega} |g_\Omega|^2 \cdot |(\Psi_i, \Omega\Psi)|^2 f(E_i)|, \\
\bar{E}_\beta &= \sum_{i=0}^{n} \frac{\lambda^{(i)}}{\lambda} (Q - \epsilon_i) C^{(i)}, \\
\bar{E}_\gamma &= \sum_{i=0}^{n} \frac{\lambda^{(i)}}{\lambda} \epsilon_i,
\end{aligned}$$

where i means the $i-th$ final state of energy ϵ_i, Q the Q value of beta decay, $C^{(i)}$ the ratio of the average electron kinetic energy to the maximum electron kinetic energy $Q-\epsilon_n$, Ω the type of beta decay operator, g_Ω the coupling constant and $f(E_i)$ the Fermi function. In the "Gross Theory" the discrete levels of the daughter nuclide are treated as continuous ones. The decay constant is, therefore, represented as follows:

$$\lambda = \frac{1}{2\pi^3} \int_{-Q}^{0} \sum_{\Omega} |g_\Omega|^2 \cdot |M_\Omega(E_g)|^2 f(-E_g + 1) dE_g$$

The matrix element $|M_\Omega(E)|^2$ is given by the following equation.

$$|M_\Omega(E)|^2 = \int_{\epsilon_m in}^{\epsilon_m ax} D_\Omega(E, \epsilon) W(E, \epsilon) \frac{dn_1}{d\epsilon} d\epsilon$$

where

$D_\Omega(E,\varepsilon)$: one-particle strength function inferred from sum rules,

E : energy of final nuclear state measured from initial state,

ε : one-particle energy of decaying nucleon,

$\frac{dn_1}{d\varepsilon}$: energy distribution of one particle,

$W(E,\varepsilon)$: weight function to take into account the Pauli exclusion principle.

The beta and gamma ray spectrum are calculated using the matrix elements and the level density formula. When the calculated spectrum is incorporated into the file, the measured spectrum, if exits, is kept in the original data but the normalization factor is changed in order to keep consistency between the average energy values and the spectrum data.

4 Test of the File

The file is now being tested through comparison with decay heat measurements and aggregate fission products spectrum of beta and gamma rays. The examples of the results are shown in Figs. 1 through 3 for the decay heat after ^{235}U thermal neutron fission.

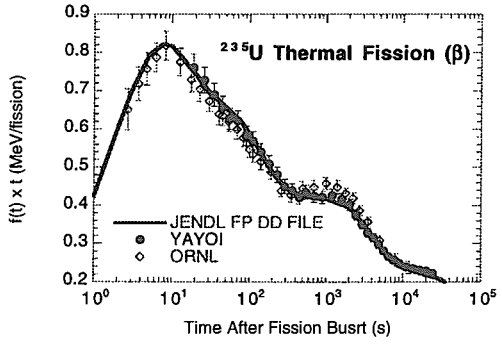

Fig. 1 Beta ray component of the decay heat after ^{235}U thermal neutron fission

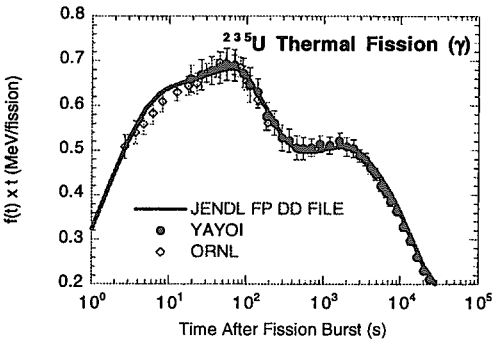

Fig. 2 Gamma ray component of the decay heat after ^{235}U thermal neutron fission

In these figures the decay heat is represented by those of energy release rate multiplied by time. The measured data are taken from those at Oak Ridge National Laboratory (ORNL in figures) [6] and Tokyo University (YAYOI in figures) [7]. The decay heat calculations are in good agreement with the measured data for beta, gamma and total decay heat. These figures show that the FP Decay Data File seems to be applicable to decay heat estimation of fission products. It is also interesting to compare the calculated decay heat values between those calculated with the present file and the JNDC file. The JNDC file is the basis of the calculation to produce the recommendation of reactor decay heat by Atomic Energy Society of Japan because of its success to reproduce the measured decay heat values of various fissioning nuclides. The comparison was made for ^{235}U thermal neutron fission. The differences of the decay heat values between them are shown Figs. 4 through 6. The calculations are made for ^{235}U thermal neutron fission. The differences are represented by percentage from the calculated values using the JNDC file. The comparisons were made for the cooling time region upto 10^{13} seconds after fission burst. As seen in these figures the gamma component shows about 12 % differences at about 10^{10} seconds after fission. The differences of the beta component, however, are 5 % at most. For the total decay heat the differences

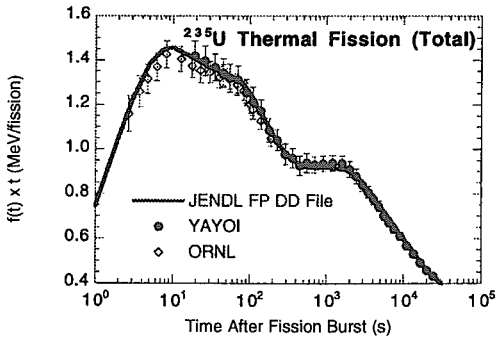

Fig. 3 Total decay heat after ^{235}U thermal neutron fission

are within 4 %. The main source of the difference seen in the gamma component at about 10^{10} seconds is the decay energy values of ^{126m}Sb. The average gamma energy value of the JNDC file is 1.7995 MeV, but it is 1.550 MeV in the new file. As there are a few nuclides which contribute to the decay heat at this cooling time region, the the data of one nuclide cause large effect on the calculation. The data in the JNDC file are based on old measured data. We should adopt new measured data for the JENDL FP DD File even if the differences are more than 10 %.

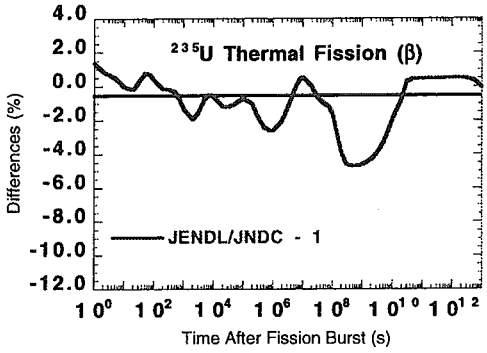

Fig. 4 Differences of beta ray component between the decay heat calculations with the JNDC file and the present JENDL DD file

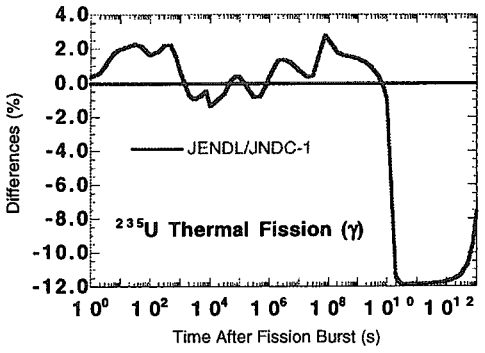

Fig. 5 Differences of gamma ray component between the decay heat calculations with the JNDC file and the present JENDL DD file

We also made comparison with the AESJ recommendation [8] of decay heat values. The Atomic Energy Safety Committee in Japan approved the usage of the AESJ recommendation as decay heat source in ECCS (Emergency Core Cooling System) analysis when the uncertainties of the recommendation are suitably taken into account. So the recommended values added three times of the uncertainties are used for the ECCS analysis. It is interesting to compare the decay heat values using new file with the recommended values. In Fig. 7 the comparison is shown. In this figure the AESJ recommendation is represented as that added three times of the uncertainties. If the new decay heat values happened to exceed the recommendation with three times of the uncertainties, it would be needed to reconsider the recommendation. The new decay heat values, however, don't exceed the AESJ recommendation at any cooling time regions and it would not need revise the recommendation.

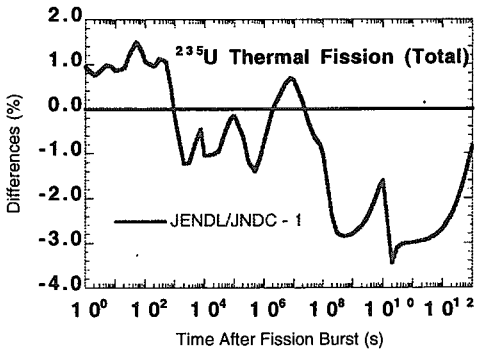

Fig. 6 Differences of total decay heat between the calculations with the JNDC file and the present JENDL DD file

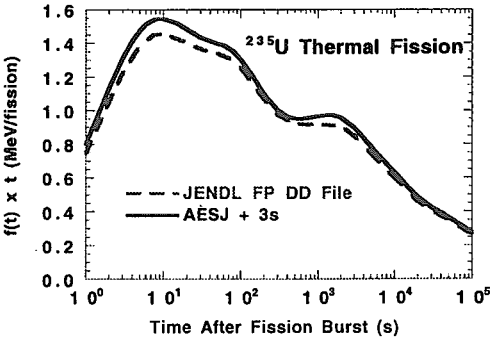

Fig. 7 Comparison of decay heat between the AESJ recommendation and the calculation with JENDL DD file

At present the decay heat comparisons with measured data are limited to some fissioning nuclides. Further comparisons for other fissioning nuclides will be needed before release of the file in order to confirm the applicability to decay heat evaluation of any fissioning nuclides. Such comparisons are now being done.

The spectrum data of the file are also tested by comparing the measured aggregate fission product spectra of beta and gamma rays. The examples of the spectrum calculation are shown in Figs. 8 and 9. Both spectra were taken at 2.2 seconds after the ^{235}U target was irradiated by thermal neutrons for

1 second. The measurements were performed at Oak Ridge National Laboratory [6]. In the figures the results of two kind of calculations are shown: one is the calculated result using the present JENDL FP Decay Data File which includes the model calculated spectra, another is that using ENDF/B-V FP Decay Data File [9] which includes only the measured spectrum data of fission products. The present version of the ENDF is 6th, which also includes the model calculated spectra but the old version is shown here in order to see the effectiveness of the model calculated spectra.

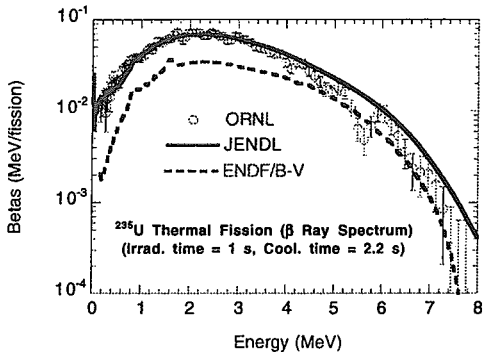

Fig. 8 Aggregate beta ray spectrum after ^{235}U thermal neutron fission

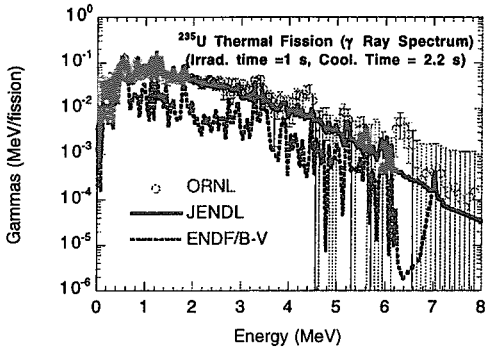

Fig. 9 Aggregate gamma ray spectrum after ^{235}U thermal neutron fission

As seen in these figures the adoption of the model calculated spectra shows good agreement with the measured spectra even in the short cooling time where the nuclides with no measured or incomplete data make major contribution to the spectra. The calculations using only the measured spectral data of fission products largely underestimate the measured spectra. This fact shows that the the model calculated spectra of individual fission product nuclides are effective to estimate the aggregate spectra of both beta and gamma rays. We will continue the comparison with the measured spectra for other fissioning nuclides before the release of the file.

5 Summary

The present status of JENDL FP Decay Data File is described. The primary file of the file has been compiled and is under the test of assessing the quality of the file. The test which has been performed by now has showed good agreement with the measured data of both decay heat values and aggregate fission products spectra of both gamma and beta rays for ^{235}U thermal neutron fission. The further test of the file will be performed for other fissioning nuclides. The file will be released after the test is finished. The release will be made until the end of next March.

References

[1] Tasaka, K. et al.: "JNDC Nuclear Data Library of Fission Products -Second Version-", JAERI 1320 (1990)

[2] The Cross section Evaluation Working Group: "Data Formats and Procedures for the Evaluated Nuclear Data File ENDF-6", BNL-NCS-44945 (ENDF-102), edited by V. McLane et al.(1995)

[3] Bhat, M. R.: "Evaluated Nuclear Structure Data File (ENSDF)", Nuclear Data for Science and Technology, pp817, edited by S. M. Qaim (Springer-Verlag, 1992)

[4] Katakura, J. and England, T. R: "Augmentation of ENDF/B Fission Product Gamma-Ray Spectra by Calculated Spectra", LA-12125-MS (ENDF-352) (1991)

[5] Takahashi, K., Yamada, M., and Kondoh, T.: Atom. Data and Nucl. Data Tables, 12, 101 (1973) and references therein.

[6] Dickens, J. K. et al.: "Fission Product Energy Release for Times Following Thermal Neutron Fission of ^{235}U Between 2 and 14,000 Seconds", ORNL/NUREG-14 (1977)

[7] Akiyama, M. et al.: J. Atom. Ener. Soc. of Japan, 24, 709 (1982) [in Japanese]; Akiyama, M. et al.: J. Atom. Ener. Soc. of Japan, 24, 803 (1982) [in Japanese]

[8] Research Committee on "Standardization of Decay Heat Power in Nuclear Reactors": "Decay Heat Power in Nuclear Reactor and Its Recommended Values", Atom. Ener. Soc. of Japan (1989) [in Japanese]

[9] England, T. R. et al.: "Summary of ENDF/B-V Data for Fission Products and Actinides", NP-3787, LA-UR 83-1285, ENDF-322 (1984)

This is a blank page.

3. Papers Presented at Poster Session

This is a blank page.

3.1 Capture Cross Section Measurement of Np-237 below 1 keV with Lead Slowing-down Spectrometer

Katsuhei Kobayashi[1], Hyun-Je Cho[1*], Shuji Yamamoto[1],
Takaaki Yoshimoto[1], Yoshiaki Fujita[1], and Yasushi Ohkawachi[2]

1 Research Reactor Institute, Kyoto University
Kumatori-cho, Sennan-gun, Osaka 590-0494, Japan
* Visiting Scientist from University of Ulsan, Korea
2 The O-arai Engineering Center, Japan Nuclear Cycle Development Institute,
O-arai-machi, Higashi-ibaraki-gun, Ibaraki 311-1393, Japan

Making use of the Kyoto University Lead slowing-down Spectrometer (KULS) driven by a 46 MeV electron linear accelerator (linac) at the Research Reactor Institute, Kyoto University (KURRI), the relative cross section for the ^{237}Np(n,γ) reaction has been measured from 0.01 eV to 1 keV with energy resolution of about 40 % (FWHM). The neutron flux/spectrum has been measured by a BF_3 counter. The cross section of the ^{10}B(n,α) reaction in ENDF/B-VI was used as a reference one for the cross section measurement. The measured result has been normalized to the reference value of the ^{237}Np(n,γ)^{238}Np reaction in ENDF/B-VI at 0.0253 eV, and the measurement has been compared with the experimental and the evaluated data in ENDF/B-VI and JENDL-3.2, whose data were broadened by the energy resolution of the KULS.

1. Introduction

The neptunium (Np)-237, which is abundantly produced in light water reactors, is one of the minor actinides with a long half-life. In order to make nuclear power more acceptable and practical, much interest has been paid to the disposal of radioactive waste matter [1-3]. One of the waste management methods for ^{237}Np is to adopt the nuclear transmutation using reactor neutrons. The Np-237 has a large capture cross section in the low/resonance energy region. It has also a relatively large fission cross section in the MeV energy region. Accurate determination of these cross sections is very important for the evaluation of the transmutation of ^{237}Np which is produced in large quantities in power reactors.

Although several measurements of the ^{237}Np(n,f) cross section have been reported at higher energies, the capture cross section has rarely been measured in the lower/resonance energy region. Hoffman et al. measured the neutron capture cross section of Np-237 by the neutron time-of-flight (TOF) method and Moxon-Rae detector[4]. Weston et al. measured the capture cross section between about 10^{-2} eV and 0.2 MeV by the neutron TOF method using an Oak Ridge Electron Linear Accelerator [5]. The evaluated fission cross section data are appeared in ENDF/B-VI [6] and JENDL-3.2 [7].

In the present study, we measure the neutron capture cross section of Np-237 in the range of

0.01 eV to 1 keV relative to that of the $^{10}B(n, \alpha)$ reaction by using the lead slowing-down spectrometer [8] coupled to the 46 MeV electron linear accelerator (linac) of the Research Reactor Institute, Kyoto University (KURRI). Below 1 keV, the relative measurement has been carried out with an Ar-gas counter, and the neutron flux/spectrum has been measured with a BF_3 counter. The relative cross section obtained has been normalized to the reference value of the thermal cross section at 0.0253 eV. The present result is compared with the existing experimental and evaluated data in ENDF/B-VI and JENDL-3.2.

2. Experimental Methods

2.1. Lead Slowing-down Spectrometer

A lead slowing-down spectrometer has been installed in coupling to the 46 MeV linac at KURRI. This Kyoto University Lead Slowing-down Spectrometer (KULS)[8] is composed of 1600 lead blocks (each size : 10 x 10 x 20 cm^3, purity : 99.9 %) and the blocks are piled up to make a cube of 1.5 x 1.5 x 1.5 m^3 (about 40 tons in weight) without any structural materials. The KULS is covered with Cd sheets of 0.5 mm in thickness to shield it against low energy neutrons scattered from the surroundings. At the center of the KULS, an air-cooled photoneutron target of Ta is set to generate pulsed fast neutrons. One of the experimental holes in the KULS is covered by Bi layers of 10 to 15 cm in thickness to shield from high energy capture γ -rays (6 to 7 MeV) produced by the $Pb(n, \gamma)$ reaction in the spectrometer.

Characteristics of behavior of neutrons in the KULS have been studied by experiments using the resonance filter method[8]. The slowing-down constant K in the relation of $E=K/t^2$ was determined to be 190 ± 2 (keV μs^2) for the Bi hole in the KULS by the least squares method using the measured relation between the neutron slowing-down time t in μs and the average neutron energy E in keV. The energy resolution for the experimental holes was also deduced from the measured data to be about 40 % at energies between a few electron-volts and about 500 eV and was worse than that below a few electron-volts and above about 500 eV [8]. The relation between the neutron slowing-down time and the energy, and its energy resolution were also verified by Monte Carlo calculations [8].

2.2. The Np-237 sample

Neptunium oxide powder of 1.13 gram was purchased from Amersham, which was packed in an aluminum disk container of 20 mm in diameter and 1.4 mm in thickness. The purity of the sample is 99.6 % by weight and the major impurities are about 4 μg in total weight of Ga, K, P, Rb, and S. The gamma-rays of 86.5 keV to 300, 312, 341 keV from Pa-233, which was produced through the α-decay of Np-237, were measured with a high-purity germanium detector (HPGe). The pulse height distribution of the Np-237 is shown in **Fig. 1.** No peak from the impurities is found in the figure.

2.3. Ar-gas counter

The Ar-gas counter, which is filled with a mixed gas of 97 % Ar and 3 % CO_2 at the pressure of 1 atm., was of a cylindrical type, 12.7 mm in diameter, 6.3 cm in effective length, and high-voltage bias was 1400 V. The Np-237 sample was put together by the side of the counter as seen in **Fig. 2** and inserted into the Bi hole of the KULS.

A BF_3 counter, 12.7 mm in diameter and 5.8 cm in effective length was applied to measure the neutron flux / spectrum at the Bi hole of the KULS. In order to monitor the neutron intensities between the experimental runs, another BF_3 counter was placed in an experimental hole of the KULS.

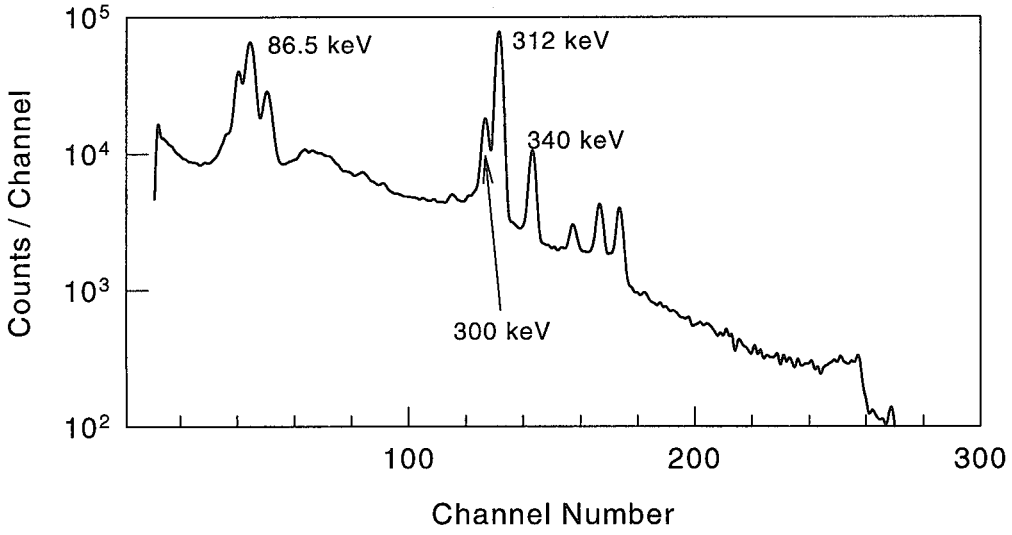

Fig. 1. The pulse height spectrum of the Np-237 sample measured with a HPGe detector.

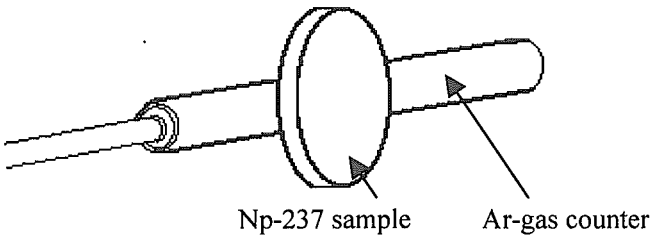

Fig. 2. The Ar-gas counter and the Np-237 sample.

3. Measurement and Analysis

3.1. Capture Cross Section Measurement

The relative cross section of the $^{237}Np(n, \gamma)$ reaction is given by the following relation :

$$\sigma_{Np}(E) = \frac{C_{Np}(E)}{C_B(E)}\sigma_B(E), \quad (1)$$

where $C_{Np}(E)$ is capture counts of Np-237 at energy E, $C_B(E)$ is counts from the BF_3 counter at energy E, and $\sigma_B(E)$ is the energy-dependent reference cross section of the $^{10}B(n,\alpha)$ reaction. The cross section of the $^{10}B(n,\alpha)$ reaction is a well-known reference one and has been used to determine the neutron flux in the current measurement. The cross section values of $\sigma_B(E)$, whose data were broadened by the resolution function of the KULS, were taken from ENDF/B-VI[6]. The typical operating conditions that the KULS was driven were as follows ; the pulse repetition rate was 200 Hz, the pulse width 6.8 ns, the electron peak current 600 mA, and the electron energy 30 MeV. A background run was carried out without the NpO_2 powder using the same size of empty aluminum disk container instead of the Np-237 sample.

3.2. Electronics and Data Taking

Through the amplifiers and the discriminators, signals from the Ar-gas counter or the BF_3 counter for the neutron flux/spectrum monitor were fed into the time digitizer, which was initiated by the linac electron burst. Two sets of 4096 channels with a channel width of 0.5 μ s were allotted to the slowing-down time measurements for the Ar-gas counter or the BF_3 counter and the BF_3 counter for the neutron intensity monitor between the experimental runs. Pulse height distributions for these counters were also measured together with the slowing-down time measurements.

For the relative measurement to the $^{10}B(n, \alpha)$ cross section, output signals from the BF_3 counter were also fed to the time digitizer through the amplifiers and the discriminators, and were stored in almost the same way as for the measurement with the Ar-gas counter.

3.3. Self-shielding Correction

As mentioned above, the NpO_2 powder of 1.13 gram was encapsulated in the aluminum disk container of 20 mm in diameter and 1.4 mm in thickness. Then, the self-shielding effects of neutrons has to be taken into account in the capture cross section measurements, especially near the large resonance region. We have assumed that the sample is isotopically irradiated from the surrounding in the Bi hole of the KULS. The self-shielding correction in the Np-237 sample has been calculated by the MCNP Monte Carlo Code using the following relation.

$$\langle \sigma_c(E) \rangle = \frac{\int_r \int_E N\sigma_c(E)\varphi(r,E)drdE}{\int_r \int_E N\varphi(r,E)drdE} \quad (2)$$

where, N is atomic density of the Np-237 sample, $\sigma_c(E)$ is capture cross section, ϕ (r,E) is neutron energy spectrum at the position r. The correction function has been obtained from the ratio of the effective capture cross section for the Np-237 sample and that for the infinite diluted sample (the atomic density is multiplied by 10^{-6}).

The correction function broadened by the resolution function of the KULS is illustrated in **Fig. 3.** The broadened function has been applied to the self-shielding correction for the present measurement of the $^{237}Np(n,\gamma)^{238}Np$ reaction cross section with the KULS.

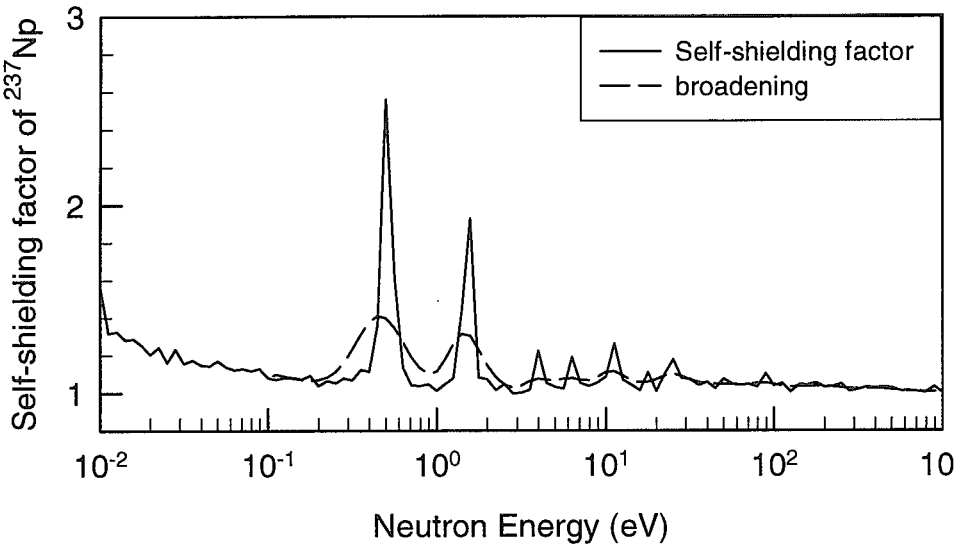

Fig. 3. The self-shielding factor of ^{237}Np. The solid-line is self-shielding factor of ^{237}Np and dot-line is broadened by the resolution function of the KULS.

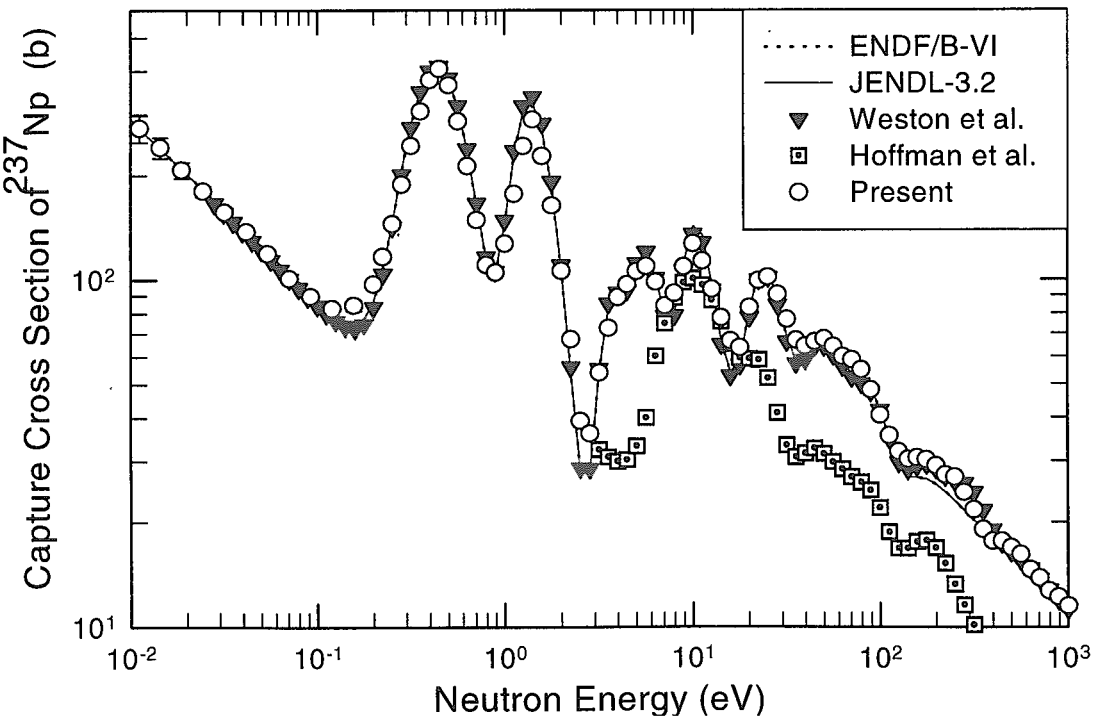

Fig. 4. Comparison of the measured and the evaluated data for the $^{237}Np(n,\gamma)^{238}Np$ reaction, whose values are broadened by the resolution function of the KULS.

4. Results and Discussion

Making use of the KULS, the cross section of the $^{237}Np(n,\gamma)$ reaction has been measured relative to that of the $^{10}B(n,\alpha)$ reaction at energies below 1 keV. The cross section data were obtained by summing up the slowing-down time data in intervals of about 0.12 lethargy width. The result obtained has been normalized to the reference value of the thermal neutron cross section in ENDF/B-VI at 0.0253 eV. The experimental uncertainties are in the range from 2 % to 10 %, and the major uncertainties are due to the statistical error (2~10 %) and that in the reference cross section (~2 %). Since the Np-237 sample was almost free from impurities, no correction was made for the impurity effect.

The capture cross sections measured by Weston et al. are in good agreement with the present measurement as seen in **Fig. 4**, but the data measured by Hoffman et al. are remarkably lower than the present values. In **Fig. 4**, the experimental and the evaluated data are broadened by the resolution function of the KULS. The evaluated data in ENDF/B-VI and JENDL-3.2 are close to the present measurement in the relevant energy region.

5. Conclusion

The cross section of the $^{237}Np(n,\gamma)$ reaction has been measured from 0.01 eV to 1 keV relative to that of the $^{10}B(n,\alpha)$ reaction, making use of the lead slowing-down spectrometer KULS at KURRI. The data by Weston et al. and the evaluated data in ENDF/B-VI and JENDL-3.2 are in good agreement with the present measurement in the relevant energy region. However, the data by Hoffman et al. are lower obviously.

References

(1) Mukaiyama. T., et al., "Conceptual Study of Actinide Burner Reactors", Proc. Of the 1988 Int. Reactor Phys. Conf., Jackson Hale. Vol. IV, 369 (1988).
(2) Berwald, D. H. and Duderstadt, J. J., Nucl. Technol., Vol. 42, 34 (1979).
(3) Takano, H., et al., "Concept of Actinide Transmutation with Intense Proton Accelerator", 6th Int. Conf. On Emerging Nuclear Energy System, Monterey, USA 1991.
(4) Hoffman, M. M., Sanders, W. M. and Semon, M. D., "Fission, Scattering and Capture Cross Sections for 237-Neptunium", BAP, 21, 655 (JE3) (1976).
(5) Weston, L. W. and Todd, J. H., "Neutron Capture Cross Section of Np-237", Nucl. Sci. Eng., Vol. 79, 184 (1981).
(6) Rose, R. F. (Ed.), "ENDF-201, ENDF/B-VI Summary Documentation", BNL-NCS-17541, 4th Ed. (ENDF/B-VI) Brookhaven National Laboratory (1991), and "ENDF/B-VI MOD 2 Evaluation", by P.G. Young (1996).
(7) Shibata, K. and Narita, T. (Eds.), JAERI-Data/Code 98-006 (part II) (1998).
(8) Kobayashi, K. et al., Nucl. Instr. and Meth. in Phys. Research A, **385**, 145 (1997).

3.2 Measurement of Neutron Total Cross-Sections of Dy and Hf in the Energy Region from 0.002 eV to 100 keV

Hyun-Je Cho[1*], Katsuhei Kobayashi[1], Shuji Yamamoto[1], Yoshiaki Fujita[1], Guinyun Kim[2] and Seung Kook Ko[3]

1 Research Reactor Institute, Kyoto University, Kumatori-cho, Sennan-gun, Osaka 590-0494, Japan
* Visiting Scientist from University of Ulsan, Korea
2 Pohang Accelerator Laboratory, POSTECH, San 31, Hyojadong Namgu, Pohang 790-784, Korea
3 Department of Physics, University of Ulsan, San 1, Moogedong Namgu, Ulsan 680-749, Korea

The neutron total cross-sections of Dy and Hf have been measured in the energy region from 0.002 eV to 100 keV by the neutron time-of-flight method with a 46 MeV electron linear accelerator (linac) of the Research Reactor Institute, Kyoto University. A ^{6}Li glass scintillator has been used as a neutron detector and metallic plates of Dy and Hf samples, 0.5 to 5.0 mm thick, have been applied to the neutron transmission measurement. The neutron flight path from the water-cooled Ta target to the ^{6}Li glass scintillator is 22.1±0.01 m. The background level has been determined by the block-off method and/or by using notch-filters of Co (132 eV), Ag (5.2 and 16.3 eV) and Mn (336 eV) and a Cd sheet. The figures show the present measurements, the previous data and the evaluated data in ENDF/B-VI.

1. INTRODUCTION

An electron linear accelerator is a most powerful tool to produce intense pulsed neutrons. Most of the electron linear accelerators were constructed for various fundamental research programs including neutron spectroscopy. They have been used for neutron cross-section measurements by the time-of-flight (TOF) methods covering the energy range from thermal neutron to a few tens of MeV. Pulsed neutrons from an electron linear accelerator (linac) are suited for measuring the energy dependent cross-section with high resolution using the TOF technique.

The neutron total cross-sections of Dy and Hf are of great importance not only for the design and development of nuclear reactors but also for the basic study of neutron interaction with nuclei. Dysprosium (Dy) and hafnium (Hf) are useful absorbing materials for the control rod of thermal reactors because of their large neutron cross-sections in the thermal neutron energy region. Up to now, a few data of their neutron total cross-sections have been reported below 10 eV and a few measurements have been made above a few hundreds keV energy region.

Moore [1] and Okamoto [2] measured the total cross-sections of Dy in the thermal neutron energy region by the transmission method. Sturm *et al.* [3] obtained the cross-sections from 0.08 eV to 20 eV using a heavy water pile and the Bragg reflection method. Brunner *et al.* [4] obtained the total cross-sections in the energy region from 0.015 eV to 2.5 eV with a fast-chopper installed in a thermal reactor. Knorr *et al.* [5] have reported the total cross-sections measured in the energy region below 3.2×10^{-3} eV in a reactor. In the higher energy region, Egelsaff [6] measured the total cross-sections

from 144 eV to 36 keV by the TOF method using a fast-chopper.

The total cross-section of Hf has been measured in the thermal neutron energy region by Joki *et al.* [7], Bernstein *et al.* [8], Moore [1], and Schermer [9]. Bollinger et al. [10] obtained the experimental data from 1 eV to 8 keV. Sherwood *et al.* [11] and Divadeenam *et al.* [12] measured the total cross-section of Hf in the energy region from 0.11 keV to 0.15 keV and from 0.12 MeV to 0.64 MeV using a Van-de-Graaff accelerator.

Although these total cross-sections of Dy and Hf have been reported, there exist discrepancies among the data, especially in the resonance energy region. Therefore, the experimental data in the relevant energy range are strongly requested to measure.

In the present work, the total cross-sections of natural Dy and Hf have been measured between 0.002 eV and 100 keV by the neutron TOF method using the 46 MeV electron linear accelerator of the Research Reactor Institute, Kyoto University (KURRI). A ^{6}Li glass scintillator has been used as we applied in the previous work [13]. The measured results are compared with the previous measurements and the evaluated data in ENDF/B-VI [14].

2. EXPERIMENTAL METHOD

The transmission measurements were made by the neutron TOF method with the 46 MeV electron linac at the Research Reactor Institute, Kyoto University (KURRI). Bursts of fast neutrons were produced from a water-cooled photoneutron target, which was made of twelve sheets of Ta plates of 5 cm in diameter and about 3 cm in effective thickness. This target was set at the center of an octagonal water tank, which was 30 cm in diameter and 10 cm thick, to moderate fast neutrons. A shadow bar made of Pb block, 7 cm thick and 20 cm long was placed in the neutron flight path in front of the Ta target to reduce the gamma-flash generated by the electron burst in the target. The neutron collimation system was mainly composed of B_4C-hardened epoxy resin, H_3BO_3 and Pb collimators, which were symmetrically tapered from 10 cm diameter at both the beginning and the end of the flight tube to 4 cm diameter at the middle position where the transmission sample was located. For the cross-section measurement in the energy range above 0.5 eV, a 0.5-mm-thick Cd sheet was inserted in the TOF beam to suppress overlap of thermal neutrons from the previous pulses due to the high-frequency operation of the linac. During the experiment, the linac was operated in two different modes: One was that the linac operating conditions without a Cd sheet were for the thermal neutron energy region (thermal region) with a repetition rate of 25 Hz, a pulse width of 3 μs, a peak current of 200 mA, and an electron energy of 30 MeV, and the other with a Cd sheet was for the higher energy region (epi-cadmium region) with a repetition rate of 100 Hz, a pulse width of 22 ns, a peak current of 1 A, and an electron energy of 30 MeV.

In the total cross-section measurements, we have used three kinds of Dy metal samples and four kinds of Hf metal samples. The transmission samples were placed at the midpoint of the flight path and were cycled into the neutron beam by an automatic sample changer with four sample-positions. A set of notch filters of Co, Ag, Mn and a Cd sheet were mounted in front of the sample changer when we made the background measurement.

For the neutron TOF spectrum measurement, a ^{6}Li glass scintillator of 12.7 cm in diameter and 1.27 cm in thickness was mounted on an EMI-9618/R photomultiplier and used as a neutron detector located at 22.1 ± 0.01 m distant from the photoneutron target. Neutron signals were amplified,

discriminated and sent to the data acquisition system. The neutron intensity during the TOF measurement was monitored with a BF_3 proportional counter, which was inserted into the neutron beam. The monitor counts by the BF_3 counter were also amplified and led to the computer for storage through a discriminator.

2. DATA REDUCTION

2.1 . TOF Measurement

For the transmission measurement, three sample-in positions with different samples in thickness and a sample-out (open) position were cycled periodically into the neutron TOF beam for a preset time interval by the automatic sample changer. The cycle time was 8 to 12 min.-period, and the time was allotted to each sample so as to minimize the statistical error in the cross-section measurement.

The TOF signals from the ^{6}Li glass scintillator were fed into a time digitizer, which was initiated by the electron burst of the KURRI linac, and the counts versus TOF channel for each sample position were recorded in each section of the data acquisition system linked to a personal computer. The multi-channel time analyzer was operated as four 2048-channel analyzers corresponding to each transmission sample-in or sample-out position. Another four 2048-channel analyzers were used for the TOF measurements using the BF_3 monitor system in order to normalize the neutron intensity between the experimental runs.

The channel width of the time analyzer in this experiment was set to be 16 μs/ch for the thermal neutron energy region and 0.5 μs/ch for the epi-cadmium energy region. The energy calibration of the TOF neutron beam was performed with the well-known resonance energies of thin Ag, Co, and Mn filters. Total running times for the thermal and the epi-cadmium regions were about 248 hours; 62, 16 and 24 hours for 0.5 mm, 3 mm and 5 mm thick Dy samples and 65, 21, 11 and 49 hours for 0.5 mm, 1.5 mm, 2 mm and 3 mm thick Hf samples, respectively.

2.2 . Background Measurement

In order to estimate the background level, we have used two kinds of methods: One was the block-off method using a borated paraffine block of 15 cm in thickness, which was placed in front of the sample to black out the neutron beam. The other was to apply notch-filters of Ag, Co, and Mn and a 0.5-mm-thick Cd sheet. The magnitude of the background level has been interpolated using the fitting function $F(I) = aI^b$, where a and b are constants and I is the channel number of the time analyzer.

4. DATA ANALYSIS

The total cross-section is determined by measuring the transmission of neutrons through the sample. The transmission rate of neutrons at energy E_i is defined as a fraction of incident neutrons passing through the sample to the open beam. Thus, the neutron total cross-section is given as follows, using the neutron transmission rate $T(E_i)$:

$$\sigma(E_i) = (1/N) \ln T(E_i) \quad (1)$$

$$T(E_i) = \frac{[I(E_i) - IB(E_i)] / M}{[O(E_i) - OB(E_i)] / MB} \quad (2)$$

where N is the atomic density of the transmission sample, and the bracket (E_i) means the total counts in i-th energy group corresponding to each TOF channel. $I(E_i)$ and $O(E_i)$ are the foreground counts for sample-in and sample-out, $IB(E_i)$ and $OB(E_i)$ are the background counts for sample-in and sample-out, and M and MB are the monitor counts for the foreground and the background runs, respectively. The monitor counts are obtained by integrating TOF counts in each channel corresponding to the relevant energy region.

5. RESULTS AND DISCUSSION

The total cross-sections of natural Dy and Hf have been obtained in the energy range from 0.002 eV to 100 keV by the neutron TOF method. The results obtained have been summed up in every δU=0.01 lethargy width in order to obtain better statistics. In the data processing, the following corrections have been made: The dead time of the time analyzer used in this experiment was estimated to be less than 0.1 μsec, and the dead time correction could be neglected in the present work. The effect of attenuation of neutron beam due to the thickness of sample was estimated to be less than 0.01 % for the transmission samples. The major impurity elements are Ta (< 0.1 %) and Al (0.05%). The effect due to the impurities on the transmission measurement is estimated to be < 0.1% considering their total cross-section values. The total uncertainties in the present experiment are estimated to be less than 3% as follows. Main sources of the uncertainties are due to the statistical errors (0.65~1.53 % for Dy, 0.36~1.25 % for Hf), the detection efficiencies (1.85~1.98 %), the geometric factor for the samples (< 0.1 %), and the systematic errors (0.5~1.0 %) including some other corrections.

For the Dy cross-section, generally, good agreement can be seen between the existing measured and evaluated data and the present measurement, as shown in **Fig. 1**, although the data by Moore [1] and Sailor et al. [15] and the ENDF/B-VI data show a tendency to be lower a little than the present result at energies between 0.01 eV and 1.5 eV. In **Fig. 1** (a), the data from 0.26 meV to 3.21 meV measured by Knorr et al. [5] are a little bit higher and the data from 0.015 eV to 2.512 eV by Brunner et al. [4], and from 0.63 meV to 0.02 eV by Okamoto [2] are in good agreement with the present measurement. The data by Moore [1] seem to have a structure around 0.2 eV. The data from 0.1 eV to 1 eV measured by Sturm et al. [3] are markedly discrepant from the previous measurements and the evaluated data in ENDF/B-VI. In the **Fig. 1** (b) for the total cross-section of Dy, the data from 2.41 eV to 43 eV measured by Carter [16] are in good agreement with the present measurement and the evaluated ones. But, the data from 144 eV to 10 keV measured by Egelstaff [6] show extremely low values compared to the present measurements. The evaluated data in ENDF/B-VI are rather close to the measurements, although they are higher in the energy range from 500 eV to 2 keV.

For the Hf cross-section, previous data measured by Bernstein et al. [4], Bollinger et al. [10], Okazaki et al. [17], Moore [1], Joki et al. [7], and Schermer [9], are in good agreement with the present

measurement. The evaluated data in ENDF/B-VI are also in general agreement except for the resonance region or above 300 eV, as shown in **Fig. 2.** In the resonance energy region, the resonance parameters for Dy and Hf have to be investigated in the future by analyzing the measured data with a computer code in the future.

6. CONCLUSIONS

The neutron total cross-sections of natural Dy and Hf have been measured in the energy region from 0.002 eV to 100 keV by using the neutron TOF method and the ^{6}Li glass scintillator as a neutron detector. For the total cross-section of Dy, it has been found that the previous measurements and the evaluated data in ENDF/B-VI are in good agreement with the present measurement except for the data from 0.1 eV to 1.0 eV by Sturm et al. and from 144 eV to 10 keV by Egelstaff. The evaluated values in ENDF/B-VI are higher than the present measurement in the energy range from 500 eV to 2 keV. The evaluated cross-section of Hf in ENDF/B-VI are higher than the measured cross-section in the energy region above 300 eV, although the evaluation and most of the previous measurements are close to the present data in general. The data measured in the resonance energy region should be analyzed in the future to get the resonance parameters.

ACKNOLEDGEMENT

The authors would like to express their sincere thanks to the staff of the Research Reactor Institute, Kyoto University (KURRI) for the excellent linac operation. One of the authors (H. J. Cho) is grateful to the Korea Science and Engineering Foundation (KOSEF) for the 1999 Post-Doc. Program.

REFERENCES

[1] Moore, W.M., Bull. Am. Phys. Soc. 6, 70 (X11) (1961).
[2] Okamoto, K., Report JAERI-1069 (1964).
[3] Sturm, W. J. and Arnold, G. P., Phys. Rev. 71, 556 (1947).
[4] Brunner, J. and Widder, F., Report EIR-123 (1967).
[5] Knorr, K. and Schmatz, W., Atomk-ernenergie (AKE) 16(9), 49 (1970).
[6] Egelstaff, P. A., Proc. Phys. Soc. A 70, 51 (1957).
[7] Joki, E. G., Evans, J. E. and Smith, R. R., Nucl. Sci. and Engi. 11, 298 (1961).
[8] Bernstein, S., Borst, L. B., Stanford, C. P., Stephenson, T. E. and Dial, J. B., Phys. Rev. 87, 487 (1952).
[9] Schermer, R., AEC reports to the NCSAG, WASH-1031, 16 (1961).
[10] Bollinger, L. M., Harris, S. P., Hibdon C. T. and Muehlhause, C. O., Phys. Rev. 92, 1527 (1953).
[11] Sherwood, G. L., Smith, A. B. and Whalen, J. F., Nucl. Sci. and Engi. 39, 67 (1970).
[12] Divadeenam, M., Bilpuch, E. G. and Newson, H. W., Report NCSAC-31, 218 (1970).
[13] Kobayashi, K., Fujita, Y. and Kimura, I., Ann. Nucl. Energy, **15**, 381 (1988).

[14] Ross, R. F., (Ed.) "Endf-201, ENDF/B-VI Summary Documentation," BNL-NCS-17541, 4th Ed. (ENDF/B-VI) Brookhaven National Laboratory (1991), and "ENDF/B-VI MOD 2 Evaluation," by P. G. Young (1996).
[15] Sailor, V. L., Landon, H. H., and JR. Foote, H. L., Phys. Rev. 96, 1014 (1954).
[16] Carter, R. S., Exfor Data File 6424001 (1955).
[17] Okazaki, A., Darden, S. E. and Walton, R. B., Phys. Rev., 93, 461 (1954).

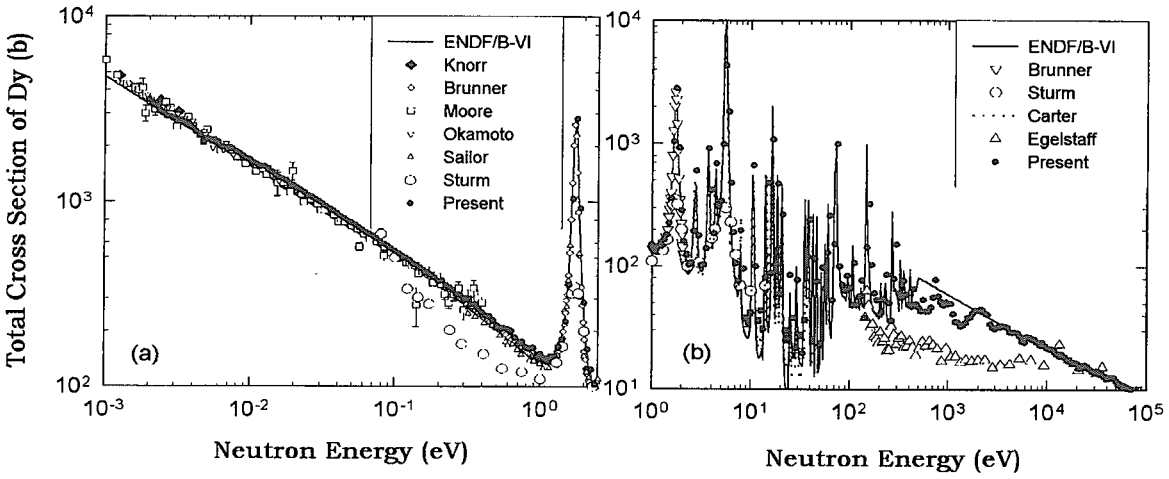

Fig. 1. Comparison of the neutron total cross-section of Dy with the experimental data and the evaluated : (a) in the lower energy region below 3 eV and (b) in the higher energy region between 1 eV and 100 keV.

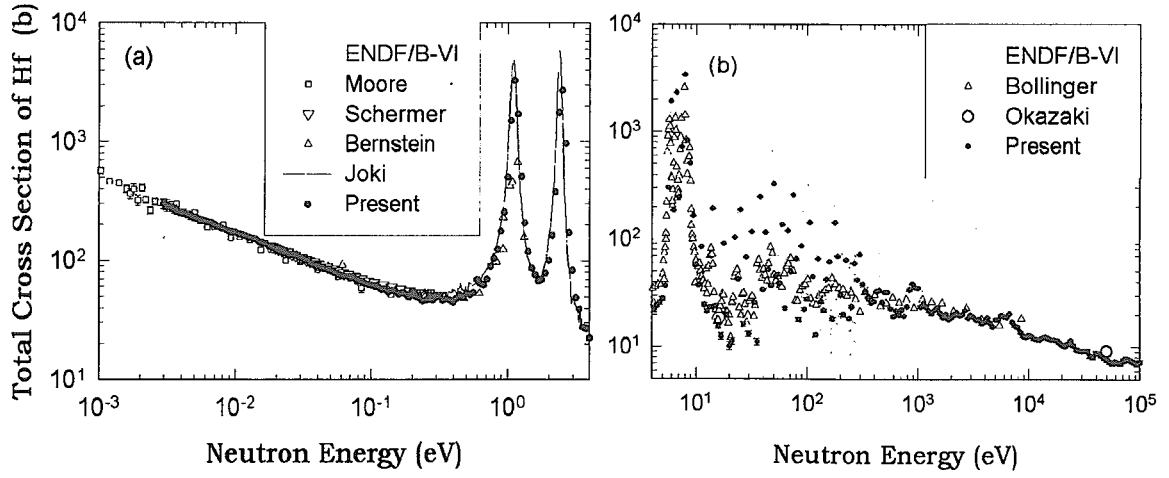

Fig. 2. Comparison of the neutron total cross-section of Hf with the experimental data and the evaluated data : (a) in the lower energy region below 4 eV and (b) in the higher energy region between 4 eV and 100 keV.

3.3 Measurement of keV-Neutron Capture Cross Sections and Capture Gamma-Ray Spectra of Er Isotopes

A.K.M. HARUN-AR-RASHID*, Masayuki IGASHIRA, Toshiro OHSAKI
Research Laboratory for Nuclear Reactors, Tokyo Institute of Technology
2-12-1 O-okayama, Meguro-ku, Tokyo 152-8550, Japan
e-mail: iga@nr.titech.ac.jp

Neutron capture cross sections and capture γ-ray spectra of ^{166,167,168}Er were measured in the energy region of 10 to 550 keV. The measurements were performed with a pulsed ^{7}Li(p,n)^{7}Be neutron source and a large anti-Compton NaI(Tl) γ-ray spectrometer. A pulse-height weighting technique and the standard capture cross sections of gold were used to derive the capture cross sections. The errors of the derived cross sections were about 5 %. The present results were compared with other measurements and evaluations. The observed capture γ-ray pulse-height spectra were unfolded to obtain the corresponding γ-ray spectra. An anomalous shoulder was observed around 3 MeV in each of the capture γ-ray spectra.

1. Introduction

The study of keV-neutron capture cross section is important in nuclear engineering, nuclear physics and nuclear astrophysics. Capture γ-ray spectra as well as capture cross sections are necessary for studies on neutron capture reaction mechanisms and nuclear excitation modes.

The element Er is proposed as one of burnable poisons in nuclear reactors, but JENDL-3.2 does not contain Er data. On the other hand, ENDF/B-VI contains data of ^{166,167}Er, but the evaluation was made many years ago[1]. Therefore, the Er data in ENDF/B-VI seem to have a considerable uncertainty. As for the experimental data of Er isotopes, there are a few available data for the keV-neutron capture cross sections and no data for the keV-neutron capture γ-ray spectra.

The aim of the present study is to measure the capture cross sections and capture γ-ray spectra of Er isotopes in the keV-neutron region in order to provide accurate nuclear data and to investigate neutron capture reaction mechanisms and nuclear excitation modes.

---

*Permanent Address: Department of Physics, The University of Chittagong, Chittagong 4331, Bangladesh.

2. Experimental Procedure

A typical experimental set up is shown in Fig.1. The measurement was performed in the neutron energy region of 10-90 keV and at 550 keV. The details of the experimental procedure were described elsewhere[2]. A 1.5-ns pulsed proton beam from the 3-MV Pelletron Accelerator of the Research Laboratory for Nuclear Reactors at the Tokyo Institute of Technology was used to produece keV neutrons by the $^{7}Li(p,n)^{7}Be$ reaction. The proton energy was set to 1.905 MeV, 24 keV above the threshold energy of the $^{7}Li(p,n)^{7}Be$ reaction, in the 10-90 keV measurement, and neutrons with energies of 2 to 95 keV were emitted within about 50° with respect to the proton beam direction. In the 550 keV measurement, the proton energy was set to about 2.3 MeV so as to generate neutrons with an average energy of 550 keV. The proton pulse repetition rate was 2 MHz or 4 MHz for the 10-90 keV or 550 keV measurement, respectively. The spectrum of neutrons incident on a capture sample was measured by means of time-of-flight (TOF) method with a ^{6}Li-glass scintillation detector.

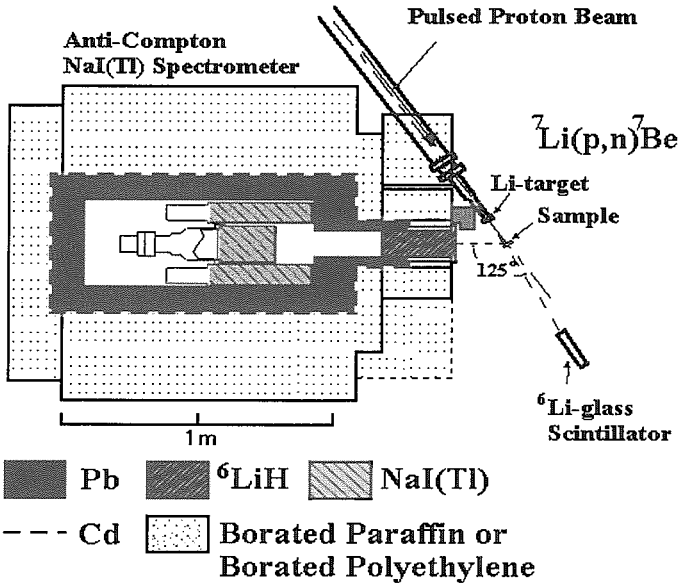

Fig. 1 Experimental setup for the 10-90 keV measurement

Table 1. Characteristics of samples

Sample		^{166}Er	^{167}Er	^{168}Er	^{197}Au
Chemical form		Er_2O_3	Er_2O_3	Er_2O_3	Au
Physical form		Powder	Powder	Powder	metal plate
Weight of powder(g)		1.139	1.140	1.140	—
Chemical purity(%)		> 98.6	> 99.6	> 99.997	99.999
Isotopic composition(%)	^{197}Au	—	—	—	100
	^{162}Er	<0.02	<0.02	<0.002	—
	^{164}Er	0.06	0.06	0.022	—
	^{166}Er	96.31	1.14	0.62	—
	^{167}Er	2.78	95.60	1.21	—
	^{168}Er	0.71	3.08	97.75	—
	^{170}Er	0.15	0.18	0.40	—
Net weight of sample(g)		0.952	0.950	0.974	12.04
Thickness of sample (mm)		3.0	2.2	1.3	2.0
(10^{-3} nuclei/barn)		1.100	1.090	1.138	11.7
Diameter of sample (mm)		20.0	20.0	20.0	20.0
Outer diameter of case (mm)		24.0	24.0	24.0	—
Outer thickness of case (mm)		5.0	4.2	3.3	—

Each of the Er samples was enriched oxide power (Er_2O_3) contained in a graphite case. The net weight of each sample was about 1 g. A gold (Au) sample was used as a standard. The characteristics of the Er and Au samples are shown in Table 1. Each sample was set at a distance of 12 cm or 20 cm from the neutron source for the 10-90 keV or 550 keV measurement, respectively.

The capture γ rays emitted from each sample were measured with a large anti-Compton NaI(Tl) spectrometer, employing a TOF method. The main detector of the γ-ray spectrometer was an NaI(Tl) detector with the diameter of 15.2 cm and the length of 20.3 cm. The main detector was centered in a hollow Compton-suppression NaI(Tl) detector with the outer diameter of 33.0 cm and the length of 35.6 cm. The spectrometer was set in a heavy shield consisting of borated paraffin, borated polyethylene, cadmium and potassium free lead. A ^{6}LiH neutron shield was also interposed between the sample and the main detector. The distance between the capture sample and the front surface of the main detector was 86.0 cm and all the characteristics, such as response functions, weighting function[2], etc., of the spectrometer were defined on this geometrical condition. The capture γ rays were measured at an angle of 125° with respect to the proton beam direction so as to approximately observe the angle-integrated γ-ray spectrum for the dipole transition. The capture events detected by the spectrometer were stored into a workstation as two-dimensional data on TOF and pulse height (PH). The Au, Er and blank runs were made cyclically to average out changes in the experimental conditions.

3. Data Processing

The detail description of the data processing has also been given elsewhere[2]. The incident neutron spectra were obtained from the TOF spectra measured by the ^{6}Li-glass detector. Typical incident neutron spectra are shown in Fig. 2.

Figure 3 shows the TOF spectra observed with the γ-ray spectrometer in the 10-90 keV measurement of ^{167}Er. Several digital gates (DGs) were set in the foreground and background regions in the TOF spectra to obtain foreground and background PH spectra. The net capture γ-ray PH spectra of Er and Au for each DG were obtained by subtracting the background PH spectrum normalized with the ratio of the gate widths from the foreground PH spectra. In the 550 keV measurement, only one DG was set in the foreground region and several ones in the background region. Figure 4 shows the net

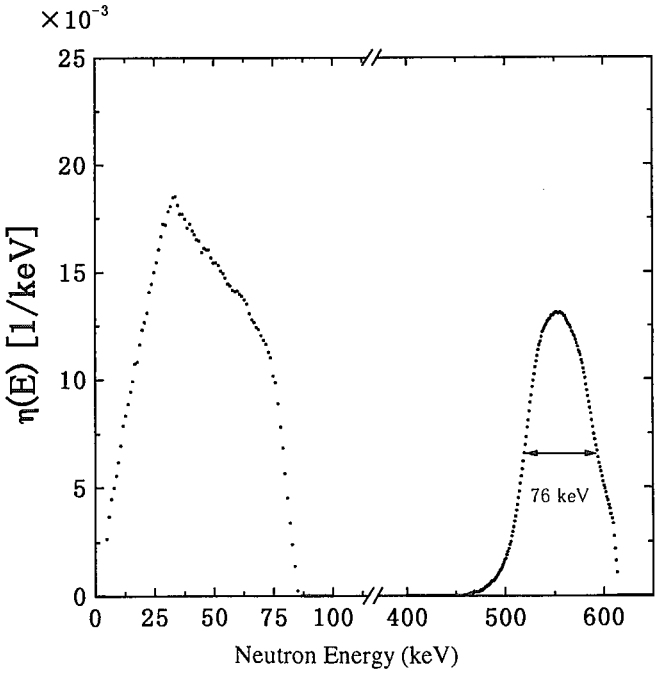

Fig.2. Incident neutron spectra in the ^{166}Er measurements

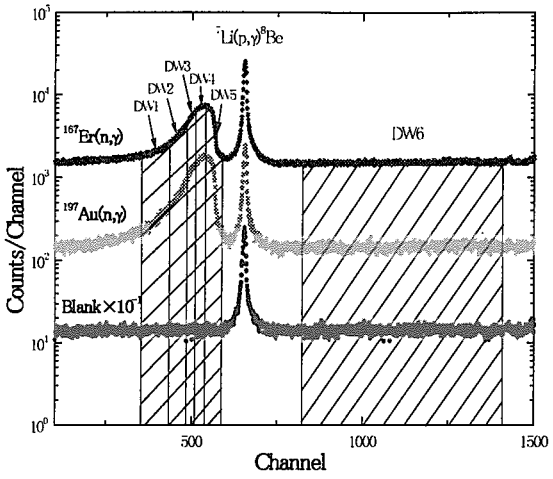

Fig. 3 TOF Spectra observed in the 10–90 keV measurement of ^{167}Er

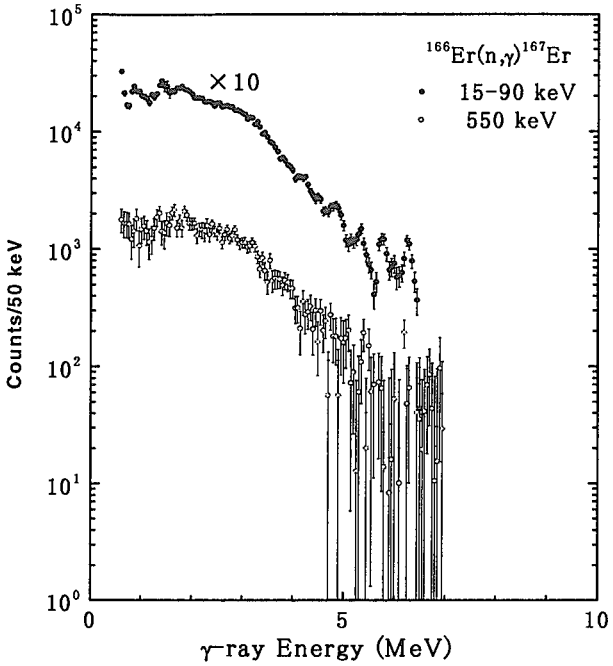

Fig. 4 Net capture γ-ray PH spectra of ^{166}Er

capture γ-ray PH spectra of ^{166}Er in the incident neutron energy region of 15 to about 90 keV and at 550 keV.

A PH weighting technique[3] with the weighting function[2] of the γ-ray spectrometer was applied to each of the net capture γ-ray PH spectra, and the capture yields (the numbers of capture events) of both Er and Au samples for each DG were obtained. The number of incident neutrons for each DG of Au was derived from the corresponding capture yield and an average capture cross section of Au for the DG. The standard capture cross sections of Au were taken from ENDF/B-VI[4]. Then, the number of incident neutrons for the corresponding DG of Er was obtained by using the neutron monitor counts. Finally, the average capture cross section of Er was derived from the corresponding capture yield of Er and the number of incident neutrons.

The capture γ-ray spectrum was obtained by unfolding the net capture γ-ray PH spectrum with a computer code, FERDOR[5], and the response matrix[2] of the γ-ray spectrometer. Then, each γ-ray spectrum was normalized.

Corrections were made for the neutron self-shielding and multiple scattering in the sample, for the γ-ray scattering and absorption in the sample, for chemical and isotopic impurities in the sample, for the dead time, etc.

4. Results and Discussion

(1) Capture Cross Sections

The capture cross sections of ^{166,167,168}Er were derived with errors of about 5 % in the incident neutron energy region of 10 to 90 keV and at 550 keV. The present results are shown in Fig. 5 and compared with previous measurements[6,7] and the ENDF/B-VI evaluations[1].

In the region of 10 to 90 keV, the present results of ^{167,168}Er are in good agreement with those of Shorin

et al.[6] or Kononov et al.[7], but the present results of ^{166}Er are larger than those of Kononov et al. by 5 to 15 %. At 550 keV, there are no available data to be compared.

Shorin et al. and Kononov et al. used a pulsed neutron source by the ^{7}Li(p,n)^{7}Be reaction and the liquid scintillation tank of Institute of Physical and Power Engineering (IPPE). They used the tank of 17l filled with C_6F_6 scintillator as a total energy absorption detector.

The ENDF/B-VI evaluation of ^{166,167}Er in the keV region was mainly based on the statistical model calculation with a spherical optical potential. In the calculation, the γ-ray strength function was adjusted so as to reproduce the measured capture cross sections: 0.74 b at 30 keV of Kononov et al. for ^{166}Er and 1.50 b at 30 keV of Shorin et al. for ^{167}Er. Therefore, the evaluations of ^{167}Er are in agreement with the present results in the 10-90 keV region, but those of ^{166}Er in the 10-90 keV region are smaller than the present results by 5-15%. At 550 keV, the evaluation of ^{167}Er is about 10 % larger than the present result, and that of ^{166}Er is about 20 % larger than the present result. It is worth noting that ENDF/B-VI does not contain data of other Er isotopes.

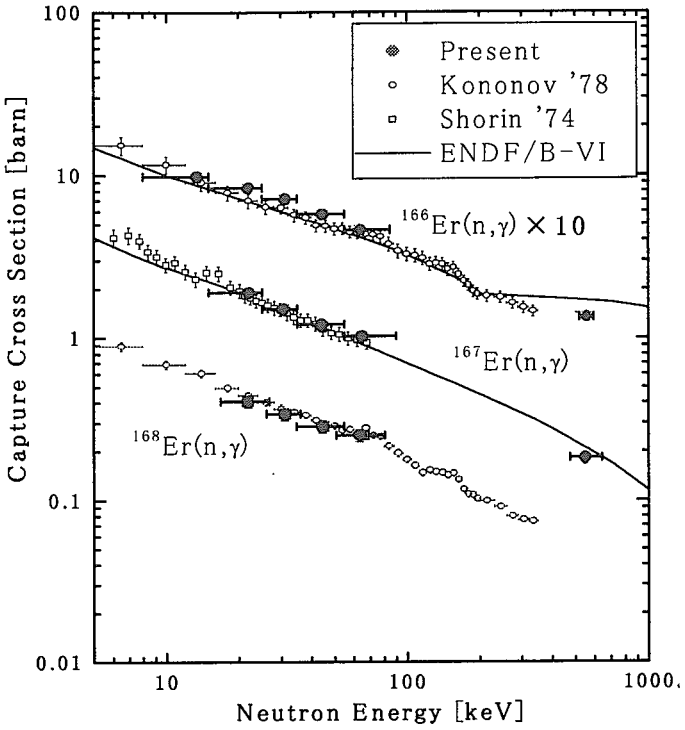

Fig.5. Capture Cross Section of ^{166,167,168}Er

(2) Capture γ-ray Spectrum

The capture γ-ray spectra of ^{166,167,168}Er were derived at the average incident neutron energy of 45 keV (energy region of 15 to about 90 keV) and at 550 keV. The results at 45 keV are shown in Fig. 6. The spectrum at the incident neutron energy of 550 keV was similar to that at 45 keV, especially in the low γ-ray energy region. From the 10-90 keV measurements, the γ-ray spectra corresponding to the individual DGs were also derived, but no difference in the spectral shape was observed.

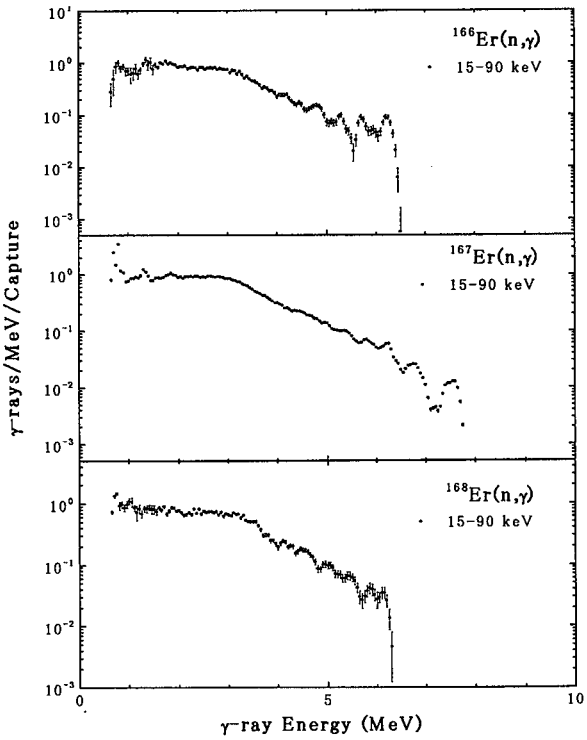

Fig. 6 Unfolded γ-ray spectra of ^{166,167,168}Er

An anomalous shoulder, which was called an anomalous "bump" in our previous work[8], is clearly observed around 3 MeV in the spectra of ^{166,167,168}Er in Fig. 6. The energy position of the shoulder is independent of the incident neutron energy and is consistent with the systematics obtained in our previous work[8]. The anomalous shoulder or bump was ascribed to a resonance structure of the electric-dipole (E1) γ-ray strength function in the previous work, but its origin should be investigated also from different aspects such as the excitation of magnetic-dipole (M1) scissors mode[9].

5. Conclusion

The capture γ rays of ^{166,167,168}Er were measured in the incident neutron energy region of 10 to 90 keV and at 550 keV with an anti-Compton NaI(Tl) γ-ray spectrometer and a 1.5-ns pulsed neutron source. The capture cross sections of ^{166,167,168}Er were derived with errors of about 5 %. In the 10-90 keV region, the present results of ^{167,168}Er were in good agreement with the previous measurements, but the present results of ^{166}Er were larger than the previous ones by 5-15 %. At 550 keV, the present measurements were the first ones. The ENDF/B-VI evaluations of ^{167}Er were in good agreement with the present measurements in the 10-90 keV region but about 10 % larger than the present result at 550 keV. As for ^{166}Er, the evaluations of ENDF/B-VI were larger than the present results by 5-20 %.

The capture γ-ray spectra of ^{166,167,168}Er were derived with good accuracy and good γ-ray energy resolution. An anomalous shoulder was clearly observed around 3 MeV in the spectra of ^{166,167,168}Er. The energy position of the shoulder was independent of the incident neutron energy, and was consistent with the systematics obtained in our previous work. The origin of the anomalous shoulder should be investigated not only from the aspect of the resonance structure of E1 γ-ray strength function but also from different aspects such as the excitation of M1 scissors mode.

Acknowledgements

The present study was partly supported by Japan Atomic Energy Research Institute.

References

[1] ENDF/B-VI data file for ^{166}Er (MAT=6837) and ^{167}Er (MAT=6840), evaluated by R. Q. Wright et al. (1990).

[2] Mizuno S. et al.: J. Nucl. Sci. Technol., **36**, 493 (1999).

[3] Macklin R. L. and Gibbons J. H.: Phys. Rev., **159**, 1007 (1967).

[4] ENDF/B-VI data file for ^{197}Au (MAT=7925), evaluated by P. G. Young (1984).

[5] Kendrick H. and Sperling S. M.:GA-9882 (1970).

[6] Shorin V. S. et al: Sov. J. Nucl. Phys., **19**, 2 (1974); EXFOR 40222.011 (1974).

[7] Kononov V. N. et al: Sov. J. Nucl. Phys., **27**, 5 (1978); EXFOR 40520.024, 40520.025 (1977).

[8] Igashira M. et al.: Nucl. Phys., **A457**, 301 (1986).

[9] Lo Iudice N. and Palumbo F.: Phys. Rev. Lett., **41**, 1532 (1978).

3.4 Measurements of Fast Neutron-Induced Fission Spectra of ^{233}U, ^{238}U, ^{232}Th

Takako MIURA, Than WIN, Mamoru BABA, Masanobu IBARAKI,
Yoshitaka HIRASAWA, Tsutomu HIROISHI, Takao AOKI
Department of Quantum Science and Energy Engineering, Tohoku University
Aramaki-Aza-Aoba 01, Aoba-ku, Sendai, 980-8579, Japan
Email: takako@rpl.qse.tohoku.ac.jp

The prompt fission neutron spectra of ^{233}U, ^{238}U, and ^{232}Th for fast neutron-induced fission were measured by using the time-of-flight (TOF) method at Tohoku University 4.5 MV Dynamitron facility. We obtained new experimental data for ^{233}U at En=0.55, 1.9, 4.1 MeV, ^{238}U at En=1.9, 4.1 MeV, and ^{232}Th at En=4.1 MeV following our previous works for ^{238}U and ^{232}Th at 2.0 MeV, and ^{237}Np at 0.55 MeV.

1. Introduction

^{233}U, ^{238}U, and ^{232}Th are one of the main constituents of fast breeder reactors and accelerator-driven breeder reactors. Their prompt fission spectra for neutron-induced fission are, therefore, of great importance for the design of reactors. These data are of high priority also as the basis for evaluation of nuclear data for actinide. Fission spectra are described by conventional Maxwellian or Watt type functions, or theoretical one by Madland-Nix model and others with appropriate parameters like the level density or the nuclear temperature. For determination of the parameters, experimental data are indispensable, but not enough both in quantity and quality, in particular for ^{233}U and ^{232}Th.

Following our previous works for ^{238}U and ^{232}Th at 2.0 MeV [1], and for ^{237}Np at 0.55 MeV [2], new experimental data were obtained in the present work for ^{233}U at En=0.55, 1.9, 4.1 MeV, ^{238}U at En=1.9, 4.1 MeV, and ^{232}Th at En=4.1 MeV. The results were compared with the evaluation and the Maxwellian temperatures were also deduced by least square fitting in order to compare with other data.

2. Experiment and Data reduction

The measurement was performed by using the time-of-flight (TOF) method at Tohoku University 4.5 MV Dynamitron accelerator facility. The experimental arrangement is shown in **Fig.1**. The details of experiment for ^{233}U at 0.55 MeV were similar with that for ^{237}Np [2].

The fission samples were solid ones of ^{233}U, ^{238}U, ^{232}Th and Pb. The ^{233}U sample consisted of 24 plates, 12.7 mm x 12.7 mm x 1 mm, of U_3O_8 powder dispersed in an aluminum metal and the amount of ^{233}U is only 2.28 g. The ^{238}U and ^{232}Th samples were metallic cylinders of elemental uranium and thorium, 2 cmϕ x 5cm, and encased in 0.5 mm-thick aluminum cans. The Pb sample was employed in order to evaluate background components and the tail of the elastic peak to the high energy side.

Neutron source was the $^{7}Li(p,n)$ reaction for En=0.55 MeV, the T(p,n) reaction for En=1.9 MeV and the D(d,n) reaction for En=4.1 MeV. These targets were metallic lithium, solid Ti-T, and D_2-gas cell for the $^{7}Li(p,n)$, the T(p,n) and the D(d,n) reactions, respectively. The ion beam was 2 MHz repetition rate with

3~3.5μA.

The neutron detector was a massively shielded 12.7 cmϕ x 5.1 cm NE213 scintillator and the flight path was 2 m. Observation angle was selected to minimize contribution of elastic scattering; 90° for En=0.55 MeV, 135° for En=1.9 MeV, and 115° for En=4.1 MeV. Data were acquired by 3-parameter list mode for pulse-height, pulse-shape, and TOF to enable flexible data analysis with optimal experimental parameters. Total time taken for the measurements is shown in ***Table 1***.

The TOF spectrum of ^{238}U for 1.9 MeV is shown in **Fig.2** as a typical one without n-γ discrimination to show the γ-ray peak. Raw list data were processed for optimum n-γ discrimination and pulse-height bias by software treatment. The experimental spectra were corrected for two effects of 1) time resolution which make apparent spectrum harder and 2) the neutron attenuation within the sample.

3. Results and Discussion

Figure 3 shows the present prompt fission spectra divided by $\sqrt{E}$ with a best-fit line of the Maxwellian function,

$$\chi(E)_M = C\sqrt{E}\exp(-E/T_M),$$

where $\chi(E)_M$, T_M, and C are the Maxwellian function (fission spectrum) expressed by the energy of prompt fission neutrons, the Maxwellian temperature and normalization constant, respectively. The uncertainty for En=4.1 MeV data is fairly large, because they do not have enough counting statistics and are affected by large backgrounds due to a deuteron beam. All of the present data are in close agreement with the Maxwellian function below ~10 MeV. The present data of ^{233}U for En=0.55 MeV, in particular, are of enough counting statistics in spite of small amount of the sample and in good agreement with the Maxwellian function.

The present Maxwellian temperatures deduced by fitting are presented in ***Table 2***. The present result of ^{238}U for En=1.9 MeV is consistent with our previous one [1] within the quoted uncertainty. The present temperatures are also shown in **Fig.4** with other experimental data and Howerton-Doyas formula as a reference data. Howerton-Doyas formula is a semi-empirical one based on the average number of neutrons emitted per fission, which is known accurately. This formula was employed in evaluations, while it is replaced with theoretical models in the current evaluations. Our data are generally consistent with other experimental data, but Howerton-Doyas formula deviate systematically from the experimental data.

The present fission spectra were compared with the evaluated nuclear data, JENDL-3.2 and ENDF/B-VI. For ^{233}U at En=0.55 MeV, the both evaluated data are of good agreement with the present data as shown in **Fig.5**. The difference between the evaluated data become larger as incident neutron energy goes higher. In particular in the case of ^{232}Th at En=4.1 MeV, difference is large markedly. The spectra for ^{232}Th at En=4.1 MeV are shown in **Fig.6**, where the present data are normalized to JENDL-3.2 because of relative value in the present data. For more detailed discussion, therefore, comparison in absolute value is desirable.

The uranium-233 samples are on loan from Kyoto University Research Reactor Institute.

[1] M. Baba et al., Nucl.Sci.Technol., 27(7) (1990) 601-616
[2] Than Win et al., Nucl.Sci.Technol., 36(6) (1999) 486-492

Table 1 Total measurement times

Sample	En (MeV)	Time (h)
U-233	0.55	13
	1.90	14
	4.10	3.5
U-238	1.90	5
	4.10	1.2
Th-232	4.10	2

Table 2 Maxwellian Temperatures (preliminary)

Present		
U-233	En = 0.55 MeV	$T_M = 1.31 \pm 0.04$ MeV
	En = 1.90 MeV	$T_M = 1.36 \pm 0.04$ MeV
	En = 4.10 MeV	$T_M = 1.39 \pm 0.05$ MeV
U-238	En = 1.90 MeV	$T_M = 1.28 \pm 0.05$ MeV
	En = 4.10 MeV	$T_M = 1.34 \pm 0.04$ MeV
Th-232	En = 4.10 MeV	$T_M = 1.28 \pm 0.08$ MeV
Previous		
U-238	En = 2.00 MeV	$T_M = 1.26 \pm 0.03$ MeV
Th-232	En = 2.00 MeV	$T_M = 1.24 \pm 0.03$ MeV

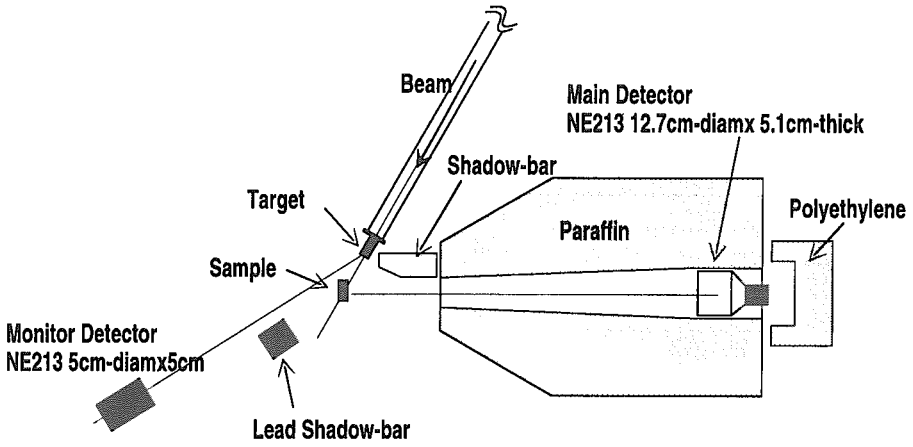

Fig.1 Experimental setup

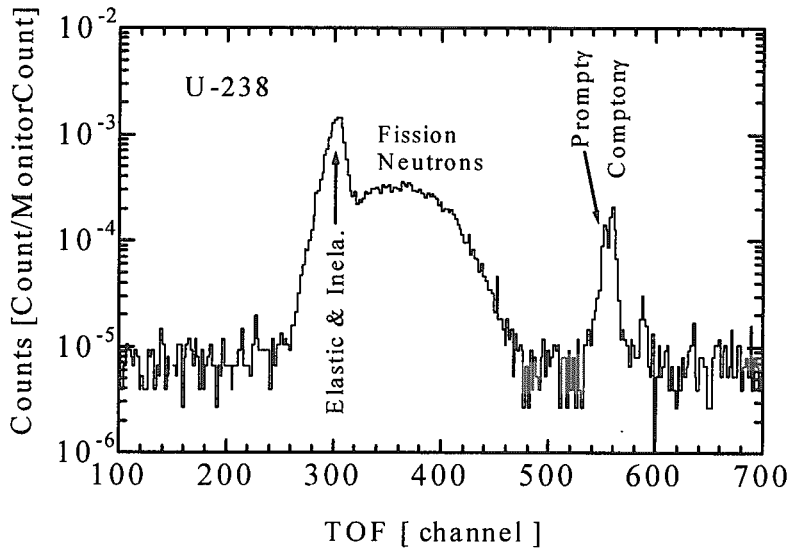

Fig.2 TOF spectrum for ^{238}U at En=1.9 MeV (without n-γ discrimination)

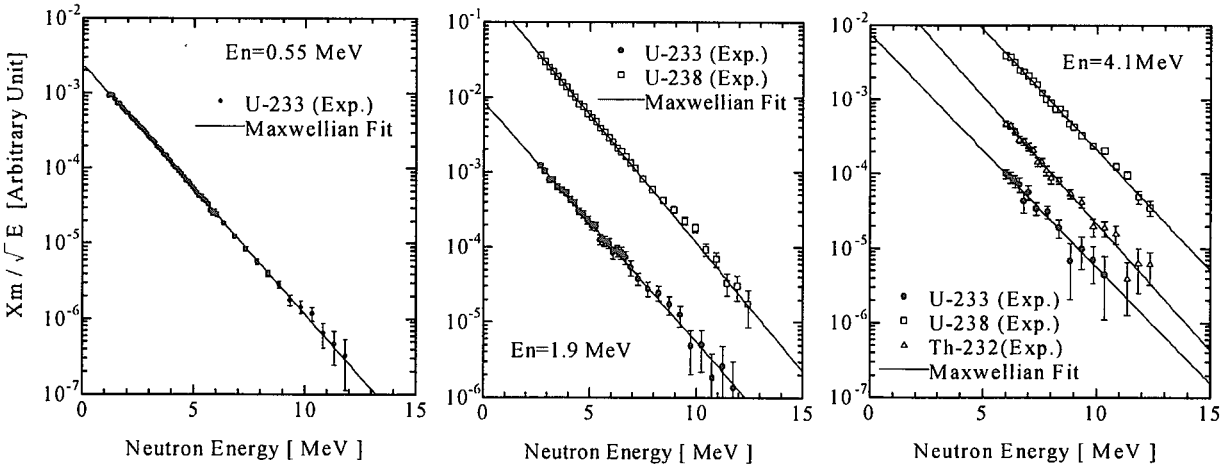

Fig.3 Fission spectra divided by $\sqrt{E}$ for En=0.55 MeV, 1.9 MeV, 4.1 MeV

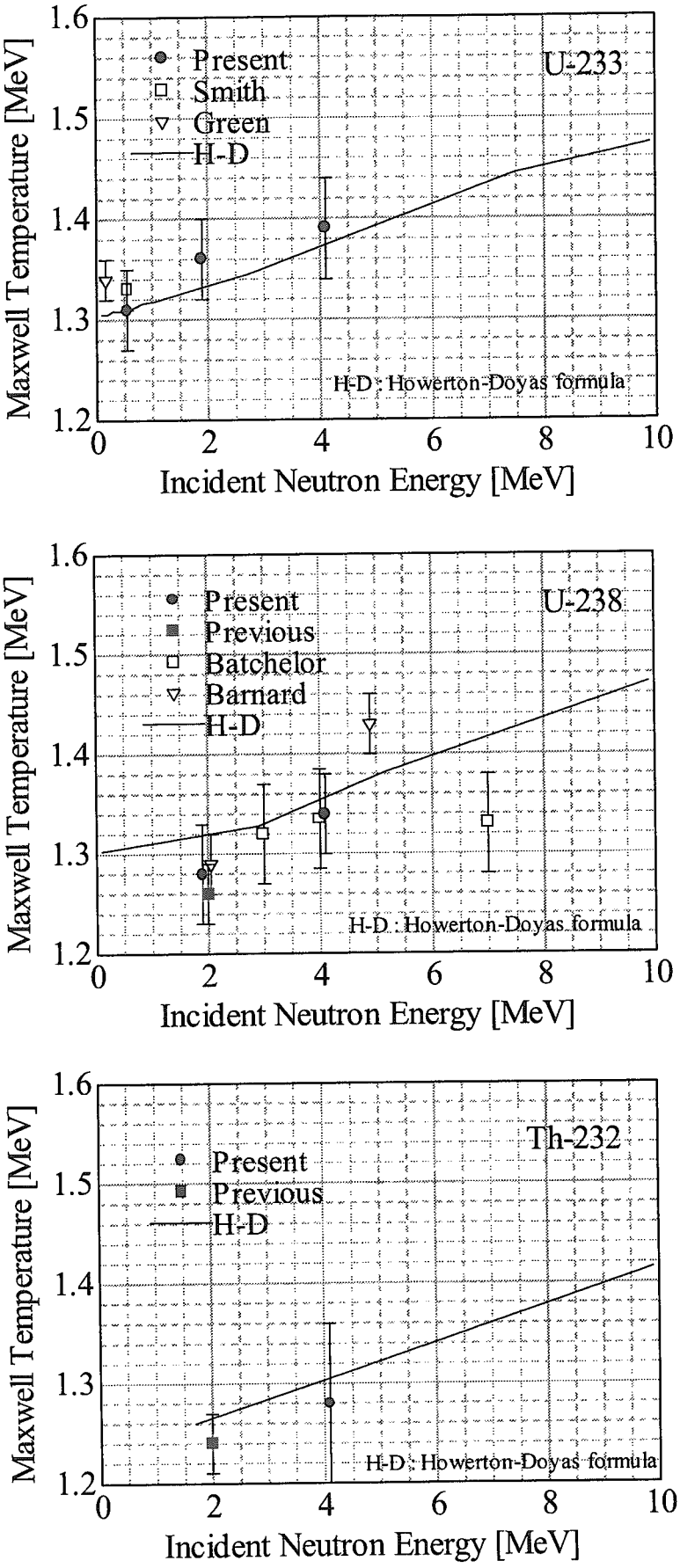

Fig.4 Maxwellian Temperature

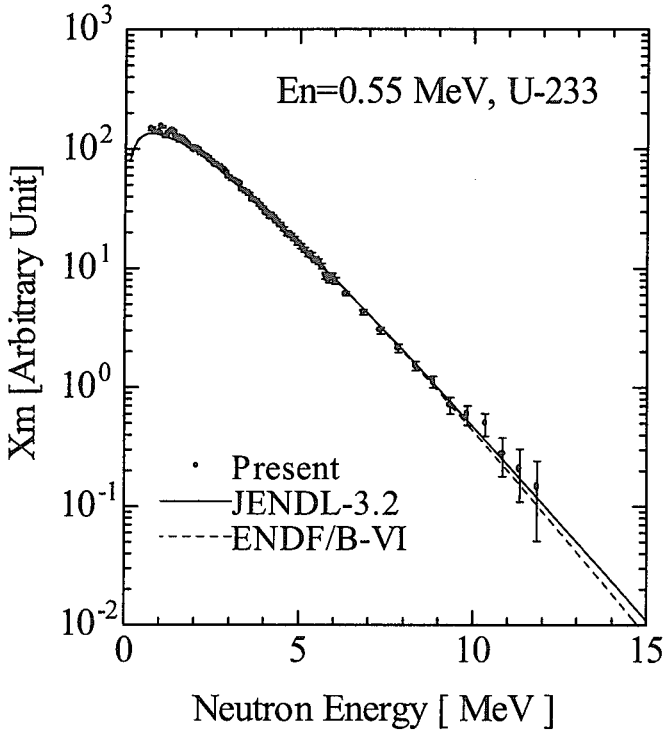

Fig. 5 Fission spectrum of ^{233}U at En=0.55 MeV compared with JENDL-3.2 and ENDF/B-VI

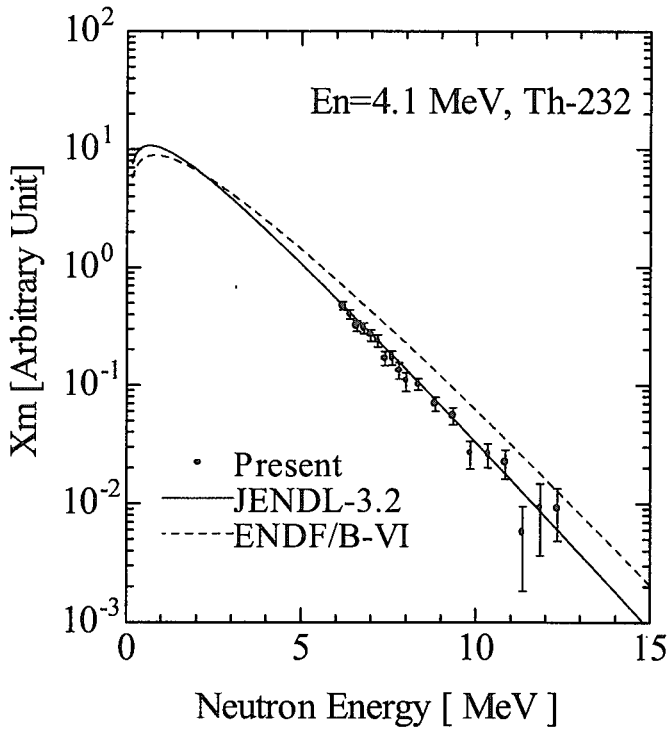

Fig. 6 Fission spectrum of ^{232}Th at En=4.1 MeV compared with JENDL-3.2 and ENDF/B-VI
(Experimental data are normalized to JENDL-3.2)

3.5 Effect of Anisotropic Scattering on MOX fuel Analysis

Daisuke Sato and Toshikazu Takeda
Department of Nuclear Engineering, Osaka University
2-1, Yamada-oka, Suita, 565-0871, Japan
E-mail: dsato@nucl.eng.osaka-u.ac.jp

The effect of anisotropic scattering on neutronic performances is investigated for MOX fuel analysis not only in the fuel cell but also in one-dimensional core geometry. It is found that the effect of anisotropic scattering for UO_2 fuel is small, but it is large for MOX fuel. To treat the high order anisotropic scattering, the treatment up to P_3 scattering is enough for the MOX fuel analysis.

1. Introduction.

The conventional method treats the effect of anisotropic scattering by the transport correction, but this method is inadequate for MOX fuel cell [1]. So the high order anisotropic scattering is considered for MOX fuel cell and numerical results are obtained. Furthermore, to treat the effect of anisotropic scattering on core characteristics, we investigate the effect in one-dimensional core geometry.

2. Calculation model.

The effective macroscopic cross section was obtained by SRAC95 [2] based on JENDL-3.2 [3]. For the cell calculation, we used the MARIKO [1] code (method of characteristics) and both MOX and UO_2 fuel cells are investigated: the cell pitch is 1.26cm, the fuel inner diameter is 0.403cm and the cladding outer diameter is 0.475cm. To change the moderator to fuel volume ratio, the cell pitch was changed. For one-dimensional core geometry calculation, we used the TWOTRAN-II [4] and calculated the core characteristics of MOX fuel: the width of core region is 80cm or 300cm, and the core is consisted of several fuel, cladding and moderator regions and the each region has been chosen close to the real cylindrical cell preserving the volumes, the thickness of the reflector varies from 0cm to 30cm and the boundary condition is vacuum.

3. Calculation Results and Discussions.

a. Effect of moderator subdivision

We divided the moderator region up to 120. The effect of moderator subdivision on k_∞

is presented on Table 1. In the case of no moderator subdivision, the average neutron current is zero, so the effect of P_1 scattering becomes zero. By increasing the moderator subdivision, the effect of P_1 scattering for MOX fuel cell varies up to about -0.16%, although the effect of transport correction varies from about +0.19% to +0.17%. The total effect (of replacing the transport corrected cross section with P_1 scattering) varies from about -0.19% to -0.33%. Figure 1 shows the difference of neutron spectrum for MOX fuel cell in the moderator region between transport correction (or the P_1 scattering case) and the P_0 scattering case in the case of 4 regions subdivision. The transport correction has soft neutron spectrum compared to the P_0 scattering case, so the effect of transport correction has positive sign; +0.19%. On the other hand, the P_1 scattering case has hard neutron spectrum compared to the P_0 scattering case, so the effect of P_1 scattering has negative sign; -0.12%.

b. Effect of high order anisotropic scattering

The effect of high order anisotropic scattering on k_∞ is presented on Table 2. The effect of high order anisotropic scattering is smaller than that of P_1 scattering; the effect of treatment up to P_5 scattering for MOX fuel cell is about -0.23%, but the effect of P_1 scattering is about -0.16%. The effect of treatment up to P_3 scattering is about -0.22%, it is enough to treat the anisotropic scattering. The effect of anisotropic scattering for UO_2 fuel cell is small; the effect of treatment up to P_5 scattering is about -0.03%.

c. Effect of moderator to fuel volume (Vm/Vf) ratio

The effect of Vm/Vf ratio on k_∞ is presented on Table 3. In the case of Vm/Vf ratio of 1.7, the effect (of replacing the transport corrected cross section with P_5 scattering) is about -0.39%. In the case of Vm/Vf ratio of 1.0, the effect is not changed; about -0.36%. In the case of Vm/Vf ratio of 3.0, the effect decreases to about -0.26%. This is because the effect of transport correction decreases with large Vm/Vf ratio (soft neutron spectrum); the effect is +0.22% with Vm/Vf ratio of 1.0, the effect is +0.17% with that of 1.7, the effect is +0.06% with that of 3.0. Figure 2 shows the macroscopic transport and total cross section for MOX fuel cell in fuel and moderator regions. The difference of macroscopic cross section between transport and total cross section decreases with the decrease of energy, so the effect of transport correction decreases with the softening of neutron spectrum.

d. Effect of anisotropic scattering in 1-D core geometry

Table 4 shows the effect of anisotropic scattering on k_{eff} in 1-D core geometry for MOX fuel. The effect depends on the core width; the effect is about -2.55% for core width of

80cm, but is about -0.56% for that of 300cm, this is because the outside of the reflector is vacuum and the neutron current for core width of 80cm is larger than that of 300cm; Figure 3 shows that the neutron current for core width of 300cm is quite different from that of 80cm.

4. Conclusion.

The effect of anisotropic scattering for MOX fuel cell is about -0.39%. The effect of high order anisotropic scattering is small and the treatment up to P_3 scattering is enough for MOX fuel analysis. The large Vm/Vf ratio decreases the effect of anisotropic scattering. It is concluded that the effect of anisotropic scattering is small for UO_2 fuel, but it is large for MOX fuel, so the transport correction is inadequate for MOX fuel.

References

[1] Petko T. Petkov and Takeda, T.: *J. Nucl. Sci. Technol.*, 35[12], 874 (1998).

[2] Okumura, K., *et al.*: *JAERI-DATA/Code* 96-015.

[3] Shibata, K., *et al.*: "Japanese Evaluated Nuclear Data Library, Version-3.2" ---JENDL-3.2---, JAERI-1319 (1990).

[4] Lathlop, K.: LA-4848-MS (1973).

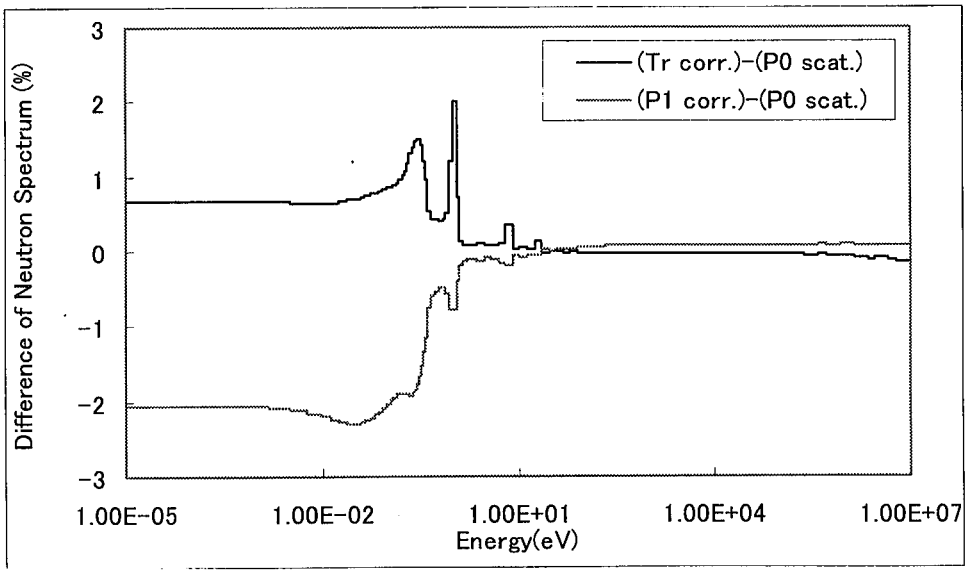

Figure 1 Difference of Neutron Spectrum for MOX Fuel Cell in Moderator Region

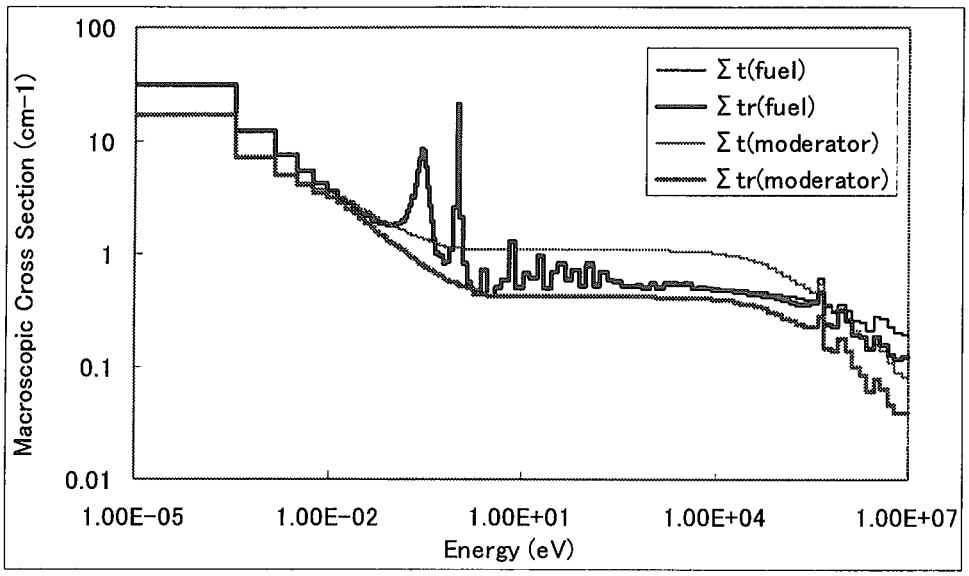

Figure 2 Macroscopic Cross Section for MOX Fuel

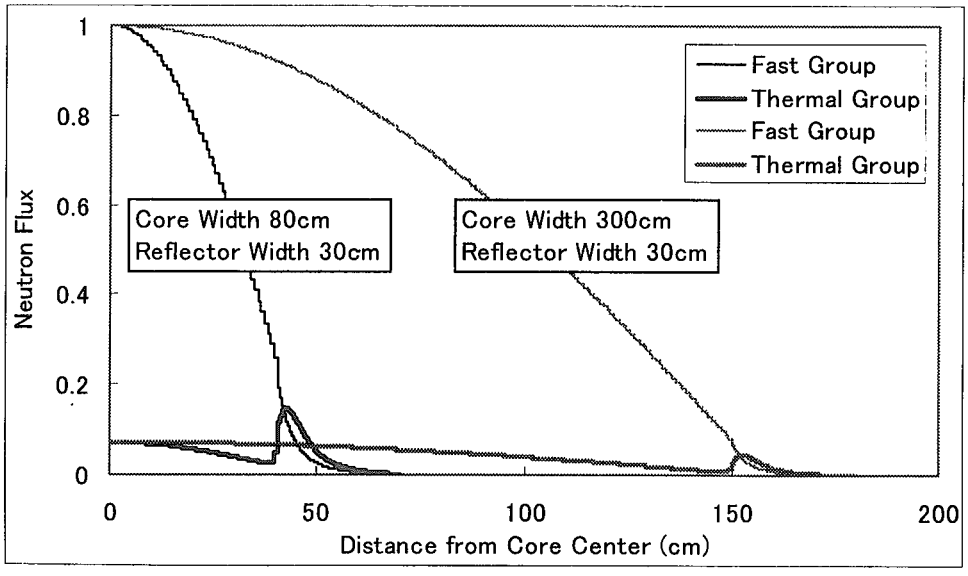

Figure 3 Neutron Flux Distribution for MOX Fuel

Table 1 Effect of moderator subdivision on k_∞

No subdivision.

	k_∞	Δk_∞		
	P_0 scattering	Transport correction*	P_1 scattering*	Δk_{P1}-Δk_{tr}**
MOX	1.19598	+0.191	+0.000	-0.191
UO_2	1.36798	+0.046	+0.000	-0.046

4 regions.

	k_∞	Δk_∞		
	P_0 scattering	Transport correction	P_1 scattering	Δk_{P1}-Δk_{tr}
MOX	1.19598	+0.191	-0.118	-0.309
UO_2	1.36798	+0.047	-0.011	-0.058

8 regions.

	k_∞	Δk_∞		
	P_0 scattering	Transport correction	P_1 scattering	Δk_{P1}-Δk_{tr}
MOX	1.19604	+0.177	-0.136	-0.313
UO_2	1.36762	+0.048	-0.008	-0.056

120 regions.

	k_∞	Δk_∞		
	P_0 scattering	Transport correction	P_1 scattering	Δk_{P1}-Δk_{tr}
MOX	1.19607	+0.165	-0.163	-0.328
UO_2	1.36721	+0.051	-0.004	-0.055

* Relative difference of k_∞ from P_0 scattering case.

** Difference of k_∞ for P_1 scattering and transport correction.

Table 2 Effect of high order scattering on k_∞

Vm/Vf=1.7

	k_∞	Δk_∞						
	P_0	Tr corr.*,+	P_1**,+	P_2**,+	P_3**,+	P_4**,+	P_5**,+	Δk_{P5}-Δk_{tr}++
MOX	1.19607	+0.165	-0.163	-0.209	-0.221	-0.221	-0.225	-0.390
UO_2	1.36721	+0.051	-0.004	-0.026	-0.030	-0.030	-0.030	-0.081

* Transport correction.

** Treatment up to P_n scattering.

+ Relative difference of k_∞ from P_0 scattering case.

++ Difference of k_∞ for P_5 scattering and transport correction.

Table 3 Effect of moderator to fuel volume ratio on k_∞

Vm/Vf=1.0

	k_∞	Δk_∞						
	P_0	Tr corr.$^{*,+}$	$P_1^{**,+}$	$P_2^{**,+}$	$P_3^{**,+}$	$P_4^{**,+}$	$P_5^{**,+}$	Δk_{P5}-Δk_{tr}^{++}
MOX	1.11465	+0.216	-0.109	-0.139	-0.143	-0.143	-0.146	-0.362
UO_2	1.25045	+0.100	-0.043	-0.070	-0.074	-0.074	-0.074	-0.174

Vm/Vf=3.0

	k_∞	Δk_∞						
	P_0	Tr corr.	P_1	P_2	P_3	P_4	P_5	Δk_{P5}-Δk_{tr}
MOX	1.28818	+0.062	-0.135	-0.179	-0.196	-0.196	-0.200	-0.262
UO_2	1.40320	+0.070	+0.100	+0.087	+0.083	+0.083	+0.083	+0.013

* Transport correction.

** Treatment up to P_n scattering.

+ Relative difference of k_∞ from P_0 scattering case.

++ Difference of k_∞ for P_5 scattering and transport correction.

Table 4 Effect of anisotropic scattering on k_{eff} in 1-D geometry

Core width: 80cm

	Thickness of Reflector	k_{eff}	Δk_{eff}		
		P_0 scattering	Tr corr.*	P_1 scattering*	Δk_{P1}-Δk_{tr}**
MOX	0cm	1.15171	-1.124	-2.548	-1.424
	10cm	1.16215	-0.882	-2.261	-1.379
	30cm	1.16242	-0.865	-2.235	-1.370

Core width: 300cm

	Thickness of Reflector	k_{eff}	Δk_{eff}		
		P_0 scattering	Tr corr.	P_1 scattering	Δk_{P1}-Δk_{tr}
MOX	0cm	1.19878	-0.193	-0.559	-0.366
	10cm	1.19909	-0.185	-0.552	-0.367
	30cm	1.19909	-0.183	-0.551	-0.368

Core width: ∞

	Thickness of Reflector	k_∞	Δk_∞		
		P_0 scattering	Tr corr.	P_1 scattering	Δk_{P1}-Δk_{tr}
MOX	0cm	1.20305	-0.091	-0.357	-0.266

* Relative difference of k_∞ from P_0 scattering case.

** Difference of k_∞ for P_1 scattering and transport correction.

3.6 Development of JOYO MK-II Core Characteristics Database

Shiro TABUCHI　Takafumi AOYAMA

4002 Narita-cho Oarai-machi Higashiibaraki-gun Ibaraki 311-1393

Oarai Engineering Center, Japan Nuclear Cycle Development Institute

e-mail : tabuchi@oec.jnc.go.jp

The MK-II core of the experimental fast reactor JOYO served as the irradiation bed for testing fuels and materials for FBR development since 1982 for 15 years. During the MK-II operation, extensive data were accumulated from the core management calculations and characteristics tests conducted in thirty-one duty operations and thirteen special test operations. These core management data and core characteristics data were compiled into a database recorded on CD-ROM for user convenience.

1. Introduction

The MK-II core of the experimental fast reactor JOYO served as the irradiation bed for testing fuels and materials for FBR development since 1982. The MK-II operation was completed and the transition to the MK-III core has started in 1997. During the MK-II operation, extensive data were accumulated from the core management calculations and core characteristics tests conducted in thirty-one duty operations and thirteen special test operations. These results were introduced on J. At. Energy Soc. Japan in 1997 [1], but the data had not been compiled as a database so that the users of these data were limited. The completion of JOYO MK-II core presented an opportunity for compiling core management calculation data and measured core characteristics data into a database, recorded on CD-ROM [2] for user convenience.

2. Operating History of JOYO MK-II Irradiation Bed Core [3]

JOYO is a sodium-cooled fast reactor, which is located at the Oarai Engineering Center of JNC. In 1982, the initial MK-I breeding core was replaced by a MK-II to be used as an irradiation bed for FBR fuels and materials testing. The MK-II core attained criticality on 22 Nov. 1982, and in 1983 it reached 100MWth and began irradiation testing. During the MK-II operation, extensive data were accumulated from the core management calculations and the core characteristics tests conducted in thirty-one duty operation cycles and thirteen special test operations. In 1997, the transition to the MK-III high performance irradiation bed core has started. It is shown in Fig.1 that the operating history of JOYO MK-II core. The MK-II core operated for 41,200 hours and the integrated power was 3,770GWh.

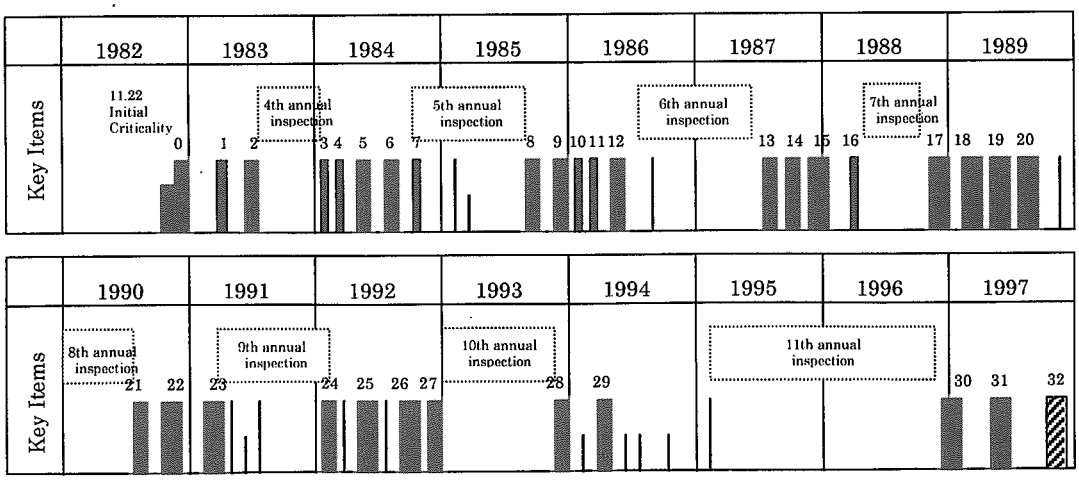

Fig.1 Operating History of JOYO MK-II

3. Specifications of JOYO MK-II Irradiation Bed Core

JOYO is a Plutonium-Uranium oxide fueled fast reactor with two main primary sodium loops, two secondary loops, and an auxiliary system. The auxiliary system consisting of primary and secondary loops are used for decay heat removal in the event that the main cooling systems are not available. The sodium enters the core at 370℃ at a flow rate of 1,100 tons/hr/loops, and exits the reactor vessel at 500℃. The main reactor parameters of MK-II core are shown in Table.1.

This fast reactor is relatively small, and has a large burn-up reactivity change and the burden of irradiation subassemblies, but has a sufficient excess reactivity due to mixed oxide fuel of enriched uranium and plutonium. The plutonium content is about 30wt%. At the beginning of the MK-II operation, ^{235}U enrichment of J1 fuel is about 12wt%. To improve the rate of operation, J2 fuel with ^{235}U enrichment of about 18wt% was introduced and the operation period was extended from 45 days to 70 days.

Three types of the irradiation subassemblies, type A, B and C, have been used for different purposes of the irradiation testing. Reflector subassemblies surround the core and are made of stainless steel to flatten the neutron flux distribution in the core and as a neutron shield.

JOYO has six control rods to control the excess reactivity and shut down the reactor. In normal operation all the control rods are equally inserted. The absorber materials of the control rod are sintered pellets of the boron carbide.

Table.1 Main Core Parameter of JOYO MK-II

Specifications		
Reactor Power	MWth	100
Primary Coolant Flow Rate	t/h	2,200
Reactor Inlet Temperature	℃	370
Reactor Outlet Temperature	℃	500
Core Height	cm	55
Core Volume	l	235
Number of Fuel Subassemblies		≦67
Fuel Pin Diameter	mm	5.5
Type of Fuel		UO_2/PuO_2
Pu Content	wt%	≦ 30wt%
235U Enrichment	wt%	12 (J1) 18 (J2)
Theoretical Density	%	93 (J1) 94 (J2)
Fast Neutron Flux	n/cm²/sec	3.8×10^{15} (J1) 3.6×10^{15} (J2)
Total Neutron Flux	n/cm²/sec	5.1×10^{15} (J1) 4.9×10^{15} (J2)
Max. Excess Reactivity	%Δk/kk'	5.5
Control Rod Worth	%Δk/kk'	≧9
Max. Burn-up (pin-av.)	MWd/t	75,000
Operation Period	days / cycle	70

4. The Structure of the Database

The completion of JOYO MK-II core presented an opportunity for compiling core management calculation data and measured core characteristics data into a database, recorded on CD-ROM for user convenience. The structure of the database is shown in Fig.2.

The calculated core management data are the text style data in the CD-ROM. The "Configuration Data" include the history of the fuel exchange and core arrangement for each cycle. The "Subassembly Library Data" include the atomic number density, neutron fluence, burn-up, integral power of about 300 fuel subassemblies, and 60 irradiation subassemblies. The "Output Data" include the neutron fluxes, gamma fluxes, power density, linear heat rates, coolant and fuel temperature

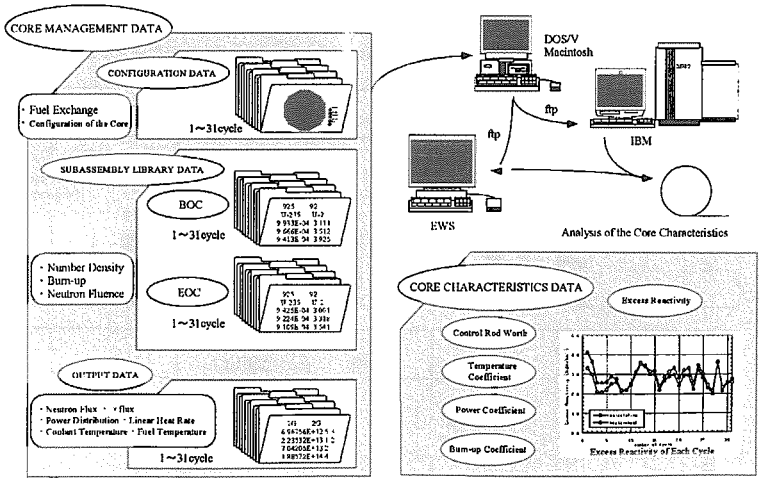

Fig.2 JOYO MK-II Core Characteristics Database

distributions of each core position at the beginning and end of each cycle.

The measured core characteristics data, such as the excess reactivity, control rod worths, temperature coefficient, power coefficient, and burn-up coefficient are also included in the CD-ROM along with the measurement conditions.

Hence, the users can edit these core management data with personal computer and can analyze the core characteristics of JOYO, by forwarding these data to engineering workstations or a super computer. By comparing the results with the measured core characteristics data, the users will be able to reflect these estimations to core designing and the analytical development of core characteristics.

5. The Core Management Data

For core management and operational planning purposes, the core management code system "MAGI" has been developed. The calculation flow of "MAGI" is shown in Fig.3. "MAGI" is a nuclear thermal hydraulic calculation code system for calculating the effective multiplication factors, neutron and gamma flux distributions, power distributions, fuel burn-ups, reactivity coefficients, coolant flow rate distributions, coolant and fuel temperature distributions, etc.

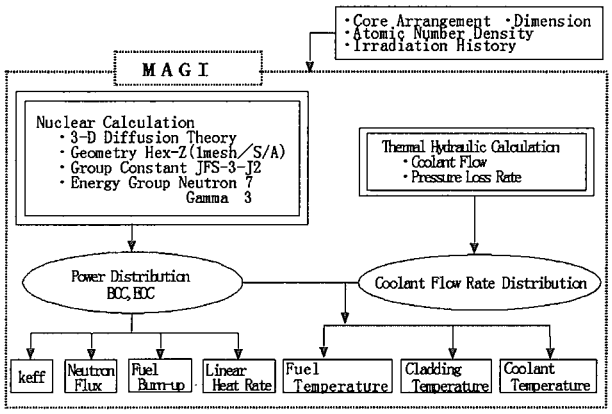

Fig.3 JOYO MK-II Core Management Code System "MAGI"

In the nuclear calculation of "MAGI", 70 group effective cross sections are made using the group constant JFS-3-J2 [4] based on JENDL-2 [5], and the effective cross sections are collapsed into 7 groups of neutrons and 3 groups of gamma by using the neutron flux distribution calculated in the two dimensional RZ geometry. Then the basic core characteristics are calculated in the three dimensional hexagonal-Z geometry by the diffusion theory based on the core arrangement and the operating history of the each cycle. A description of the diffusion calculation is as follows. In the X-Y direction, the core is divided into 331 subassemblies, and the pitch is 8.15cm. In the axial direction, the region is 140cm height, which is divided into 20 meshes, and the core height is divided into 11 meshes. The atomic number density and neutron fluxes of all the subassemblies calculated by "MAGI", based on the fuel exchange and operating history of the each cycle, are also included in the CD-ROM. Examples of the atomic number density data and neutron flux data are shown in Table.2 and Table.3 respectively.

Table.2 The Atomic Number Density Data

BUNDLE ID= PFDS12 CALCU .DATE= 1997. 5. 19. 18. 55. LOC= 1 ==> 000 TYPE NO= 1

UNIT N/D : N.10**24/C.C.

/ FLUENCE : NVT : CUM.POWER: MWD

0 TOTAL NUCLIDE NUMBER = 33

0	925	926	928	937	939	948	949	940	941	942	951
	U-235	U-236	U-238	NP-237	NP-239	PU-238	PU-239	PU-240	PU-241	PU-242	AM-241
1	0.000E+00	0.000E+00	0.000E+00	0.000E+00	0.000E+00	0.000E+00	0.000E+00	0.000E+00	0.000E+00	0.000E+00	0.000E+00
2	0.000E+00	0.000E+00	0.000E+00	0.000E+00	0.000E+00	0.000E+00	0.000E+00	0.000E+00	0.000E+00	0.000E+00	0.000E+00
3	0.000E+00	0.000E+00	0.000E+00	0.000E+00	0.000E+00	0.000E+00	0.000E+00	0.000E+00	0.000E+00	0.000E+00	0.000E+00
4	4.028E-06	1.189E-07	2.197E-03	1.665E-09	4.046E-07	4.152E-11	2.623E-05	3.966E-07	5.667E-09	3.558E-11	4.005E-10
5	1.020E-03	2.569E-05	5.032E-03	6.819E-07	8.566E-07	2.276E-05	1.402E-03	5.581E-04	1.247E-04	8.621E-05	5.607E-05
6	9.978E-04	2.914E-05	5.015E-03	7.634E-07	9.957E-07	2.242E-05	1.373E-03	5.547E-04	1.226E-04	8.598E-05	5.500E-05
7	9.762E-04	3.275E-05	4.999E-03	8.657E-07	1.130E-06	2.215E-05	1.358E-03	5.525E-04	1.209E-04	8.584E-05	5.402E-05
8	9.575E-04	3.625E-05	4.986E-03	9.782E-07	1.251E-06	2.196E-05	1.341E-03	5.517E-04	1.196E-04	8.579E-05	5.321E-05
9	9.451E-04	3.859E-05	4.977E-03	1.061E-06	1.334E-06	2.183E-05	1.330E-03	5.513E-04	1.188E-04	8.577E-05	5.268E-05
10	9.391E-04	3.973E-05	4.973E-03	1.104E-06	1.373E-06	2.177E-05	1.325E-03	5.511E-04	1.185E-04	8.576E-05	5.243E-05
11	9.397E-04	3.969E-05	4.973E-03	1.102E-06	1.367E-06	2.179E-05	1.325E-03	5.514E-04	1.186E-04	8.578E-05	5.247E-05

In the thermal hydraulic calculation of "MAGI", the coolant flow rate distribution, maximum temperature of the coolant, cladding and fuel are calculated. An example of the thermal hydraulic data is shown in Table.4. The coolant flow rate, coolant temperature, maximum temperature of the fuel and cladding of each subassembly are included in the CD-ROM.

Table. 3 The Neutron Flux Data

S/A ID. NAME>>>(PFD512) : S/A TYPE>>>(DRIVER) NO.= 1 : S/A LOACTION >>>(000) NO.= 1

***R-6 NUCLEAR CHAR. 3RD REC. (FLUX BOC) NEUTRON FLUX

NODE	1G	2G	3G	4G	5G	6G	7G	: TOTAL(1-3G)	TOTAL(1-7G)
1	6.96473E+12	5.39380E+13	1.36790E+14	1.27021E+14	4.83874E+13	3.62416E+13	1.38090E+13	: 1.97693E+14	4.23151E+14
2	2.23457E+13	1.20916E+14	2.56822E+14	2.22210E+14	8.10405E+13	5.51012E+13	1.85598E+13	: 4.00083E+14	7.76994E+14
3	7.04012E+13	2.52787E+14	4.48715E+14	3.54541E+14	1.15961E+14	6.32047E+13	1.71864E+13	: 7.71903E+14	1.32280E+15
4	1.88513E+14	4.45922E+14	6.89897E+14	4.94952E+14	1.22957E+14	4.05054E+13	6.46692E+12	: 1.32433E+15	1.98921E+15
5	3.45488E+14	6.45950E+14	9.18434E+14	5.96573E+14	1.02223E+14	1.56808E+13	7.76838E+11	: 1.90987E+15	2.62512E+15
6	4.64717E+14	8.35123E+14	1.15338E+15	7.12647E+14	1.05919E+14	9.81404E+12	1.24070E+11	: 2.45322E+15	3.28172E+15
7	5.58428E+14	9.93582E+14	1.35768E+15	8.22953E+14	1.17025E+14	8.83052E+12	4.78548E+10	: 2.90969E+15	3.85854E+15
8	6.28020E+14	1.11600E+15	1.51905E+15	9.15242E+14	1.28959E+14	9.08535E+12	3.78027E+10	: 3.26308E+15	4.31640E+15
9	6.71034E+14	1.19716E+15	1.62798E+15	9.80496E+14	1.38857E+14	9.19465E+12	1.29420E+10	: 3.49617E+15	4.62473E+15
10	6.91719E+14	1.23476E+15	1.67870E+15	1.01320E+15	1.44014E+14	9.47642E+12	1.07940E+10	: 3.60518E+15	4.77187E+15
11	6.87837E+14	1.22603E+15	1.66768E+15	1.01128E+15	1.44273E+14	9.73479E+12	1.45635E+10	: 3.58155E+15	4.74684E+15
12	6.58912E+14	1.16937E+15	1.59371E+15	9.74986E+14	1.39826E+14	1.03234E+13	4.62208E+10	: 3.42199E+15	4.54717E+15
13	5.99923E+14	1.06402E+15	1.45711E+15	9.06657E+14	1.33065E+14	1.11654E+13	7.72367E+10	: 3.12105E+15	4.17202E+15

CORE AVE. FLUX(NODE NO 5-15) 3.95927E+15

Table. 4 The Thermal Hydraulic Data

S/A ID. NAME>>>(PFD512) : S/A TYPE>>>(DRIVER) NO.= 1
: S/A LOACTION >>>(000) NO.= 1

***R-31 THERMO-HYDRAULIC 4TH REC. (BOC)

FLOW RATE (G/SEC)

BUNDLE	:	9.08553E+03
LOWER PLENUM	:	2.47059E+02
UPPER PLENUM	:	1.15784E+02

TEMPERATURE (C-DEG)

COOLANT OUTLET	:	549.9		
NODAL-MAXIMAUM	:	NOMINAL	: HOT SPOT	: NODE-POSITION
COOLANT	:	581.8	: 611.8	: 1
CLAD	:	591.2	: 623.0	: 5
FUEL	:	2011.0	: 2256.6	: 10
FUEL FOR OVER POWER	:	2124.7	: 2384.6	: 10

6. Measured Core Characteristics Data

The measured core characteristics data, such as excess reactivity, control rod worth, temperature coefficient, and power coefficient are part of the CD-ROM.

The calculated and measured excess reactivity of the each cycle are shown in Fig.4. Although the value of the excess reactivity varies with the cycle, the measured data correspond very well with the calculated values.

The control rod worth is measured by the periodic method and the substitution method at the low power criticality state at beginning of each cycle.

The temperature coefficients are measured at the low power criticality state of before and after the temperature increase in the primary cooling system. The temperature coefficient of the each cycle is shown in Fig.5. The temperature coefficients are about -4×10^{-3}% Δk/kk'/℃ all through the cycles, which are independent of the core arrangement.

The power coefficients, which are the excess reactivity changes at different reactor powers, are also measured at the beginning and end of each cycle. The power coefficient of the each cycle is shown in Fig.6. The relation between the power coefficient and the core burn-up is shown in Fig.7. The power coefficients have the tendency to decrease with an increase in core burn-up.

The burn-up coefficients are obtained by the core averaged burn-up and measured and calculated excess reactivity at the beginning and end of each cycle. The

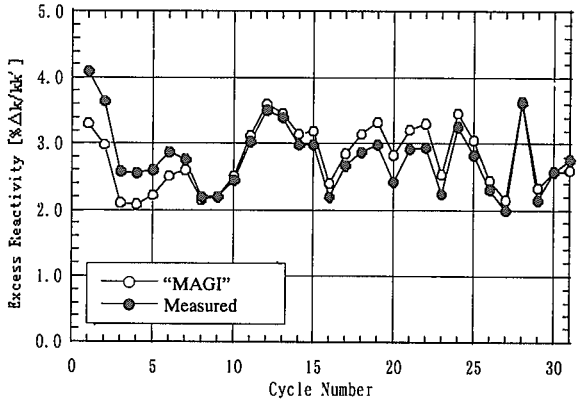

Fig. 4 Excess Reactivity of Each Cycle

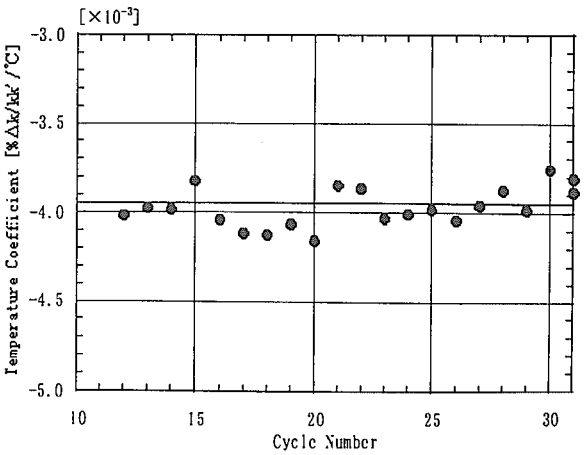

Fig. 5 Temperature Coefficient of Each Cycle

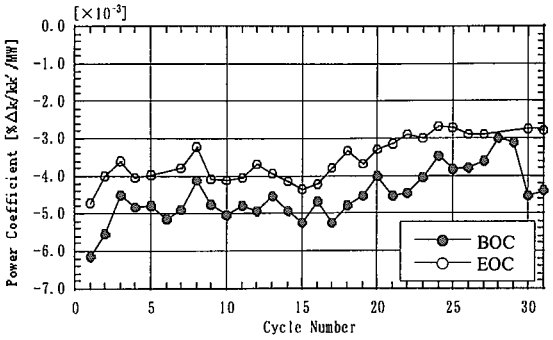

Fig.6 Power Coefficient of Each Cycle

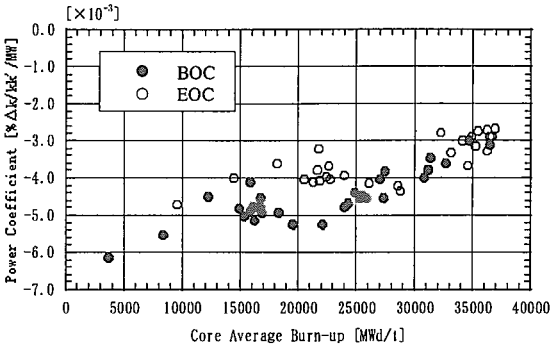

Fig7 Relation between Power Coefficient and Core Burn-up

measured and calculated burn-up coefficients are shown in Fig.8. The burn-up coefficients are about -1.7×10^{-4}% Δ k/kk'/MWd/t all through the cycles.

These reactivity coefficients are obtained by the excess reactivity measured at the core physics testing of the each operation. The measurement conditions such as the control rod positions, reactor inlet temperature, etc. are also included in the database.

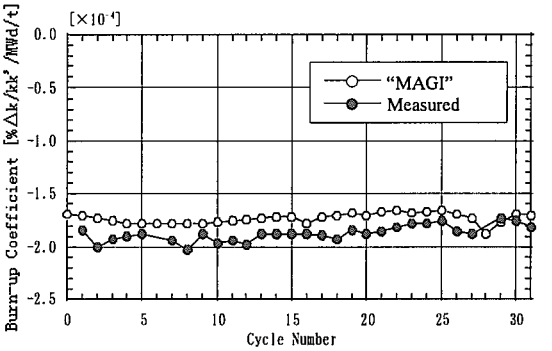

Fig.8 Burn-up Coefficient of Each Cycle

7. Conclusion

The completion of JOYO MK-II core presented an opportunity for compiling core management calculation data and measured core characteristics data into a database, recorded on CD-ROM for user convenience.

The core management data is about 300 MB of numerical data, including the atomic number density, neutron flux distribution, neutron fluences, power distribution, fuel and coolant temperature, etc. for approximately 300 fuel subassemblies and 60 irradiation subassemblies.

The core characteristics data of JOYO are very precious data and are considered the state of the art for FBR. This database is expected to be used in various FBR fields, such as the development of the core designing and core characteristics analysis.

Acknowledgements

The authors would like to note the contribution of Mr. H.Nagasaki of Nuclear Energy System Inc. for collecting and arranging measured core characteristics data, and Mr. Y.Kato of Information Technologies Japan Inc. for the core management calculation by ""MAGI".

References

(1) Arii, et al.: "Core and Fuel Management Experience of the JOYO Irradiation Core (the MK-II Core)", J. At. Energy Soc. Japan, Vol.39, No.4, p.315 (1997)
(2) Tabuchi, et al.: "JOYO MK-II Core Characteristics Database", JNC TN9410 99-003 (1998)
(3) No.104, PNC Technical Review, pp.3~13 (1997)
(4) H.Takano, et al.: "Revision of Fast Reactor Group Constant Set JFS-3-J2", JAERI-M 89-141, JAERI (1989)
(5) T.Nakagawa : "Summary of JENDL-2 General Purpose File", JAERI-M 84-103, JAERI (1984)

3.7 Properties of Fission-Product Decay Heat from Minor-Actinide Fissioning Systems

Kazuhiro Oyamatsu* and Hideki Mori
Department of Energy Engineering and Science, Nagoya University
Furo-cho, Chikusa-ku, Nagoya, 464-8603, Japan
e-mail : oyak@asu.aasa.ac.jp

The aggregate Fission-Product (FP) decay heat after a pulse fission is examined for Minor Actinide (MA) fissiles ^{237}Np, ^{241}Am, ^{243}Am, ^{242}Cm and ^{244}Cm. We find that the MA decay heat is comparable but smaller than that of ^{235}U except for cooling times at about 10^8 s (≈3 y). At these cooling times, either the β or γ component of the FP decay heat for these MA's is substantially larger than the one for ^{235}U. This difference is found to originate from the cumulative fission yield of ^{106}Ru ($T_{1/2}$=3.2×10^7 s). This nuclide is the parent of ^{106}Rh ($T_{1/2}$=29.8 s) which is the dominant source of the decay heat at 10^8 s (≈3 y). The fission yield is nearly an increasing function of the fissile mass number so that the FP decay heat is the largest for ^{244}Cm among the MA's at the cooling time.

1. Introduction

The Fission-Product (FP) decay heat from Minor Actinide (MA) fissiles has growing importance to realize innovative MA burners such as accelerator driven nuclear reactors. In this paper, we examine the difference of the decay heat between MA fissiles and ^{235}U. The MA's studied here are ^{237}Np, ^{241}Am, ^{243}Am, ^{242}Cm and ^{244}Cm. For simplicity, we confine ourselves to the fast neutron induced fission because relatively hard spectra are expected in accelerator driven reactors. No neutron capture effects are taken into account as a natural consequence of a pulse fission.

---

* present address : Faculty of Studies on Contemporary Society, Aichi Shukutoku University, 9 Katahira, Nagakute, Nagakute-cho, Aichi, 480-1197, Japan

2. Method of calculating FP decay heat

Input data required to calculate the FP decay heat are categorized into two. They are the fission-yield and decay data. The decay data consist of branching ratios (decay chains), half lives (decay constants) and average decay energy releases. These data are needed for about 1000 FP nuclides.

In this paper, the fission-yield and decay data are taken from ENDF/B-VI [1,2] because it is the only nuclear data library that has the fission-yield data for all the MA's of our interest.

The calculation of the decay heat power is straight forward in the summation method once the input database is prepared. In this paper, we use a handy computer code for personal computers [3] developed by one of the authors.

3. FP decay heat for MA fissiles

The FP decay heat power after a pulse fission of each MA is compared with that of ^{235}U as a function of cooling time.

Figure 1 shows the MA-to-^{235}U ratio of the aggregate FP decay heat after a pulse fission. The MA decay heat is comparable but smaller than that of ^{235}U except for cooling times at about 10^8 s (≈3 y). At these cooling times, either the β or γ component of the FP decay heat for each MA is substantially larger than that for ^{235}U.

In order to identify the source of the marked difference at 10^8 s, we examine decay energy releases from individual FP nuclides. Figure 2 shows the major sources of the decay heat at 7×10^7 s. The listed FP's in this figure cover 99% of the aggregate decay heat at the cooling time. It is clearly seen that the difference comes dominantly from ^{106}Rh. However, the half life of ^{106}Rh is only 29.8 s that is negligibly small compared with the cooling time. As shown in Fig. 3, at the cooling time ^{106}Rh is fed by its parent ^{106}Ru whose half-life is 3.2×10^7 s. Hence, the cumulative fission yield of ^{106}Ru is the dominant source of the difference between MA's and ^{235}U. Actually, we see from Fig. 4 that the ^{106}Ru yields from these MA's are substantially larger than that from ^{235}U. Moreover, the fission yield is nearly an increasing function of the fissile mass number. As a result, the FP decay heat is the largest for ^{244}Cm among the MA's as shown in Fig. 1.

4. Conclusion

We examine the aggregate FP decay heat after a pulse fission for ^{237}Np, ^{241}Am, ^{243}Am, ^{242}Cm and ^{244}Cm. We find that the MA decay heat is comparable but smaller than that of ^{235}U except for cooling times at about 10^8 s

(≈3 y). At these cooling times, either the β or γ component of the FP decay heat for these MA's is substantially larger than that for ^{235}U. This difference is found to originate from the cumulative fission yield of ^{106}Ru ($T_{1/2}$=3.2×10^7 s). This nuclide is the parent of ^{106}Rh ($T_{1/2}$=29.8 s), which the dominant source of the decay heat at 10^8 s (≈3 y). The fission yield is nearly an increasing function of the fissile mass number so that the FP decay heat is the largest for ^{244}Cm among the MA's.

References

[1] T.R. ENGLAND and B.F. RIDER, "Evaluation and Compilation of Fission-Product Yields 1993," LA-UR-94-3106, Los Alamos National Laboratory, 1994.
[2] T.R. ENGLAND, et al., "Decay Data Evaluation for ENDF/B-VI", Proc. Int. Sympo. on Nuclear Data Evaluation Methodology, Upton, 1992, pp. 611-22, 1993.
[3] K. OYAMATSU, Easy-to-use Application Programs to Calculate Aggregate Fission-Product Properties on Personal Computers, Proc. 1998 Sympo. on Nucl. Data, JAERI-Conf 99-002, pp. 234-239, 1999.

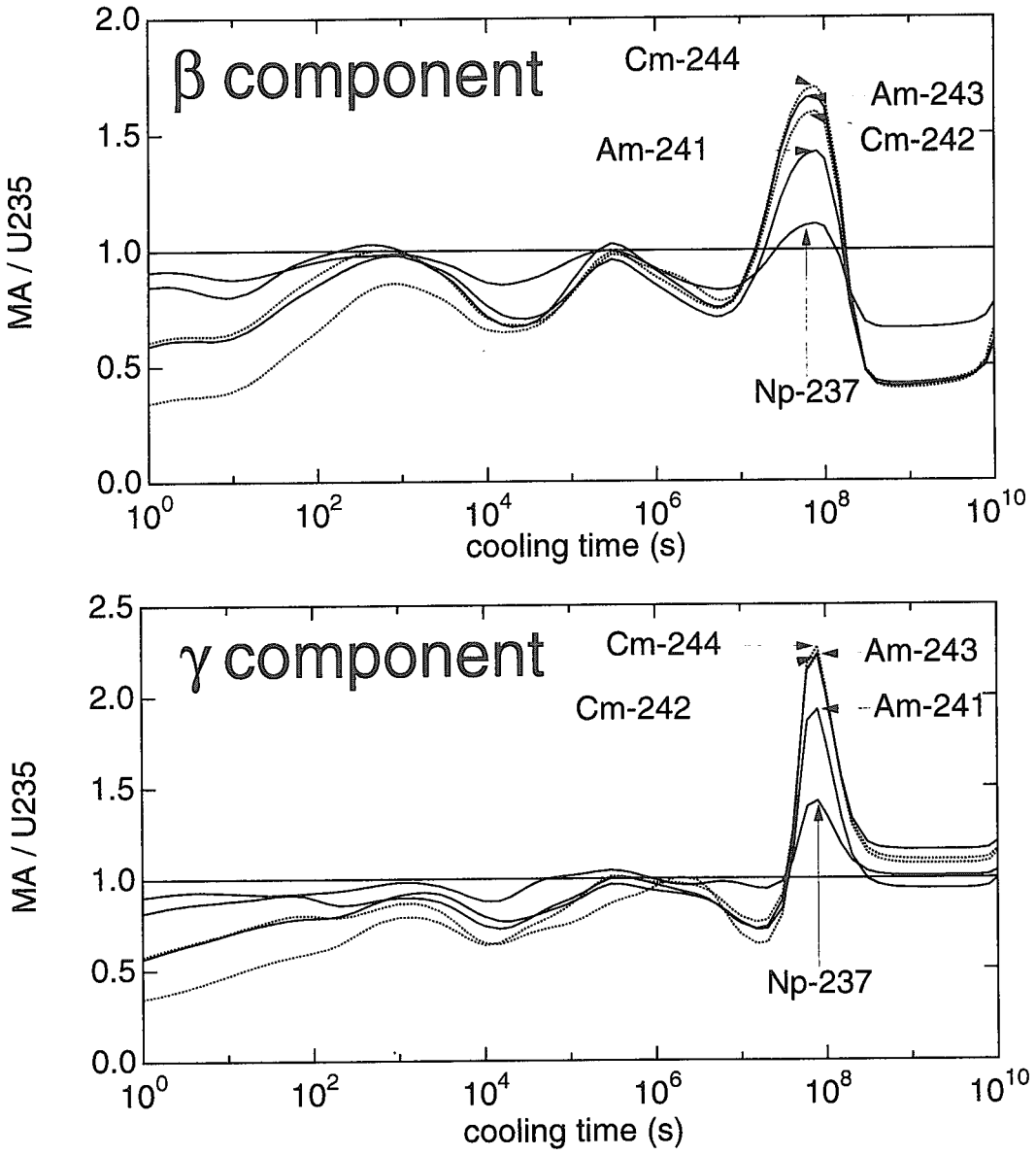

Fig. 1. The MA-to-^{235}U ratio of the aggregate FP decay heat after a pulse fission induced by a fast neutron.

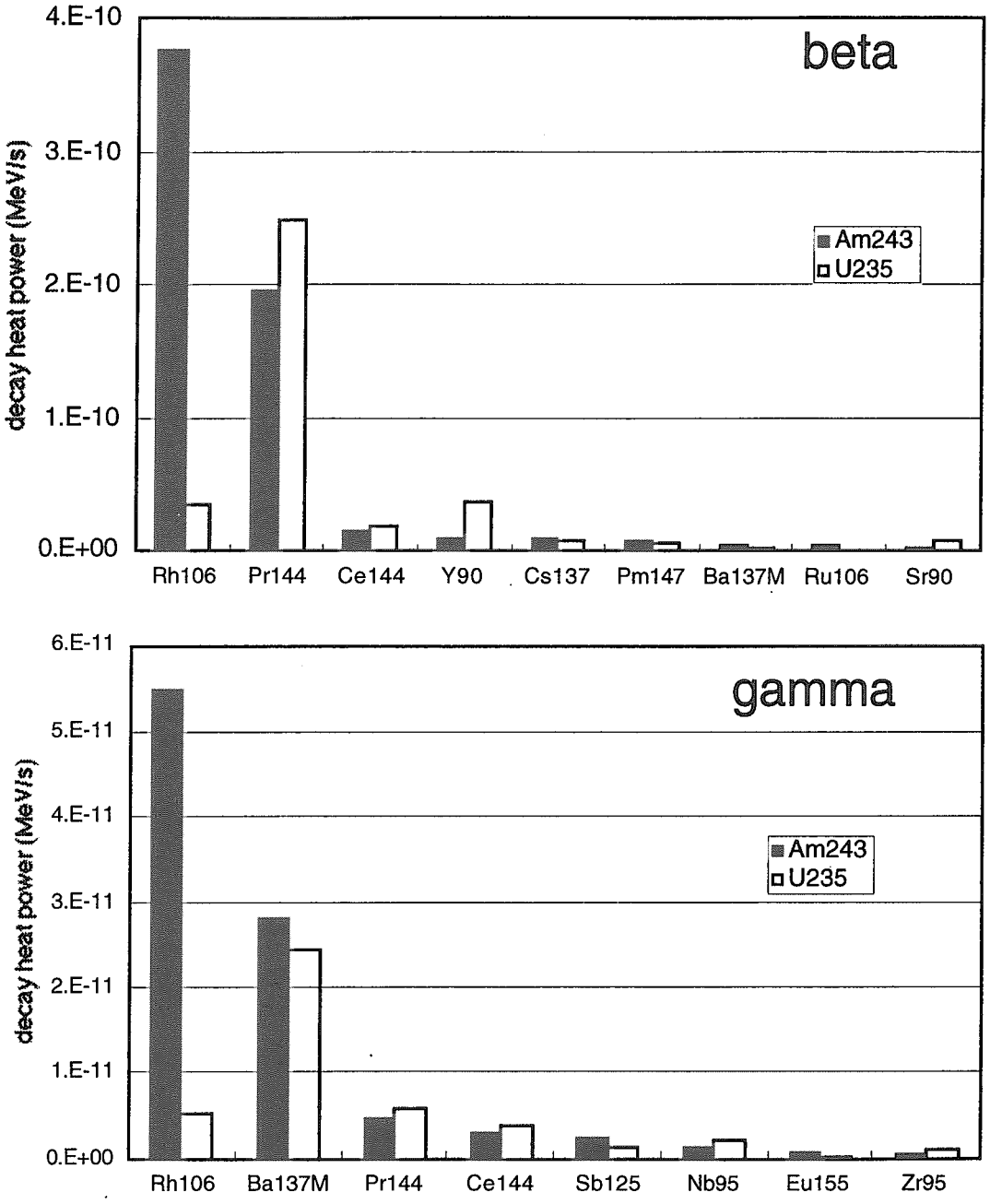

Fig. 2. The major sources of the FP decay heat at 7×10^7 s.

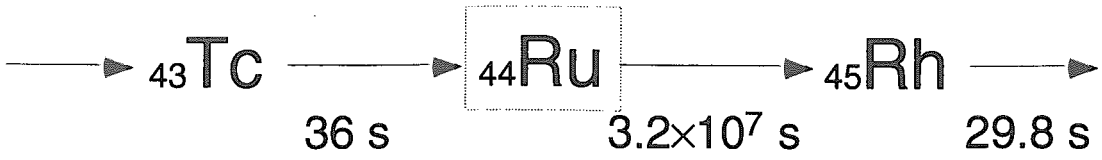

Fig. 3 The portion of A=106 decay chain relevant to ^{106}Rh decay at 10^8 s.

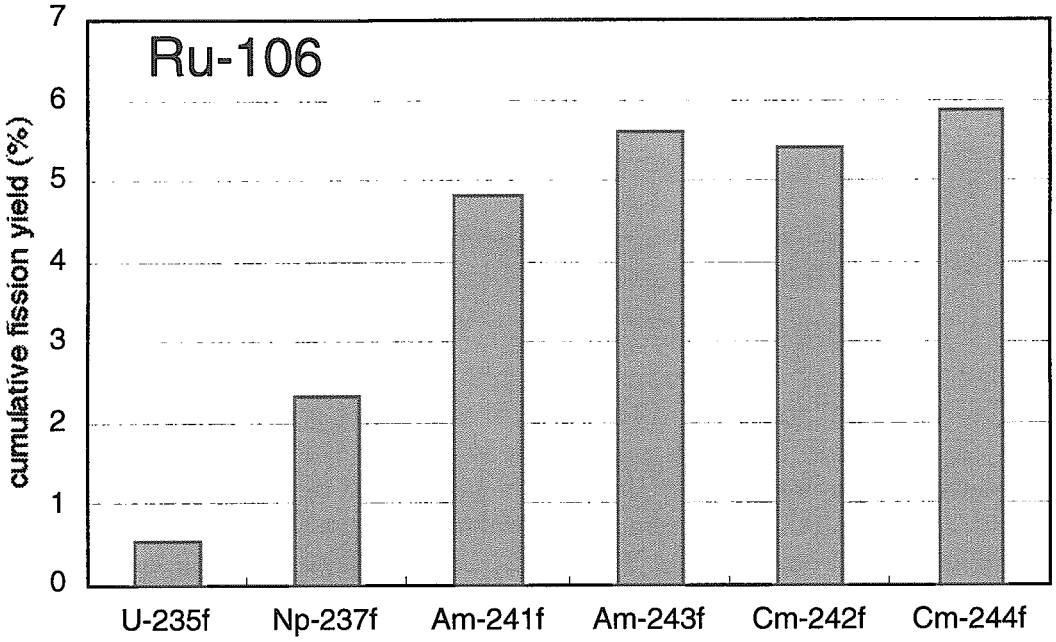

Fig. 4. The cumulative fission yield of ^{106}Ru for the fast neutron induced fission.

3.8

A β-γ Coincidence Measurement System for Precise Determination of γ-ray Emission Probabilities of Short-Lived FP Nuclides

Kazuyoshi FURUTAKA, Shoji NAKAMURA, Hideo HARADA and Toshio KATOH

Japan Nuclear Cycle Development Institute, Tokai works,
Tokai-mura, Naka-gun, Ibaraki-ken 319-1194
email : furutaka@tokai.jnc.go.jp

For the precise determination of γ-ray emission probabilities of short-lived FP nuclides, a β-γ coincidence measurement system has been developed, which utilizes a thin plastic scintillation detector as a β-ray detector. To demonstrate the performance of the developed system, it was applied to the measurement of absolute γ-ray emission probability I_γ of short-lived nuclide, ^{28}Al ($T_{1/2}$ = 2.24 (min)), whose I_γ is well known.

1 Introduction

For the nuclear transmutation study of radioactive waste, it is of fundamental importance to obtain precise nuclear data, such as thermal neutron capture cross sections, σ_0. However, some of the available nuclear data are poor in accuracy. In recent years, many works have been extensively done to improve accuracy of such nuclear data using modern radiation detectors and electronics, usually with the activation method[1].

In a conventional activation method, a sample is irradiated with reactor neutrons and γ rays emitted are measured, and the cross sections are deduced from the γ-ray yields. In the calculation, absolute γ-ray emission probabilities I_γ are used. Therefore, precision of I_γ is one of the major factors which determine the precision of the final result, and it is essential that I_γ is precisely determined.

For nuclides with their half lives longer than several minutes, a 4π β-γ coincidence method has been successfully applied. However, in this method, a radioactive sample has to be set inside a 4π β-ray gas flow proportional counter so as to attain β-ray detection efficiency to be close to unity, and it takes a couple of minutes to prepare a sample and to set up a β-ray counting system. It is, therefore, difficult with the method to determine absolute γ-ray emission probabilities of short-lived nuclides, whose half lives are considerably shorter than few minutes.

For precise determination of γ-ray emission probabilities of short-lived nuclides, a β-γ coincidence measurement system has been developed, which utilizes a plastic scintillation counter as a β detector and a fast data acquisition system. In this system, energy and timing information are accumulated in event-by-event mode. By using a plastic scintillator for β-ray detection instead of a 4π β-ray gas flow proportional counter, the time required for the preparation of the radiation detection equipments is greatly reduced, because there is no need of putting a sample inside a detector and setting up a gas-flow β-ray counting system. It is also essential for efficient measurement of radiation from short-lived nuclei to use a fast data processing system which operates

at high counting rates. In addition to these, it is inevitable in such high counting condition to determine dead times precisely to extract true coincidence events unambiguously.

2 The β-γ coincidence System

A schematic diagram of the β-γ coincidence system is shown in Figure 1. The system consists of a Ge γ-ray detector, a plastic scintillation β-ray detector and a fast data acquisition system.

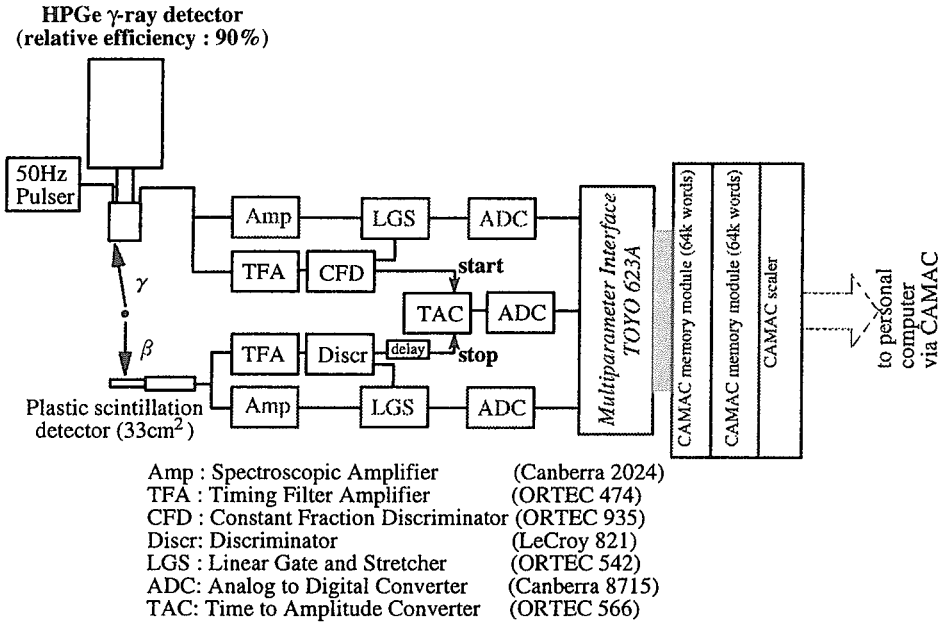

Figure 1: A schematic diagram of the β-γ coincidence system.

A large volume Ge detector whose relative detection efficiency is 90% of that of 7.6 cm×7.6 cm NaI is employed to measure γ rays from short-lived nuclei efficiently. For β-ray detection, a thin and small plastic scintillation detector is used, which is 4 mm in thickness and has an area of 33 cm^2. By using a plastic scintillator as a β-ray detector, the time required for preparation of the irradiated sample and the detection equipments is greatly reduced, and one can efficiently measure radiations from short-lived nuclei. In principle, it is applicable to the measurement of I_γ of a nuclide whose half life is the order of a second.

The energy signal of each detector is fed into an amplifier and then converted by a fast analog-to-digital converter (ADC, Canberra 8715). The timing signal is fed into a discriminator circuit and timing information is extracted. Time difference between the two signals are recorded using a time-to-amplitude converter (TAC) and an ADC. For an efficient measurement of radiations from short-lived nuclei, one should perform a measurement at a high counting rate so as to improve a statistical accuracy. In such

a measurement, the TAC information is inevitable to eliminate accidental coincidence events and to extract true number of coincidences.

The data converted by ADCs are processed by a multi-parameter interface module (TOYO 623A) to compose a list of event data. The data are recorded in event-by-event mode to distinguish true coincidence events and to eliminate spurious events such as that caused by accidental coincidence. To reduce dead times in the course of the data acquisition, the data are temporarily accumulated in one of the two memory modules with large capacity (LeCroy MM8206A), which are cyclically connected to operate as a ring buffer, and are transferred to a personal computer for storage when the other memory module is active.

The system is operated in singles trigger condition: when at least one of the two detectors detects a radiation, data of both detectors are stored. The coincidence events are extracted in later off-line analysis.

3 An application to the determination of I_γ in ^{28}Al

To demonstrate the system for an actual I_γ determination of a short-lived nuclide, an experiment was done for 1779 keV γ ray of ^{28}Al. Decay scheme of ^{28}Al is shown in Figure 2. The ^{28}Al decays into ^{28}Si with a half life of 2.24 minutes. In the decay, only one γ ray (1779 keV) is emitted, and the I_γ is known to be unity[2]. In this case, I_γ is expressed as

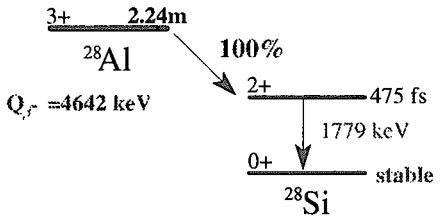

Figure 2: Decay scheme of ^{28}Al.

$$I_\gamma = \frac{1}{\epsilon_\gamma}\frac{n_c}{n_\beta}, \tag{1}$$

where ϵ_γ is detection efficiency of the γ ray, n_β is counting rate of β detector, and n_c is counting rate of β-γ coincidence event.

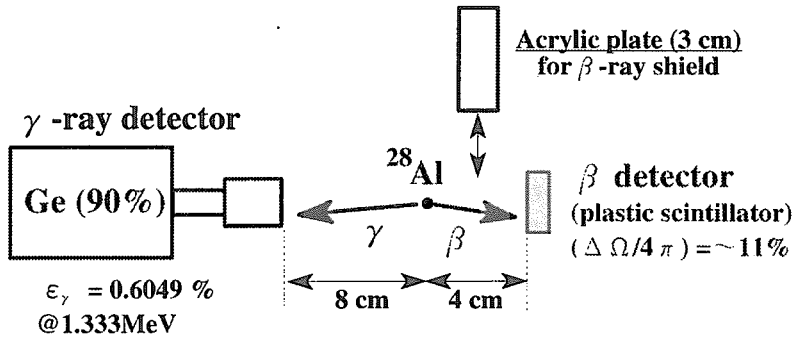

Figure 3: Experimental setup of the I_γ measurement for 1779 keV γ ray in ^{28}Al.

The setup of the experiment is shown in Figure 3. Natural Al foils of 6.76 mg/cm^2 in thickness and 99.0% in chemical purity were irradiated in Rotating Specimen Rack

of the research reactor in Rikkyo University. Activity of about 1 MBq was produced by one minute of irradiation, and after cooling of about six minutes, β- and γ-rays were measured for ten minutes. The data were saved every 20 seconds. Measurements were also done with a β-ray shield placed between the irradiated sample and the β detector in order to estimate contribution of γ rays to the β detector. An acrylic plate of 3 cm thickness was used as the β-ray shield.

Shown in upper half of Figure 4 is a typical γ-ray spectrum. As can be seen in the figure, no remarkable γ ray is observed other than 1779 keV γ ray in ^{28}Al. Depicted in lower half of the figure is a decay curve of the 1779 keV γ ray after a correction for dead times. Drawn in the figure in a solid line is a result of fitting the data by a function of the time, t,

$$A\,e^{-\frac{ln(2)}{\tau}t} + C, \quad (2)$$

where A, τ and C are fitting parameters. The τ means a half life. By averaging the values of τ obtained in all runs, a half life was obtained as $T_{1/2} = 2.248 \pm 0.018$ (min), which agrees with that reported in ref.[2] within the errors, and therefore the γ ray was assigned to be originated from ^{28}Al.

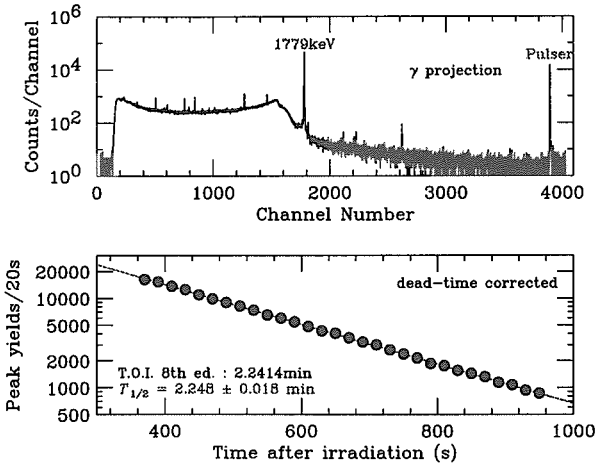

Figure 4: (Upper) : A γ-ray singles spectrum observed in a run. (Lower) : A decay curve of the 1779 keV γ ray in ^{28}Al in the same run, after dead-time correction.

The histogram shown in Figure 5 is a singles β-ray spectrum in a run without the β-ray shield, after subtraction of data in runs with the β shield. A β-ray spectrum obtained by imposing a gate on the 1779 keV γ-ray peak region is also plotted in the figure, which is normalized to the singles one. The singles data deviates from the one gated by 1779 keV γ ray only below about 30 channel, which suggests that there are some events which were not caused by β rays emitted from ^{28}Al. Therefore, lower boundary of summing was varied and the influence to the result was examined when extracting the number of β rays.

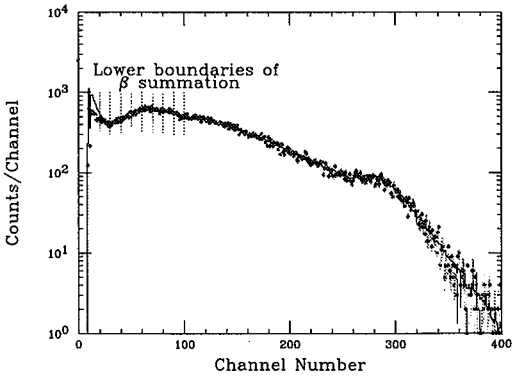

Figure 5: A singles (histogram) and a 1779 keV γ-ray gated (dots) β-ray spectrum in a run.

The number of β rays coincident with the 1779 keV γ ray was deduced by imposing several gates; Γ_P, Γ_H and Γ_L were applied on the γ ray data, while gates T_P and T_O on the TAC data, as shown in Figure 6. Let $n(\Gamma_i, T_j)$ be the number of β counting rate obtained by applying the gates Γ_i and $T_j (i = P, H, L, j = P, O)$ on the γ-ray and the TAC data, respectively. The true β coincidence counting rate n_c is obtained using the following relation,

$$n_c = n(\Gamma_P, T_P) - R \times n(\Gamma_P, T_O) - R' \left(\frac{n(\Gamma_L, T_P) + n(\Gamma_H, T_P)}{2} - R \frac{n(\Gamma_L, T_O) + n(\Gamma_H, T_O)}{2} \right) \quad (3)$$

where R represents the ratio of width of T_P to that of T_O, and R' the ratio of width of Γ_P to that of Γ_L.

Shown in Figure 7 are decay curves of β singles (n_β) and coincidence (n_c) counting rates above the 20 channel of β-summing threshold, after the subtraction of data with β-ray shield and the dead-time correction. Dashed lines in the figure represent the result of fitting the data by a function of the same form as in (2), with C and τ fixed at 0 and 2.24 minutes, respectively. A slight deviation is observed in the singles data after about 800 seconds, which seems to be caused by the remaining long life backgrounds. Therefore, the data were fitted with the function (2) and component with half life of 2.24 (min) was extracted. In the fit, τ was fixed at 2.24 minutes and both A and C were varied as free parameters.

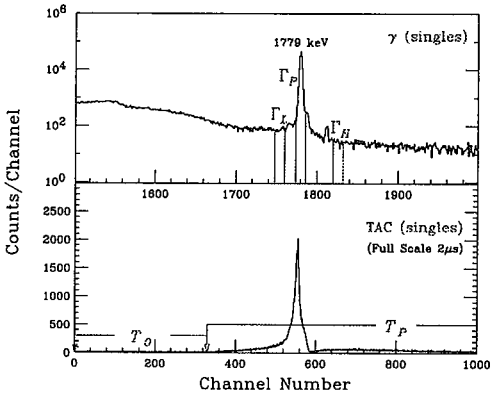

Figure 6: Gates imposed on the γ-ray and TAC data to extract the true number of coincidences.

From the n_β and n_c obtained as above, I_γ of the 1779 keV γ ray was calculated using the relation (1) for each lower limit of β summation. The γ-ray detection efficiency at 1779 keV was determined using ^{60}Co, ^{137}Cs and ^{152}Eu standard sources. Precision of the efficiency was about 2%. The preliminary values of the obtained I_γ are plotted in Figure 8 against the lower limits of β summation. Errors shown in the figure include all the errors except the one of the γ-ray detection efficiency. Above the 30 channel of β summation limit,

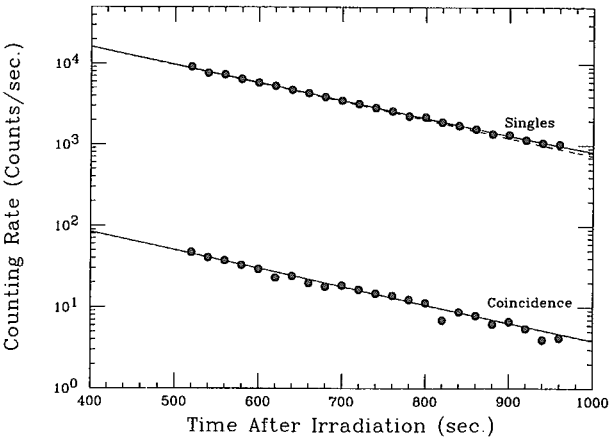

Figure 7: (Points) : Decay curves for β and coincidence channels. (Lines) : Results of the fit with (solid) and without (dashed) a constant term.

the results agree with one another within the errors. The results with errors less than one percent is obtained except an error originated from the determination of ϵ_γ. The obtained results are about two percents smaller than that reported previously [2]. Including the error of the γ-ray detection efficiency, the result agrees with the previous data within the limits of errors.

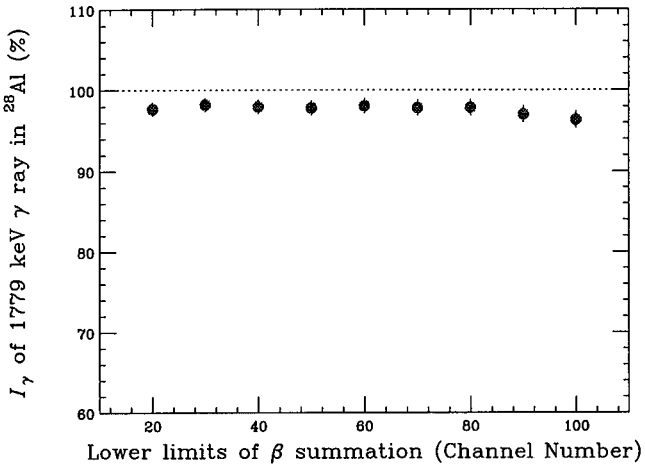

Figure 8: Results obtained in the present experiment for I_γ of 1779 keV γ ray in ^{28}Al.

4 Conclusion

For the precise determination of absolute γ-ray emission probabilities I_γ of short-lived nuclides, a β-γ coincidence measurement system has been developed, which utilizes a thin plastic scintillation detector as a β-ray detector.

The system was applied to the measurement of the absolute γ-ray emission probability of a short-lived nuclide ^{28}Al. The system was demonstrated to have the ability to measure the absolute γ-ray emission probabilities of short-lived nuclides with the precision of $\lesssim 2\%$. By improving accuracy of γ-ray detection efficiency, an absolute γ-ray emission probability will be determined with the total error less than 1%.

References

[1] Nakamura, S.: Talk given in this conference.

[2] Firestone, R. B.: "Table of Isotopes", 8th ed., John Wiley & Sons, Inc., New York (1996)

3.9

Measurements of ^{9}Be(d,x) and ^{9}Be(p,x) Cross Sections at Low Energy

Kimiya ISHII, Kentaro OCHIAI, Isao MURATA, Hiroyuki MIYAMARU and
Akito TAKAHASHI
Department of Nuclear Engineering, Osaka University,
2-1 Yamadaoka, Suita,Osaka, 565-0871, Japan
E-mail: kimiya@newjapan.nucl.eng.osaka-u.ac.jp

The cross sections and S(E)-factors for ^{9}Be(p,α) and (p,d) reactions were measured for proton energies from about 30 to 300 keV. The measured S(E)-factors for ^{9}Be(p,x) reactions increased as the proton energy decreases below 50keV. However our measured S(E)-factors increase more slowly with energy change than the other measured data and moreover more rapidly than the theoretical data.

1. INTRODUCTION

Differential cross section data of charged-particle emission from light elements with incident low-energy protons/deuterons are useful for estimating dose-rate (PKA, KERMA) and material damage in a fusion reactor. Beryllium (^{9}Be) metal and ^{9}Be-compound material are prospective candidates for fusion-reactor materials. The use of neutral beam injector with several hundred keV and several amperes has been reported recently for elevating the temperature and density of plasma. To study plasma-particle/first-wall interaction problems on low energy nuclear reactions, we have measured charged-particle emission cross sections of ^{9}Be (d,x) and ^{9}Be (p,x) reactions at low energy, where x = p, d, t and α, since, up to now, there are only few experimental data available for differential charged-particle emission cross sections of the ^{9}Be(d,x) and ^{9}Be(p,x) reactions at low energy.

We had already reported that the measured astrophysical S(E)-factors [1] for every branch of the ^{9}Be-d reaction increased as the deuteron energy decreases below 300 keV [2]. Unexpectedly the increase rate of the S(E)-factors was much higher than the theoretical data. In the present study we confirmed the similar tendency of the increase through the comparison of, measured data for ^{9}Be-p reaction and our previously measured data for^{9}Be-d reaction.

2. EXPERIMENTAL PROCEDURE

All the experiments were carried out at the Cockcroft-Walton type accelerator, OKTAVIAN of Osaka University, Japan. Figure 1 shows the schematic view of experimental system with components in the vacuum chamber. A beryllium metal (100 μm in thickness) is bombarded by proton or deuteron beam. The beam is induced into the target through three apertures (ϕ=10, 7 and 0.8 mm). At the lower energy region (the energy of proton beam was below 40 keV and that of deuteron is below 100 keV), we use H_3^+ or D_3^+ molecular beam instead of single atomic beam. Charged-particles emitted by the nuclear reactions are detected by Si-Surface Barrier Detector (Si-SBD). Depletion layer of this detector is about 200 μm. In front of the Si-SBD, we set an aluminum foil (3 μm in thickness) as an absorber and not to detect Rutherford scattering particles. The Si-SBD is smoothly movable between the angle from 30 to 160 degree with respect to the beam direction keeping a solid angle for the measurement of angular-distributions of the cross sections. The beam irradiation point of the target is adjusted by a manipulator with a stepping motor to keep the flesh surface point. A Faraday cup for beam-current monitor is set up at the backward of the beryllium target. A current integrator monitors the induced particles as a target current. We measure real beam current by the Faraday cup without target and calibrate the number of incident particle.

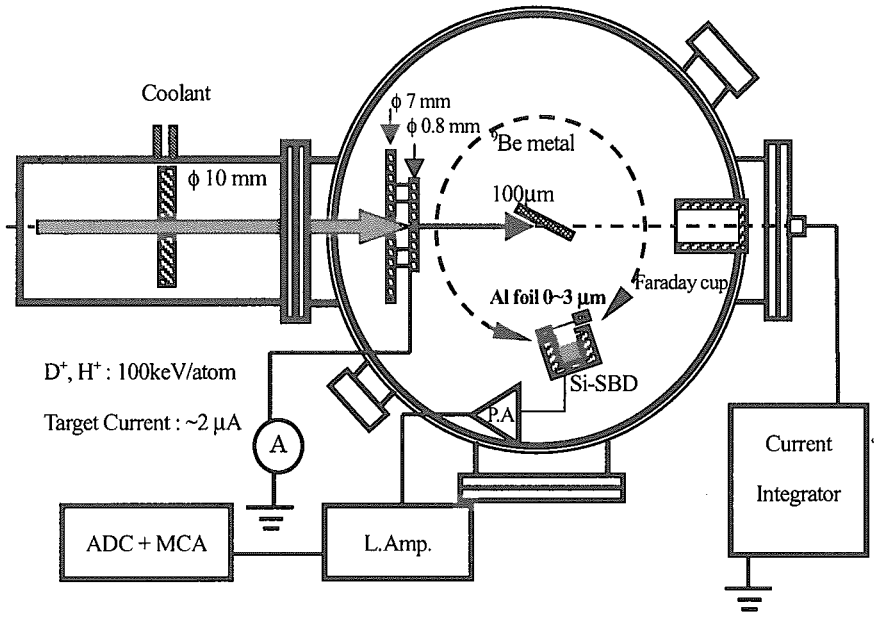

Figure 1 Experimental arrangement

3. EXPERIMENTAL RESULT

3.1 Astrophysical S(E)-factor and ^{9}Be-d nuclear reaction

The astrophysical S(E)-factor is defined by the relation

$$\sigma(E) = S(E)E^{-1}\exp(-2\pi\eta) \qquad (1)$$

Where η is the Sommerfeld parameter given by

$$2\pi\eta = 2\pi Z_1 Z_2 e^2 / \hbar v = 31.29 Z_1 Z_2 (\mu / E)^{1/2}$$

The quantities Z_1 and Z_2 are the nuclear charges of the interacting particles in the entrance channel, μ is the reduced mass in units of AMU, and E is the center-of mass energy in units of keV. In the case of non-resonant reactions, the S(E)-factor varies slowly with energy. In solid target, electron clouds surrounding the interacting nuclides act as a screening potential. So, the projectiles see reduced Coulomb barrier. The ratio of the bare cross section(σ_b(E))and the cross section with an electron screening effect(σ_s(E)) is

$$f(E) = \frac{\sigma_s(E)}{\sigma_b(E)} \approx \exp\left(\frac{\pi\eta U_e}{E}\right) \quad . \qquad (2)$$

Where U_e is the height of Coulomb barrier(e.g. $U_e \sim Z_1 Z_2 e^2 / r_i$ approximation, with r_i is an atomic radius ;$U_e \fallingdotseq 450$ eV at Be-d/p reaction)

Table1 shows astrophysical S(E)-factors obtained from the measured cross sections of ^{9}Be(d,p), (d,t_0), (d,a_0) and (d,a_1) at $E_{lab.}$ =90-290 keV, respectively.

Table 1. S(E)-factors of ^{9}Be-d nuclear reactions below E=290 keV

$\langle E \rangle_{lab.}$ KeV	S-factor MeV·barn			
	^{9}Be(d,α_0)^{7}Li	^{9}Be(d,α_1)^{7}Li*	^{9}Be(d,p_0)^{10}Be	^{9}Be(d,t)^{8}Be
90	3.5±0.70	5.7±1.2	2.0±0.40	0.85±0.18
140	1.9±0.38	3.1±1.1	1.4±0.30	0.40±0.075
190	2.7±0.55	4.2±0.83	1.7±0.35	0.52±0.10
240	4.3±0.85	6.5±1.3	2.6±0.5	0.85±0.18
290	5.7±1.2	7.6±1.5	2.8±0.55	0.95±0.2

Measured S(E)-factors slightly decreased as E decreases. However, each S(E)-factor at E=90 keV enhanced about twice larger than the one at E =140 keV. We assumed that it was not due to the resonance effect, because exited levels of ^{11}B* which enhance S(E)-factors of ^{9}Be-d reactions

have not found up to now. We suggest that S(E)-factors increase due to an electron screening effect. According to C.Rolfs et al.[3], the effect cannot be disregarded and become important for the understanding of the low-energy data at the energy region below $E/U_e \leqq 100$. Unexpectedly our measured S(E)-factors were enhanced at E= 90keV($E/U_e \fallingdotseq 200$) and increase rate of our measured S(E)-factors was much higher than the theoretical data(eq.(2)). We confirmed the similar tendency of the increase through the comparison of measured data for ^{9}Be-p reaction.

3.2. The nuclear reaction of ^{9}Be-p

Figure 2 shows the ^{9}Be-p reaction branches, as Figure 3 Energy spectrum.

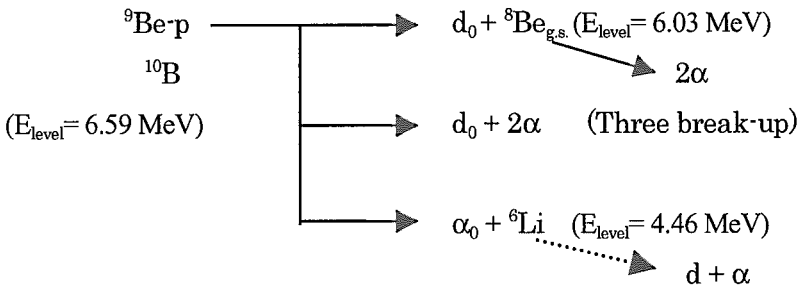

Figure 2 Branches of ^{9}Be-p nuclear reactions at low energy

The Q-value of ^{9}Be-p reaction is not enough large to separate peaks of the emitted particles with absorber foil.

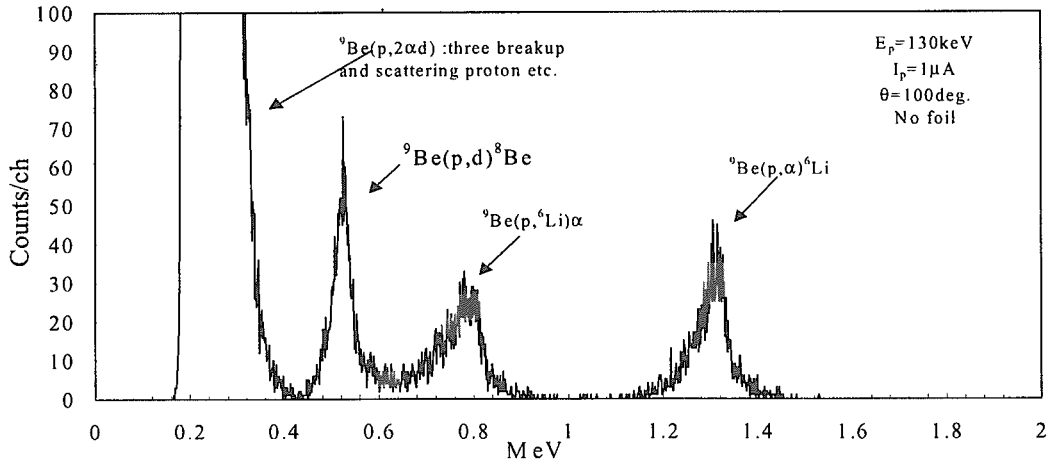

Figure 3 Energy spectrum of the charged-particles emitted from ^{9}Be-p nuclear reaction

The reactions of $^{9}Be(p,\alpha_0)^{6}Li$ and $^{9}Be(p,d)^{8}Be$ were measured for proton energies from about 30 to 300 keV(lab.) in backward angles(over 80 degree(lab.)). The total cross section was estimated from extrapolating approximation curve to measured angular distributions. Figure 4 shows the S(E)-factors obtained from out measurement and other's[4].

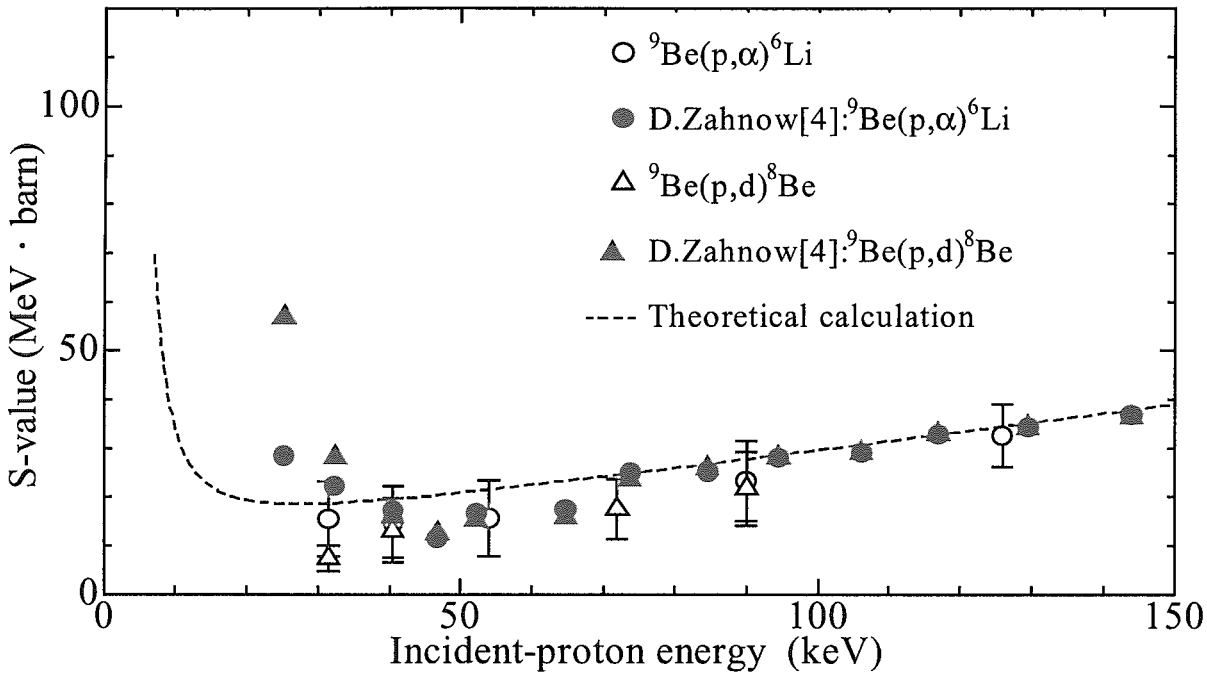

Figure 4. S(E)-factors of ^{9}Be-p nuclear reactions

As for our measurement data, the S(E)-factor of $^{9}Be(p,\alpha)^{6}Li$ reaction increases as proton energy decreases below 50 keV. That of $^{9}Be(p,d)^{8}Be$ reaction does not have the same tendency. Other measured S(E)-factors increased together as proton energy decreases below 50 keV. Theoretical curve is calculated briefly from other measured data and the equation (2). We can see a rapid enhancement about 10 keV in calculation data, while about 40 keV in other and our measured data. Our measured S(E)-factors increase more slowly with energy change than the other measured data and more rapidly than the theoretical data.

4. SUMMARY

The reactions of $^{9}Be(p,\alpha_0)^{6}Li$ and $^{9}Be(p,d)^{8}Be$ were measured for proton energies from about 30 to 300 keV in backward angles.

The increase of the S(E)-factors were observed toward lower energies region below 50 keV. However our measured S(E)-factors increase more slowly with energy change than the other

measured data and more rapidly than the theoretical data. This result is consistent with our previous ^{9}Be-d experiment. The S(E)-factors increased as deuteron energy decreases below 100 keV. From our study, we estimate that the equation (2) which approximate the S(E)-factor considering with the electron screening effect needs some other parameters. For example, we presume that they include isotopic effect of incident particle or target sample. To approximate this phenomenon more precisely, we need improved experiments at lower energy region.

ACKNOWLEDGEMENT

The authors wish to thank Messrs. H. Sugimoto and J. Datemichi of Osaka University for their assistance in experiments.

REFERENCES

[1] Assenbaum H.J., Langanke K. and Rolfs C.: Z. Phys., A327, 461 (1987)

[2] Ochiai K. et al.: Proc. 10th Int. Symp. on Reactor Dosimetry, Osaka, JAPAN (1999), in press

[3] Rolfs C. and Somorjai E.: Nucl. Inst. Meth., B99, 297 (1995)

[4] Zahnow D. et al.: Z.Phys.,A359, 211 (1997)

3.10

Measurement of Leakage Neutron Spectra from Advanced Blanket Materials and Structural Materials Induced by D-T Neutrons

Takashi Nishio, Tetsuo Kondo, Hiroyuki Takagi, Kokooo[1)], Isao Murata, Akito Takahashi, Fujio Maekawa[2)], Yujiro Ikeda[2)] and Hiroshi Takeuchi[2)]
[1)] Department of Physics, University of Mawlamyine
[2)] Japan Atomic Energy Research Institute.

Department of Nuclear Engineering, Osaka University
Yamadaoka, 2-1, Suita, 565-0871, Japan
e-mail: nishio@newjapan.nucl.eng.osaka-u.ac.jp

D-T neutron benchmark experiments for $LiAlO_2$, Li_2TiO_3, Li_2ZrO_3, Cu and W have been conducted at FNS of JAERI to validate five nuclear data files. The former three are promising advanced breeder materials and the latter two are important structural materials in a fusion reactor. From the results, all the nuclear data files were confirmed to be fairly reliable with respect to the prediction of neutron spectrum in the use of Li_2TiO_3 and Cu. For $LiAlO_2$ and W, some large discrepancies between the experimental and calculated data were observed. For Li_2ZrO_3, the C/E values became very large for all the nuclear data files.

1. Introduction

In a fusion reactor, blanket and structural materials are placed adjacent to the reactor core. Of course they must be kept their intactness during operation. In a fusion reactor design to predict their intactness accurately, it is very important to carry out the benchmark experiments and to analyze their results for candidate blanket and structural materials. In the present study, we focus on ceramic materials including lithium such as $LiAlO_2$, Li_2TiO_3 and Li_2ZrO_3 and Cu and W as an important structural material. Especially, $LiAlO_2$, Li_2TiO_3 and Li_2ZrO_3 are regarded as advanced solid breeder materials because of their inherent advantages such as chemical stability at high temperature, good tritium recovery characteristic and so on. However no integral experiments exist using these blanket materials until now.

In Japan Atomic Energy Research Institute (JAERI), a project started several years ago and is now progressing including various fusion integral benchmark experiments [1]~[4]. The present benchmark study is a part of the project and has been undertaken under the collaboration of JAERI and Osaka University.

In the present study, leakage neutron spectra from $LiAlO_2$, Li_2TiO_3, Li_2ZrO_3, Cu, and W assemblies have been measured and the analysis of the measured spectra has been carried out to validate accuracy of evaluated nuclear data files.

2. Experiment

The experiments were carried out at Fusion Neutronics Source (FNS) of JAERI. Table 1 shows the shape and thickness of used sample assemblies. Leakage neutron spectra from the sample assemblies

Table1 Sample assembly description

Sample	Shape*1	Dimensions (cm)
$LiAlO_2$	Slab	25.4 x 25.4 x ^{t}10.2, ^{t}25.4
Li_2TiO_3	Slab	25.4 x 25.4 x ^{t}10.2, ^{t}25.4
Li_2ZrO_3	Pseudo-cylinder	47.6 ϕ *2 x ^{t}10.2, ^{t}25.4,^{t}40.6
Cu	Slab	45.7 x 45.7 x ^{t}10.2, ^{t}25.4, ^{t}40.6
W	Slab	35.6 x 35.6 x ^{t}10.2, ^{t}20.3, ^{t}30.5

*1 Sample are made by piling up unit bricks, the size of which is 5.08 x 5.08 x 5.08 cm^3.
*2 Equivalent diameter to conserve the front surface area.

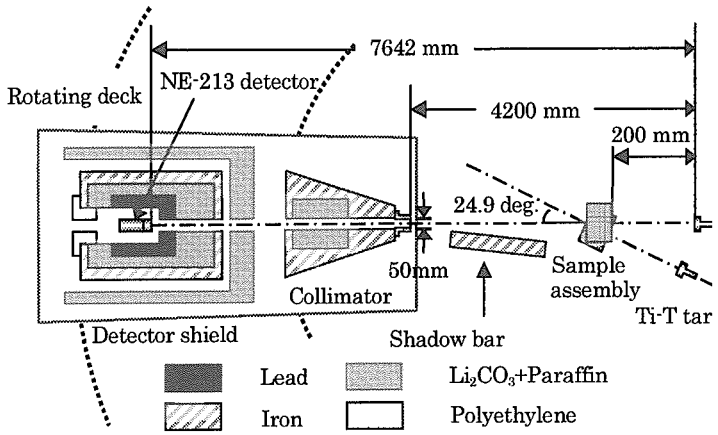

Fig.1 Cross-sectional view of the experimental arrangement

were measured using an NE-213 (2"-diam by 2"-long) scintillation detector by the time of flight (TOF) method for two emission angles of 0 and 24.9 degs. Fig.1 shows the experimental arrangement. A high energy-resolution measurement ranging from 0.05 to 15 MeV was successfully achieved by adoption of a long flight path as well as the pulse-shape-discrimination technique with three delay-line amplifiers, which were set to different gains. The block diagram of measuring system is shown in Fig.2.

The detector efficiency was determined through three measurements to cover a wide energy dynamic range of the detector: (1) leakage neutron spectrum from a beryllium slab for lower energy, (2) Energy and angle differential elastic scattering cross section of hydrogen using a polyethylene sample for several to 13 MeV and (3) neutron source spectrum for 14 MeV. The fitted curve with these experimental results was used for data reduction of the measurements. Fig.3 shows the efficiency curve.

3. Data analysis

Analyses of the experiments were carried out with the three-dimensional Monte Carlo code MCNP-4B. For validation of cross section data, five evaluated nuclear data files, i.e., JENDL-3.2, JENDL-FF, ENDF/B-VI, FENDL/E-1.0, and FENDL/E-2.0 were selected as the cross section libraries listed in Table 2. The assemblies as well as the detector collimator were modeled precisely for the MCNP calculation. The measured source neutron spectrum was used as the neutron source in the calculation.

4. Results

i) $LiAlO_2$

Figures 4 and 5 show the measured leakage neutron spectra for $LiAlO_2$ of 25.4 cm in thickness and scattering angle of 24.9 deg., and the C/E values, respectively. The calculated spectra are in fairly good agreement with the experimental data. However, an opposite trend is seen at the elastic peak, that is overestimation for 0 deg. and underestimation for 24.9 deg.

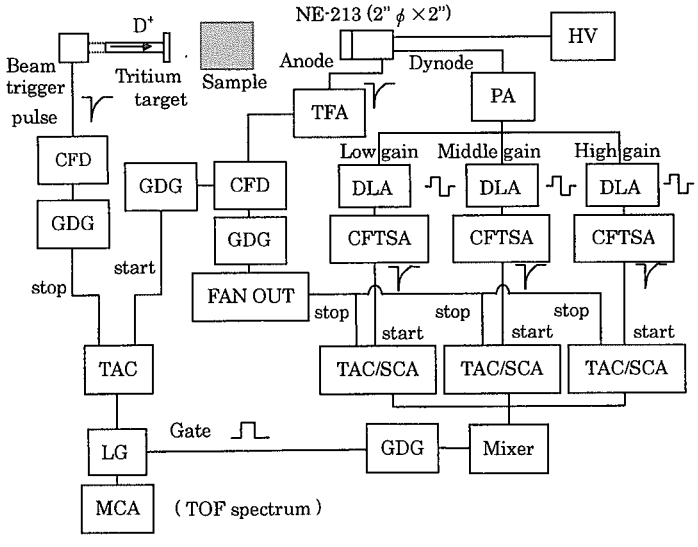

HV: High Voltage Power Supply
PA: Pre-Amplifier
TFA: Timing Filter Amplifier
DLA: Delay Line Amplifier
CFD: Constant Fraction Discriminator
CFTSCA: Constant Fraction Timing Single Channel Analyser
TAC/SCA: Time to Amplitude Converter Single Channel Analyser
GDG: Gate and Delay Generator
TAC: Time to Amplitude Converter
LG: Linear Gate
MCA: Multi Channel Analyser

Fig.2 Block diagram of the measuring system

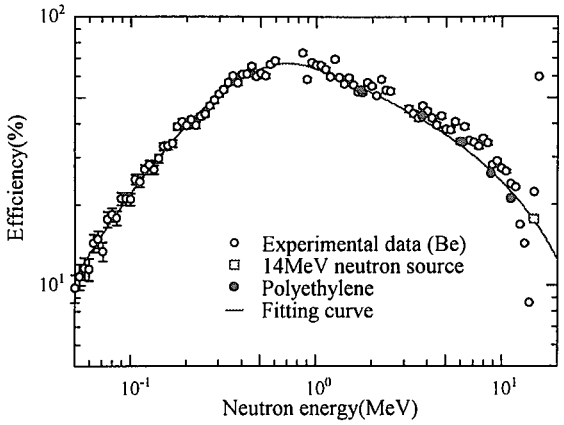

Fig.3 Measured efficiency of the NE-213 detector

In the spectrum of 24.9 deg., there exists a valley in the calculation, not in the measured spectrum, around 10 MeV. Compared to the neutron emission DDX of aluminum as is shown in Fig.6, underestimation of evaluated nuclear data is seen around 10 MeV. Some nuclear reactions around 14 MeV probably play an important role for leading to the phenomenon.

ii) Li_2TiO_3

Figures 7 and 8 show the measured leakage neutron spectra for Li_2TiO_3 of 25.4 cm in thickness and scattering angle of 24.9 deg., and the C/E values, respectively. A good agreement is seen between the experiment and calculation for the whole energy range and for all nuclear data files. However, the spectrum calculated with ENDF/B-VI is smaller than other calculations. This is understood from the neutron emission DDX comparison in Fig.9.

A valley around 10 MeV is observed similar to $LiAlO_2$ in the calculated spectrum for only 24.9 deg. The valley might be caused by the discrepancy around about 10MeV of the neutron emission DDX for Ti as is shown in Fig.9. However Li or O might cause it, because this is also observed in $LiAlO_2$.

iii) Li_2ZrO_3

Figures 10 and 11 show the measured leakage neutron spectra for Li_2ZrO_3 of 25.4 cm in thickness and scattering angle of 24.9 deg., and the C/E values, respectively. The discrepancy between the experimental and calculated spectra is very large, that is overestimation of the calculation. This discrepancy is observed in all the other results, i.e., the more the thickness of assembly increases, the lager the discrepancy becomes. From the neutron emission DDX comparison as is shown in Fig.12., one can understand the difference among the calculated spectra below 1MeV, also in the C/E spectra. Similarly it is understood that the structures of spectra calculated with ENDF/B-VI were different from those of other nuclear data files.

iv) Cu

Figures 13 and 14 show the measured leakage neutron spectra for Cu of 10.16 cm in thickness and scattering angle of 24.9 deg., and the C/E values, respectively. The calculated spectra are in fairly good agreement with the experimental data. However, the elastic scattering peaks for 0 deg, do not agree with the calculations.

ENDF/B-VI and FENDL/E-2.0 are in excellent agreement with the experimental data among five nuclear data files as one can see it from the comparison of the neutron emission DDX as is shown in Fig.15. The others show underestimation around 7 MeV.

Table 2 Nuclear data files used in the calculation

Library name used in the present paper	Nuclear data quoted*1						
	Li	O	Al	Ti	Zr	Cu	W
JENDL-3.2	J32	J32	J32	J32	J32	J32	J32
JENDL-FF	J32	J32	JFF	JFF	JFF	JFF	JFF
ENDF/B-VI	B-VI	B-VI	B-VI	B-VI	B-VI	B-VI	BVI
FENDL/E-1.0	B-VI	B-VI	J31	J31	B2	B-VI	B-VI
FENDL/E-2.0	B-VI	J32	EF3	J31	JFF	B-VI	JFF

*1 J32, JFF, B-VI, J31, EF3 and B2 are abbreviations of JENDL-3.2, JENDL-FF, ENDF/B-VI, JENDL-3.1, EFF-3 and BROND2, respectively.

v) W

Figures 16 and 17 show the measured leakage neutron spectra for W of 20.32 cm in thickness and scattering angle of 0 deg., and the C/E values, respectively. Some significant discrepancies between the experimental and calculated spectra are observed. From the

comparison of the neutron emission DDX as is shown in Fig.18, one can understand the overestimation around 3 MeV for JENDL-FF and FENDL/E-2.0 and the underestimation around 10 MeV for ENDF/B-VI and FENDL/E-1.0.

As a whole, ENDF/B-VI and FENDL/E-1.0 are mostly reliable from the present measurement, though they show a little underestimation around 10 MeV from the DDX comparison.

5. Conclusion

D-T neutron benchmark experiments for advanced breeder materials and structural materials have been conducted to validate five nuclear data files. From the result, all the nuclear data files were confirmed to be fairly reliable with respect to the prediction of neutron spectrum in the use of Li_2TiO_3 and Cu. For $LiAlO_2$ and W, some large discrepancies between the experimental and calculated data were observed. For Li_2ZrO_3, the C/E values became very large for all the nuclear data files.

Reference:

[1] Kokooo, et al., Fusion Technol., 34, 980 (1998).
[2] Maekawa F., et al., Fusion Technol., 34, 1018 (1998).
[3] Maekawa F., et al., J. Nucl. Sci. Technol., (1998).
[4] Murata I., et al., "Benchmark Experiment on $LiAlO_2$, Li_2TiO_3 and Li_2ZrO_3 Assemblies with D-T Neutrons - Leakage Neutron Spectrum Measurement -" Proc. 5th Int. Symp. on Fusion Nucl. Technol., Roma, Sept. 19~24 (1999) to be published.
[5] Takahashi A., et al., OKTAVIAN Report, A-92-01 (1992).

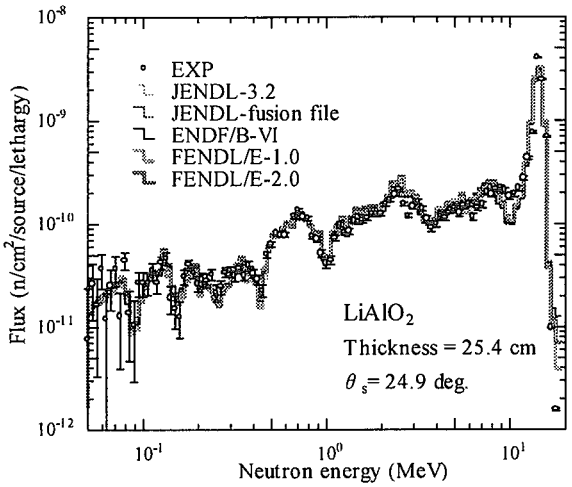

Fig.4 Neutron flux for $LiAlO_2$ of 25.4 cm[t] at 24.9 deg.

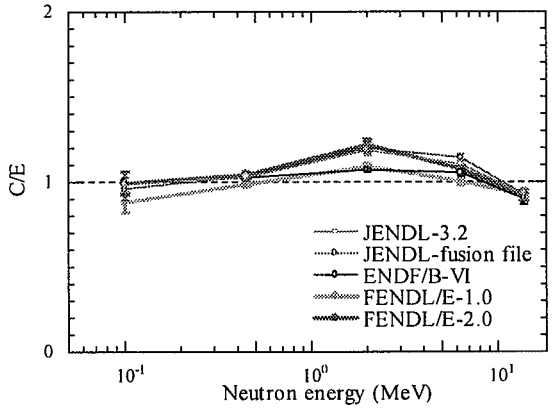

Fig.5 C/E for $LiAlO_2$ of 25.4 cm[t] at 24.9 deg.

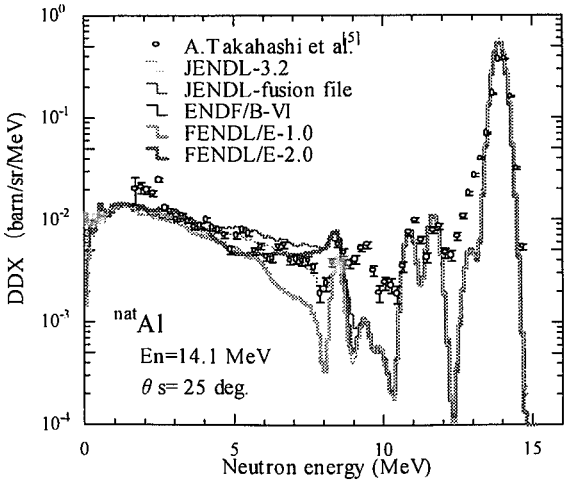

Fig.6 Evaluated neutron emission DDX of ^{nat}Al at 25 deg. compared with the experimental data.

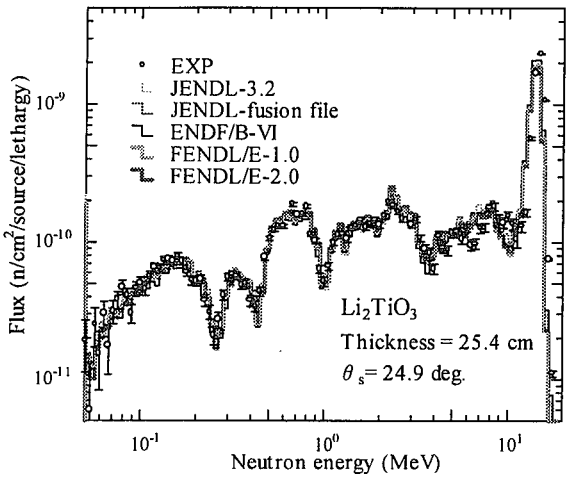

Fig.7 Neutron flux for Li_2TiO_3 of 25.4 cm^t at 24.9 deg.

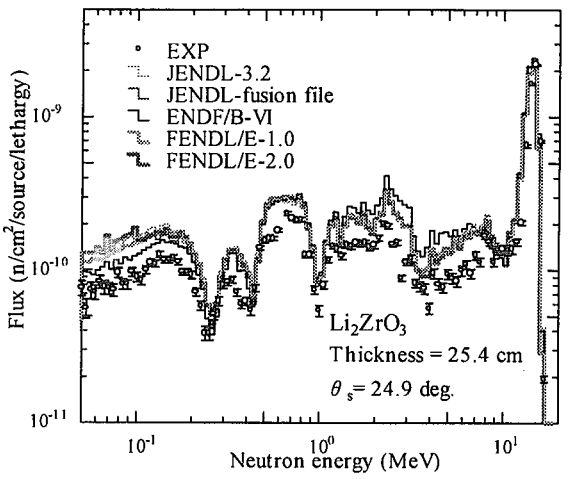

Fig.10 Neutron flux for Li_2ZrO_3 of 25.4 cm^t at 24.9 deg.

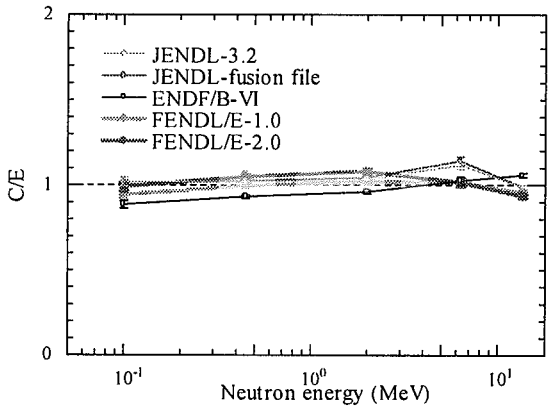

Fig.8 C/E for Li_2TiO_3 of 25.4 cm^t at 24.9 deg.

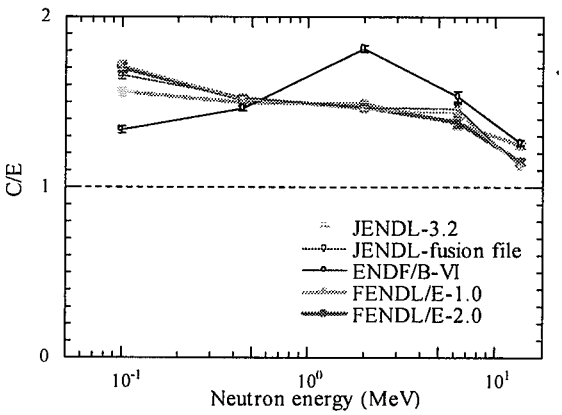

Fig.11 C/E for Li_2ZrO_3 of 25.4 cm^t at 24.9 deg.

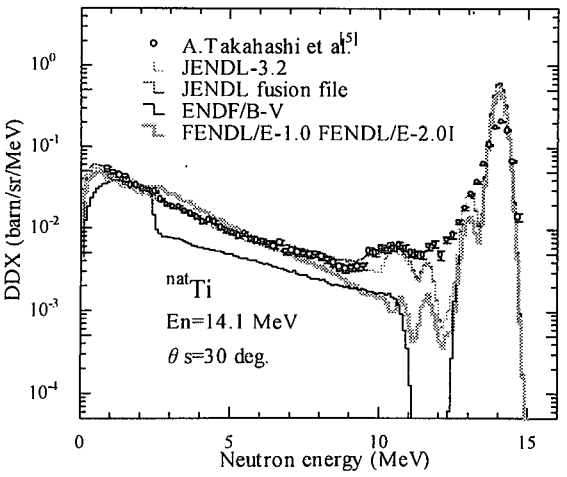

Fig.9 Evaluated neutron emission DDX of ^{nat}Ti at 30 deg. compared with the experimental data.

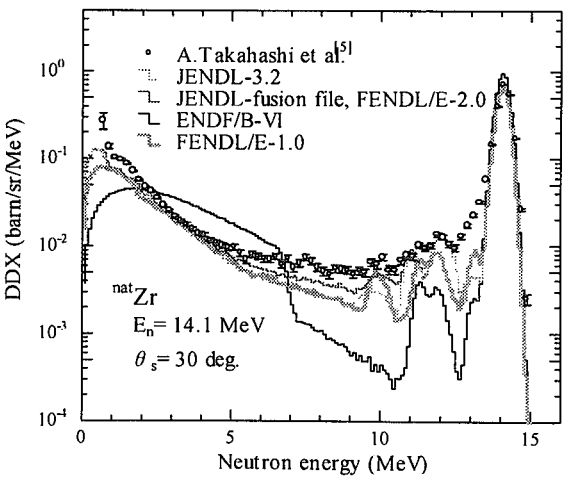

Fig.12 Evaluated neutron emission DDX of ^{nat}Zr at 30 deg. compared with the experimental data.

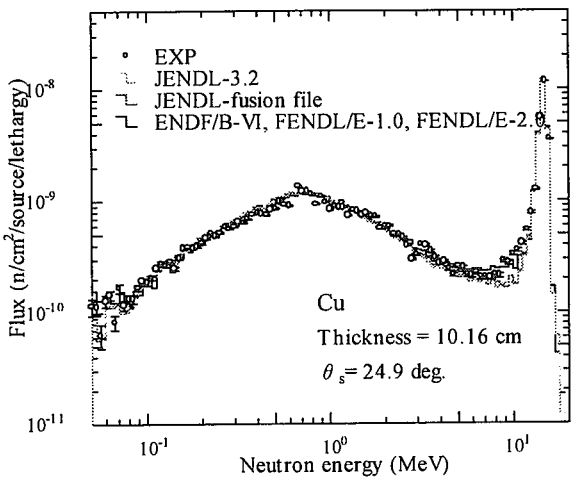

Fig.13 Neutron flux for Cu of 10.16 cm ^{t} at 24.9 deg.

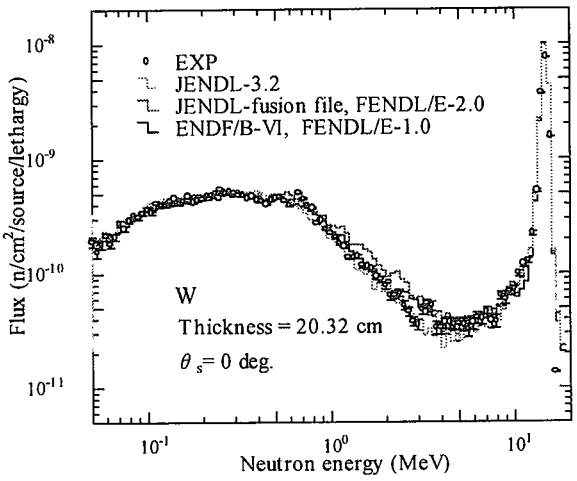

Fig.16 Neutron flux for W of 20.32 cm ^{t} at 0 deg.

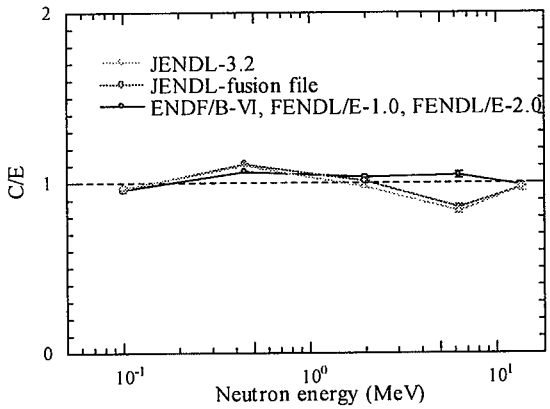

Fig.14 C/E for Cu of 10.16 cm ^{t} at 24.9 deg.

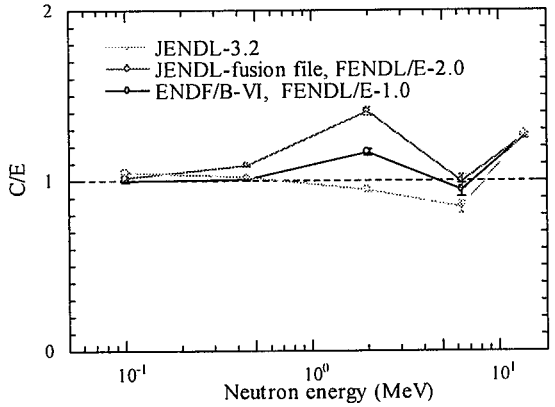

Fig.17 C/E for W of 20.32 cm ^{t} at 0 deg.

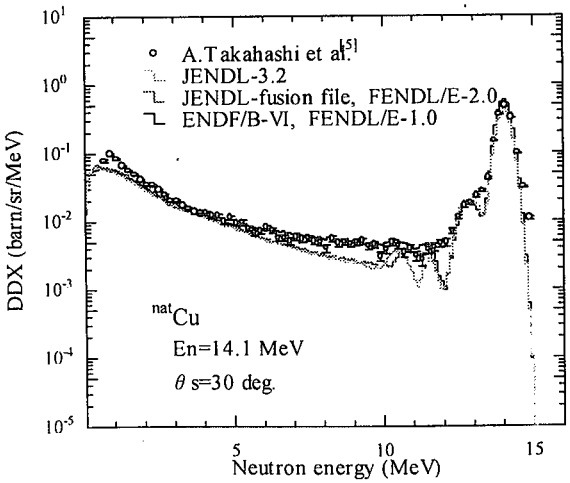

Fig.15 Evaluated neutron emission DDX of ^{nat}Cu at 30 deg. compared with the experimental data.

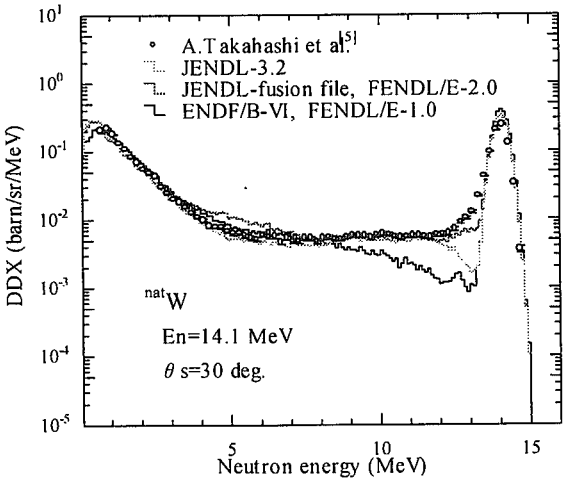

Fig.18 Evaluated neutron emission DDX of ^{nat}W at 30 deg. compared with the experimental data.

3.11

Measurement of Double Differential Cross Sections of Charged Particle Emission Reactions by Incident DT Neutrons －Correction for Energy Loss of Charged Particle in Sample Materials－

Hiroyuki Takagi, Yasuaki Terada, Isao Murata, Akito Takahashi
Department of Nuclear Engineering, Osaka University
Yamadaoka 2-1, Suita, Osaka, 565-0871, Japan
E-mail: takagi@newjapan.nucl.eng.osaka-u.ac.jp

In the measurement of charged particle emission spectrum induced by neutrons, correcting the energy loss of charged particle in sample materials becomes a very important inverse problem. To deal with this inverse problem, we have applied the Bayesian unfolding method to correct the energy loss, and tested the performance of the method. Although this method is very simple, it was confirmed from the test that the performance was not inferior to other methods at all, and therefore the method could be a powerful tool for charged particle spectrum measurement.

1. Introduction

Correction for the energy loss of charged particle in sample materials is a serious problem in measurement of charged particle emission spectrum induced by neutrons. Recently, a new simple method was developed for unfolding various measured radiation spectra by extending Bayes theorem [1]. In the present study, we have, thus, tried to apply this method to our experimental data of charged particle emission cross-section measured by the E-TOF two-dimensional analysis at OKTAVIAN of Osaka University [2].

In the past, our experimental data (double differential charged particle emission cross section (DDXc) induced by DT neutrons) were corrected by the conventional method based on an assumption that any charged particle passes half thickness of sample material. This method was applicable if only the energy loss could be suppressed to very small value by using a thin sample foil. For example, we used 25 μ m and 10 μ m thick foil for proton and α-particle measurements, respectively. However, recently elements that cannot be supplied as an enough thin sample are planning to be used for cross section measurement, like light elements. In this study, focusing on a measurement in which there exists a remarkable energy loss in the sample material as a result of using a thick sample foil, we developed an unfolding code based on the Bayes theorem to accurately correct the energy loss.

2. The New Method

The Bayes' unfolding method is applicable to almost all kind of radiation measurement analysis. There are some variations in the Bayes' estimation method. In this work, *spectrum type Bayes estimation method* has been applied to our charged particle spectrum unfolding problem. In the method, estimation calculation can be realized using just measured pulse height spectrum (histogram) data.

The estimation procedure is expressed as

$$est_j^{(l+1)} = \sum_i^m \left(d_i \times \frac{est_j^{(l)} \times r_{ij}}{\sum_j^n est_j^{(l)} \times r_{ij}} \right) \quad ,(j = 1, n) \tag{1}$$

where r_{ij} called *likelihood* is the response of the detection system which provides the probability of a

detection event giving pulse height h_i for the charged particle energy E_j. d_i (i=1,m) is the detected pulse height spectrum. $est_j^{(l)}$ (j=1,n) is the estimated spectrum revised by lth estimation calculation. The above formula is repeatedly used for the pulse height spectrum d_i in this work. Revised $est_j^{(l)}$ is used for prior information to the next revise calculation.

3. Application and verification

In order to verify the above method in the charged particle spectrum unfolding problem, several analyses were carried out using numerical simulation and practical measured results, i.e., α -particles spectrum measurement and its unfolding for ^{27}Al samples (60mm ϕ ×10 μ m, 25 μ m, 100 μ m thick) with incident DT neutrons.

3-1. Evaluation of Response Function

In order to carry out unfolding, the response function should be prepared. They are evaluated on the assumption that energy loss occurs only in sample material not in the detector. It means that response, in this case, is made considering energy loss in the sample. The response function is calculated by using SRIM (TRIM-96) code. The obtained response function is shown in Fig. 1.

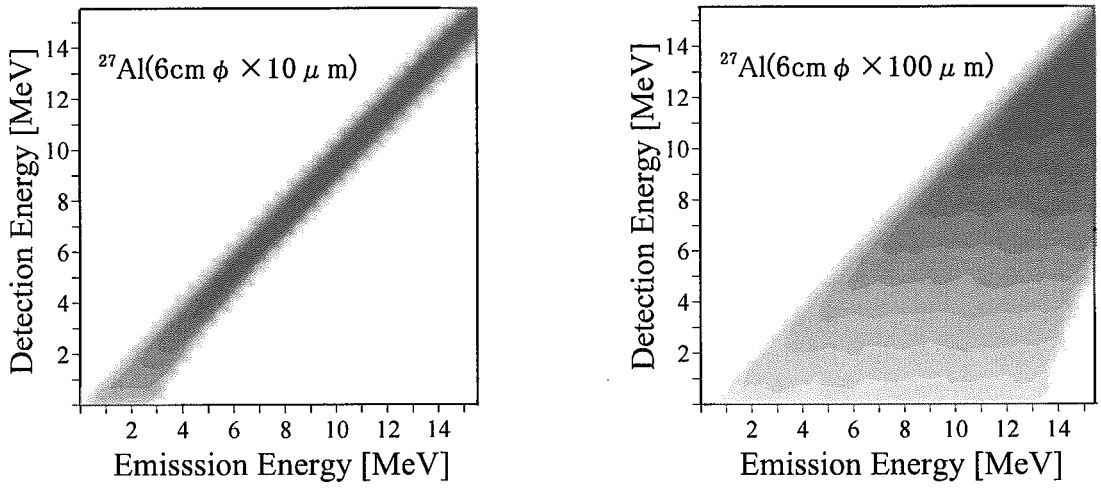

Fig. 1 Response Function for ^{27}Al(n,x α) measurement calculated by SRIM (θ =45deg.).

3-2. Verification Using Numerical Simulations for ^{27}Al Sample

The verification of the new unfolding method was confirmed through numerical simulation using infinite statistic pseudo-measured spectrum (folded spectrum; $\vec{d}$), which was given as

$$\vec{d} = \boldsymbol{R} \cdot \vec{p} \tag{2}$$

where $\boldsymbol{R}$ is the response function. $\vec{p}$ is the ideal spectrum quoted from the evaluated nuclear data(JENDL-FF). Fig. 2 shows the unfolded results. In these figures, an excellent spectrum reproduction is seen even if the diagonality of response function is not good, i.e., in case of 100 μ m in thickness. In such a case, more iteration is required to reproduce the ideal spectrum than thinner ones. For evaluating reproducibility, we introduce the amount of information entropy, $\boldsymbol{B}$, which is defined as

$$B = \sum_{j=1}^{n} p_j \log\left(\frac{est_j}{p_j}\right) \tag{3}$$

where p_j(j=1,n) is the ideal spectrum. est_j(j=1,n) is the unfolded spectrum. Unfolding performance is

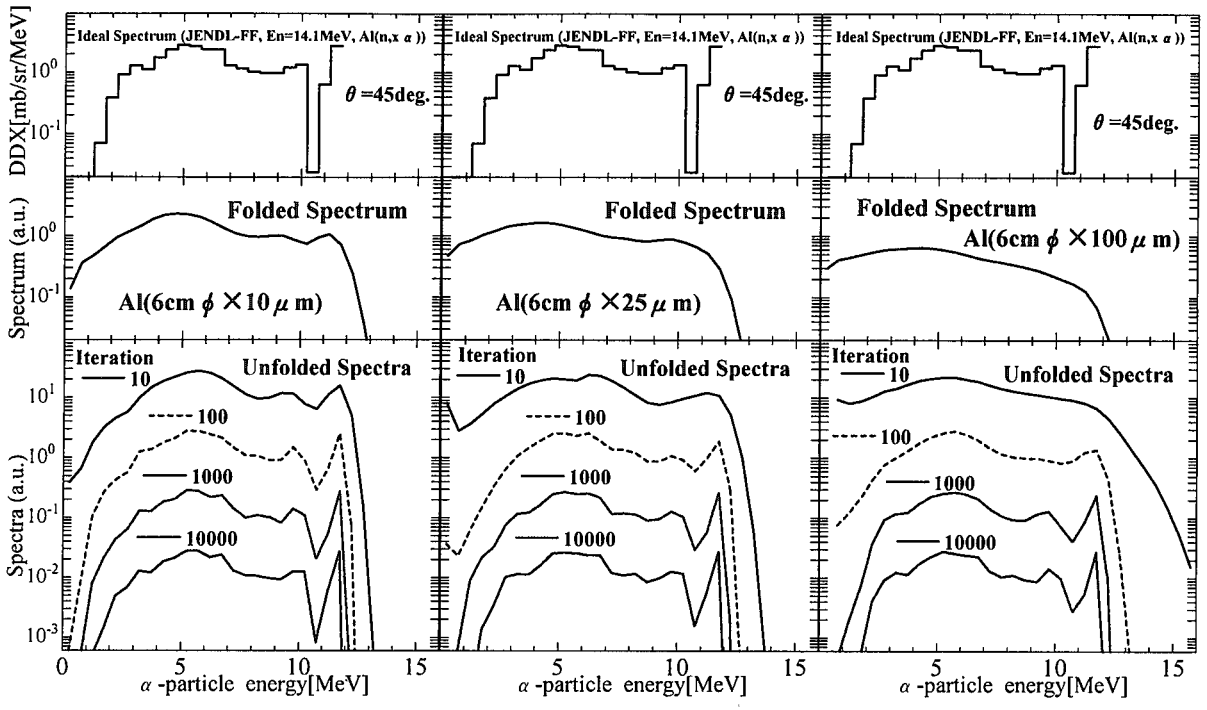

Fig. 2 Unfolding tests using infinite statistic spectra.

estimated by this value. The larger the ***B*** value becomes, the better reproduction of the ideal spectrum is realized. The relation between the ***B*** value and the number of iteration is shown in Fig.3. It is verified from the figure that the unfolded spectrum approaches the ideal spectrum with increase of the number of iteration, and therefore the ideal spectrum can be reproduced by sufficient iteration even if using a thick sample.

In the next step, an unfolding test using finite statistic pseudo-measured spectrum, derived from random sampling of infinite statistic folded spectrum (the number of sampling: N_{ran}), was carried out. The unfolded results are shown in Figs. 4-7. These figures show that this method can reproduce the ideal spectrum to a certain extent. However, as increasing iteration, an unpleasant oscillation is observed as a result of propagation of the statistical fluctuation in the initial folded spectrum, as shown in Figs. 4 and 6. From the Figs. 5 and 7, it is found that there is an optimum iteration number which increases with increase of the statistical accuracy, (N_{ran}). It can be concluded that an acceptable result can be expected, if N_{ran} is set to be an enough large (meaning that a high statistical accuracy is required in actual case.), though in such a case the number of iteration is obliged to increase.

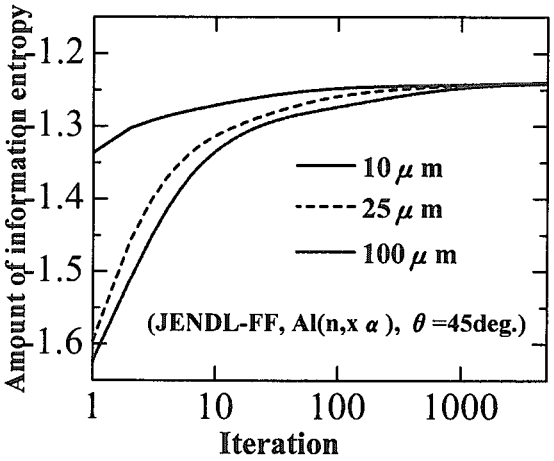

Fig. 3 Behavior of convergence in the case of infinite statistic as a function of the number of iteration.

3-3. Verification Using Experimental Results for ^{27}Al Sample

To confirm the conclusion in the previous section, the developed method was applied to a measured spectrum data. Double differential cross section (DDX) of $^{27}Al(n,x\alpha)$ reaction induced by DT neutrons have been measured at OKTAVIAN of Osaka university. Experiments were carried out

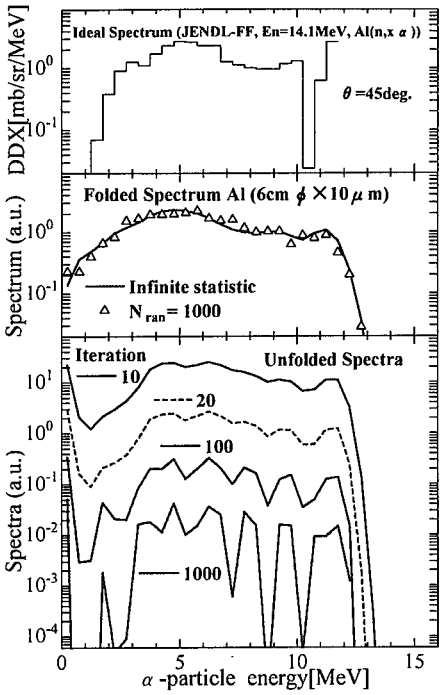

Fig. 4 Unfolding using finite statistic spectra of 1000 counts for ^{27}Al(10 μ m) sample.

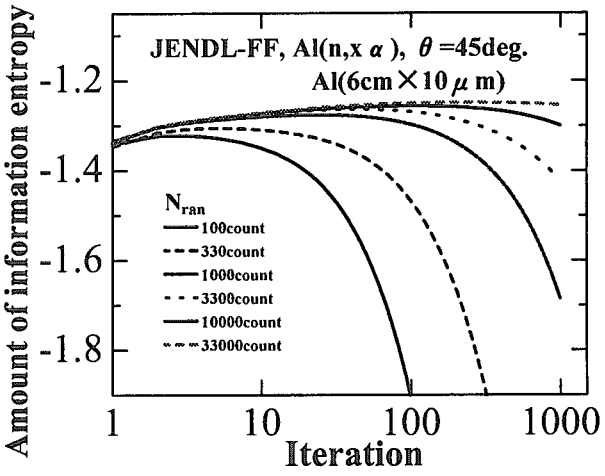

Fig. 5 Unfolding performance using finite statistic spectra of various counts for ^{27}Al(10 μ m) sample.

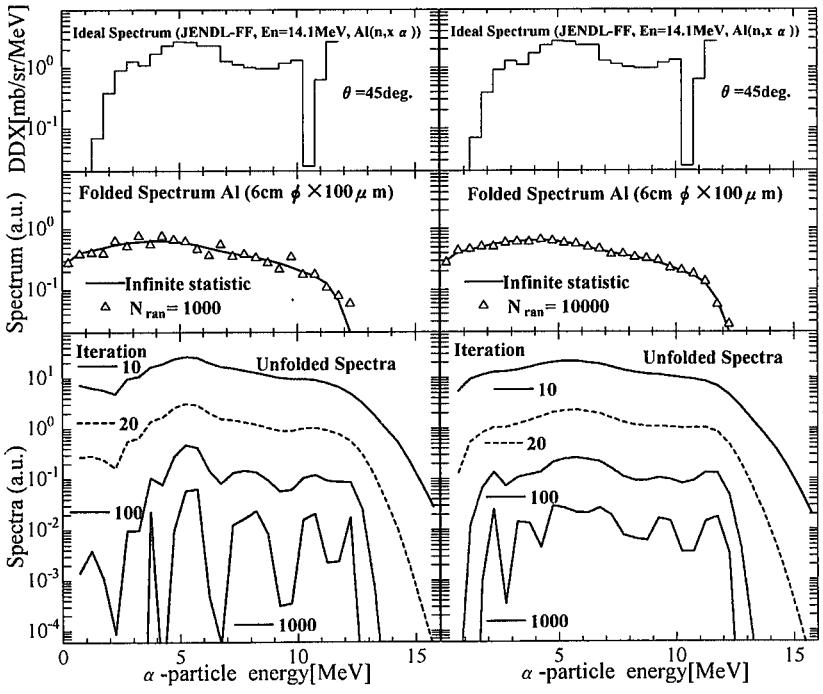

Fig. 6 Unfolding using finite statistic spectra of 1000 counts and 10000 counts for ^{27}Al(100 μ m) sample.

by using the charged particle spectrometer based on the two-dimensional analysis of energy and time-of-flight of emitted charged particle [2]. The schematic arrangement of the spectrometer is shown in Fig. 8. The CsI(Tl) scintillator, 2mm in thickness and 50mm in diameter, was used as a charged particle detector.

Similar to the previous section, three ^{27}Al samples with different thickness (60mm ϕ ×10 μ m, 25 μ m, 100 μ m thick) were used. The measured raw spectra for each sample are shown in Fig. 9. The optimized iteration frequency, that is the revise number of estimation calculation, was evaluated from the amount of information entropy ***B*** calculated using JENDL-FF data. Unfolding was carried out by formula (1) for each spectrum. Fig. 10 shows the respective unfolded spectra (DDX data) together with the corrected spectrum obtained by the conventional method (10 μ m thick sample)[3]. Although the measured raw spectra for three thicknesses show different shape, unfolded spectra present equal data. Further, the unfolded spectrum for 10 μ m shows almost the same as the corrected spectrum with the conventional correction method. It should be noted that the conventional method can not deal with the results for 25 μ m and 100 μ m. These results prove the applicability of this new method to measurements for thicker samples.

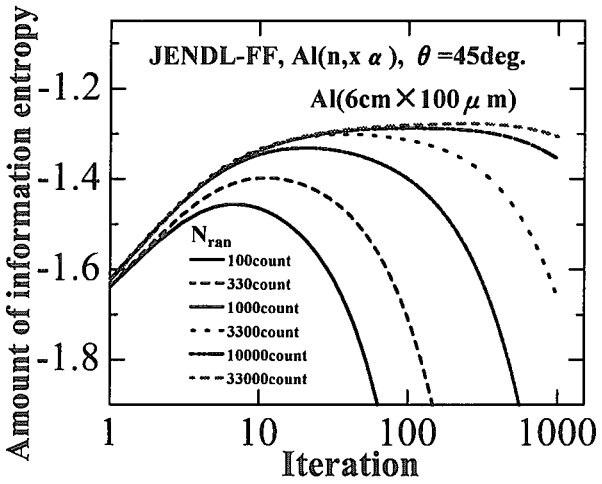

Fig. 7 Unfolding performance using finite statistic spectra of various counts for ^{27}Al(100 μ m) sample.

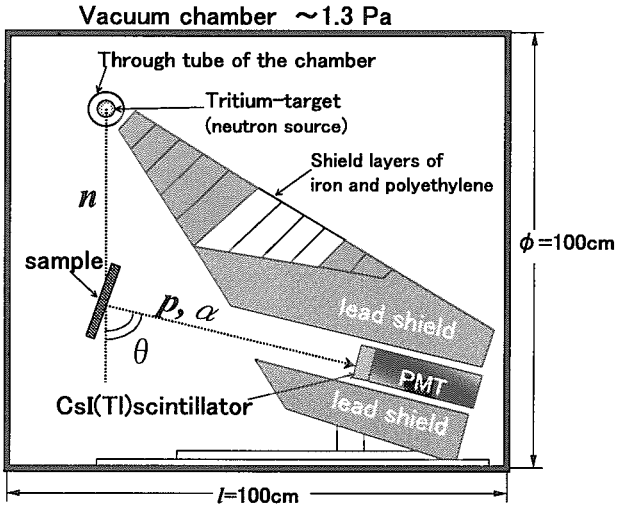

Fig.8 Schematic arrangement of the charged particle spectrometer.

4. Discussion

Taking into account the unfolding results using numerical simulation in Sec. 3-2, one can understand the following opposite two requirements exist. One is requirement of thinner sample, because thicker sample makes diagonality of response function worse. The other is thicker sample, because sufficiently accurate result cannot be obtained with a thinner sample. Thus, "*Optimum sample thickness*" exists. The thickness should be determined considering these inconsistent requirements as well as available measurement time.

Unfolding tests using the measured DDX spectra show a fairly good agreement among unfolded spectra. However, there is a slight difference with each other. These differences might be caused by selection of the sample thickness, i.e., the number of iteration considering the measurement accuracy, or by the difference between the simulated response function and actual one. Though the difference is mostly within the statistical error, further investigation about it should be performed in the future.

5. Conclusion

The Baysian statistical unfolding method has been applied to correction for energy loss of charged particle in sample materials on measurement of charged particle emission cross section with DT neutrons. And the unfolding applicability has been tested using numerically simulated spectra and practical measured results. From the test results, it is important in the use of the method to determine *optimum condition*, such as sample thickness, iteration frequency and so on. Also the results showed

the validity of the method. Although this method is very simple, it was found that the performance was not inferior to other methods at all. Thus, it was confirmed that this method could be a powerful unfolding tool for charged particle spectrum measurement.

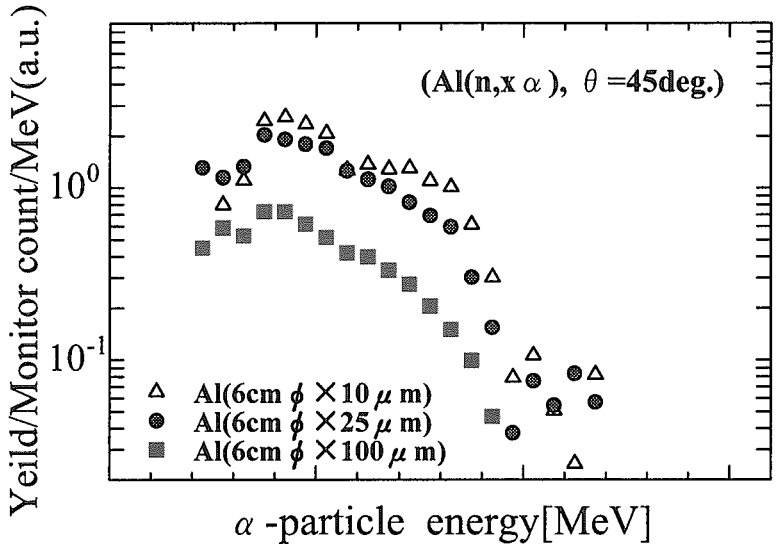

Fig. 9 The measured raw spectra of ^{27}Al(n,x α) reaction for each sample thickness.

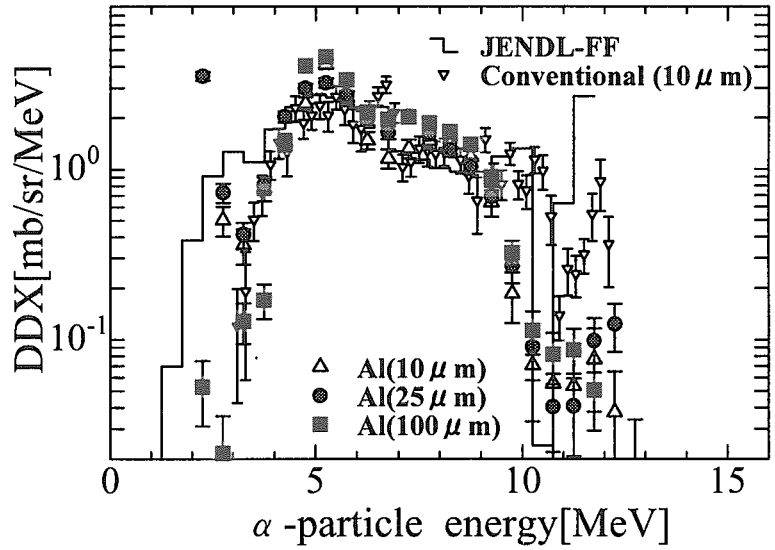

Fig. 10 The unfolded spectra for respective thickness estimated by Bayesian method and corrected spectrum for 10 μ m thick sample obtained by conventional method.

References

[1] Iwasaki, S., :"A New Approach for Unfolding Problems Based Only on the Bayes' Theorem", 9th International Symposium on Reactor Dosimetry, Prague, Chezk, Sep. 2-6, (1996).

[2] Takahashi, A., *et al.*: "A Time-of-Flight Spectrometer with Pulse-Shape Discrimination for Measurement of Double Differential Charged-Particle Emission Cross Section", *Nucl. Instr. Meth.*, A401, 93 (1997).

[3] Takagi, H., *et al.*: "Measurement of Double Differential Cross Section of Charged Particle Emission Reactions for ^{nat}Zr, ^{27}Al and ^{nat}Ti by Incident DT Neutrons", *Proc. 1998 Sympo.Nucl. Data, JAERI-Conf* 99-002, 204 (1998).

3.12 Measurement of secondary gamma-ray production cross sections of structural materials for fusion reactor

—Extraction of discrete and continuum components—

Tetsuo Kondo, Ryutaro Morotomi, Takashi Nishio, Isao Murata, and Akito Takahashi

Department of Nuclear Engineering, Osaka University
Yamada-oka, 2-1, Suita, 565-0871, Japan
e-mail : tkondo@newjapan.nucl.eng.osaka-u.ac.jp

Abstract

A new method to deal with measured spectrum of secondary gamma-rays induced by D-T neutrons with Ge detector is proposed. Subtracting background components and discrete peaks from the raw secondary gamma-ray spectrum, the continuum component of secondary gamma-ray was successfully extracted. By using unfolding process, the continuum component of the secondary gamma-ray production cross section was derived. The measured cross section data obtained by this method are very useful for precise evaluation of secondary gamma-ray production cross sections.

1. Introduction

In a fusion reactor design, secondary gamma-ray production cross section data are important because of the necessity of estimations for nuclear heating, radiation damage, radiation exposure, and so on. The experimental data are discrete gamma-rays(S_{DC}) obtained with Ge detector or continuum energy spectrum(S_{NaI}) with NaI detector. In nuclear data files, continuum spectra are mainly included considering the measured continuum spectra(S_{NaI}) with NaI detector. Because with Ge detector, only prominent discrete gamma-rays can be measured, but residual continuum component(S_{CC}) can not be extracted.

In the present study, we propose a new method to process a measured gamma-ray spectrum with Ge detector. At first, we separate gamma-rays induced by D-T neutrons into two components shown in Fig .1 : One is the discrete component(S_{DC}) including relatively prominent discrete peaks. The other is the continuum component(S_{CC}) which includes a continuous energy spectrum containing small discrete peaks. The gamma-ray spectrum for the latter has not been obtained experimentally. We extract these two data from the measured spectra with Ge detector by a special data processing procedure. The obtained data were compared with the theoretical calculation result with SINCROS-Ⅱ as well as the evaluated nuclear data. The calculation contained the effect of direct reactions calculated with DWUCKY. These measured data are very useful for precise evaluation of secondary gamma-ray production cross section, i.e., mixture of discrete and continuum components.

2. Experiment

Measurements of secondary gamma-ray production cross sections have been carried out at the D-T neutron source facility OKTAVIAN of Osaka University. We adopted the TOF method to separate prompt gamma-ray signals from the whole time spectrum. An HP-Ge detector was used as a gamma-ray detector. The Ge crystal volume was 177.9 cm^3. Elements which are considered as candidates of the structural material for the fusion reactor were chosen as sample materials. In the present paper, the result for vanadium was presented. The shape of the vanadium sample was a hollow cylinder(OD : 30 mm, ID : 26 mm, length : 70 mm). Using such a thin sample, we could suppress neutron multiple scattering and attenuation of produced gamma-rays in the sample.

The experimental arrangement is shown in Fig. 2. The scattering angle was fixed at 125 deg. so that we didn't have to consider the angular distribution for secondary gamma-rays to estimate the total gamma-ray production cross section. The detector was heavily shielded with lead, heavy concrete, polyethylene, and so on. With the electronic circuit shown in Fig. 3, we obtained foreground spectrum, background spectrum and TOF spectrum.

3. Measured spectra

Figures 4, 5a and 5b show TOF, foreground and background spectra, respectively. Utilizing the signals in the areas of FG and BG described in Fig.4, spectra for FG and BG were obtained as shown in Figs. 5a and 5b, respectively. In the foreground spectrum, several discrete gamma-rays were observed. Though some of them were background gamma-rays, the peaks from the vanadium sample could be found by comparing Fig. 5a with 5b, Besides gamma-rays from the sample, the FG spectrum contains time-independent background component(TIB) and time-dependent background component(TDB). The BG spectrum in Fig. 5b corresponds to the TIB component. Fig. 6 shows the sample-out FG spectrum which contains the TIB and TDB components. The TDB component was obtained with FG and BG spectrum in the sample-out measurement.

4. Data analysis

At the first step, we subtracted the TIB and TDB components from the foreground spectrum in the sample-in measurement to obtain the net foreground spectrum. Then the prominent discrete peaks were removed from the net foreground spectrum using the response functions of the peaks were calculated with MCNP-4B. The residual spectrum is shown in Fig. 7 together with the net foreground spectrum. On the second step, the spectrum was unfolded using the unfolding code HEPRO to obtain the S_{CC} having only the continuum component.

5. Result and discussion

Experimental data of discrete gamma-ray production cross sections above 0.35 MeV are listed in Table 1 compared with the theoretical calculation result by the SINCROS-Ⅱ system and DWUCKY. The DWUCKY is based on the DWBA theory. The data includes the evaluated nuclear data in ENDF-B/Ⅵ not JENDL-3.2 because JENDL-3.2 includes just continuum energy spectra. In addition to them, the measured data were compared with the compiled data by S.P. Simakov et al[1]. Simakov's data were prepared by normalizing and averaging other experimental data which had been measured over the world. The calculation results supported our experimental value as a whole. On the other hand, Simakov's data deviated from our experimental data. Since the number of data which had been used to obtain the compiled data was very small, we concluded that some of his data were not reliable. ENDF-B/Ⅵ didn't have adequate discrete data to compare with ours.

Table 2 shows the total discrete data, the total continuum data and the total cross section data. And Fig. 8 shows the calculated energy differential cross sections together with our experimental data for the continuum component. In the table, discrete data are the sum of discrete cross sections above 0.35 MeV. We excepted the data for gamma-ray energies of 684, 815, 1777 and 2004 keV from the discrete data because these values could not be included in the theoretical calculation or Simakov's data. The experimental continuum data are obtained with the method developed in this study. It is noted that the present continuum value in Table 2 is preliminary. The energy region of the continuum and total cross section data is from 0.35 to 3.0 MeV. Evaluated data of JENDL-3.2 and ENDF-B/Ⅵ are also shown in the total cross section data. Our continuum and total cross section data are larger than the calculation result and ENDF-B/Ⅵ data. According to Fig. 8, our result shows a little larger data above 1 MeV. But we think that we could extract the S_{CC} component successfully. Consequently, this method has a promising potential to enable to estimate the secondary gamma-ray production cross section data consisting mixture of discrete and continuum components from the measured spectra with Ge detector.

6. Conclusion

In design of a fusion reactor, secondary gamma-ray production cross section data are important. We

introduced a new method to estimate discrete and continuum secondary gamma-ray production cross sections from the measured spectra with Ge detector. The procedure is as follows :

Step 1 : Subtracting TDB and TIB components from FG spectrum.

Step 2 : Removing dominant discrete peaks from net FG spectrum.(Then we got the residual Pulse Height Spectrum of S_{CC}.)

Step 3 : Unfolding the PHS to obtain the S_{CC} .

We applied this method to secondary gamma-ray spectra measurement of vanadium with an HP-Ge detector at the D-T neutron source facility OKTAVIAN. Though our result is not in agreement with the theoretical calculation result, by means of this method we will be able to estimate separately discrete and continuum components valuable for accurate evaluation of secondary gamma-ray production cross sections.

Table 1 **Discrete γ-ray Production Cross Sections above 0.35 MeV from vanadium sample**

energy	cross section(mb)			
(keV)	125 deg.	Cal.*	S.P.Simakov	ENDF-B/VI
684	21.9±2.7	27.6		
815	3.1±1.0		19±1.6	
836	10.7±1.5	19.2	31±3	
910	42.8±5.0	66	88±6.9	
929	38.0±4.3	51.6	49±2.4	0.9
946	10.0±1.4	5.5	19±1.5	
1090	65.7±6.6	58	60±2.4	
1121	3.6±1.0	3.0	13.4±1.5	
1174	18.8±3.5	1.5	20±1.9	
1437	17.2±2.0	17.6	18±2.9	
1494	13.8±1.7	13.5	17.1±2.8	0.1
1554	15.8±1.7	16.5	30.3±1.8	
1609	184±17	163	214±8	2.6
1777	10.0±1.3		32.5±8.5	0.7
1813	46.9±4.7	47.8	68.1±4.4	0.7
2004	6.52±1.0		11.6±3.8	
2334	6.97±1.0	1.69	17.3±1.7	

* : Theoretical Calculation with SINCROS-II and DWUCKY

References :

[1] S.P. Simakov et al.
Report INDC(CCP)-413
IAEA (1998)

Table 2 **Total and continuum secondary gamma-ray production cross section**

*Except 684, 815, 1777, 2004 keV
** Energy range is between 0.35 MeV and 3.00MeV

Component	Cross Section Unit : barn				
	Exp. Value	Theoretical Cal.	Simakov et al.	Nuclear Data JENDL-3.2	Nuclear Data ENDF-B/VI
Discrete*	0.444±0.052	0.465	0.645±0.050	----------	----------
Continuum**	1.270±0.15	0.502	----------	----------	----------
Total**	1.776±0.17	0.967	----------	0.807	0.985

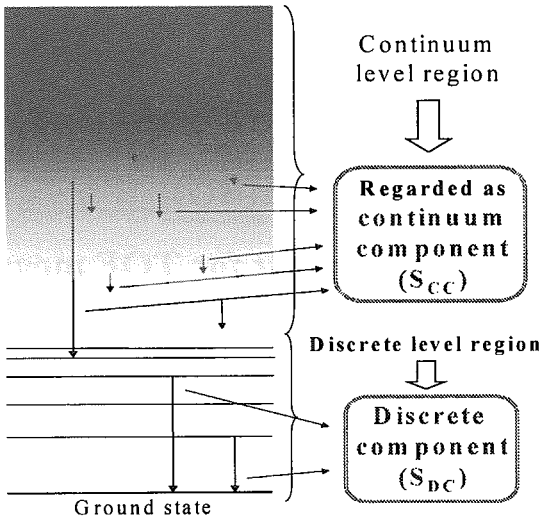

Fig. 1 **Image of secondary gamma-ray and excited levels**

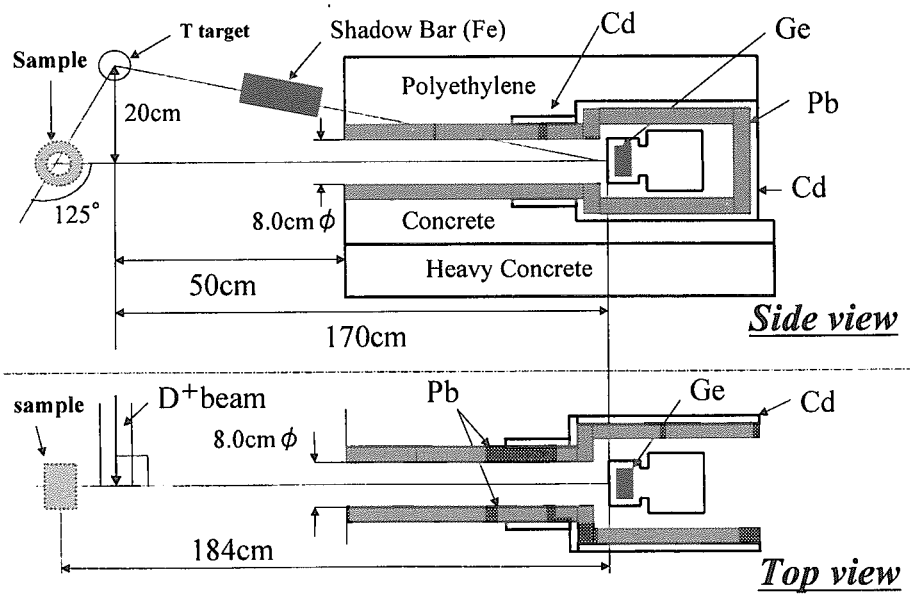

Fig.2 **Schematic Experimental Arrangement**

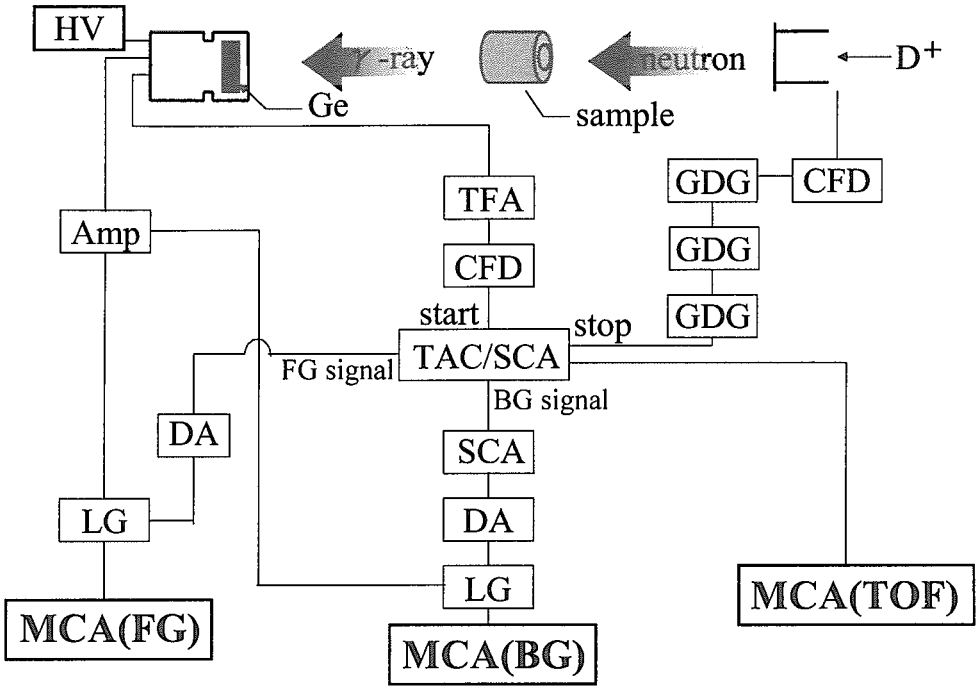

Fig. 3 Electronic circuit for TOF measurement

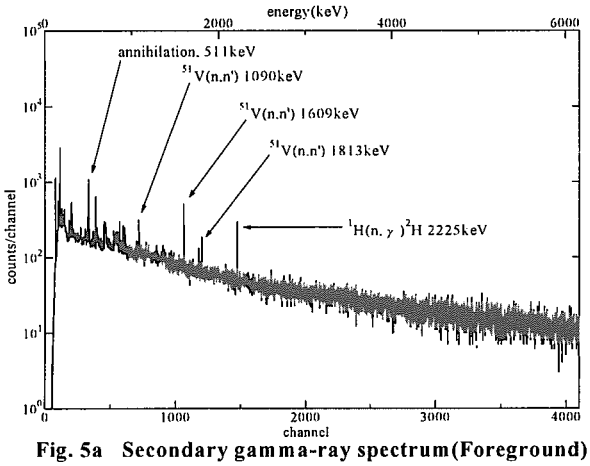

Fig. 5a Secondary gamma-ray spectrum(Foreground) of 51-V in sample-in system (at 125 deg.)

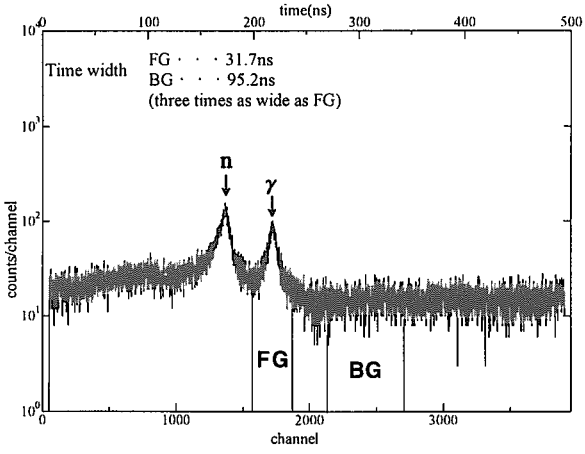

Fig. 4 TOF Spectrum for V-51 with sample-in system

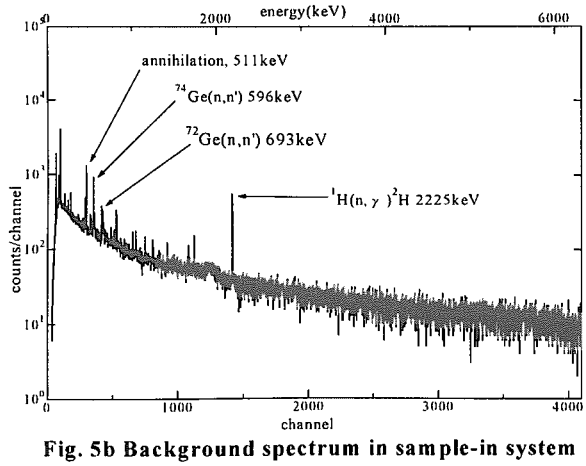

Fig. 5b Background spectrum in sample-in system

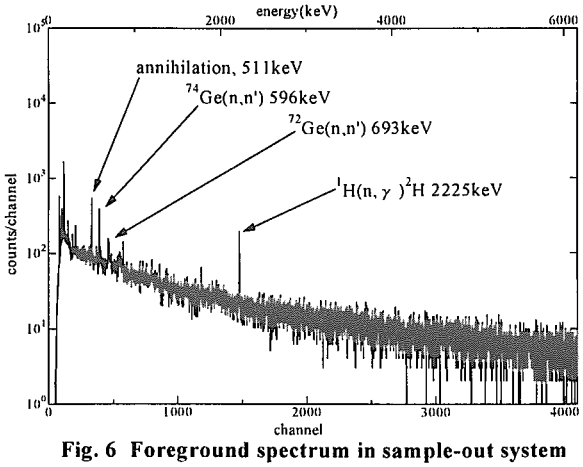

Fig. 6 Foreground spectrum in sample-out system

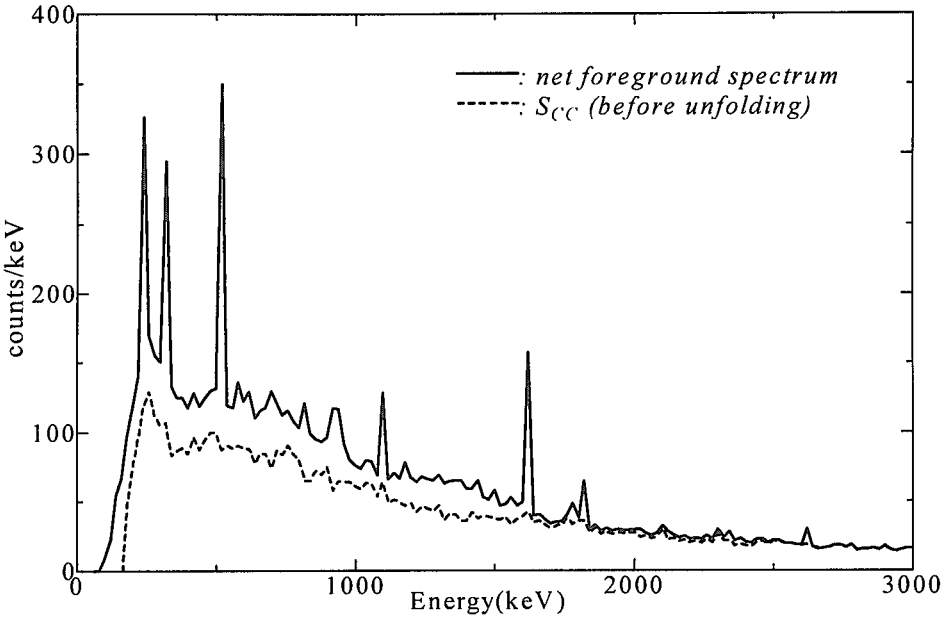

Fig. 7 Comparison of net foreground spectrum and Scc

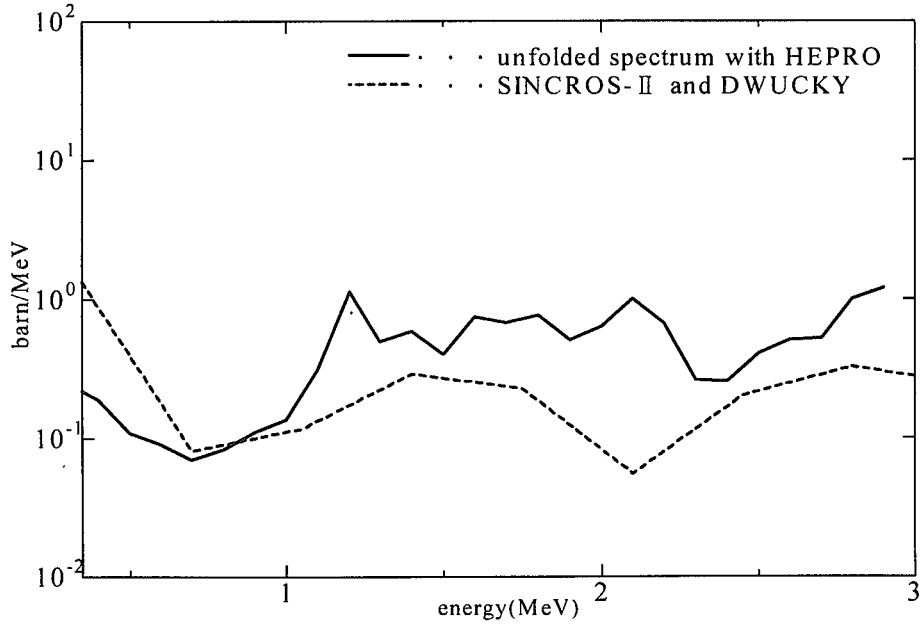

Fig. 8 Comparison of the theoretical calculation result and the unfolding result

3.13 Development of Helium Measurement System for Neutron Dosimetry

Yoshiyuki TAKAO, Masatomo MURAMASU, Shuji OZAKI,
Hirofumi SOU, and Hideki NAKASHIMA
Advanced Energy Engineering Science
Interdisciplinary Graduate School of Engineering Sciences
Kyushu University, Kasuga, Fukuoka 816-8580, Japan
e-mail: takao@aees.kyushu-u.ac.jp

Yukinori KANDA
Oita National College of Technology
1666 Maki, Oita, 870-01, Japan

A system for measurement down to 10^8 atoms of helium contained in a solid sample within the range of mass between 10mg and 1g has been developed for a neutron dosimetry system. The system has an apparatus based on ultra-high vacuum techniques, computer codes to estimate suitable parameters for the given experimental conditions and to control the sequence of data acquisition, and an appropriate routine of the operation of the system. The system apparatus is comprised basically of a gas releaser, a mass spectrometer, and a standard helium supply. Gases in a sample are extracted by evaporating it in the gas releaser and are purified by two titanium getter pumps cooled by liquid nitrogen to decrease background gases. The amount of helium is determined by analyzing the gases with the mass spectrometer in current measurement mode or pulse counting. Several sample measurements are carried out to estimate performance of this apparatus. The apparatus and the results of the performance tests are reported.

1. Introduction

The helium atoms measurement system (HAMS) was developed to measure He production cross sections for several kinds of elements in our previous work[1]. The cross sections are obtained by measuring the amount of He atoms down to 10^{10} in solids[2, 3]. The purpose of this work is to advance the lower helium measurement limit of the HAMS to less than 10^8 He atoms in a solid. The improvement is for applying this system to a new type of area monitoring system employing a He gas accumulation method. The amount of He produced in a dosimeter by neutron irradiation is measured with the absolutely calibrated mass spectrometer in the method. The amount of He is in proportion to neutron fluence at the dosimeter position and is independent of variation in neutron flux. The only He production cross section is required to obtain absolute values of neutron fluence.

Two important points should be considered to advance the lower limit of He measurements. One is to produce a high quality vacuum in the system chambers to decrease the background gas during the sample measurement. The other is to detect a very small output signal from the mass spectrometer. A pulse counting system is applied to achieve high sensitivity in helium measurements. This paper presents the detail description of architecture of the improved HAMS and several results of performance tests.

2. Apparatus

A block diagram and a photograph of the HAMS are shown in Fig.1 and 2 respectively. The HAMS is composed of three blocks, which are a gas releaser, a mass spectrometer, and a standard He supply. The measurement procedure is briefly described. A solid sample containing He is set in the furnace of the gas releaser and is evaporated. The released gases are purified with a trap of the gas releaser and then are introduced into the mass spectrometer to measure the amount of He in the sample. The mass spectrometer has a quadrupole mass spectrometer (QMS), a digital electrometer, a multichannel analyzer and a personal computer that controls the QMS and stores data from the digital

electrometer or the multichannel analyzer, and additional information. The sensitivity of the HAMS to He is calibrated by measuring standard He. The standard He is produced by using the standard He supply.

2.1. Vacuum evacuation

Vacuum vessels of the HAMS are redesigned to decrease background gases at the He measurement. Welding at the inside wall are employed to assemble their parts. The inside wall of the vessels are cleaned by emery polishing and electric polishing. The total volume of the vessels is decreased and conductance for pumping is increased. The three blocks (the gas releaser, the QMS, and the standard He supply) have individual turbo-molecular pumps to keep them at the high quality vacuum. The QMS block, especially, has tandem jointed turbo-molecular pumps and is evacuated to lower than 1.2×10^{-8} Pa. The tandem jointed pumps also pump the gas releaser. Two Ti-getter pumps cooled by liquid nitrogen are attached to the gas releaser and the QMS to trap the background gases and purify the released gas. Valves employed in this system are metal seal valves to prevent He permeation.

2.2. Gas releaser

The gas releaser (Fig.3) is composed of a furnace, a sample loader, and a trap. The furnace is a device for releasing He from the solid sample by vaporizing it. The furnace has a pair of electrodes and a shield. An evaporating boat, that is heated electrically, is located between the electrodes that are made of stainless steel 304. The material of the evaporating boat is selected from tungsten, molybdenum, tantalum and graphite and is chosen according to melting point and chemical characteristic of the sample.

2.3. Mass spectrometer

The mass spectrometer is composed of a quadrupole-type mass spectrometer (QMS), a personal computer, a digital electrometer, a multichannel analyzer, and a trap. The QMS is adjusted to be able to measure the mass from 1 to 6 in atomic mass units with the mass analyzing power of 0.025amu(10% valley).

The released gas is introduced into the QMS from the gas releaser and is then analyzed. The output current is amplified by a pulse counting type of secondary electron multiplier (gain: max.$1x10^8$) in the QMS, and is led to the digital electrometer or the multichannel analyzer. The improved HAMS operates in the current measurement mode or the pulse counting mode. The pulse counting with a multichannel analyzer is applied to measure the very small amount of He of less than 10^{10}. The computer code for these procedures controls and computes the timing for measurements. The process of producing the standard He gases are also indicated by the code when we input the operating conditions.

2.4. Standard He supply

Figure 4 shows a block diagram of the standard He supply producing the standard He which is used to calibrate the HAMS absolutely. The standard He supply comprises four vessels: the glass standard volume vessel (V1), the sub-standard vessel (V2), the inlet vessel (V3), and the dilution vessel (V4) and three absolute pressure gauges. The furnace is used as the fifth vessel to produce the standard He, so it is called V5. Standard He in the range of 1×10^9 to 5×10^{15} He atoms can be produced with dilution method.

3. Performance

Several kinds of tests were carried out to determine performance of the HAMS on helium measurement. The tests were done both in the current measurement mode ($>10^{10}$ He atoms) and in the pulse counting mode ($<10^{10}$ He atoms). The tests are as follows.

Current measurement mode

(1) Standard He gas measurement (1×10^{10} ~1×10^{13} He atoms)

(2) Measurement of chromium samples irradiated by neutron

The amount of He produced in Cr samples by neutron irradiation is measured with the improved HAMS. The measured results are compared with the calculated values with JENDL-3.2 to confirm reliability of He measurement with the improved HAMS.

Pulse counting mode

(3) Standard He gas measurement (8×10^{7} ~1×10^{10} He atoms)

(4) Background measurement of an aluminum-boron alloy sample(dummy)

Actual lower limit of helium measurement of the improved HAMS will be determined by measuring this alloy sample.

4. Conclusion

The results of standard He measurements (test 1 and 3) with a regression curve are shown in Fig.5 and 6 respectively. The curves indicate a good linearity. In the test 2, the calculated values with JENDL-3.2 (Cr(n, α)+Cr(n, nα)) are fairly agree with our measured results (Table1). These results indicate that the HAMS has sensitivity to the amount of He between 10^{8} and 10^{13} He atoms. The constituents of the measured Al-Cr alloy sample are written in Table 2. The result of the alloy measurement (test 4) is shown in Table 3. The value indicate that the background is $1.7\text{x}10^{7}$ He atoms, on actual dosimeter sample measurements. This background is low enough to measure a sample containing around 10^{8} atoms of He.

The HAMS has developed and has an analyzing power from 10^{8} to 10^{13} He. It has a possible use in neutron dosimetry from an area monitor to reactor surveillance.

References

[1] Takao Y., Kanda Y.: Rev. Sci. Instrum., **67** 198(1996).

[2] Takao Y., Kanda Y., Uenohara Y., Takahashi T., Itadani S., Iida T., Takahashi A.: J. Nucl. Sci. Technol., **34**[1], 1(1997).

[3] Takao Y., Kanda Y., Hashimoto H., Yamasaki K., Yamaguchi K., Yonemoto T., Miwa M., Etoh H., Nagae K.: J. Nucl. Sci. Technol., **34**[2], 109 (1997).

Table 1 Results of neutron irradiated Cr sample measurements.

Sample No.	The amount of produced He (He atoms)	The calculated values with JENDL-3.2 (Cr(n,α)+Cr(n,nα)) (He atoms)
Cr-5	$(1.05\pm0.08)\text{x}10^{11}$	$1.17\text{x}10^{11}$
Cr-9	$(8.70\pm0.70)\text{x}10^{10}$	$8.84\text{x}10^{10}$

Table 2 Constituents of the Al-B alloy sample.

Element	Weight (g)	Chemical purity	Melting point
B	0.065	99.8%	2092℃
Al	0.577	99.99%	660.5℃
Al-B Alloy	0.642	10.1(B Weight %)	1200℃

Table 3 Result of background measurement with the Al-B alloy sample.

The amount of He without a sample	The amount of He with Alloy sample
$3.5\text{x}10^{7}$ He atoms	$5.2\text{x}10^{7}$ He atoms

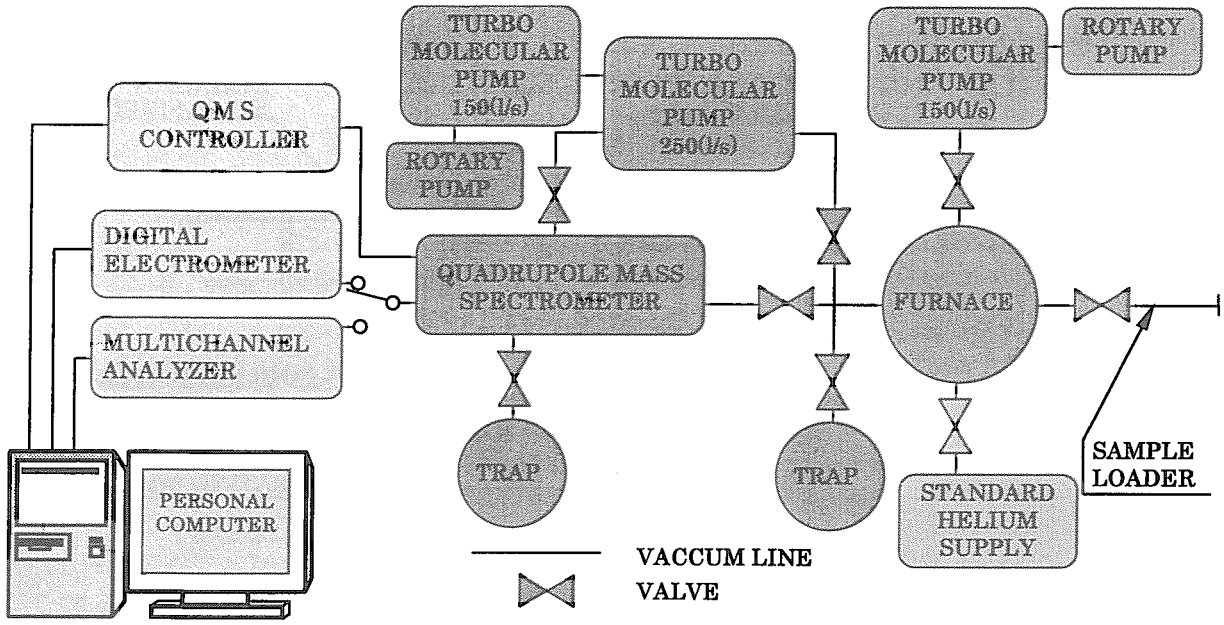

Fig.1 Block diagram of the improved Helium Atoms Measurement System.

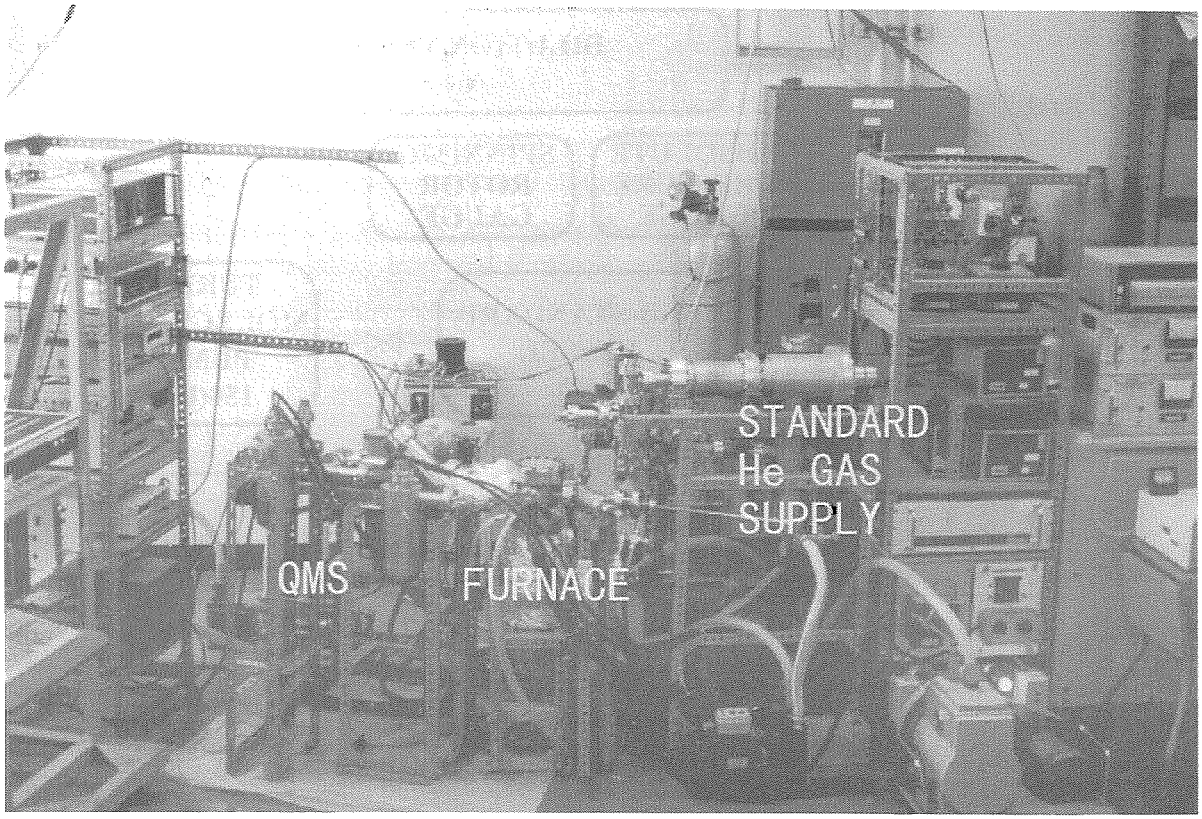

Fig.2 Photograph of the improved Helium Atoms Measurement System.

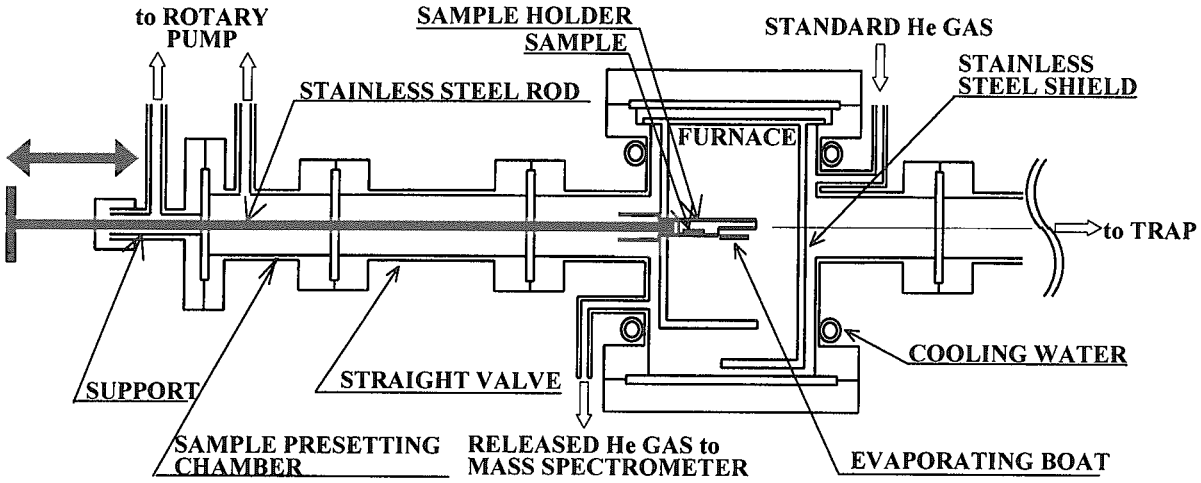

Fig.3 Schematic diagram of the gas releaser.

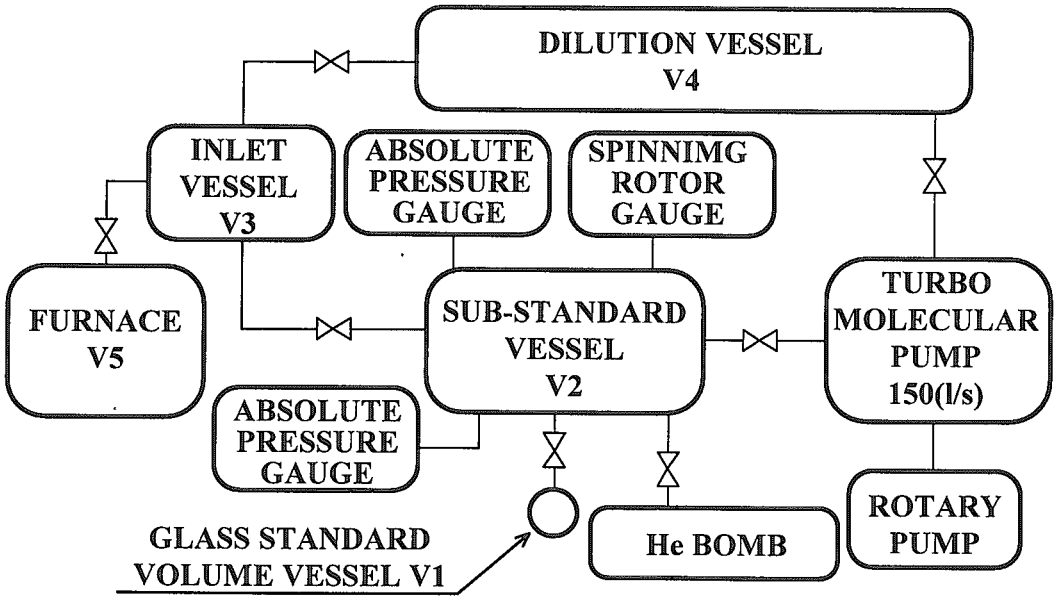

Fig.4 Block diagram of the standard He supply.

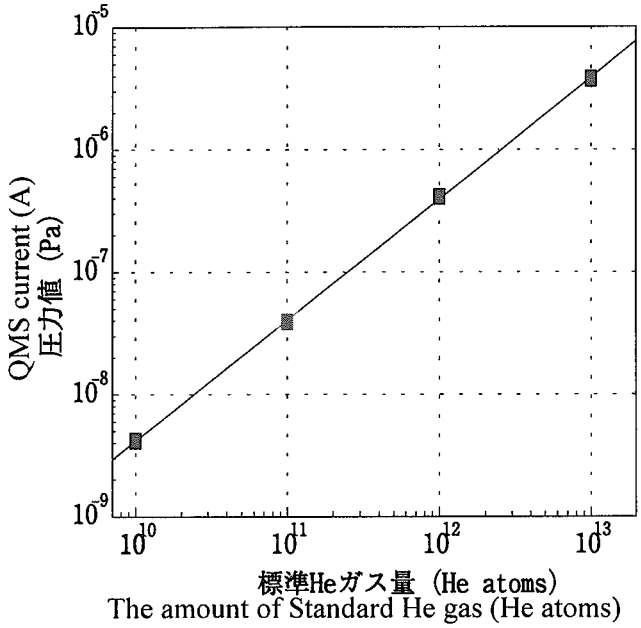

Fig.5 The results of standard He gas measurement (1×10^{10} ~1×10^{13} He atoms) in current measurement mode.

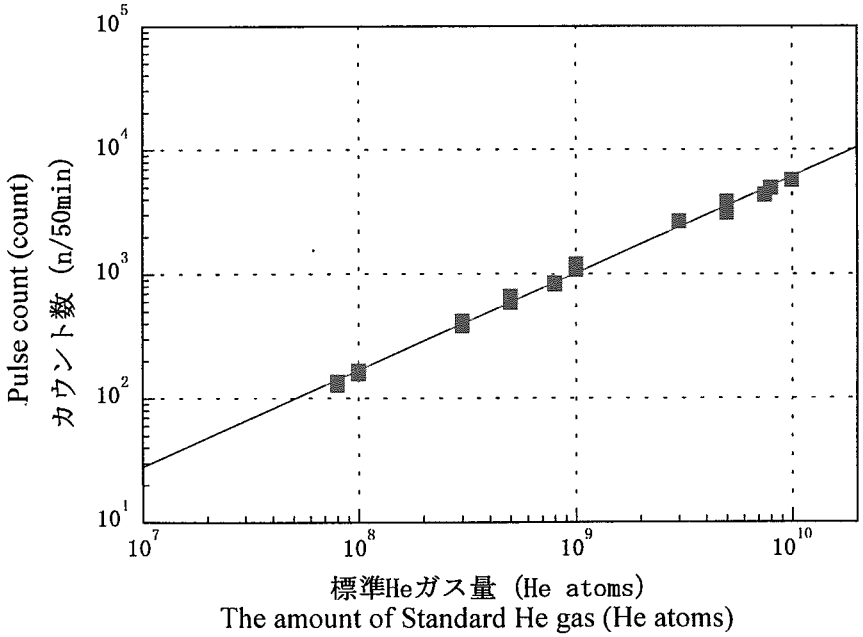

Fig.6 The results of standard He gas measurement ($8x10^{7}$~$1x10^{10}$ He atoms) in pulse counting mode.

3.14
Secondary Gamma-ray Skyshine From 14MeV Neutron Source Facility(OKTAVIAN)

-Comparison of Measurement with its Simulation-

*Ryutaro MOROTOMI *Tetsuo KONDO *Isao MURATA
*Shigeo YOSHIDA *Akito TAKAHASHI **Takayoshi YAMAMOTO
*Department of Nuclear Engineering, Osaka University **Radio Isotope Research Center, Osaka University
Yamadaoka 2-1,Suita, Osaka, 565-0871 Japan
e-mail: rmoro@newjapan.nucl.eng.osaka-u.ac.jp

Abstract

Measurement of secondary gamma-ray skyshine was performed at the Intense 14MeV Neutron Source Facility (OKTAVIAN) of Osaka University with NaI and Hp-Ge detectors. From the result of measurements, some mechanism of secondary gamma-ray skyshine from 14MeV neutron source facility was found out. The analysis of the measured result were carried out with MCNP-4B for four nuclear data files of JENDL-3.2, JENDL-F.F., FENDL-2, and ENDF/B-Ⅵ. It was confirmed that all the nuclear data are fairly reliable for calculations of secondary gamma-ray skyshine.

1. Introduction

Evaluation of skyshine effect of radiation is important for estimating dose equivalent near nuclear facilities. Especially for a neutron source facility, though it was thought that contribution of neutron was dominant on skyshine dose, recently H.W.Kugel et al.[1] at TFTR found that dose equivalent due to secondary gamma-ray skyshine was as large as that of neutron at distances below 200m from the facility. We think from this result that direct gamma-rays from the facility play an important role as the skyshine effect. This suggests that it is very important to take into account the facility building configuration in dose-equivalent evaluation around the facility. It means therefore that experimental approaches are quite important as well as their analysis.

Generally, the word 'Skyshine effect' is a phenomenon that leakage radiation from the facility shines on the ground due to scattering or nuclear reaction with oxygen and nitrogen atoms in the upper air. However in this study, the skyshine effect includes all the contributions from the facility (direct contribution), from the ground (groundshine contribution) as well as from the upper air (real skyshine) ,because in a nuclear facility design we have to evaluate the dose-equivalent containing all possible contributions. Each contribution of the skyshine effect is schematically described in Fig.1.

In the Intense 14MeV Neutron Source Facility OKTAVIAN of Osaka University, investigation of the mechanism for secondary gamma-ray skyshine has been proceeded to propose semi-empirical expression of dose equivalent for each contribution above as a function of distance from the facility. With Hp-Ge detector, high energy-resolution gamma-ray spectra were measured and used to investigate the skyshine mechanism through identification of nuclear reaction. On the other hand, with NaI detector gamma-ray spectra were measured for evaluation of dose equivalents as a function of the distance from the facility. In this paper, the abstract of the mechanism we found out[2~4] was briefly described. Preliminary calculated results of dose equivalents with MCNP-4B performed using several nuclear data files were presented.

2. Experiment

Secondary γ -rays have been measured around the OKTAVIAN facility with an large Hp-Ge (180cc) detector and an NaI(Tl) scintillation detector (5 inch ϕ by 5 inch long).[4] The intensity of the neutron source is

about 10^9 neutrons/sec. Measurements were done at 24m, 43m, 100m, and 150m from the facility for NaI, while 31m, 55m, 88m, and 165m for Hp-Ge detector. In this study, to measure each contribution in Fig.1, we used bare-detector (total contribution) and shielded detector (real skyshine contribution and groundshine contribution). Every measurement was performed at a point which can directly view the facility. To measure 'real skyshine contribution' and 'groundshine contribution, the detectors were shielded with some lead block and 1mm-thick cadmium sheet as described in Figs.2 and 3. The lead block was employed to eliminate gamma-rays which come from directions we don't need. The cadmium sheet was used to suppress neutron capture reaction in the lead shield.

To evaluate the dose equivalent originating from the skyshine gamma-ray, we performed unfolding of the spectra measured with the NaI detector. The response function of the detector was calculated with the Monte Carlo method. Unfolding code FERDO was used to estimate the gamma-ray spectra at the detector. The dose equivalent was obtained with the measured gamma-ray spectra and the flux-to-dose conversion factor.

3. Results and discussion

Figure 4 shows the obtained spectra measured with the Hp-Ge detector. All the foreground(on-beam) spectra (①,②and③in the figure) are distinctly different from the background(off-beam) spectrum (④in the figure) in high energy region above 3 MeV. Many discrete gamma-ray peaks were observed in the 'total contribution'. Also in the 'groundshine contribution', discrete peaks of hydrogen and silicon capture gamma-rays were observed. However in the 'real skyshine contribution', there is no discrete peaks in high energy region. These spectra enabled us to propose some mechanism of secondary gamma-ray skyshine as shown in Fig.5. As for the 'real skyshine' spectrum, Compton scattered gamma-rays produced in the air are dominant in the 'Real skyshine contribution', because the reaction cross section of $^{16}O(n,\gamma)$ and $^{14}N(n,\gamma)$ for thermal neutrons are exceptionally small as shown in Table 1. Consequently, significant peaks were not observed. Also in the 'Groundshine contribution', Compton scattered gamma-rays generated in soil and discrete secondary gamma-rays produced by (n,γ) reactions of hydrogen and silicone existing in soil are dominant. Almost all discrete peaks in the total contribution are generated in the shielding wall of the facility, because few peaks exist in the real skyshine and groundshine spectra. Their nuclear reactions were identified by ascertaining the emitted gamma-ray energies. The result is shown in Table 1 and Fig.4. It is confirmed that all the nuclides corresponding to the nuclear reactions are contained in the shield wall, and gamma-ray produced with (n,γ) reactions induced by slowing down neutrons in the wall are dominant.

Dose equivalents around the facility obtained by the NaI detector are shown in Fig.6 together with the calculation. The calculation was performed with MCNP-4B assuming that the shape of the OKTAVIAN facility is a co-axial cylinder as shown in Fig.7. The ring detector was employed to evaluate the gamma-ray spectra considering the statistical accuracy. The measured dose equivalents were in good agreement with the calculated values using JENDL-3.2, JENDL-F.F., FENDL-2, and ENDF/B-Ⅵ. The calculated values with ENDF/B-Ⅵ and FENDL-2 show a slightly smaller than other nuclear data. However, the nuclear data are fairly reliable for calculations of secondary gamma-ray skyshine. Fig.8 shows the energy differential dose equivalent at 60m from the facility calculated with MCNP-4B using the nuclear data of JENDL-3.2, JENDL-F.F., FENDL-2, and ENDF/B-Ⅵ. The spectrum calculated with ENDF/B-Ⅵ has larger discrete peaks than the results by other nuclear data, because the secondary gamma-ray spectrum in ENDF/B-Ⅵ includes some significant discrete peaks. The spectrum for ENDF/B-Ⅵ in Fig.8 shows lower than the others in high energy region. This tendency is observed in all the calculated cases for distances of 40m to 200m. We think that this is one of the reason why the calculated dose equivalent spectrum using ENDF/B-Ⅵ shows smaller than others.

The 'n-value' in a function $1/r^n$ which is approximately evaluated as an attenuation curve of gamma-ray skyshine, where r is the distance from the facility. This equation is available within several hundreds meters from the facility.[3] In the present study, using the integral counts above 3MeV in the Hp-Ge spectra for several distances from the facility, the 'n-values' are evaluated for 'total', 'real skyshine', and

'groundshine' contributions. Also MCNP-4B calculations were carried out to obtain 'n-values' for JENDL-3.2. The results are shown in Table 2. The 'n-value' of 'Real skyshine' contribution is slightly smaller than those of 'Total contribution' and 'Groundshine contribution'. Table 2 shows an excellent agreement between the experimental and calculated 'n-values'. Consequently, the dose equivalents decay on the attenuation curve $1/r^n$ where n=1.6～2.1. These data are approximately interpreted as decay phenomenon of a point source; n=2. It is thought that the reason why the 'n-value' of real skyshine is lower than 2 is that the atmosphere, i.e., gamma-ray source region in which Compton scattering occurs becomes a volume source.

4. Conclusion

Measurements of secondary gamma-ray skyshine with NaI and Hp-Ge detectors had been carried out around the OKTAVIAN facility of Osaka University. From the result of measurements with Hp-Ge detector, the on-beam spectrum had a structure distinctly different from the off-beam spectrum above 3MeV. The mechanism of secondary gamma-ray skyshine was discussed with three measurements including real skyshine, groundshine, and total contributions. It was found that the contribution of direct gamma-rays from the facility was large and important in dose equivalent evaluation.

Moreover as for n-value in the attenuation curve ($1/r^n$) of dose equivalent, an excellent agreement was obtained between the experiment and calculation. It was found that all the nuclear data used for the analysis are reliable for calculations of secondary gamma-ray skyshine. Also dose equivalents around the facility were measured with NaI detector. The analysis was carried out using MCNP-4B with JENDL-3.2,JENDL-F.F.,FENDL-2,ENDF/B-Ⅵ. As a result, the measured dose equivalents were in good agreement with the calculated values.

In the next step, it is planning to carry out experiments at YAYOI Reactor (fast neutron source of Univ. of Tokyo) and UTR-KINKI (thermal neutron source of Kinki Univ.), in order to study the relation between initial neutron energy and decrease of dose equivalent as a function of distance from the facility.

Acknowledgement

The authors wish to acknowledge H.Sugimoto and J.Datemichi for their excellent continuous operation of OKTAVIAN.

References

[1] Kugel H.W et al. :"Measurements of tokamak fusion test reactor D-T radiation shielding efficiency" Fusion Engineering and Design 28 (1995) 534-544

[2] Yoshida S et al. :"Measurement of Secondary Gamma-ray Skyshine from Intense 14MeV Neutron Source Facility with Hp-Ge detector" Ploc. Int. Conf. on Nucl. Data for Sci. and Technol. Trieste, 1338 (1997)

[3] Murata I et al. :"Mechanism of secondary gamma-ray skyshine from Intense 14MeV Neutron Source Facility with Hp-Ge detector," Fusion Technol., 34,997(1998)

[4] Yoshida S et al. :"Measurement of Secondary Gamma-ray Skyshine and Groundshine from Intense 14MeV Neutron Source Facility", Proc, 9th Int. Conf. Radiation Shielding (1999)to be appeared

Table 1 Reaction cross section of main nuclides existing in and around the facility

Nuclides	Reaction cross section		Total contribution	Real skyshine	Groundshine
	(n,γ)	(n,n'γ)			
H	0.29	-	Observed	Not observed	Observed
N-14	6.60E-02	0.4	Observed	Not observed	Not observed
O-16	1.70E-04	0.51	Observed	Not observed	Not observed
Si-nat	0.15	0.43	Observed	Not observed	Observed
Ca-nat	0.39	0.27	Not observed	Not observed	Not observed
Al-27	0.2	0.43	Not observed	Not observed	Not observed
Fe-56	2.24	0.73	Observed	Not observed	Not observed
Cl-nat	29.4	0.35	Observed	Not observed	Not observed

Table 2 Comparison of 'n-values' in a gamma-ray attenuation function $1/r^n$ calculated with MCNP-4B and the measured results with Hp-Ge detector

	Total contribution	Real skyshine contribution	Groubdshine contribution
Experiment	2.1 ± 0.3	1.6 ± 0.2	(2.0 ± 0.5)
Calculation	1.97 ± 0.02	1.78 ± 0.09	2.1 ± 0.2

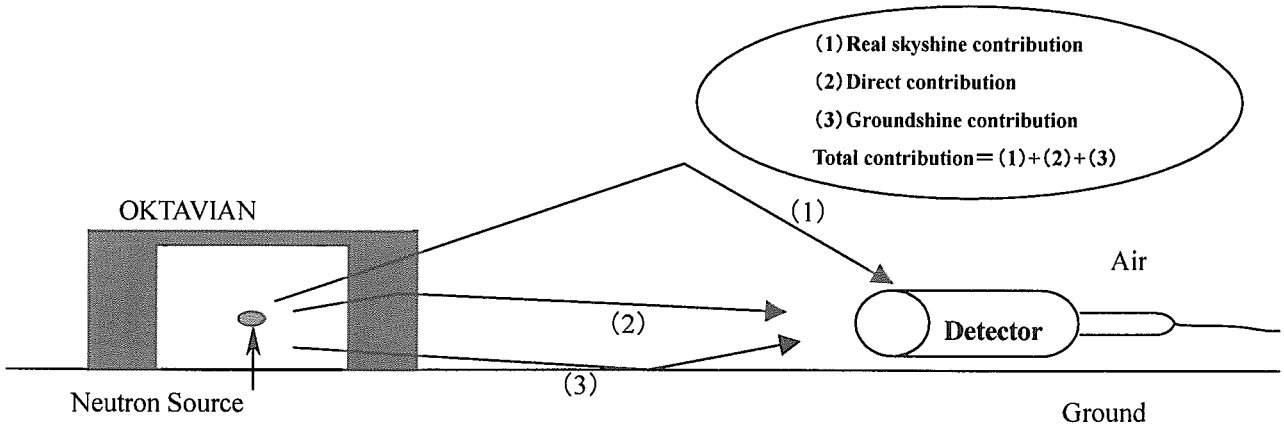

Fig.1 Schematic description of secondary gamma-ray skyshine effect

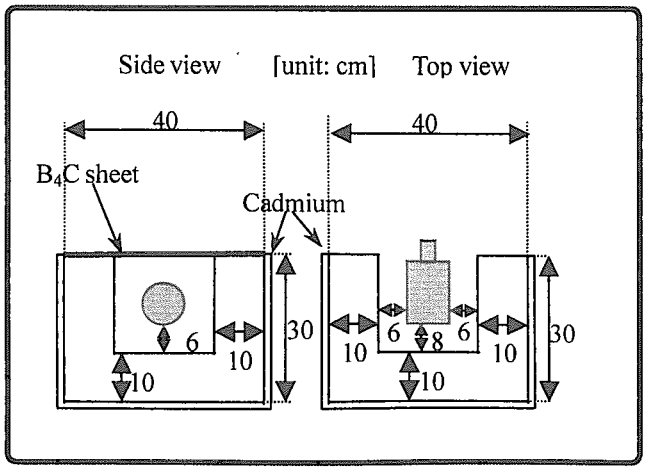

Fig.2 Ge detector arrangement for measurement of 'Real skyshine'

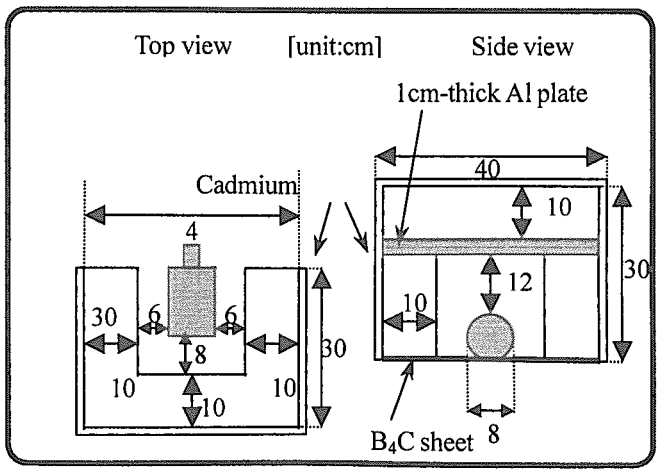

Fig.3 Ge detector arrangement for measurement of 'Groundshine'

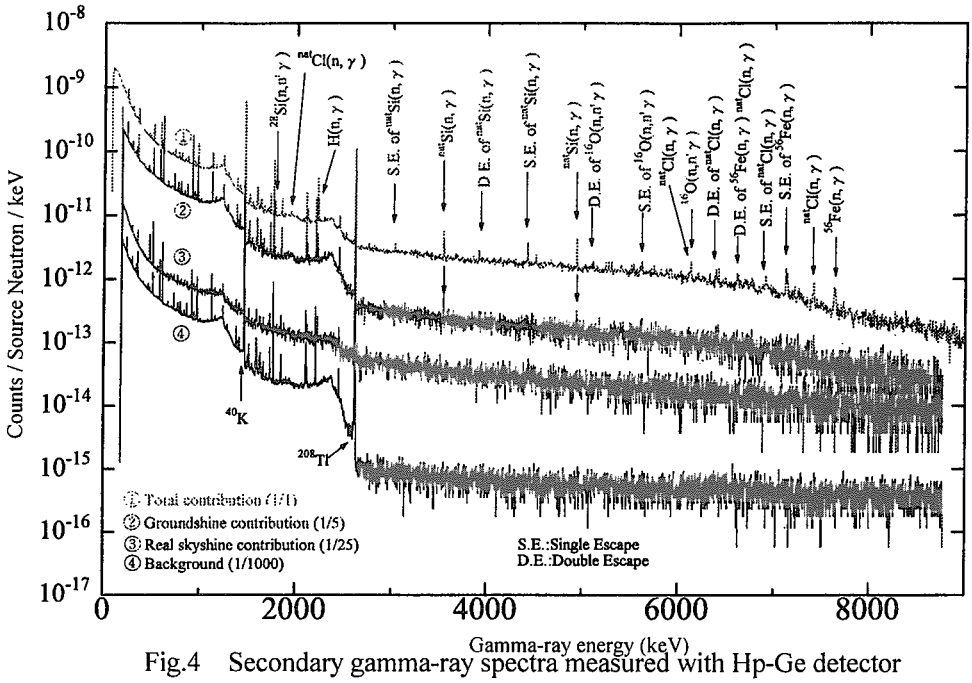

Fig.4 Secondary gamma-ray spectra measured with Hp-Ge detector at distance of 50m from the facility

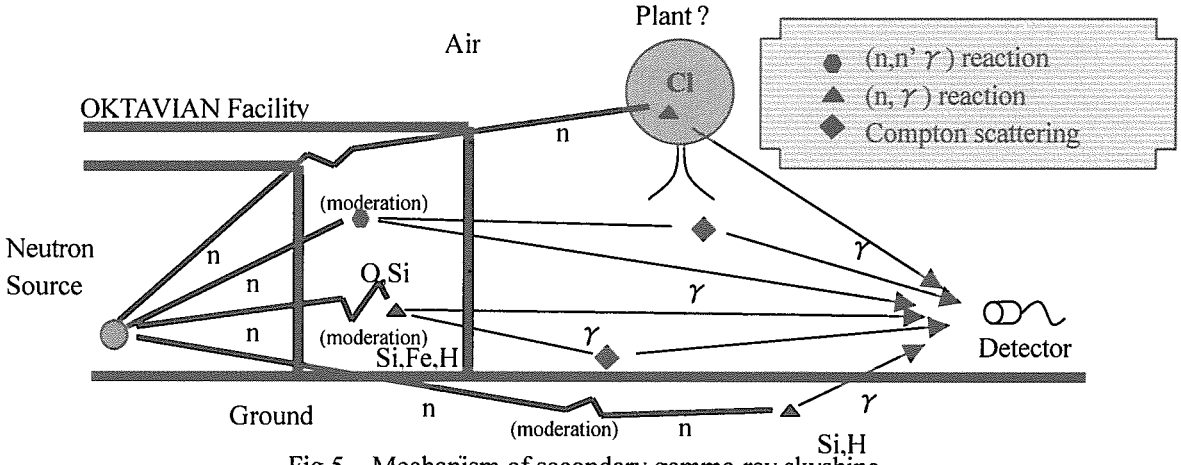

Fig.5 Mechanism of secondary gamma-ray skyshine

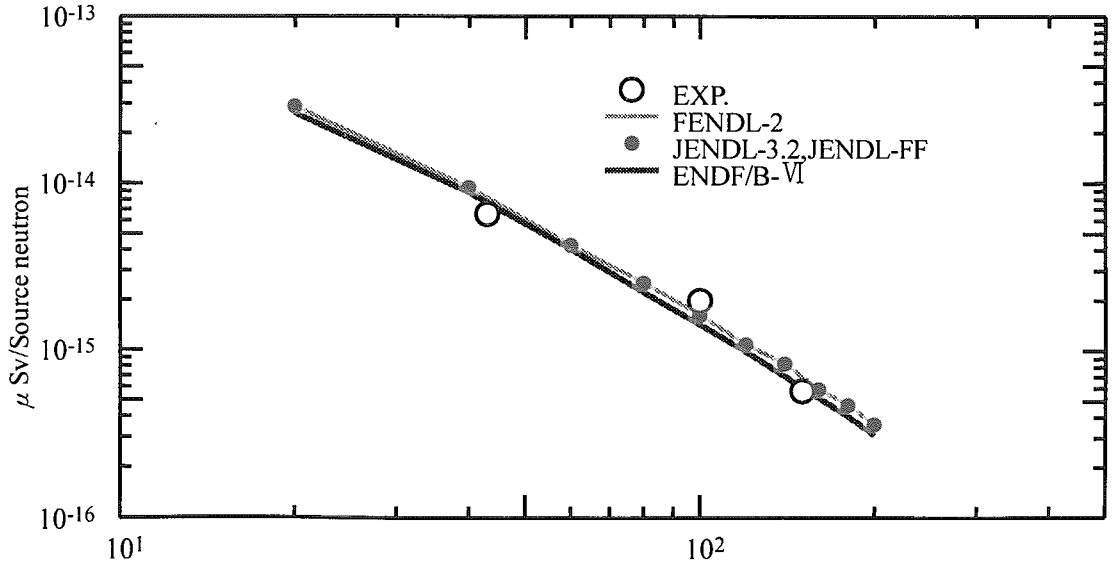

Fig.6 Comparison of measured dose equivalent with NaI detector and the calculations with MCNP-4B

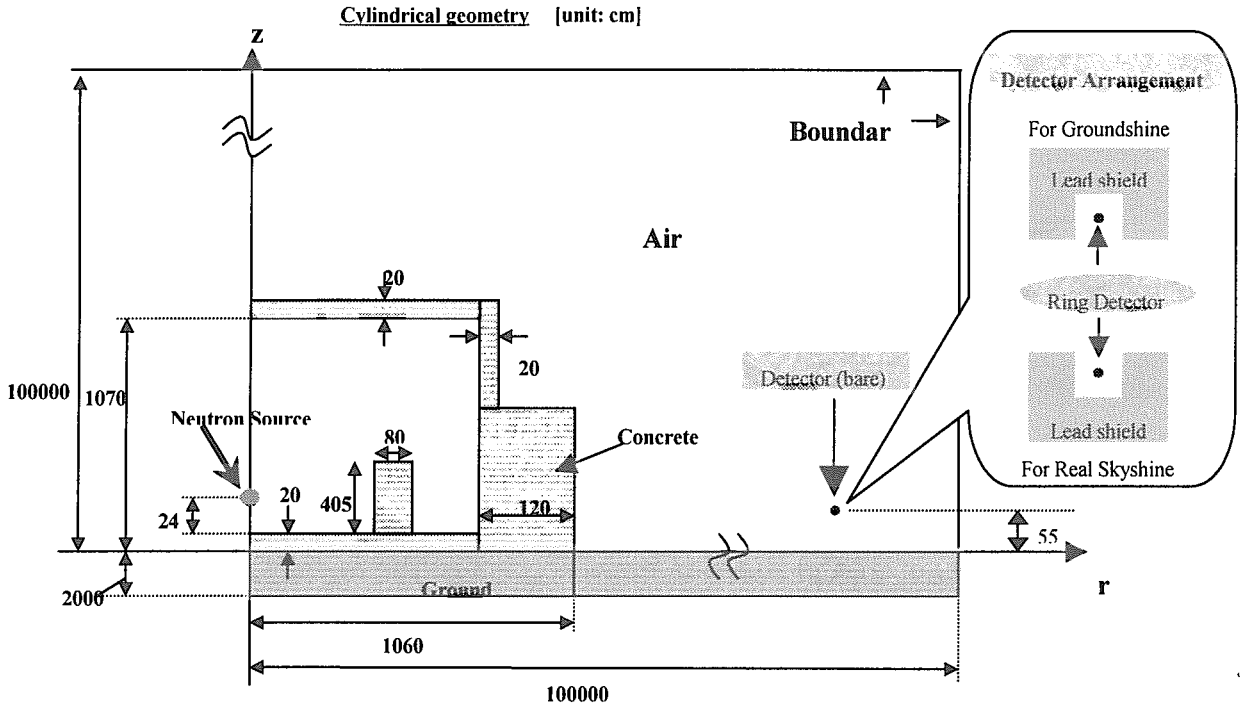

Fig.7 Two-dimensional model employed for MCNP calculation

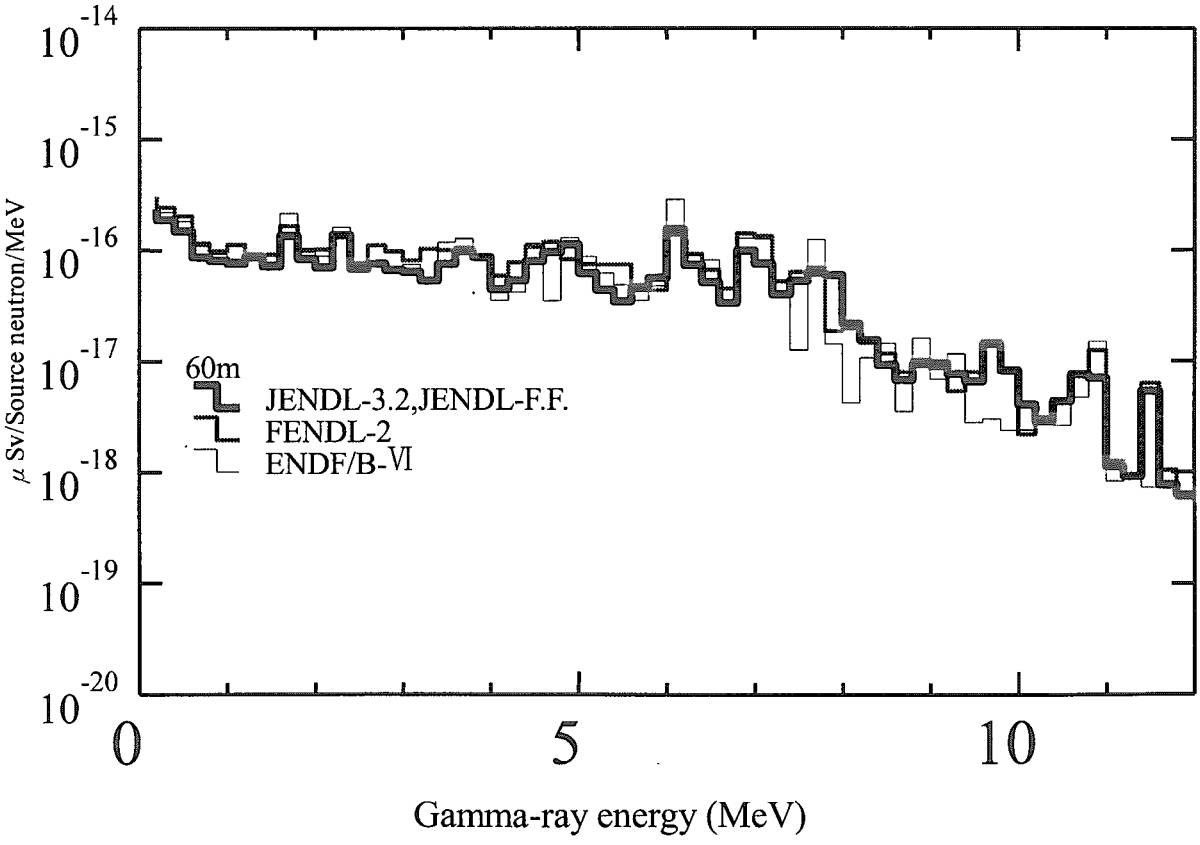

Fig.8 Calculated energy differential dose equivalent with MCNP-4B

3.15 Systematics of (n,n'p) reaction cross sections by 14 MeV Neutron

H. Sakane*, M. Shibata*, K. Kawade*, Y. Kasugai** and Y. Ikeda**
*Energy Engineering and Science, Nagoya University,
Furo-cho, Chikusa-ku, Nagoya 464-8603
** Japan Atomic Energy Research Institute
Tokai-mura, Naka-gun, Ibaraki-ken 319-1195
e-mail: h986304d@mbox.media.nagoya-u.ac.jp

Systematics of (n,n'p) reaction cross section in the energy range between 13.4 and 14.9 MeV were studied on the basis of experimental data measured by the Nagoya and Fusion Neutronics Source groups. Our group have been measured 31 (n,n'p) reaction cross section. In present work, 8 (n,n'p) cross sections were newly measured in the neutron energy range between 13.4 and 14.9 MeV by using a high efficiency well-type HPGe detector. The measured isotopes were ^{113}Cd, ^{123}Te, ^{148}Nd, ^{160}Gd, ^{170}Er, ^{174}Yb, ^{184}W and ^{186}W. Preliminary empirical formulae of a cross section at 14.7 MeV based on 37 data were deduced as a function (N-Z+2)/A, where N, Z and A are neutron, proton and mass numbers of the target nuclei. Comparing the experimental data with the calculated value, we estimated that the accuracy of the proposed empirical formulae was ±50 %.

1 Introduction

Neutron activation cross section data around 14 MeV are important from the view point of the fusion reactor technology in terms of estimations of radiation damage, nuclear transmutations, induced activity and so on. In the view point of gas production, we need to obtain the (n,p), (n,α) and (n,n'p) reaction cross section data. Systematic cross section measurement programs have been performed by using the d-T neutron generator (the Fusion Neutronics Source: FNS) at Japan Atomic Energy Research Institute (JAERI). The FNS group measured 199 cross section data. A group of Nagoya University has also measured 74 activation cross section data, mostly for short-lived products ($T_{1/2}$ <20min) by using rotating T-target (OKTAVIAN) at Osaka University. In addition of data taking, we are about to propose empirical formulae which can reproduced partial excitation function of cross section around 14 MeV. Recently the systematics was proposed

on the basis of 65 cross section data of (n,p) and 33 data of (n,α) reaction[1),2)]. The systematics for (n,p) and (n,α) reaction predicts well the excitation functions around 14 MeV within ± 20 % and 30 %, respectively. To construct the systematics for (n,n'p) reaction, we needs to obtain more cross section data for (n,n'p) reaction. By using a high efficiency well-type HPGe detector, (n,n'p) cross section in the region of μbarn could be measured. As shown in Fig. 1, the cross section at 14 MeV as a function of (N-Z)/A was plotted[3)], where N, Z, A, Sn and Sp are neutron, proton, mass numbers, neutron separation energy and proton separation energy of the target nuclei. However the data fall on two curves, one for nuclei with Sn<Sp and the other for nuclei with Sn>Sp. We tried to propose the single empirical formulae as a function of a simple parameter.

2 Experiment

Experiments were carried out at the FNS (Fusion Neutronics Source) facility. A pneumatic sample transport system was used for the irradiation of samples as shown in Fig. 2. The angles of the irradiation position to the d^+ beam were 0, 45, 70, 95, 120 and 155 degree, which covered the neutron energies from 14.9 to 13.4 MeV. The distance between the D-T neutron target and the irradiation position was 10 cm. The average neutron flux at the irradiation position was about 1×10^8 n/cm^2-s. The effective incident neutron energy at the irradiation position was determined by the ratio of the ^{90}Zr(n,2n)^{89}Zr and ^{93}Nb(n,2n)^{92m}Nb reaction rates. The induced activities were measured with a well-type HPGe detector[4)]. The efficiency in the bottom of the detector is 6-7 times larger than those at the surface position of the detector as shown in Fig. 3. Corrections were made for time fluctuation of neutron flux, contribution of low energy neutron below 10 MeV, thickness of samples, self-absorption of the gamma ray and sum-peak effect of the gamma ray. The details of each correction are described elsewhere[1)]. The total errors (δ_t) were described by combining the experimental errors (δ_e) and the errors of nuclear data (δ_r) in quadratic: $\delta_t^2=\delta_e^2+\delta_r^2$.

Measured reactions and decay parameters are listed in Table 1.

3 Experimental Results

Numerical data of the present cross section were given in Table 2. Present cross section data were shown in Fig. 4 together with the previous data and the evaluation data of JENDL 3.2 and ENDF/B-VI. The cross section data of 6 reactions were obtained around 14 MeV for the first time. The cross section data of ^{186}W(n,np)^{185}Ta reported by Kasugai et. al., which was measured by using the

rotating target (OKTAVIAN) at Osaka University, were good agreement with present result.

4 Preliminary systematics of (n,n'p) reaction cross section

To study the systematics of the cross sections of (n,n'p) reaction at 14.7 MeV, our cross section data in present work and the data in ref. (7) were used. In Fig. 5, the cross section data at 14.7 MeV were plotted as a function of (N-Z+2)/A. It is evident that the cross sections depend on the (N-Z)/A. The systematics is expressed by the formulae given by

$$\sigma_{14.7}(mb) = 10500(N - Z + 2)) \times \exp\left(-68.2 \times \frac{(N - Z + 2)}{A}\right)$$

To find the overall quality of proposed empirical formulae, the distribution of the deviation which given by $R=(\sigma_{exp}-\sigma_{sys})/\sigma_{exp}$ is shown in Fig. 6. Sixty-five percent of the data are in between –0.50 and 0.50. This means that one standard deviation of the R-distribution is about 0.50. The accuracy of proposed formulae are within ±50% as a whole.

5 Conclusion

Eight cross sections of (n,n'p) reaction were measured in the energy range between 13.4 and 14.9 MeV. The measured isotopes were ^{113}Cd, ^{128}Te, ^{148}Nd, ^{160}Gd, ^{170}Er, ^{174}Yb, ^{184}W and ^{186}W. The cross section data except for ^{128}Te and ^{186}W were obtained for the first time.

Preliminary empirical formulae of cross section ($\sigma_{14.7}$) was deduced as a function of (N-Z+2)/A. The accuracy of empirical formulae was ±50%. The proposed on a relative slope formula of excitation function around 14 MeV are now in progress

Reference

1) Y.Kasugai et al.: Ann. Nucl. Energy, 23, 429 (1996)
2) Y.Kasugai et al.: Ann. Nucl. Energy, 25, 421 (1996)
3) S.M.Qaim: Nucl. Phys. A382, 255 (1982)
4) H. Sakane et al.: JAERI-Conf 99-002, 210 (1999)
5) E.Browne et al.: "Table of Radioactive Isotope" John Wiley & Sons, New York (1986)
6) R.B.Firestone et al.: "Table of isotopes 8th Edition" John Wiley & Sons, NewYork (1996)
7) Y. Ikeda et al.: JAERI 1312 (1988)

Table 1 Measured reactions and decay parameters [5),6)]

Reaction	Half-life	Gamma-ray Energy (keV)	Intensity per decay (%)	Q-value(MeV)
^{113}Cd(n,np)^{112}Ag	3.13h	617.27	43(4)	-8.92
^{128}Te(n,np)^{127}Sb	3.85d	685.7	36.6(8)	-9.58
^{148}Nd(n,np)^{147}Pr	13.4m	314.68	13.2(17)	-9.23
^{160}Gd(n,np)^{159}Eu	18.1m	67.8	19(4)	-9.18
^{170}Er(n,np)^{169}Ho	4.7m	788.4	22.0(22)	-8.60
^{174}Yb(n,np)^{173}Tm	8.24h	398.9	87.9(20)	-7.98
^{184}W(n,np)^{183}Ta	5.1d	246.06	28.0(10)	-7.70
^{186}W(n,np)^{185}Ta	49.4m	177.59	25.6(5)	-8.40

Table 2 Activation cross sections

Neutron Energy (MeV)	^{113}Cd(n,n 'p)^{112}Ag				^{128}Te(n,n 'p)^{127}Sb			
	σ(mb)	δ_t(%)	δ_e(%)	δ_r(%)	σ (mb)	δ_t(%)	δ_e(%)	δ_r(%)
14.87	1.0_2	16	12	11	0.7_2	30	30	3.6
14.64	0.5_1	25	22	11				
14.35	0.2_1	51	50	11	0.3_2	64	64	3.6

Neutron Energy (MeV)	^{148}Nd(n,np)^{147}Pr				^{160}Gd(n,np)^{159}Eu			
	σ (mb)	δ_t(%)	δ_e(%)	δ_r(%)	σ (mb)	δ_t(%)	δ_e(%)	δ_r(%)
14.87	0.20_4	21	17	13	0.3_2	60	56	21
14.64	0.16_4	26	22	13				
14.35	0.10_4	37	35	13				
14.02	0.06_3	54	52	13				

Neutron Energy (MeV)	^{170}Er(n,np)^{169}Ho				^{174}Yb(n,np)^{173}Tm			
	σ (mb)	δ_t(%)	δ_e(%)	δ_r(%)	σ (mb)	δ_t(%)	δ_e(%)	δ_r(%)
14.87	0.05_2	61	45	10	0.82_{15}	18	18	3.2
14.64					0.82_{15}	19	19	3.2
14.35					0.41_8	20	19	3.2
14.02					0.28_6	20	20	3.2
13.70					0.30_7	23	23	3.2
13.40					0.12_5	38	38	3.2

Neutron Energy (MeV)	^{184}W(n,np)^{183}Ta				^{186}W(n,np)^{185}Ta			
	σ (mb)	δ_t(%)	δ_e(%)	δ_r(%)	σ (mb)	δ_t(%)	δ_e(%)	δ_r(%)
14.87	1.3_3	21	20	4.7	0.40_6	15	15	3.6
14.64	0.8_2	30	30	4.7	0.25_4	16	16	3.6
14.35	0.4_2	45	45	4.7	0.18_4	20	20	3.6
14.02					0.05_3	50	50	3.6

* δ_e: experimental error, δ_r: nuclear data error, δ_t: total error, $\delta_t^2 = \delta_e^2 + \delta_r^2$

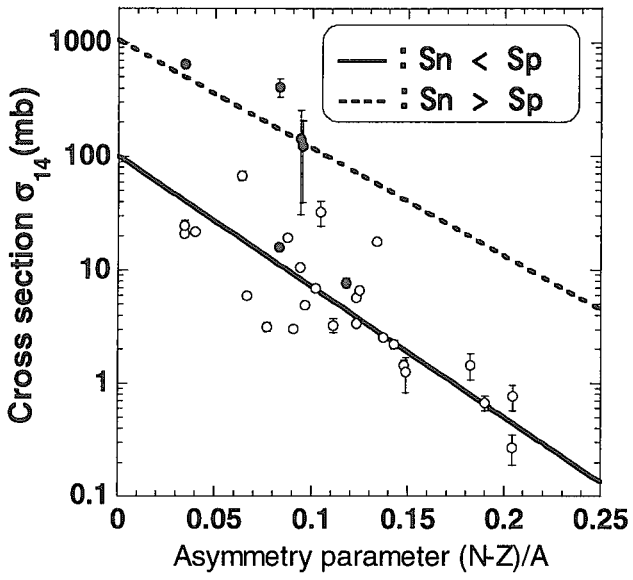

Fig.1 The cross sections σ_{14} for (n,np) reactions at 14.0 MeV as a function of asymmetry parameter (N-Z)/A. N, Z and A are neutron, proton and mass number of target nuclei.

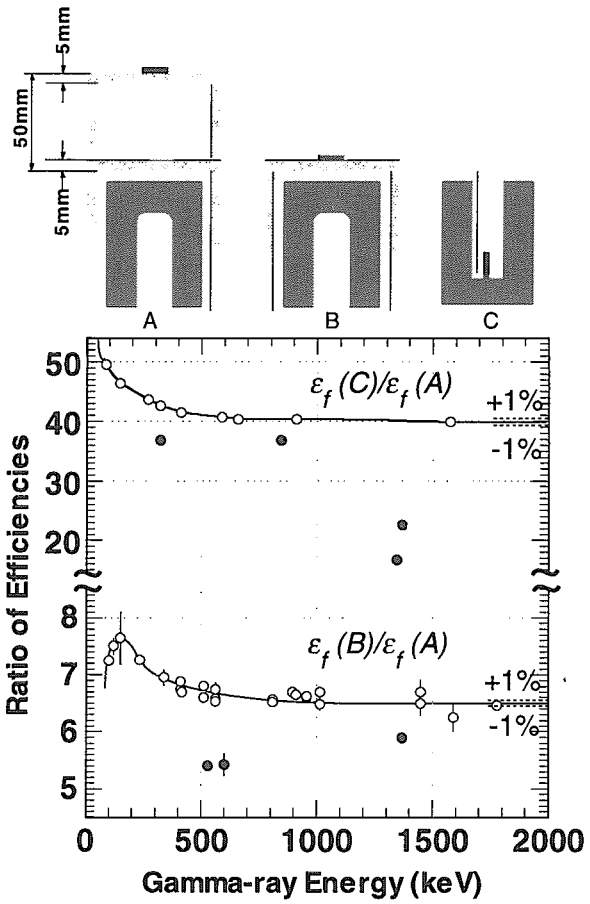

Fig. 3 Efficiency calibration method. A standard position is 5 cm for detector A. Practical positions are on the surface and in the bottom for a well type detector C. Ratio of detection efficiencies at the surface and in the bottom to that at 5 cm. Open circle show single gamma-ray emitters and closed ones show cascade gamma-ray emitters.

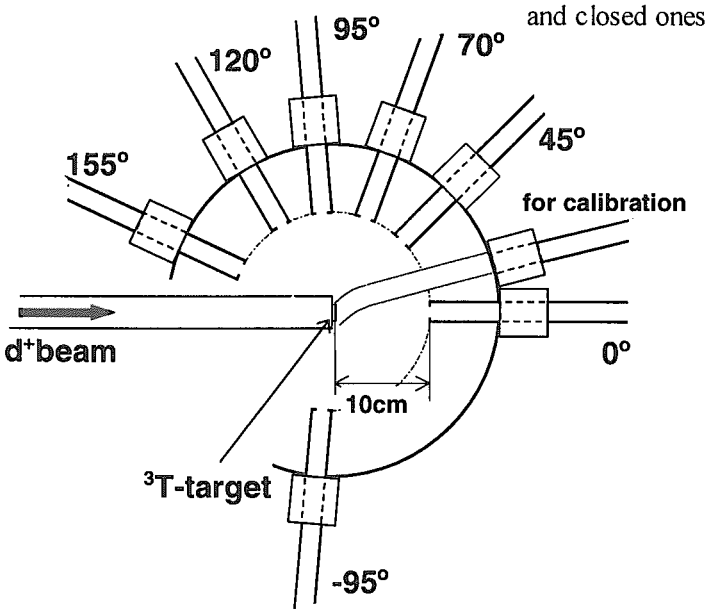

Fig. 2 Pneumatic sample transfer system.

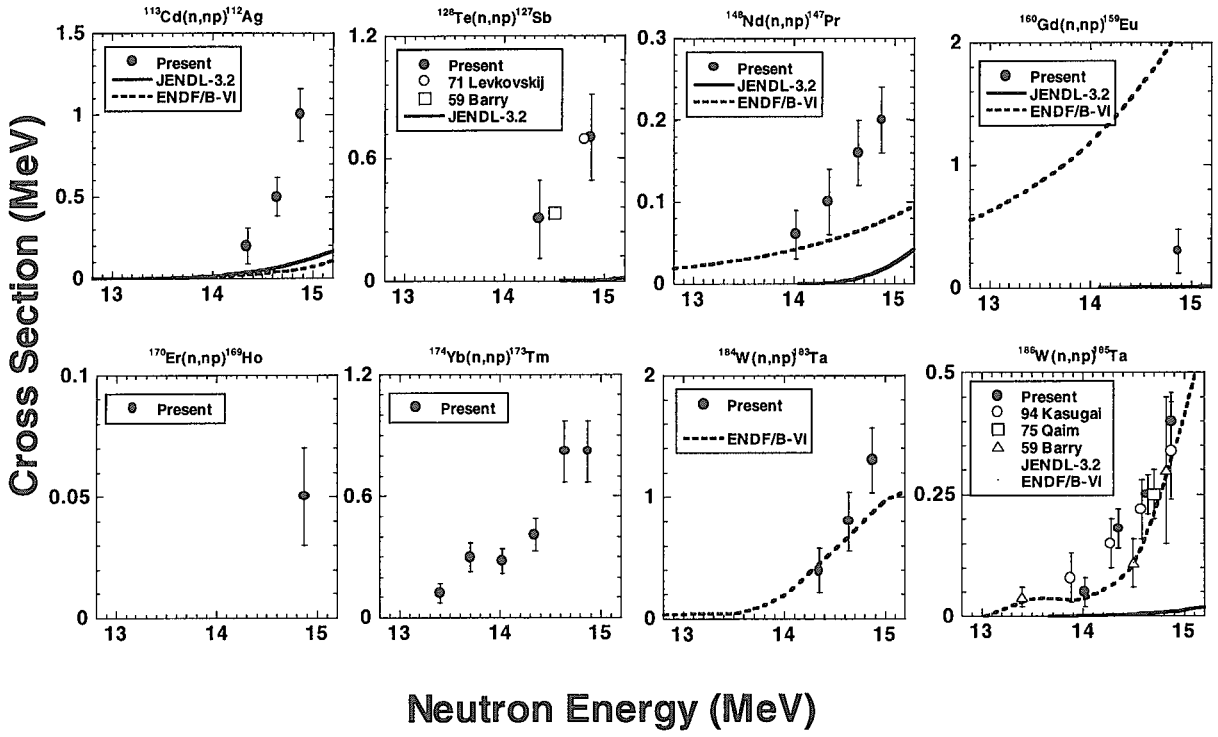

Fig. 4 Measured (n,n'p) reaction cross section data for isotopes of ^{113}Cd, ^{128}Te, ^{148}Nd, ^{160}Gd, ^{170}Er, ^{174}Yb, ^{184}W and ^{186}W.

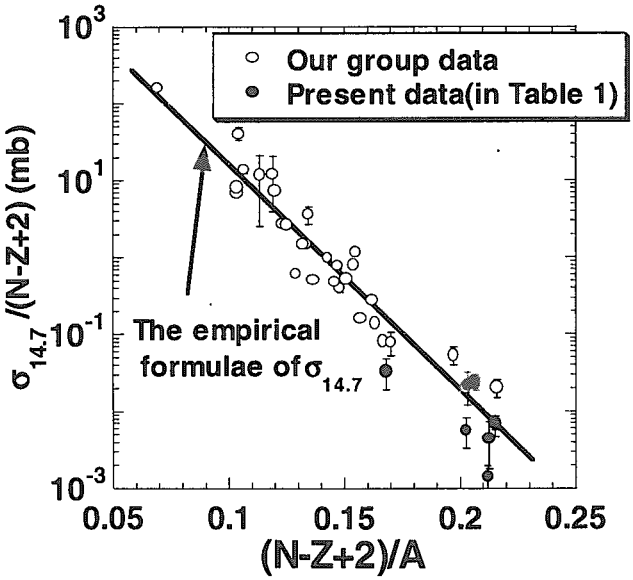

Fig. 5 The Value of $\sigma_{14.7}$/(N-Z+2) as a function of (N-Z+2)/A. The solid line shows the fitting function which leads to the empirical formula of $\sigma_{14.7}$.

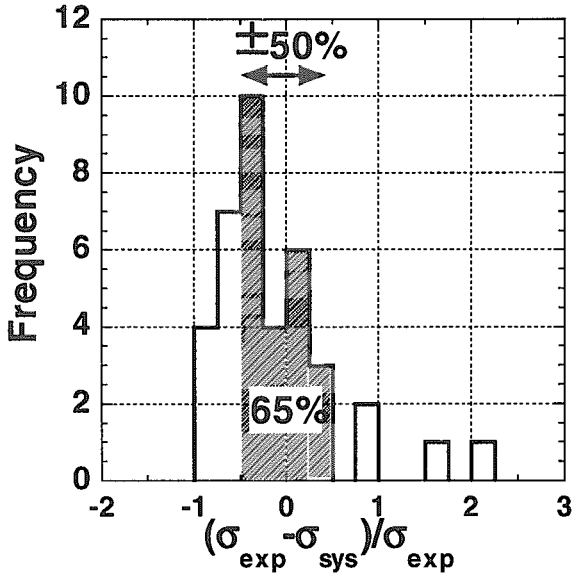

Fig. 6 The distribution of R=(σ_{exp}-σ_{sys})/σ_{exp}, where σ_{exp} is the experimental cross sections and σ_{sys} is the calculated cross section dedused by the empirical formulae in Fig. 5.

3.16 Measurement of Neutron Activation Cross Sections in the Energy Range between 2 and 7 MeV by Using a Ti-deuteron Target and a Deuteron Gas Target

T. Senga, H. Sakane*, M. Shibata*, H. Yamamoto*, K. Kawade*,
Y. Kasugai**, Y. Ikeda** and H. Takeuchi**
* Energy engineering and science, Nagoya University
** Japan Atomic Energy Research Institute
e-mail: h952521b@mbox.media.nagoya-u.ac.jp.

Using a Ti-deuteron target in the neutron energy range between 2 and 4.5 MeV and a deuteron gas target between 4.5 and 7 MeV, mono-energetic neutrons could be generated enough for activation cross section measurements. The KN-3750 Van de Grraff accelerator at Nagoya University and the Fusion Neutronics Source (FNS) at Japan Atomic Energy Research Institute (JAERI) were used. Preliminary results of activation cross sections were obtained for reactions of $^{27}Al(n,p)^{27}Mg$, $^{47}Ti(n,p)^{47}Sc$, $^{58}Ni(n,p)^{58}Co$. The evaluation data of JENDL-3.2 showed reasonable agreement with our results.

1 Introduction

Database of activation cross sections for neutron energy up to 15 MeV was required for a design of fusion reactors. Available cross section data in the neutron energy range between 13 and 15 MeV were reported. However, in the energy range between 2 and 13 MeV, the experimental data were rather scarce owning to the lack of available intense neutron source. In the energy range of 5 to 10 MeV, Qaim et al.[1] reported cross section data by using a deuterium gas target at a compact cyclotron. In order to obtain adequate neutron flux, we also used a deuteron gas target until now. However, below 5 MeV, an influence of energy straggling of the incident deuteron in deuteron gas became a serious problem. In this work, two type target systems (a Ti-deuteron target and a deuteron gas target) were combined for measurements of neutron reaction cross section.

2 Neutron Source

The range of neutron energy, which was covered by using 2 type target systems and 2 type accelerators, were shown in Fig. 1. In the 4.5 to 7 MeV energy range, as shown in Fig. 2, a deuteron gas-target system[2] was used to obtained a high neutron flux. The characteristic of a deuteron gas target was described in Ref. 2. In the 2 to 3 MeV energy range, the d-D neutrons were generated by

bombarding a Ti-d target occluded deuteron with a d^+ beam of 1.5 mA and 350 keV using FNS facility[3]. In the 3 to 4.5 MeV energy range, as shown in Fig. 3, a Ti-deuteron target system consists of a Ti board (0.5 mm-thick) and water-cooled system was used. The neutrons were generated by bombarding Ti-deuteron target with a d^+ beam of 10 μA and 0.35-1.4 MeV using the KN-3750 Van de Graff accelerator at Nagoya university. The neutron flux was measured with use of the standard reaction $^{115}In(n,n')^{115m}In$ reaction[4] ($T_{1/2}$=4.486h). In Fig. 4, as a implantation of deuteron in Ti was increased, neutron flux was increased. As a result, a typical neutron flux in the deuteron energy of 1.4 MeV was 1×10^6 n/cm^{2}s at 1 cm from the surface of Ti board. The effective neutron energies of incident neutrons at each kinematics energies of d^+ beam were determined by the reaction ratio of $^{64}Zn(n,p)^{64}Cu$[4] to that of $^{115}In(n,n')^{115m}In$[4]. Effective neutron energy was shifted about 500 keV lower than calculated value of neutron energy, due to deuteron beam size and irradiation position.

3 Cross Section Measurement

In this paper, the experiment by using Ti-D target at V. d. G. in Nagoya-University was described. Other experiments were described in Ref. 2, 5.

In Fig. 5, Samples were irradiated at 0 degree to incident deuteron beam and at 1.0cm from the surface of Ti-board. As shown in Fig. 6, irradiated samples were send back from neutron irradiation position (4) to measuring position (6) by using pneumatic transport system (5). The neutron flux at the sample position was measured with use of the $^{115}In(n,n')^{115m}In$ reaction[4]. The sample were sandwiched by two In foils of 10 mm × 10 mm and 0.5 mm in thickness, and were put in a sample cartridge as shown in Fig. 5. Each sample size was 10 mm × 10 mm and (0.2-0.5) mm in thickness. The fluctuation of neutron flux during the irradiation was monitored at interval of 10 s with a NE213 scintillator. Gamma-ray emitted from the irradiated samples were measured with coaxial-type 22% and well-type HPGe detectors. The efficiencies in the bottom of the well-type detector were 6-7 times larger than those at the surface position of coaxial-type 22% detector. Details of the corrections were described elsewhere.[5]

Measured reactions and decay parameters of the products were listed in Table 1.

4 Experimental results and Discussion

Preliminary cross section data of (n,p) reaction were obtained with a high efficiency well-type HPGe detector in an energy range between 2 and 7 MeV. Measured reactions were $^{27}Al(n,p)^{27}Mg$, $^{46}Ti(n,p)^{46}Sc$ and $^{58}Ni(n,p)^{57g+m}Co$.

Present cross section data were shown in Fig. 7 together with the evaluation data of JENDL 3.2 library. The evaluated values of JENDL 3.2 showed good agreement with our data.

5 Conclusion

Using a Ti-deuteron target in the neutron energy range between 2 and 4.5 MeV and a deuteron gas target between 4.5 and 7 MeV, mono-energetic neutrons could be generated enough for activation cross section measurements. In particular, neutron flux at 1.0 cm from the surface of target could be obtained 1×10^6 n/cm^{2}s by using Ti-deuteron implanted target.

Preliminary cross section data of ^{27}Al(n,p)^{27}Mg, ^{46}Ti(n,p)^{46}Sc and ^{58}Ni(n,p)$^{57g+m}$Co reaction were obtained. The evaluated values of JENDL 3.2 showed good agreement with our data.

Reference

1) Qaim, A. M., et al.: Nucl. Sci. Eng., 88, 143 (1984).
2) Furuta, T., et al.: JAERI-Conf 99-002, 186 (1995).
3) Nakamura, T., et al.: Proc. 4-th Symposium on Accelerator Science and Technology, RIKEN, Saitama, Japan, Nov. 24-26, 155 (1982).
4) Shibata, K., et al.: JAERI-Data/Code 98-006, (1998).
5) Kawade, K., et al.: JAERI-M 90-171 (1990).

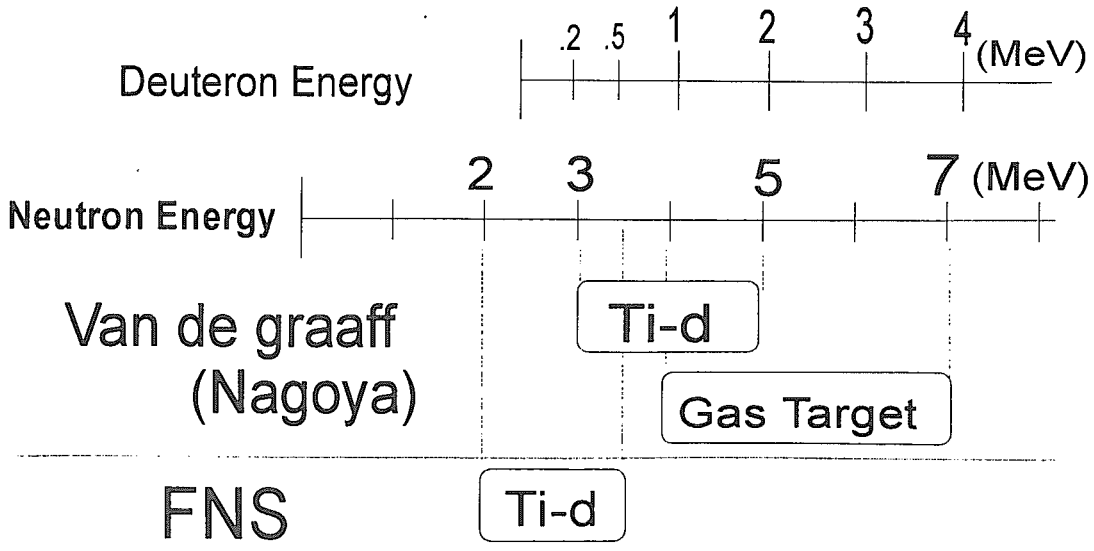

Fig. 1 A correlation between neutron energy range and neutron generator.

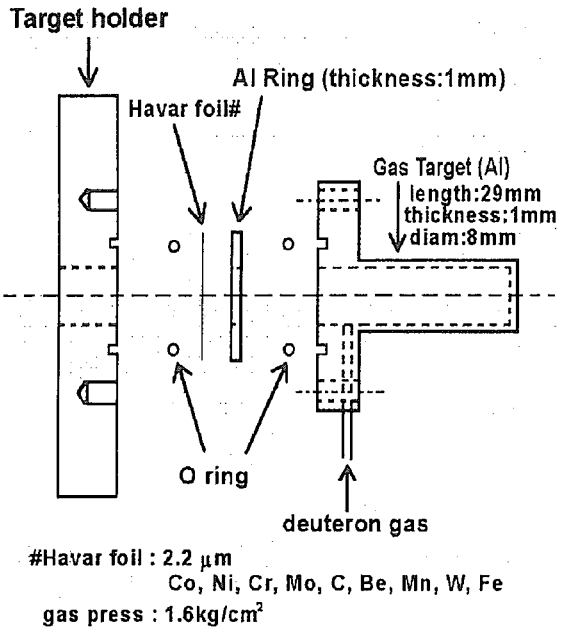

Fig.2 cross sectional view of deuteron gas target assembly.

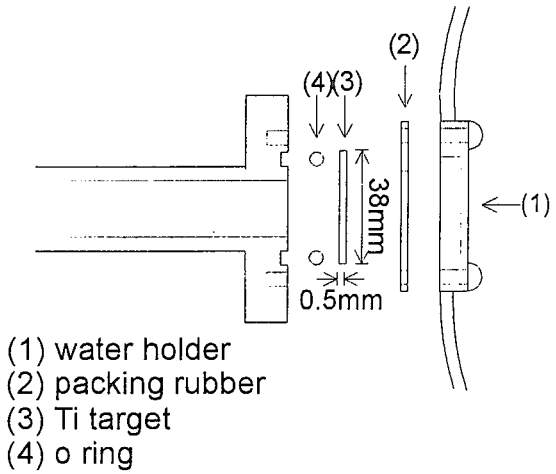

Fig.3 cross sectional view of Ti-d target assembly.

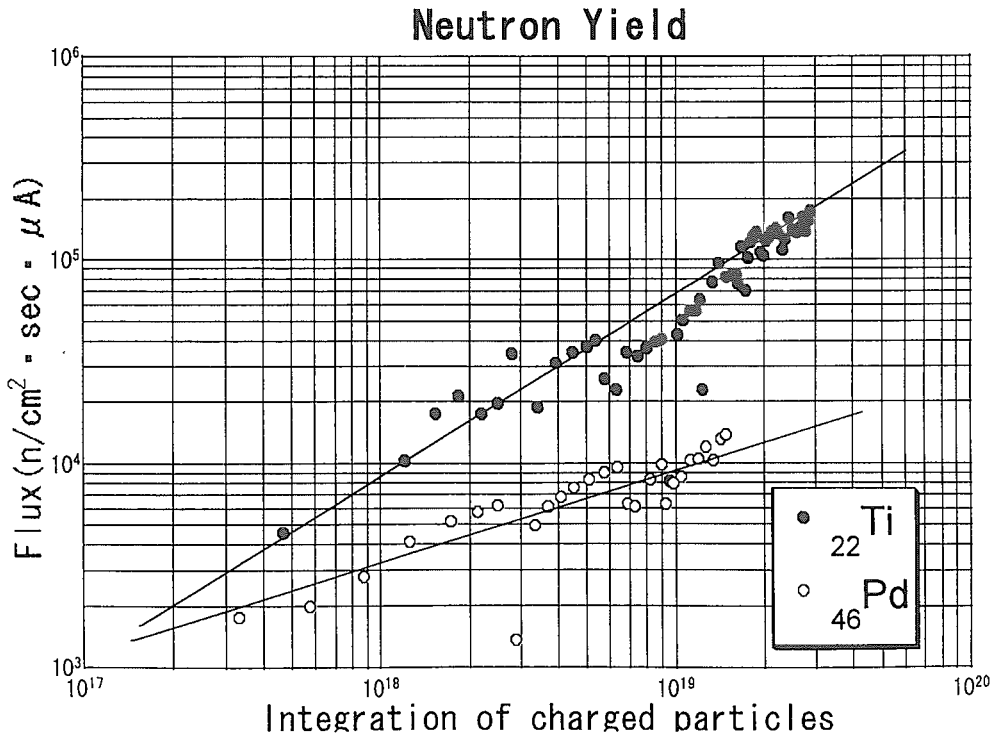

Fig.4 A correlation between integration of charged particles and neutron flux.

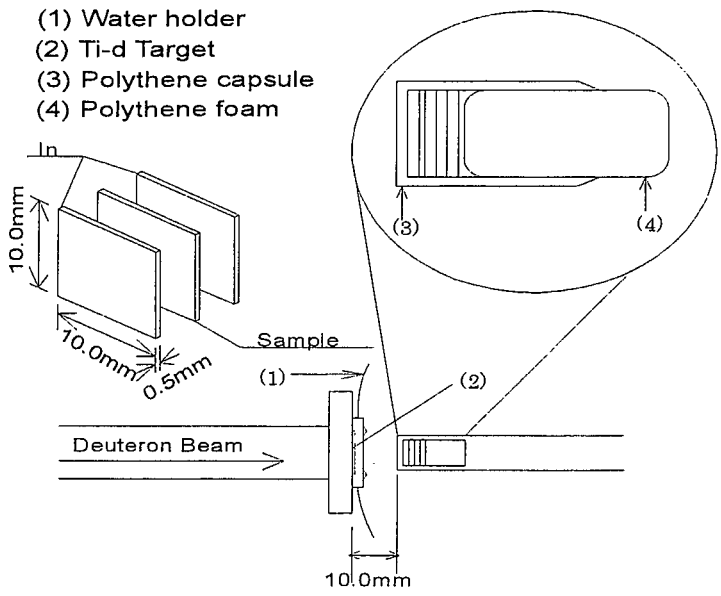

Fig.5 Pneumatic sample transport system.

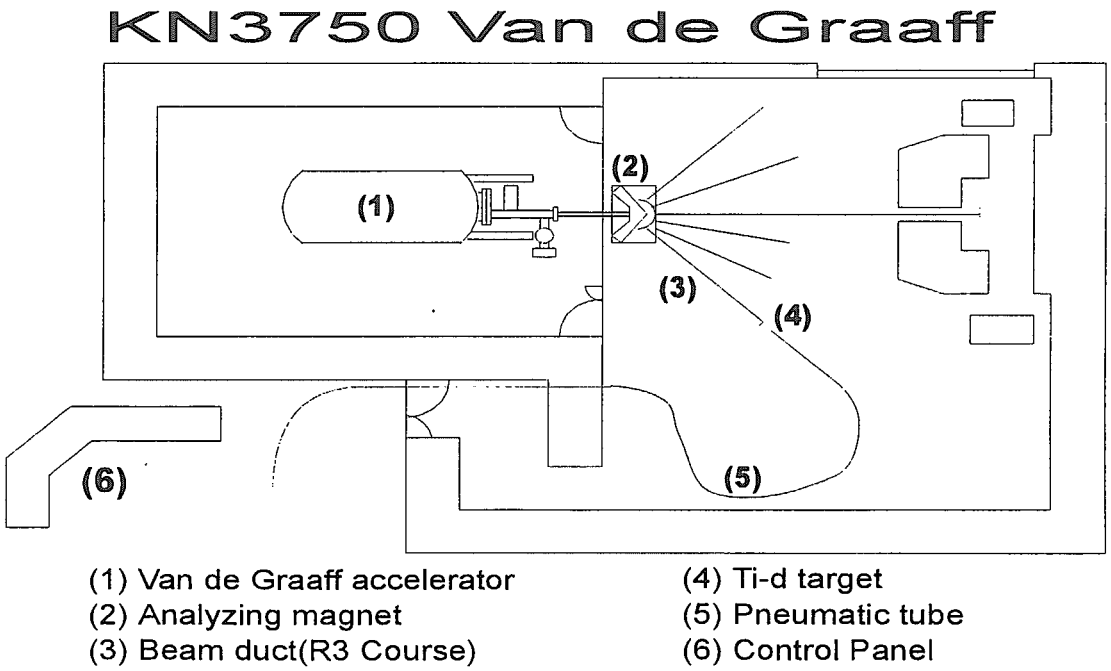

Fig.6 A sketch of KN3750 Van de Graaff accelerator in Nagoya University

Table1. Measured reactions and decay parameters.

Reaction	Half life	E_γ (keV)	I_γ (%)	Q-value(keV)
$^{27}Al(n,p)^{27}Mg$	9.462m	843.7	73(1)	-1827.9
$^{47}Ti(n,p)^{47}Sc$	3.422d	159.38	68.3(27)	182.2
$^{58}Ni(n,p)^{58}Co$	70.78d	810.7	99.44(2)	-400.0
$^{115}In(n,n')^{115m}In$	4.486h	336.4	45.9(1)	-340.0

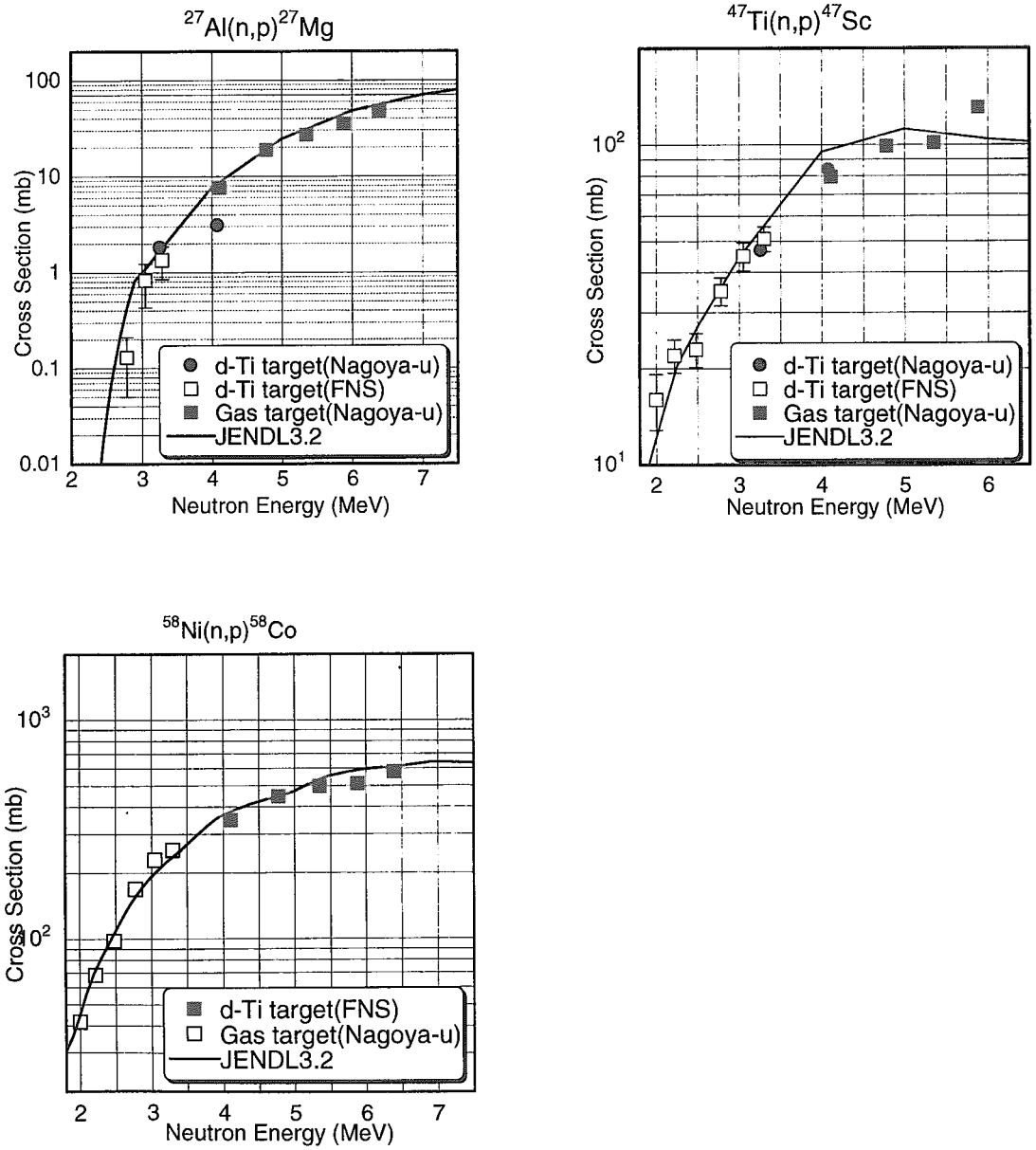

Fig.7 Experimental cross section data of (n,p) reaction.

3.17

Integral Data Test of FENDL-2 Fusion Nuclear Data Library with Neutronic Integral Experiments

Yican WU*, Yixue CHEN*, Ulrich FISCHER**, Yuan CHEN***, Li AN***

* Institute of Plasma Physics, Chinese Academy of Sciences, P.O. Box 1126, Hefei, Anhui, 230031, China
Tel.: +86 551 5591397, Fax: +86 551 5591310, E-mail: ycwu@mail.ipp.ac.cn
** Karlsruhe Research Center, Postfach 3640, 76021 Karlsruhe, Germany
*** Southwest Institute of Nuclear Physics and Chemistry, P.O. Box 525-74, Chengdu, 610003, China

FENDL-2 , the latest version of Fusion Evaluated Nuclear Data Library, had been developed based on selection of evaluated data from ENDF/B-VI, JENDL-3, JENDL-FF, BROND-2 and EFF-3 and distributed for benchmark analysis recently. Integral data test of FENDL-2 has been performed to qualify and validate the working library with a variety of neutronic integral experiments. Calculations and analyses of neutron leakage spectra and reaction rates have been performed with the 3-D Monte Carlo transport code MCNP and FENDL-2 data library. The results were compared with the measured results and the results obtained previously with FENDL-1, EFF, JENDL-FF.

I. Introduction

The Fusion Evaluation Nuclear Data Library (FENDL) is a compilation of fusion-oriented data evaluations selected from the national nuclear data files ENDF/B (USA), BROND (Russian Federation), JENDL (Japan) and EFF (Europe) in an international effort initiated and coordinated by the IAEA Nuclear Data Section. The first version of the file, FENDL/E-1, has been compiled and released [1]. And the file has served as the reference library for design calculations in the Engineering Design Activity (EDA) phase of the International Thermonuclear Experimental Reactor (ITER) project. The second version of the file, FENDL/E-2 [2], contains evaluated neutron, photon-atom and photon production cross sections, in ENDF format, with resonance parameters where appropriate, for 57 nuclides of importance for coupled neutron-photon transport calculations for fusion reactor design selected from the evaluated data files BROND-2, ENDF/B-VI, JENDL-3.1, JENDL-FF and EFF-3. A preliminary working library (Version 1 of March 1997) is available from the IAEA Nuclear Data Section for the purpose of benchmark analysis, which contains the processed cross sections in pointwise ACE format, for use with the Monte Carlo transport code MCNP4A [3], and in the multigroup GENDF and MATXS formats, for use in coupled neutron-photon transport calculations with discrete-ordinates codes such as ANISN[4], ONEDANT[5], etc. Prior to FENDL-2 evaluation selection, a great amount of benchmark work, including integral fusion neutronic experiments and data testing, has been performed in the world for FENDL validation [6,7]. In particular, in the Ref.[7], a large variety of existing integral 14MeV benchmark experiments had been analyzed for that purpose by means of coupled neutron-photon transport calculations with the Monte Carlo code MCNP4A, the discrete ordinates code ONEDANT and the nodal transport code NGSN/1D [8]. The analyzed experiments covered a wide range of fusion-relevant materials such as 14 MeV neutron transmission experiments on rectangular slabs and on shells with measurements of neutron leakage spectra were analyzed. This work has been performed to validate and qualify the second version of FENDL based on benchmark calculations with the code MCNP4A and the preliminary release of the processed FENDL-data and also comparisons to the previous calculation results in Ref.[7]. In this paper, we do not intend to present the detailed analysis of any evaluation status. However, brief benchmark calculation results and major findings are presented for 14 MeV neutron transmission experiments on spherical Fe, Be, Al, Si, Mo, Co, Cr, Cu, Ti, Mn, Zr, Nb, W and V shells with measurements of neutron leakage spectra, which had been performed previously at Institute of Physics & Power Eng. (IPPE, Russian Federation), University of Osaka (OKTAVIAN facility, Japan) and for shielding experiments on multi-layer alternating iron-water spherical and cylindrical shells-combined assembly and multi-layer iron-polyethylene-lead slabs-combined with measurements of activation reaction rates, which have been performed recently at Southwest Institute of Nuclear Physics and Chemistry (SWINPC), China [9,10,11].

II. Benchmark Calculation and Analysis

1. Iron spherical shell experiment (IPPE)

Iron spherical shells with various thicknesses of 2.5, 7.5, 12, 18.1 and 28 cm were irradiated by 14 MeV D-T neutrons at Institute of Physics & Power Eng., Russian Federation. The neutron leakage spectra from the outer surface of five shells were measured by the Time-of-Flight (TOF) method[12]. Calculations have been

performed for the three-dimensional (3D) spherical geometrical model with MCNP4A and FENDL-2. The measured leakage with specified uncertainty and C(calculational)/E (Experimental) ratios of integral neutron spectra for the shells with thicknesses of 2.5 and 28.1 cm are listed in Table 1 where the previous results with EFF-3 from Ref.[7] are also included for comparison purpose. The results show that FENDL-2 Fe data underestimated the measured leakage spectrum in the thin shell experiment by above 20%. However, a clear improvement can be observed for the thick shell experiment. In addition, we note that the results for FENDL-2 are different from those with the previous EFF-3 data file, where FENDL-2 Fe data originated.

Table 1 C/E data for integrated neutron leakage spectra in the IPPE iron shell experiment

Shell Thickness (cm)	Energy Range (MeV)	Experimental Leakage (1/sn)	C/E of Integral Leakage			
			FENDL-2	FENDL-1	JENDL-FF	EFF-3
2.5 (0.5 MFP)*	0.05~1.0	.099 (5)**	*0.95*	0.93	1.09	*0.96*
	1.0~5.0	.140 (4)	*1.00*	0.99	1.01	*1.05*
	5.0~10.0	.032 (5)	*0.72*	0.98	0.84	*0.76*
	10.0~20.0	.740 (7)	*1.04*	1.05	1.05	*1.05*
	>0.05	1.01 (5)	*1.02*	1.03	1.04	*1.03*
28.0 (6.1 MFP)*	0.05~1.0	.786 (5)	*1.08*	1.08	1.09	*1.09*
	1.0~5.0	.115 (4)	*1.06*	1.04	0.99	*1.06*
	5.0~10.0	.0063 (6)	*0.98*	1.27	1.09	*0.98*
	10.0~20.0	.034 (7)	*1.08*	0.94	0.93	*0.98*
	>0.05	.94 (5)	*1.08*	1.07	1.07	*1.08*

*MFP represents Mean Free Path of neutron in the materials; ** percentage experimental errors in parentheses

2. Beryllium spherical shell experiment (OKTAVIAN)

A beryllium spherical shell experiment with various thicknesses was conducted at the intense 14 MeV neutron source facility OKTAVIAN at Osaka University, Japan. Neutron leakage spectra were measured applying the TOF technique[13]. In this work, the sphere shell with inner radius of 5.7 cm and outer radius of 17.35 cm has been calculated using MCNP4A and FENDL-2 with isotropic 14.1MeV point neutron source and the measured neutron energy spectrum. Results are shown in Table 2 in comparison with the results obtained previously with FENDL-1and JENDL-FF. The calculation shows that the results obtained with FENDL-2 fairly well represents the measured neutron spectra although there is an overestimation of 20% around the source energy peak. In addition, the results with the current FENDL-2 beryllium data, which originated from JENDL-FF beryllium data file, well agree with those with JENFL-FF. The very slight differences probably come from the statistic errors in the calculations.

Table 2 C/E data for integrated neutron flux spectra in the OKTAVIAN Be shell experiment

Energy Range (MeV)	Experimental Leakage (1/sn)	C/E of Integral Leakage		
		FENDL-2	FENDL-1	JENDL-FF
0.003~1.0	.469 (5.7)*	*0.99*	.98	*.98*
1.0~5.0	.315 (1.0)	*0.84*	.83	*.85*
5.0~10.0	.143 (1.7)	*0.90*	.88	*.90*
10.0~20.0	.324 (1.1)	*1.20*	1.18	*1.21*
>0.003	1.26 (2.9)	*0.99*	.98	*1.00*

* percentage experimental errors in parentheses

3. Vanadium spherical shell experiment (IPPE)

Neutron leakage spectra were measured at the IPPE neutron source facility for two vanadium spherical shells. The inner/outer radii of the two shells amounted to 1.5cm/5cm and 1.5cm/12cm, respectively. The total uncertainty of the measured fluences is estimated at about 7%[14]. An isotropic neutron source was adopted in the calculation with MCNP4A and FENDL-2 V data. A uniform source energy spectrum distribution between 13.36 and 14.89 MeV and the simplified 1-D geometry model was used in the calculation. The comparison of calculated and measured integral spectra is given in Table 3. The results obtained previously with FENDL-1, JENDL-FF and EFF-3 are also listed in Table 3. The calculations have shown that FENDL-2 vanadium data agrees with JENDL-FF V evaluation and has the best agreement with the measured leakage spectra among the three evaluated data files. A slight difference between FENDL-2 results and previous results with JENDL-FF in the low energy range for thin shell experiment was caused by the fact that we had included the measured source energy spectrum distribution in the

previous calculation with JENDL-FF.

4. Various spherical pile experiment (OKTAVIAN)

Sphere pile experiments were performed at the intense 14 MeV neutron source facility OKTAVIAN at Osaka University, Japan, for various materials using the TOF technique. The neutron leakage spectra and the source neutron spectrum were measured. The sample piles were made by filling spherical vessels with sample powder or flakes. The characteristic parameters of the sample piles may be seen in Ref.[13]. In this work, the sphere pile experiments for Al, Si, Mo, Co, Cr, Cu, Ti, Mn, Zr, Nb, W have been calculated using MCNP4A with continuous energy cross-section data FENDL-2. The isotropic angular distribution of source neutrons along with the measured energy spectra and the simplified 1-D geometry model has been adopted in all the calculations. The C/E values of integrated neutron leakage are listed in Table 4. The experimental uncertainty listed in Table 4 includes only counting statistic error. From Table 4, the following facts can be observed.

For both Al and Si, a clear improvement in the estimation of neutron spectra can be found with FENDL-2 in comparison to other data files although there is still a slight underestimation in the energy range below source peak energy with all the data files.

For Mo, the measured neutron leakage spectrum can be well reproduced by all the data evaluations except for an underestimation in the energy range 3-10 MeV. However, FENDL-2 Mo data, originating from JENDL-FF Mo data, show a much better agreement with the measured spectrum in that energy range due to an improved neutron emission spectrum. The measured total neutron leakage (>0.1 MeV) is underestimated by some 10% in total.

For Co, a serious underestimation by about 17% of the leakage spectrum as measured in the experiment is found for all of the applied data evaluations. Note the shape of leakage spectrum is nevertheless well reproduced by all the calculations. Thus there may be a normalization problem in this experiment.

For Cr, FENDL-2 Cr data, originating from ENDF/B-VI (FENDL-1) data, has a good agreement with experiment except for an overestimation of some 10% in the energy range 0.1-10 MeV. For Cu, FENDL-2, FENDL-1 and EFF-2, which all make use of the Cu ENDF/B-VI evaluation, give a strong overestimation of measured integral leakage spectra by 27% in the energy range 5-10 MeV.

For Ti, all the data totally overestimate the measured leakage spectra by about 20% whereas JENDL-FF shows much better agreement in the energy range of above 1 MeV. FENDL-2 show the same results as FENDL-1 and EFF-2 due to application of the same Ti ENDF/B-VI evaluation. For Mn, FENDL-2, FENDL-1 and EFF-2 data rather well reproduce the experimental spectrum except for a slight overestimation of about 10% in the energy range below 5 MeV.

For Zr, FENDL-2, which makes use of JENDL-FF Zr evaluation, shows the best agreement with the experimental spectrum among the evaluations. However, an overall overestimation of above 15% can still be observed with FENDL-2 and other data although FENDL-2 shows an improvement.

For Nb, FENDL-2 Nb data shows an improvement in reproduction of the experimental leakage spectrum above 1 MeV although the measured leakage spectrum is overestimated by about 15% in total with all the evaluations.

For W, the measured leakage spectrum is underestimated by some 10% in total with all the evaluations. In particular, there is a strong underestimation for FENDL-2, originating from JENDL-FF, around 1 MeV and for EFF-2 in the energy range 2-6 MeV.

In addition, it is noted that all the calculated results with FENDL-2 for the OKTAVIAN spherical shell experiments are nearly the same as those with the other corresponding data files, from which FENDL-2 originated.

5. Iron-water combination experiment

The experimental assembly was constructed from a combination of alternating iron-water multi-layers of spherical and cylindrical shells. The spherical shell was made of three layers of iron and two layers of water. The inner and outer radii were as follows: R (inner/outer, cm) =7.1/13.1(Fe)/18.1(H_2O)/23.8(Fe)/30.5(H_2O)/35(Fe). The D-T target was surrounded by foam polystyrene of 0.04 g/cm^3 in density inside the spherical shell and placed at the center of spherical shell. An extended cylinder shell with a radius of 17.5cm was arranged just outside the spherical shell. The thicknesses (cm) of multi-layers of cylindrical shell are: 1.5(Fe)/8.1(H_2O)/5(Fe)/7.6(H_2O)/5(Fe)/7.3(H_2O)/0.5(Fe). The measurements of activation reaction rates, neutron angular flux spectra, neutron leakage spectra were performed at the D-T neutron source facility of SWINPC[9].

The calculation for 3-D geometrical model with 14.1 MeV isotropic neutron source has been performed with FENDL-2. In this work, the measured and calculated reaction rates of $^{56}Fe(n,p)^{56}Mn$ and $^{27}Al(n,\alpha)^{24}Na$ at the positions with various penetration depths are presented in Fig.1, where the calculated results with ENDF/B-IV and ENDF/B-V data are also included for comparison purpose. The calculation shows the all calculated results fairly represent the spatial distribution trend of the measured rates, expect for ~20% underestimation over the measured results at all positions. In addition, the underestimation with FENDL-2 appears to be ~3% stronger than those with

ENDF/B-IV and ENDF/B-V at the inner surface position (7.1 cm) of iron-water spherical assembly and nearly the same at other positions.

Table 3 C/E data for integrated neutron leakage spectra in the IPPE V shell experiment

Shell Thickness (cm)	Energy Range (MeV)	Exper. Leakage (1/sn)	C/E of Integral Leakage			
			FENDL-2	FENDL-1	*JENDL-FF*	EFF-3
3.5 (0.6MFP)	0.1~1	.123	*1.31*	1.11	*1.25*	1.00
	1~5	.170	*1.07*	1.02	*1.05*	1.14
	5~10	.0308	*1.14*	1.06	*1.12*	.87
	10~20	.737	*0.99*	.996	*.99*	1.00
	>0.1	1.06	*1.05*	1.02	*1.03*	1.02
10.5 (1.8MFP)	0.1~1	.391	*1.23*	1.06	*1.22*	1.01
	1~5	.301	*1.03*	1.04	*1.02*	1.14
	5~10	.0377	*1.27*	1.13	*1.25*	.96
	10~20	.0381	*0.97*	1.00	*.98*	1.00
	>0.1	1.11	*1.09*	1.04	*1.08*	1.04

6. Iron-lead-polyethylene combination experiment

The experiment assembly was constructed from a combination of 100x80 cm^2 plates of iron, lead, polyethylene (PE) and iron with thicknesses of 5.5, 10, 6, 5.5 cm. Measurements of neutron angular spectra and activation reaction rates were performed at the D-T neutron source facility of SWINPC. The 14 MeV D-T neutron source was located in the front of the plates at the axis of the slab assembly. The activation foils were placed at the middle vertical plane inside the lead plate and at the cross surface of polyethylene plate and iron plate. The reaction rates at various distances away from the axis of the experimental assembly were measured [10].

The calculation for 3-D geometrical model with 14.1 MeV isotropic neutron source has been performed with MCNP4A and data files FENDL-2, ENDF/B-IV and ENDF/B-V. The measured and calculated reaction rates of $^{56}Fe(n,p)^{56}Mn$ and $^{27}Al(n,\alpha)^{24}Na$ are presented in Fig.2 for the measured positions inside lead plate, and in Fig. 3 for the measured positions between iron plate and polyethylene plate. An underestimation of 10%~40% is observed for all the calculations expect for an overestimation of 10%~30% at the measured positions near the axis of the experimental assembly inside lead plate with the three data files. That underestimation and overestimation with FENDL-2 are ~10% stronger than those with ENDF/B-IV and ENDF/B-V data files.

III. Summary

A variety of 14 MeV neutronic experiments have been analyzed by means of Monte Carlo transport calculations with the preliminary release of Fusion Evaluated Nuclear Data Library FENDL-2. The calculated results with FENDL-2 were compared with the measured neutron spectra and reaction rates and the calculated results obtained previously with FENDL-1, EFF-2/-3 and JENDL-FF from which FENDL-2 evaluations originated. Transmission experiments on spherical shells made of iron, vanadium, aluminum, silicon, molybdenum, cobalt, chromium, copper, titanium, manganese, zirconium, niobium, tungsten, respectively and on a combined spherical and cylindrical shell assembly consisting of iron-water alternating layers and on a combined slab assembly consisting of iron, lead and polyethylene plates were included in the analysis. In general, the FENDL-2 evaluations show a high quality level and have an overall good agreement with integral experiments. However, some exceptions were found and need to be analyzed further. All the calculated results with FENDL-2 rather well reproduced those obtained previously with the corresponding data evaluations in the libraries ENDF/B-VI, EFF and JENDL-FF, from which FENDL-2 data originated. It should be mentioned that the above found disagreements between the calculated and measured results may be caused partly by the data files and partly by the experimental data themselves. We do not intend to clarify any detailed explanation of data deficiencies in the FENDL-2, but to provide the basis for further analyses. As a next step, calculations with more integral experiments are needed for cross-checking. Furthermore, there is required a sensitivity analysis for tracing down the discrepancies to specific cross section data and further improvement of the corresponding cross section data.

References

[1] Muir, D.W., Ganesan, S. and Pashchenko, A.B.: Inter. Conf. On Nuclear Data for Science and Technology, Juelich, Germany, May 13-17, 1991.

[2] Pashchenko, A.B. and Wienke, H.: summary documentation, IAEA-NDS-175 (1997).

[3] Briesmeister, E (Ed.) : LA-12625-M (1993).
[4] Engle, W.W. : CCC-254 (1973).
[5] Alcouffe, R.E. et al : LA-1296-M (1995).
[6] Fischer. U. (Ed.): FZKA-5785, INDC(GER)-41 (1996).
[7] Wu, Y., Fischer, U. : FZKA-5953 (1998).
[8] Wu, Y.C., Xie, Z.S., Fischer U.: J. Sci. Eng., 133, 350-357 (1999).
[9] Chen, Y., liu, R., Shen, J. et al.: Fusion Technology, 34, 1023-1027 (1998).
[10] Chen, Y., Guo, H., An, L. et al.: Proc. of the 5th China-Japan Symposium on Materials for Advanced Energy Systems and Fission & Fusion Engineering, Xi'an, China , p.252-256, Nov.2-6,1998
[11] Wu, Y.C., Chen, Y.X., Fischer, U. Et al: Report ASIPP/178, Institute of Plasma Physics, Chinese Academy of Sciences (1999).
[12] Devkin, B.V., Giese, H., Kobozev, M.G. et al: Neutron Leakage Spectra from Spherical Iron Shells, Forschungszentrum Karlsruhe internal report 31-06-32/01A (1995).
[13] Maekawa, F., Yamamoto, J., Ichihara, C. et al : Collection of Experimental data for Fusion Neutronics Benchmark, JAERI-M-94-014, (1994).
[14] Moelendorff, U.V., Devkin, B.V., Fischer, U., B.I. Fursov et al.: Proc. the 19th Symposium on Fusion Technology , Lisbon, Portugal, Sept.16-20, 1996

Table 4 C/E of integral leakage spectra for various materials sphere pile experiments

Element	Energy Range (MeV)	Measured Leakage (1/sn)	C/E of Integral leakage			
			FENDL-2	FENDL-1	EFF-2	JENDL-FF
Al	0.1~1.0	.069 (1.9)	*0.90*	0.89	0.81	0.88
	1.0~5.0	.148 (3.1)	*0.85*	0.92	0.89	0.79
	5.0~10.	.050 (1.4)	*0.74*	0.60	0.79	0.81
	10.0~20	.675 (3.7)	*1.10*	1.10	1.10	1.11
	>0.1	.942 (3.3)	*1.03*	1.03	1.03	1.02
Si	0.1~1.0	.093 (3.7)	*0.89*	1.63	0.67	0.89
	1.0~5.0	.171 (5.0)	*0.93*	0.69	0.79	0.89
	5.0~10.	.047 (2.1)	*0.94*	0.71	0.79	0.83
	10.0~20	.482 (4.6)	*1.11*	0.97	1.17	0.93
	>0.1	.793 (4.4)	*1.03*	0.97	1.00	0.90
Mo	0.1~1.0	.516 (8.5)	*0.90*	0.90	0.81	*0.89*
	1.0~5.0	.287 (6.9)	*0.89*	0.96	1.03	*0.89*
	5.0~10.	.043 (2.1)	*0.82*	0.60	0.63	*0.83*
	10.0~20	.524 (4.7)	*0.93*	0.97	0.97	*0.93*
	>0.1	1.37 (6.5)	*0.91*	0.93	0.91	*0.90*
Co	0.1~1.0	.242 (4.3)	*0.63*	*0.63*	0.63	0.62
	1.0~5.0	.295 (6.2)	*0.61*	*0.61*	0.61	0.64
	5.0~10.	.055 (2.1)	*0.49*	*0.49*	0.49	0.65
	10.0~20	.729 (5.2)	*1.02*	*1.02*	1.02	1.00
	>0.1	1.32 (5.1)	*0.83*	*0.83*	0.83	0.83
Cr	0.1~1.0	.211 (4.9)	*1.07*	*1.07*	1.07	1.15
	1.0~5.0	.221 (3.2)	*1.13*	*1.13*	1.25	1.11
	5.0~10.	.041 (1.2)	*1.14*	*1.14*	0.98	0.96
	10.0~20	.549 (2.8)	*0.97*	*0.97*	0.96	0.96
	>0.1	1.02 (3.3)	*1.04*	*1.03*	1.05	1.03
Cu	0.1~1.0	.660 (10)	*1.09*	*1.08*	1.09	1.04
	1.0~5.0	.145 (4.8)	*1.05*	*1.06*	1.06	0.97
	5.0~10.	.013 (1.2)	*1.28*	*1.27*	1.27	0.99
	10.0~20	.079 (2.0)	*0.99*	*0.99*	0.99	1.04
	>0.1	.898 (8.4)	*1.07*	*1.07*	1.07	1.03
Ti	0.1~1.0	.086 (2.2)	*1.31*	1.31	1.31	1.38
	1.0~5.0	.152(3.8)	*1.33*	1.34	1.34	1.06
	5.0~10.	.038 (1.5)	*0.98*	0.98	0.98	1.00
	10.0~20	.598 (4.4)	*1.19*	1.19	1.19	1.23
	>0.1	.874 (4.0)	*1.22*	1.21	1.21	1.20
Mn	0.1~1.0	.661 (9.4)	*1.08*	1.08	1.08	1.08
	1.0~5.0	.271 (6.5)	*1.14*	1.14	1.14	1.13
	5.0~10.	.028 (1.7)	*1.00*	1.00	1.00	1.15
	10.0~20	.154 (2.7)	*0.95*	0.94	0.94	1.00
	>0.1	1.14 (7.5)	*1.05*	1.07	1.07	1.08
Zr	0.1~1.0	.442 (7.7)	*1.21*	1.07	0.95	*1.21*
	1.0~5.0	.307 (8.2)	*1.07*	1.24	1.58	*1.07*
	5.0~10.	.033 (2.2)	*0.99*	1.20	1.74	*0.98*
	10.0~20	.317 (4.9)	*1.21*	1.26	1.19	*1.21*
	>0.1	1.10 (6.9)	*1.16*	1.18	1.22	*1.16*
Nb	0.1~1.0	.335 (6.1)	*1.37*	1.27	1.12	*1.37*
	1.0~5.0	.219 (3.2)	*1.04*	1.26	1.47	*1.04*
	5.0~10.	.036 (1.1)	*0.93*	1.09	1.17	*0.94*
	10.0~20	.510 (2.7)	*1.04*	1.04	1.05	*1.04*
	>0.1	1.10 (3.8)	*1.14*	1.15	1.16	*1.14*
W	0.1~1.0	.360 (7.2)	*0.93*	0.84	0.87	*0.94*
	1.0~5.0	.241 (7.0)	*0.79*	0.86	0.84	*0.79*
	5.0~10.	.040 (2.1)	*0.69*	0.67	0.61	*0.68*
	10.0~20	.710 (6.3)	*0.94*	0.94	0.95	*0.94*
	>0.1	1.35 (6.6)	*0.90*	0.90	0.89	*0.90*

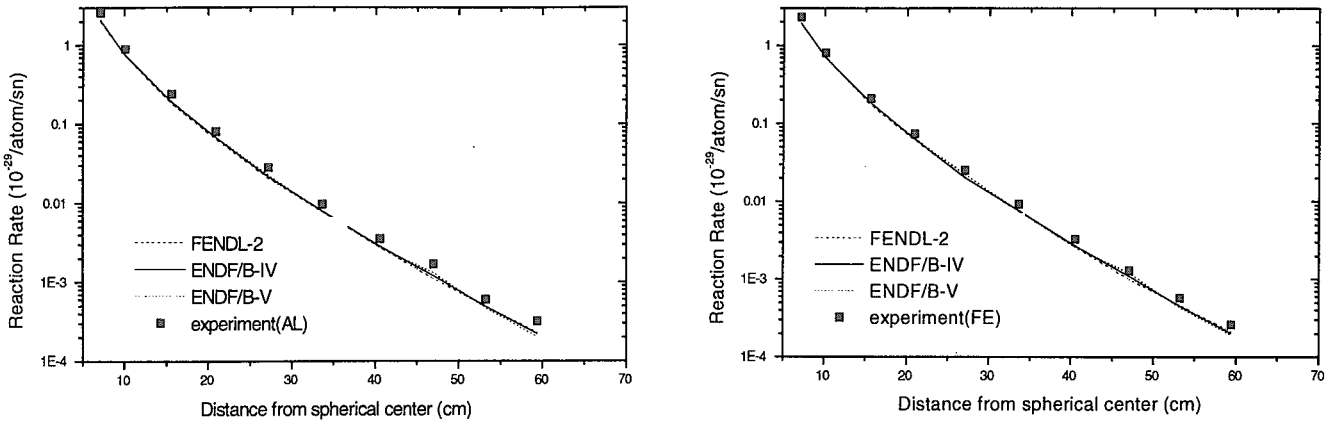

Fig.1 Measured and calculated reaction rates for iron water combination experiment

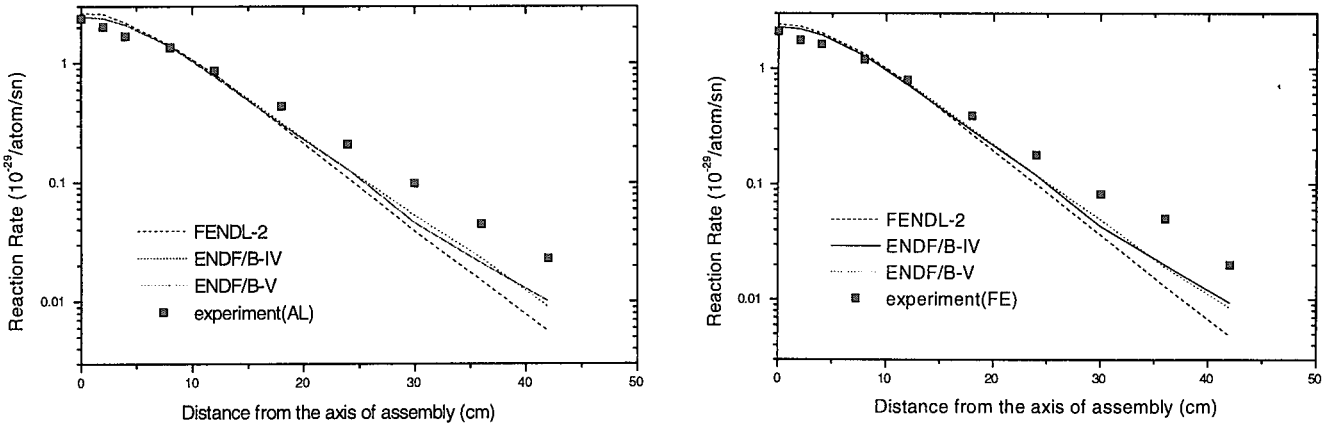

Fig.2 Measured and calculated reaction rates inside lead plate for Fe-Pb-PE combination experiment

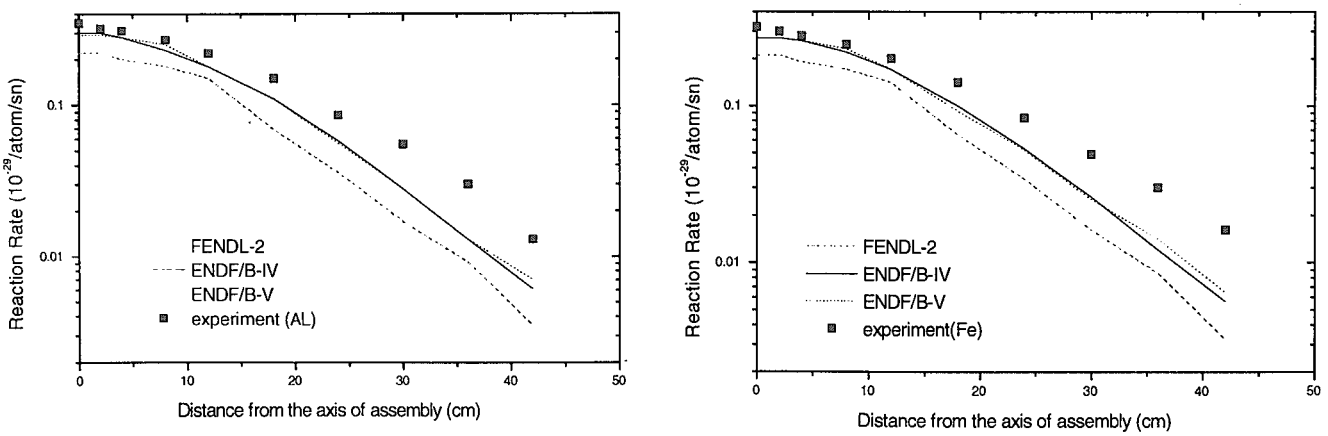

Fig.3 Measured and calculated reaction rates between lead and polyethylene plates for Fe-Pb-PE combination experiment

3.18 Tritium Release from Ceramic Breeders with Catalytic Function

Kenzo Munakata[1], Toshihiko Kawano[1], Atsushi Baba[1], Takahiro Kawagoe[1], Yoshihiro Yokoyama[1], Toshiharu Takeishi[1], Masabumi Nishikawa[1], Hideki Nakashima[1], Hirotake Moriyama[2], Keizo Kawamoto[2], Kenji Okuno[3]
[1]Kyushu University, Department of Advanced Energy Engineering Science, Interdisciplinary Graduate School of Engineering Science, Kasuga 816-8580, Japan
[2]Kyoto University, Research Reactor Institute, Osaka 590-0494, Japan
[3]Shizuoka University, Radiochemistry Research Laboratory, Faculty of Science, 422-8529, Japan
Phone: +81-92-642-3784 Fax: +81-92-642-3784
E-mail: kenzo@nucl.kyushu-u.ac.jp

1. Introduction

Most current designs of D-T fusion reactor blankets employ ceramic breeders such as Li_2O, $LiAlO_2$, Li_2ZrO_3 and Li_4SiO_4. With regard to these ceramic breeders, a helium gas containing approximately 0.1 % of hydrogen would be used to extract tritium via isotopic exchange reactions that take place at the surface. In previous studies, the isotope exchange reactions and water adsorption at the surface of several ceramic blanket materials were investigated[1-3]. The results revealed that these isotope exchange reactions proceed fast only at higher temperatures. Because of the strong temperature dependency of the exchange reactions, a considerable decrease in the reaction rate takes place as the temperature is lowered. Taking into consideration that there is a broad temperature distribution within a blanket module[2], it is anticipated that the tritium bred in regions of lower temperature will presumably be poorly recovered, which would lead to increased overall steady state tritium inventories in the blanket module.

In order to obtain an improved recovery of tritium from a blanket over a broad range of temperatures, the effect of catalytic active metal additives, such as platinum and palladium, on the heterogeneous isotope exchange reactions at the breeder - sweep gas interface was examined in our previous work[4]. The results of the study revealed that isotope exchange reactions proceed fast if catalytic additive metals are deposited on the surface of a Li_4SiO_4 ceramic breeder; we designated this type of breeders as "Catalytic Breeders". This time, the authors conducted out of pile annealing tests using the catalytic breeder materials irradiated in a research reactor and investigated the effect of catalytic additives on the tritium release from the ceramic breeder material.

2. Preparation of catalytic breeder

Platinum was deposited on ceramic breeder pebbles (Li_4SiO_4, 0.51-0.94 mm (av. 0.68 mm) in diameter, >98 %TD) by the incipient wet impregnation method generally used for the fabrication of catalysts. The Li_4SiO_4 pebbles were donated by FzK (Research Center Karlsruhe) in Germany. In the fabrication procedure, a solution of platinum tetra ammonium nitrate $Pt(NH_3)_4(NO_3)_2$ was pored dropwise onto the previously dried Li_4SiO_4 pebbles. After this treatment, the wet Li_4SiO_4 pellets were dried in an oven. The obtained precursors were

calcined and reduced in a quartz tube reactor at 400°C. The details of the fabrication procedure are cited in our previous report[4]. The sample ceramic breeder (Pt/ Li_4SiO_4) used in this work is the exactly same one as that used in our previous study[4]. The exact content of the deposited Pt has not yet been determined, but according to the mass balance in the fabrication process the concentrations can be estimated being within a range of 0.7 to 2 wt %.

3. Irradiation of ceramic breeders and experiments

Li_4SiO_4 and Pt/ Li_4SiO_4 breeder materials were irradiated in Kyoto University Research Reactor with the neutrons flux of 2.75×10^{13} $cm^{-3}s^{-1}$ for 1 min. The research reactor has several ports for irradiation tests, and the port Pn-2 was used to irradiate the breeder materials. The neutron energy spectrum at Pn-2 is shown in Fig. 1[6]. The breeder pebbles were encapsulated in quartz tubes (6 mmϕ×60 mm) with low-pressure He gases, and which were placed in sample holders made of polyethylene. Before encapsulation, breeder pebbles were dried under dry He gas streams for 12 h by raising their temperature stepwise up to 400°C. The sample holders were transported to the core of the thermal reactor with the help of pressurized air. After irradiation, the quartz tubes were mechanically broken and the breeders were placed in reaction tubes for annealing experiments. All procedures are carried out in a glove box of which moisture level is less than 1 ppm. Accordingly, the breeder materials were never exposed to the atmosphere before and during experiments.

Figure 2 shows the neutron spectrum at Pn-2 calculated from the data shown in Fig. 1. Figure 2 also shows the cross section of the reactions related to tritium production from ^{6}Li and ^{7}Li, which were taken from JENDL-Dosimetory file[7]. As shown in this figure, there are higher neutron fluxes in the lower energy region. The cross section of the ^{6}Li(n,t) reaction is high at the lower energy region, whereas the cross section of the ^{7}Li(n,n't) is very low in the region of thermal neutron. Therefore, the ^{6}Li and neutron reaction is the dominating path for the production of tritium. Figure 3 shows the response (production of neutron flux $\phi(E)$ and cross section $\sigma(E)$) for ^{6}Li as a function of neutron energy. This figure verifies that almost all

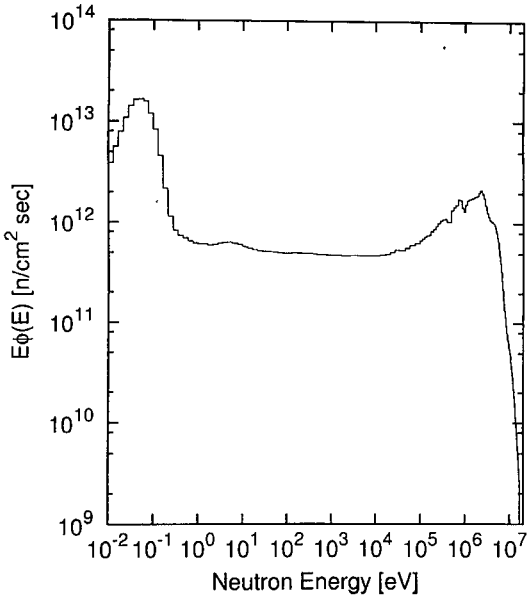

Fig. 1 Neutron energy spectrum at Pn-2 in KUR

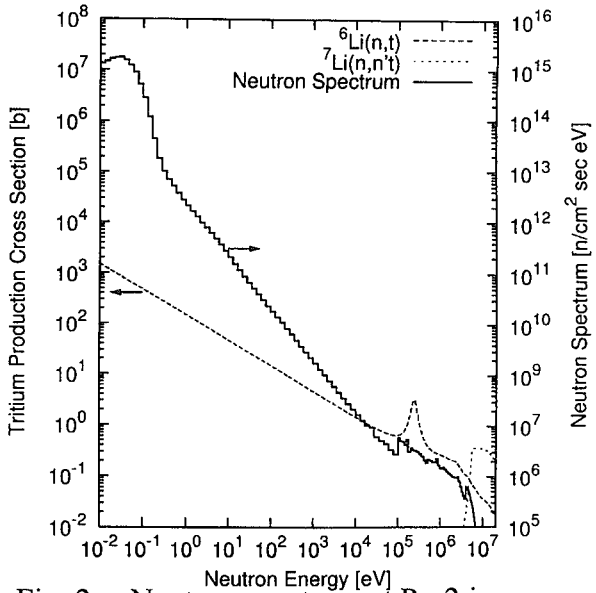

Fig. 2 Neutron spectrum at Pn-2 in KUR and cross section of nuclear reaction for tritium production

tritium is produced by low energy neutrons.

A schematic diagram of the annealing experiment is shown in Fig. 4. The experimental conditions are summarized in Table 1. 0.2 g of Pt/Li_4SiO_4 or Li_4SiO_4 pebbles were placed in the quartz tube reactor. The reactor tube was heated with an infrared image furnace, and thus the bed temperature can be raised to set temperatures within 1 - 2 min. A 1000 ppm H_2/Nitrogen gas was used as the purge gas, and the gas flow rate was controlled with conventional mass flow controllers. The gases employed were purified with a trap containing 5A molecular sieve (MS5A) to remove residual water vapor. The concentrations of tritium in inlet and outlet streams of the reactor were traced with an ionization chamber (made of stainless steel) of which effective volume was 90 cm^3. The applied voltage between the electrodes of the ion chamber was 90 V. Just before the process gas was introduced into the ionization chamber, the gas was mixed with a nitrogen gas containing 10000 ppm of H_2O to avoid system effects in the ionization chamber. The system effects are caused by tritium sorbed on the surface of the electrodes, which induces incorrect electric outputs from the ionization chambers. Tritium are sorbed via adsorption or isotope exchange reactions, and thus the addition of high concentration water vapors to the process gases enables to prevent the sorption of tritium on the surface of the electrodes[5]. The exit gas was treated with MS5A adsorbent beds and water bubblers.

Table 1 Experimental conditions

Breeder	(1) Li_4SiO_4 (pebble size 0.68 mm, >98 %TD) (2) Pt/Li_4SiO_4
Irradiation condition	Neutron flux: 2.75×10^{13} $cm^{-3}s^{-1}$ Irradiation time: 1 min
Amount of breeders	0.2 g
Sweep gas	1000 ppm H_2/N_2 (1000ppm H_2O/N_2 only at 900 °C)
Gas velocity	100 cm^3/min
Bed diameter	~4 mm
Temperature	20 – 900 °C

4. Results of out of pile annealing experiments

Figure 5 shows a result of out of pile annealing tests for the Li_4SiO_4 pebbles irradiated in the thermal reactor; the figure shows the change in tritium level in the outlet

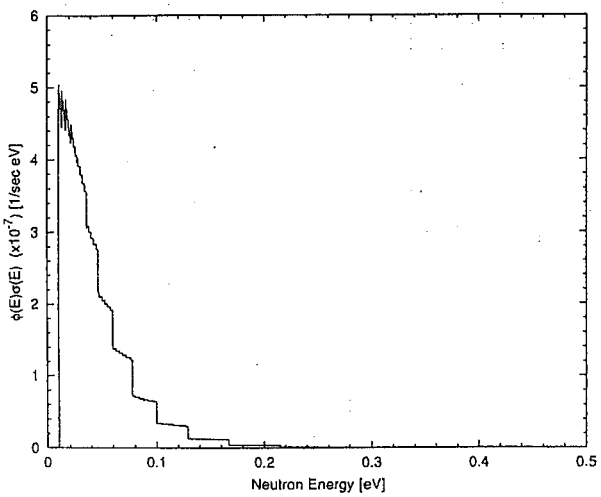

Fig. 3 Response of nuclear reaction for tritium production

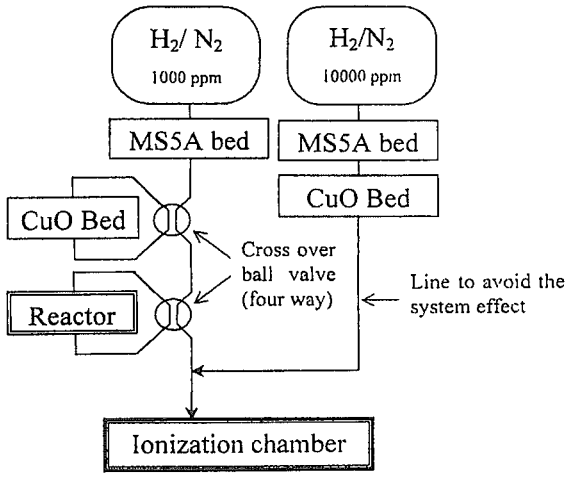

Fig. 4 Schematic diagram of apparatus for the annealing experiment

stream of the reactor. The flow rate of the sweep gas (1000 ppm H_2/N_2) was 100 ml/min. The reactor temperature was raised stepwise from ambient temperature to 300, 500, 700 and finally 900 °C. At each temperature (300, 500 and 700 °C), the reactor temperature was held constant for 15 min. The sweep gas was replaced with a 1000 ppm H_2O/N_2 gas at 15 min after the reactor temperature was raised to 900 °C to ensure the release of total amounts of tritium bred in the breeder materials via exchange reactions. As seen in this figure, the amount of tritium released from the Li_4SiO_4 pebbles increased with increasing temperature when the reactor temperature was lower than 900 °C. In total, 14.5 μCi (5.4×10^5 Bq) of tritium was released. The amounts of tritium released at each temperature are presented in Table 2. The largest amount of tritium (46 % of the total amount of tritium) was released at 700 °C, but only 15 % of the total amount of tritium was released at 300 °C.

The result of out of pile annealing tests for the Pt/Li_4SiO_4 breeder is shown in Fig. 6. The reactor temperature was raised stepwise as described above. The flow rate of the sweep gas was also 100 ml/min; the experimental condition for this experiment was same as that for the experiment shown above. In this case, 13.3 μCi (4.9×10^5 Bq) of tritium was totally released. The amounts of tritium released at each temperature are presented in Table 2. The largest amount of tritium (54 % of the total amount of tritium) was released at 500 °C. 28 % of the total amount of tritium was released even at 300 °C. By comparing this result with that for the Li_4SiO_4 pebbles, it is seen that the amount of tritium released was increased at lower temperatures

Table 2 Fractional amount of tritium released at each temperature

Temp. [°C]	Fractional release [%]	
	Li_4SiO_4	Pt/Li_4SiO_4
20	0.1	0.7
300	15.3	27.5
500	32.8	54.3
700	46.4	15.6
900	3.7	1.8
900 (water purge)	1.5	0.1
Total amount Released	14.5 μCi (5.4×10^5 Bq)	13.3 μCi (4.9×10^5 Bq)
Total amount of tritium estimated	19.5 mCi (7.20×10^5 Bq)	19.2 mCi (7.10×10^5 Bq)

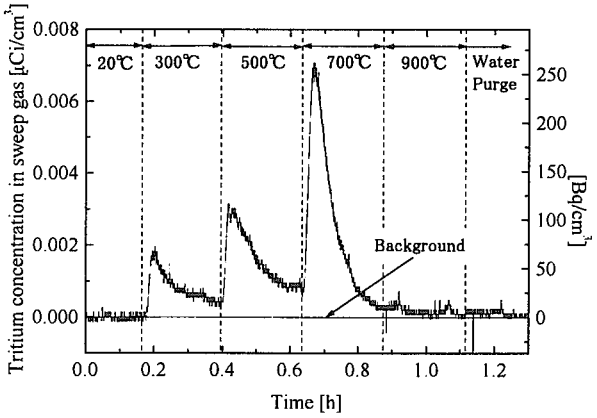

Fig. 5 Change in tritium concentration in outlet stream of Li_4SiO_4 bed

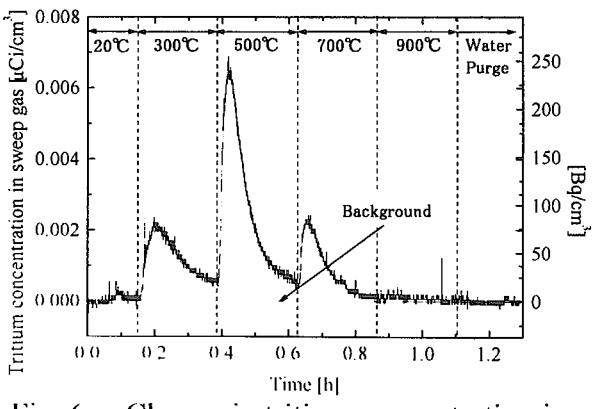

Fig. 6 Change in tritium concentration in outlet stream of Pt/Li_4SiO_4 bed

when the catalytic additive was impregnated into the Li_4SiO_4 pebbles. These results suggest that addition of catalytic additive metals to the ceramic breeder is an effective way to enhance the tritium release rate at lower temperatures.

As shown in Table 2, the total amounts of tritium produced in the breeder materials were 14.5 mCi for Li_4SiO_4 and 13.3 mCi for 1.5% Pt/ Li_4SiO_4, which were calculated from the results of the out of pile annealing experiments. The amounts of tritium produced in the breeder materials were also estimated from the neutron spectrum and the nuclear cross section shown in Figs. 2 and 3. In the estimation, the self-shielding effect was ignored. The amounts of tritium calculated in this way were 19.5 mCi for Li_4SiO_4 and 19.2 mCi for 1.5% Pt/ Li_4SiO_4 (see Table 2). The difference between the experimental and estimated values is approximately 25 %. This difference is probably because of change in neutron spectrum at Pn-2 in KUR; the neutron spectrum shown above was measured more than ten years ago and the present neutron spectrum is though to be somewhat different from the result of the previous measurement. The other probable reason is the negligence of the self-shielding effect in neutronic calculations, since ^6Li has a high cross section for the consumption of neutrons.

5. Conclusions

Catalytic breeders were fabricated by impregnating lithium silicate with platinum. Out of pile annealing experiments were conducted using irradiated ceramic breeders. The results of the experiments indicate that tritium bred in the catalytic breeder material is released at lower temperatures compared with the breeder material with no catalyst.

The amounts of tritium produced in the breeder materials were estimated by using the neutron spectrum and the nuclear cross section without consideration of self-shielding effects. In the estimation, the self-shielding effect was ignored. Comparison of experimental and calculated amounts of tritium produced indicates that the difference between the values is approximately 25 %.

Acknowledgment

The authors wish to thank to Prof. K. Kobayashi for giving data for the neutron spectrums in KUR.

References

[1] Munakata, K., et al.: J. Nucl. Mater. **170,** 187 (1990).
[2] Munakata, K., et al.: Fusion Technol. **15**, 1451(1989).
[3] Baba, A., et al.: J. Nucl. Mater. to be published.
[4] Munakata, K., et al.: J. Nucl. Sci. Technol. **35,** 511(1998).
[5] Munakata, K., et al.: M.: Proc. International Workshop on Present Status and Prospect of Tritium – Material Interaction Studies, p.68(1996).
[6] Kobayashi, K., et al.: KURRI-TR-287, (1987).
[7] Chiba, S., et al.: JAERI-M 88-164, (1988).

3.19 Integral Activation Experiment of Fusion Reactor Materials with d-Li Neutrons Up to 55 MeV

Fujio MAEKAWA [1], Ulrich von MÖLLENDORFF [2],
Masayuki WADA [3] and Yujiro IKEDA [1]

1 Spallation Neutronics Laboratory, Japan Atomic Energy Research Institute,
Tokai-mura, Naka-gun, Ibaraki-ken 319-1195
2 Forschungszentrum Karlsruhe, Postfach 3640, 76021 Karlsruhe, Germany
3 Business Automation Co., Ltd., 1-24-10, Toranomon, Minato-ku, Tokyo, 105-0001
e-mail: fujio@fnshp.tokai.jaeri.go.jp

An integral activation experiment of fusion reactor materials with a deuteron-lithium neutron source was performed. Since the maximum energy of neutrons produced was 55 MeV, the experiment with associated analysis was one of the first attempts for extending the energy range beyond 20 MeV. The following keywords represent the present study: d-Li neutrons, 55 MeV, dosimetry, SAND-II, spectrum adjustment, LA-150, MCNP, McDeLi, IFMIF, fusion reactor materials, integral activation experiment, low-activation, F82H, vanadium-alloy, IEAF, ALARA, and sequential charged particle reaction.

1. Introduction

An integral activation experiment of fusion reactor materials with a deuteron-lithium (d-Li) neutron source was performed at Forschungszentrum Karlsruhe (FZK), Germany, for the sub-task "Fusion Neutronics" under the IEA Collaboration [1, 2]. Since the maximum energy of neutrons produced was 55 MeV, the experiment with associated analysis was one of the first attempts for extending the energy range beyond 20 MeV that has been the upper limit energy for fusion applications. Accordingly, several codes and data developed recently for higher energy applications were used for practical analysis, and several important experimental facts were found. This report summarizes the experiment focusing on important experimental findings and code & data newly introduced.

2. Neutron Field Characterization

2.1. Experiment

A lithium target shown in Fig. 1 was used for the experiment. Metallic lithium was contained in a stainless

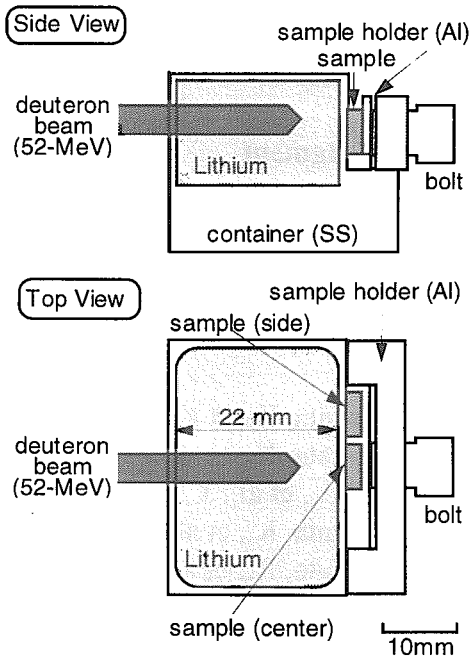

Fig. 1 The lithium-target and sample arrangement.

steel case. A deuteron beam of 52 MeV of typically 3 μA was impinged into the target to produced neutrons. An approximate energy of deuterons entering into the lithium regionwas 40 MeV due to energy loss in the stainless steel wall of 1 mm. The lithium thickness of 22 mm was enough to stop the deuteron beam. Samples were placed at the center and side positions on the downstream side surface of the target. The d-Li neutron source was a simulation of a neutron environment for the International Fusion Materials Irradiation Facility (IFMIF). Before the integral activation experiment, a neutron field characterization was performed by means of multiple-foil activation technique to define neutron flux spectra at the sample positions precisely.

Twenty-seven threshold reactions listed in Table 1 were selected as activation detectors. In addition to the low threshold reactions which have been used for fusion neutronics studies, such as the (n,n'), (n,p), (n,α) and (n,2n) reactions, the (n,3n) ~ (n,6n) reactions having high threshold energies were selected to characterize the high energy neutron flux up to 55 MeV. The most important point for selecting the high threshold reactions was availability of experimental cross section data beyond 20 MeV which were measured with quasi-monoenergetic p-Li neutron sources [3-6]. All the activation foil samples were pure metal in a uniform size of 5 x 5 mm^2. Thicknesses of bismuth samples were 2 mm while those of the other samples ranged from 0.01 mm to 0.1 mm.

The samples were irradiated by the d-Li neutrons for 20 min, 2 hours or 12 hours. After the irradiations, gamma-rays emitted from the samples were measured with a high purity germanium (HP-Ge) detector. Radioactivity of reaction product for each sample was then determined from the measured gamma-ray peak count, detection efficiency, decay constant, etc. in a unit of reaction per atom per coulomb. A typical overall experimental uncertainty of the measured reaction rates was 5 %.

According to the experience in higher energy dosimetry, features of each dosimetry reaction when it was used practically were revealed. The most remarkable finding is suitability of the $^{169}Tm(n,xn)$ (x=2, 3 and 4) reactions as dosimeters. Thulium is an element consisting of a single isotope, and the three (n,xn) reactions can be measured very easily in a single and short measurement. Since the only one drawback of the reactions is lack of experimental cross section data above 30 MeV, measurements of the $^{169}Tm(n,xn)$ reaction cross sections above 30 MeV with quasi-monoenergetic p-Li neutron sources are strongly desired.

2.2. Calculation of Initial Guess Spectra

The initial guess spectrum to be adjusted was calculated by the Monte Carlo neutron transport

Table 1 Dosimetry reactions used for the neutron field characterization experiment.

Reaction	E_{th}[MeV]	Half-Life	Reaction	E_{th}[MeV]	Half-Life
$^{27}Al(n,p)^{27}Mg$	1.9	9.46 m	$^{93}Nb(n,2n)^{92m}Nb$	8.9	10.15 d
$^{27}Al(n,\alpha)^{24}Na$	3.2	14.96 h	$^{115}In(n,n')^{115m}In$	0.3	4.49 h
$^{55}Mn(n,2n)^{54}Mn$	10.4	312.1 d	$^{169}Tm(n,2n)^{168}Tm$	8.1	93.1 d
$Fe(n,x)^{54}Mn$	0.0	312.1 d	$^{169}Tm(n,3n)^{167}Tm$	15.0	9.25 d
$Fe(n,x)^{56}Mn$	3.0	2.58 h	$^{169}Tm(n,4n)^{166}Tm$	23.7	7.70 h
$^{59}Co(n,2n)^{58m+g}Co$	10.6	70.82 d	$^{197}Au(n,2n)^{196m}Au$	8.7	9.7 h
$^{59}Co(n,3n)^{57}Co$	19.4	271.9 d	$^{197}Au(n,2n)^{196m+g}Au$	8.1	6.18 d
$^{59}Co(n,p)^{59}Fe$	0.8	44.5 d	$^{197}Au(n,3n)^{195}Au$	14.8	186.1 d
$^{59}Co(n,\alpha)^{56}Mn$	0.0	2.58 h	$^{197}Au(n,4n)^{194}Au$	23.2	38.0 h
$Ni(n,x)^{58}Co$	0.0	70.82 d	$^{209}Bi(n,3n)^{207}Bi$	14.4	31.6 y
$Ni(n,x)^{57}Co$	8.3	271.8 d	$^{209}Bi(n,4n)^{206}Bi$	22.6	6.24 d
$Ni(n,x)^{57}Ni$	12.4	35.60 h	$^{209}Bi(n,5n)^{205}Bi$	29.6	15.31 d
$^{89}Y(n,2n)^{88}Y$	11.6	106.7 d	$^{209}Bi(n,6n)^{204}Bi$	38.0	11.22 h
$^{89}Y(n,3n)^{87m+g}Y$	21.1	79.8 h			

code MCNP-4B [7] combined with the Monte Carlo Deuteron Lithium (McDeLi) source model [8]. In the calculation, the experimental configuration consisting of the lithium target, container, sample, copper base, cooling water system and surrounding cyclotron parts was modeled. Track length estimators (cell detectors) of 5 x 5 x 1 mm^3 were used for the tally. The Los Alamos LA-150 library [9] up to 150 MeV processed into the ACE type format for MCNP was used as transport cross sections. Since no neutron transport cross section data for lithium was available in the energy range above 20 MeV, cross section data for beryllium up to 100 MeV in the 100XS library [10] was used instead.

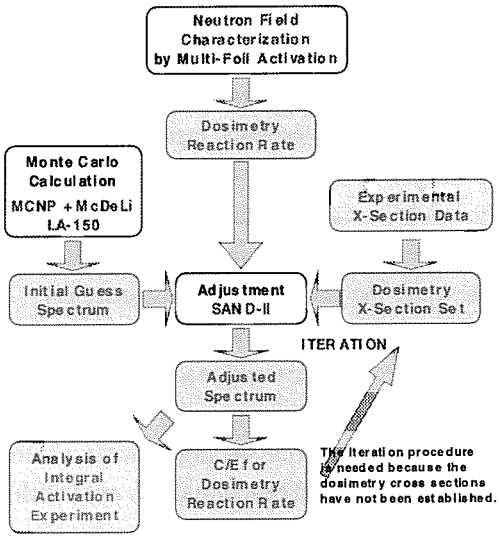

Fig. 2 Flow of the spectrum adjustment.

2.3. Spectrum Adjustment

Figure 2 illustrates a flow of a spectrum adjustment procedure presently adopted. The adjustment required a set of well known dosimetry cross sections. However, such a cross section set extending to 55 MeV was not available especially in the energy region above 20 MeV. Hence, a cross section set was tentatively produced by considering experimental cross section data [3-6], a cross section set extending to 24 MeV determined previously [11], the Intermediate Energy Activation File (IEAF) [12] up to 150 MeV evaluated at Institute of Physics and Power Engineering, Obninsk, Russia, and so on.

The initial guess spectra were adjusted by the SAND-II code [13] with the dosimetry cross section set so as to be consistent with the measured reaction rates. The SAND-II code provided ratios of calculated reaction rates with the adjusted spectrum and the cross section data to the experimental reaction rates (C/E). These C/E values distributed around 1.0 while some of them deviated more than 10 % apart from 1.0. Since the most probable reason for the deviation was lay in uncertainty in the cross section data, cross sections for the largely deviated reactions were revised within a range where consistency with

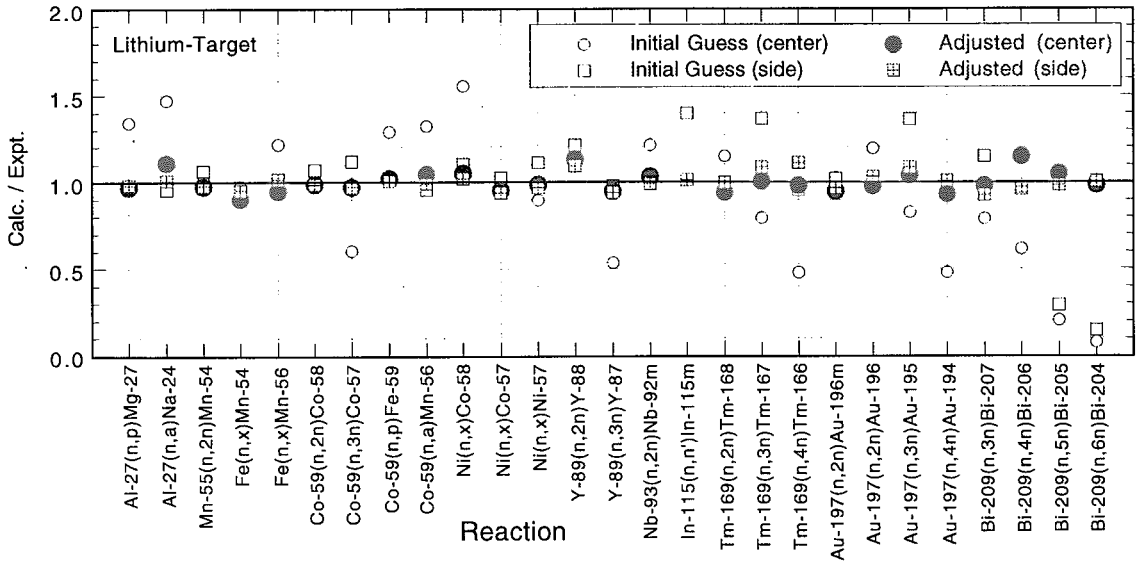

Fig. 3 The C/E values for the dosimetry reactions before and after the adjustment.

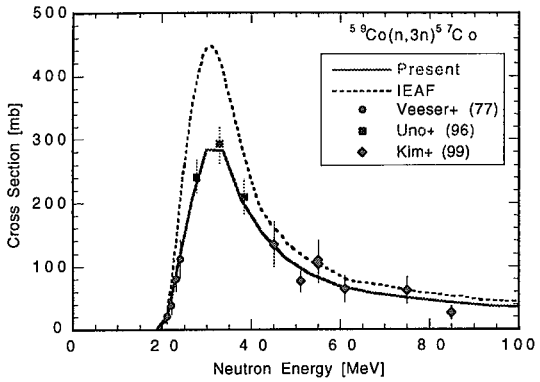

Fig. 4 The ^{59}Co(n,3n)^{57}Co reaction cross sections.

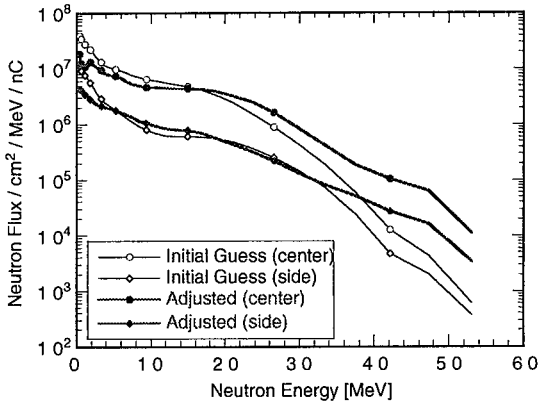

Fig. 5 The initial guess and adjusted neutron flux spectra for the d-Li neutron field.

the experimental cross section data was kept. The initial guess spectra were then adjusted again with the revised cross section data. The procedure of the adjustment and the revision of cross section data was repeated five times to attain convergence of the C/E ratios approximately in a range of 0.9 ~ 1.1 as shown in Fig. 3. An example of the dosimetry cross sections presently adopted is shown in Fig. 4, and more detailed discussion on the dosimetry cross section is given elsewhere [14].

Figure 5 compares the initial guess and adjusted neutron flux spectra at the center and side sample positions. Discrepancies between the initial and adjusted spectra can be explained by deficiencies in the calculation of initial guess spectra: omission of neutron production in the stainless steel case and the use of the beryllium cross section data for lithium. Nevertheless, the initial guess and adjusted neutron flux above 10 MeV agree within 10 % with each other for both the center and side positions. This good agreement gives experimental validation for the MCNP/McDeLi codes which are used for IFMIF neutronics designs.

3. Integral Activation Experiment

3.1. Experiment

Four samples of fusion reactor structural materials, i.e., pure-vanadium, vanadium-alloy (Ti: 4%, Cr: 4%, V: balance), SS-316LN of ITER-grade (Cr: 17.5%, Ni: 12.3%, Mo: 2.5%, Mn: 1.8%, Si: 0.4%, Fe: balance) and low activation ferritic steel F82H (Cr: 7.7%, W: 1.95%, Mn: 0.16%, V: 0.16%, Si: 0.11%, Fe: balance), were irradiated at the center position in the d-Li neutron field for 1 hour. After the irradiation, radioactivities induced in these samples were measured by the HP-Ge detector at several cooling times ranging from 1 hour to 5 months.

3.2. Low-Activation Property

Low-activation properties for the sample materials irradiated in the IFMIF-like neutron field were demonstrated. After 5 months since the irradiation, the total activity of F82H steel, 1.6 x 10^4 Bq/g, was considerably less than that of SS-316LN, 5.1 x 10^4 Bq/g, mainly due to the reduction of nickel and molybdenum content in F82H. Low-activation property was further enhanced in vanadium-based materials: the total activities after 5 months cooling were 2.9 x 10^3 Bq/g and 1.1 x 10^3 Bq/g for vanadium-alloy and pure-vanadium samples, respectively, which were less than the total activity of F82H steel by about one order.

3.3. Sequential Charged Particle Reaction

Figure 6 shows a gamma-ray spectrum for the pure-vanadium sample measured after 1 month cooling. Although vanadium does not produce ^{51}Cr via the ordinary neutron induced reactions, the strongest radioactivity observed is ^{51}Cr. Contents of impurity elements that can produce ^{51}Cr, such as chromium and manganese, are too low to explain the ^{51}Cr production. The reaction mechanism to produce ^{51}Cr in vanadium is the sequential charged particle reaction (SCPR) which is illustlated in Fig. 7. A charged particle, a proton in this case, is produced by the V(n,xp) reaction, then the proton induces the $^{51}V(p,n)^{51}Cr$ reaction sequentially. The SCPR process should be considered when we estimate radioactive inventories in low-activation materials irradiated in higher energy neutron fields.

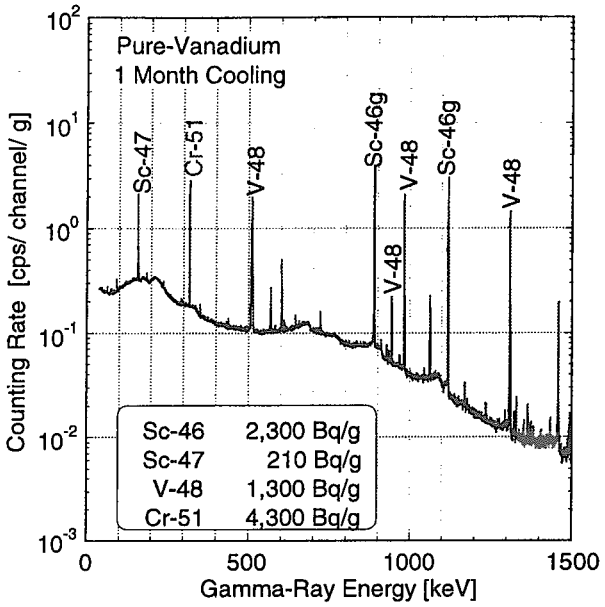

Fig. 6 Gamma-ray spectrum for the pure-vanadium sample measured after 1 month cooling.

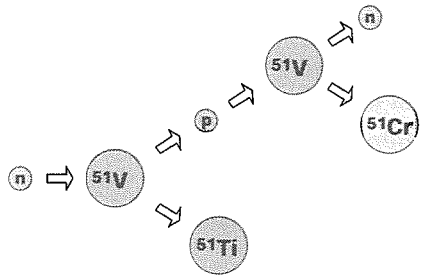

Fig. 7 Sequential charged particle reaction.

3.4. Validation of IEAF and ALARA

An experimental analysis was performed with IEAF and ALARA. The IEAF [12] is practically the only existing activation cross section library which includes activation cross section data for higher energy

Table 2 The C/E ratios of radioactivities intensely observed (> 1% to the total activity).

Nuclide	Half-Life	SS-316LN	F82H Steel	Vanadium-Alloy	Pure-Vanadium
Sc-43	3.9 hr			0.024± 30%	
Sc-44	3.9 hr			1.50 ± 20%	
Sc-46	84 d			0.91	0.77
Sc-47	3.4 d			7.73	8.67
Sc-48	44 d			0.98	1.05
V-48	16 d			1.11	1.14
Cr-49	42 min			0.75 ± 15%	
Cr-51	28 d	1.06	1.08	1.00	*0.0004*
Mn-52	5.6 d	3.28	3.78		
Mn-54	312 d	1.05	1.06		
Mn-56	2.6 hr	1.11	1.12		
Co-56	77 d	3.60	*0.02*		
Co-57	272 d	1.02			
Co-58	71 d	1.13			
Ni-57	36 hr	1.25 ± 20%			
Nb-92m	10 d				1.32 ± 30%
Mo-99	66 hr	1.26			
Tc-99m	6.0 hr	1.26			
W-187	24 hr		0.54		

Estimated experimental uncertainty ± 10% except where indicated.

neutrons beyond 20 MeV. The IEAF adopts cross section data in EAF-97 [15] in the energy range below 20 MeV. The ALARA, "Analytic and Laplacian Adaptive Radioactivity Analysis", is a radioactivity inventory calculation code developed at FZK [16].

Table 2 summarizes ratios of C/E values for radioactivities which are observed intensely (> 1% to the total activity). Tow very low C/E values, 0.0004 for ^{51}Cr in pure-vanadium and 0.02 for ^{56}Co in F82H, can be attributed to omission of the SCPR process in the calculation. The ^{56}Co is produced mainly by the ^{56}Fe(p,n)^{56}Co reaction where protons are provided by neutron induced proton emission reactions. The very large C/E values of ~ 8 for ^{47}Sc are due to a problem in the ^{51}V(n,nα)^{47}Sc cross section in EAF-97 which has been pointed out previously [17]. Except for these particular cases, the calculated values agrees with the experimental data. Accordingly, the activation cross sections in IEAF were validated experimentally by the integral activation experiment that dealt with neutrons up to 55 MeV.

References

[1] Maekawa F., et al.: "Determination of Neutron Spectra Formed by 40-MeV Deuteron Bombardment of a Lithium Target with Multi-Foil Activation Technique," to be published in *Fusion Eng. Des.* (2000).

[2] Möllendorff U., et al.: "Experimental Test of Structural Materials Activation in the IFMIF Neutron Spectrum," to be published in *Fusion Eng. Des.* (2000).

[3] Kim E., et al.: *Nucl. Sci. Eng.*, 129, pp. 209-223 (1998).

[4] Kim E., et al.: *J. Nucl. Sci. Technol.*, 36, pp. 29-40 (1999).

[5] Uno Y., et al.: *Nucl. Sci. Eng.*, 122, pp. 247-257 (1996).

[6] Uno Y., et al.: "Measurements of Activation Cross Sections for the Neutron Dosimetry at an Energy Range from 17.5 to 30 MeV by using the ^{7}Li(p,n) Quasi-Mono-Energetic Neutron Source," *Proc. 9th International Symposium on Reactor Dosimetry*, September 2-6, 1996, Prague, Czech Republic, pp. 465-472 (1998).

[7] Briesmeister J. F. (Ed.): *LA-12625-M*, Los Alamos National Laboratory (1997).

[8] Wilson P. and Fischer U.: "Analysis and Implementation of a Monte Carlo High Energy Neutron Source for IFMIF," *Proc. 19th Symposium on Fusion Technology*, Lisbon, Portugal, September 16-20, 1996, pp. 1599-1602 (1998).

[9] Chadwick M., et al.: *Nucl. Sci. Eng.*, 131, 293 (1999).

[10] Little R. C.: *LA-UR-96-24*, Los Alamos National Laboratory (1995).

[11] Maekawa F., et al.: *Fusion Technol.*, 36, 165 (1999).

[12] Korovin Yu. A., et al.: "Evaluated Nuclear Data Files for Intermediate and High Energy Applications," to be published in *Nucl. Inst. Meth. A* (2000).

[13] Mcelroy W., S. Berg and G. Gigas, *Nucl. Sci. Eng.*, 27, 533 (1967).

[14] Maekawa F., et al.: "Production of a Self-Consistent Dosimetry Cross Section Set Up to 50 MeV", *Proc. 10th International Symposium on Reactor Dosimetry*, September 12-17, 1999, Osaka, Japan , to be published (2000).

[15] Sublet J-Ch, et al.: *UKAEA FUS 351* (1997).

[16] Wilson P., et al.: *Fusion Technol.*, 34, 784 (1998).

[17] Möllendorff U., et al.: "Activation Test of Vanadium Alloys with a Deuteron-Beryllium Neutron Source," *Proc. 20th Symposium on Fusion Technology*, Marseille, France, September 7-11, 1998, pp. 1449-1452 (1998).

3.20 Measurements of double differential charged-particle production cross sections for 55,65,75 MeV neutrons

Yoshitaka Hirasawa[1],*, Mamoru Baba[1], Yasushi Nauchi[1], Masanobu Ibaraki[1]
Takako Miura[1], Tsutomu Hiroishi[1], Takao Aoki[1]
Hiroshi Nakashima[2], Shin-ichiro Meigo[2], Susumu Tanaka[3]

*E-mail : yhira@rpl.qse.tohoku.ac.jp
[1]*Department of Quantum Science and Energy Engineering, Tohoku University, Sendai 980-8579*
[2]*Tokai Establishment, Japan Atomic Energy Research Institute, Tokai-Mura 319-1196*
[3]*Takasaki Establishment, Japan Atomic Energy Research Institute, Takasaki 370-1292*

Abstract: We have performed the measurements of double differential charged-particle production cross section ((n,xz)DDXs) of iron and nickel for 55, 65, 75 MeV neutrons using the ^{7}Li(p,n) quasi-monoenergetic source of TIARA[1]. The experimental data were compared with the LA-150 data library, which agreed generally with the present data.

KERMA[2] coefficients(of Fe) were deduced from the experimental data and compared with the integral measurement and calculations by the LA-150 data library.

1 Introduction

Neutron-induced reactions play an important role in the particle transport, radiation effects in accelerator-based systems for transmutation, medicine and material research. Especially, charged-particle production reactions, (n,xz), are important to estimate neutron KERMA required for the evaluation of the radiation effects and the nuclear heating. For Fe and Ni, KERMA measured by integral measurements are generally lower than that derived from microscopic cross sections [1, 2]. To trace these problems , energy and angular distribution data are indispensable. However, experimental data are very scarce.

We are conducting experiments to obtain (n,xz)data, at a ^{7}Li(p,n) monoenergetic neutron source of TIARA [3, 4]. We reported the double differential proton and deuteron production cross sections data of aluminum and carbon for 75,65 MeV neutrons, at five angles by using SSD-NaI(Tl) telescopes, and compared the data with theoretical calculation codes [4]. Then, to expand the energy range and particle species, a wide range spectrometer was developed by Nauchi et al. [5].

In the present paper, we report double differential charged-particle production cross sections data of Fe and Ni taken by using the developed spectrometer and KERMA coefficient(of Fe) deduced from the present data.

2 Experiments

The experiments were carried out at the ^{7}Li(p,n) neutron source of TIARA, JAERI. The incident neutrons energies were 55, 65, 75 MeV. Figure 1 shows neutron source spec-

[1]Takasaki Ion Accelerator for Radiation Application
[2]Kinetic Energy Released in MAtter

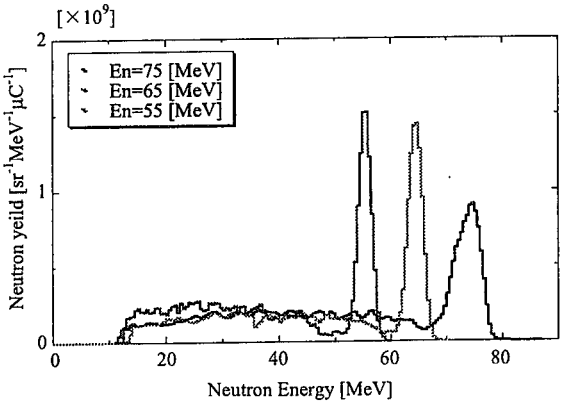

Figure 1: Neutoron source spectra

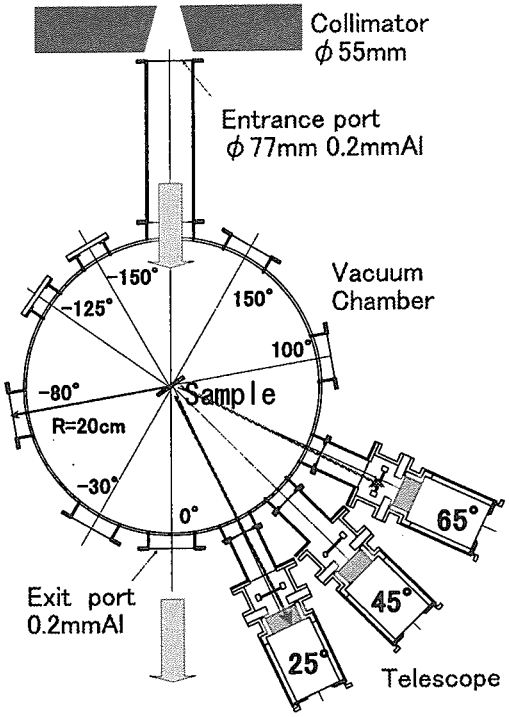

Figure 2: Experimental setup

tra, which consist of a peak part and a continuum one by break up reactions. Samples were metallic foil of elemental Fe(0.62mm×ϕ50) and Ni(0.57mm×ϕ50). The experimental setup is shown Fig.2. A spectrometer consists of three counter telescopes mounted on a vacuum chamber to reduce energy loss of secondary particles and charged particles from the air. The measurement was made mainly with a combination of a SSD(as ΔE counter) with a BaF_2 scintillator(as E counter), but α particles of a few MeV which stop in the SSD were measured by combination of a low-pressure proportional-counter(GPC, as ΔE counter) and a SSD(as E counter). The measurement angles were 25°-75° with 10° step for 75 MeV neutrons, 25°-65° with 25° step for 55 MeV neutrons, and 25°,65°,125° for 65 MeV neutrons.

We used a CAMAC system for data acquisition. Data were accumulated for 6 parameters : the pulse height(PH) of GPC, high and low gain PH of SSD, PH of BaF_2, and TOF signals of SSD and BaF_2. Valid events are chosen by either GPC-SSD coincidence or BaF_2-SSD coincidence. The signals from telescopes were amplified and converted into digital signal by voltage-type ADC. More details are described in ref. [5].

3 Data reduction

First, particle identification was made using ΔE-E spectra, then, the ^{7}Li(p,n)peak events were selected by using TOF information and pulse height of BaF_2 scintillator because the source spectra include a continuum low energy neutrons(see Fig.1). The energy scales of the spectra were determined by peak of the α particles from ^{241}Am and

protons from the H(n,p) reaction using polyethylene. Then DDX $\frac{d^2\sigma}{dEd\Omega}$ [mbMeV^{-1}sr^{-1}] was determined using

$$\frac{d^2\sigma}{dEd\Omega} = \frac{1}{\Omega N\phi}\frac{dY}{dE} \tag{1}$$

where N[#] is a number of atoms in the sample, Ω [sr] is a solid angle, ϕ [cm^{-2}] is the neutron flux obtained with a proton recoil telescope and $\frac{dY}{dE}$ [MeV^{-1}] is a measured spectrum.

We had to use thick samples to obtain acceptable counts because of limited neutron flux. Therefore, it was necessary to do energy loss correction. The correction was done using "average method" for protons, deuterons and tritons. This method was based on the relation between primary particle energy and average energy of detected particles obtained from response function by calculation. For α particles and low energy protons with large energy loss, this method was not appropriate. We applied to unfolding method based on Bayesian theorem by S.Iwasaki [6](Bayesian method).

4 Results and discussion

DDXs were obtained for proton, deuteron, triton, and α particle production for three incident energies. No experimental data of Fe and Ni are available for ten's MeV neutrons, the results are compared with the LA-150 data library [7]. Figures 3, 4 and 5 show DDXs data of Fe and Ni for 75 MeV neutrons, 65 MeV neutrons, and for 55 MeV neutrons, respectively. The solid line shows the LA-150 data library, and the present data of Ni is multiplied by 100.

The spectra have no distinct structures and are continuous. The LA-150 data agree generally with the present data, but it overestimates the high energy parts at forward angle, and this trend is enhanced especially the for deuterons, similarly in the case of the Al(n,xd)reaction [4]. In addition, it underestimates the low energy parts for deuterons at low incident neutron energy(55 MeV). Angular distributions of the LA-150 are based on the Kalbach-systematics. This angular distribution follow the present data generally.

Figure 6 shows DDXs data for α particle production of Ni and Fe. There is a same tendency that the library overestimates the high energy parts.

Figure 7 shows KERMA coefficients for Fe by the present data together with integral measurement and calculations by the LA-150 library. Partial KERMA coefficients for each type of secondary charged particle are derived by

$$k_\phi^i = \frac{C}{M_\mathrm{A}}\bar{\epsilon}_i\sigma_i^{prod} = \frac{C}{M_\mathrm{A}}\int\left[\int E\cdot\frac{d^2\sigma_i^{prod}}{dEd\Omega}dE\right]d\Omega \tag{2}$$

where σ_i^{prod}[b] is the production cross section of ejectile i, $\bar{\epsilon}_i$ is the average energy of ejectile i, M_A is the target mass, and the factor C converts partial KERMA coefficients from MeV$\cdot$b unit to S.I. units of fGy$\cdot$m^2[femto(f)=10^{-15};Gray(Gy)=Jkg^{-1}]. The calculations by LA-150 include estimations of the inelastic contribution [1]. The present KERMA coefficients are sum over proton, deuteron, triton, α partial KERMA coefficients. The KERMA coefficients deduced from the present data were deduced with interpolation of log liner for angles and for events above $\sim$ 10 MeV because energy loss correction in low

energy part was rather uncertain. The difference of KERMA according to the angular extrapolation scheme is smaller than 10%. The contribution to the KERMA coefficients of low energy part is 20-30%. The present results are smaller than both integral measurement and calculations by the LA-150 library. The energy correction in low energy part should be checked to trace the difference.

References

[1] M.B.Chadwick te al., Med. Phys., 26(1999)974

[2] I.Slypen et al., Phys. Med. biol., 40(1995)73

[3] M.Baba et al., Nucl. Instr. and Meth., A428(1999)454

[4] Y.Nauchi et al., J. Nucl. Sci. Technol., 36(1999)143

[5] Y.Nauchi et al. JAERI Conf. 99-002, (1998)

[6] S.Iwasaki, KEK Proc. 95-1(1995)319

[7] M.B.Chadwick et al., Nucl. Sci. Eng., 131(1999)293

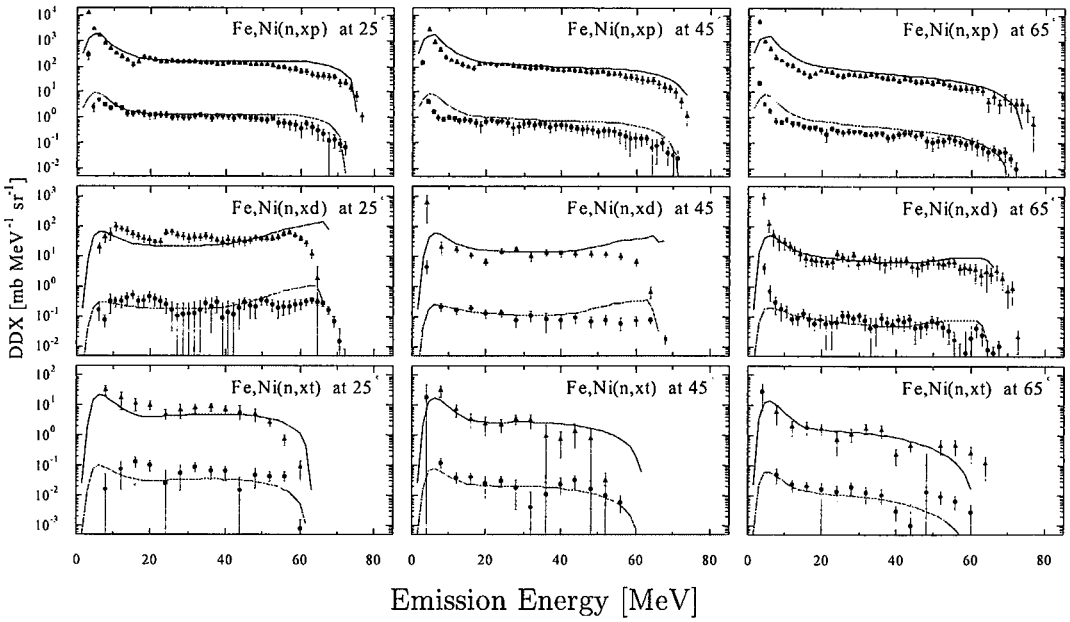

Figure 3: (n,xz)DDXs data of Ni(upper) and Fe at 25°, 45° and 65° for 75MeV neutron with LA-150 library

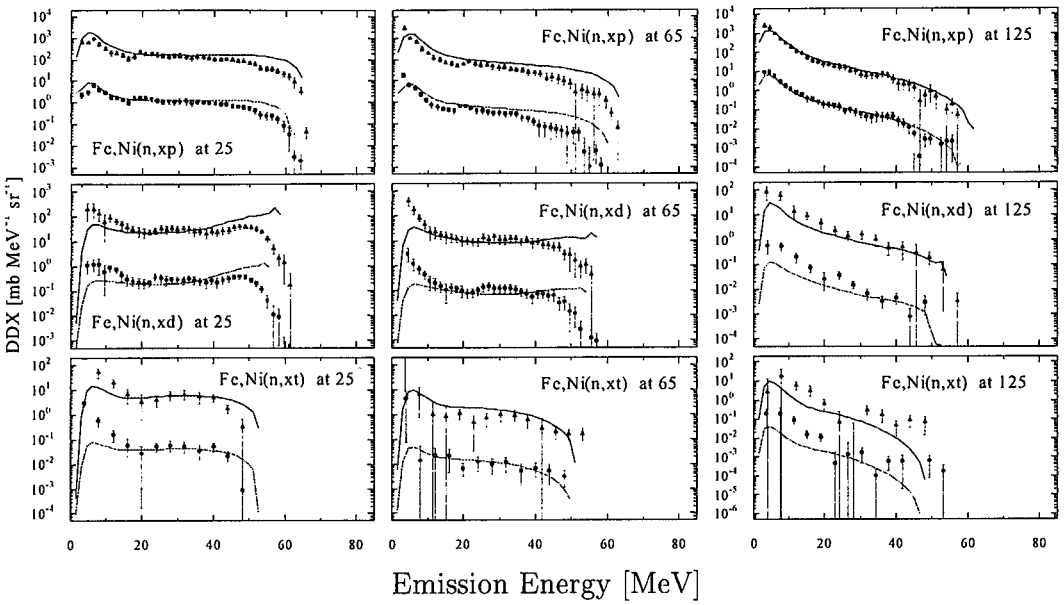

Figure 4: (n,xz)DDXs data of Ni(upper) and Fe at 25°, 65° and 125° for 65MeV neutron with LA-150 library

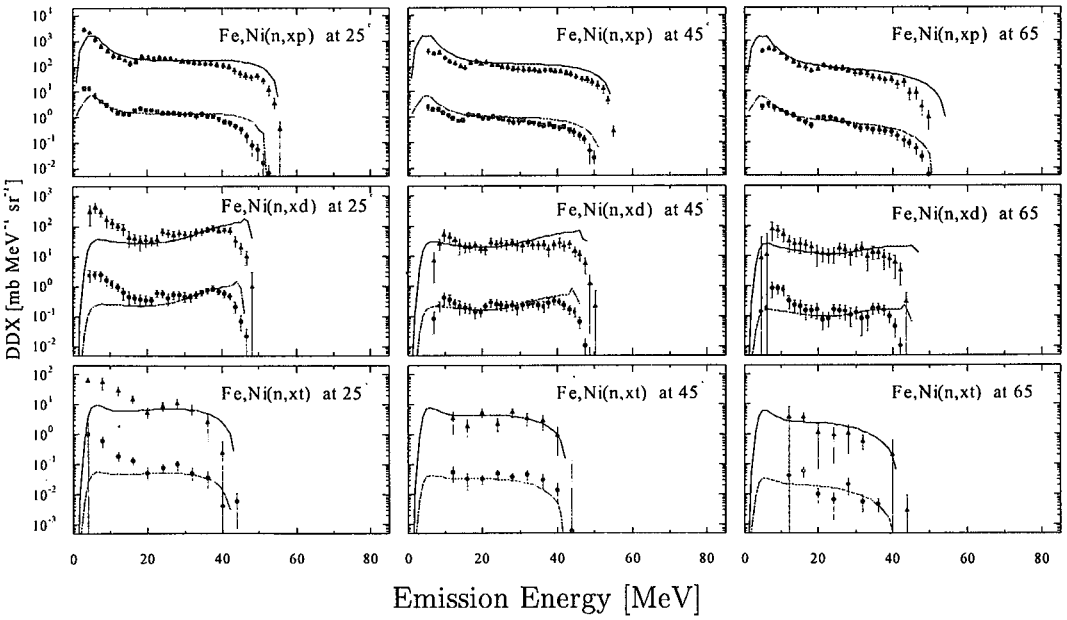

Figure 5: (n,xz)DDXs data of Ni(upper) and Fe at 25°, 45° and 65° for 55MeV neutron with LA-150 library

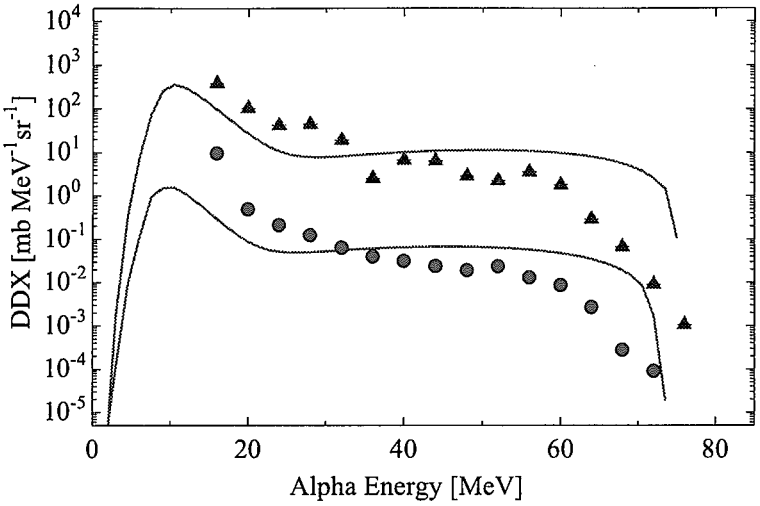

Figure 6: DDXs data for α particle production of Ni(upper) and Fe at 25° for 75MeV neutron with LA-150 library

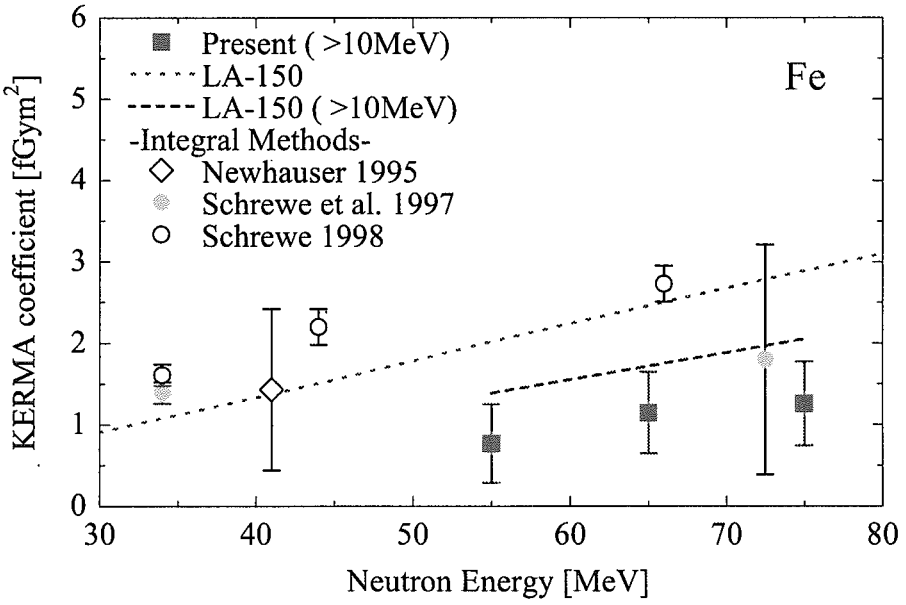

Figure 7: KERMA coefficient of Fe with integral measurement and calculations by the LA-150 data library

3.21 Projectile Dependency of Radioactivities of Spallation Products Induced in Copper

Hiroshi Yashima H. Sugita, T. Nakamura, T. Shiomi
Cyclotron and Radioisotope Center, Tohoku University, Aoba, Aramaki, Aobaku, Sendai 980-8578,Japan
e-mail:yashima@cyric.tohoku.ac.jp

Y. Uwamino
Institute of Physical and Chemical Research, Hirosawa, Wako, Saitama 351-01, Japan

A. Fukumura
National Institute of Radiological Sciences, 4-9-1, Anagawa, Inage-ku
Chiba-shi, Chiba, 263-8555, Japan

The reaction cross sections of spallation products in a Cu target by 230MeV/u C and Ne ions were obtained. Irradiation experiments were performed at HIMAC (Heavy Ion Medical Accelerator in Chiba), National Institute of Radiological Sciences. Gamma-ray spectra from activation samples were measured with a HPGe detector. From the gamma-ray spectra, we obtained the variation of reaction cross sections of Cl-38, Cr-49, Mn-55, Cu-60, Cu-61 and Co-62m in Cu sample with Cu target thickness, and compared it with the experimental data by Kim et al.. The results showed that the dependence of the cross sections to the projectile mass is very small for the same projectile energy per nucleon.

1. Introduction

Recently the high-energy and high-intensity accelerators have increasingly been used for nuclear physics, solid-state physics, radiotherapy, material damage study, and so on. Safety design consideration for the accelerator facilities requires reaction cross section data for high-energy ions to estimate the radioactivities induced in the accelerator components and in the shielding materials. We therefore irradiated 230MeV/nucleon C and Ne ions onto a Cu target, and investigated the projectile dependency of induced radioactivities of spallation products.

2. Experiment and Analysis

Irradiation experiments were performed at HIMAC (Heavy Ion Medical Accelerator in Chiba), National Institute of Radiological Sciences. A schematic view of the experimental set-up is shown in Fig.1. The Cu target was composed of a stack of 100mm×100mm×5mm Cu plates, and C, Al, Cr, Fe, Ni, Cu, Pb samples were inserted between the Cu plates. The thickness of Cu target is longer than the flight path of the projectile beam. The flight path of the projectile beam calculated by the SPAR code [1] is 10.5mm for 230MeV/u Ne and 17.4mm for 230MeV/u C. After irradiation, we measured the gamma-ray spectra from samples with a HPGe detector. Fig.2 shows a schematic view of the gamma-ray detection system. The reaction rates of radionuclides produced in samples which were identified from the gamma-ray spectra and the decay curves were estimated after being corrected for the peak efficiency of the HPGe detector and the coincidence-summing effect.

3. Results and Discussions

From the reaction rates, we obtained the reaction cross sections of Cl-38, Cr-49, Mn-56 Cu-60, Cu-61 and Co-62m in a Cu target by 230 MeV/u Ne and C ions. The results were compared with the data for 290, 400MeV/u C and 400MeV/u Ne ions by Kim [2].

Fig.3 shows the variation of reaction cross sections of Cl-38 produced in the Cu sample with Cu target thickness. In Fig.3, the reaction cross sections of Cl-38 are almost constant down to the beam flight path and rapidly decrease beyond it. The reaction cross sections of Cl-38 produced by 230MeV/u C and Ne ions are almost equal each other. Since the mass number difference between Cu and Cl-38 is large, Cl-38 is almost produced by a primary projectile beam. But, for 400MeV/u C and Ne ions, the cross sections by Ne ions are about 40% higher than those by C ions, which implies some contribution of secondary particles to the production of Cl-38.

Fig.4 shows the variation of reaction cross sections of Cr-49 produced in the Cu sample with Cu target thickness. In Fig.4, the reaction cross sections of Cr-49 increase down to the beam flight path and decrease beyond it. Since the mass number of Cr-49 becomes closer to Cu than that of Cl-38, the fraction of Cr-49 produced by secondary particles increases, but the projectile dependence of the reaction cross sections is very small for the same projectile energy per nucleon.

Figs.5 to 8 show the variation of reaction cross sections of Mn-56,Cu-60,Cu-61,Co-62m produced in the Cu sample with Cu target thickness, respectively. In these figures, the reaction cross sections of these nuclides show the similar tendency as that of Cr-49 although the cross section increase with the target thickness is much higher for lighter mass products .

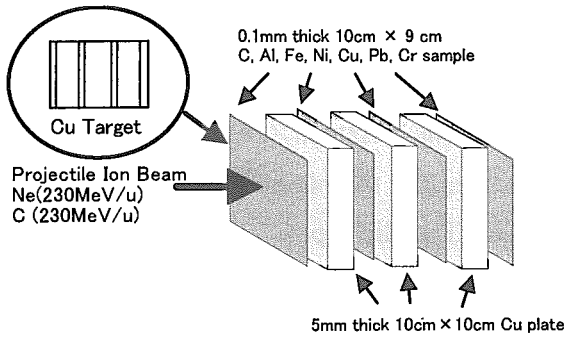

Fig.1 Schematic view of the experimental geometry.

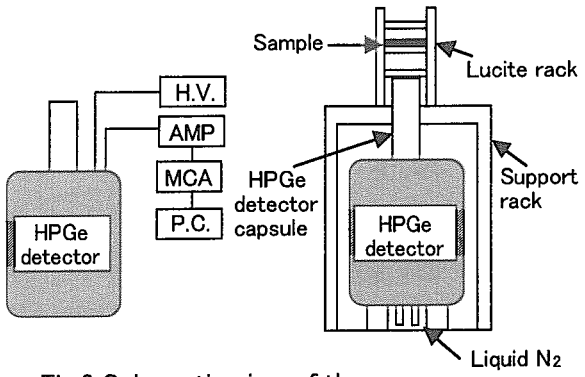

Fig.2 Schematic view of the gamma-ray detection system

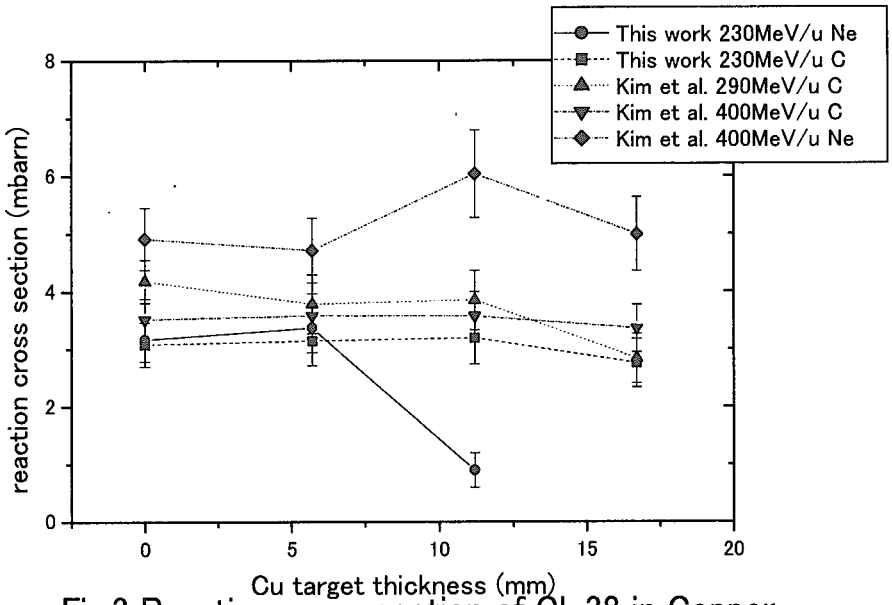

Fig.3 Reaction cross section of Cl-38 in Copper

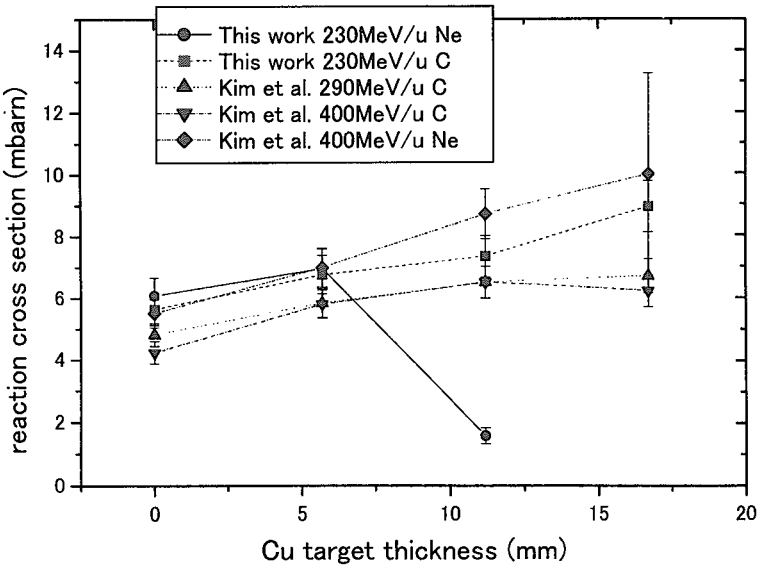

Fig.4 Reaction cross section of Cr-49 in Copper

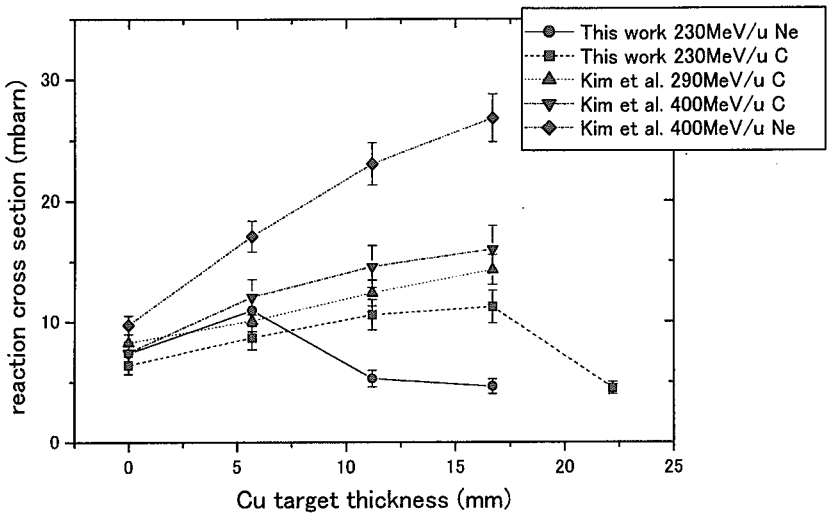

Fig.5 Reaction cross section of Mn-56 in Copper

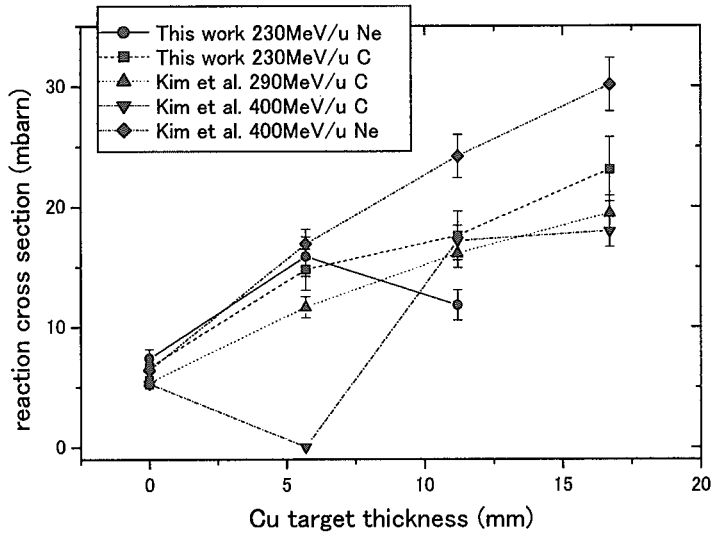

Fig.6 Reaction cross section of Cu-60 in Copper

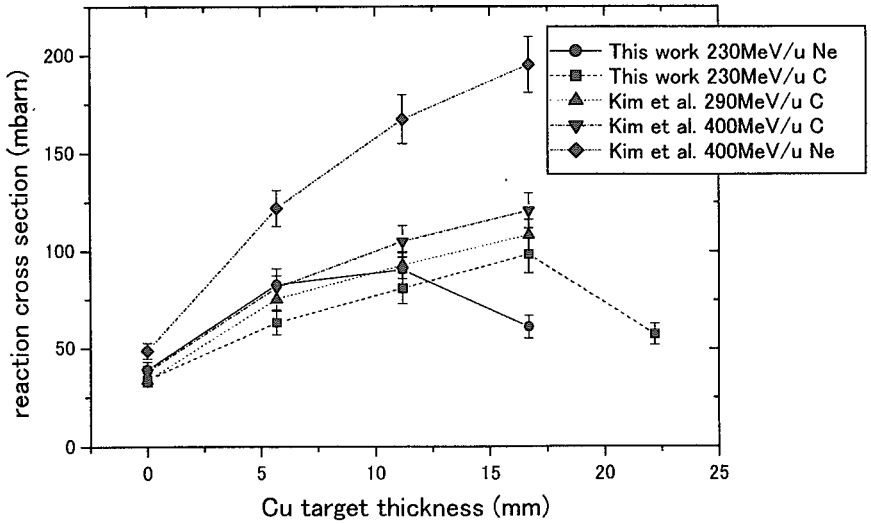

Fig.7 Reaction cross section of Cu-61 in Copper

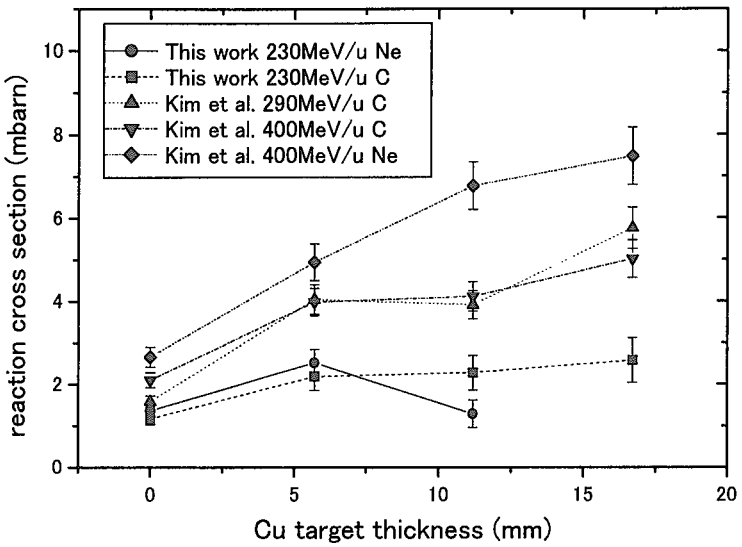

Fig.8 Reaction cross section of Co-62m in Copper

4.Conclusion

We performed the irradiation experiments by 230MeV/u Ne and C ions, and obtained the variation of reaction cross sections of nuclides produced in Cu sample with Cu target thickness. It was found that these cross sections have little dependence to the projectile mass having the same energy per nucleon. We are now analyzing the induced radioactivities produced in other samples.

Acknowledgments

We wish to thank the synchrotron machine group of HIMAC for synchrotron operation during the irradiation experiment. We are also very much obliged to the members of the Nakamura Laboratory of the Cyclotron and Radioisotope Center, Tohoku University.

References

[1] T. Nakane, Nucl. Phys., A491, 130 (1989).

[2] E. Kim, Doctor Thesis, Tohoku University, Faculty of Engineering, Department of Quantum Science and Energy Engineering, March, 1999 (in Japanese)

3.22 Measurements of Elastic Scattering and Total Non-Elastic Cross Sections for 40-80 MeV Neutrons at TIARA

Masanobu IBARAKI[(1)], Hiroshi NAKASHIMA[(2)], Shin-ichiro MEIGO[(2)], Mamoru BABA[(1)], Takako MIURA[(1)], Yoshitaka HIRASAWA[(1)], Tsutomu HIROISHI[(1)], Takao AOKI[(1)], Susumu TANAKA[(3)]

E-mail: iba@rpl.qse.tohoku.ac.jp

(1)Department of Quantum Science and Energy Engineering, Tohoku University, Sendai 980-8579

(2)Tokai Establishment, Japan Atomic Energy Research Institute, Tokai-Mura 319-11

(3)Takasaki Establishment, Japan Atomic Energy Research Institute, Takasaki 370-123

We have performed the measurements of neutron elastic scattering and total non-elastic cross sections of carbon, silicon, iron, zirconium and lead in 40-80 MeV region using a ^{7}Li(p,n) quasi-monoenergetic neutron source at TIARA of JAERI. Elastic scattering cross sections for 55, 65 and 75 MeV neutrons were measured by time-of-flight method at 25 laboratory angles between 2.6° and 53.0°. Total non-elastic cross sections for 40-80 MeV neutrons were measured by attenuation methods. The experimental data were compared with the other experimental data and the libraries.

1 Introduction

Neutron cross section data above 20 MeV become more and more important for the shielding design of the high-energy accelerator facilities, estimation of radiation damage and for various applications. Total, elastic scattering and non-elastic cross section data with appropriate accuracy are required for the evaluation of intermediate nuclear data. However, experimental data of elastic scattering and non-elastic cross section are very scarce above 40 MeV because of the experimental difficulties, in contrast to the total cross section data for which very accurate data are available[1, 2].

In this study, we have performed measurements of elastic scattering and non-elastic cross section for carbon, silicon, iron, zirconium and lead in 40-80 MeV region at TIARA facility of JAERI[3]. Elastic scattering cross sections were measured by the time-of-flight (TOF) method at 25 laboratory angles between 2.6° and 53.0° with five liquid scintillator detectors. Total non-elastic cross sections were measured by the attenuation method adopting a "close-geometry"[4, 5] and a large plastic scintillator detector. The experimental results were compared with the other experimental data and libraries.

2 Elastic Scattering Measurements

2.1 Experiment and data reduction

Measurements were done at 75, 65 and 55 MeV by using the time-of-flight (TOF) method and the ^{7}Li(p,n) quasi-monoenergetic neutron source [3]. The details of experimental and data reduction method is described elsewhere[6, 7]. Data were obtained for carbon, silicon, iron, zirconium and lead at 25 laboratory angles between 2.6° and 53.0°. The effects of inelastically scattered neutrons were corrected by calculating the fraction of the inelastic neutrons to the total (sum of the elastic and inelastic) ones considering experimental energy resolution using the LA 150 data [8].

2.2 Results

Figure 1 shows the results of carbon, iron and lead in comparison with the data reported by the U.C.Davis group[9, 10]. They measured neutron elastic scattering cross sections for 65 MeV by a ^{7}Li(p,n) source and 52.5-225 MeV by a spallation neutron source. By adopting the TOF method with a longer flight path at TIARA facility, our data cover much wider angular range than that of Davis ones. In comparison of 65 MeV data, the Davis's data for iron around 25° differ from the present one by about 40%, while they are in good agreement for other elements. The Davis's data by spallation source were restricted to angular range of 7°-23°, and show milder distribution than our results.

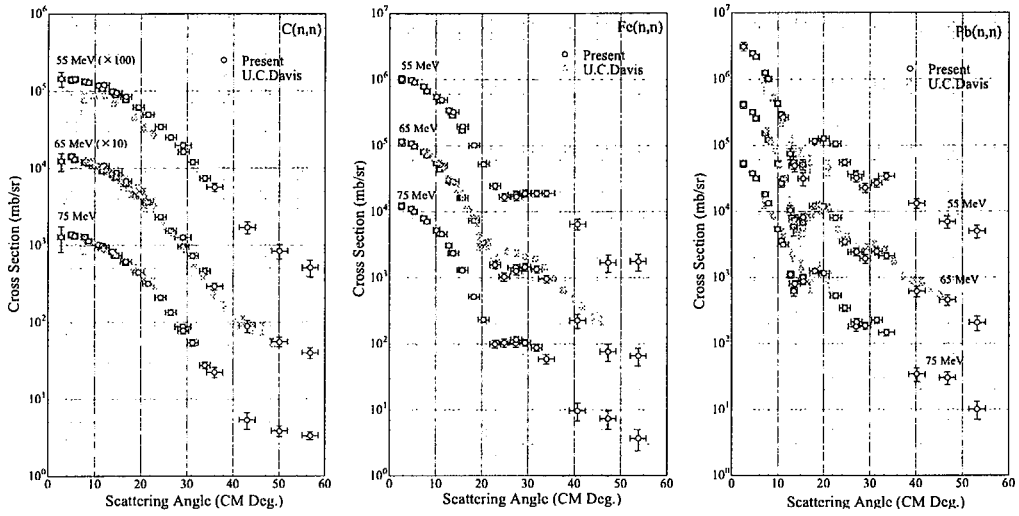

Figure 1: Elastic scattering cross sections of C(n,n), Fe(n,n) and Pb(n,n) in comparison with U.C.Davis data

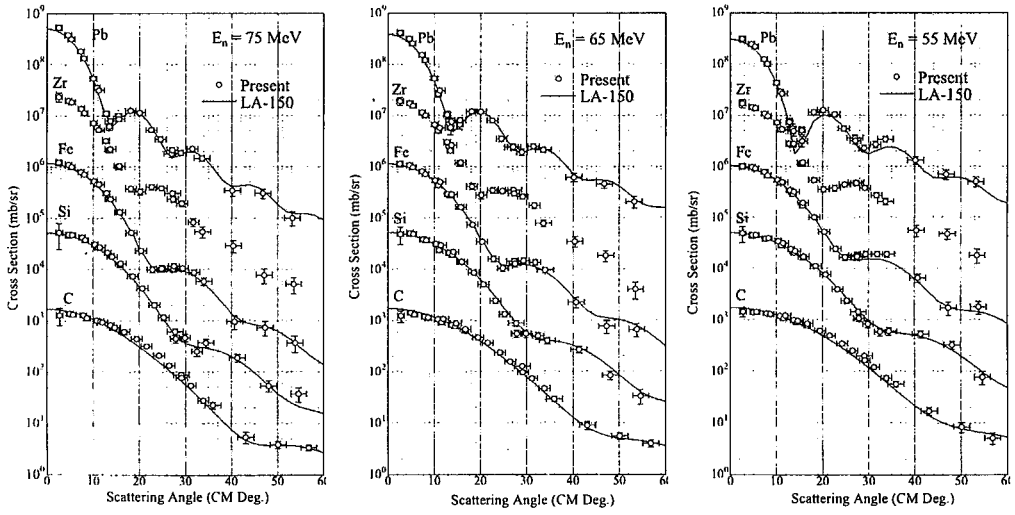

Figure 2: Elastic scattering cross sections in comparison with LA 150

Figure 2 shows the present result in comparison with the LA 150 data[8]. LA 150 is the evaluated neutron and proton cross section library up to 150 MeV. The neutron optical potentials by A.S.Meigooni et al.[11] for carbon, D.G.Madland[12] for silicon and iron, R.E.Shamu and P.G.Young[13] for lead, are used, in this energy region. In general, LA150 data agree well with the present results for all nuclei and incident energies, but in detail, are smaller by 10-15% for Pb at forward angles.

Figure 3 shows angle-integrated elastic scattering cross sections in comparison with the LA150 data, Pearlstein's systematics[14] and other experimental data. The present angle integrated cross sections were deduced by least-square fitting of optical model calculation using a code, *ECIS88*, to each differential cross section. LA 150 data agree well present data except for lead, ~10% smaller.

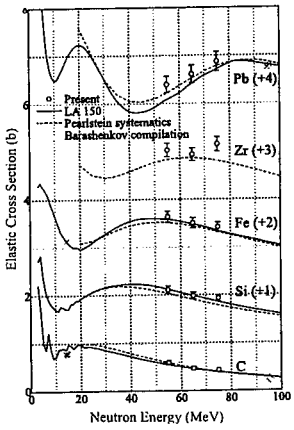

Figure 3: Angle integrated elastic scattering cross sections

3 Total Non-elastic Measurements

3.1 Experiment and data reduction

Neutron total non-elastic cross sections of carbon,silicon, iron, zirconium and lead were measured in 40-80 MeV region based on the attenuation method adopting with "close-geometry"[4, 5]. Figure 4 shows the setup of the total non-elastic measurements. In this method, the neutron detector subtends large solid angle to the sample, and detects both the transmitted neutrons which did not receive any reaction in the sample and most of the elastically scattered neutrons by the sample. The total non-elastic cross section was deduced by following equation while some corrections are needed,

$$\sigma_{ne} \approx -\ln(I_m/I_0)/(Nt), \tag{1}$$

where I_0 is the incident neutron flux measured by the sample-out run, I_m is the neutron flux transmitted through the sample measured by the sample-in run. The thickness of the samples, t, 3~4cm, was chosen so that $\exp(-\sigma_{ne}Nt) = 0.8 \sim 0.9$. The neutron beam was collimated to 1 cm diam. by iron so that the beam spot was smaller than the diameter of the samples, 2 cm. The transmissions, I_m/I_0, were obtained concurrently for 40-80 MeV neutrons by using a peak and continuous part of the ^{7}Li(p,n) neutron source with E_p=80 MeV [3]. We used an NE 102 plastic scintillator, 20.3cm $\phi\times$ 7.6cm, located at 12 cm or 18 cm from the sample. The detector subtending a large angle, θ_{max}=30~40°, intercepted most of the elastically scattered neutrons, 95% typically. Table 1 shows the structure of the energy bin and the detector threshold energy. The threshold for each incident neutron energy was selected as a compromise between the detector efficiency and the effects of inelastically scattered neutrons.

Table 1: Structure of the energy group and detector threshold

E_n(MeV)	75	65	60	55	50	45
ΔE_n(MeV)	72.5-78.5	62.5-67.5	57.5-62.5	52.5-57.5	47.5-52.5	42.5-47.5
Bias(MeV)	50	40	30	30	20	20

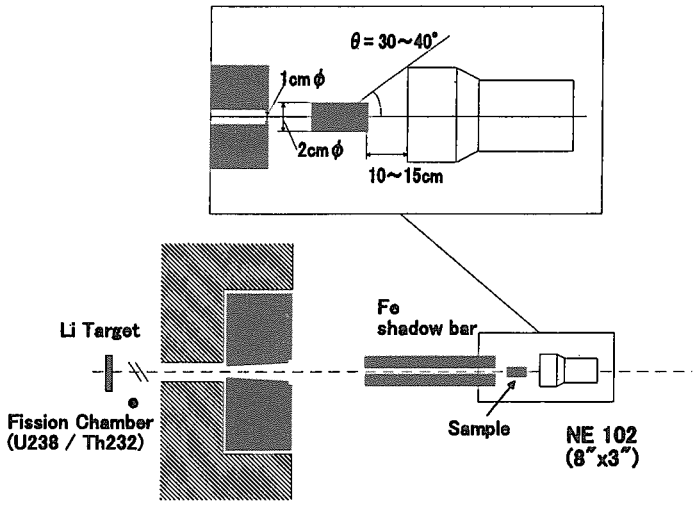

Figure 4: Experimental set up of total non-elastic cross section measurement

Figure 5 shows the attenuated (sample-in, iron) and direct (sample-out) TOF spectra. The I_m and I_0 for each energy group were deduced by integrating over the corresponding ROI in TOF spectra. To deduce total non-elastic cross section, the corrections were considered for the probabilities of 1) the neutrons elastically scattered to the angles larger than θ_{max}, $f_1 = \frac{1}{\sigma_{el}} \int_{\theta_{max}}^{\pi} d\Omega \frac{d\sigma_{el}}{d\Omega}$, 2) the neutrons inelastically scattered to the angles smaller than θ_{max}, $f_2 = \frac{1}{\sigma_{ne}} \int_{E_b}^{E_{in}} dE \int_0^{\theta_{max}} d\Omega \frac{d^2\sigma_{nx}}{d\Omega dE}$, where E_b is detector threshold energy and 3) the neutrons elastically scattered to the angles smaller than θ_{max} are not detected because of multiple-scattering, $f_3 = \frac{1}{\sigma_{el}} \int_0^{\theta_{max}} d\Omega \frac{d\sigma_{el}}{d\Omega}(1 - e^{-\sigma_t N \overline{x}}) \frac{\sigma_{ne}}{\sigma_t}$, where $\overline{x}$ is mean path length in the sample. To calculate $f_{1,2,3}$, we used the experimental data[1, 2] for total cross section and the LA 150 data[8] for the angular distribution of elastic scattering. The experimental total cross sections have relatively small uncertainties, 1% or smaller, and the elastic scattering cross sections of LA 150 reproduce the experimental data as seen in Fig.2. Because f_3 explicitly includes the σ_{ne} we want, we made iterative calculations to find a solution. Typically, f_1, f_2 and f_3 were respectively 2%~10%, 4%~8% and 4%~10% but depend on the neutron energy and sample. The corrected cross section was deduced by the following equations.

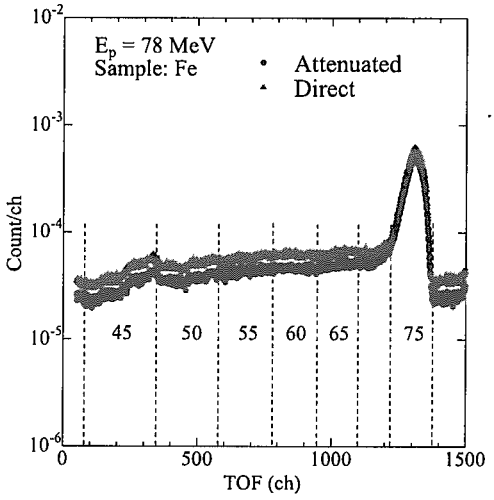

Figure 5: Attenuated (sample-in) and direct (sample-out) TOF spectra

$$\frac{I_m}{I_0} = e^{-\sigma_t N t} + (1 - e^{-\sigma_t N t}) \frac{1}{\sigma_t}((1 - f_1 - f_3)\sigma_{el} + f_2 \sigma_{ne}), \quad (2)$$

then we substitute $\sigma_t - \sigma_{ne}$ to σ_{el},

$$\sigma_{ne} = \frac{\frac{\frac{I_m}{I_0}-1}{1-e^{-\sigma_t N t}} + f_1 + f_3}{f_1 + f_2 + f_3 - 1}\sigma_t \tag{3}$$

where σ_t is experimental total cross section[1, 2]. Figure 6 shows the comparison with raw and corrected total non-elastic cross sections. The differences between corrected and uncorrected data are 5% to 15%.

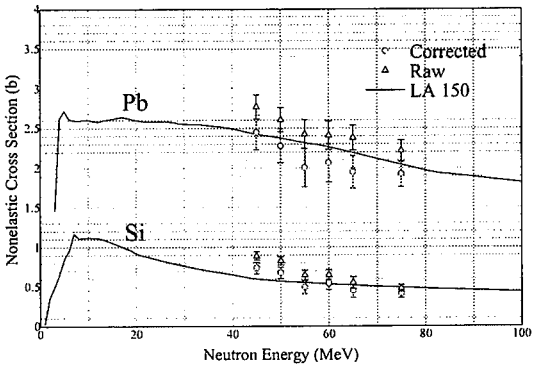

Figure 6: Comparison with raw and corrected total non-elastic cross sections

3.2 Results

Figure 7 shows the present results in comparison with other experimental data, Pearlstein's systematics[14] and LA 150 data. The circles are deduced from the present (n,n) data by subtracting the present elastic scattering cross section from well-known total cross section[1, 2]. The data by our two experiments agree each other with experimental uncertainties except for zirconium at 75 MeV. The present experiment provide the data at 40-80 MeV region where there were only few experiments, and are useful to verify the calculations. Above 50 MeV, our results supports the LA 150 data and systematics except for lead case. For lead, the present results are close to systematics rather than the LA 150 data which are larger by 15% in 50-80 MeV region. Figure 8 shows the present results for lead in comparison with proton data as well as neutron one. The present results are close to proton data by LA 150 and experiments, and neutron total-nonelastic cross sections by LA 150 seem to be too large.

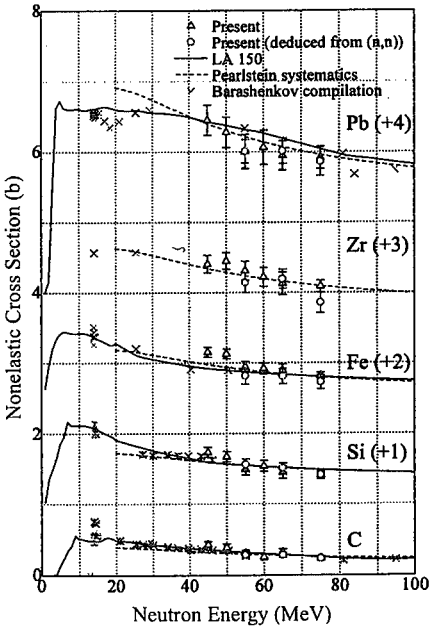

Figure 7: Total non-elastic cross section

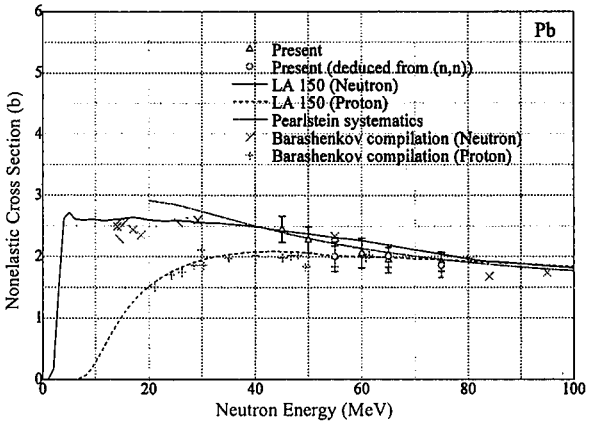

Figure 8: Total non-elastic cross sections for lead

4 Summary

Neutron elastic and total non-elastic cross sections were measured in 40-80 MeV region by TOF and attenuation methods, respectively. Elastic scattering measurements were done for 75, 65 and 55 MeV neutrons, and the data at 25 laboratory angle points between 2.6° and 53.0° were obtained. LA 150 reproduced the elastic scattering cross sections very well except for lead at very forward angles. The total non-elastic cross sections by two experiments were consistence within experimental uncertainties. LA 150 data reproduced experiments very well except for lead, ~15% larger of total non-elastic cross sections.

References

[1] R.W.Finlay et al., Phys. Rev. C 47 (1993) 237

[2] F.S.Dietrich et al., Proc. Int. Conf. on Nuclear Data for Sci. and Technol, 1997 Trieste, (1998) p.402

[3] M.Baba et al., Nucl. Instrum. and Methods A 428 (1999) 454

[4] R.G.P.Voss and R.Willson, Proc. Phil. Soc. (London), A 236 (1956) 41

[5] F.P.Brady et al., Nucl. Instrum. and Methods, 178 (1980) 427

[6] M.Ibaraki et al., Nucl. Instrum. and Methods A, to be published.

[7] M.Ibaraki et al., Proc. Ninth International Conf.on Rad. Shielding (ICRS9), 1999 Tsukuba, to be published.

[8] M.B.Chadwick et al., Nucle. Sci. Eng. 131, (1999) 293

[9] E.L.Jort et al., Phys. Rev. C 53 (1996) 237

[10] J.H.Osborn, Dissertation, University of California, Davis (1995)

[11] A.S.Meigooni et al., Nucl. Phys. A, 445 (1985) 305

[12] D.G.Madland, Proc. OECD/NEANDC Specialist's Mtg. on Preeq. Nucl. Reac., 1988 Semmering, NEANDC-245 (1988)

[13] R.E.Shamu and P.G.Young, J. Phys. G 19 (1993) L169

[14] S.Pearlstein, Astrophys. Jounal, 346 (1989) 1049

3.23 Measurements of Neutron Spectra Produced from a Thick Tungsten Target Bombarded with 1.1 and 2.3 GeV/c Protons and π^+ Mesons

Shin-ichiro Meigo*,†, Hiroshi Takada*, Nobuhiro Shigyo**, Kiminori Iga**, Yousuke Iwamoto**, Hirohiko Kitsuki**, Kenji Ishibashi**, Keisuke Maehata**, Hidehiko Arima**, Tatsushi Nakamoto*** and Masaharu Numajiri***

*Center for Neutron Science, Japan Atomic Energy Research Institute
Tokai-mura, Naka-gun, Ibaraki-ken 319-1195

**Department of Applied Quantum Physics and Nuclear Engineering, Kyushu University
Hakozaki, Higashi-ku, Fukuoka 812-8581

***High Energy Accelerator Research Organization (KEK)
Oho, Tsukuba, Ibaraki 305-0801 Japan

e-mail: †meigo@linac.tokai.jaeri.go.jp

For the validation of the nucleon-meson transport code, spectra of neutrons produced from a thick tungsten target bombarded with 1.1 and 2.3 GeV/c protons and π^+ mesons were measured. The calculated results with NMTC/JAERI97 was compared with the present experimental results. It is found the NMTC/JAERI97 generally shows in good agreement with experiment for protons and pions incident. However, for the neutrons in the energy region between 20 and 100 MeV, the NMTC/JAERI97 shows 50 % underestimation of the experiment, which is consistent with the results of lead target.

1. Introduction

Applications of high energy particle accelerators are rapidly growing in many fields such as spallation neutron source and accelerator driven system. For the design of the target and shielding of the accelerator facilities, it is necessary to estimate the reaction rate and the neutron production in a thick medium in the energy region up to several GeV. Nucleon-Meson Transport codes such as NMTC/JAERI[1, 2] and LAHET[3] have been widely employed for the neutronics calculation.

It is generally known that the codes can describe the particle productions and the transport in a thick medium. The accuracy of the codes, however, has not been completely satisfactory yet. In order to comprehend and improve the accuracy of the code, studies[4]have been performed from both the theoretical and the experimental points of view. A series of the measurements of neutron production double differential cross sections were carried out at LANL and High Energy Accelerator Organization (KEK)[5]. For the spectrum of the thick target, the spectrum of neutrons produced from a thick lead target was measured[6]. The experiment data of the spectrum are, however, very scarce for incident energies higher than 256 MeV.

For the validation of the calculation code employed in the design of the accelerator facilities, it is required the spectrum of neutrons produced from a thick target which is longer than the mean free path of the outgoing particles. However, these experimental data were scarce for the projectiles above 0.8 GeV, especially for pion projectiles measurements have not been performed. In this study, the spectrum produced in the tungsten target bombarded with 1.1-

and 2.3 GeV/c protons and π^+ mesons was measured. These experimental data were compared with the calculation of NMTC/JAERI.

2. Experimental procedure

2.1 Incident particles and target

The experiment was carried out at the $\pi 2$ beam line of the 12-GeV Proton Synchrotron at KEK in a series of double differential neutron production cross section measurements[7]. Schematic view of the experimental arrangement is shown in Fig. 1. The incident particles were supplied as the secondary particle generated by an internal target which was placed in the primary 12-GeV proton beam. After passing the bending magnet, the secondary beam having a unique momentum was introduced to the thick target. The interval between and duration of the primary proton pulses were 4 and 2.5 s, respectively. The intensity of the incident particles was so weak ($\leq 10^5$ particles/pulse) that incident particles were counted one by one with beam scintillators. As incident projectiles, 1.1 and 2.3 GeV/c protons and π^+ mesons were employed, whose energies are 0.5- and 1.5- GeV for protons and 0.96- and 2.1- GeV for π^+, respectively. The incident particles were identified by the time-of-flight (TOF) technique with a pair of scintillators (Pilot U) located at a separation distance of 4 m. The size of the incident beams was 2.0 and 1.6 cm in FWHM on the perpendicular and horizontal plains, respectively. Each Pilot U scintillator was connected with two photomultipliers on opposite sides to obtain good time resolution. Čerenkov detector was employed so as to eliminate the μ^+ from the π^+ projectiles. In order to subtract the neutrons produced from the beam scintillator, background measurements were performed without target.

A tungsten target was bombarded by the proton and π + beams. The target was a rectangular parallelepiped $15\times15\times20$ cm^3 whose purity was 94.81%. It was thick enough to stop 0.5-GeV protons completely, while it caused the partially energy loss for other projectiles. For 1.5-GeV protons, 0.96- and 2.1-GeV π^+ mesons, the average energy deposition is 1.0, 0.49 and 0.56 GeV, respectively.

2.2 Neutron detector

As neutron detectors, NE213 scintillators(12.7 cm in diam. and 12.7 cm in thick.) were used. The detectors were placed at angles of 30°, 60°, 90°, 120° and 150° to the beam axis and at a common distance of 1.5 m from the center of the target. At the angle 15°, the distance was chosen 2.0 m so that the higher energy resolution was achieved. In order to reject the detection of the charged particles (i.e. π, p, d), NE102A scintillators of $17\times17\times1$ cm^3 were used as veto counters. They were placed at a distance of 2 cm from the surface of the NE213 scintillators. The pulse height of the neutron detectors was calibrated using gamma-rays from ^{137}Cs, ^{60}Co and ^{241}Am-Be.

As the neutron detection efficiency, the calculation results of SCINFUL-R[8] were used. Hence, the results of SCINFUL-R were utilized for detection efficiencies below 80 MeV. Above 80 MeV, the calculated efficiency of CECIL[9] adjusted to connect smoothly with that of SCINFUL-R at 80 MeV was employed. The detection efficiencies for ^{60}Co and ^{137}Cs biases were employed for the analysis of the neutron spectrum above and below 20 MeV, respectively.

2.3 Electronic Circuit

The diagram of the electronic circuit is shown in Fig. 2. A personal computer (PC-AT) was utilized for controlling CAMAC ADCs and TDCs. The events arising from μ^+ projectiles were

eliminated by the unti-coincidence of all beam scintillators. The number of incident particles was accumulated by the scaler. A good discrimination for the incident proton against the π^+ was achieved so that the uncertainty of the incident proton counts could be less than 1 %.

Anode signals of the photomultipliers coupled with NE213 scintillators were branched out to three pulses. One pulse was put into a CFD to produce the start signal of TOF measurement. Other two pulses were put into three ADCs (Fast, Total) which collected the charge of pulse during each gate signal duration. In order to eliminate gamma-ray counting, the two-gate integration method was adopted. After the elimination of the photons, the TOF spectrum of the neutrons was obtained.

3. Calculation

The neutron spectrum calculation was carried out with NMTC/JAERI97[2] and MCNP-4A. NMTC/JAERI97 calculated the nuclear reactions and the particle transport above 20 MeV. MCNP-4A calculated the neutron transport below 20 MeV using a continuous energy cross section library FSXLIB-J3R2 processed from the nuclear data file JENDL-3.2 In NMTC/JAERI97, the Pearlstein's systematics[10] was implemented to estimate total, elastic and non-elastic nucleon-nucleus cross sections in the transport calculation part. The level density parameter derived by Baba[11] was also employed in the statistical decay calculation in NMTC/JAERI97.

Furthermore, additional calculations were performed by substituting the in-medium nucleon-nucleon cross sections (NNCS) for the free NNCS in the nuclear reaction calculation part of NMTC/JAERI97. The in-medium NNCS parametrized[12] similarly to those of Cugnon[13] were employed in this calculation.

In order to compare the experimental results, the calculation results are smeared with the energy resolution. By the comparisons of both results with and without smearing, it is found that the effect of the energy resolution on the spectra is smaller than 25 % for the energy up to 150 MeV.

4. Results and Discussion

4.1 Neutron spectra produced from the tungsten target

The calculated results with the NMTC/JAERI97-MCNP-4A code system are compared with the present experimental results shown in Figs. 3 and 4 for protons and Figs. 5 and 6 for π^+ mesons, respectively. It is observed that the calculation with the free NNCS (shown by solid lines in the figures) is in good agreement with the experiment at an energy region below $\sim$10 MeV for both incident energies. In an energy range 20 and 80 MeV, free NNCS , however, gives about 50 % or more lower than that of the experiment.

On the other hand, the calculation with the in-medium NNCS (shown by dot lines in the figures) gives much better agreement with the experiment in the an energy region above 20 MeV. This improvement is ascribed to the fact that the high energy nucleon emission is enhanced in the calculation because the mean free path of nucleon in a target nucleus is estimated longer by in-medium NNCS than the free one. It is simply because of being smaller n-p cross sections. The enhancement of high energy nucleon emission diminishes the excitation energy of a residual nucleus so that the neutron emission from the evaporation process is suppressed. Consequently, the calculation gives slightly lower neutron flux than the experiment does for the energy range below 10 MeV for 0.5 GeV protons. For the backward emission of neutron above 20 MeV, the underestimation still remains.

4.2 Consistency with lead target results

In order to comprehend the discrepancy between calculation and experiment, here we discuss the results comparing with the results for the study on lead target[6]. In the result of the lead target, the same discrepancy between the calculation with free NNCS and experiment was found above 20 MeV. Furthermore, it is reported in Ref. [6] that the calculation using in-medium NNCS improves the transport of secondary particles in that energy region. The result obtained from the comparison between calculation and experiment of the tungsten target is consistent with those of the lead target.

In Ref [6], the calculated result of double-differential cross sections of the Pb(p,xn) reaction were compared with the experiment. The calculations using both free and in-medium NNCS gave good agreement with the experiment as same as the calculations for the thick target using in-medium NNCS. For the neutrons in the energy region between 20 and 80 MeV, the difference between those calculations for the thin target was smaller than the difference for the thick target. As a result, these facts will suggest that the calculation using in-medium NNCS improves the transport of secondary particles in the energy region above 20 MeV.

The calculation of the differential cross sections showed that the results for the backward neutron emission, however, gave smaller results than the experiment. By this fact, the underestimation for the thick target at deeper angles can be explained. A study [12] suggested that the inclusion of the pre-equilibrium process or the refraction and reflection process improved the backward neutron emission significantly. It is, thus, anticipated that the disagreement for the thick target will be reduced by the inclusion of those processes.

5. Conclusion

For the validation of the nucleon meson transport code, the neutron spectra from a thick lead target bombarded with 1.1- and 2.3-GeV/c protons and π^+ mesons were measured at 6 angles between 15° and 150°. The accurate neutron spectra were obtained in the energy region between 2 and 150 MeV by the time-of-flight technique.

The calculation was carried out with the NMTC/JAERI97-MCNP-4A code system. It was found that results showed fairly good agreement with the experiments, but gave about 50 % lower neutron flux in the energy region between 20 and 80 MeV. This discrepancy was consistent with the result of lead target. For the neutrons between 20 and 80 MeV, the calculation using with the in-medium nucleon-nucleon cross sections(NNCS) reproduced the experiment fairly well. It suggests that the calculation by using in-medium NNCS improves the agreement with the experiment for the transport of particles. By the inclusion of pre-equilibrium process or the refraction and reflection process, a better agreement with the experiment can be anticipated for the backward neutron emission.

References

[1] Nakahara Y. and Tsutsui T.: JAERI-M 82-198 (1982).

[2] Takada H. et al.: JAERI-Data/Code 98-005 (1998).

[3] Prael R. E. and Linchtenstein H.: LA-UR 89-3014 (1989).

[4] Intermediate Energy Nuclear Data: Models and Code, Proc. of OECD/NEA Mtg., Paris (1994).

[5] Ishibashi K., et al.: *J. Nucl. Sci. Technol.*, **34** 529 (1997).

[6] Meigo S. et al.,: *Nucl. Instr. and Meth. A* **431** 521 (1999).

[7] Iwamoto Y., et al.: Presented in this symposium.

[8] Meigo S.: it Nucl. Instrum. Meth., **A401**, 365 (1997).

[9] Cecil R. A., et al.: *Nucl. Instrum. Meth.* **161** 439 (1979).

[10] Pearlstein S.: *Astrophys. J.*, **346** 1049 (1989).

[11] Baba H.: *Nucl. Phys.*, **A159** 625 (1970).

[12] Takada H. : *J. Nucl. Sci Technol.*, **33**, 275 (1996).

[13] Cugnon J., Mizutani T. and Vandermeulen J.: *ibid.*, **A352**, 505 (1981).

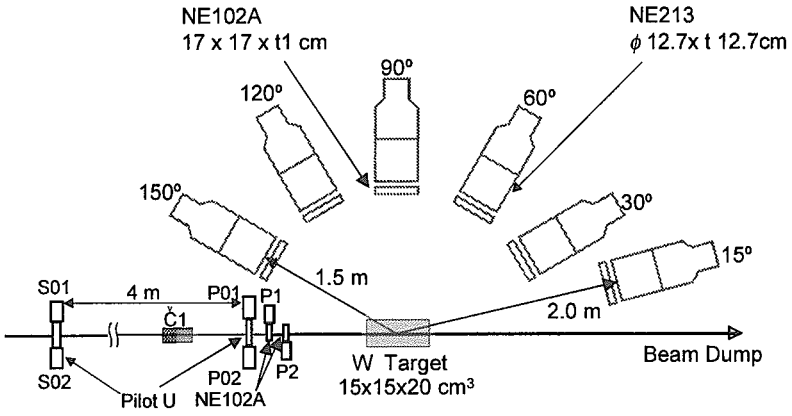

Fig. 1: Illustration of the experimental arrangement.

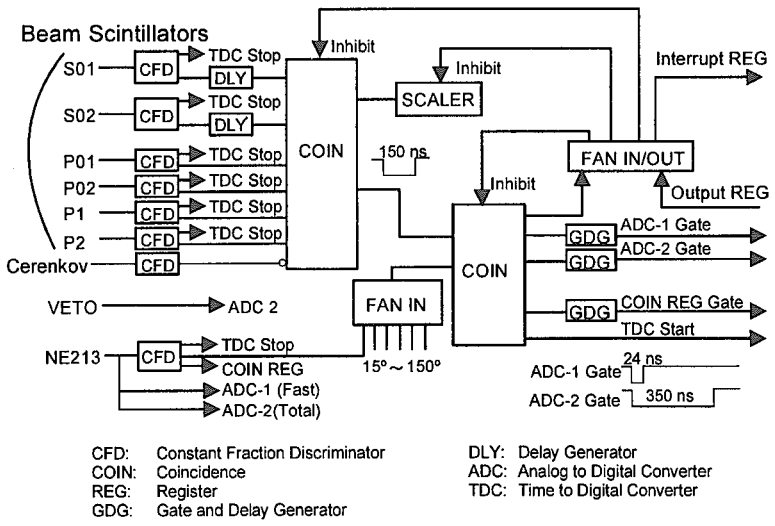

Fig. 2: Diagram of the electronic circuit used in the present experiment.

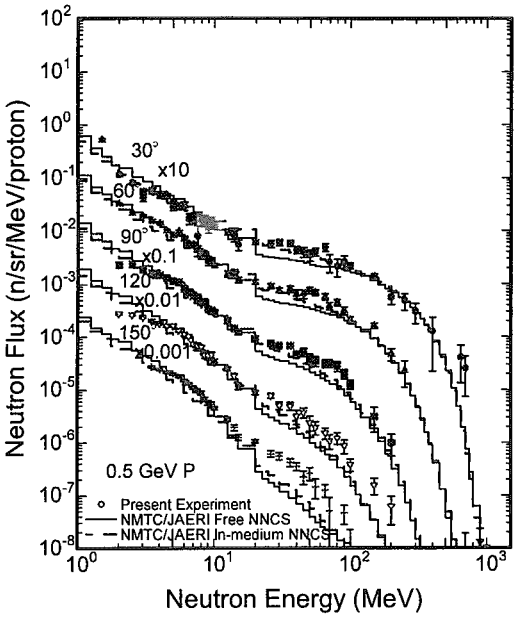

Fig. 3: Comparison of neutron spectra for 0.5-GeV protons between NMTC/JAERI97 and present experiment.

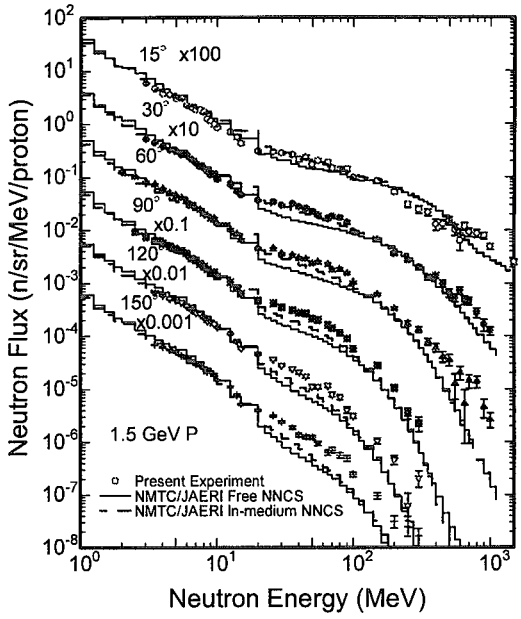

Fig. 4: Comparison of neutron spectra for 1.5-GeV protons between NMTC/JAERI97 and present experiment.

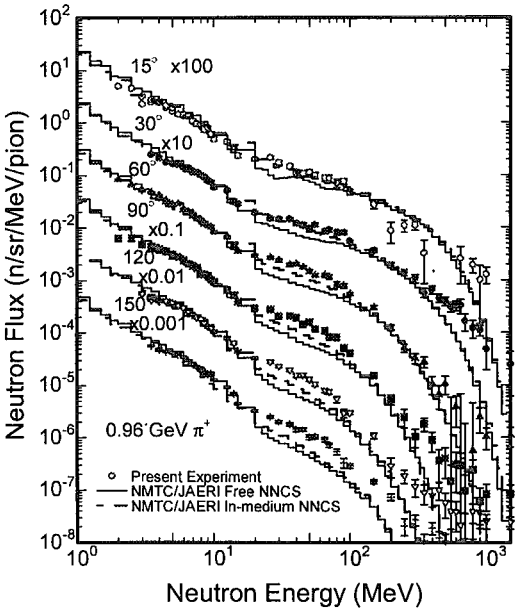

Fig. 5: Comparison of neutron spectra for 0.9-GeV π^+ mesons between NMTC/JAERI97 and present experiment.

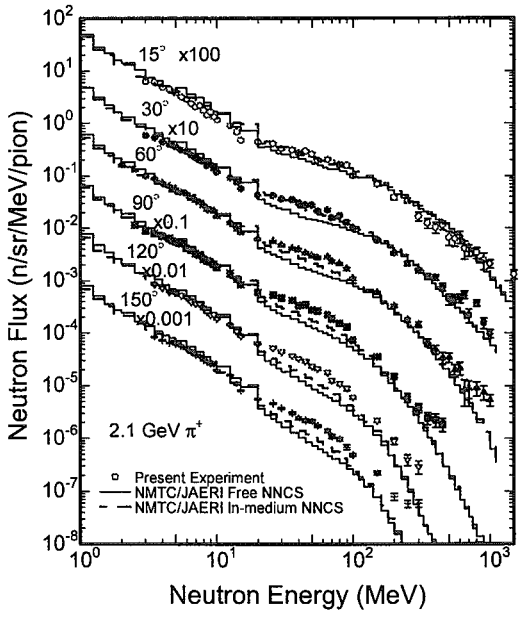

Fig. 6: Comparison of neutron spectra for 2.1-GeV π^+ mesons between NMTC/JAERI97 and present experiment.

3.24

Measurements of Photo-Neutron Energy Spectra from Thick Targets Produced by Irradiation of 2.0 GeV Electron Beam

Tatsuhiko Sato[1], Kazuo Shin[1], Ryuta Yuasa[1], Syuichi Ban[2], and Heeseock Lee[3]

1:*Department of Nuclear Engineering, Kyoto University, Yoshida, Sakyo, Kyoto 606-8501, Japan*
E-mail: tatsu@nucleng.kyoto-u.ac.jp
2:*High Energy Accelerator Research Organization (KEK), Oho, Tsukuba, Ibaraki, 305-0801, Japan*
3:*Pohang Accelerator Laboratory, POSTECH, Nam-gu, Pohang, 790-784, Korea*

ABSTRACT

Photo-neutron spectra produced by 2.04 GeV electron incident on thick Al, Cu, Sn and Pb targets were measured by TOF method. A Pb attenuator was placed at the middle point of the flight path to suppress γ-flash signals. The thickness of the attenuator was changed from 10 cm to 30 cm for each target, and the effects of the attenuator on the neutron spectra were calculated by a combination of small changed LAHET2.7 code and ENDF-HE/VI data. Obtained neutron spectra are larger than calculated values predicted by a combination of EGS4, our modified PICA95 and LAHET2.7 codes.

1 Introduction

Recently high-energy electrons have been used rather widely for Synchrotron Orbital Radiation and other purposes. They produce high-energy photons as bremsstrahlung, and induce photospallation reactions in a beam stop. Therefore, photo-neutron spectra data are indispensable not only for a better understanding of the reaction mechanisms but also for the safety of electron accelerators.

Over the years, a lot of measurements of photo-neutron yield above the giant resonance region were carried out. However, only a few experiments [1]−[4] were to measure their energy spectra. Bremsstrahlung induced by striking electron beams into thick targets were used as photon source. Most of the other photo-neutron measurements were for evaluating total cross section of photo-nuclear reaction by summing up cross section of all neutron emitted channels. Pseudo mono-energetic photons were usually used for these cases.

In general, time of flight (TOF) method is adopted to measure neutron energy spectrum emitted from a beam bombarded target. However, it is difficult to measure the photo-neutron spectrum because of too large electromagnetic background. Especially, photo-neutrons with high energies are very hard to be measured because those neutrons tend to reach a detector within the detector dead time caused by strong γ-flash signals.

On the other hand, several calculation codes (CEM95, [5] DINREG, [6] FLUKA, [7] MARS, [8] and PICA95 [9] etc.), which are able to predict high energy photo-neutron spectrum, have been developed. These codes are based on the intra-nuclear cascade evaporation model except for DINREG. However, there is large discrepancy between calculated spectra by those codes because detail calculation models are different from code by code. Therefore, it is very hard to decide the most sophisticated model because of the lacking of the experimental data.

From these considerations, a photo-neutron spectra produced by 2.04 GeV electron incident on thick targets were measured by TOF method. A Pb attenuator was placed at the middle point of the flight path to suppress the electromagnetic background, and the effects of the attenuator on the spectra were calculated by a combination of LAHET2.7 code [10] with small modification and

ENDF-HE/VI data. [11] The obtained results are compared with calculated spectra by a combination of EGS4, [12] our modified PICA95, [13] and LAHET2.7 codes. The detail experimental procedures are described in Section 2. Analyses and discussions about the obtained results are given in Section 4. The final section is for conclusions.

2 Experimental Procedures

1. Geometry

The experiments were performed at the injection linac in Pohang Accelerator Laboratory. A simplified schematic diagram of the experimental set-up is shown in fig.1. An Al, Cu, Sn and Pb target was placed in front of the accelerator tube window, and its thickness was 8.0, 14.0, 12.1 and 5.5 cm, respectively. The distance between the window and the center of the targets was 21.0 cm.

2. Beam Status

The 2.04 GeV electron beam from the accelerator is focused on a center of the target about 2 cm diameter. The beam frequency was 10 Hz and the pulse width was 1 nsec. The beam intensity measured by a wall-current monitor was approximately 500 pC/pulse. The integrated currents during each measurement were monitored by current integrator. The accuracy of the integrator was confirmed by an activation measurement of Au foils, which were inserted in the Pb target. The foils were irradiated by the electron beam for 22 minutes. After the irradiation, yields of ^{196}Au in the Au foils were determined by measuring their activities. Comparing these values with calculated ones which were evaluated by EGS4 and our modified PICA95, it was found out that the error associated with the current integrator was less than 5 %. The detail description of this checking method was written in our previous paper. [14]

3. Detector Efficiency

A detector of PILOT-U (2 inchϕ ×2 inch) was located at a fixed angle of 90 degrees to the beam axis and 557.5 cm separation from the target. The detector was surrounded by a Pb collimator whose outside and inside diameter are 30 cm and 6 cm, respectively. Since the discriminate level was set to 4.2 MeVee checked by an Am-Be reference source, the lower limit of measurable neutron energy was approximately 9 MeV. The higher limit was approximately 300 MeV.

The detector efficiency was calculated by SCINFUL [15] for neutron energy below 80 MeV, and Cecil's code [16] for above the energy. It should be noted that the calculated values by SCINFUL were for NE110 efficiencies, and the values by Cecil's were for NE213 values because the calculation codes were not adapted to PILOT-U. The results by Cecil's code were normalized to those by SCINFUL at the neutron energy 80 MeV because the performance of PILOT-U was closer to that of NE110 compared with NE213. For a determination of the effect of the surrounded collimator, and also for a confirmation of the calculated results, the efficiency of the detector with the collimator were measured for neutron energies 14.9, 33.0, 64.7, 66.0, 86.5, and 132.0 MeV. The measurements were performed by using quasi-monoenergetic neutron sources of four different facilities, OKTAVIAN [17] for neutron energy 14.9 MeV, CYRIC [18] for 33.0 MeV, TIARA [19] for 64.7 MeV, and RIKEN [20] for other energies. The obtained efficiencies were shown in fig.2.

From the figure, it is obvious that the experimental values agree with the calculated ones well.(within 15%) It means that the effects of the Pb collimator surrounded the detector are almost negligible to the detector efficiency. This results are consistent with Bahr's result. [21] From these consideration, we can say the calculated efficiency is enough precise to be used in the analysis of the photo-neutron spectra.

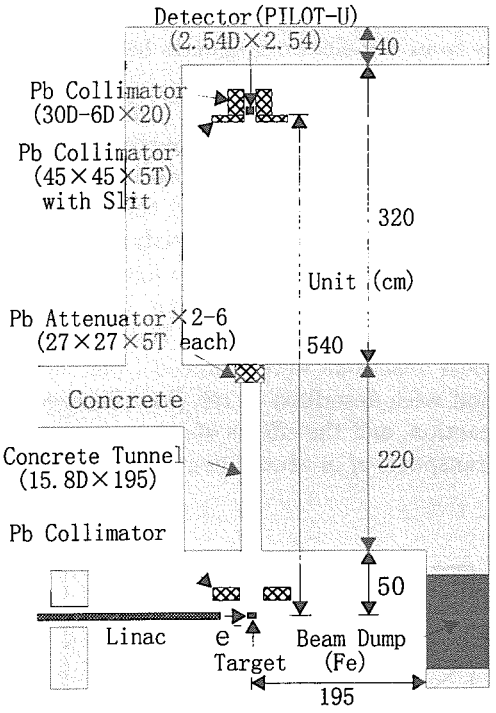

Fig.1 Experimental arrangement.

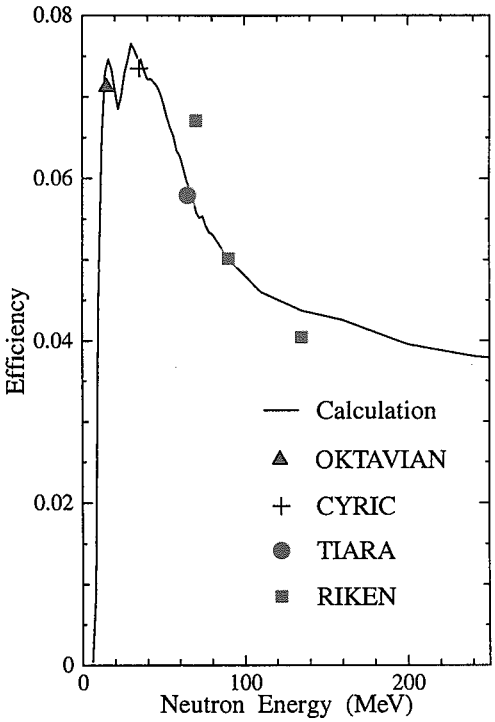

Fig.2 Measured and calculated detector efficiency.

4. Attenuator Effect

Neutrons emitted from the target were collimated by passing through a lead and concrete collimator of 10 cm and 220 cm thickness, respectively. A lead attenuator was placed at the end of the concrete collimator to suppress the electromagnetic background. The thicknesses of the attenuator for the cases of the Cu, Sn and Pb targets were changed from 15 cm to 30 cm at an interval of 5 cm. However, the data of high and low neutron energy part for 15 cm attenuator case were not reliable due to too large electromagnetic background. The thicknesses for the Al target case were 5 cm or 10 cm because radiation length of the Al target was much smaller than those of the other targets.

The effects of the attenuator on the neutron spectra were determined by calculating probabilities of neutrons getting to the detector after passing through the attenuator. The detail calculation method of the probability was described in other paper. [22] The neutron spectra at the target surface can be evaluated from the probabilities and detected neutron spectra.

3 Results and Discussion

For a confirmation of the attenuator effects, and checking an accuracy of the experiment, the yields at the Sn target surface for several neutron energy bins are plotted in fig. 3 as a function of the attenuator thickness. Those yields are normalized to the values for 25 cm attenuator cases. The errors are only associated with the counting statistics. From the figure, it is found out that the yields are almost independent of the attenuator thickness for neutron energy between 10 MeV and 300 MeV.

Since neutrons with energies above 300 MeV tend to reach the detector within the detector dead time caused by the strong γ-flash specially for thinner attenuator cases, the yield for the energy region becomes larger by increasing of the attenuator thickness. On the contrary, the yields of neutrons with energies below 10 MeV become smaller by increasing of the thickness. It is due

to an increasing of the number of the neutron whose light output is above the threshold level by decreasing of the attenuator thickness, since light outputs from the electro-magnetic background are added to the value from the neutron.

Obtained photo-neutron spectra at the Al and Pb targets surfaces are shown in fig. 4. The attenuator thickness is 10 cm and 25 cm for the case of the Al and Pb target, respectively. The errors are also associated with the counting statistics only. There may be an additional 10 % and 15 % of systematic errors at maximum in the value of the current monitor and the detector efficiency, respectively. Calculated values corresponding to the experimental data evaluated by a combination of EGS4, our modified PICA95, and LAHET2.7 were also shown in the figures.

The photon, electron and positron track length in the targets were calculated by EGS4. Photo-neutron production cross sections were evaluated by our modified PICA95. Neutron production cross sections of electron-nuclear or positron-nuclear reactions were deduced from those of photo-nuclear ones. The detail methods of the evaluation were described in ref. [14]. However, almost all the neutrons were produced by photo-nuclear reaction, and the effects of other reactions were only a few percents of the total neutron yields. The transports of produced neutrons, protons, and pions in the targets were calculated by LAHET2.7.

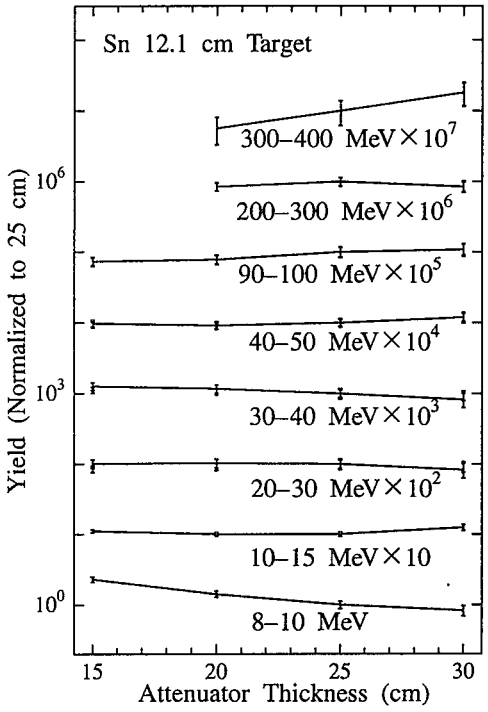

Fig.3 Photo-neutron yields of the Sn target as a function of the attenuator thickness. Those yields are normalized to the values for 25 cm attenuator cases.

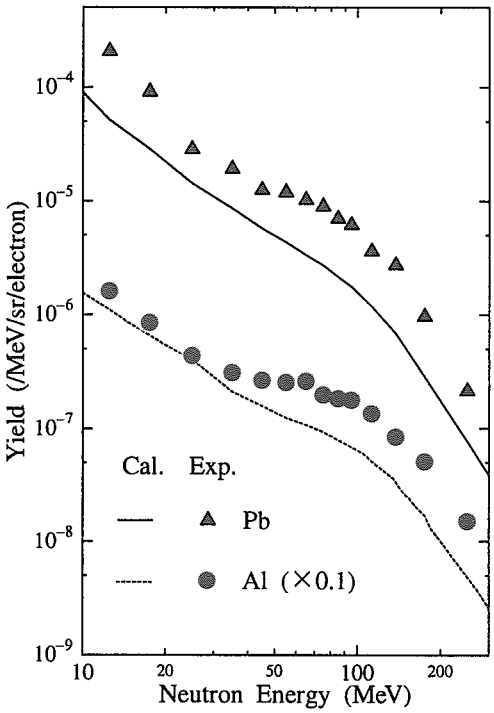

Fig.4 Photo-neutron spectra at the Al and Pb targets surfaces

Comparing experimental data with the calculated ones, it is obvious that the calculated values underestimate the experimental ones. This discrepancy is clearly seen for neutron energy less than 20 MeV, and greater than 50 MeV. This tendency is also observed for the other targets' cases.

One reason of the discrepancy for lower energy neutron yields is an ignorance of pre-equilibrium process in the PICA95 calculation. Neutrons having an intermediate energy (greater than an average energy of neutron produced by evaporation process, and less than that by direct process) are mainly produced by the pre-equilibrium process. Therefore, the ignorance of the process causes an underestimation of the neutron yields below 20 MeV.

The reason of the discrepancy for higher energy neutron yields has not been figured out. One considerable reason is an underestimation of quasi-deuteron disintegration (QDD) for incident photon energies above 150 MeV, because the average kinetic energy of emitted neutrons produced by the reaction is higher than the value by Δ resonance. The QDD reaction mechanism proposed by Levinger [23] is the dominant photo-nuclear reaction for incident photon energies between 30 MeV and 150 MeV. The modified PICA95, which adopts the model, can reproduce the experimental total photo-nuclear reaction cross section for the energy region very well. [13] However, there is no experimental data to prove the accuracy of the model above 150 MeV because Δ resonance become a dominant reaction for the energy region, and it is very hard to extract the QDD reaction contribution from experimental data. Another considerable reason is a difference between experimental and calculated angular distributions of emitted neutrons. However, both of them can not explain such a large discrepancy sufficiently.

4 Conclusions

The photo-neutron spectra produced by striking 2.04 GeV electron into various thick targets were measured by placing a Pb attenuator at the middle point of the TOF flight path, and the obtained spectra are almost independent of the attenuator thickness for neutron energies between 10 MeV and 300 MeV.

The neutron spectra calculated by a combination of EGS4, our modified PICA95, and LAHET2.7 underestimate the experimental ones. This discrepancy is clearly seen for neutron energy less than 20 MeV, and greater than 50 MeV. One reason of the discrepancy for lower energy neutron yields is an ignorance of pre-equilibrium process in the PICA95 calculation. The reason for higher energy neutron yields has not been figured out.

More experimental data, especially the yields for higher and lower neutron energies which can not be measured in these experiments, are required. The spectra for other angles are also needed because the angular distribution of emitted neutron may become a key to solve the discrepancy between experimental and calculated results. Recently, we have performed a similar experiments by using longer flight path (10.4 m) to obtain the spectra with better energy resolution. The results of the experiments will be published soon.

References

[1] W. C. Barber, and W. D. George, Phys. Rev. 116, 1551 (1959).

[2] N. N. Kaushal, E. J. Winhold, P. F. Yergin, H. A. Medicus, and R. H. Augustson, Phys. Rev. 175, 1330 (1968).

[3] J. A. Rawlins, C. Glavina, S. H. Ku, and Y. M. Shin, Nucl. Phys. A122, 128 (1968).

[4] H. J. von Eyss, and G. Luhrs, Z. Phys. 262, 393 (1973).

[5] S. G. Mashnik, A. J. Sierk, O. Bersillon, and T. A. Gabriel, "Cascade-Exciton Model Detailed Analysis of Proton Spallation at Energies from 10 MeV to 5 GeV", LA-UR-97-2905, Los Alamos National Laboratory (1997).

[6] P. Degtyarenko, "Application of the Photonuclear Fragmentation Model to Radiation Protection Problems", Proc. SATIF-2, Geneva, 12-13 October, 1995, p.67.

[7] A. Fasso, A. Ferrari, J. Ranft, and P. R. Sala, "An Update about FLUKA", Proc. SARE-2, Geneva, 9-11 October, 1995, p.158.

[8] O. E. Krivosheev and N. V. Mokhov, "New MARS and Its Applications", Proc. of SARE-3, Tsukuba, 7-9 May, 1997, p.12.

[9] C. Y. Fu, "PICA95, An Intra-Nuclear Cascade Code for 25-MeV to 3.5-GeV Photon-Induced Nuclear Reactions", presented at SATIF-3, Sendai, 12-13 May, 1997.

[10] R. E. Prael and H. Lichtenstein, "User's Guide to LCS: The LAHET Code System", LA-UR-89-3014, Los Alamos National Laboratory (1989).

[11] ENDF/HE-VI, Evaluated Nuclear Data Files W3 Retrieval System, National Nuclear Data Center (NNDC), 1998. WWW address: http//www.nndc.bnl.gov/.

[12] W. R. Nelson, H. Hirayama and D. W. O. Rogers, "The EGS4 Code System", SLAC-265 Stanford University, Stanford (1985).

[13] T. Sato, K. Shin, S. Ban, Y. Namito, H. Nakamura, and H. Hirayama, Nucl. Inst. Meth. A437, 471 (1999).

[14] T. Sato, K. Shin, S. Ban, Y. Namito, H. Nakamura, and H. Hirayama, Nucl. Inst. Meth. A401, 476 (1997).

[15] J. K. Dickens, "SCINFUL: A Monte Carlo Based Computer Program to Determine Scintillator Full Energy Response to Neutron Detection for E_n between 0.1 and 80 MeV: User's Manual and FORTRAN Program Listing", ORNL-6462, Oak Ridge National Laboratory (1988).

[16] R. A. Cecil, B. D. Anderson, and R. Madey, Nucl. Inst. Meth. 161, 439 (1979).

[17] K. Sumita *et al.*, "Osaka University 14 MeV Intense Neutron Source and Its Utilization for Fusion Studies" Proc. 12th Symp. Fusion Technology, Julich, 13-17 September, 1982, Vol.1, p.681.

[18] M. Takada, T. Nakamura, M. Baba, T. Iwasaki, and T.Kiyosumi, Nucl. Inst. Meth. A372, 253 (1996).

[19] JAERI TIARA Annual Report Vol. 1 (1992), JAERI-M 93-047(1993).

[20] N. Nakao *et al.*, Nucl. Inst. Meth. A420, 218 (1999).

[21] C. Bahr *et al.*, Nucl. Inst. Meth. A411, 430 (1998).

[22] T. Sato, K. Shin, R. Yuasa, S. Ban, H. S. Lee, and G. N. Kim, "Experimental Setup for Measurements of High Energy Photo-Neutron Spectra from Thick Targets", presented at ICRS-9, Tsukuba, 17-22 Oct. 1999.

[23] J. S. Levinger, Phys. Rev. 84, 43 (1951).

3.25 Measurement of Neutron Production Cross Sections by High Energy Heavy Ions

H. Sato T. Kurosawa, H. Iwase, T. Nakamura
Cyclotron and Radioisotope Center,Tohoku University,Aoba,Aramaki,Aobaku,Sendai 980-8578,Japan
e-mail:hisaki@cyric.tohoku.ac.jp

N.Nakao
High Energy Accelerator Research Organization, Tsukuba, Ibaraki 305-0801, JAPAN

Y.Uwamino
Institute of Physical and Chemical Research, Hirosawa 2-1, Wako, Saitama, JAPAN

The double-differential cross section (DDX) of neutron production from thin C, Al, Cu, Pb targets bombarded by 135MeV/nucleon C ion were measured using the RIKEN Ring Cyclotron of the Institute of Physical and Chemical Research, Japan. The neutron energy spectra were obtained by using the time-of-flight method coupled with the ΔE-E counter telescope system. The ΔE counter of the NE102A plastic scintillator was used to discriminate charged particles from noncharged particles, neutrons and photons. The E counter of the NE213 liquid scintillator was used to measure the neutron energy spectra. The experimental spectra were compared with the calculation using the HIC and the QMD codes.

1. INTRODUCTION

Recently, the use of high-energy heavy ions have been increasing in various fields. To design the accelerator facility, it is important to protect workers from radiation, particularly penetrating neutrons produced by high energy heavy ions. There exist a few published data on the double-differential cross sections (DDX) of neutron production for 337 MeV/nucleon Ne ions on C, Al, Cu, U targets [1], but still very poor. In this work we present the double-differential cross sections (DDX) of neutron production from thin C, Al, Cu, Pb targets bombarded by 135MeV/nucleon C ion. These results will be useful as a benchmark experimental data to investigate the accuracy of high energy particle transport calculation code. Here, the measured spectra are compared with the calculation using the two heavy-ion Monte Carlo codes of internuclear-cascade and evaporation model (HIC) and the quantum molecular dynamics model (QMD).

2. EXPERIMENT

The measurements were carried out at the RIKEN Ring Cyclotron, the Institute of Physical and Chemical Research. A schematic view of the experimental set-up is shown in Fig.1. The NE213 liquid scintillator (12.7cm diameter by 12.7cm thick), which was designed to expand the dynamic range of output pulses for high energy neutron measurements, was used for E counter, and the NE102A plastic scintillator (15cm by 15cm square and 0.5cm thick) for ΔE counter was placed in front of the E counter to discriminate charged particles from noncharged particles, neutrons and photons. The target thicknesses are 1mm of C, 0.6mm of Al, 0.3mm of Cu, 0.3mm of Pb. The direction of incident beam was rotated around the target from 0 to 110 degrees through the beam swinger, for measuring the energy-angle distribution of neutrons produced from the target by the time-of-flight (TOF) method having the flight path of 847cm. In order to shield the spurious scattered neutrons, the neutrons from the target were introduced to the detector through the iron-concrete collimator of 120cm thickness. The measurements were carried out at 0° ,15° ,30° ,50° ,80° and 110° .

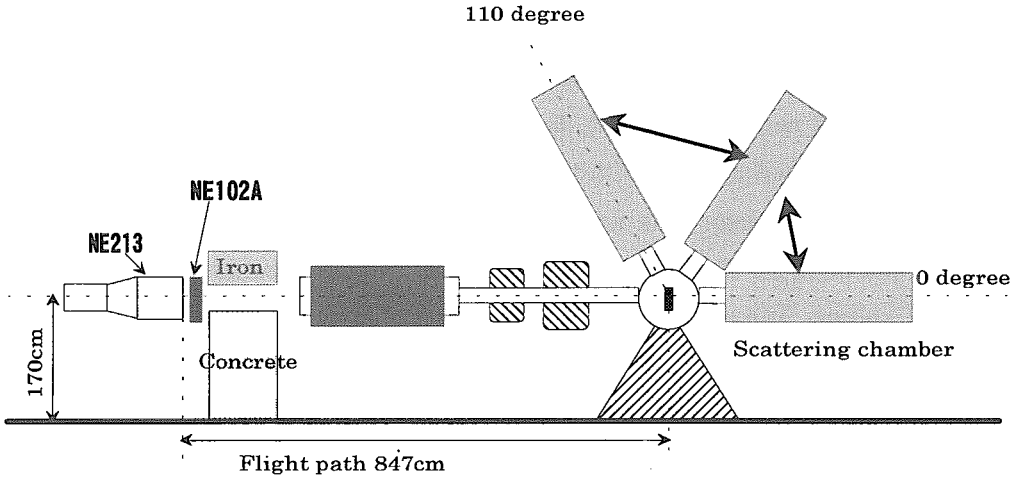

Fig.1 Schematic view of the experimental set-up

3. RESULTS AND DISCUSSIONS

We obtained neutron energy spectra for C,Al,Cu, and Pb targets bombarded by 135 MeV/nucleon C ion. These experimental results were compared with the calculation using the HIC [2] and the QMD [3] codes. Figs.2-5 show the experimental and calculated double differential cross sections of neutron production from C, Al, Cu, and Pb targets, respectively. Neutron energy spectra measured in the forward direction have a peak near the projectile energy per nucleon. This peak is due to a knock-on process in which a neutron is knocked out by the direct collision between the target nucleon and the projectile nucleon. This peak becomes more prominent in the forward direction and for a lighter target, since the momentum transfer from projectile to target nuclei is higher for lighter

nucleus than for heavier nucleus [4]. The high energy end of neutrons in the forward direction reaches about 300-400MeV. This influences the Fermi motion of a nucleon in a nucleus. The neutron spectra have another two components based on cascade-preequilibrium emission process and evaporation-equilibrium emission process. At small angles, knock-on process is dominant, and at large angles, evaporation process is dominant. Two calculations of HIC and QMD show a tendency to underestimate the high energy neutron components beyond the peak at all angles. The HIC overestimates the peak, while the QMD underestimates the peak. At large angles, the calculated spectra become in good agreement with the measured spectra. In general, the QMD gives better agreement with the experimental results, especially for heavy target, than the HIC.

4. CONCULUSIONS

We measured double-differential cross sections of neutron production from thin C, Al, Cu, Pb targets bombarded by 135 MeV/u C ion. The experimental spectra were compared with the calculation using the HIC and the QMD codes. The calculated spectra tend to underestimate the high energy neutron region. At large angles, the calculated spectra, particularly the QMD, are in rather good agreement with the measured spectra. These experimental results will be useful as the benchmark data for investigating the accuracy of high energy particle transport calculation code.

References

[1] Cecil, R. A. , *et al.* : Inclisive neutron production by 337 MeV/nucleon neon ions on carbon, aluminum, copper, and uranium, *Phys. Rev. C* 24, 2013 (1981)

[2] Bertini, W. H. : HIC-1 : First Approach the Calculation of Heavy-ion Reactions at Energy>50MeV/nucleon., ORNL-TM-4134.

[3] Aichelin, J. : *Physics Report* 202, 233 (1991).

[4] Kurosawa T. and Nakamura S. ,*et al.* : Spectral measurements of neutrons, protons, deuterons and tritons produced by 100 MeV/nucleon He bombardment., *Nucl. Instrum. Methods. A*430, 440(1999)

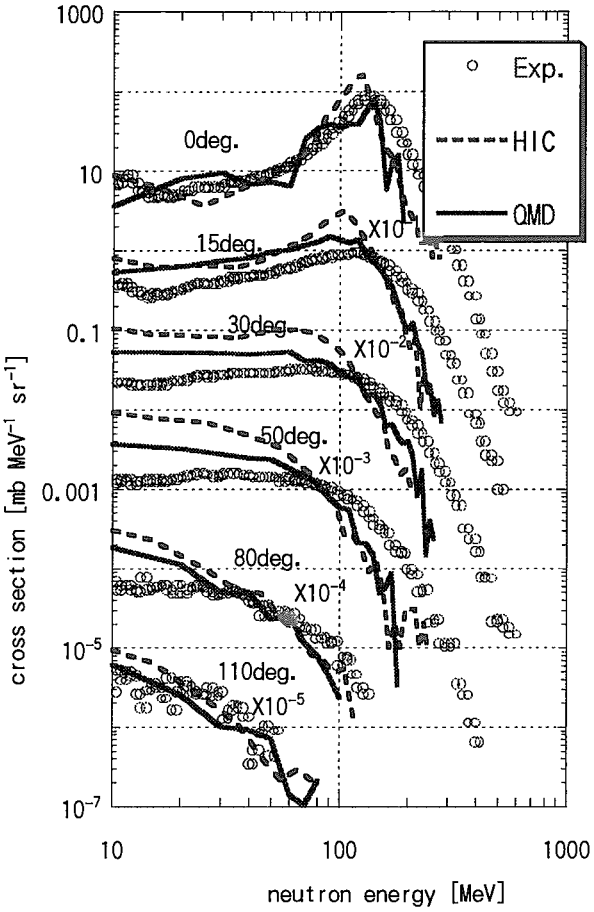

Fig.2 Neutron energy spectrum for C

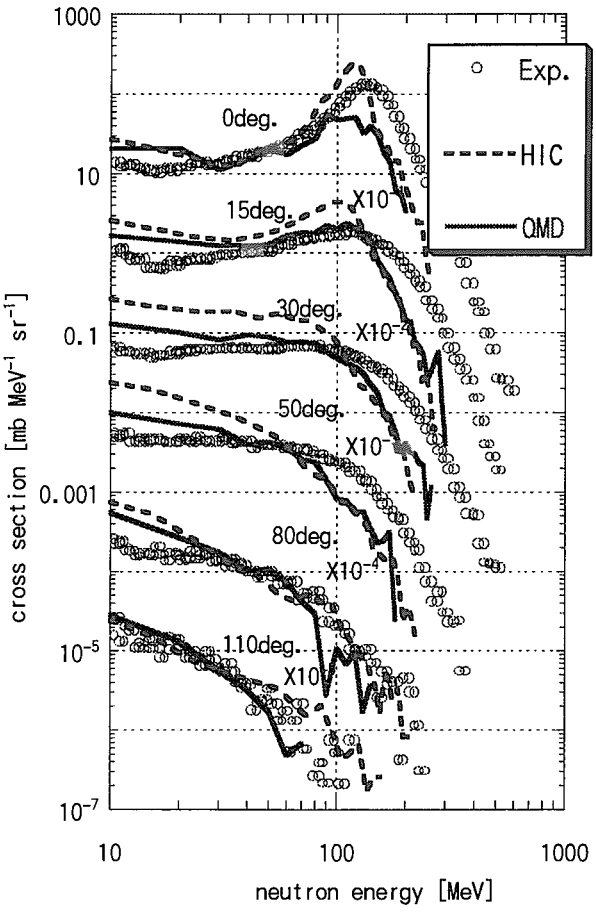

Fig.3 Neutron energy spectrum for Al

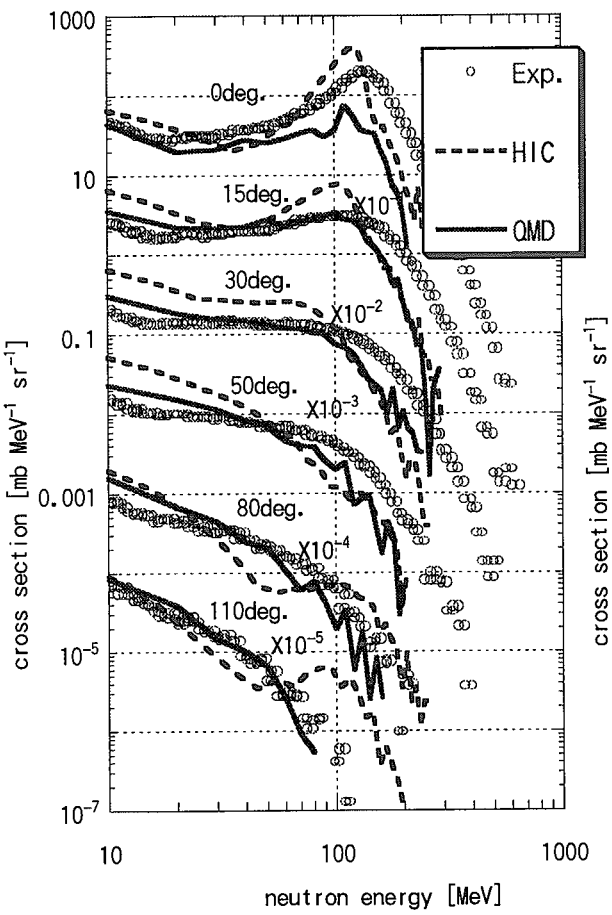

Fig.4 Neutron energy spectrum for Cu

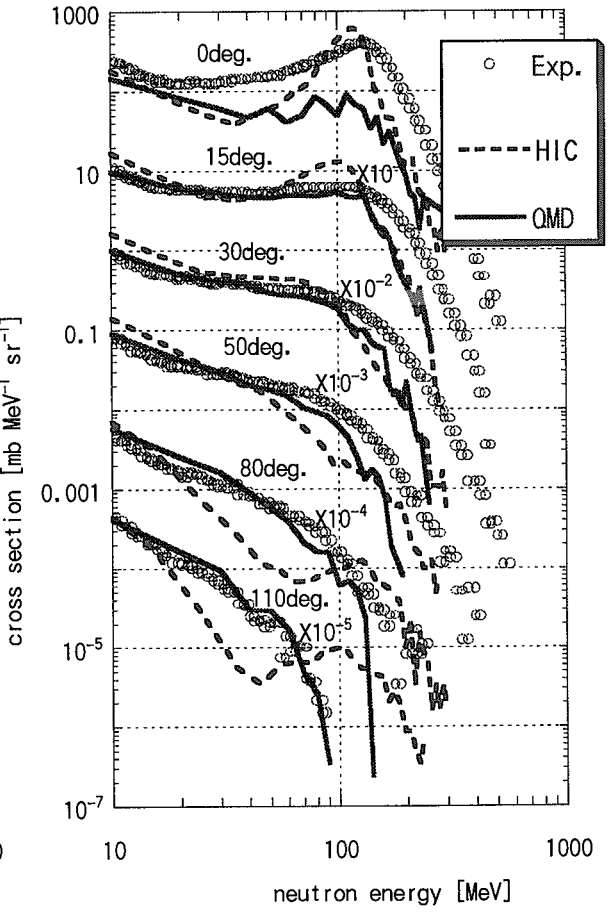

Fig.5 Neutron energy spectrum for Pb

3.26

Design and Development of Quasi-Monoenergetic Neutron Source using the Inverse Kinematics of (p,n) Reaction

Y. Matsuoka, Y. Watanabe [a)], S. Hachiya, H. Nakamura, Y. Tanaka
N. Ikeda* and K. Sagara*
Department of Advanced Energy Engineering and Science, Kyushu University, Kasuga-kouen, Kasuga, Fukuoka-ken 816-8580
**Department of Physics, Kyushu University, Hakozaki, Higashi-ku, Fukuoka 812-0053*
[a)] e-mail: watanabe@aees.kyushu-u.ac.jp

We has started to develop a new quasi-monoenergetic neutron source using the inverse kinematics of (p,n) reaction at Kyushu University Tandem Laboratory. A preliminary experiment was performed for a neutron source using the $^{1}H(^{13}C,n)^{13}N$ reaction at an incident energy of 59.3MeV. It was experimentally observed that monoenergetic neutrons with about 7 MeV were produced at 0° in the laboratory system and the produced neutrons were collimated to a forward cone restricted by the kinematics.

1. Introduction

There are various types of accelerator-based monoenergetic neutron sources that are widely used in basic science and applications. In the energy region covered by tandem Van de Graaf accelerators, light-ion induced reactions on light element targets, such as the $D(d,n)^{3}He$, $T(d,n)^{4}He$, $T(p,n)^{3}He$ and $^{7}Li(p,n)^{7}Be$ reactions, are popular as the nuclear reactions to produce monoenergetic neutrons. However, these reactions cannot produce the real monoenergetic neutrons in the energy region between 8 and 14 MeV because of the breakup of the projectile and/or the target nucleus. Therefore, only few neutron cross section data is now available in this "gap" region, whereas the data in this energy region is required in several applications, e.g., the development of D-T fusion reactors.

Recently, new types of monoenergetic neutron sources with heavy ion (HI) beams have been proposed as one of the candidates to fill in the "gap" region and the feasibility has so far been investigated.[1,2,3] A neutron source with the $^{1}H(^{11}B,n)^{11}C$ reaction were practically used for measurements of some activation cross sections in the 9 to 13 MeV region [4] and the usefulness was demonstrated.

Under these circumstances, we have started the development of a monoenergetic neutron source in this "gap" region by using the $^{1}H(HI,n)$ reaction at Kyushu University Tandem Laboratory (KUTL). The $^{1}H(^{13}C,n)^{13}N$ reaction was chosen as a suitable candidate for KUTL from consideration about the performance of accelerator and its feasibility test has been performed.

2. The $^{1}H(HI,n)$ neutron source

Characteristic features of the $^{1}H(HI,n)$ neutron source are summarized as follows:

1) In an endothermic reaction, the produced neutrons are emitted at angles smaller than θ_{max} defined by two-body kinematics, that is, the neutrons are "kinematically collimated" into a forward cone. This situation is schematically illustrated in Fig. 1, and a calculation of the kinematics for the $^{1}H(^{13}C,n)^{13}N$ reaction is shown in Fig. 2.

By this collimation, the shielding design of neutron facilities is expected to become easier.

2) The $^{1}H(HI,n)$ cross section at 0° in the laboratory system is enhanced strongly by the compression into the forward cone, which leads to large neutron yield at 0°.
3) The emitted neutrons at one angle have two energies as shown in Figs. 1 and 2. The neutrons with higher energy are called "primary" neutrons and those with lower energy are called "satellite" neutrons. However, the energy and yield of the "satellite" neutrons is considerably smaller than the "primary" neutrons under most experimental conditions.
4) The smaller backgrounds of neutrons and γ rays from the beam stopper can be expected because the heavy projectiles have much higher Coulomb barrier than protons and deuterons.

3. Design of the neutron source and simulation of neutron production

As a hydrogen target for the $^{1}H(^{13}C,n)^{13}N$ reaction, we have chosen a gas target. A schematic drawing of the fabricated gas target is shown in Fig. 3. It is made of stainless steel and has the effective size of 30 mm long and 33 mm in diameter. The entrance window is made of tantalum foil of 3 μm in thickness and 12 mm in diameter, and a 0.2 mm thick tantalum disk is used as the beam stopper so that associated backgrounds of neutrons and γ rays may be reduced as much as possible by using high Z materials. The escape of the electrons produced by beam bombardment on the entrance window is suppressed by the permanent magnets.

In the design of the neutron source, we have estimated neutron yields at 0° in laboratory system using a modified version of the simulation code [5] developed for $^{1}H(^{11}B,n)^{11}C$ neutron source. Since there is no available cross section data of the $^{1}H(^{13}C,n)^{13}N$ reaction, we used the cross sections derived from the $^{13}C(p,n)^{13}N$ cross sections[6] in terms of the inverse kinematics. The calculated result for an incident energy of 58.2 MeV is shown in Fig. 4. The pressure of H_2 gas was taken to be 1 atm. One can see two peaks that correspond to two neutron components. It is found that the yield of the "primary" neutrons (about 7 MeV) is much larger than the "satellite" neutrons (about 1 MeV).

4. Preliminary experiment and results

4.1. Experimental procedure

The first test experiment was carried out using 59.3 MeV $^{13}C^{6+}$ beam. The experimental setup is shown in Fig. 5. The average beam current was about 40 enA. The pressure of H_2 gas in the gas cell target was 2 atm. The neutron yields were measured at angles, 0°, 10°, 20° and 30°, by using an active radiator proton recoil counter telescope (ARPRT)[7] which was placed 20 cm far from the center of the gas cell target.

4.2. Neutron yield at 0°

The recoil proton spectrum at 0° measured by ARPRT is shown in Fig. 6. The "satellite" neutrons shown in Fig. 4 could not be detected in this experiment, because the threshold energy of ARPRT was about 2 MeV. The experimental yield of 7.2 MeV neutrons for emission at 0° was $(1.58\pm0.06)\times10^{7}$ [n/sr/μC]. This value was about 2.5 times smaller than the result estimated from the number of incident ^{13}C ions, the pressure of H_2 gas and the cross section of the $^{13}C(p,n)^{13}N$ reaction[6]. One of the reasons may be due to the $^{13}C(p,n)^{13}N$ cross section used, because the experimental values [6,8,9] in the energy region of interest are scattered within a factor of about two.

4.3. Angular distributions

In Fig. 7, the measured angular distribution of produced neutrons is compared with the two calculated results of $^{1}H(^{13}C,n)^{13}N$ and $D(d,n)^{3}He$ neutron sources. Each angular distribution is normalized to each value at 0°. The experimental yield shows remarkable reduction at 30°. And, this trend is similar to the simulation result given by the solid line. Thus, it was experimentally confirmed that the neutrons produced by the $^{1}H(^{13}C,n)^{13}N$ reaction are emitted within the forward cone restricted by the kinematics. As shown in Fig. 7, however, a small fraction of neutrons are observed even at 30° over the kinematically allowed angle. The reason may be due partly to the reactions on some impurities in the H_2 gas cell target, such as H_2O and/or air.

5. Summary

We have investigated the properties of the $^{1}H(^{13}C,n)^{13}N$ neutron source at KUTL. The preliminary experiment with 59.3 MeV $^{13}C^{6+}$ beam showed that the $^{1}H(^{13}C,n)^{13}N$ reaction can produce the "kinematically collimated" monoenergetic neutrons with 7.2 MeV at 0°. The present work is in the first stage toward the completion of the monoenergetic neutron source using the $^{1}H(^{13}C,n)^{13}N$ reaction at KUTL. In the future, further optimization of the design will be necessary for the enhancement of neutron yields and the reduction of backgrounds in order to satisfy several requirements for practical use.

References

[1] M. Drosg.: Nucl. Sci. Eng. **106**, 279 (1990)
[2] S. Chiba et al.: Nucl. Inst. Meth. **A281**, 581 (1989)
[3] K. Hasegawa et al., Proc. 11th Int. Conf. Cyclotrons and Their Applications, Oct. 20-24, 1987, Tokyo, Japan, 642 (1987)
[4] Y. Ikeda et al., Proc. of Int. Conf. on Nucl. Data for Sci. and Tech., May. 13-17, 1991, Julich, 294 (1992)
[5] S. Meigo.: JAERI M-94-019, 243 (1994)
[6] P. Dagley, et al.: Nucl. Phys. **24**, 353 (1961).
[7] S. Hachiya.: Master thesis, Kyushu Univ., unpublished (1999).
[8] O. Dietzsch.: Nucl. Phys. **85**, 689 (1966).
[9] J. Gibbons, et al.: Phys. Rev. **114**, 571 (1959).

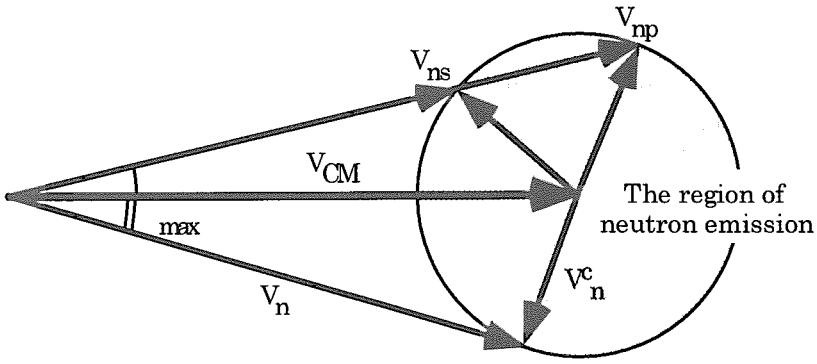

Fig. 1: Schematic diagram of two-body kinematics for the $^{1}H(HI,n)$ reaction under the condition $V_{CM} > V^{C}_{n}$, where V_{CM} denotes the velocity of the CM, and V^{C}_{n} that of the produced neutron in the CM. θ_{max} is the maximum angle of neutron production in laboratory system.

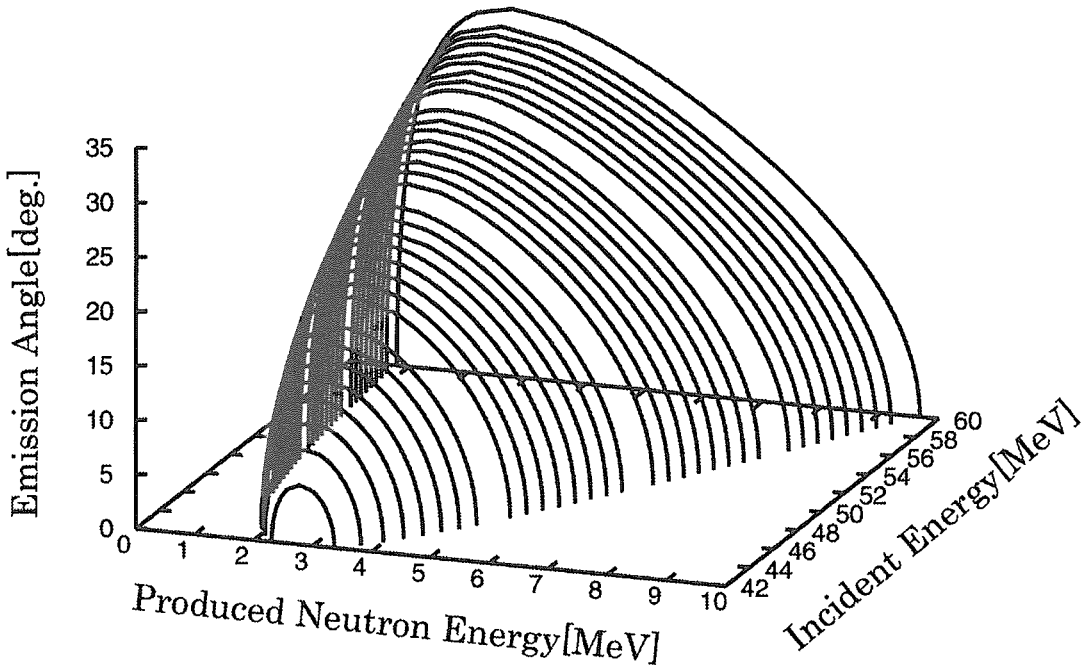

Fig.2: Neutron emission angle as a function of neutron emission energy and incident heavy-ion energy calculated using the two-body kinematics for the $^{1}H(^{13}C,n)^{13}N$ reaction.

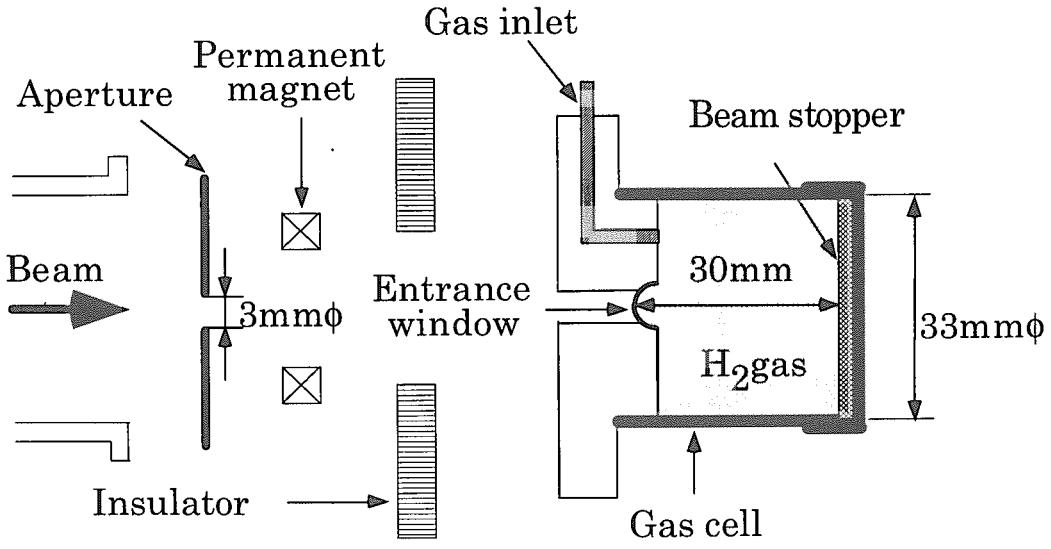

Fig. 3: Schematic drawing of the H_2 gas cell target

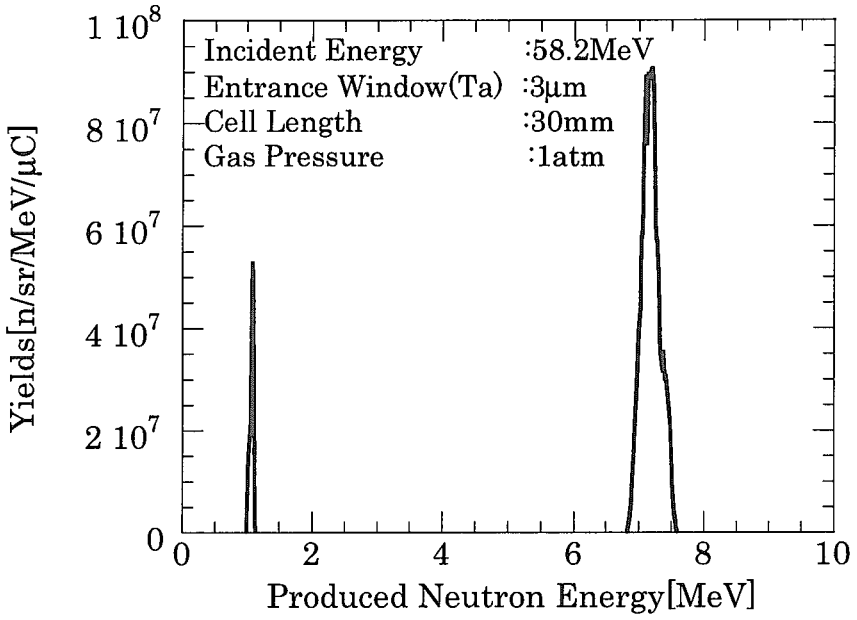

Fig. 4: Calculated spectrum of neutrons produced by the $^{1}H(^{13}C,n)^{13}N$ reaction at 58.2 MeV in the 0° direction.

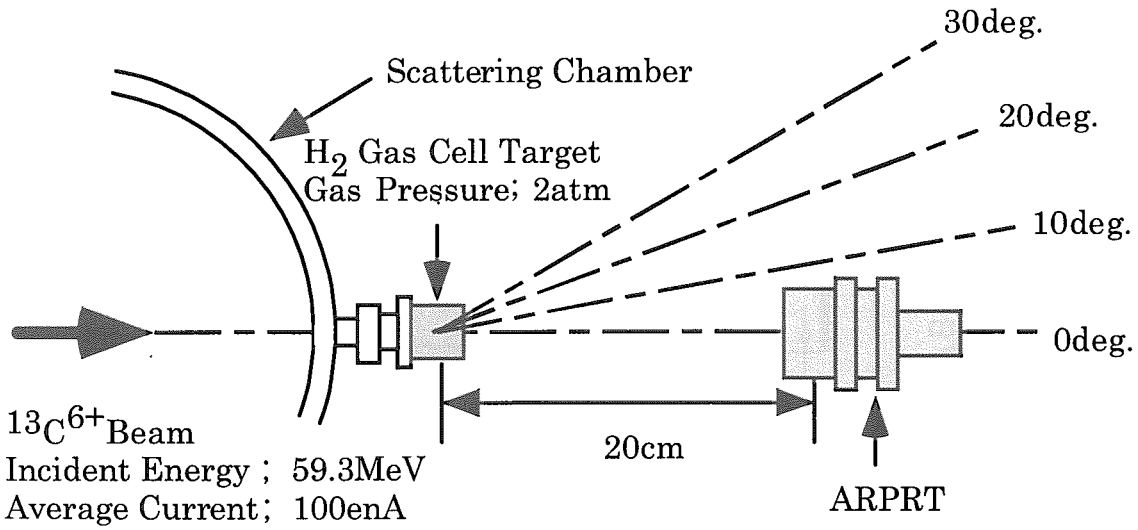

Fig. 5: Experimental setup at KUTL

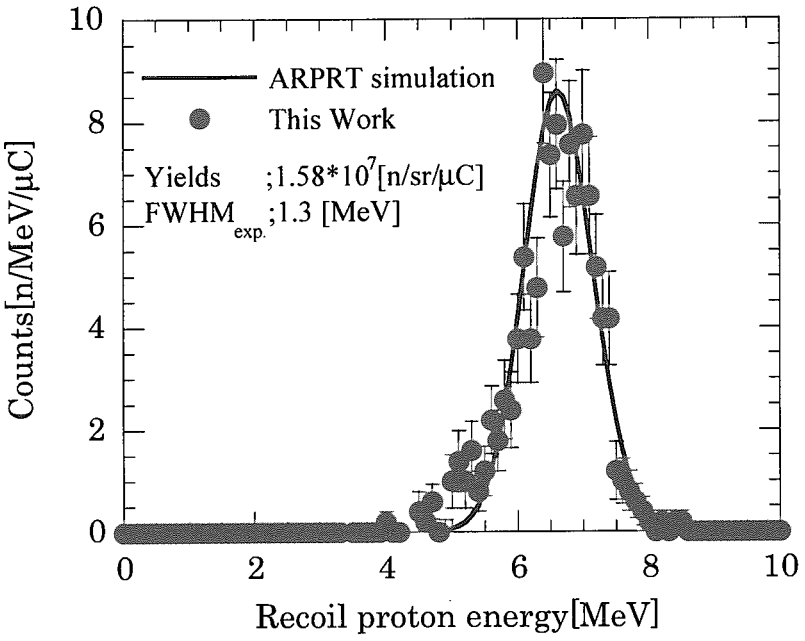

Fig. 6: Measured proton spectrum for 7.2 MeV neutrons produced by the $^{1}H(^{13}C,n)^{13}N$ reaction using ARPRT. The solid line represents the calculated response of ARPRT.

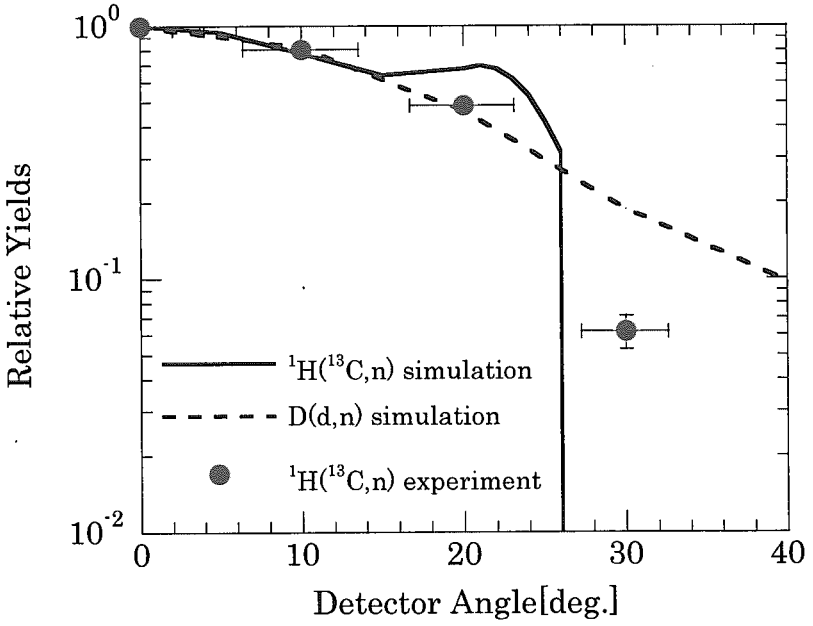

Fig. 7: Angular distributions of neutrons produced by the $^{1}H(^{13}C,n)^{13}N$ reaction. They are normalized to the values at 0° . The solid circles are the experimental data. The solid line is the calculated angular distribution. The dash line represents the calculated angular distribution of neutrons produced by the $D(d,n)^{3}He$ reaction for comparison.

3.27 Measurement of Neutron-Production Double-Differential Cross Sections for High-Energy Pion-Incident Reaction

Yousuke IWAMOTO[1], Kiminori IGA[1], Hirohiko KITSUKI[1], Hideki TENZOU[1], Shunsuke ISHIMOTO[1], Nobuhiro SHIGYO[1], Keisuke MAEHATA[1], Kenji ISHIBASHI[1]

Tatsushi NAKAMOTO[2], Masaharu NUMAJIRI[2], Shin-ichiro MEIGO[3] and Hiroshi TAKADA[3]

1 Department of Applied Quantum Physics and Nuclear Engineering, Kyushu University

2 High Energy Accelerator Research Organization

3 Japan Atomic Energy Research Institute

email: yousuke@meteor.nucl.kyushu-u.ac.jp

Abstract

Double-differential neutron-production yields for 870-MeV π^+, π^- and 2.1-GeV π^+ incident on iron and lead targets were measured with NE213 liquid scintillators by time-of-flight technique. The two-gate integration method was used for the pulse shape discrimination between neutrons and gamma-rays. Neutron detection efficiencies were derived from the calculation results of SCINFUL and CECIL codes. The experimental results were compared with the calculation including the neutron transport in the actual thickness target by the contribution use of both NMTC/JAERI97 and MCNPX.

1. Introduction

Nuclear data in the intermediate energy region up to GeV-grade are recently getting more important because of necessity in applications to a spallation neutron source and an accelerator-based nuclear-waste transmutation system. For such applications, proton incident reactions are used for generating neutrons. At incident energies above 0.5 GeV, a number of pions are yielded from the primary proton reaction. The pions easily induce the secondary reactions, and accordingly create secondary neutrons in the target. Calculation codes such as High Energy Transport Code (HETC) [1][2] are based on Birtini's intranuclear-cascade-evaporation (INCE) model [3]. These codes have been formed to be applicable to the nuclear reaction for both nucleon and meson incidences. The validity of the codes has been comfirmed by a comparison between the proton-incident experimental data and the computed ones. For neutron-production cross section by pion incidence, however, there are no experimental data at incident energies around 1GeV. The INCE model has not been checked for neutron-production double-differential cross section on the intermediate-energy pion-incident nuclear reaction. Therefore, we measured the double-differential yields for 870-MeV (momentum of 1.0GeV/c) $\pi+$, $\pi-$ mesons and 2.1-GeV (that of 2.25GeV/c) $\pi+$ mesons incident on iron and lead. In this work, we describe the experimental method and the data analysis.

2. Experiment

2.1 Incident Pion Beam

The experiments were carried out at the π 2 beam line of the 12GeV proton synchrotron (12GeV-PS) at High Energy Accelerator Research Organization (KEK). The experimental arrangement is illustrated in **Fig.1**. Since the beam intensity was very weak, the pions were able to be individually counted one by one. Incident pions were generated in a secondary beam from an internal target mounted in the accelerator ring. The secondary beam contains several kinds of particles. In selection of positive beam polarity, unresolved particles of π^+, proton, μ^+ and positron come together with the same momentum, whereas π^-, electron and μ^- are available at negative polarity. At a momentum of 1GeV/c, the fractions of μ and positron are less than several percents. For positive beam incidence, the Time-of-Flight (TOF) of incident particles was measured for separation of protons from π^+ mesons and other lighter particles by the use of a pair of Pilot U scintillators. These scintillators were located at beam line with a flight distance of 4.5m. Time differences between π^+ and protons are 4.9 and 1.07ns at momentums of 1.0 and 2.25GeV/c, respectively. Since the time resolution was 0.29ns for the incident-beam TOF measurement, protons were well separated by the electronic circuit. We set up a Cerenkov counter at the beam line to separate π^+ (π^-) from μ^+ and positron (μ^- and electron) by means of the difference of Cerenkov light emission. NE102A plastic scintillators served to define the pion beam with Pilot U scintillators. The coincidence of these scintillators was counted to give the number of incident pions.

2.2 Target and Detector Arrangement

A target was located at beam line height of 1.0m and all neutron detectors were faced to the target. A iron target was 4.9cm in diameter and 3.0cm thick, while a lead target 4.9cm in diameter and 1.7cm thick. Since the targets were not quit thin, we had to take correction of multiple-scattering effects into consideration.

For neutron TOF measurements, NE213 neutron detectors 12.7cm in diameter and 12.7cm thick were placed in directions of 15, 30, 60, 90, 120 and 150°, as indicated in **Fig.1** . Flight pass lengths were 1.5 to 2m. The scintillators were connected with Hamamatsu H1161. In front of individual neutron detectors, NE102A plastic scintillators 1cm thick were mounted as veto detectors to eliminate charged particle events by the anticoincidence method.

2.3 Pulse-Shape Discrimination

It was very important to perform the pulse-shape discrimination between neutrons and gamma rays particularly in the short flight path experiment. This is because prompt gamma-rays peak are not completely separated from neutron events in the TOF spectra. For the pulse-shape discrimination method, there are mainly two methods, the zero-cross method[4][5][6][7] and the two-gate integration method[8][9][10]. It was known that the latter is capable of reducing the saturation effect on the neutron-gamma discrimination in the high-energy region. The two-gate integration method was chosen for this experiment. For this reason, the photomultiplier signal was branched into two pulses and they were input into individual ADCs as fast or slow gate pulses. The prompt gate on one ADC covered the initial peak of the photomultiplier signal, whereas the delayed gate made the other ADC to accept the long-tail part. The time duration of the prompt gate was 40 ns and that of the delayed gate was 350 ns after

delay of 150 ns. The discrimination results of 870MeV π^+ on Fe target are shown in **Fig.2**. The discrimination characteristics were sufficiently good above a few MeV and the saturation effect did not deteriorate the discrimination results.

3. Data Analysis

Target-in and -out experiments were performed in the neutron measurements. Neutron spectra were derived by subtracting the results of target-out experiment from those of the target-in with normalizing the incident number of pions. **Fig.3** presents the TOF spectra of the target-in and -out measurements at incident π^+ energy of 870MeV on iron. In this figure, the pulse-shape discrimination was not made and the TOF spectra include both of neutrons and gamma-rays. The flash gamma-rays which emitted from target nuclei exited by incident pions make a peak at 156ns. The flash gamma-ray peak was taken as the time standard of the neutron TOF, since the gamma-rays came along on the flight path as the light velocity. The TOF of neutrons is given as the time difference between flash gamma-rays and neutrons. The neutron production double differential yields were extracted from the neutron TOF spectra, which were separated from gamma-rays by the pulse-shape discrimination. The number of neutron events were converted into the differential cross sections by using the efficiencies of the neutron detectors and making the data corrections.

3.1 Neutron Detection Efficiencies

Neutron detection efficiencies are required to convert the neutron events into absolute values of the cross sections. It is desired to adopt the measured detection efficiencies to the data analysis. However, it was difficult to measure the neutron detection efficiencies in the neutron energy range up to a GeV. The neutron detection efficiencies were obtained from calculation results of the SCINFUL [11] and the CECIL [12] codes. SCINFUL is well known to reproduce the detection efficiencies of the NE213 and NE110 scintillators at neutron energies below 80MeV. SCINFUL is supposed to be more reliable than CECIL in this region. In fact, SCINFUL takes account of many reaction channels for n+C reaction and light output values for all charged particles generated by this reaction. For this reason, SCINFUL was utilized for the neutron detection efficiencies below 80MeV. CECIL was adjusted to smoothly connect with the result of the SCINFUL at 80MeV and was employed above 80MeV.

The neutron detection efficiencies were calculated with four threshold levels. Calculation results of the neutron detection efficiencies with the four threshold levels are plotted in **Fig.4**. The lowest threshold level was determined by the photo-peak of 60keV gamma-rays from ^{241}Am. The other threshold levels were determined by the half-height of the Compton edge produced by radiation source by ^{137}Cs, ^{60}Co, and Am-Be. In the case of ^{60}Co bias, we adopted the mean value of 1.17 and 1.33 MeV gamma-rays as the threshold level because the poor resolution of the NE213 scintillator made these Compton edges unresolved.

4. Double differential yield

The experimental neutron yields were obtained after data analysis. The yields was presented in units of double differential neutron cross sections for iron and lead are plotted in **Figs. 5** to **9**. Solid lines show the calculation

results including the neutron transport in the actual thickness target by the use of nucleon-meson transport code (NMTC/JAERI97) [13] and MCNPX code[14]. The neutron transport at energies below 150MeV was made by MCNPX with a continuous energy cross section library, which were processed from the nuclear data of ENDF-B/VI and an additional data base. The calculation results overestimate the experimental data in the neutron energy range from 3 to 50 MeV in all degrees. Compared with iron and lead targets, the agreement between the experimental data and calculation ones for lead is somewhat better than iron in the energy range from 3 to 50 MeV. The experimental data for 870MeV π^- incidence are better agreement with the calculation ones than π^+ incidence above 100MeV, and the experimental ones for 2.1GeV π^+ incidence better agree with the calculation ones than 870MeV π^+ incidence.

The difference between yields and cross sections is within about 10% under 50MeV. We will take into the actual beam profile consideration. After correction of the beam transport effects in the target, the double differential cross sections will be obtained.

5. Conclusion

Neutron-production double-differential yields induced by 870MeV π^+, π^- mesons and 2.1 GeV π^+ meson on iron and lead targets were obtained in the emitted neutron energy range from 1 MeV to 1 GeV by the TOF method with a typical flight pass length of 1.5 m. NE213 liquid scintillators were utilized in directions of 15, 30, 60, 90, 120 and 150° for the measurements. For the pulse-shape discrimination between neutron and gamma-ray, the two-gate integration method was used. Neutron detection efficiencies were derived from the calculation results of the SCINFUL and the CECIL codes. The effects of multiple-scattering neutrons will be corrected later.

Acknowledgements

The authors express their gratitude to Prof. Y. Yoshimura and beam channel staff of KEK for their continuous encouragement and generous support of this experiment.

Reference

(1) CHANDLER, K. C., ARMSTRONG, T. W.: *CCC*-178, (1977).

(2) COLEMAN, W. A., ARMSTRONG, T. W.: *ORNL*-4606, (1970).

(3) BERTINI, H. W., et al.: *Phys. Rev.*, **188**, 1711 (1969).

(4) BROOKS, F. D., *Nucl. Instrum. Methods* **4**, 151 (1959)

(5) MCBETH, G. W., LUTKIN, J.E. and WINYARD, R. A., *Nucl. Instrum. Methods* **93**, 99 (1971)

(6) GLASGOW, D. W., VELKLEY, D. E., BRANDENBERGER, J. D. and MCELLISTREM, M. T., *Nucl. Instrum. Methods* **136**, 579 (1976)

(7) PLISCHKE, P., SCHRODER, V., SCOBEL, W., WILDE, L. and MCELLISTREM, M. T., *Nucl, Instrum. Methods* **114** 535 (1974)

(8) BELL, Z. W., *Nucl. Instrum. Methods* **188**, 105 (1981)

(9) ZUCKER, M. S. and TSOUPAS, N., *Nucl. Instrum. Methods* A **299**, 281 (1990)

(10) MOSZYNSKI, M., et al., *Nucl. Instrum. Methods* A **343**, 563 (1994)

(11) DICKENS, J. K., ORNL-6452 (1988)

(12) CECIL, R. A., et al., *Nucl. Instr. And Meth.*, **161**, 439 (1979)

(13) TAKADA, H., et al., *JAERI-DATA/CODE* 98-005 (1998)

(14) BRIESMEISTER, J.F, et al., *LA*-12625-*M* (1997)

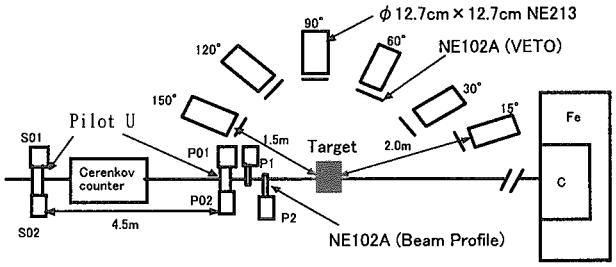

Fig. 1 Illustration of the experimental arrangement

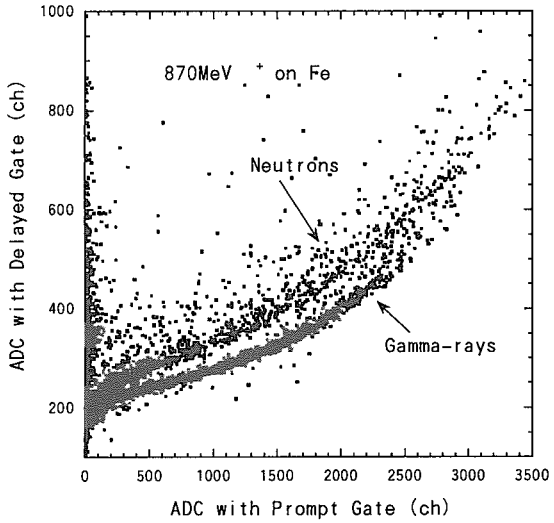

Fig. 2 Neutron and gamma-ray pulse-shape discrimination by two-integration method.

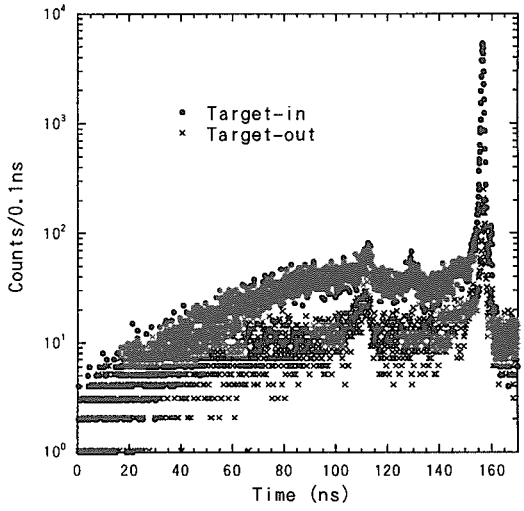

Fig. 3 TOF spectra of the target-in and -out measurements at 30°for 870 MeV + on Fe.

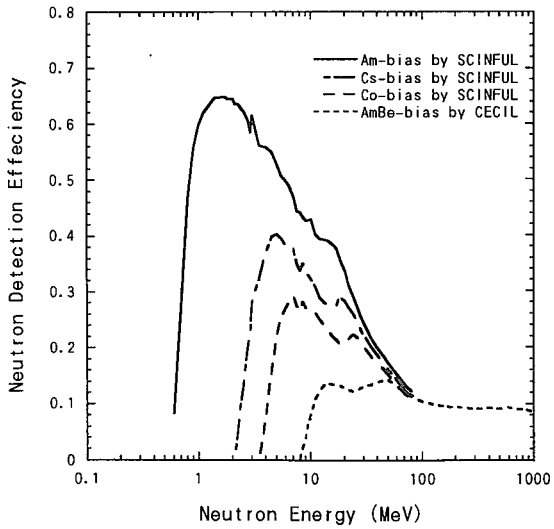

Fig. 4 Calculated neutron detection efficiencies for NE213 liquid scintillatos.

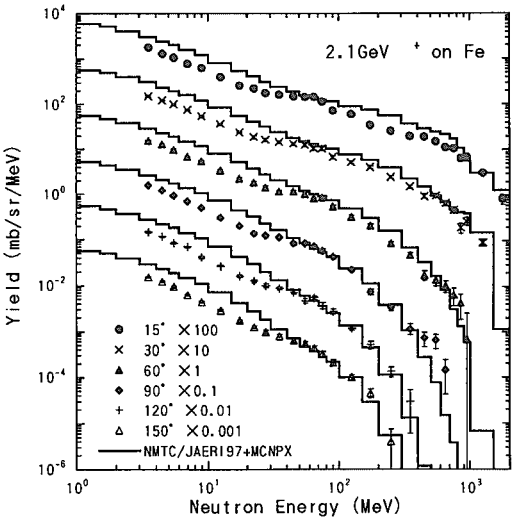

Fig. 5 Neutron production double differential yield for 2.1GeV + on Fe.

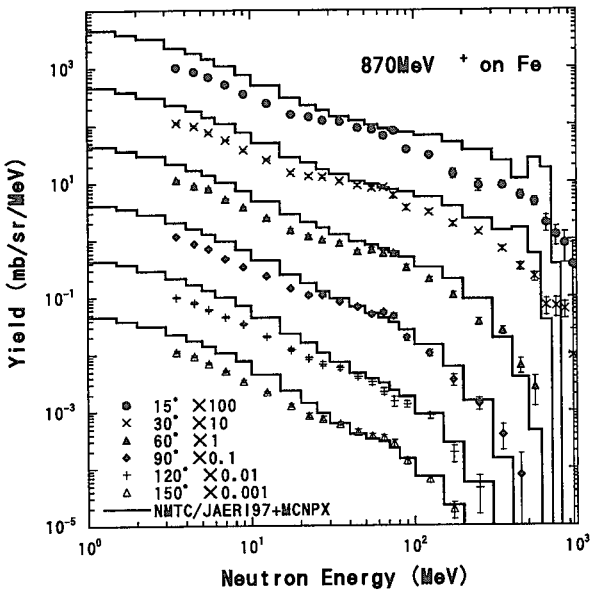

Fig. 6 Neutron production double differential yield for 870MeV $^{+}$ on Fe.

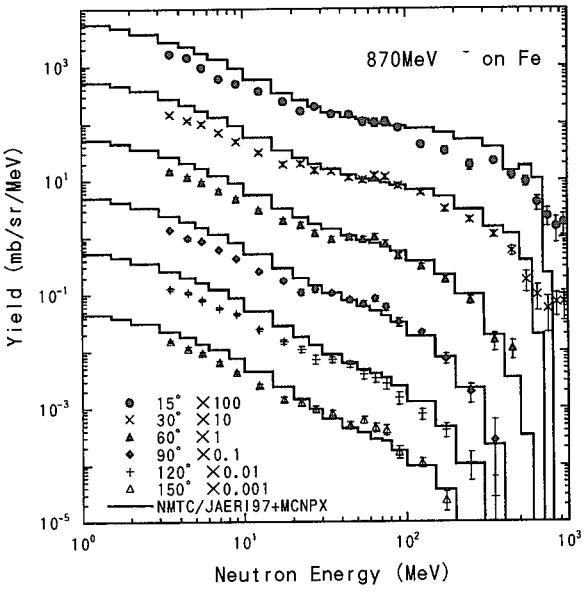

Fig. 7 Neutron production double differential yield for 870MeV $^{-}$ on Fe.

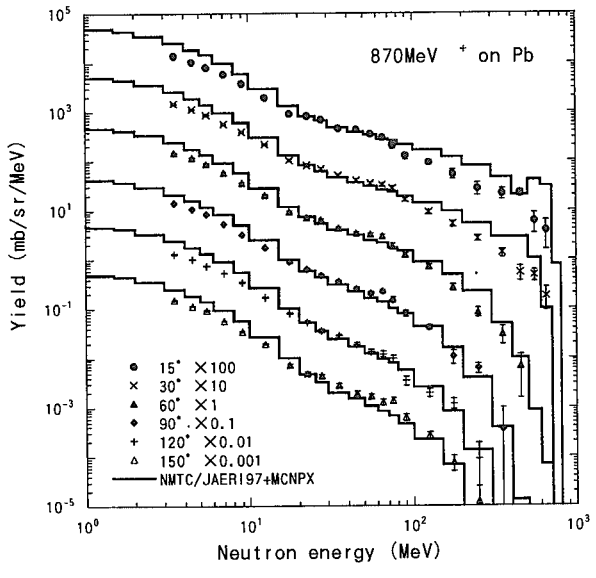

Fig. 8 Neutron production double differential yield for 870MeV $^{+}$ on Pb.

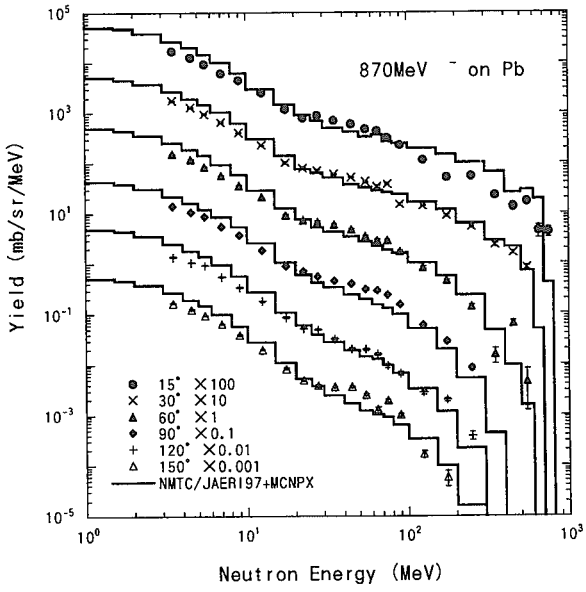

Fig. 9 Neutron production double differential yield for 870MeV $^{-}$ on Pb.

3.28 Parameterization of Neutron Production Double-differential Cross Section above Several Tens-MeV by the Use of Moving Source Model

Hirohiko KITSUKI, Nobuhiro SHIGYO, Kenji ISHIBASHI
Department of Applied Quantum Physics and Nuclear Engineering, Kyushu University
Hakozaki, Higashi-ku, Fukuoka 812-8185
e-mail:kituki@meteor.nucl.kyushu-u.ac.jp

The moving source model based on the Maxwell-like energy distribution with Gaussian shape terms are employed for analyzing the neutron emission spectra from proton-induced spallation reaction. The parameterization of the double differential cross section is made for the experimental and calculated neutron data in the energy region from several-tens MeV to 3 GeV.

1 Introduction

Accurate nuclear data covering incident energies up to several GeV are required for applications such as radiation transport simulations in the cancer radiotherapy and the accelerator-driven transmutation of nuclear wastes. Neutron production double differential cross sections, however, have been measured for several targets at some incident energies. Therefore, it is important to find the systematic behaviors in the neutron data, and to parameterize them to extend to different incident energies and target nuclei. The moving source (MS) model[1] which is based on the Maxwell-like distribution has been employed for analyzing the experimental neutron emission data. The parameters obtained from this type of analysis represented well the experimental (p,xn) double differential neutron spectra in the incident energy region from 113 MeV to 800 MeV[2]. This method made use of angle-independent parameters for specifying individual components of experimental spectra, i.e. cascade, preequilibrium and evaporation processes Three parameters were required in the model for specifying each evaporation component of experimental spectra, and were determined with simultaneous consideration of whole-direction data.

In this study, the parameterization of the (p,xn) double differential cross sections is made for the neutron emission from the spallation reaction induced by protons from several tens-MeV to 3 GeV. The experimental neutron data at incident proton energies of 22 MeV[3], 25 MeV[4], 113 MeV[5], 597 MeV[6], 800 MeV, 1.5 GeV and 3.0 GeV[7] are analyzed for each component of cascade, preequilibrium and evaporation process by the MS model. In addition, HETC-3STEP[8] and QMD+SDM[9] are employed to calculate the cross sections which were not measured.

2 MS model

The MS model is based on the view that a locally heated spot is moving with isotropically evaporating particles in a nucleus. Since the particle emission behavior in the high energy reaction is also explained to a considerable extent by such models as the intranuclear-cascade model, the reaction may not always produce the physical moving source. In the MS model, the collision phenomena are at first seen from an observation point moving with an appropriate velocity β (moving frame). Neutrons are assumed to be emitted isotopically with an exponential-type energy distribution at a temperature T (MeV) in the moving frame. The neutron emission double cross section is expressed in the laboratory frame by

$$\frac{d^2\sigma}{d\Omega dE_{kin}} = p\frac{A}{T}\exp\left\{-\left(\frac{E_{kin}+m-p\beta\cos\theta}{(1-\beta^2)^{\frac{1}{2}}}-m\right)/T\right\}, \quad (1)$$

where, E_{kin} (MeV) and P (MeV/c) is kinetic energy and momentum of an emitted neutron in the laboratory frame, respectively. The parameters A (mb/sr/(MeV/c)), β and T (MeV) are called amplitude, velocity and temperature, respectively. The parameters are adjustable in fitting the equation to double differential cross section data.

For the spallation reaction, the MS model is applied in a form of summation of three components as

$$\frac{d^2\sigma}{d\Omega dE_{kin}} = \sum_{i=1}^{3} p\frac{A_i}{T_i}\exp\left\{-\left(\frac{E_{kin}+m-p\beta_i\cos\theta}{(1-\beta_i^2)^{\frac{1}{2}}}-m\right)/T_i\right\}. \quad (2)$$

Three components of i=1 to 3 correspond to the intranuclear-cascade, the preequilibrium and the nuclear-evaporation processes, respectively. In this study,the parameters for each process are adjusted to the experimental neutron emission spectra and the calculation results by HETC-3STEP and QMD + SDM.

Figures. 1 and 2 show the results of fitting for the 22-MeV proton incidence on Fe and the 25-MeV proton incidence on W, respectively. The marks stand for the experimental cross sections[3][4]. The dotted lines show the results obtained by HETC-3STEP. The solid lines show the results of fitting for the experimental data and calculated data. This MS model reproduces the neutron spectra in the energy region below 25 MeV well.

Figures. 3 and 4 show the results of fitting for the 113-MeV proton incidence on the Fe and W target, respectively. The dotted lines show the calculated data by QMD+SDM. In this figure, the results by this MS model are indicated by dash-dotted-line. The MS model reproduces the experimental and calculated cross sections at whole emission angles in the energy region below 100 MeV. In the forward direction below 60°, however, the MS model underestimates the neutron data at neutron energy above 20 MeV. It is supposed that the quasi-elastic and quasi-inelastic scattering processes are dominant in the reaction, where neutron emission spectrum is known to be forward-peaked.

3 Consideration for quasi-elastic scattering

A Gaussian shaped term[10] is introduced into the usual MS model for analyzing the neutron spectra originated from the quasi-elastic and quasi-inelastic scattering processes. The equation is thus written as

$$\frac{d^2\sigma}{d\Omega dE_{kin}} = \sum_{i=1}^{3} p\frac{A_i}{T_i}\exp\left\{-\left(\frac{E_{kin}+m-p\beta_i\cos\theta}{(1-\beta_i^2)^{\frac{1}{2}}}-m\right)/T_i\right\} + A_G\exp\left\{-\frac{(E_{kin}-E_G)^2}{\sigma_G^2}\right\}, \quad (3)$$

where A_G (mb/sr/MeV), E_G (MeV) and σ_G (MeV) in the last term are adjustable parameters, and are dependent on the emission neutron angle at this stage. The other terms are the same one in the usual MS model of Eq. 2. The values of parameters A_G, E_G and σ_G are showed in Fig. 7, where q_{NN} (MeV/c) is momentum transfer. The marks stand for the value obtained from fitting for 113 and 597 MeV proton incidence on Fe. The solid lines show systematics of parameters obtained by smooth functions as

$$\begin{aligned} A_G &= a_1 e^{a_2 q_{NN}}, \\ E_G &= \left\{b_1 + b_2 q_{NN} + b_3 q_{NN}^2\right\} E_{NN}, \\ \sigma_G &= \left\{c_1 + c_2 q_{NN} + c_3 q_{NN}^2\right\} E_{NN}, \end{aligned} \quad (4)$$

where E_{NN} (MeV) that neutron kinetic energy after elastic collision with incident proton, a_i, b_i and c_i that adjustment parameter. The quantity of q_{NN} and E_{NN} are determined by the incident proton and the angle of emitted neutron. The values of E_G and σ_G are almost constant, while A_G depends on momentum transfer strongly. Figures 3 - 6 present neutron production double differential cross section on Fe, W and Pb target. The solid lines show the neutron spectra obtained by the MS model including the gaussian-term obtained by Eqs. 3 and 4. The marks and the dashed lines indicate the experimental data[5][6] and the calculated results by QMD+SDM, respectively. The MS model with the Gaussian shaped term represents the experimental and calculated neutron data over the whole angle well.

4 Systematics of parameters

The systematics of parameters of MS model was obtained by fitting of the experimental neutron data and the results calculated by HETC-3STEP and QMD+SDM in the incident proton energy region from

several-tens MeV to 3 GeV. The parameters A, β and T for Fe and Pb target are shown as function of incident proton energy in Figs. 8 and 9, respectively. In these figures, subscripts 1, 2 and 3 indicate the intranuclear-cascade, preequilibrium and nuclear-evaporation processes, respectively. The marks present the values obtained from fitting for experimental and calculated neutron data. The solid lines show systematics of parameters A, β and T. The Amplitude A_1 for cascade process on Fe and Pb target vanish in the incident proton energy region below 100 MeV. For preequilibrium process, the amplitude A_2 on Fe target shows different behavior from one on Pb target. Temperature T_1 and T_2 are supposed to combine together at the incident proton energy around 100 MeV. The Velocity β on Pb smoothly depends on incident proton energy for each reaction process.

5 Conclusion

The experimental neutron data and the calculated results above several tens-MeV were reproduced for the three components of cascade, preequilibrium and evaporation reaction by the use of MS model. The introduction of the gaussian shaped term into MS model were found to lead to good agreement with the neutron emission spectra originated from quasi-elastic and quasi-inelastic spectra. The Maxwell MS model with the Gaussian term were found to be applicable to the nuclear data evaluation for the wide incident energy range.

References

[1] Bogatoskaya, I. G., *et al.* : *Phys. Rev.* **C22**, 209 (1980).

[2] Ishibashi, K., *et al.* : *J. Nucl. Sci. Tech.*, **29**, 499 (1992).

[3] Birjukov, B. V., *et al.* : *Yad. Fiz.* **31**, 561 (1980).

[4] Harder, K., *et al.* : *Hamburg University* HH-87-01 (1987).

[5] Meier, M. M., *et al.* : *Nucl. Sci. Eng.*, **102**, 310 (1989).

[6] Amian, W. B., *et al* : *Nucl. Sci. Eng.*, **115**, 1 (1993).

[7] Ishibashi, K., *et al.* : *J. Nucl. Sci. Tech.*, **34**, 529 (1992).

[8] Yoshizawa,Y. *et al.* : *J. Nucl. Sci. Tech.*, **32**, 601 (1995).

[9] Niita, K., *et al.* : *Phys. Rev.*, **C52**, 2620 (1995).

[10] Kitsuki, H. *et al.* : *Proc. 1998 Symposium on Nuclear Data*, JAERI-Conf 99 002, 257 (1998).

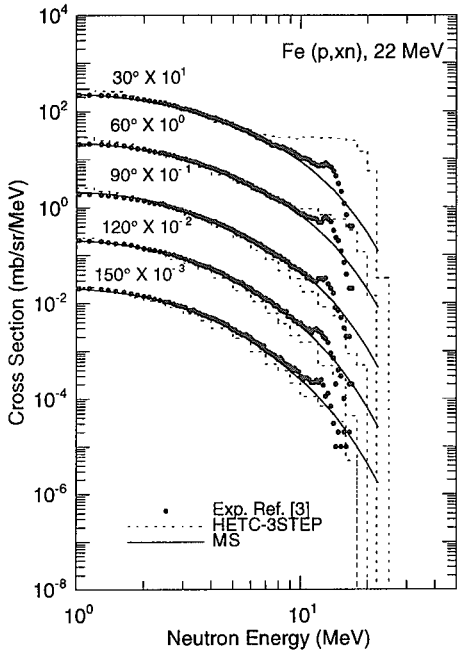

Figure 1: Neutron production double differential cross section for 22 MeV-proton incidence on Fe.

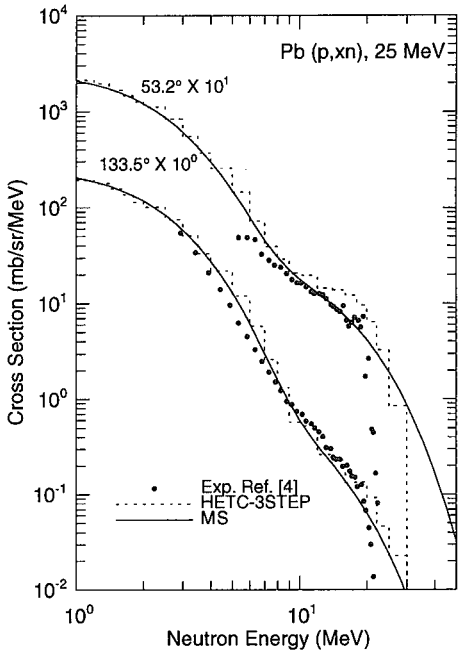

Figure 2: Neutron production double differential cross section for 25 MeV-proton incidence on Pb.

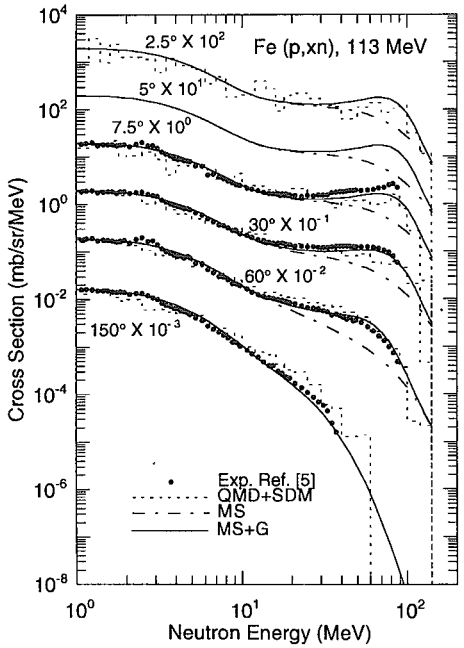

Figure 3: Neutron production double differential cross section for 113 MeV-proton incidence on Fe.

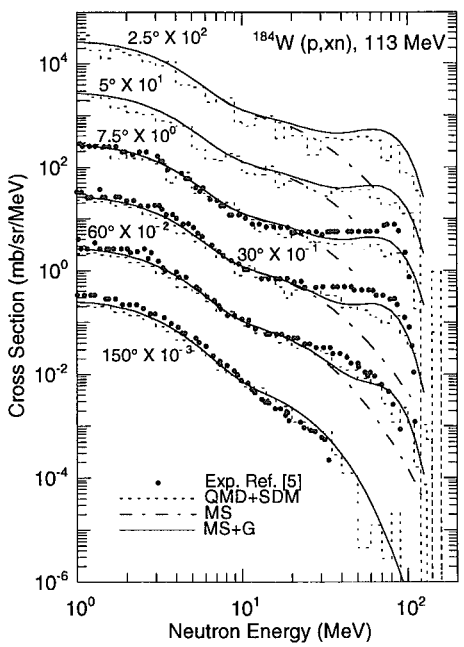

Figure 4: Neutron production double differential cross section for 113 MeV-proton incidence on W.

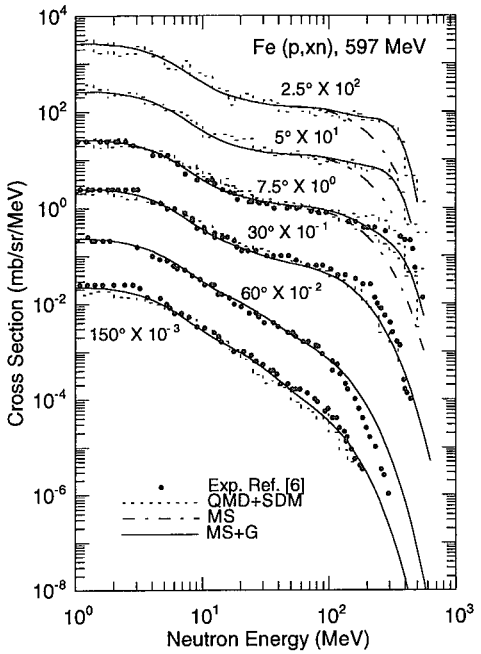

Figure 5: Neutron production double differential cross section for 597 MeV-proton incidence on Fe.

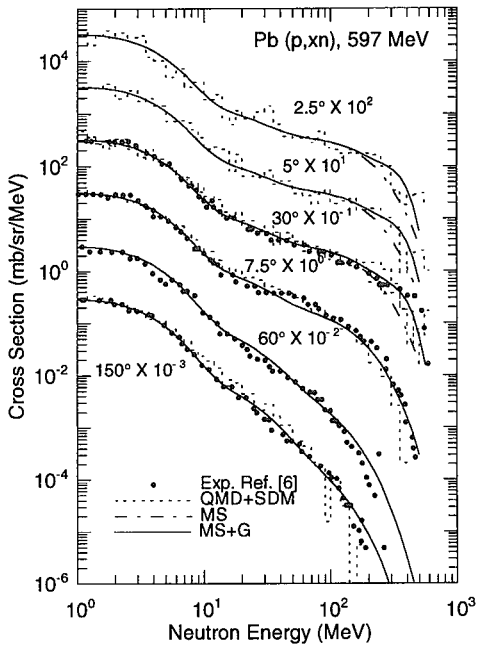

Figure 6: Neutron production double differential cross section for 597 MeV-proton incidence on Pb.

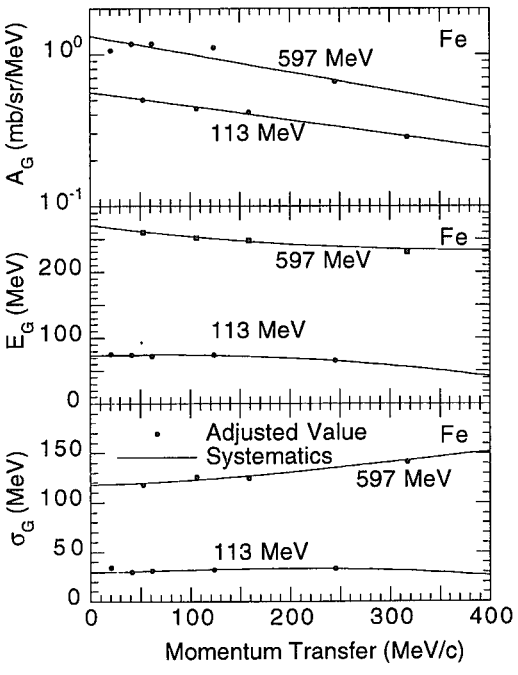

Figure 7: The parameters A_G, E_G and σ_G of Gaussian term obtained by fitting for the experimental and calculated neutron data

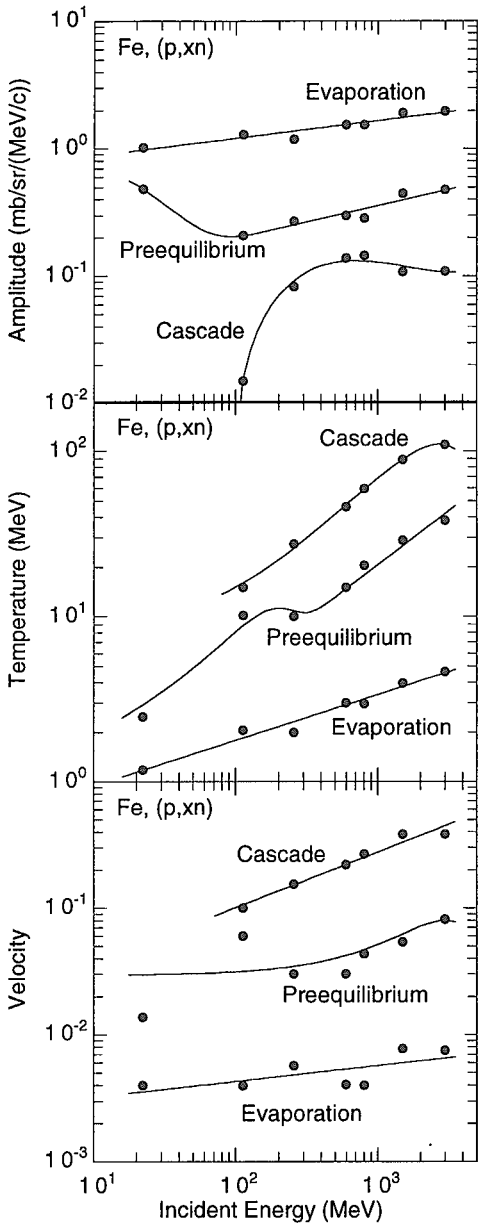

Figure 8: Incident energy dependence of parameters A, T and β on Fe target

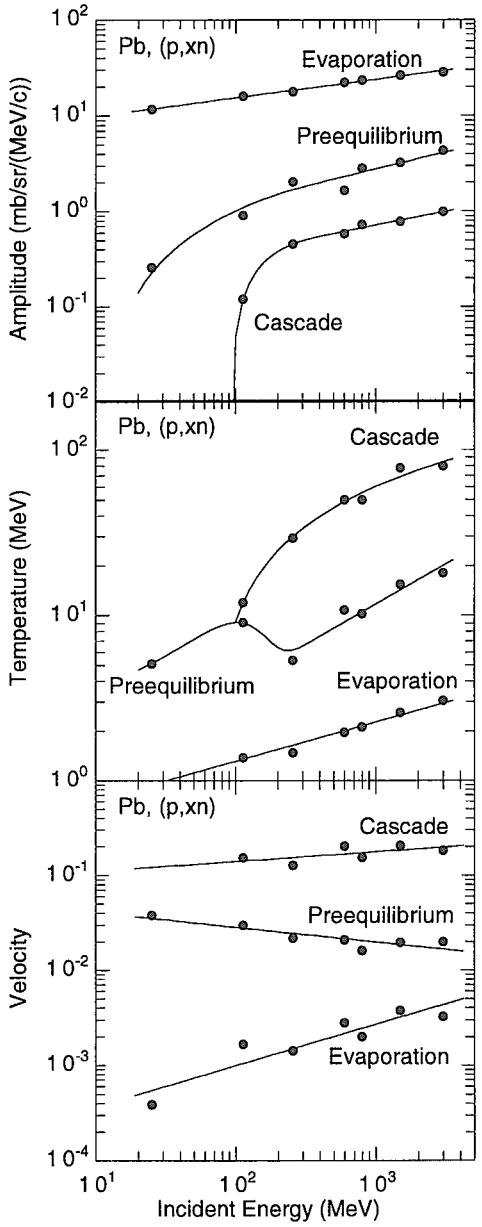

Figure 9: Incident energy dependence of parameters A, T and β on Pb target

3.29 Calculation of the MSD Two-Step Process with the Sudden Approximation

YOSHIDA Shiro† and KAWANO Toshihiko‡
† *Department of Physics, Tohoku University*
Aoba-ku, Sendai 980-8578, Japan
e-mail: shiro@nucl.phys.tohoku.ac.jp
‡*Advanced Energy Engineering Science, Kyushu University*
6-1 Kasuga-kouen, Kasuga 816-8580, Japan
e-mail: kawano@aees.kyushu-u.ac.jp

A calculation of the two-step process with the sudden approximation is described. The Green's function which connects the one-step matrix element to the two-step one is represented in r-space to avoid the on-energy-shell approximation. Microscopically calculated two-step cross sections are averaged together with an appropriate level density to give a two-step cross section. The calculated cross sections are compared with the experimental data, however the calculation still contains several simplifications at this moment.

1. Introduction

Quantum mechanical theories of the preequilibrium nuclear reaction have been developed in recent years. There are three well-known statistical multi-step direct (MSD) theories, those are the theories of Feshbach, Kerman, and Koonin (FKK)[1], Tamura, Udagawa, and Lenske (TUL)[2], and Nishioka, Weidenmüller, and Yoshida (NWY)[3]. The FKK theory has a rather simple and feasible formulation in contrast with the TUL and NWY models, and it has been applied to analyses of the medium- and high-energy nuclear reactions. A long-standing problem exists, however, *i.e.* the on-energy-shell approximation in the Green's function made by FKK is inadequate.

The other two theories employ the different statistical assumptions — the adiabatic and sudden approximations. According to an argument of the time scale of nuclear reactions, an additional particle-hole pair creation is much faster than residual configuration mixing. Therefore the sudden approximation is favored. However no calculation has been done with the NWY model so far, because of its somewhat complicated formulation.

In this study, we calculate the MSD two-step process with the sudden approximation. The nuclear state is expressed by the single-particle shell model. The residual interaction is assumed to be a central Yukawa form with the range of 1 fm. Calculated inelastic scattering cross sections are compared with the experimental data.

2. Microscopic Cross Section of the Two-Step Process

Cross sections of a two-step process in Fig. 1, $A + a \rightarrow C + c \rightarrow B + b$, is given by

$$\left(\frac{d\sigma}{d\Omega}\right)_{\text{2step}} = \frac{2I_B+1}{(2I_A+1)(2S_a+1)} \sum_j \frac{\mu_a \mu_b}{(2\pi\hbar^2)^2} \frac{k_b}{k_a} \sum_{m m_b m_a} \left| t_{lsj}^{m m_b m_a} \right|^2, \tag{1}$$

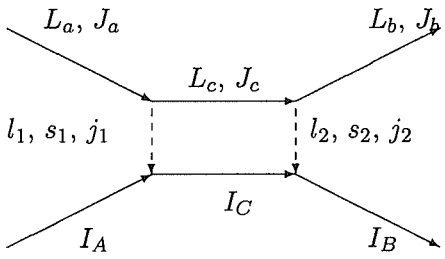

$$\boldsymbol{l} = \boldsymbol{j} + \boldsymbol{s}, \qquad \boldsymbol{s} = \boldsymbol{s}_1 + \boldsymbol{s}_2$$
$$\boldsymbol{j} = \boldsymbol{j}_1 + \boldsymbol{j}_2 = \boldsymbol{I}_B - \boldsymbol{I}_A = \boldsymbol{J}_a - \boldsymbol{J}_b$$
$$\boldsymbol{j}_1 = \boldsymbol{I}_C - \boldsymbol{I}_A = \boldsymbol{J}_a - \boldsymbol{J}_c$$
$$\boldsymbol{j}_2 = \boldsymbol{I}_B - \boldsymbol{I}_C = \boldsymbol{J}_c - \boldsymbol{J}_b$$

Fig. 1: 2-step process, coupling of angular momenta.

where I is the spin of nucleus, S, L, J are the intrinsic spin, angular momentum, and total spin of nucleon, k the wave number, and l, s, j the transfered angular momentum and spin. The transition matrix element t is given by[4]

$$\begin{aligned} t_{lsj}^{mm_bm_a} &= \sum_{L_aJ_aL_bJ_b} \hat{J}_b \hat{l}\hat{s} \langle L_a S_a 0 m_a | J_a m_a \rangle \langle L_b S_b m, -m_b | J_b m - m_b \rangle \\ &\times \langle J_a j m_b - m, m_a - m_b + m | J_a m_a \rangle A_{L_aL_b}^m(\theta) I_{L_aJ_aL_bJ_b}^{lsj}, \end{aligned} \tag{2}$$

where $A_{L_aL_b}^m(\theta)$ is the angle factor, and $I_{L_aJ_aL_bJ_b}^{lsj}$ is the radial overlap integral,

$$I_{L_aJ_aL_bJ_b}^{lsj} = \frac{4\pi}{k_a k_b} \int r_b dr_b \int r_a dr_a \chi_{L_b}^{J_b}(k_b r_b) h_{L_aJ_aL_bJ_b}^{lsj} \chi_{L_a}^{J_a}(k_a r_a), \tag{3}$$

which contains a radial kernel $h_{L_aJ_aL_bJ_b}^{lsj}$ of the two-step process. When one uses the zero-range approximation, the kernel becomes[5]

$$\begin{aligned} h_{L_aJ_aL_bJ_b}^{lsj} &= \sum_{l_1l_2s_1s_2j_1j_2L_cJ_c} i^{L_a-L_b-l_1-l_2}(-)^{j_1+j_2-j} \hat{j}_1\hat{j}_2^2\hat{s}_1\hat{s}_2\hat{l}_1\hat{l}_2\hat{L}_b\hat{J}_b\hat{L}_c\hat{J}_c^2\hat{I}_C \\ &\times \langle L_c l_1 00 | L_a 0 \rangle \langle L_b l_2 00 | L_c 0 \rangle W(J_a\, j_1\, J_b\, j_2\, ;\, J_c\, j) W(I_A\, j_1\, I_B\, j_2\, ;\, I_C\, j) \\ &\times \begin{Bmatrix} L_c & S_c & J_c \\ l_1 & s_1 & j_1 \\ L_a & S_a & J_a \end{Bmatrix} \begin{Bmatrix} L_b & S_b & J_b \\ l_2 & s_2 & j_2 \\ L_c & S_c & J_c \end{Bmatrix} F_{L_cJ_c}(r_b, r_a), \end{aligned} \tag{4}$$

$$F_{L_cJ_c}(r_b, r_a) = f_{l_2}(p_2 h_2; r_b) G_{L_cJ_c}^{(+)}(r_b, r_a) f_{l_1}(p_1 h_1; r_a), \tag{5}$$

where $G_{L_cJ_c}^{(+)}(r', r)$ is the partial-wave expanded Green's function which connects the one-step matrix element to the two-step one. The Green's function in r-space representation[6] can be calculated as

$$G_{L_cJ_c}^{(+)}(r_b, r_a) = -\frac{2\mu}{\hbar^2 k_c} \chi_{L_cJ_c}(k_c r_<)\, \mathcal{H}_{L_cJ_c}(k_c r_>), \tag{6}$$

where $\chi_{L_cJ_c}(k_c r)$ is the distorted wave for the intermediate state, $\mathcal{H}_{L_cJ_c}(k_c r)$ is the out-going wave which is an irregular solution of the Schrödinger equation. These functions have asymptotic forms

$$\chi(k_c r) \sim \{F(k_c r) + C\,[G(k_c r) + iF(k_c r)]\}\, \mathrm{e}^{i\delta_C}, \tag{7}$$
$$\mathcal{H}(k_c r) \sim \{G(k_c r) + iF(k_c r)\}\, \mathrm{e}^{-i\delta_C}, \tag{8}$$

where $G(k_c r)$ and $F(k_c r)$ are the Coulomb functions, and δ_C the Coulomb phase shift.

In Eq. (5), $f_l(r)$ is the form factor which expresses p-h state excitation. We assumed that the particle-hole residual interaction has the Yukawa form with the range of 1 fm. According to an expression of the two-step process with the sudden approximation, an intermediate state is always $1p$-$1h$ state. Therefore the formfactor for the first collision f_{l_1} in Eq. (5) is $\langle 1p1h|V|0\rangle$, and the second formfactor becomes $\langle 2p2h|V|1p1h\rangle$. However we replaced the second one by $\langle 1p1h|V|0\rangle$ for the sake of simplicity. This simplification will be removed in future.

3. Transition to Continuum

Double differential cross sections of the two-step process to the continuum state are calculated as

$$\left(\frac{d^2\sigma}{d\Omega dE_b}\right)_{\rm 2step} = \frac{\mu_a\mu_b}{(2\pi\hbar^2)^2}\frac{k_b}{k_a}\sum_l \sum_{p_1h_1p_2h_2} (2l+1)\hat{\rho}^{(l)}_{p_1h_1p_2h_2}(E_x) \sum_{mm_bm_a} |t^{mm_bm_a}_{l0l}|^2, \qquad (9)$$

where the target spin I_A and the spin transfer s are assumed to be zero, $\hat{\rho}$ is the true level density[7]. As seen in Fig. 2 there are four different paths to arrive the same $2p$-$2h$ state. Amplitudes corresponding to those paths are coherently summed up to give the final two-step amplitude. An example of this rearrangement is shown in Fig. 3, which is the angular distribution of ^{208}Pb(p,p') reaction, for E_{in} = 22 MeV, l = 3, and the excited $2p$-$2h$ state is $|1f_{7/2}0h_{9/2}(2s_{1/2})^{-1}(1d_{3/2})^{-1}\rangle$ in the Z shell. The optical potential used is the Walter-Guss' potential and the strength of the residual interaction V_0 is taken to be 30 MeV. The thick solid line stands for the coherent sum of four amplitudes which correspond to the different intermediate state. The dot-dashed line is the incoherent sum of the cross sections shown by the thin lines.

Since the $2p$-$2h$ state density in the residual nucleus is very large, it is difficult to calculate Eq. (9) directly. We approximate Eq. (9) by

$$\left(\frac{d^2\sigma}{d\Omega dE_b}\right)_{\rm 2step} = \sum_l (2l+1)\omega(2,2,E_x)R_4(l)\overline{\left(\frac{d\sigma}{d\Omega}\right)_l}, \qquad (10)$$

where $\overline{(d\sigma/d\Omega)_l}$ is the averaged two-step cross section for the angular momentum transfer of l, $\omega(2,2,E_x)$ is the state density of Betak-Dobes[8], $R_4(l)$ the spin distribution.

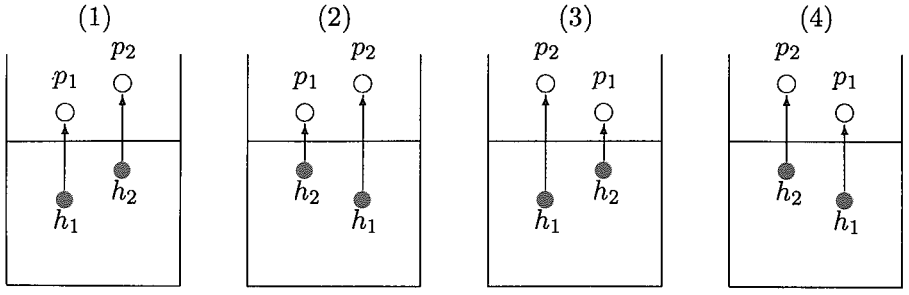

Fig. 2: Four paths to arrive a 2-particle 2-hole state. (1) is the basic configuration, (2) shows an exchange of the two holes, (3) shows an exchange of the two particles, and (4) shows exchanges of the two holes and two particles, respectively.

The average cross section in Eq. (10) is calculated by means of a random sampling of the $2p$-$2h$ state, and the microscopic cross sections for those states are Gaussian averaged. Figure 4 shows various two-step cross sections (light lines) and the average of them (heavy line).

A comparison of the calculated angular distribution of inelastically scattered neutrons from ^{93}Nb for E_{in} = 25.7 MeV and E_{out} =12.5 MeV, with the experimental data[9] is shown in Fig. 5. The dashed line is the one-step cross section, and the dotted line is the two-step one. The effective interaction strength V_0 used was 30 MeV. This result is similar to the NWY calculation of Koning and Akkermans[10], although they made some additional approximations to make calculations easier.

Figure 6 shows a comparison of the angle-integrated energy spectra for the 25.7 MeV neutron incident reaction on ^{93}Nb. The energy spectrum consists of the one-step, two-step, and Hauser- Feshbach components, and the elastic scattering, collective, and $(n, 2n)$ reactions are not included. The sum of one-step and two-step processes well reproduces the experimental data near 15 MeV.

4. Conclusion

We described how the two-step cross sections with the sudden approximation are calculated. At this moment it contains several approximations, such as the replacement of the formfactor at the second collision, use of a phenomenological level density formula, and so on. Such simplifications will be removed in future to give a calculation which is more in line with the NWY theory.

References

[1] H. Feshbach, A. Kerman, and S. Koonin, *Ann. Phys.*, (N.Y.) **125**, 429 (1980).

[2] T. Tamura, T. Udagawa, and H. Lenske, *Phys. Rev. C,* **26**, 379 (1982).

[3] H. Nishioka, H. A. Weidenmüller, and S. Yoshida, *Ann. Phys.*, (N.Y.) **183**, 166 (1988).

[4] G. R. Satchler, *Nucl. Phys.*, **55**, 1 (1964).

[5] N. Hashimoto and M. Kawai, *Prog. Theo. Phys.*, **59**, 1245 (1978); N. Hashimoto, *Prog. Theo. Phys.*, **59**, 1562 (1978).

[6] N. Austern, R. M. Drisko, E. Rost, and G. R. Satchler, *Phys. Rev.*, **128**, 733 (1962).

[7] K. Sato, Y. Takahashi, and S. Yoshida, *Z. Phys. A,* **339**, 129 (1991).

[8] E. Betak and J. Dobes, *Z. Phys. A,* **279**, 319 (1976).

[9] A. Marcinkowski, R. W. Finlay, G. Randers-pehrson, C. E. Brient, R. Kurup, S. Mellema, A. Meigooni, and R.Tailor, *Nucl. Sci. Eng.*, **83**, 13 (1983).

[10] A. J. Koning and J. M. Akkermans, *Phys. Rev. C,* **47**, 724 (1993).

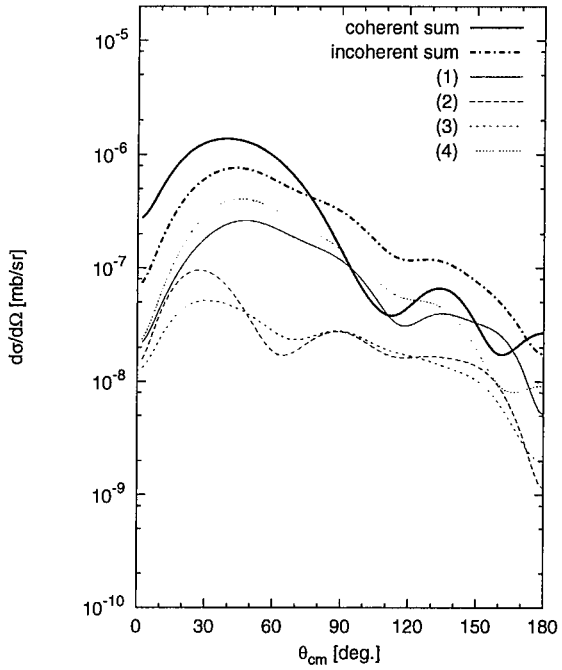

Fig. 3: Microscopic two-step cross sections for ^{208}Pb(p,p'), for E_{in} =22 MeV. The $2p$-$2h$ pairs are created in the Z shell. The thin lines are the contributions of each path in Fig. 2, the thick sold line is the coherent sum of the four paths, and the thick dot-dashed line is the incoherent sum.

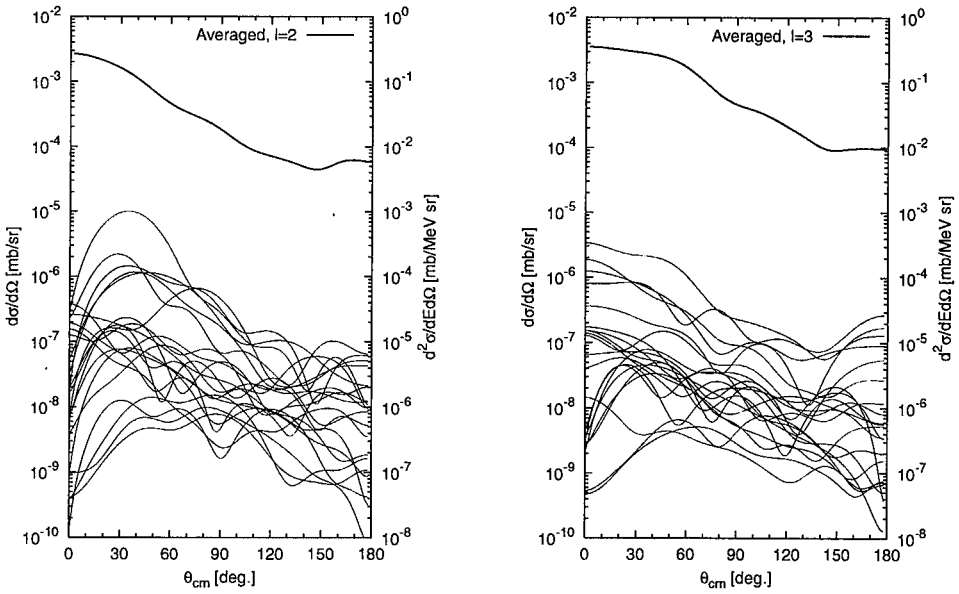

Fig. 4: Averaged microscopic two-step cross sections for the angular momentum transfers of 2 and 3. The heavy solid lines are averaged values multiplied by the state density (on the right axis), and the light lines are some typical microscopic cross sections (on the left axis).

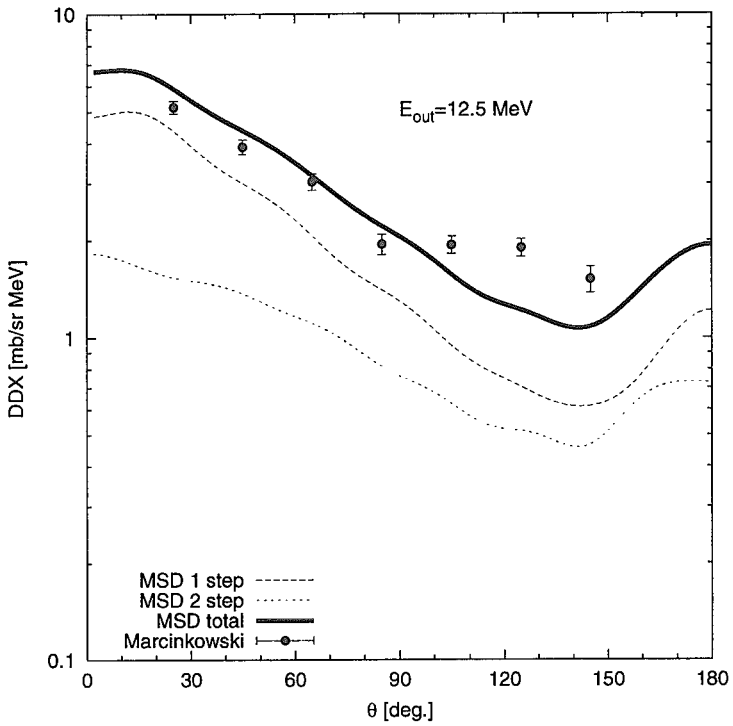

Fig. 5: Comparison of the calculated angular distribution of inelastically scattered neutrons from ^{93}Nb for E_{in} =25.7 MeV, and E_{out} =12.5 MeV, with the experimental data.

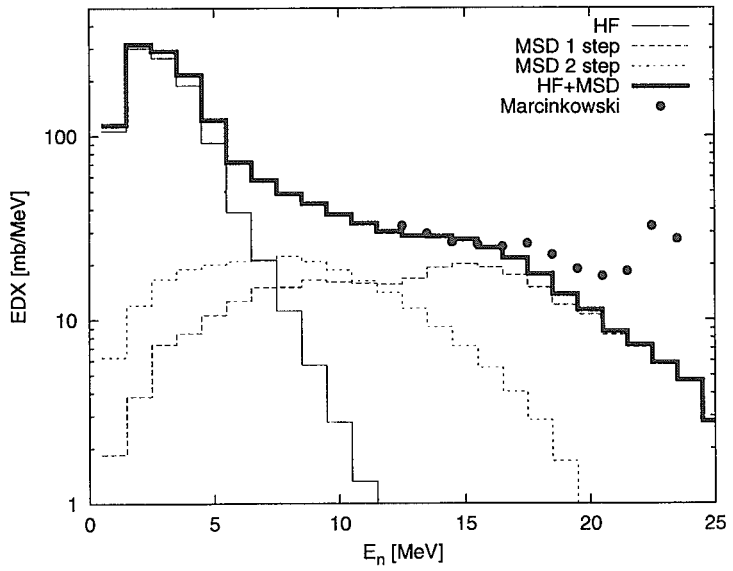

Fig. 6: Energy distribution of the emitted neutrons for the 25.7 MeV neutron incident reaction on ^{93}Nb.

3.30

A Systematics of Optical Model Compound Nucleus Formation Cross Sections for Neutron,Proton,Deuteron,^{3}He and Alpha Particle Incidents

Toru Murata
AITEL corporation
1-5-9 Shiba,Minatoku,Tokyo 105-0014
e-mail: murata@aitel.toshiba.co.jp

Simple formulae to reproduce the optical model compound nucleus formation cross sections for neutron,proton,deuteron,triton,^{3}He and alpha particles are presented for target nuclei of light to medium weight mass region.

Many nuclear reaction calculation codes utilize optical model compound nucleus formation cross sections repetitiously many times to obtain nuclear reaction behavior. For ordinary personal computers, the cross section calculation is quite heavy work. So, simple fitting formula or simple systematics of the cross sections over many target nucleus are useful for the nuclear reaction calculation. As an example, in the statistical multi-step reaction code EXIFON /1/, the cross sections for neutron, proton and alpha particle incidents are reproduced with several tenth of fitting parameters, over target nucleus mass number A>20 in the incident energy region below 100MeV. Modification of the EXIFON code were made /2/ to apply it to light nucleus and to include deuteron, triton and ^{3}He emission, and fitting parameters for these particles were also determined to reproduce the cross sections in the target nucleus mass region A<=16.

In the present study, target nucleus are extended to the medium weight nuclei, and the cross sections are calculated with optical potential parameters given in the ref./3/. Incident energy dependence of the cross section ratio R(E): charged particle (p,d,t,^{3}He and alpha-particle) to neutron are well reproduced with the following formulae. Incident energy region was divided into two region, using a Coulomb barrier related parameter E_0:

$E_0 = Q_b * R_C$, $Q_b = E_{qb} * R_q$,

where E_{qb} is Coulomb barrier and given by $E_{qb} = 1.4399 * Z_p * Z_T / R$ (MeV) using the interaction radius: $R = R_0 * (A_T^{1/3} + A_p^{1/3})$ and $R_0 = 1.3$ fm.

In the incident energy region: $E <= E_0$, R(E) is given by approximated Coulomb barrier penetration factor and

$R(E) = Exp[-2*G/A_g]$

$G = \{Arccos(E_b^{1/2}) - E_b^{1/2}*(1- E_b)^{1/2}\}*Q_b/Z_p/ E_b^{1/2})$

In the incident energy region: $E > E_0$

$R(E) = R(E_0)+\{1-Exp(-A_0*(E-E_0))\}*\{A_1+A_2*(E-E_0)^{1/2}\}$

where, $R_c, R_q, A_g, A_0, A_1, A_2$ are fitting parameters.

Examples of the fitting are shown in Fig.1 for ^{12}C and ^{90}Zr. The fitting parameters dependence on target nucleus atomic number is shown in Fig.2.

Neutron incident compound nucleus formation cross section was reproduced by,

in the incident energy region: $E_1 =< E < E_2$,

$\sigma_n(E) = A_l*E+A_m+A_n/E$,

in $E < E_1$,

$\sigma_n(E) = B_l*(E-E_1)+\sigma_n(E_1)+B_n*(1/E-1/E_1)$,

and in $E > E_2$,

$\sigma_n(E) = \sigma_n(E_2)*(E/ E_2)^{A0}$,

where $A_l, A_m, A_n, B_l, B_n, E_1$, and E_2 are fitting parameters.

Examples of the cross section fitting are shown in Fig.3 and values of the fitting parameters are given in Table 1.

As is shown in Figures, the cross section ratios and the neutron incident cross sections are reproduced well with the present simple formulae.

[References]

/1/ Kalka,H.: Z.Phys.A341,289(1992), /2/ Murata,T.: JAERI-Conf 97-005, p.286

/3/neutron: Wilmore,D.,hodgson,P.E.: Nucl.Phys.32,353(1962), proton: Perey,F.G.:Phys. Rev.131,745(1963), deuteron:P erey,C.M.,Perey.F.G.:Phys.Rev.132,755(1963), triton& ^{3}He:Becchetti,F.D.,Greenlees,G.W.:"Polarization Phenomena in Nuclear Reaction" ,p.628, alpha: Arthur,E.D.,Young,P.G.:LA-8636-MS(ENDF-304)

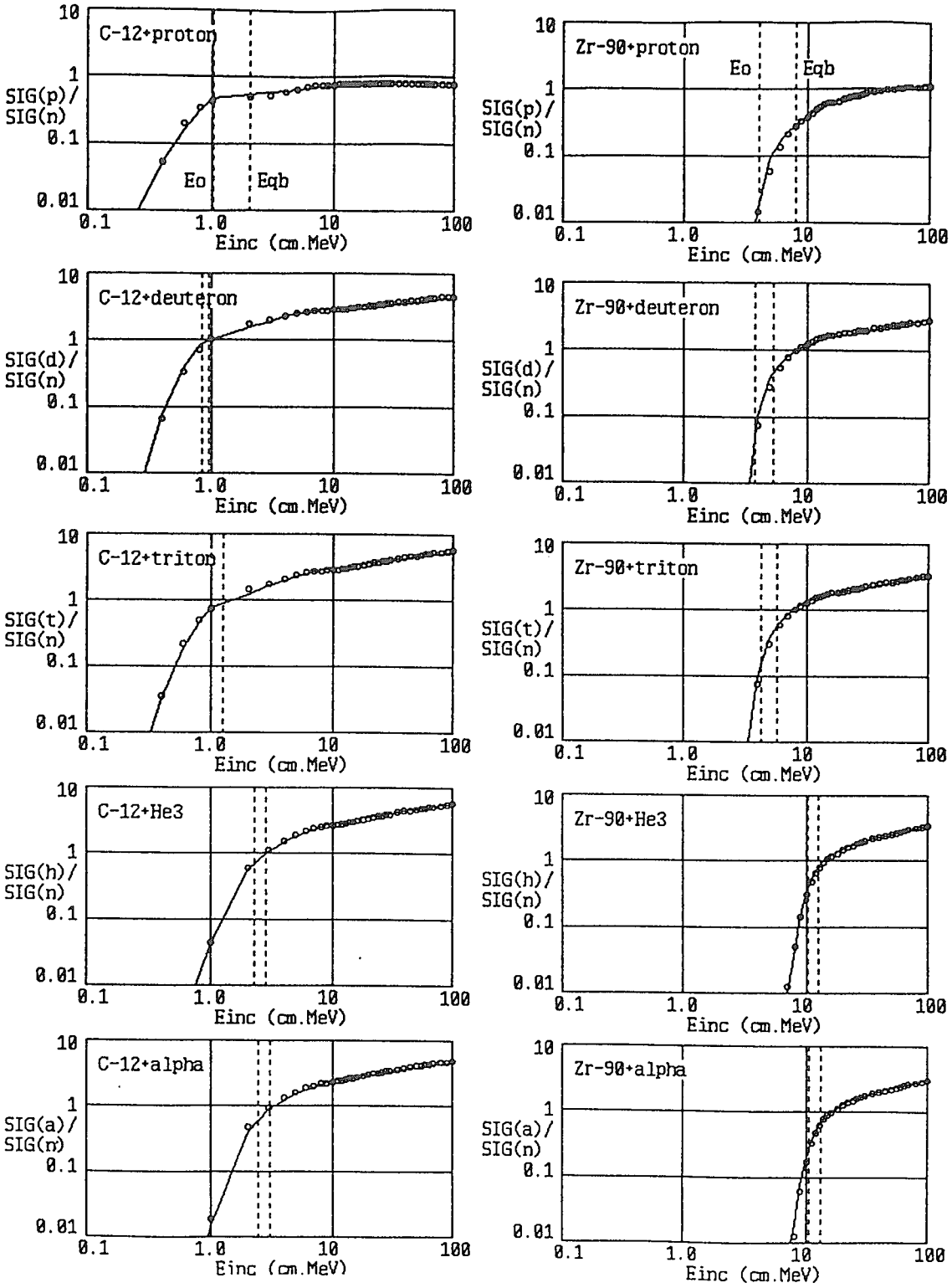

Fig.1 Ratio of charged particle incident compound nucleus formation cross section to that of neutron incident on ^{12}C and ^{90}Zr. Optical model calculation ratios are shown by circles and reproduced ratios using present formulae are shown by solid lines.

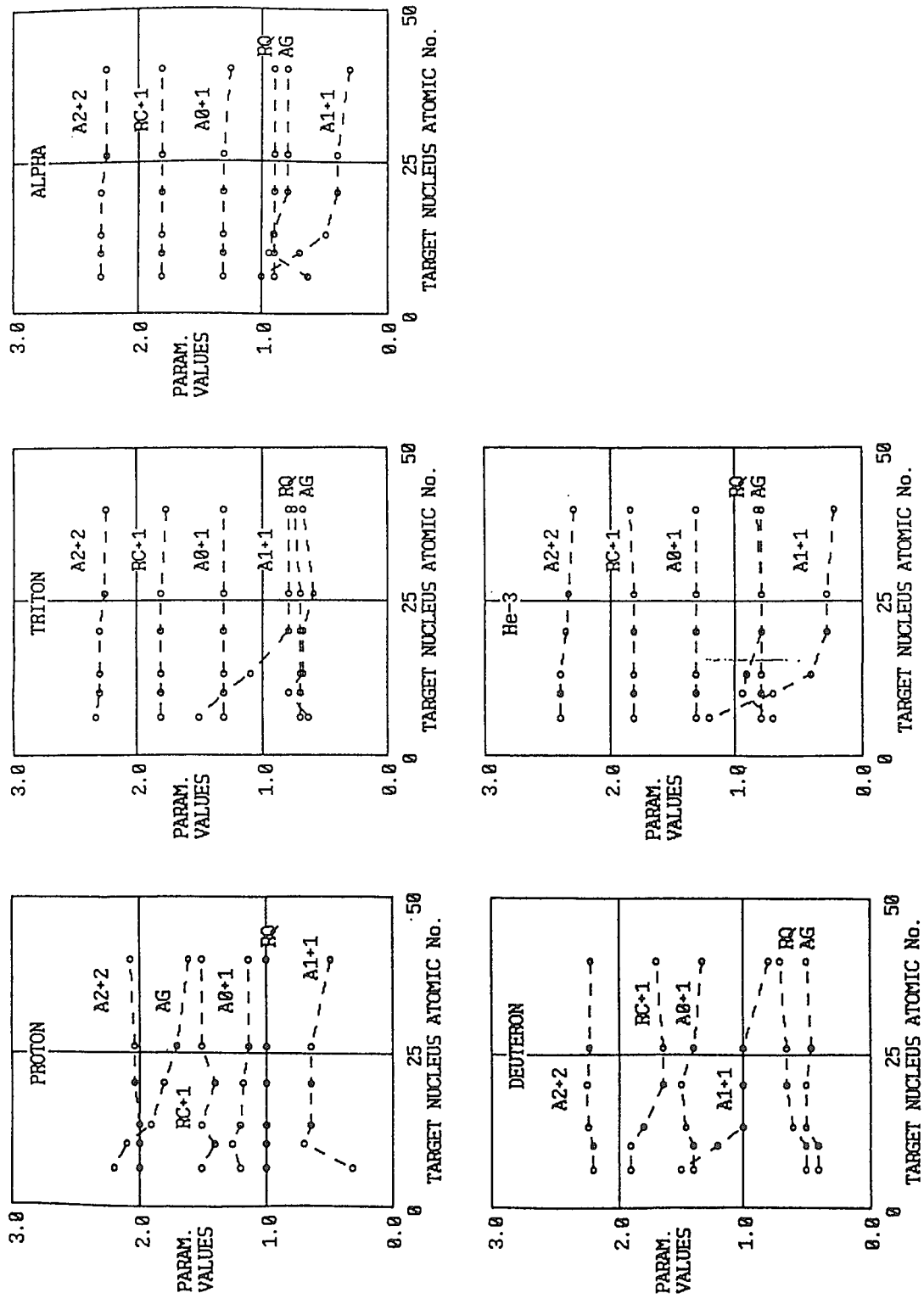

Fig.2 Target nucleus atomic number dependence of the parameters to reproduce the cross section ratios (See text). For distinction, some parameters are shifted by given value in the figure.

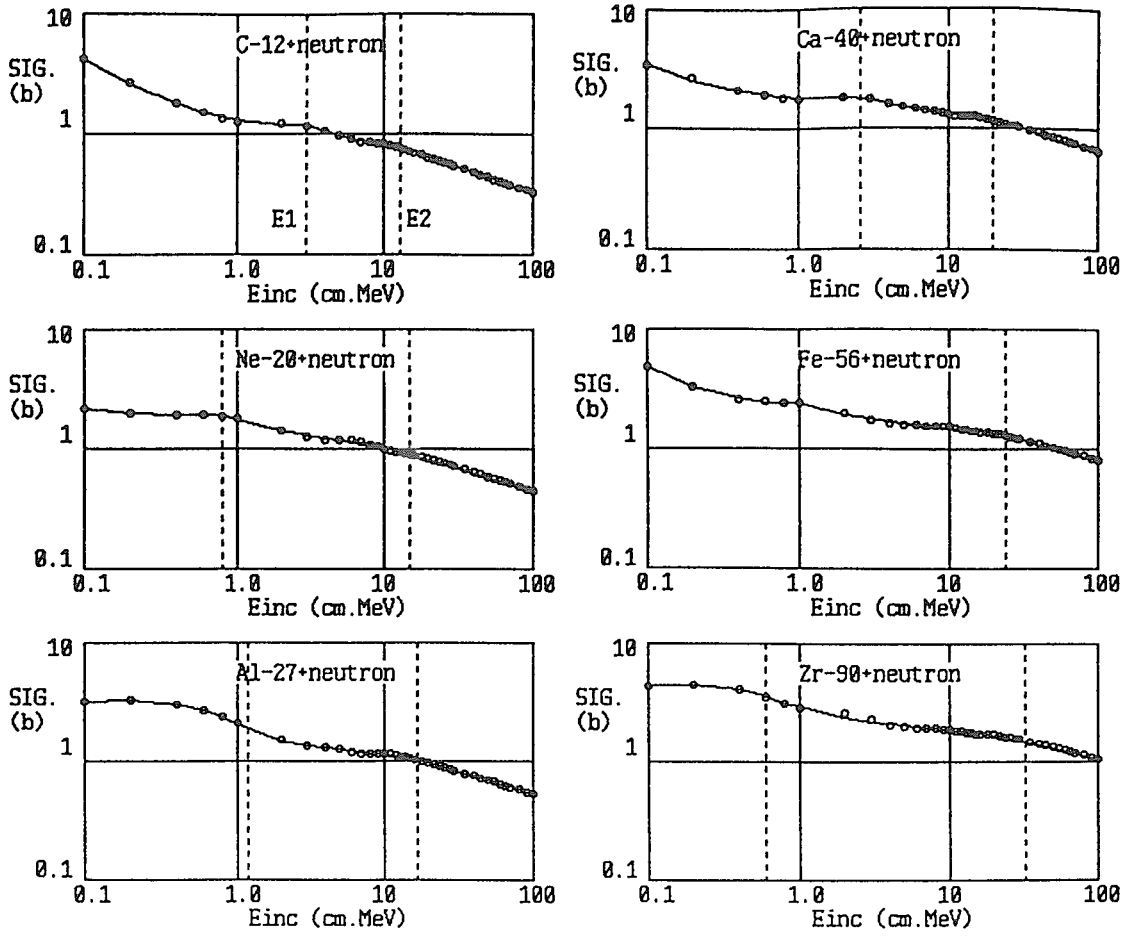

Fig.3 Examples of neutron incident compound nucleus cross sections reproduced by present formulae. Optical model calculated values are shown by circles and reproduced ones using present formulae are shown by solid lines.

Table 1 Values of fitting parameters for neutron incident compound nucleus formation cross sections (See text)

TARGET	AL	AM	AN	BL	BN	A0	E1	E2
C-12	-3.87E-01	6.66E+02	1.55E+03	3.72E+01	3.28E+02	-4.19E-01	3.00E+00	1.30E+01
Ne-20	-2.14E+01	1.18E+03	6.04E+02	9.74E+01	3.64E+01	-3.69E-01	8.00E-01	1.50E+01
Al-27	-9.28E+00	1.16E+03	7.17E+02	-1.69E+03	-4.00E+01	-3.74E-01	1.20E+00	1.68E+01
Ca-40	-7.43E+00	1.25E+03	1.56E+03	6.42E+01	1.89E+02	-3.53E-01	2.60E+00	2.00E+01
Fe-56	-9.87E+00	1.51E+03	9.32E+02	3.96E+02	3.06E+02	-3.41E-01	1.00E+00	2.40E+01
Zr-90	-1.39E+01	1.91E+03	1.01E+03	-2.99E+03	-8.11E+01	-2.99E-01	6.00E-01	3.25E+01

3.31 Neutron and Proton Optical Potentials for ^{12}C, ^{16}O, ^{27}Al, ^{56}Fe, ^{90}Zr and ^{208}Pb up to 250 MeV

Young-Ouk LEE and Jonghwa CHANG
Korea Atomic Energy Research Institute,
Tokio FUKAHORI and Satoshi CHIBA
Japan Atomic Energy Research Institute
e-mail: yolee@lui.kaeri.re.kr

In order to perform nuclear data evaluation without unphysical discontinuities, optical models should cover the whole mass and energy range of interest continuously. In this work, the best set of optical model parameters were obtained with energy dependent potential forms which incorporate effects of dispersion relationship for neutron and proton up to 250 MeV on ^{12}C, ^{16}O, ^{27}Al, ^{56}Fe, ^{90}Zr and ^{208}Pb. Applicability of adopting an identical geometrical factor for the real volume, imaginary volume and imaginary surface potentials has been investigated as well in the process of parameter search.

1. Introduction

Nuclear data for conventional fission reactors and fusion devices mainly consist of neutron-induced cross sections in energy below 20 MeV. However, recent new applications, such as radiation transport simulations of cancer radiotherapy and the accelerator-driven transmutation of nuclear wastes require evaluated nuclear data on neutron- and proton-induced reaction above 20 MeV up to a few GeV.

The optical model provides the basis for theoretical evaluations of nuclear corss sections that are used in providing nuclear data for applications. In addition to offering a convinient means for calculations of reaction, shape elastic, and (neutron) total cross sections, optical model potentials are widely used in quantum-mechanical preequilibrium and direct-reaction theory calculation. But the most important role of the optical model anaysis is to supply particle transmission coefficients for Hauser-Feshbach statistical theory anayses used in nuclear data evaluations.

In order to perform nuclear data evaluation without unphysical discontinuities, optical models should cover the whole energy range of interest continuously. Currently many optical model segments are available for the nuclear date evaluations, but most of them have been derived over very limited energy and mass regions. In the Reference Input Parameter Library (RIPL) published by IAEA [1], only Koning, Wijk and Delaroche [2] potential for neutron reactions on Zr-90 has a truly broad energy range of validity. Recently Chadwick *et al.* [3] applied Madland's global medium energy optical model [4] over wide mass and energy region. It is reported that this global potential gives a good description of measured neutron and proton cross sections for some isotopes up to 160 MeV. But it is also mentioned in the reference that the Madland's global optical potential can not reproduce in more detail the all the measured data. To supplement the Madland's global optical model, they adopted the energy dependent potential forms [5] which incorporate effects of dispersion relationship proposed by Delaroche *et al.* for some isotopes, giving better agreements with measurements. Lee *et al.* [6] also adopted the same potential form in evaluating neutron and proton cross sections of Al-27 up to 250 MeV successfully.

This work aims for a part of ground work to establish a global optical potential form having effects of dispersion relationship over wide mass range and up to 250 MeV. In this work, energy dependent optical model parameters of Delaroche type OMP were searched up to 250 MeV for some isotopes of interest: ^{12}C, ^{16}O, ^{27}Al, ^{56}Fe, ^{90}Zr and ^{208}Pb. As a byproduct, applicability of adopting an identical geometrical factor for the real volume, imaginary volume and imaginary surface potentials has been investigated as well in the process of parameter search.

2. Potential Form : Type I

The potential form factor was chosen to be of Woods-Saxon form for V_r and W_v, derivative Woods-Saxon for W_d and Thomas-Fermi form for spin-orbit parts as

$$U(r) = -V_r f_v(r) - iW_v f_w(r) + 4i\, a_{wd}\, W_d \frac{df_{wd}(r)}{dr}$$

$$-\frac{1}{r}\left(\frac{\hbar}{m_\pi c}\right)^2\left(V_{so}\frac{d}{dr}f_{vso}(r)+iW_{so}\frac{d}{dr}f_{wso}(r)\right)\ \boldsymbol{l}\cdot\boldsymbol{s}\ +V_{Coul}. \tag{1}$$

Figure 1 presents general shapes of potential depths of real volume(V_r), volume absorptive(W_v) and surface absorptive (W_d) adopted in this work to incorporate effects of the dispersion relationship.

$V_r(E)$ decreases exponentially down to few MeV for incident nucleon energies around 250 MeV. On the other hand. $W_d(E)$ increases to reach a plateau at around 10 MeV and then decreases smoothly with energy. W_v(E) is negligible for incident energies below 10 MeV, then increases to reach plateau at around 70 MeV.

These shapes have following functional forms:

$$\begin{aligned}
V_r(E) &= V_0 e^{-\lambda_{vr}(E-E_f)}+V_1+V_2E\\
W_v(E) &= W_{v0}\frac{(E-E_f)^4}{(E-E_f)^4+W_{v1}^4}\\
W_d(E) &= W_{d0}e^{-\lambda_{wd}(E-E_f)}\frac{(E-E_f)^4}{(E-E_f)^4+W_{d1}^4},\\
r_i(E) &= r_{i0}+r_{i1}E\\
a_i(E) &= a_{i0}+a_{i1}E
\end{aligned} \tag{2}$$

where the Fermi energy E_f for neutron and proton is given by

$$\begin{aligned}
\text{neutron}\quad E_f(Z,A) &= -\frac{1}{2}[S_n(Z,A)+S_n(Z,A+1)]\\
\text{proton}\quad E_f(Z,A) &= -\frac{1}{2}[S_p(Z,A)+S_p(Z+1,A+1)]
\end{aligned} \tag{3}$$

The geometry factor of W_v is assumed to be the same as that of V_r as

$$\begin{aligned}
r_v(E) &= r_{wv}(E)\neq r_{wd}(E)\\
a_v(E) &= a_{wv}(E)\neq a_{wd}(E)
\end{aligned} \tag{4}$$

Above leaves 17 adjustable parameters for the enrgy range 0 - 250 MeV of incident neutron and proton.

3. Potential Form : Type II

One thing which make this work different from all other OMP analyses is adopting the same geometry factor for all three potentials as

$$\begin{aligned}
r_v(E) &= r_{wv}(E)=r_{wd}(E)\\
a_v(E) &= a_{wv}(E)=a_{wd}(E)
\end{aligned} \tag{5}$$

This reduces the number of adjusterble parameters to 13.

4. Parameter Search

The best sets of Type-I and Type-II OMP were determined by adjusting the 17 and the 13 adjustable coefficients defined in eq. (2), (4) and (5) with the use of ECISPLOT [7], an interactive optical parameter searcher with the simulated annealing algorithm, developed by the author. It is an X-Window based software system incorporated into the nuclear reaction code ECIS-96 [8]. In ECISPLOT, the potential parameters are adjusted interactively based on eye-guide, then the final parameter set is searched automatically by the simulated annealing algorithm to have minimum χ^2. During the ECISPLOT operation, smooth-varying potential depths and form factors could be collected with respect to the incident energies. With these points, rough fittings and interactive tuning were applied to get initial 17 (for Type-I) or 13 (for Type-II) coefficients. Finally, simulated annealing algorithm were applied to get the best optimum coefficient set within the ranges for each coefficient.

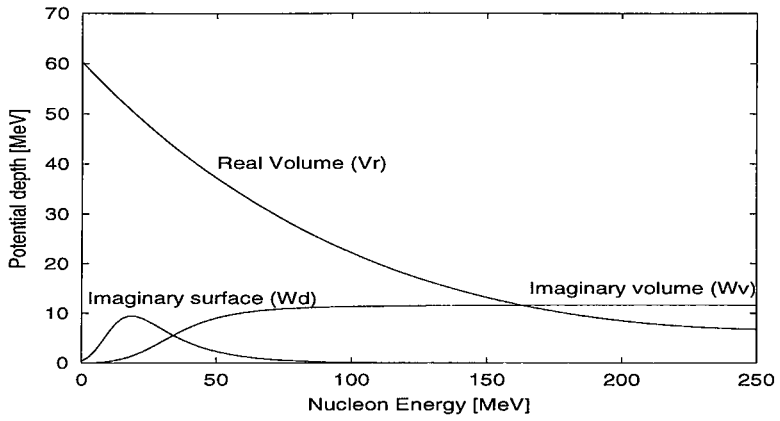

Figure 1: Depths of the real volume, imaginary volume and surface potentials as a function of incident nucleon energy

5. Results and Future Work

The total (for neutron), reaction (for proton) cross sections and elastic angular distributions resulted from Type-I OMP and Type-II OMP set are shown in Figs. 2 -7 with various measurements and LANL evaluations. Our optical model parameters give excellent agreements with most of experimental data over entire energy range for both incident neutron and proton.

Based on the results of present work, appropriate systematics will be tried to establish a global optical potential form form having effects of dispersion relationship, covering wide mass and energy range.

References

[1] Young, P. G.: *Ch4: Optical model parameters*. Tech. Rep. IAEA TECDOC-1034, International Atomic Energy Agency, Vienna, Austria (1998).

[2] Koning, A. J., *et al.*: *Neutron and proton data files up to 150 mev for 54fe, 56fe, 58ni and 60ni*. Tech. Rep. ECN-RX-97-047, Netherlands Energy Research Foundation ECN, Petten, The Netherlands (1997).

[3] Chadwick, M., *et al.*: *Nucl. Sci. Eng.*, **131**, 293 (1999).

[4] Madland, D. G.: In B. Strohmaier, ed., *Proc. of a Specialists Meeting on Preequilibrium Reactions*, no. NEANDC-245, 103–116, Paris, France (1988). Semmering, Austria, 1988, Organization for Economic Cooperation and Development (OECD) Nuclear Energy Agency.

[5] Delaroche, J., *et al.*: *Phys. Rev. C*, **39**, 391 (1989).

[6] Lee, Y., *et al.*: In *Proc. of the 1998 Symposium on Nuclear Data, Nov. 19-20, 1998, JAERI, Tokai, Japan*, no. JAERI-Conf 99-002, 246 (1999).

[7] Lee, Y.: *ECISPLOT: An interactive optical model parameter searcher with simulated annealing algorithm*. Tech. Rep. NDL-9/99, KAERI (1999).

[8] Raynal, J.: *Notes on ECIS94*. Tech. Rep. CEA-N-2772, pp. 1–145, Commisariat á l'Energie Atomique (CEA), Saclay, France (1994).

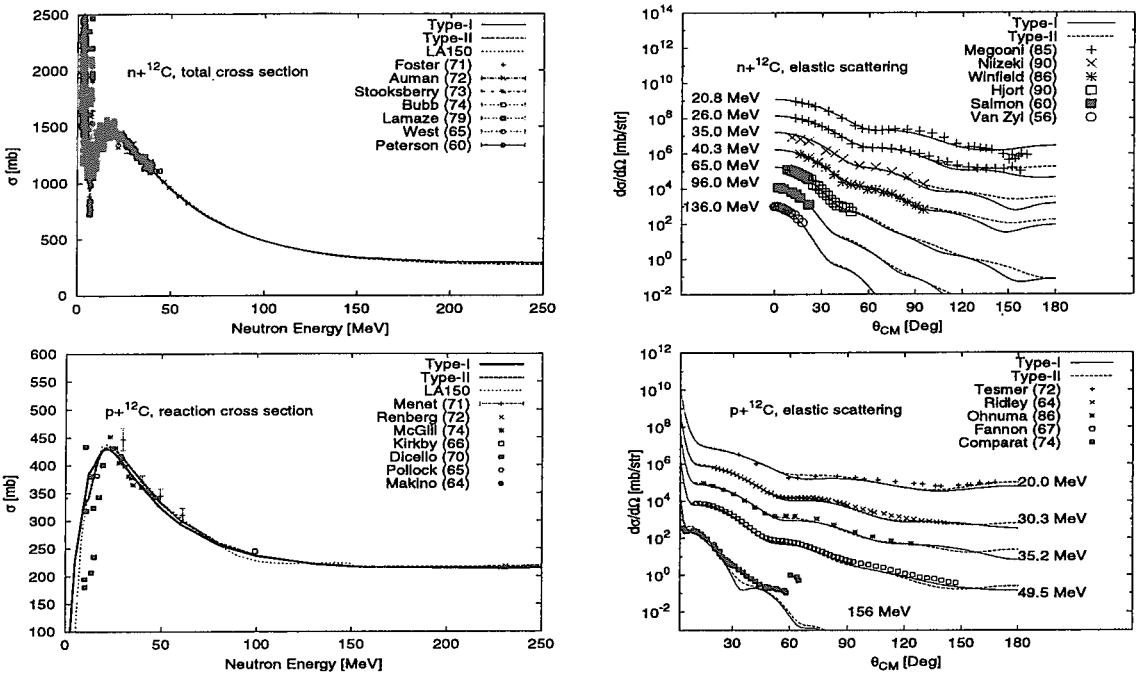

Figure 2: Total, Reaction Cross Section and Elastic Angular Distbution for n,p + ^{12}C Reactions

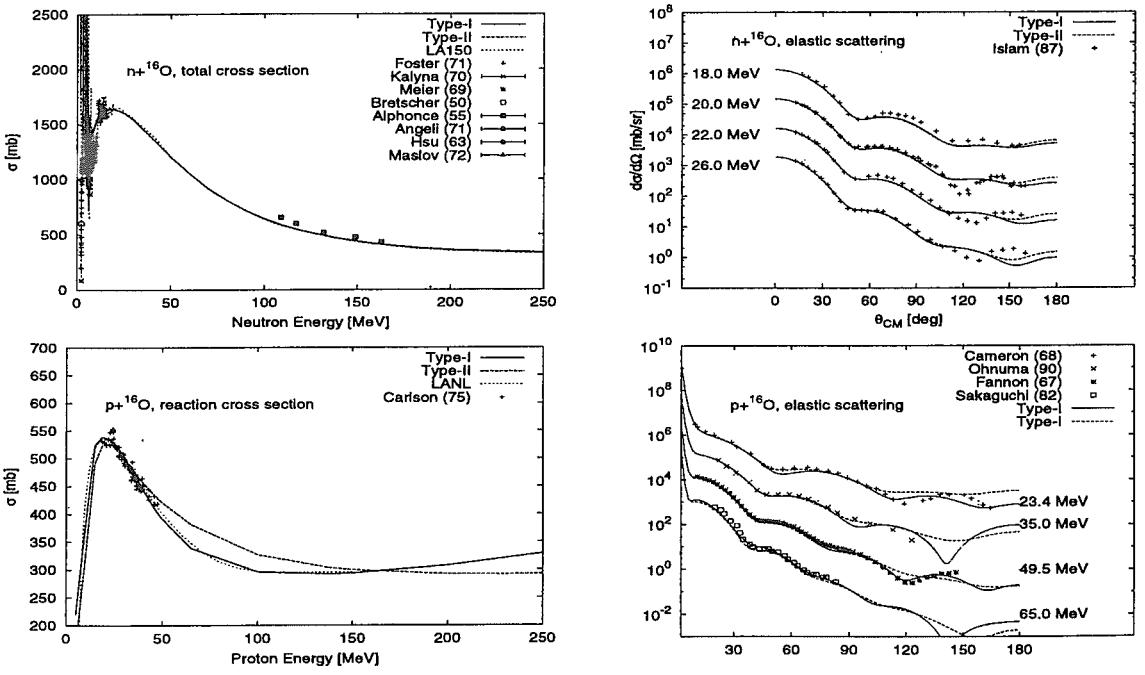

Figure 3: Total, Reaction Cross Section and Elastic Angular Distbution for n,p + ^{16}O Reactions

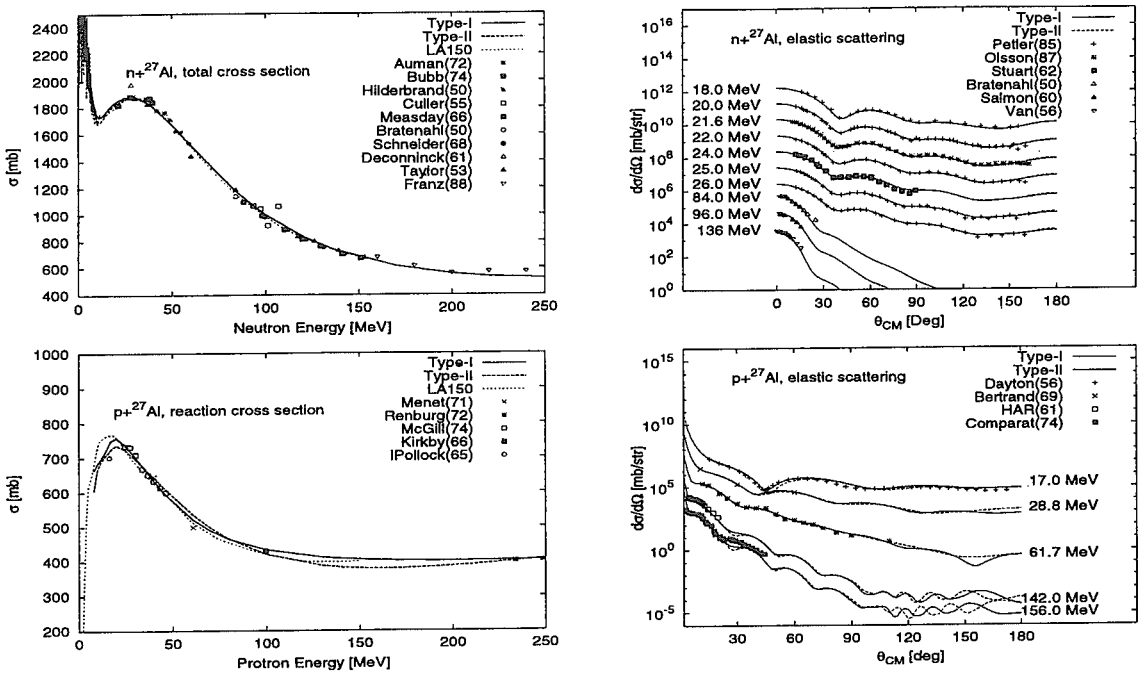

Figure 4: Total, Reaction Cross Section and Elastic Angular Distbution for n,p + ^{27}Al Reactions

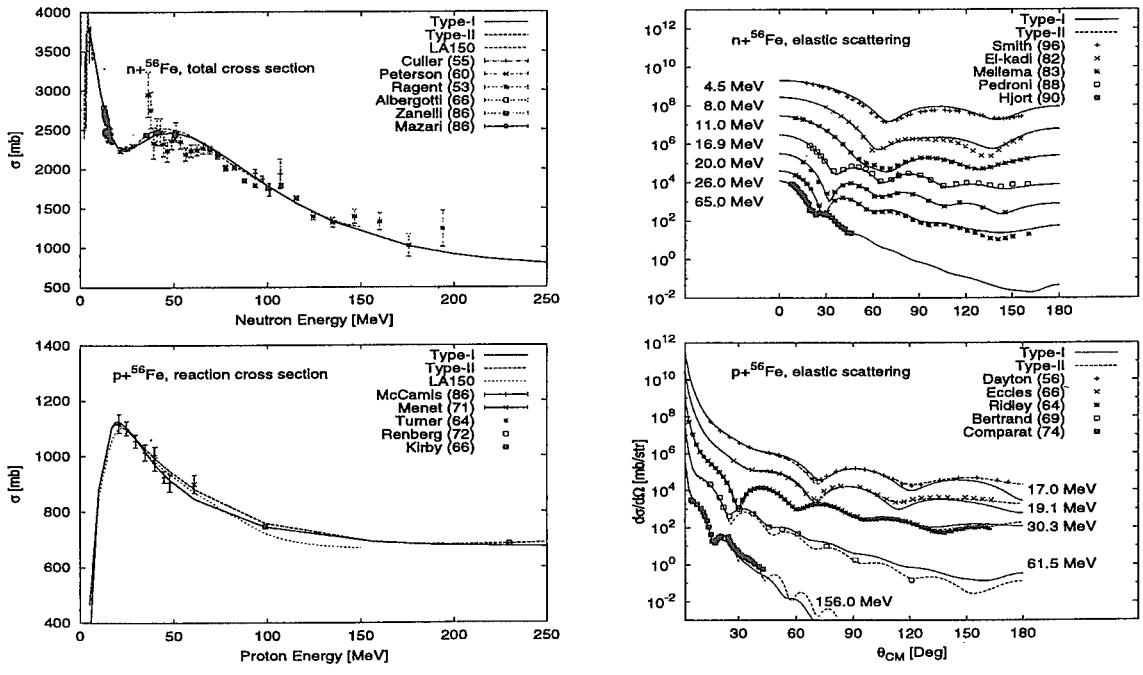

Figure 5: Total, Reaction Cross Section and Elastic Angular Distbution for n,p + ^{56}Fe Reactions

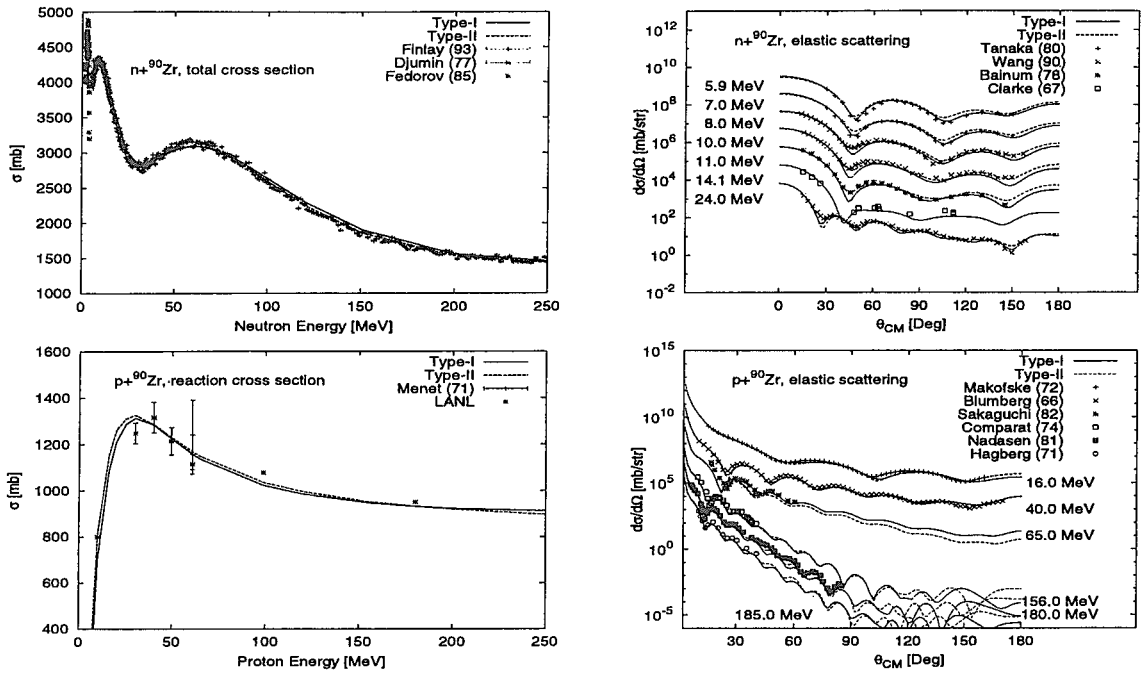

Figure 6: Total, Reaction Cross Section and Elastic Angular Distbution for n,p + ^{90}Zr Reactions

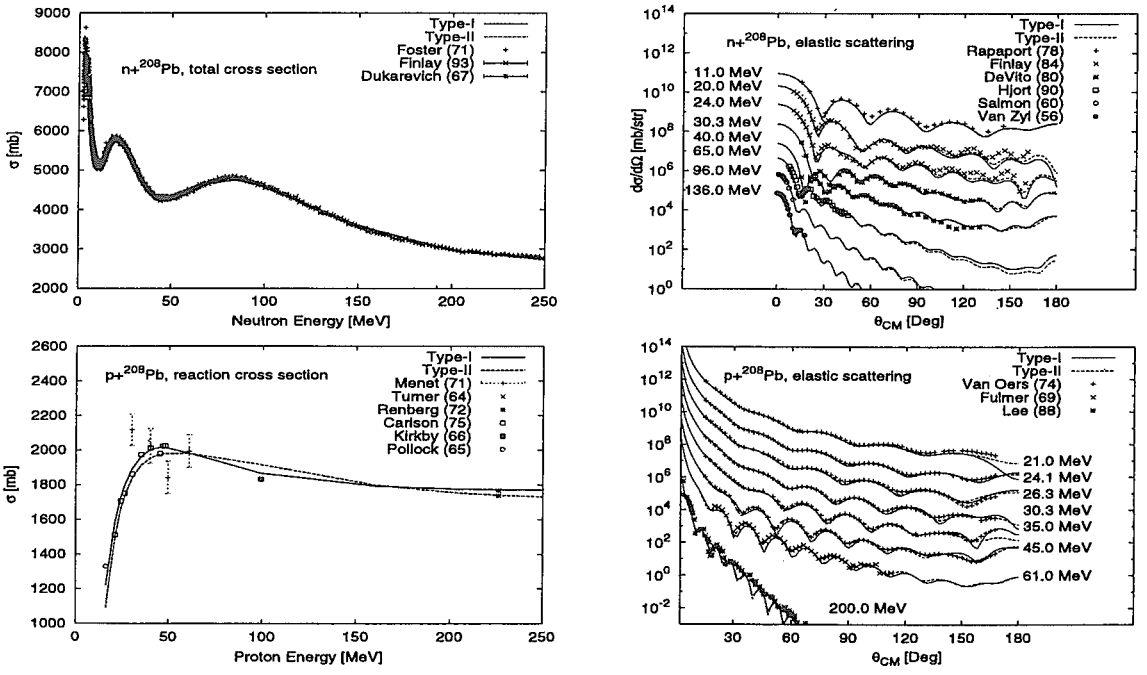

Figure 7: Total, Reaction Cross Section and Elastic Angular Distbution for n, p + ^{208}Pb Reactions

3.32 High Energy Nucleon Incident Optical Potential by Relativistic Impulse Approximation

Nobuhiro SHIGYO, Kazuo NAKAMURA, Hirohiko KITSUKI and Kenji ISHIBASHI
Department of Applied Quantum Physics and Nuclear Engineering, Kyushu University
Hakozaki, Higashi-ku, Fukuoka-shi 812-8581.
e-mail:shigyo@kune2a.nucl.kyushu-u.ac.jp

The optical potentials by relativistic impulse approximation (RIA) are utilized for the high energy nucleon incidence. The nucleon-nucleon scattering amplitudes are derived from the phase shift and parametrized as a function of the incident nucleon energy. The optical potential by RIA reproduces the experimental data.

1. Introduction

It is expected that a number of neutrons generated by the high energy spallation reaction are utilized to engineering purposes such as high intensity neutron source, accelerator-driven transmutation system, accelerator-driven subcritical nuclear reactor and so on. Because of lack of the experimental data of neutron production cross section in the spallation reaction, simulation codes such as Nucleon Meson Transport Code (NMTC) [1] and High Energy Transport Code (HETC) [2] and based on the intranuclear-cascade-evaporation model [3] are often used to the engineering design. Calculation results of the codes, however, is poor agreement with experimental data in the forward direction as near 0 degree. The neutron production cross section in the forward direction is much larger than the backward direction and important in the case such as the shielding calculation of the facility. One of the reason of the disagreement is that HETC is no consideration of the elastic scattering in the forward direction. Improvement of the neutron production cross section in the forward direction, the nucleon-nucleus Dirac optical potential is used. The potential is obtained by the relativistic impulse approximation (RIA) [4]. In RIA the nucleon-nucleus Dirac optical potential is derived from the summation of the nucleon-nucleon scattering amplitude for each nucleon in the target nucleus. The nucleon-nucleon scattering amplitude mainly has five components (scalar, vector, tensor, pseudoscalar and axial vector) [5]. The components except for the scalar and the vector ones are neglected because of small contribution in the energy around 1 GeV. The nucleon-nucleon scattering amplitudes for each orbit are given by fitting empirical phase shift data [6]. To simplify calculation of the potential, the neutron-proton and proton-proton scattering amplitudes are parameterized in a Gaussian shape as a function of the momentum transfer for each incident energy. The Dirac equation is also changed to the Dirac-Schrödinger equation. The neutron production cross section is obtained by solving the equation. The cross sections by this method are good agreement with the experimental data in high incident energy region.

2. Relativistic Impulse Approximation

The optical potential is represented by [7]

$$U_{opt}(r) = -\frac{4\pi p_{lab}}{M}\left\langle \Psi|\hat{F}|\Psi \right\rangle \tag{1}$$

where, p_{lab} and M are the momentum of incident particle in the laboratory frame, and the rest mass, respectively. $|\Psi\rangle$ is the wave function in the ground state. $\hat{F}$ is the Dirac scattering amplitude for the relativistic nucleon-nucleus scattering and is represented by

$$\hat{F} = F^S + F^V \gamma^{\mu}_{(0)}\gamma_{(i)\mu} + F^{PS}\gamma^5_0\gamma^5_i + F^T \sigma^{\mu\nu}_{(0)}\sigma_{(i)\mu\nu} + F^A \gamma^5_{(0)}\gamma^{\mu}_{(0)}\gamma^5_{(i)}\gamma_{(i)\mu} \tag{2}$$

where, suffix (0), (i) stand for the incident particle and a particle of the target nucleus, respectively. Suffix S, V, PS, T and A are scalar, vector, pseudoscalar, tensor and axial vector, respectively. σ and γ are the Pauli σ matrix and the Dirac γ one, respectively. The pseudoscalar and the axial vector elements

are neglected for the sphere nucleus. The tensor term is smaller than the scalar or the vector terms. Then, the optical potential is represented by

$$\hat{U}_{opt}(q) = -\frac{4\pi i p_{lab}}{M}\left[\langle\Psi|F^S(q)|\Psi\rangle\,\rho^S(q) + \gamma^0_{(0)}\,\langle\Psi|F^V(q)|\Psi\rangle\,\rho^V(q)\right] \tag{3}$$

where, q is the momentum transfer and $\rho^S(q)$ and $\rho^V(q)$ are shown as

$$\rho^S(q) = \left\langle\Psi|\sum_i^A e^{i\vec{q}\cdot\vec{r}_i}|\Psi\right\rangle \tag{4}$$

$$\rho^V(q) = \left\langle\Psi|\sum_i^A \gamma^0_{(}i)e^{i\vec{q}\cdot\vec{r}_i}|\Psi\right\rangle \tag{5}$$

The scattering amplitude F^S and F^V are parametrized as

$$F^S(q) = F_{S0}e^{-q^2\beta_S} \tag{6}$$

$$F^V(q) = F_{V0}e^{-q^2\beta_v} \tag{7}$$

where, F_{S0}, F_{V0}, β_S and β_V are parameters obtained from fitting the nucleon-nucleon scattering cross sections. These parameters are derived from the phase shifts. In this work, the phase shift is obtained by fitting the empirical data [6]. The phase shift of P and D shells are shown in Fig. 1. In the figures, marks and solid lines stand for the empirical data and the fitted values, respectively. The cross section of pp scattering is fitted by the nucleon-nucleon potential U_{NN}as

$$U_{NN}(r) = V_{NN}(r) + i\alpha V_{NN}(r) \tag{8}$$

$$V_{NN}(r) = V_0\exp\left(-r^2/a_0^2\right) + V_1\exp\left(-r^2/a_1^2\right) \tag{9}$$

where, V_0, V_1, a_0, a_1 and α are parameters obtained by fitting. The nucleon-nucleon cross section by the fitted phase shift value is represented in Fig. 2. Figures 3 and 4 show the parameters of Eqs. (6) and (7) as a function of the incident energies. Then, the Dirac optical potential is represented by

$$U_{opt}(r) = \int\frac{d^3\vec{q}}{(2\pi)^3}e^{i\vec{q}\cdot\vec{r}}\hat{u}_{opt}(q) \tag{10}$$

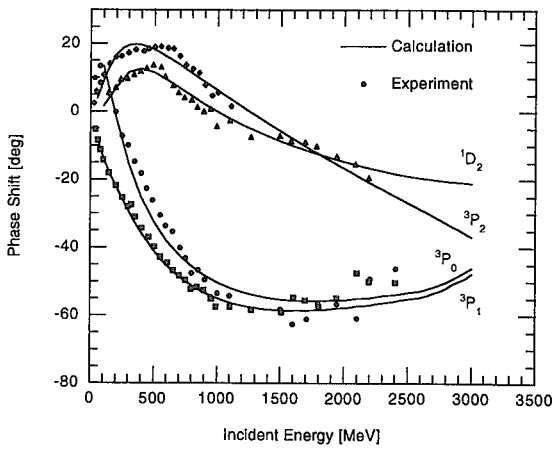

Fig. 1: Phase shift of P and D shell for $p-p$ and $p-n$ scattering. Solid marks stand for the values derived from the experimental data. Solid lines show the values by fitting.

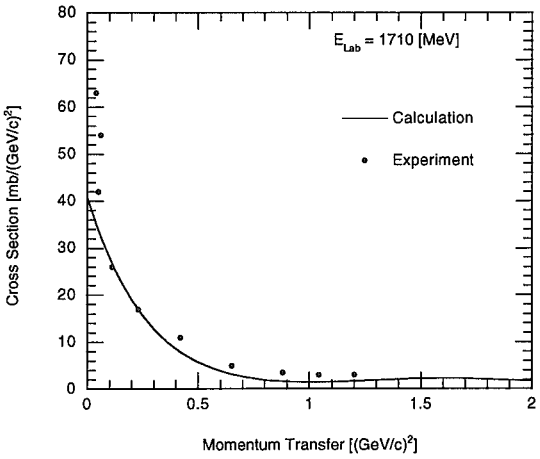

Fig. 2: $p-p$ scattering cross section for collision energy of 1710 MeV. Solid marks stand for the values derived from the experimental data. Solid lines show the values by fitting.

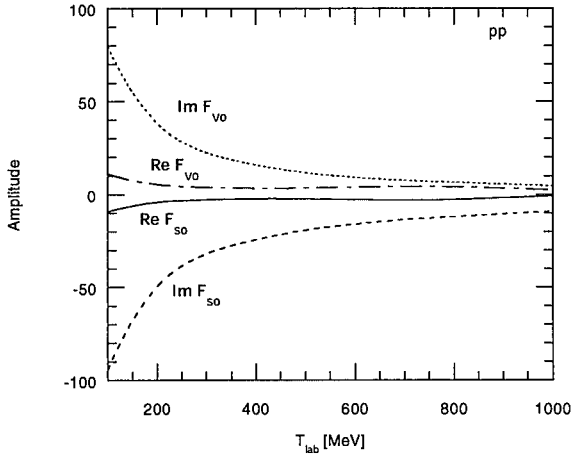

Fig. 3: Parameters of F_{S0} and F_{V0} of equations (6) and (7).

In figs. 5 and 6, the Dirac optical potential of the lead target for 500 MeV neutron incidence and the copper one for 1000 MeV incidence are represented, respectively.

To simplify the calculation, Dirac equation is converted to Shrödinger form as follows,

$$[p^2 + 2E(U_{cent} + U_{so}\vec{\sigma}\cdot\vec{L})]\Phi(r) = [(E - V_c)^2 - m]\Phi(r) \tag{11}$$

where p is momentum, m mass, E total energy, $\vec{\sigma}$ spin, $\vec{L}$ orbital momentum, V_c coulomb potential, U_S and U_V Dirac scalar and vector potential, respectively. The central and spin orbit potentials U_{cent}, and U_{so} are represented as,

$$U_{cent} = \frac{1}{2E}(2EU_V + 2mU_S - U_V^2 + U_S^2 - 2V_cU_V + 2EU_{Darwin}) \tag{12}$$

$$U_{so} = -\frac{1}{2EBr}\frac{\partial B}{\partial r} \quad . \tag{13}$$

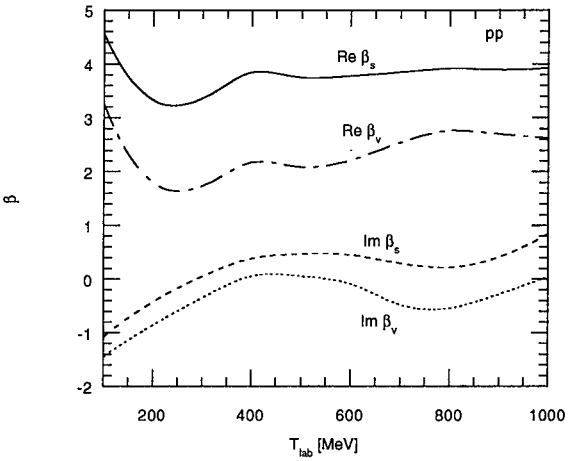

Fig. 4: Parameters of β_S and β_V of equations (6) and (7).

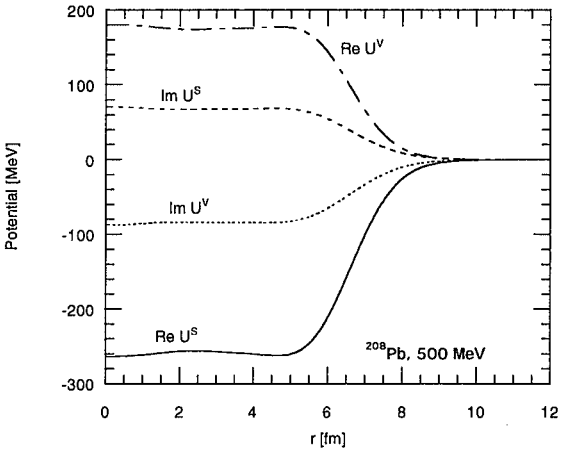

Fig. 5: The scalar and vector potentials for 500 MeV neutron incidence on ^{208}Pb target.

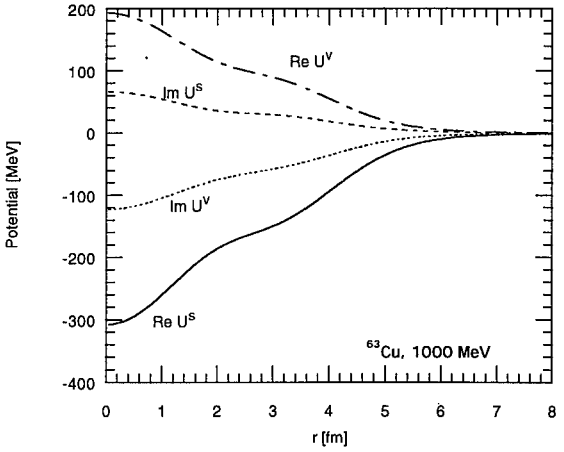

Fig. 6: The scalar and vector potentials for 1000 MeV neutron incidence on ^{63}Cu target.

Darwin and B terms are

$$U_{Darwin} = -\frac{1}{2}\frac{1}{Br^2}\left(\frac{\partial}{\partial r}r^2 - \frac{\partial}{\partial r}B\right) + \frac{3}{4}\frac{1}{B}\left(\frac{\partial}{\partial r}B\right) \quad (14)$$

$$B = \frac{E + m + U_S - U_V - V_c}{E + m} \quad . \tag{15}$$

3. Calculation Results

Figure 7 shows the neutron incident total cross sections for ^{239}U, ^{209}Bi, ^{208}Pb, ^{191}Ta, ^{107}Ag targets. Marks, dashed lines and solid ones stand for the experimental data [8], the results by global potential by Maruyama *et al.* [8] and by RIA, respectively.The proton incident reaction cross sections for ^{209}Pb, ^{63}Cu, ^{40}Ca, ^{27}Al and ^{12}C are shown in Fig. 8. Marks and solid lines are the experimental data [9] and the results by RIA. Figure 9 stands for the scattering cross section of ^{40}Ca for 1044 MeV proton incidence. Marks and solid lines show the experimental data [8] and the results by RIA. In the Figs. 7 - 9 the cross sections by RIA are reproduced the experimental data.

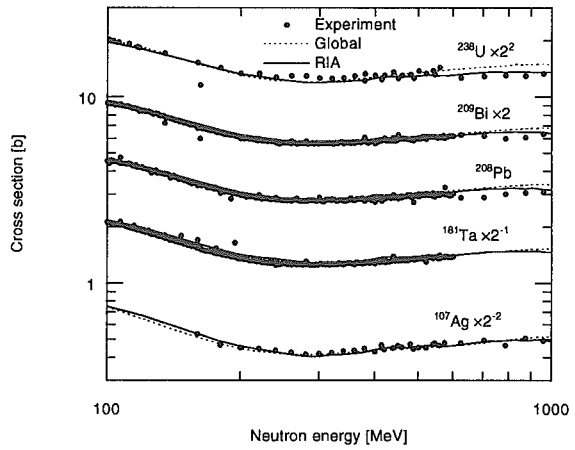

Fig. 7: Neutron incident total cross sections. Marks show the experimental data, dashed lines the global potential by Maruyama *et al.*, solid ones the results of RIA, respectively.

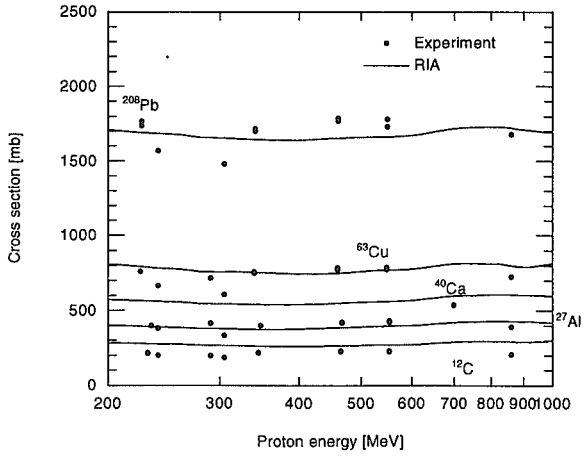

Fig. 8: Proton incident reaction cross sections. Marks show the experimental data, dashed lines the global potential by Maruyama *et al.*, solid ones the results of RIA, respectively.

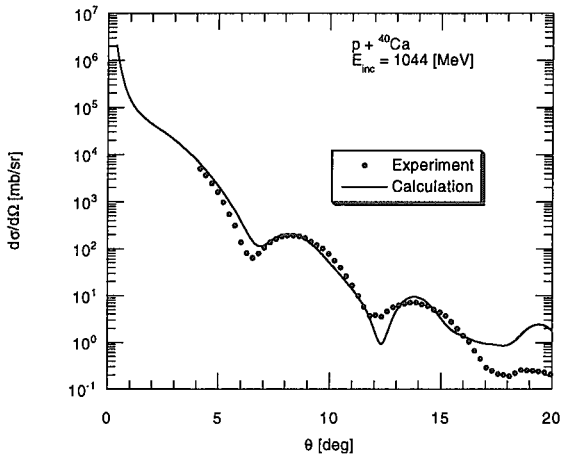

Fig. 9: Elastic scattering cross section of ^{40}Ca for 1044 MeV proton incidence.

4. Summary

Improvement of the neutron production cross section in the forward direction, the nucleon-nucleus Dirac optical potential obtained by RIA. The nucleon-nucleus Dirac optical potential is derived from the nucleon-nucleon scattering amplitude for each nucleon in the target nucleus. The nucleon-nucleon scattering amplitudes for each orbit are given by fitting empirical phase shift data. To simplify calculation of the potential, the neutron-proton and proton-proton scattering amplitudes are parameterized in a Gaussian shape as a function of the momentum transfer. The cross sections by this method are good agreement with the experimental data in high incident energy region.

References

[1] Coleman W.A., *et al.*: *ORNL-4606* (1970).

[2] Chandler K.C., and Armstrong T.W.: *ORNL-4744* (1972).

[3] Bertini H.W., *et al.*: *Phys. Rev.*, **188**, 1711 (1969).

[4] Horowitz C.J.: *Phys. Rev.*, **C31**, 1340 (1985).

[5] McNeil J.A., *et al.*: *Phys. Rev.*, **C27**, 2123 (1983) and their in.

[6] Arndt R.A., *et al.*: *Phys. Rev.*, **C28**, 97 (1983), *ibid*, **C56**, 3005 (1997).

[7] Murdock D.P. and. Horowitz C.J: *Phys. Rev.*, **C31**, 538 (1985).

[8] Maruyama S., *et al.*: *Proc. Int. Conf. Nuclear Data for Science and Technology*, 336, Trieste (1998), and their in.

[9] Cooper E.D., *et al.*: *Phys. Rev.*, **C47**, 297 (1993) and their in.

JP0050665

JAERI－Conf 2000－005

3.33 SCDW Analysis of DDX in (*N,N'X*) Reactions for a Wide Range of Mass Number

Sun Weili[a)*], Y.Watanabe[b)], K. Ogata[c)], M. Kohno[d)], and M. Kawai[c)]

[a)] *Department of Energy Conversion Engineering, Kyushu University, Kasuga, Fukuoka 816-8580, Japan*

[b)] *Department of Advanced Energy Engineering and Science, Kyushu University, Kasuga, Fukuoka 816-8580, Japan*

[c)] *Department of Physics, Kyushu University, Fukuoka 812-8581*

[d)] *Physics Division, Kyushu Dental College, Kitakyushu 803-8580*

**email: sun@aees.kyushu-u.ac.jp*

The applicability of a newly improved semiclassical distorted wave model with Wigner transform of a one-body density matrix has been investigated to a wider range of target mass number. The (*p,p'x*) reactions on ^{12}C, ^{27}Al, ^{58}Ni, ^{90}Zr, and ^{197}Au, and (*p, nx*) reaction on ^{90}Zr are chosen to be analyzed. Comparisons with the calculations of other models, AMD, QMD, and FKK, are also carried out. The results shows that our model can reproduce the experimental double differential data well over a wider range of target mass number, and have predictive powers similar to the other models. The possible reason for overestimation in (*p,nx*) reaction is discussed from the viewpoint of two-body nucleon-nucleon scattering. The sensitivity of SCDW calculations to single particle potential parameters is also investigated.

1. Introduction

Recently we have proposed a new semiclassical distorted wave (SCDW) model with Wigner transform of a one-body density matrix[1], in which the jj-coupling shell model is used to describe the single particle wave functions in a finite range of single particle potential, instead of the local density Fermi gas (LFG) model used in the previous SCDW model [2]. We also performed practical analyses of experimental data for the ^{90}Zr(*p, p'x*) reactions at 80 and 160 MeV incident energies. The results showed that the new SCDW model improved remarkably the previous calculations of the SCDW model. In particular, the one-step cross sections increased greatly at backward angles. The reason was explained from the viewpoint of nucleons momentum distributions. In the LFG model, the target nucleons have only momenta less than the local Fermi momentum. The range of scattering angles, therefore, is subject to a stringent kinematic restriction. In the new SCDW model, the higher momentum components are incorporated into the calculations because of the use of realistic single particle wave functions. Accordingly the stringent kinematic restrictions of the Fermi models that tend to reduce the cross sections at large and very small angles are relaxed.

In this paper, we present more comparisons of new SCDW calculations in order to investigate the applicability of this model for other reactions over a wider range of target mass and incident energy. Since there exists several MSD calculations by FKK, AMD, and QMD, for ^{58}Ni(*p,p'x*) and ^{90}Zr(*p,p'x*) reactions, it is also interesting to see the similarities and differences among the calculations by these models and the SCDW model.

2. Applications to a wider range of target mass number and incident energy

The (*p,p'x*) reactions on ^{12}C, ^{27}Al, ^{58}Ni, ^{90}Zr, and ^{197}Au and (*p, nx*) reaction on ^{90}Zr are chosen for our analyses. Their experimental data show the evidence that MSD processes provide the significant

fraction of the cross sections, *i.e.*, the presence of smoothly forward-peaked angular distributions (over a wide range of outgoing energy), which is of interest for the present study. On the other hand, these reactions cover an interesting range of mass and incident energy. In the all SCDW calculations, the Woods-Saxon potential with global parameters[3] is used as the finite range of single particle potential.

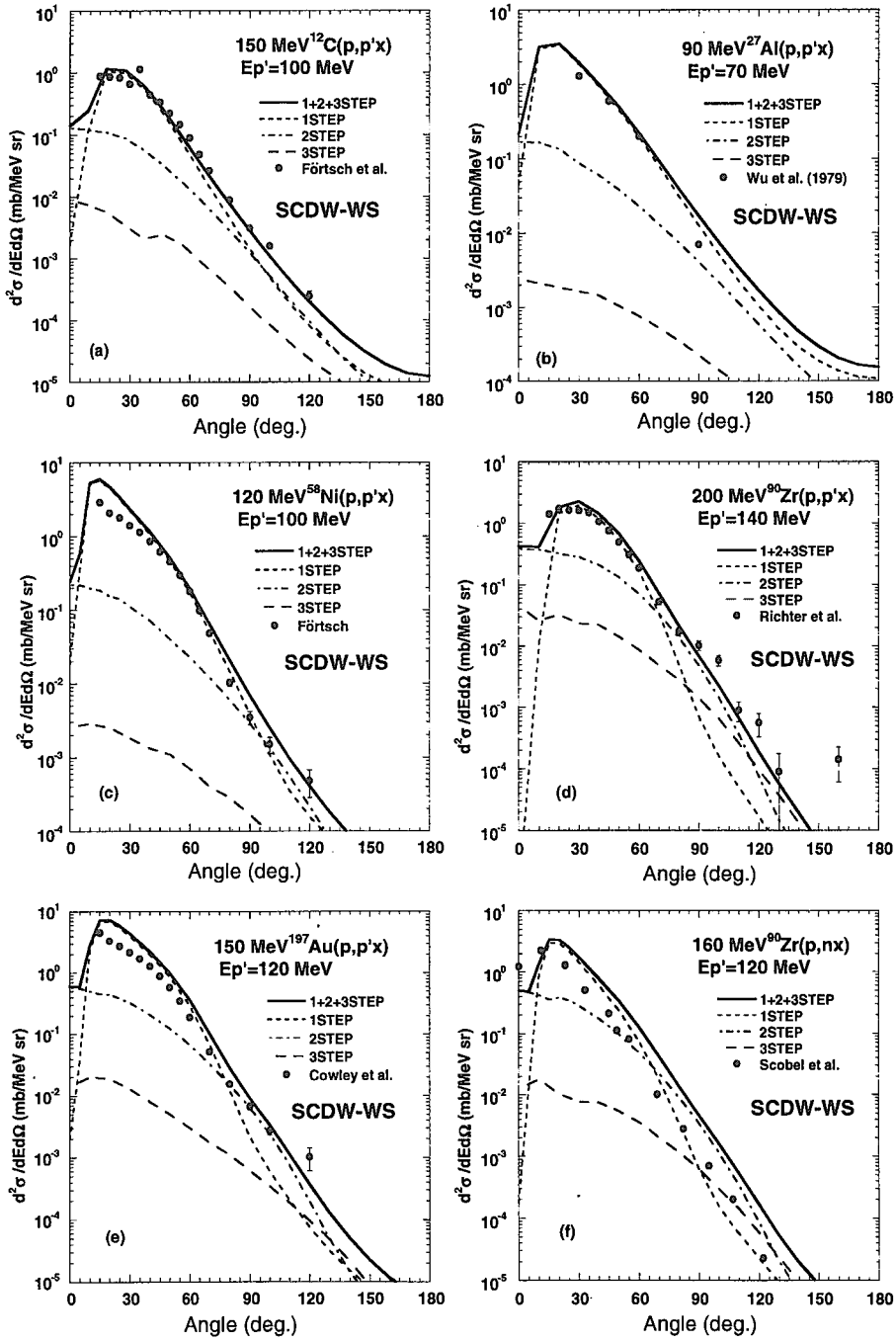

Fig. 1. Comparison of SCDW calculations with measured double differential cross sections for the $(p,p'x)$ reactions on ^{12}C, ^{27}Al, ^{58}Ni, ^{90}Zr, and ^{197}Au, as well as the (p,nx) reaction on ^{90}Zr. In each panel, the cross sections of one-, two-, and three-step processes are represented by the short-dashed, the dashed-dotted, and the long-dashed lines. The solid lines corresponds to their sum.

Figures 1(a) through 1(e) show the applicability of the SCDW model to a wider range of mass number. It is seen that the new SCDW model reproduces well the experimental data for ($p,p'x$) reactions. Agreement of the calculations with measured data is satisfactory except at small angles for the higher emission energies. The one-step cross sections do not drop off at the very forward and large angles as the previous ones [2]. Apparently the one-step cross section provides the major part of the total cross section. In particular, the one-step is predominant at the highest emission energy, and is almost sufficient to explain the data. This result is reasonable because the one-step process dominates the pre-equilibrium reaction for high emission energy. For the highest emission energy, however, the one-step cross section still drops at the very forward angle. Also the new calculations still overestimate the experimental data near the quasielastic scattering (QES) angle by a factor of about 2-3 similar to the previous calculations, although the peak is slightly deduced and shifted to forward angles.

Figures.1(a) and 1(b) show that the SCDW calculations reproduce excellently the experimental data for light target nuclei ^{12}C and ^{27}Al. Fig 1(d) shows that the SCDW calculation is also applicable to the higher incident energy up to 200 MeV, and has similar features as those reactions shown at other incident energies. Figs. 1(f) shows the applicability to (p,nx) reaction. However, the calculation overestimates the data in the whole angular region.

3. Comparison with other models

We compare the SCDW calculations with the results of the other models, AMD, QMD, and FKK, in order to investigate whether our SCDW model is comparable in quality with the other models and to discuss the similarities and differences.

Firstly, a comparison with AMD[4] is made for ^{58}Ni($p,p'x$) at 120 MeV in Fig 2. Agreement is generally good, although the SCDW three-step cross sections are somewhat smaller than the AMD ones. It is noticeable that the AMD one-step cross sections also show peaks near the QES angles, though slightly shifted forward. Such peaks do not appear in the cross sections in QMD calculations.

Secondly, SCDW and QMD[5] are compared in Figs. 2 and 3. One sees some differences in one-step angular distributions, in particular at very forward angles. The QMD one-step cross sections show forward peaks without the steep fall in the vicinity of zero degree that is seen in the SCDW ones.

The QMD used the Gaussian-like shape of momentum distribution which also include the higher momentum components of target nucleons. The authors[5] once investigated the effect of the momentum distribution to the angular distribution by using the different momentum distributions: a) Unified Fermi gas distribution which is similar to our LFG distribution, and b) Gaussian-like shape of momentum distribution which is similar to our distribution for Woods-Saxon potential. It was found that the higher momentum components can not lead to the dramatic increase in one-step cross section in the vicinity of zero degree, but leads to the shift of the QES peak to the forward angles. In this aspect, our new SCDW model shows similar feature to the QMD model. It seems that the reason why one-step cross section drops off in the vicinity of zero degree can not be explained by the Fermi-motion of the target nucleons.

It was also mentioned in Ref.[5] that the behavior of the QMD one-step cross sections near zero degree was strongly affected by the refraction of the incident and outgoing particles by the mean field, and the steep drop at the very forward angles can be totally washed out by the refraction effect. The SCDW calculations also automatically takes account of the refraction by the distorting potentials. However, the effect was found to be small. As for the two- and three-step cross sections, the SCDW and QMD cross sections are similar in shape, although SCDW yields smaller cross sections at the highest emission energy than the QMD.

Thirdly, a comparison of SCDW with FKK[5] is made in Fig. 3. Considerable difference in one-step cross sections is seen between the predictions of the two models, although the higher-step cross sections do not differ as much. FKK gives steeper fall of one-step cross sections towards large angles than SCDW. The relative contributions of the two- and the three-step processes at backward angles

are larger in FKK than in SCDW.

From the above comparisons, we can understand that the calculated angular distribution of the one-step process is strongly model-dependent and those of the multistep processes are not. In addition, the relative magnitude of the contributions of individual multisteps is rather similar in all the models compared. It is concluded that the SCDW model can reproduce the experimental data to the same extent as the other models (FKK, QMD, and AMD).

4. Discussions

a) Two-body nucleon-nucleon scattering

Although the SCDW model is improved by introducing the realistic single particle wave functions, there still exists three problems to be further investigated: 1) the overestimation for (*p,nx*) reaction, as shown in Fig. 1(f), 2) the drop of one-step cross section near zero degree, and 3) the overestimation near the QES angle for the highest emission energy. As for the first problem, we attempt to explain the possible reason from the viewpoint of two-body nucleon-nucleon (*NN*) scattering.

In the SCDW calculations, the two-body *NN* scattering cross sections in free space, denoted by σ_{pp} and σ_{pn}, are used. The values of free space as well as the in-medium *NN* cross sections of Cugnon [6] are shown in Fig. 4(a). It is seen that the free σ_{pn} is larger than the free σ_{pp}. By considering two cases, we made test calculations of the cross sections in the ^{90}Zr(*p,nx*) and ^{90}Zr(*p,p'x*) reactions at 160 MeV incident and 120 MeV emission energies. One case is that the free σ_{pp} and σ_{pn} is taken as different, as we did in all calculations. Another case is that the value of σ_{pn} is assumed to be same as that of σ_{pp}. The results are shown in Figs. 4(b) and 4(c). It is seen that the cross section in ^{90}Zr(*p,nx*) reaction for the second case is reduced and closer to the experimental data in the magnitude. And, the cross section in ^{90}Zr(*p,p'x*) reaction is also reduced.

It is noted that, in the QMD calculations, the in-medium *NN* cross sections of Cugnon are used for the (p,p'x) and (p,nx) reactions, which have almost same magnitude with a difference less than 30 percent in the energy range of 50-300 MeV, and are closer to the free space σ_{pp} as shown in Fig. 4(a). On the other hand, the FKK calculations use the same values of the strength V_0 of effective nucleon-nucleon interactions for both types of reactions, which corresponds to our second case. The QMD and FKK calculations showed the agreement with the experimental data for both types of reactions. This might indicate that a weak isospin dependence is required for simultaneous fits to the MSD cross sections of (*p,p'x*) and (*p,nx*) reactions. Therefore, it is suggested to investigate further the effect of isospin dependence of in-medium *NN* scattering cross sections on the calculations of the MSD cross sections, because the two-body NN cross sections are important input parameters for various model calculations.

As for the other two problems, namely the drop of one-step cross section near zero degree, and the overestimation near the QES angle for the highest emission energy, the reasons are not clear at present. Further study will be necessary.

b) Sensitivity of SCDW calculations to single particle potential parameters

In the calculations of Wigner transform, the Woods-Saxon potential with global parameters is used for all target nuclei chosen for this study. It might be argued that the SCDW calculations can be further improved if the best-adjusted potential parameters are used. To investigate the effect of the potential parameters on the SCDW calculations. we calculated DDX by using two type of potential parameters for the ^{12}C(*p,p'x*) at 150 MeV incident and 100 MeV outgoing energy. One set of potential parameters is the global one, and another is the best-adjusted potential parameters given by Bear and Hodgson [7].

Figure 5 shows the SCDW calculations corresponding to two cases of potential parameters. It is seen that the results do not change so much, which indicates that the cross sections do not depend strongly on the particular choice of potential parameters. The Woods-Saxon potential with global parameters is good enough to reproduce overall the experimental data. This can be regard as one of

the advantages of the SCDW model from the viewpoint of application.

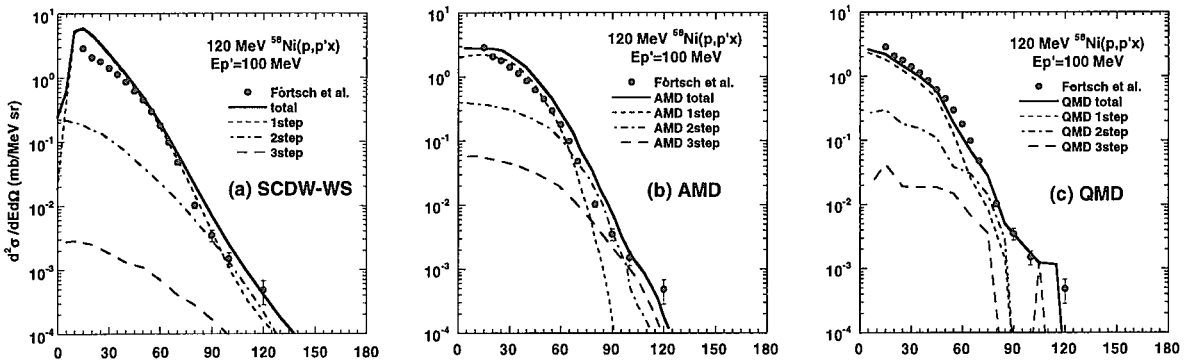

Fig. 2. Comparisons of SCDW calculations with AMD and QMD calculations for the reaction ^{58}Ni($p,p'x$) for 120 MeV incident and 100 MeV outgoing energies.

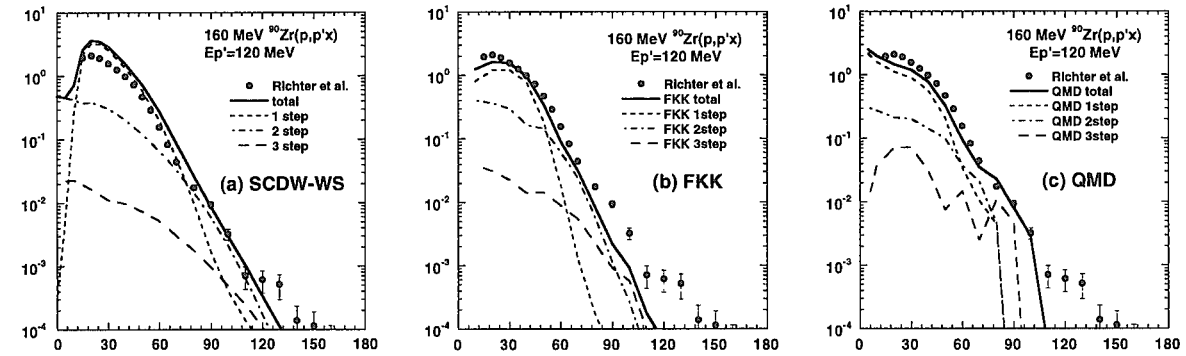

Fig. 3. Comparison of SCDW calculations with FKK and QMD calculations for the reaction ^{90}Zr($p,p'x$) for 160 MeV incident and 120 MeV outgoing energies.

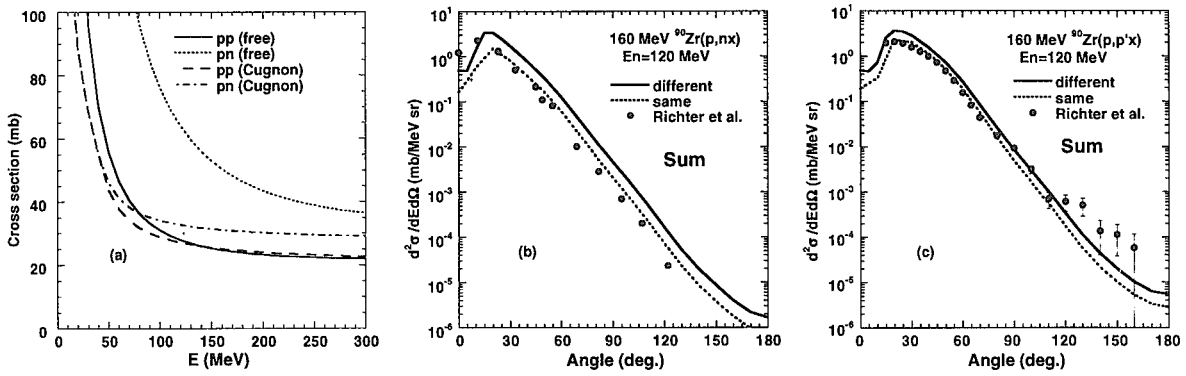

Fig. 4. Dependence of SCDW calculations on two-body nucleon-nucleon scattering. (a) The free nucleon-nucleon scattering cross sections and in-medium ones by Cugnon. (b) Comparisons of the double differential cross sections (summed over the individual step cross sections) for two cases: 1) free σ_{pp} (solid line) and σ_{pn} (dotted line). 2) σ_{pn} is assumed to be same as σ_{pp}. The reaction is ^{90}Zr(p,nx) at 160 MeV incident and 120 MeV outgoing energies. (c) Same as (b), but for ^{90}Zr($p,p'x$) at 160 MeV incident and 120 MeV outgoing energies.

5. Summary

In this paper, the SCDW analyses are carried for the (*p,p'x*) and (*p,nx*) reactions on the target nuclei ^{12}C, ^{27}Al, ^{58}Ni, ^{90}Zr, and ^{197}Au in order to examine the applicability of the SCDW model over a wider range of mass number and incident energy. The SCDW calculations are also compared with those of other models(FKK, AMD, QMD).

The results show that the SCDW model can indeed reproduce well the experimental data for both (*p,p'x*) and (*p,nx*) reactions over a wider range of mass number and incident energy. Agreement is satisfactory except at forward angles for the higher emission energies. In particular, the calculation for ^{12}C(*p,p'x*) agrees excellently well with the experimental data. The results also show that this model is applicable to higher incident energy up to 200 MeV. The comparisons with the other models show that the SCDW model can reproduce the experimental data to the same extent as these models, although there are some difference in individual step cross sections. It is noticed that there are some problems to be further investigated. One of them is the overestimation for (*p,nx*). The possible reason for this overestimation is discussed from the viewpoint of two-body nucleon-nucleon scattering. It is suggested that the effect of isospin dependence of in-medium *NN* scattering cross sections on the calculations of the cross sections should further be investigated. Finally, the sensitivity of SCDW calculations to single particle potential was investigated. It is seen that the dependence of the SCDW model on the potential parameters is not strong, which can be regard as one of the advantages of the SCDW model from the viewpoint of application.

References:

[1] Sun Weili *et al.*, Phys. Rev. C **60**, 064605 (1999).
[2] Watanabe *et al.*, Phys. Rev, C **59**, 2139 (1999).
[3] A. Bohr and B. R. Mottelson, *Nuclear Structure*, (Benjamin, New York, 1969). Vol. I, p. 238-239.
[4] E. I. Tanaka *et al.*, Phys. Rev, C **52**, 316 (1995).
[5] S. Chiba *et al.*, Phys. Rev, C **53**, 1824 (1996).
[6] J. Cugnon *et al.*, Nucl. Phys. **A352**, 505 (1981); J. Cugnon, Phys. Rev. C **22**, 1885 (1980).
[7] K. Bear and P.E. Hodgson, J. Phys. G: Nucl. Phys. Vol. **4**, L287 (1978).

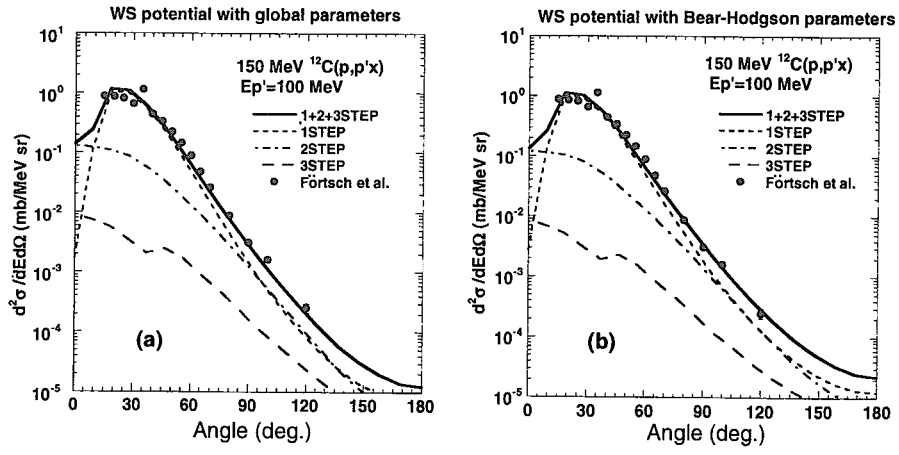

Fig. 5 Comparison of the SCDW calculations with different Woods-Saxon potentails parameters for the ^{12}C(*p,p'x*) reaction at 150 MeV incident and 120 MeV outgoing energies: (a) global ones [3], and (b) Bear-Hodgson's ones [7].

3.34 Decay Properties of Neutron-Deficient Actinides

Minoru SAKAMA,[1,2] Kazuaki TSUKADA,[2] Masato ASAI,[2] Shin-ichi ICHIKAWA,[2]
Yasuji OURA,[1] Ichiro NISHINAKA,[2] Hiromitsu HABA,[2] Shin-ichi GOTO,[2]
Yuichiro NAGAME,[2] Michihiro SHIBATA,[3] Kiyoshi KAWADE [3] Akihiko OSA,[4]
Yasuaki KOJIMA,[5] Mitsuru EBIHARA[1] and Hiromichi NAKAHARA[1]
[1]*Department of Chemistry, Tokyo Metropolitan University*
Hachioji, Tokyo 192-0397
e-mail: sakama@tdmalph1.tokai.jaeri.go.jp
[2]*Advanced Science Research Center, Japan Atomic Energy Research Institute*
Tokai, Naka-gun, Ibaraki-ken 319-1195
[3]*Department of Energy Engineering and Science, Nagoya University*
Chikusa-ku, Nagoya, Aichi-ken 464-8603
[4]*Department of Materials Science, Japan Atomic Energy Research Institute*
Takasaki, Gunma-ken 370-1292
[5]*Department of Engineering, Hiroshima University*
Higashi-Hiroshima, Hiroshima-ken 739-8527

In continuation of our study on investigation of the neutron-deficient americium isotopes, which had been the identification of ^{236}Am and ^{235}Am, we carried out the experiments aimed to produce new isotopes ^{233}Am and to determine the half-life and α-decay energy of ^{235}Am. The isotopes were identified after mass-separation from the other reaction products by the PbI_2/He-jet coupled JAERI on-line isotope separator (ISOL) and the beneficial detection system for a few events of α-decay from unknown isotopes. The assignment of unknown α-ray against ^{233}Am was made by establishing time correlations between a parent and daughter nuclides belonging to known α-decay chains. In addition the determination of the half-life, α/EC decay branching ratio and α-decay energy of ^{235}Am was made by measuring Pu Kx-rays originating from the EC decay of ^{235}Am and α-ray of the isotopes coincidentally.

1, Introduction

The known nuclides until now from thorium to 112 element in the table of nuclide are showed in Fig. 1. Decay properties of these nuclides in Fig. 1 have been investigated intensely together with the development of a measurement (alpha-ray detector, etc) and an accelerator technique. Despite it, particularly in the region of neutron-deficient actinide

isotopes there are still many unknown nuclides which decay dominantly through electron-capture (EC). Although this region is very difficult to study, the information on nuclear-decay properties of these nuclides has a significant role in the fission properties of far from stability and the mass values of transactinides in nature. For example, we have mentioned three alpha-decay chains, shown in Fig. 1, relative to the mass values of transactinides. It should be possible to determine the mass values which have only been observed as individual events from alpha-decay measurements[1]. But the mass values of ^{255,256}Db and ^{261}Bh included in the chains are entirely unknown. Because the main reason for the undecided masses is that the alpha-decay chains are interrupted because of some unknown alpha-emitters; americium and berkelium in neutron-deficient actinide region. Thus it is impossible to decide the mass values using the known masses for daughter nuclides in the end points of the alpha-decay chains. Indeed it is necessary that the decay properties of neutron-deficient actinides should be investigated. In order to study decay properties of the nuclides, we have developed the PbI_2/He-jet coupled JAERI-ISOL[2]. In this paper, we present the new information on decay properties of new isotopes ^{233}Am and ^{235}Am.

2, Experiment

Experiments have been performed using extracted ion beams of ^{6}Li delivered from 20UR tandem accelerator, Japan Atomic Energy Research Institute (JAERI). The twenty-one targets of ^{233}U with the average thickness of 100 μg/cm^2 per a target were made by being electrodeposited onto a 3 μm thick aluminum backing foil. Thier targets were set in the multiple-target chamber where they could be irradiated simultaneity. The incident energies of the ^{6}Li projectiles were chosen to be 63 MeV for the reaction ^{233}U(^{6}Li,6n)^{233}Am and 45.5 MeV for the reaction ^{233}U(^{6}Li,4n)^{235}Am. The tandem accelerator provided with the average 300 pnA beam intensity of ^{6}Li. The schematic illustration of the PbI_2/He-jet coupled JAERI-ISOL system is shown in Fig. 2. The reaction products recoiling out of the targets which are simultaneously bombarded with ion beams into the multiple-target chamber are attached to an inert gas containing PbI_2 aerosol cluster[3]. And they are transported through a Teflon capillary (1.4 mm ϕ × 8 m length) and two skimmers (2 mm ϕ and 4 mm ϕ) to a thermal ion source at 2450 K with the surface ionization method. Successively the ions were accelerated with the voltage of 30 kV in order to mass-separate at a mass fragment of interest with an electromagnet. The mass-separated nuclides are implanted respectively into four catcher foils, whose thickness is 4-7 μ/cm^2, of VYNS resin[4] (polyvinylchloride-acetate copolymer) with 45° rotating periodically at Rotating Wheel detection system. This thickness is into the stopping range of all Am^+ products accelerated by ISOL. Each foils are rotated to the detection system equipped with seven PIN-photodiodes and a short coaxial n-type HPGe detectors. The α-ray energies were calibrated by *alpha*-particle energies from known α emitter nuclei, ^{221}Fr, ^{217}At and ^{213}Po, by a α decaying ^{225}Ac source. The energy resolution for each PIN-photodiodes was not worse than 60 keV (FWHM). Singles α-rays and x/γ-rays are recorded event by event

together with time information respectively. The mass resolution $M/\Delta M$ of the ISOL at M=208 was about 850 which was good enough to separate ions of interest from those with the ±1 mass difference. The overall efficiency of ^{237}Am atoms became approximately 0.5% which is 5 times higher than the previous one and the signal-to-noise ratio (S/N) in the x/γray-spectrum was about 3.5 times larger than that in Ref[5].

3, The ^{233}Am isotope

The α-spectrum obtained at the mass-233 fraction is shown in Fig. 3. The data were accumulated for the period of 150 s × 1500 cycles at all PINphotodiodes. The α-decay chain from the daughter nuclei ^{229}Np ($T_{1/2}$=∼4.0 min)[6] following the α-decay of ^{233}Am up to ^{209}Bi are clearly observed. The α-decay chain originated from the daughter nuclei ^{229}U following the EC decaying the parent nuclei ^{229}Np also are observed. The 6.74±0.03 MeV α-particle is assigned to be ^{233}Am. By the decay curve of the α-ray intensity fitted by the exponential function, the half-life of ^{233}Am is deduced to be 2.3±0.6 min preliminarily. Unfortunately Pu Kx rays originated from the EC decaying ^{233}Am couldn't be observed with the present detection system. By this reason we would seek the α/EC decay branching ratio of $\alpha \geq$8% and EC≤92%.

4, The ^{235}Am isotope

The α-spectrum obtained at the mass-235 fraction is shown in Fig. 4. The data were accumulated for the period of 900 s × 360 cycles at all PINphotodiodes. The 6.44±0.02 MeV α-particle is assigned to be ^{235}Am. Although ^{235}Am had been identified for the first with detection for Pu Kx-rays following the EC decay by J. Guo *et al.*[7], in 1996, α-decay of ^{235}Am had been unknown than ever. In this present work we had performed to observe both α-decay and EC decay originated from ^{235}Am for the first time. By the decay curves of the α-ray and Pu Kx-rays intensities fitted by the exponential function the half-life of ^{235}Am is deduced to be 9.83±0.47 min definitely. The α/EC branching ratio is determined to be α=0.4% and EC=99.6%.

5, Discussion

Table 1 shows comparison between the experimental and the calculated half-lives of ^{233}Am and ^{235}Am with the gross theory (GT2)[8], the semi-gross theory (SGT)[9] and the microscopic *pn*-QRPA (proton-neutron quasiparticle random phase approximation) model [10]. The present values is in good agreement with those from GT2 and SGT within a factor of 1.5.

The relationship between α energy and α-decay partial half-life of their isotopes are represented in Fig. 5. The favorite α energy of ^{235}Am is well reproduced by a systematic line

developed from the favorite α-energies of the other odd-A americium isotopes, ^{237,239,241}Am With respect to ^{233}Am on the assumption that α energy of ^{233}Am is reproduced by the systematic line, the α-decay branching ratio of ^{233}Am is estimated to be ~19%. That values is compatible with the lower limit of the α-decay branching ratio of ^{233}Am.

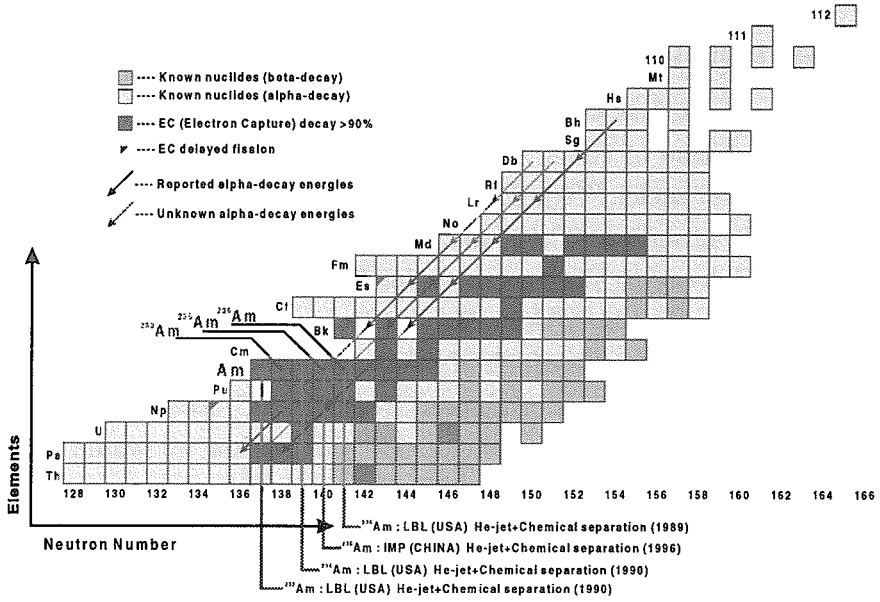

Figure 1. Chart of nuclides that shows actinides and transactinides in the region from thorium to element 112.

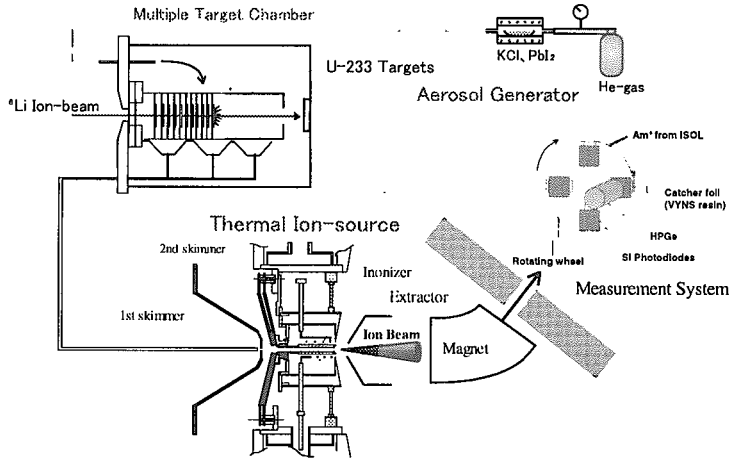

Figure 2. Schematic diagram of the PbI_2/He-jet coupled JAERI-ISOL.

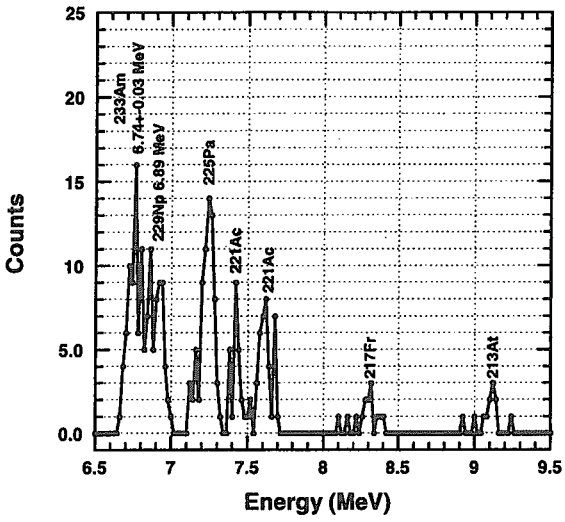

Figure 3. α-ray correlation spectrum observed at A=233 fraction.

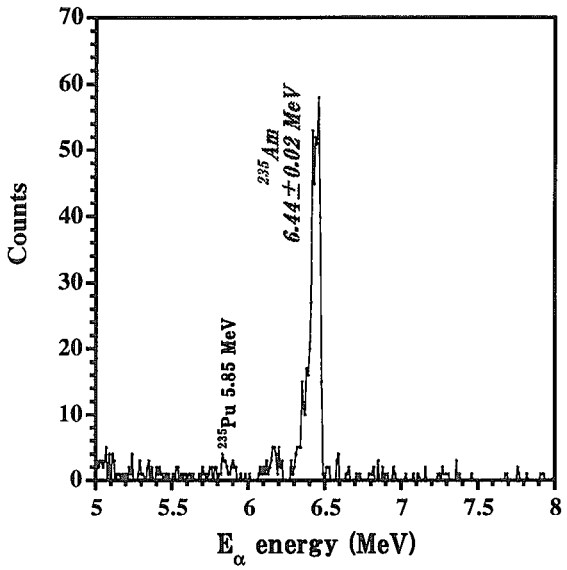

Figure 4. α-ray single spectrum observed at A=235 fraction.

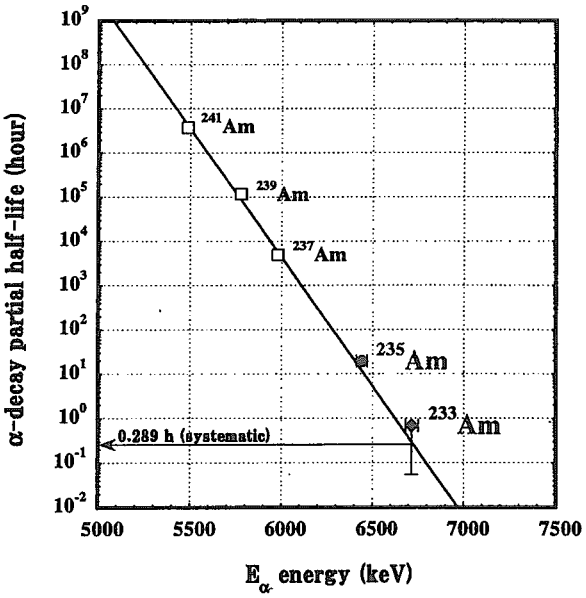

Figure 5. Experimental α-decay partial half-lives vs. α energies for odd-A americium isotopes.

Table 1. Comparison between the experimental and calculated values of half-lives on ^{233}Am and ^{235}Am.

	Present result	GT2[8]	SGT[9]	*pn*-QRPA[10]
^{233}Am	2.3±0.6 min	1.72 min[a]	1.90 min[a]	0.89 min[b]
	$T_{1/2}$(exp.)/$T_{1/2}$(cal.)	1.34	1.21	2.58
^{235}Am	9.83±0.47 min	6.95 min[c]	14.89 min[c]	3.0 min[d]
	$T_{1/2}$(exp.)/$T_{1/2}$(cal.)	1.41	0.66	3.28

[a] Q_{EC}=3.25 MeV
[b] Q_{EC}=3.24 MeV
[c] Q_{EC}=2.56 MeV
[d] Q_{EC}=2.31 MeV

References

1) H. Wollnik *et al.*
Proposal to map the masses of the isotopes of superheavy elements.
Private communication, 1995.

2) S. Ichikawa, K. Tsukada, M. Asai, A. Osa, Y. Oura, H. Iimura, Y. Kojima, T. Hirose, I. Nishinaka, Y. Hatsukawa, Y. Nagame, K. Kawade, T. Ohyama, and K. Sueki.
Search for Unknown Isotopes using the JAERI-ISOL.
Nucl. Instrum. Methods B, 126:205, 1997.

3) A. Taniguchi, K. Okano, T. Sharshar, and Y. Kawase.
Characteristic of a mixed-gas jet system in KUR-ISOL.
Nucl. Instrum. Methods A, 351:378, 1994.

4) B. D. Pate and L. Yaffe.
A new material and techniques for the fabrication and measurement of very thin films for use in 4π-counting.
Canadian Journal of Chemistry, 33:15, 1954.

5) K. Tsukada, S. Ichikawa, Y. Hatsukawa, I. Nshinaka, K. Hata, Y. Nagame, Y. Oura, T. Ohyama, K. Sueki, H. Nakahara, M. Asai, Y. Kojima, T. Hirose, H. Yamamoto, and K. Kawade.
Search for the electron-capture decaying isotopes ^{236}Am.
Phys. Rev. C, 57(4):2057, 1998.

6) R. L. Hahn, M. F. Roche, and K. S. Toth.
New Neptunium Isotopes, ^{230}Np and ^{229}Np.
Nucl. Phys., A113:206, 1968.

7) J. Guo, Z. Gan, H. Liu, W. Yang, L. Shi, W. Mu, Guo T, K. Fang, S. Shen, S. Yuan, X. Zhang, Z. Qin, J. Zhong R. Ma, S. Wang, D. Kong, and J. Qiao.
A new neutron-deficient isotopes, ^{235}Am.
Z. Phys. A, 335:111, 1996.

8) T. Tachibana, M. Yamada, and Y. Yoshida.
Improvement of the Gross Theory of β-decay. 2.
Prog, Theor. Phys., 84:641, 1990.

9) H. Nakata, T. Tachibana, and M. Yamada.
Semi-Gross Theory of Nuclear β-decay.
Nucl. Phys. A, 625:521, 1997.

10) M. Hirsch, A. Staudt, K. Muto, and V. Klapdor-Kleingrothaus.
Microscopic prediction of β^+/EC-decay half-lives.
At. Data Nucl. Data Tables., 53:165, 1993.

3.35 Nuclear mass formula with shell energies obtained by a new method and its application to superheavy elements

H. Koura[*1], M. Uno[*1,*2], T. Tachibana[*1] and M. Yamada[*1]
[*1] *Advanced Research Institute for Science and Engineering, Waseda University, 3-4-1 Okubo, Shinjuku-ku, Tokyo 169-8555, JAPAN*
[*2] *Ministry of Education, Science, Sports and Culture, 3-2-2 Kasumigaseki, Chiyoda-ku, Tokyo 100-0013, JAPAN*
koura@mn.waseda.ac.jp
unom@tanashi.kek.jp
ttachi@mn.waseda.ac.jp

A nuclear mass formula is constructed which is composed of two parts, one describing the general trend of the masses as a function of Z and N and the other representing deviations of individual masses from this general trend. These deviations, referred to as shell energies, are calculated by a new method for spherical as well as deformed nuclei only with use of spherical single-particle potentials. The root-mean-square deviation from experimentally known masses is 0.68 MeV. The obtained mass formula is applicable to any nucleus with $Z \geq 2$ and $N \geq 2$. By this mass formula α-decay energies are calculated, and α-decay half-lives of superheavy elements are estimated.

1 Introduction

Our group has been investigating for years the mass formula which is composed of two parts, one representing the general trend of the masses as a function of proton and neutron numbers (Z, N) and the other representing the deviations from this general trend [1, 2, 3]. The latter may be called shell energies in a broad sense; it is caused by the shell structure and, if any, the deformation of the nucleus. The mass formula in Ref. [4], which we obtained previously and is referred to as TUYY formula in the following, was fairly successful in estimating the nuclear masses. However, it includes many adjustable parameters, and cannot be extrapolated to the region of superheavy nuclei where no empirical data to determine the necessary parameter values are available. Recently, we have solved this problem [5]. In this report we briefly explain a new method of treating deformed nuclei in which only spherical single-particle potentials are used. The mass formula obtained by this new method is capable of predicting the masses of nuclei far from stability such as very neutron- or proton-rich nuclei and superheavy nuclei. In section 2, we outline the calculation of the spherical shell energies. In section 3, we explain how to take into account the deformation effect. In section 4, we construct a mass formula. Finally, we apply our mass formula to superheavy nuclei in section 5.

2 Crude and refined spherical shell energies

We first calculate shell energies for neutron groups and for proton groups in spherical nuclei using an extreme single-particle model; we refer to them as crude shell energies. We use a spherical single-particle potential recently proposed [6, 7]. This potential reproduces fairly well the single-particle levels of 15 double-magic or magic-submagic nuclei in a wide nuclidic region ranging from ^{4}He, ^{8}He to ^{208}Pb. The potential parameters are assumed to be smooth functions of Z and N with due consideration of the charge symmetry; several parameter sets were obtained in Refs. [6, 7], and we adopt the set HD.

Once the single-particle potential of the nucleus (Z, N) is prepared, we put n neutrons or n protons in it from its bottom. Then the sum of the single-particle energies, which is denote by $E_{\rm nsp}(n; Z, N)$ (or $E_{\rm psp}(n; Z, N)$), is a function of n, Z and N. For the purpose of extracting the deviations from a general

tendency in this sum, we construct a smooth function $\overline{E}_{\rm nsp}(n;Z,N)$ (or $\overline{E}_{\rm psp}(n;Z,N)$) to represent the general tendency of $E_{\rm nsp}(n;Z,N)$ (or $E_{\rm psp}(n;Z,N)$). Then, the deviations are given as

$$E_{i\rm fl}(n;Z,N)=E_{i\rm sp}(n;Z,N)-\overline{E}_{i\rm sp}(n;Z,N),\ (i=\mathrm{n,p}). \tag{1}$$

With these deviations, we obtain the crude shell energies as

$$E_{\rm ncr}(Z,N)=E_{\rm nfl}(N;Z,N),\ E_{\rm pcr}(Z,N)=E_{\rm pfl}(Z;Z,N). \tag{2}$$

The subtraction of the smooth function $\overline{E}_{i\rm sp}(n;Z,N)$ as in Eq. (1) is made in two steps. In the first step we subtract the Thomas-Fermi energy $E_{i\rm TF}(n;Z,N)$. Although this first step subtracts a large part of the smooth energy, a considerable amount still remains. In the second step, we further subtract a smooth function $\Delta E_{i\rm av}(n;Z,N)$ (i=n, p), which should be an approximation to $\overline{E}_{i\rm sp}(n;Z,N)-E_{i\rm TF}(n;Z,N)$ (i=n, p). For details see Ref. [5].

Next, we modify these crude shell energies by taking into account the BCS-type pairing, and also make some phenomenological reduction of the shell energies; we refer to the neutron and proton shell energies thus obtained as refined spherical shell energies. In order to include the pairing effect, we take a weighted average of the crude shell energies of neighboring nuclei with the weights related to the occupation probabilities of the BCS theory. It is likely that the simple single-particle plus pairing model is not sufficient to take full account of the configuration mixing. The remaining configuration mixing will probably reduce the magnitudes of the shell energies. This effect is simply represented by a multiplication of the shell energies by a reduction factor μ (a smooth function of $N+Z$ and $N-Z$). Then we obtain the refined spherical neutron and proton shell energies $E_{\rm ns}(Z,N)$ and $E_{\rm ps}(Z,N)$.

For a spherical nucleus the nuclear shell energy is simply the sum of the refined spherical neutron and proton shell energies:

$$E_{0\rm s}(Z,N)=E_{\rm ns}(Z,N)+E_{\rm ps}(Z,N). \tag{3}$$

3 Deformation

The shell energy of a deformed nucleus is expressed as the sum of two parts: the intrinsic shell energy and the average deformation energy. As our method was already explained in a previous report [2], we only give a sketch of it.

3.1 Intrinsic shell energy

We first assume that the intrinsic shell energy of a deformed nucleus is expressed as a superposition of the proton and neutron shell energies of some spherical nuclei with certain mixing weights:

$$E_{\rm in}(Z,N)=\sum_{Z'}W_{\rm p}(Z';Z,N)E_{\rm ps}(Z',N'')+\sum_{N'}W_{\rm n}(N';Z,N)E_{\rm ns}(Z'',N'), \tag{4}$$

where N'' and Z'' are integers closest to NZ'/Z and ZN'/N, respectively. In this equation, the mixing weights $W_{\rm p}(Z';Z,N)$ and $W_{\rm n}(N';Z,N)$ are obtained as

$$W_{\rm n}(N';Z,N)=-\frac{1}{4\pi}\frac{d\Omega_{\rm oc}(r(N'))}{dN'}, \tag{5}$$

where $\Omega_{\rm oc}(r(N'))$ is the occupied solid angle for the radial coordinate $r(N')$. This shows that the mixing weight is related to the rate of the decrease of the occupied solid angle as r increases.

In the actual calculation, some modification is made in this procedure to get a reasonably large deformation. We use an intermediary coordinate $r_{\rm im}$ and an intermediary shape $\Omega_{\rm im}(r_{\rm im})$ defined by

$$\begin{aligned} &dr_{\rm im}=\{1-h[1-\Omega_{\rm oc}(r)/4\pi]\}dr, \quad \text{with } h=0.46,\\ &\Omega_{\rm im}(r_{\rm im}){r_{\rm im}}^2dr_{\rm im}=\Omega_{\rm oc}(r)r^2dr, \end{aligned} \tag{6}$$

and with $r_{\rm im}$ and $\Omega_{\rm im}(r_{\rm im})$ we proceed as above.

3.2 Average deformation energy

We limit the deformation to axially and reflectionally symmetric shapes and assume the same shape for the neutron group and proton group. We use uniform neutron and proton distributions with a sharp-cut surface. Then the nuclear shape is described by the following radii as a function of the polar angle θ:

$$R(\theta) = \frac{R_0}{\lambda}\left[1 + \alpha_2 \mathrm{P}_2(\cos\theta) + \alpha_4 \mathrm{P}_4(\cos\theta) + \alpha_6 \mathrm{P}_6(\cos\theta) + \cdots\right], \tag{7}$$

where $\mathrm{P}_{2i}(\cos\theta)$ $(i = 1, 2, \ldots)$ are the Legendre polynomials and α_{2i} are parameters to specify the shape. Furthermore, R_0 is the radius of the sphere whose volume is equal to that of the deformed nucleus under consideration, and this volume conservation is guaranteed by the denominator λ. We take the expansion in Eq. (7) down to the $\mathrm{P}_6(\cos\theta)$ term.

As the contributions to the average deformation energy, we consider three kinds, the changes of the surface energy ΔE_{s} and the Coulomb energy ΔE_{C}, and an energy to favor prolate shapes. The third energy is usually not considered explicitly. In the present study, however, the experimentally observed dominance of the prolate deformation is not obtained without such an energy. We assume the energy to favor prolate shapes as

$$\Delta E_{\mathrm{prl}} = -C_{\mathrm{prl1}}\alpha_2 A^{2/3} \exp\left[-C_{\mathrm{prl2}}{\alpha_2}^2\right],\ C_{\mathrm{prl1}} = 0.28,\ C_{\mathrm{prl2}} = 5, \tag{8}$$

where the factor $A^{2/3}$ is introduced since this energy is a surface effect. The average deformation energy is given as the sum of the above three energies:

$$\overline{E_{\mathrm{def}}} = \Delta E_{\mathrm{s}} + \Delta E_{\mathrm{C}} + \Delta E_{\mathrm{prl}}. \tag{9}$$

3.3 Shell energies of deformed nuclei

Once the parameter values are fixed, the shell energy of the nucleus (Z, N) is obtained by minimizing the sum of the intrinsic shell energy and the average deformation energy:

$$E_{\mathrm{sh}}(Z, N) = \min_{\alpha_2, \alpha_4, \alpha_6}\left[E_{\mathrm{in}}(Z, N) + \overline{E_{\mathrm{def}}}(Z, N)\right]. \tag{10}$$

The deformation parameters α_2, α_4 and α_6 giving the minimum energy specify the shape of the ground state.

4 Mass formula

The functional form of our mass formula is similar to the TUYY formula [4]. It consists of three parts as

$$M(Z, N) = M_{\mathrm{g}}(Z, N) + M_{\mathrm{eo}}(Z, N) + M_{\mathrm{sh}}(Z, N), \tag{11}$$

where $M_{\mathrm{g}}(Z, N)$ is the term representing the gross feature of the nuclear mass surface, $M_{\mathrm{eo}}(Z, N)$ is the even-odd term, and $M_{\mathrm{sh}}(Z, N)$ is the shell term for which we use the shell energies obtained in the last section. The functional form of the gross term and even-odd term are given in Ref. [5]. The gross term is the same as Eq. (2) of Ref. [4], but we make small modifications on the constants and coefficients.

In order to determine the values of the parameters in the gross and even-odd terms we compare the calculated masses with the Audi-Wapstra95 [8] excluding the systematics values and also excluding the nuclides with $Z = 0, 1$ and/or $N = 0, 1$. Then, 1835 masses are available. We first determine the parameters in the even-odd term by inspecting the trend of the even-odd mass differences. The parameters in the gross term are determined by the least-squares method in which we take the weight for each nuclide as $1/(\Delta_i + 0.7\ \mathrm{MeV})^2$ where Δ_i is the error in the mass of that nuclide. If the absolute magnitude of a parameter becomes too large in this least-squares method, we constrain it to a reasonable magnitude not to cause a drastic variation in light nuclei. The root-mean-square (RMS) deviation of our formula from experimental data is 680.2 keV. In Fig. 1, deviations of calculated masses from experimental data are roughly shown.

5 Application to superheavy elements (SHE)

Responding to the recent increasing interest in superheavy elements we give some results based on the new mass formula. To compare our predicted quantities with, we take two recent mass formulas, the Finite Range Droplet Model (FRDM) [9] and the Extended Thomas-Fermi Strutinsky Integral (ETFSI) [10].

5.1 Nuclear shell energies of SHE

For the mass formulas other than ours we tentatively define the shell energies as follows:

$$E_{\rm sh}(Z,N)c^2 \equiv M_{\rm th}(Z,N) - (M_{\rm g}(Z,N) + M_{\rm eo}(Z,N)). \tag{12}$$

where $M_{\rm th}(Z,N)$ are their theoretical mass values and $M_{\rm g}(Z,N)$ and $M_{\rm eo}(Z,N)$ are ours.

We show these shell energies in Figs. 2, 3 and 4. These Figures show that the three kinds of shell energies are similar to each other in the region of $Z = 90 - 110$ and $N = 136 - 160$, and slightly different in the region $Z = 110 - 130$ and $N = 180 - 190$. According to our shell energies, the alleged magicity at $Z = 114$ is not so remarkable, while the nucleus $^{310}126$ is doubly-magic although its double-magicity is not so strong as ^{132}Sn and ^{208}Pb.

5.2 Q_α and T_α of SHE

The main decay mode for the known heaviest elements is α-decay. We compare the calculated α-decay Q-values, Q_α, with other formulas. We also estimate the α-decay half-lives T_α: we use the phenomenological formula by Viola and Seaborg [11],

$$\log T_\alpha(Z,N) = (aZ+b)/\sqrt{Q_\alpha} + (cZ+d), \tag{13}$$

with

$$a = 1.66175, b = -8.5166, c = -0.20228, d = -33.9069 \text{ [12]}. \tag{14}$$

We show Q_α and T_α in Figs. 5, 6 and 7. In Fig. 5(a), our α-decay Q-values present a feature of magicity at $Z = 114$ and at $Z = 126$ as relatively wide gaps between isotope lines, while those of FRDM have a large gap only at $Z = 114$, and those of ETFSI show no gap. Our α-decay half-lives T_α depend on nuclides rather moderately compared with other predictions.

References

[1] H. Koura, T. Tachibana, M. Uno and M. Yamada, JAERI-Conf **95-008** (1995) 250.
[2] H. Koura, T. Tachibana, M. Uno and M. Yamada, JAERI-Conf **96-008** (1996) 284.
[3] H. Koura, M. Uno, T. Tachibana and M. Yamada, Int. Conf. on Exotic Nuclei and Atomic Masses (ENAM98), Bellaire, Michigan, 1998, ed. B.M. Sherill, D.J. Morrissey, and C.N. Davids, (The American Institute of Physics, 1998) p. 114.
[4] T. Tachibana, M. Uno, M. Yamada and S. Yamada, Atomic Data and Nuclear Data Tables **39** (1988) 251.
[5] H. Koura, M. Uno, T. Tachibana and M. Yamada, Nucl. Phys., submitted for publication.
[6] H. Koura and M. Yamada, Nucl. Phys., to be published.
[7] H. Koura and M. Yamada, Technical Report of Advanced Research Institute for Science and Engineering, Waseda University, **No.99-14** (1999) 1.
[8] G. Audi and A.H. Wapstra, Nucl. Phys. **A 595** (1995) 409.
[9] P. Möller, J.R. Nix, W.D. Myers and J. Swiatecki, Atomic Data and Nuclear Data Tables **59**, (1995) 185.
[10] Y. Aboussir, J.M. Pearson, A.K. Dutta and F. Tondeur, Atomic Data and Nuclear Data Tables **61**, (1995) 127.
[11] V.E. Viola, Jr. and G.T. Seaborg, J. Inorg. Nucl. Chem. **28** (1966) 741.
[12] Z. Patyk, J. Skalski, A. Sobiczewski and S. Ćwiok, Nucl. Phys. **A 502** (1989) 591c.

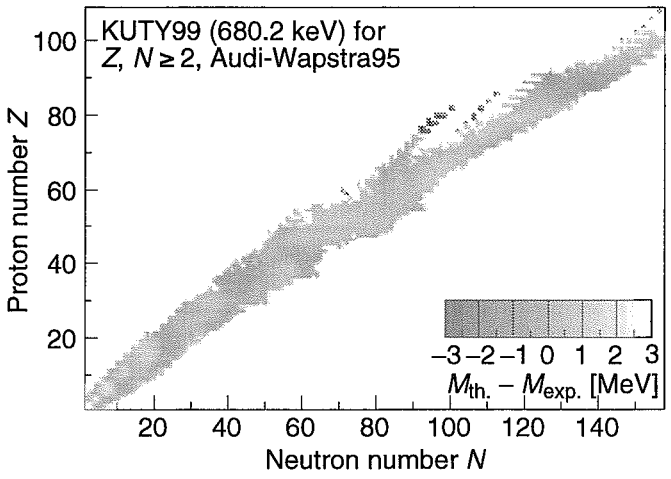

Figure 1: Calculated masses minus experimental masses.

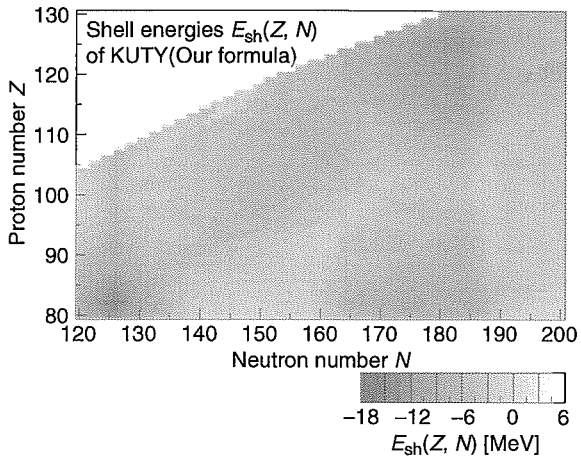

Figure 2: Shell energy of KUTY formula [5].

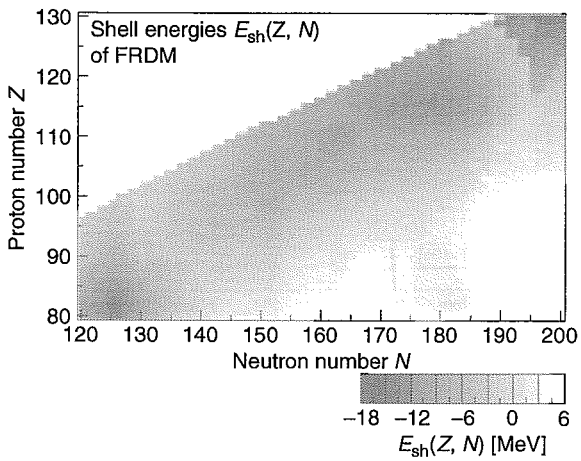

Figure 3: Shell energy of FRDM formula [9] defined by Eq. (12).

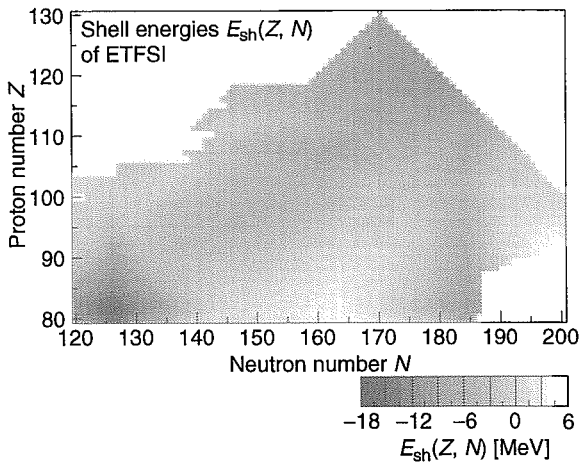

Figure 4: Shell energy of ETFSI formula [10] defined by Eq. (12).

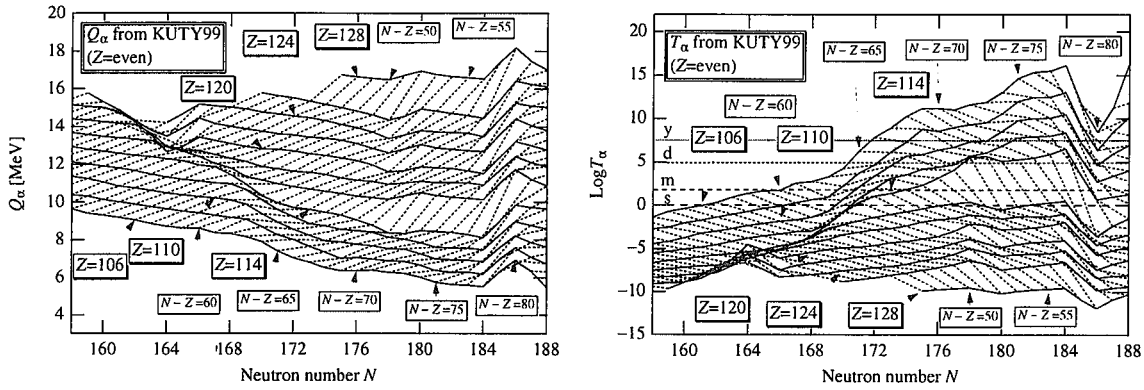

(a) (b)

Figure 5: Q_α (a) and T_α (b) of superheavy elements from KUTY formula [5] for even Z. The solid lines connect isotopes and dashed lines connect α-decay chains.

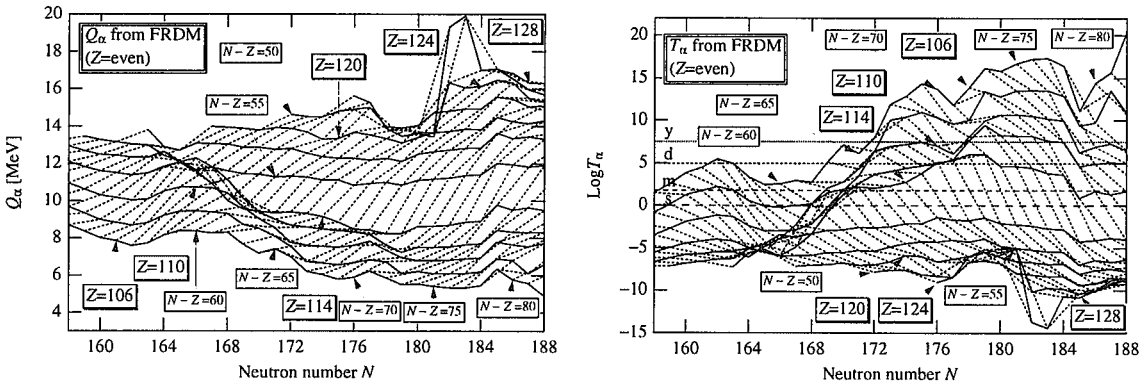

(a) (b)

Figure 6: Q_α (a) and T_α (b) of superheavy elements from FRDM formula [9] for even Z. Same notation as in Fig. 5.

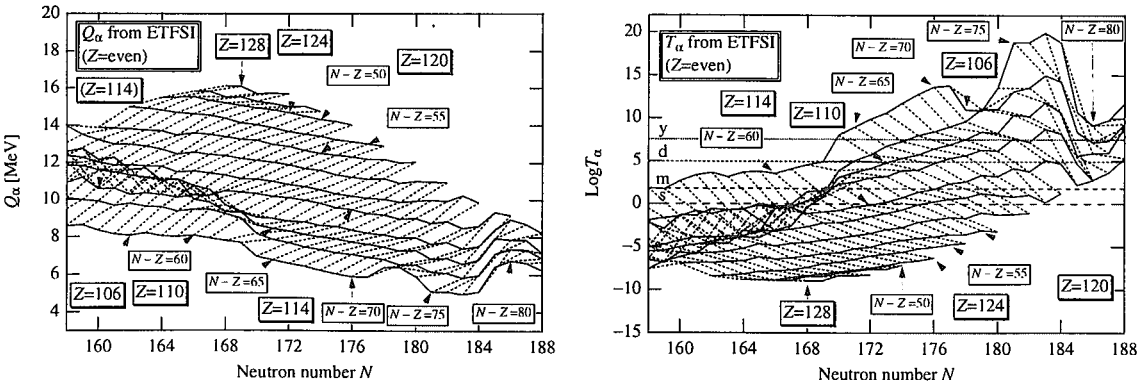

(a) (b)

Figure 7: Q_α (a) and T_α (b) of superheavy elements from ETFSI formula [10] for even Z. Same notation as in Fig. 5.

3.36

Regular level structures in s-wave neutron resonances in light or magic e-e nuclei up to several hundred keV

Makio OHKUBO+
SOHONRR 1663-39,Senba-cyo,Mito-shi, Ibaraki-ken 310-0851 Japan

Abstract
Non-statistical level distributions in s-wave neutron resonances in 15 light or magic e-e nuclei are investigated. In histogram of spacings between two arbitrary levels, dominant level spacings D_0 are found which appear most frequently. Among 30 dominant spacings (after recoil correction) of different nuclei, integer ratios are frequently found. Many of these dominant spacings are found to be equal to (C/mn), where C=34.5 MeV, and m,n are integers. Nuclear excitations are considered as a sum of C/n.

1.. Introduction

Non-statistical description of the fine structure resonances will be a developing field of the nuclear physics, where dynamical descriptions of many degrees of freedom in nuclear system will play essential role. Against prevailing statistical descriptions of neutron resonances, non-statistical distributions of observed neutron resonance levels are reported by several authors for a long time[1~5]. The methods of analyses were Dij(spacing between arbitrary two levels) distribution, Fourier analysis, and compilation of levels or spacings of many nuclei, etc. By these methods, many facets of crystalline structures of resonance levels are revealed, which can hardly be detected by the Wigner or Brody distributions on the nearest neighbor spacing.

To search for basic disposition properties of resonance levels, we try to analyze spacing distributions of two arbitrary levels Dij in light or magic e-e nuclei where level dispositions are expected to be simple because of small number of degrees of freedom involved.

In this article, the level spacings Dij and their ratios are discussed for s-wave neutron resonance levels of 15 light or magic e-e nuclei; S-32, Ar-40,Ca-40,-44, Ti-48, Cr-50,-52,-54, Fe-54,-56, Kr-86, Sr-88, Zr-90, Ce-140, and Pb-206. In these nuclei, dominant level spacing D_0 are found, which are most frequently appear among resonance levels and are construction elements of self-similar level patterns. Thirty spacings are adopted as dominat spacings for these nuclei. Among these dominant spacings D_0* (recoil energy corrected) of different nuclei, integer ratios are frequently found. For the pairs of D_0* having integer ratios, the least common energies LCE are defined. It is found that about half of the dominant spacings are equal to (34.5/mn) MeV, where m,n are integers less than 20. Physical meaning of the above relation on dominant spacing are considered based on the recurrence model of the compound nucleus[6].

2. Dominant Level Spacing

Neutron resonance parameters are taken from the book of new edition [8]. For N levels at energies Ei (i=1,2,....,N; Ej>Ei for j>i), spacings between two arbitrary levels are defined as Dij = Ej- Ei (j> i , i=1,2,..,N-1, j=2,3,...,N). Number of Dij is N(N-1)/2. The dominant spacing can be found as a peak in the distribution of Dij. In the following, brief descriptions on level dispositions are made on S-32, Ca-40 and Zr-90, on which non-statistical dispositions are fairly clear.

a) S-32

About one hundred resonances are observed below 1700keV, and 10 resonance levels are assigned as s-wave ones. Level dispositions and Dij distributions are shown in Fig.1(a). Among the 10 levels, Dij of a=593.5 ±0.5keV appears three times, and b=369.6±0.3keV two times. The spacing ratio is a:b=8:5 with 0.4% accuracy. The levels concern are 102,696,1065,1290 and 1659keV, the sequence of which can be described as /a/b/a-b/b/, where "/" means a real level. Among this sequence, symmetric patterns with spacing ratios 8:5:8 and 5:3:5 are found.

Disposition of these levels is a rare event. Probability of three times appearance of arbitrary spacing Dij within error ±0.5keV is calculated assuming random disposition of the 10 levels in energy region of 1700 keV. It is shown that such appearance is expected in one case out of 100 of the shuffled ensembles of 10 levels. This value is sufficiently small to occur by chance. We can say that assumption of random level distribution (without long range correlation of this type) is rejected with statistical significance level of 1 %. The spacings of a and b are adopted as dominant spacings.

Ca-40

About 250 resonances are observed below 2500keV, and 40 resonances are assigned as s-wave ones. Level dispositions and Dij distributions are shown in Fig.1(b). Among the 40 levels a spacing of a=232± 5keV appears 12 times, and another spacing b=186keV frequently adjacent to a=232keV. A level sequence of /a/b/a/ frequently appears. In Dij distribution, a=232keV, a+b=418keV and 2a+b=650keV show dominant peaks. The ratio of spacings is integer ratios within 1% error; a:b:a+b:2a+b = 5:4:9:14. Several level sequences composed of elements a, b, a+b, overlap in this energy region.

As described earlier [7], the frequent appearance of /a/b/a/ is rare event. The spacing of 650±10keV appears 14 times in this energy region, and in 11 cases out of 14, there exist 418±10keV spacing. Probability of 11 times appearance in 14 trials is calculated assuming random level distribution. Expectation of such appearance at any spacing with an error of ±10keV is estimated to be 0.5%, which means that in 200 ensemble of shuffled 40 levels, such appearance is expected only in one case. This value is sufficiently small to occur by chance. The spacing a,a+b, 2a+b are adopted as dominant spacings.

C) Zr-90

About 140 resonances are observed below 301 keV, and 30 resonances are assigned as s-wave ones. Level dispositions and Dij distributions are shown in Fig.1(f). In Dij spectrum for the 30 s-wave levels, a peak appears at 78.5±0.5 keV, corresponding to 9 times appearance. Probability of 9 time appearance of arbitrary spacing within error ΔE=1keV is calculated to be 15 %, assuming random distribution of 30 levels in 300keV region. This value is insufficient to say non-random structures. However, among the levels which concern the 78.5keV spacing, a regular sequence are found out. The level dispositions and series are shown in Fig.3, the members are 35, 90, 114, 129, 144, 168, 192, 208, 222, 246, and 300keV levels. Except 129 and 208keV levels, these 9 levels are placed at /a+b/a/b/a/a/b/a/a+b/, where a=24.1keV, b=30.4keV, a+b=54.5keV, and 2a+b=78.5keV. In this sequence, the spacing 2a+b=78.5keV appears 6 times. The sequence starts from 35keV and ends at 300keV resonances. These resonance levels dispose symmetrically around 168keV resonance. In the central region of the sequence, inclusion of a level at 198keV(not included in above symmetric series) give swapped structure; 168,192,198,222 as overlapping of /a/b/ and /b/a/ with common end levels. Spacing ratio is a:b =24.1:30.4 =4:5 within error of 1%. This –4-5-4- structure is similar to that found in 40Ar, and 40Ca, where -5-4-5- structures are predominant. Spacing

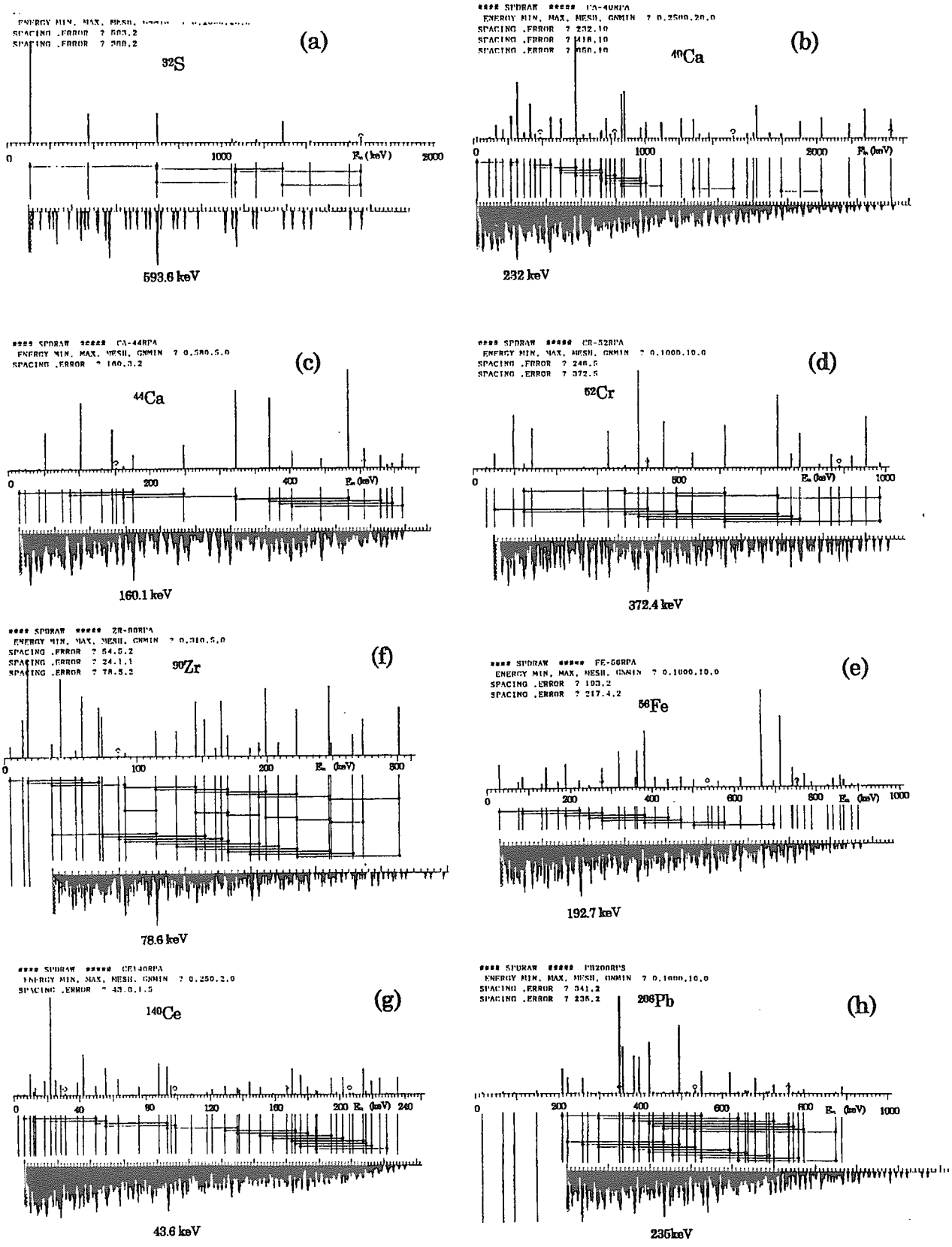

Fig.1 Level dispositions and Dij distributions for S-32, Ca-40, Ca-44, Cr-52, Fe-56, Zr-90, Ce-140 and Pb-206.

between levels of 129 and 208keV is 78.5keV, and the levels placed at symmetric point around the 168keV level. We adopted 24.1,30.4, 54.5 and 78.5keV as dominant spacings.
d) Dij distributions for other nuclei are shown in Fig.1. Dominant spacings are searched for by similar method as above. In some cases, number of observed resonances are not enough and statistical ambiguity are rather large. Nevertheless, we tried to read out dominant spacings by the aid of disposition pattern. D_0 obtained are shown in Table 1.

3. Integer ratios among D_0 of different nuclei

Curious integer ratios are found between some pairs of the dominant spacings of different nuclei. So we tried to seek integer ratios among D_0^* which are corrected for the recoil effect; $D_0^* = (A/(A+1))D_0$ where A is target mass number. The criterion of the integer ratios between $D_0 1^*$ and $D_0 2^*$ is,

$$| 1 - R/(m/n) | \leq 0.005 \quad (m,n = 1,2,3,.. < 20) \quad \ldots\ldots (1)$$

where $R = D_0 1^*/D_0 2^*$.

If $D_0 1^* = X$ and $D_0 2^* = Y$ are in integer ratio,

$$X/Y = m/n \quad (m,n = 1,2,3,..) \quad \ldots\ldots (2),$$

we can get two kind of values, the unit U and the Least common Energy LCE, defined as

$$U = X/m = Y/n = (X+Y)/(m+n) \quad \ldots\ldots (3)$$

$$LCE = nX = mY = (nX+mY)/2 \quad \ldots\ldots (4).$$

We searched for pairs of D_0 with integer ratios and U and LCE, especially LCE by a computer. Distribution of LCE is shown in Fig.2, where peaks are seen at 2032, 2655, 3834, ... keV. Based on the recurrence model of the compound nucleus [6], recurrence frequency dropped by integral ratio when a new degrees of freedom is excited in the system. Therefore, we think that there are some stable modes of excitation at the energies 2032, 2655, 3834,... keV , which are common to many compound nuclei.
Moreover, the energy ratios between these peaks are 2032/2655 =13/17, 2032/3834= 9/17, 2655/3834= 9/13. From these ratios, the peak energies are found to be simply expressed as 2032keV =C/17, 2655= C/13 and 3834 =C/9, where C is a constant,

$$C = 34.5 \text{ MeV}. \quad \ldots\ldots (5)$$

Several small peaks in Fig.2 are of this type, though different peaks are also seen. About half of D_0^* in Table 1 are equal to C/mn, where m, n are integers. These m,n are listed in Table1.

4. Meaning of dominant spacings

Many of the dominant spacings in Table 1 are described as mode ensemble coupled to the oscillator of frequency C. The time period of oscillation of C is 1.20x10-22 (s), which seems to be a time clock for the resonance reactions on nuclear surface. On the mn-th periodic points of the time mesh, resonance reaction is took place, as if "time-slit" open to interfere penetrating and passing component of the incident neutron wave[6].
For example, D_0^*=226keV in Ca-40 is described as the product of two oscillators with moderation factors of 9 and 17, and the recurrence energy is scaled as 34.5MeV/9/17 = 225.5 keV.
Unexpectedly it is found that the excitation energies Ex of lowest three s-wave resonances of S-32 can be accurately described by a sum of inverse integers as,

$$\text{(S-32)} \quad Ex = Sn + En^* = [\, 1/9 + 1/17 + 1/k \,]\, C \quad (k=10,11,12) \quad \ldots\ldots (6),$$

where C is 34.5 MeV in Eq.(5), and Sn =8641.6keV, and k=12 for the lowest resonance. Dominant spacing of S-32 D_0*=575.6keV is between first and third resonances, and is shown to be (1/10- 1/12)C = C/60 =575 keV. Other combinations of integers are possible instead of (9,17,k) in Eq.(6), such as (5,30,50),(5,30,36),and (5,20,50) for 1^{st},2^{nd} and 3^{rd} resonances. For these oscillator ensemble, recurrence energies E_{rec} are C/150, C/180, and C/100, respectively, as the least common energy of these oscillators. Energies of the 1^{st} ,2^{nd} and 3^{rd} resonances are 102.7keV (99.6keV), 377(365.4) and 696(675), where recoil corrected values En* are in parentheses. It is noted that the ratios between recurrence energies and the resonance energies are nearly equal to the integer ratios, if a correction $\delta \backsim$15keV is added to the resonance energies. This will be a confirmation of a classical image in neutron resonances, that at a resonance the incident wave frequency is in integer ratios of the recurrence frequency of the target system.[6]

On the compound nucleus, it seems that several independent oscillators of energy C/n (n: integer) are excited. Dominant spacings of C/nm type will be an energy difference of C(1/m-1/n)/(n-m), with furcation of C into C/(n-m).

It is interesting that the constant C=34.5MeV is related to the values Δ=4.6MeV presented by Sukhoruchkin [9], the mass difference between $\pi\pm$and π 0, and Δ(4.6MeV) =9m_e, where m_e is electron mass 0.511 MeV. The value C presented here is C= 7.5Δ = 67.5 m_e, with a relation Δ=(1/3 - 1/5)C. Also C is very close to the value of (average mass of pions)/4 = 34.509MeV.

5. Conclusion

For the s-wave resonance levels of light or magic e-e nuclei, spacings between two arbitrary levels are investigated. Against ordinary surmise, these dominant spacings D_0* seem to preserve themselves under complicated interactions in highly excited compound nuclei. There are integer ratios among D_0* of different nuclei, and we obtain a constant C=34.5MeV, which seems to stem from a phenomenon common to all the nuclear system. Many of D_0* can be described as (C/mn), where m,n are integers. Nuclear excitations will be considered as ensembles of oscillators with energies C/n, where C will be related to the pion interactions. Time behaviors of the oscillator ensemble will be essential to the resonance phenomena. Further efforts are needed to clarify the "Non-Statistical" features of the neutron resonances.

References

1. S.Sukhoruchkin: Proc.Conf.Nucl.Data for Reactors,Paris,1966,Vol 1,p159,Vienna, 1967
2. S.Sukhoruchkin:ISINN-4,Dubna 1996; ISINN-5,1997 Dubna; ISINN-6,1998 Dubna
3. K.Ideno, M.Ohkubo: J.Phys.Soc.Jap.30,620(1971); K.Ideno; ibid. 37,581(1974)
4. F.N.Belyaev, S.P.Borovlev: Yad. Fiz. 27, 289 (1978)
5. G.Rohr: Low Energy Nuclear Dynamics,(World Scientific, 1995) p130
6. M.Ohkubo; Phys.Rev.C, 53, 1325 (1996)
7. M.Ohkubo; JAERI-CONF 96-008, Proc.Symp.Nuclear Data, 1995.p314 (1996)
8. Landolt-Börnstein New series Vol 16/B, "Neutron Resonance Parameters" ,Springer (1998)
9. S.Sukhoruchkin: Proc.ISINN-6, Dubna 1998

Table 1 Nuclides, energy regions, number of resonances, dominant spacings, recoil corrected dominant spacings, and preliminary m,n of coupled modes.

Nuclide	Emax(keV)	N	Do (keV)	Do* (keV)	Mode Coupling
S-32	1700	10	593.6 369.6	575.6 358.4	5 12 8 12
Ar-40	1500	28	207 259.6 467.5	201.9 253.2 456.1	9 19 8 17
Ca-40	2500	40	232 418 650	226.3 407.8 634.1	9 17 7 12
Ca-44	580	24	160.1	156.5	13 17
Ti-48	370	18	74.8 95.2 229.7	73.3 93.3 225.0	9 17
Cr-50	600	32	75.2	73.7	
Cr-52	1000	23	245.7 372.4	241.0 365.4	12 12
Cr-54	820	15	308.5	302.9	6 19
Fe-54	1000	44	300.7	295.2	9 13
Fe-56	900	38	192.7 217.4	189.3 213.5	13 14 9 18
Kr-86	950	32	75.0 312.2 484.2	74.1 308.6 478.6	 7 16 6 12
Sr-88	850	13	252 541	249.1 534.9	
Zr-90	310	28	50.2 78.6	49.6 77.7	
Ce-140	240	47	43.5 86.7	43.2 86.1	
Pb-206	900	35	235 341	233.9 339.3	

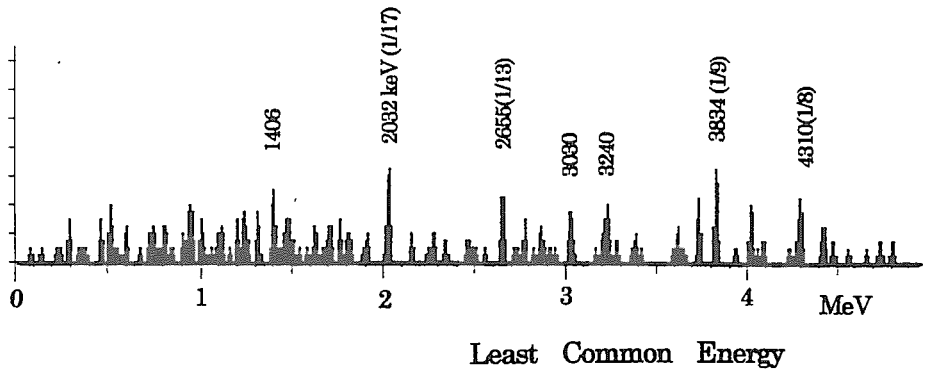

Fig.2 Distributions of the least common energies for pairs of D_0* having integer ratios. Energies of several peaks are equal to (C/n), where C=34.5MeV, and n are integers shown.

3.37 Study on Nuclear Characteristics of Sodium Cooled Accelerator-Driven Transmutation System

Vladimir Barchevtsev and Hisashi Ninokata
Research Laboratory for Nuclear Reactors
Tokyo Institute of Technology
2-12-1, O-okayama, Meguro-ku, Tokyo 152-8550, Japan
e-mail: vabar@nr.titech.ac.jp, hninokat@nr.titech.ac.jp

Series of calculations of OECD/NEA benchmark problem [1] are performed using ABBN-93 [2] cross-section data library. For an accelerator-driven system (ADS) the core neutronic characteristics and transmutation rates of minor actinides (MA) are obtained and analyzed. Discrepancies with the results of benchmark participants are found due to the differences in cross-section data and due to different methods used in calculations.

1. Introduction

Transmutation calculations are not as well established as the conventional uranium and plutonium burn-up reactor systems, because nuclear data for minor actinides are less reliable and the burn-up chains for decay and generation are not completely modeled in the computation.

We suggest to compare calculational results of neutronic characteristics for the ADS benchmark concerning MA transmutation using the ABBN-93 cross-section data library. This data library has been verified and validated by a wide set of various fast and thermal critical experiments and benchmarks.

The main idea of this work is to evaluate the status of MA transmutation calculations and also to validate codes and data for the benchmark.

The ABBN-93 cross-section data library includes group constants for nearly all-chemical elements, all long-lived actinides, all important fission product nuclides and for many isotopes. The range of considered neutron energies is from 0 to 20 MeV. Number of neutron groups is 28 or 299 as a standard and variants can be assumed between 28 and 299. The ABBN-93 is prepared from the evaluated data files library FOND-2 (File Of evaluated Nuclear Data). This library contains data for nuclides selected from BROND-2, JENDL-3, ENDF/B-V, -VI, and JEF-2 libraries. The selection is based on the detailed study of the relative performances of the above libraries in predicting the results of several micro and macro experimental results. The ABBN-93 cross-section data library can be applied in different scientific and technical fields for calculations.

2. Evaluation Method

The system subject to analysis consists of a proton accelerator and sodium cooled subcritical region driven by a proton beam of 1 GeV energy and current of 10 mA in a subcritical state of $k_{eff} \approx 0.9$. Specifications of this ADS are given in Table 1. Solid tungsten is used as a target material. Fuel is a mixture of plutonium (10%) and minor actinides (90%). Two types of fuel compositions are considered, which are denoted as MOX11 and MOX12. These compositions are given in Table 2.

Table 1. Specifications of target / core transmutation system

Specification	Value
Proton beam	1.0 GeV, 10 mA
Beam radius	15 cm
Beam profile	Uniform
Target	Tungsten (disk layers type)
Height / Radius	80 cm / 15 cm
Upper region height	26 cm
Lower region height	54 cm
Core radius	40 cm
Fuel	(10Pu-90MA)N
Pin diameter	7.3 mm
Pin pitch	9.9 mm
Pin height	80 cm
Fuel pellet diameter	6 cm
Na bond thickness	0.35 mm
Cladding thickness	0.3 mm
Reflector	Stainless steel
Inner / outer radius	40 cm / 90 cm
Top thickness	30 cm
Bottom thickness	40 cm
Coolant	Sodium

Table 2. Fuel composition (weight percent)

Fuel	MOX11	MOX12
Pu-238	1.5	2.6
Pu-239	59.3	44.5
Pu-240	23.7	31.0
Pu-241	8.7	10.7
Pu-242	5.5	9.5
Am-241	1.3	1.7
Total:	100	100
Np-237	44.6	4.5
Am-241	43.6	62.5
Am-243	9.7	24.3
Cm-244	2.1	8.7
Total:	100	100

Two-dimensional model of ADS system is used in calculations. It consists of two-region tungsten target, MA fueled core, and stainless steel reflector, each of which is cooled by sodium. The atom densities are homogenized for each region. Fig. 1 shows this caculational model.

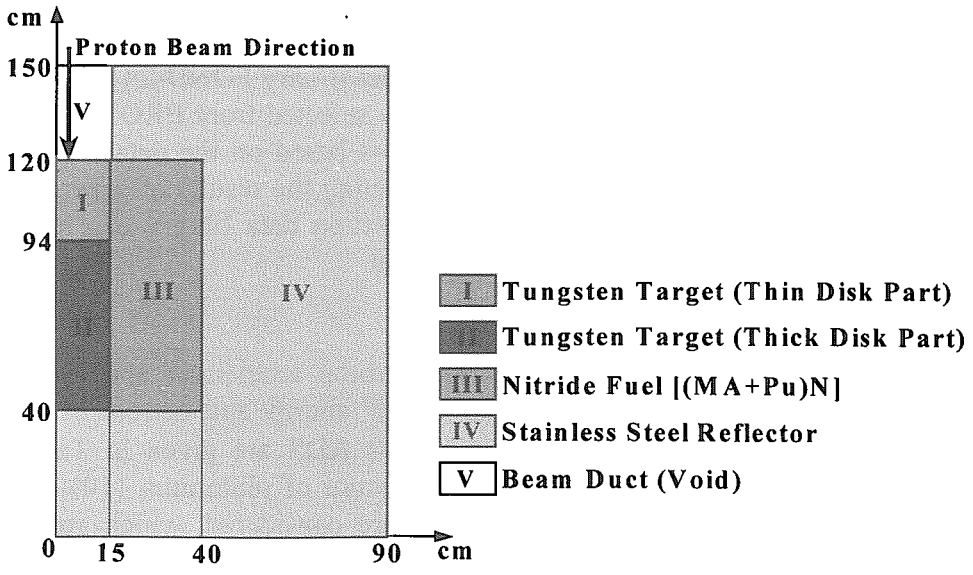

Fig.1. Two-dimensional calculational model

Calculation codes and nuclear data libraries which are used by participants of this benchmark are given in Table 3. Our calculational method is denoted as TIT. This calculational scheme is shown in more detail in Fig. 2.

Table 3. Codes and nuclear data libraries

Calculation	TIT*	JAERI**	PSI***
> 20 MeV	NMTC/JAERI	NMTC/JAERI	HETC-PSI
< 20 MeV	TWODANT	TWODANT	TWODANT
Burn-up	ORIGEN	BURNER	2DTB
Cross-section Formation	CONSYST	SCALE-4	NJOY89.62
Nuclear Data Library (Groups Number)	ABBN-93 (299 Groups)	JENDL-3.2 (73 Groups)	JEF-2.2 (33 Groups)

* TIT – Tokyo Institute of Technology
** JAERI – Japan Atomic Energy Research Institute
*** PSI – Paul Scherrer Institute

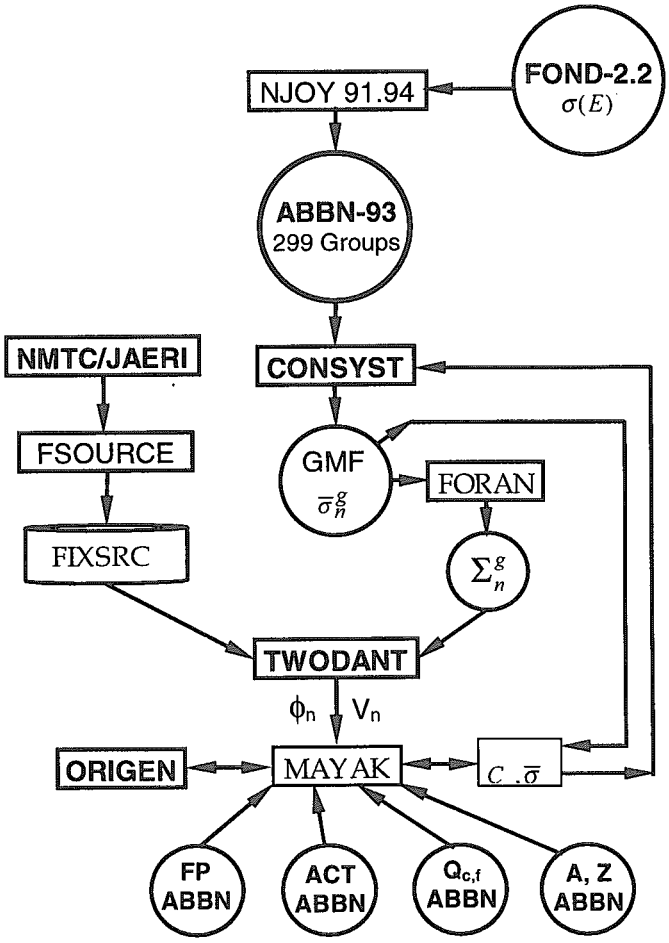

Fig. 2. Scheme of calculational method

The neutron transport process in the target/core is calculated as the fixed source problem. The nucleon-meson transport code NMTC/JAERI [3] is used for the calculations of external spallation neutron source distribution. Neutrons slowed down below 20 MeV are stored to the history file. Fixed neutron source FIXSRC file for the transport calculation is built from the history file by FSOURCE Code [3]. Only the neutron analysis below 20 MeV is considered for calculations of multiplication factor and burn-up. The transport of neutrons is calculated by TWODANT Code [4] using ABBN-93 (299 Groups) constant set. CONSYST Code [5] is used for cross-section formation. Burn-up calculations are done by the ORIGEN-S Code [6] in which cross-sections of original libraries are updated during calculations by the cross-sections of additional isotopes from the external group neutron constant set ABBN-93 libraries, which are necessary for burn-up chains. These libraries are for fission products (FP ABBN, about 170 isotopes) and actinides (ACT ABBN, about 60 isotopes). MAYAK Code [7] is used not only for intercommunication between CONSYST, TWODANT, and ORIGEN, but also for calculations of neutron reaction rates, neutron balance components, power distribution etc. MAYAK receives information about averaged fluxes and volumes of the zones from transport code. CONSYST provides MAYAK with isotopic composition and microscopic cross-sections. Then MAYAK prepares the information for burn-up code and provides the interaction of different parts of the program scheme. All complex of codes is driven by a system of batch files which give the possibility of multi-step burn-up calculations.

3. Results and Discussions

Using the calculational method and model mentioned above we have obtained main neutronic characteristics of ADS system. These results are given below in tables and figures.

Good agreement is observed for time evolution of MA, MA transmutation rates, less agreement for capture and fission reaction rates. However there are discrepancies between values of multiplication factor and core neutron spectrum. The major reasons are due to differences between fission neutron spectrum, capture and fission cross-sections used for MA nuclides in different nuclear data.

We use ABBN-93 cross-section in our standard calculations. There are only 28-group data for MA (for such as ^{237}Np, ^{241}Am, ^{243}Am, ^{242}Cm, ^{243}Cm, ^{244}Cm, ^{245}Cm, ^{246}Cm). New version of ABBN cross-section data is preparing now for release. In comparison we give results which are obtained by using ABBN with new 299-group data for MA in order to take into account more correctly the resonance part of cross-sections and threshold reactions. These results are denoted as TIT-MA.

Table 4. Neutronic characteristics analysis results

	MOX11				MOX12			
	JAERI	PSI	TIT	TIT-MA	JAERI	PSI	TIT	TIT-MA
k-eff	0.8993	0.8966	0.9359	0.9184	0.9180	0.9205	0.9609	0.9406
Na Void Reactivity (% Δk/k/k')	+7.16	+7.31	+5.17	+5.23	+7.30	+7.44	+5.31	+5.38
Av. Neutron Flux (10^{15} n/cm^2/s)	2.39	1.58	3.09	3.02	2.92	1.99	3.68	3.64

Neutron spectrum in the core is shown in Fig. 3. Harder TIT spectrum is observed. Here we give results for MOX11 fuel case only, because results of MOX12 case are similar.

Core fission and capture reaction rates normalized to unit are shown for MOX11 case in Fig. 4.

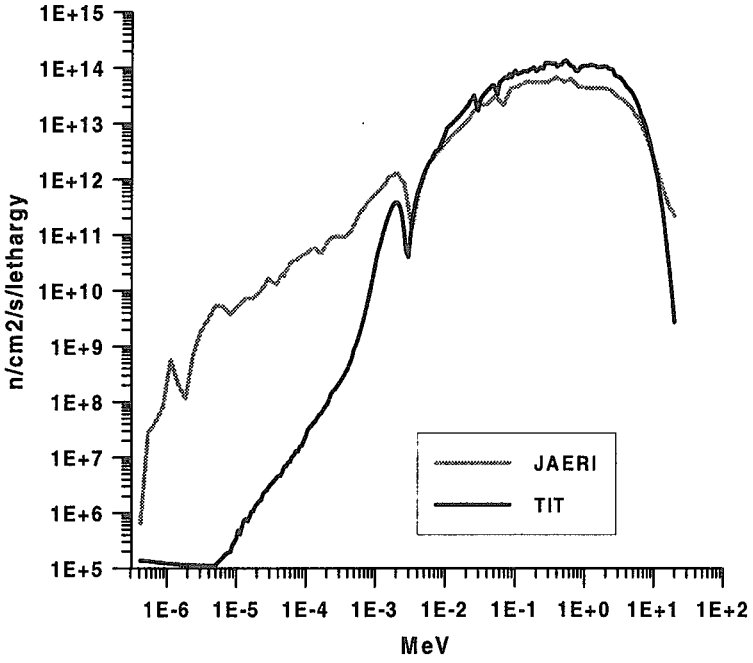

Fig. 3. Core neutron spectrum

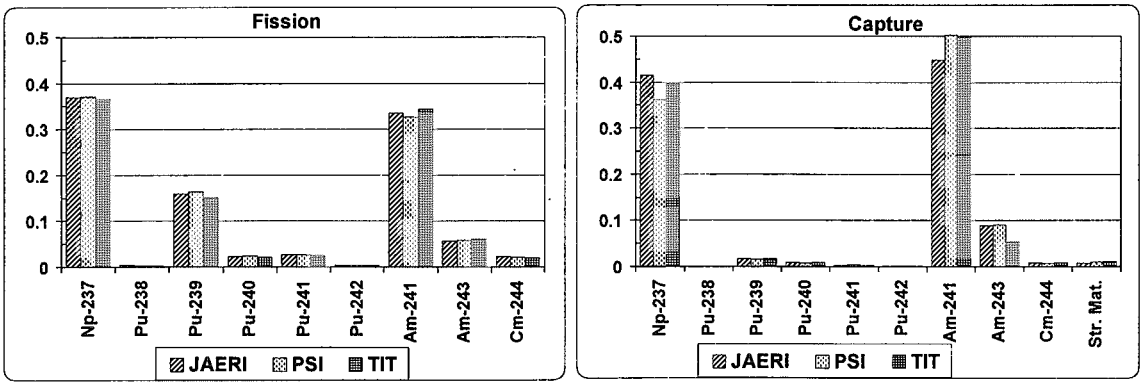

Fig. 4. Core fission and capture reaction rates for MOX11 fuel case

Some nuclides in the fuel composition of the large fractions give the contribution in reaction rates. These are ^{237}Np, ^{239}Pu, ^{241}Am and ^{243}Am. Differences between results of reaction rates for MOX11 case are reported in Table 5.

Table 5. Comparison of reaction rates results for MOX11 case, %

Nuclide	Fission		Capture	
	TIT-JAERI	TIT-PSI	TIT-JAERI	TIT-PSI
^{237}Np	-0.9	-1.1	-4.6	8.9
^{239}Pu	-4.7	-7.3	4.5	9.1
^{241}Am	2.6	5.2	10.1	-0.9
^{243}Am	6.2	5.0	-63.7	-65.1

It is necessary to note that calculations with 299-group cross-section for MA (TIT-MA results) reduce the discrepancy of the reaction rates on the average in comparison with the results of participants. Especially it is appreciable in capture rate for ^{243}Am. This discrepancy decreases from 65 to 3 percent. A similar tendency of the core reaction rates is found for MOX12 case. These results are shown in Fig. 5.

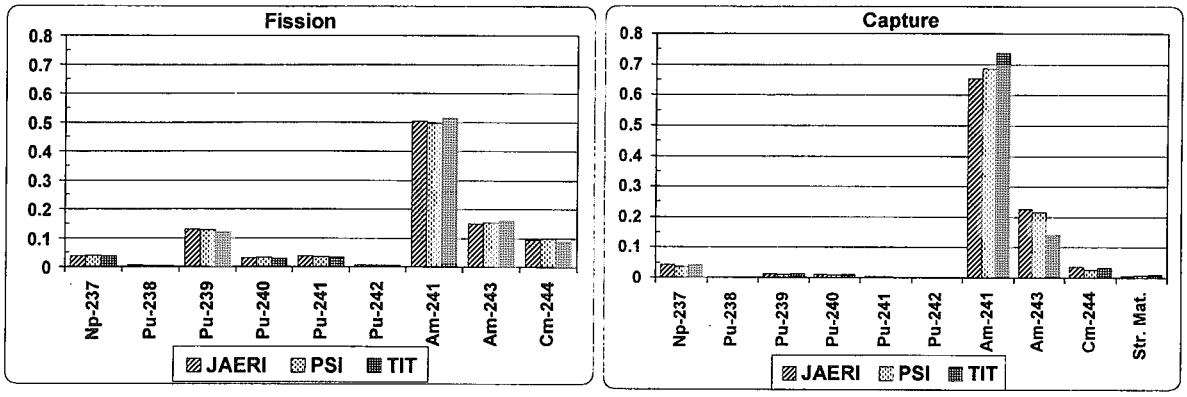

Fig. 5. Core fission and capture reaction rates for MOX12 fuel case

Time evolution of ^{237}Np number density for MOX11 and MOX12 cases is shown in Fig. 6. No big discrepancy is found between TIT and PSI results. Differences from the JAERI results are about 10 percent at the end of burn-up. It is explained by the different burn-up codes are used in calculations which consider different burn-up chains and nuclide yields.

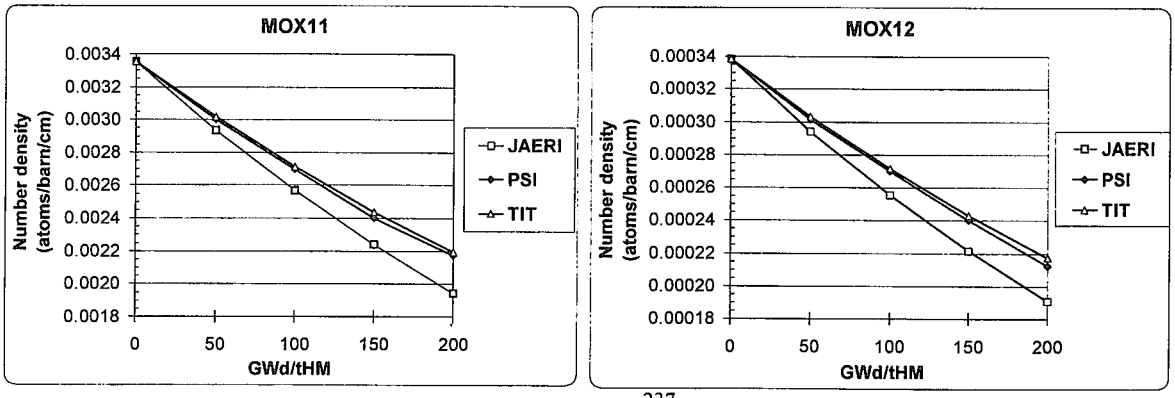

Fig. 6. Time evolution of ^{237}Np number density

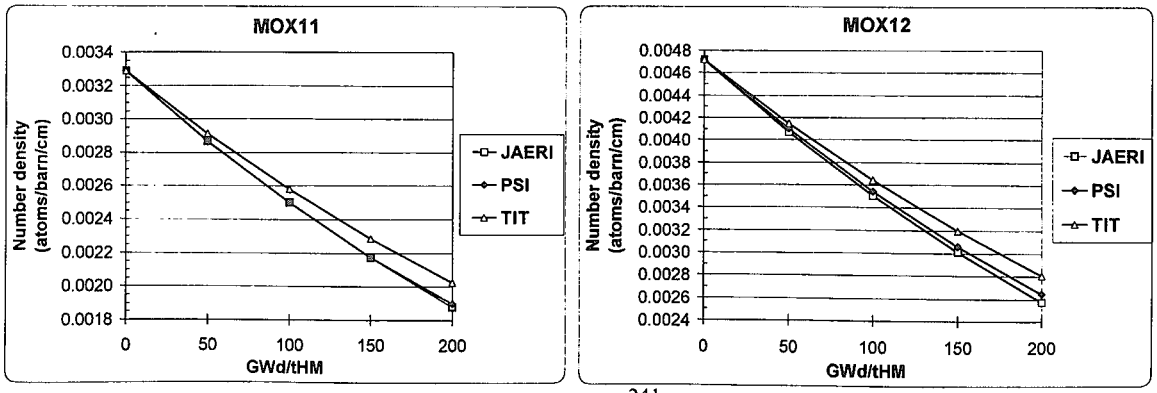

Fig. 7. Time evolution of ^{241}Am number density

Time evolution of ^{241}Am number density for MOX11 and MOX12 cases are shown in Fig. 7. The ^{241}Am number density (TIT results) for MOX11 case is 7 percent higher at the

end of burn-up in comparison with results of JAERI and PSI. For MOX12 case TIT calculational results differ from JAERI results by 8 percent and from PSI results by 6 percent.

The effective multiplication factor is one of the most important integral data. Calculational results of k_{eff} as a function of burn-up are shown in Fig. 8. Remarkable discrepancies between k_{eff} are observed. Major reasons for the discrepancies are considered to be due to fission neutron spectrum, capture and fission cross-sections used for MA nuclides in different nuclear data libraries.

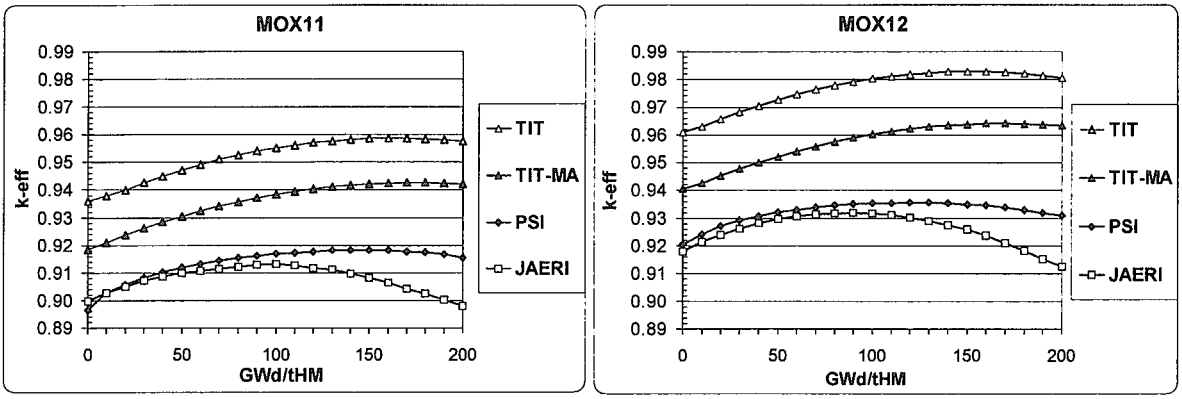

Fig. 8. Comparison of k_{eff} values as a function of burn-up

Discrepancies between k_{eff} increase at the end of burn-up. The main reason is due to the burn-up calculations by the standard ORIGEN working library for Liquid Metal Fast Breeder Reactor. It means that the fission product yields are limited by the isotopes which are included in this library for fissile nuclides. These fissile isotopes are ^{235}U, ^{238}U, ^{239}Pu, ^{240}Pu and ^{241}Pu. The subcritical system under consideration has only 10 percent of plutonium and 90 percent of MAs in the fuel. Therefore the fission product accumulation is not predicted correctly (Fig.9).

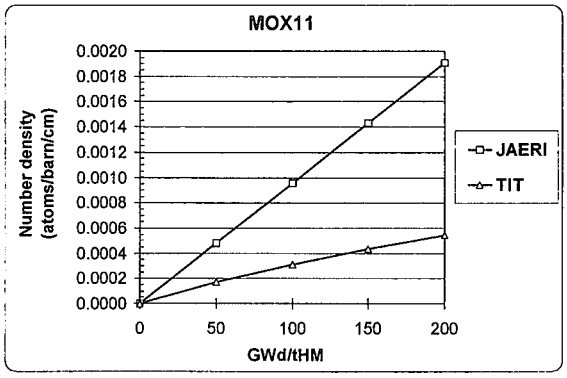

Fig. 9. Time evolution of fission products number density

Table 6. Transmutation rates of Pu and MA (only by fission), %

Nuclides	MOX11				MOX12			
	JAERI	PSI	TIT	TIT-MA	JAERI	PSI	TIT	TIT-MA
^{237}Np	36.99	37.07	36.67	36.92	3.95	3.98	3.86	3.92
^{238}Pu	0.37	0.32	0.30	0.30	0.66	0.59	0.55	0.54
^{239}Pu	15.99	16.39	15.27	14.93	13.01	12.86	12.12	11.98
^{240}Pu	2.23	2.38	2.17	2.20	3.13	3.31	2.97	3.02
^{241}Pu	2.79	2.78	2.63	2.54	3.79	3.55	3.44	3.36
^{242}Pu	0.37	0.43	0.39	0.40	0.82	0.79	0.71	0.72
^{241}Am	33.46	32.56	34.36	35.08	50.41	49.62	51.57	52.76
^{243}Am	5.76	5.83	6.14	5.56	14.99	15.54	16.11	14.61
^{244}Cm	2.23	2.21	2.06	2.09	9.39	9.76	8.90	9.09

Pu and MA transmutation rates are given in Table 6. Most discrepancies are observed for ^{238}Pu, ^{241}Pu and ^{242}Pu. Other differences do not exceed 10 percent.

4. Concluding Remarks

For an accelerator-driven system the core neutronic characteristics and transmutation rates of minor actinides are obtained and analyzed.

Good agreement is observed for time evolution of MA, minor actinides transmutation rates, less agreement for capture and fission reaction rates. However there are notable discrepancies between results for a multiplication factor k_{eff}. They are caused by differences between fission neutron spectrum, capture and fission cross-sections used for MA nuclides in different nuclear data. Increasing time evolution discrepancy between k_{eff} values is explained by underestimation of the fission products accumulation during burn-up. To consider correctly fission product yields, it is necessary to add MA nuclides to the ORIGEN working fissile isotopes library. A revision of the fission products library (FP ABBN) is required in order to add nuclides which appears due to MA fission.

Obtained results indicate that the ABBN-93 cross-section data library with appropriate modifications could be used as a basis for calculations of nuclear characteristics of subcritical MA fueled core.

Acknowledgments

Authors wish to thank Mr. T.Sasa and Dr. H.Takano (Japan Atomic Energy Research Institute) for their fruitful help. Special thanks are given to Ms. S.Zabrodskaya, Mr. Al.Tsiboulia, Dr. G.Manturov, Mr. V.Koscheev, Mrs. T.Ivanova (Institute of Physics and Power Engineering, Obninsk, Russia) for their support and many useful discussions.

References

[1] H. Takano, et al. "Benchmark Problems on Transmutation Calculation by the OECD/NEA Task Force on Physics Aspects of Different Transmutation Concepts"

[2] G.N. Manturov, M.N. Nikolaev, A.M. Tsiboulia. "ABBN-93 Group Data Library." Part 1. Nuclear Data for calculation of Neutron and Photon Radiation Fields. Vienna, IAEA, INDC(CCP)-409/L (1997)

[3] T. Sasa, K. Tsujimoto, T. Takizuka, H. Takano "Accelerator-Driven Transmutation Reactor Analysis Code System - ATRAS." Japan Atomic Energy Research Institute (1999)

[4] "Two-Dimensional Discrete Ordinates Code System." Los Alamos National Laboratory (1992)

[5] RSICC DLC-182 " ABBN-90: Multigroup Constant Set for Calculation of Neutron and Photon Radiation Fields and Functionals, including the CONSYST2 Program."

[6] RSICC CCC-545 "SCALE 4.3: Modular Code System for Performing Standardized Computer Analysis for Licensing Evaluation for Workstations and Personal Computers." (1997)

[7] T. Ivanova, M. Nikolaev, Y. Rozhikin, M. Semenov, Al. Tsiboulia "Validation of the KENO-ABBN-93 Package Based on Data from the International Handbook of Evaluated Criticality Safety Benchmark Experiments." Sixth International Conference on Nuclear Criticality Safety. Versailles, France (1999)

3.38

CALCULATION AND ANALYSIS OF NEUTRON AND RADIATION CHARACTERISTICS OF LEAD COOLANTS WITH ISOTOPIC TAILORING FOR FUTURE NUCLEAR POWER FACILITIES

A.I.Blokhin, A.P.Ivanov, V.V.Korobeinikov, V.P.Lunev, V.N.Manokhin, G.L.Khorasanov.

SSC RF A. I. Leypunsky Institute for Physics and Power Engineering
1 Bondarenko Square, Obninsk, Kaluga Region, 249020 Russia
Tel.:7-08439-94464, Fax:7-095-2302326, E-mail: blokhin@ippe.rssi.ru

I. INTRODUCTION.

The purpose of the paper is isotopically enriched material construction perspectives for fast and subcritical reactors. Last time a new type of safe fast reactor with lead coolant was proposed in Russia /1/. It is well known that natural lead is the mixture of lead isotopes, which consists of 52.3 % Pb-208, 22.6 % Pb-207, 23.6 % Pb-206 and 1.5 % Pb-204.

In the first part of paper the search of a technique for hardening the fast reactor neutron spectrum and by this way increasing the burning of Np-237, Am-243 and other minor actinides (MA) fissionable preferentially under hard neutron spectrum is given. The main concern is for using lead isotope, Pb-208, as a reactor coolant instead of natural lead, Pb-nat.

Another lead isotope, Pb-206, is considered as the low-activation material in the second part of paper. As it is shown in our previous papers /2,3/ the use of Pb-206 as a coolant for fast reactors and as a coolant-converter for accelerator-driven system seems to be very attractive, although isotopic tailoring option requires tremendous technical efforts.

II. MMKFK CODE SIMULATION

The use of coolants with low moderating properties is one of the ways to get the hard neutron spectrum in the fast reactor. The stable lead isotope, Pb-208, is proposed as the one of such coolants. The neutron inelastic scattering cross-section of Pb-208 is 3.0–3.5 times less than the one for other lead isotopes. These data are taken from JENDL-3.2 library /4/ and given in Table 1.

Table 1. Neutron inelastic scattering cross-sections of natural lead and his stable isotopes, averaged up on fission neutron spectrum, barns

Nuclide	Pb-204	Pb-206	Pb-207	Pb-208	Pb-nat
Cross-section, σ_{in}	1.325	1.316	1.265	0.361	0.804

Calculation of the MA transmutation rates in the fast reactor with different coolants is performed by Monte-Carlo method using Code MMKFK /5/. Such the simulation reproduces a broad class of parameters at operation of the standard BN-type fast reactor. The analysis of obtained results for burning neptunium and americium in the blanket having thickness of 50 cm was carried out in this paper. Six various models are simulated for the fast reactor blanket with different kinds of fuel and coolant. The composition of this blanket is listed in Table 2.

Table 2. The composition of fast reactor blanket for different models of (MA + coolant), nuclides$*10^{-20}$/cm^3

Nuclide	Model 1 (Np+Na)	Model 2 (Np+Pb-nat)	Model 3 (Np+Pb-208)	Model 4 (Am+Na)	Model 5 (Am+Pb-nat)	Model 6 (Am+Pb-208)
Np-237	12.6	12.6	12.6	0.0	0.0	0.0
Am-241	0.0	0.0	0.0	11.4	11.4	11.4
Am-243	0.0	0.0	0.0	4.0	4.0	4.0
O	25.2	25.2	25.2	23.6	23.6	23.6
Na	103.0	0.0	0.0	103.0	0.0	0.0
Pb-nat	0.0	143.0	0.0	0.0	143.0	0.0
Pb-208	0.0	0.0	143.0	0.0	0.0	143.0

The composition of structural materials is the same for all the models. The values of nuclear concentration for elements of structural materials used in homogeneous blanket are listed in Table 3.

Table 3. The nuclear concentration of structural materials in homogeneous blanket model, nuclides$*10^{20}/cm^3$

Nuclide	Model 1–6	Nuclide	Model 1–6	Nuclide	Model 1–6
Fe	140.0	Cr	30.8	Ni	16.8
Mo	2.4	Mn	1.6	Zr	21.6
C	21.6	-	-	-	-

The weight and volume portions of the main material constituents used in the MMKFK calculation are summarized in Table 4. One can see that the volume portions of main materials in all the models are following: 7.13–9.54 % for the fuel, 54.16–57.00 % for the coolant, and 35.06–37.17 % for structural materials. It is important to note that the volume share of the coolant is large for changing the neutron spectrum in the blanket.

Table 4. Weight and volume composition of materials of the blanket models (MA + coolant) for MMKFK calculation

Model	Fuel		Coolant		Structural materials	
	Weight, %	Volume, %	Weight, %	Volume, %	Weight, %	Volume, %
1. (Np+Na)	18.12	7.39	12.66	55.44	69.22	37.17
2. (Np+Pb-nat)	7.37	7.14	64.45	56.90	28.12	35.95
3. (Np+Pb-208)	7.35	7.13	64.54	57.00	28.11	35.87
4. (Am+Na)	21.10	9.54	12.20	54.16	66.70	36.31
5. (Am+Pb-nat)	8.78	9.23	63.47	55.62	27.75	35.15
6. (Am+Pb-208)	8.76	9.21	63.56	55.73	27.68	35.06

The objective for simulating the considered system is the establishment of difference between a neutron temperature in the blanket charged with various metal coolants: sodium, Pb-nat, and Pb-208. Results of MMKFK calculation include the values for combined collision, capture of neutrons, and fission of MA. The MMKFK runs above 10^6 particles are taken into account for the blanket area. The incident particle energy corresponded to the reactor core spectrum. In order to show the results, the neutron temperature as a ratio of the fission cross-section to the sum of that and the cross-section of neutron capture, $\sigma_{fis}/(\sigma_{fis}+\sigma_{cap})$ is used, due to monotonous dependence of this ratio on the neutron energy over the MA threshold. The higher value of the ratio, the harder neutron spectrum is. The obtained values of this ratio are listed in Table 5.

Table 5. The fission portion in summarized cross-section of neutron capture and fission for neptunium and americium in the fast reactor with different coolants, $\sigma_{fis}/(\sigma_{fis}+\sigma_{cap})$

MA	Sodium	Pb-nat	Pb-208
Np-237	0.200	0.210	0.265
Am-241	0.177	0.175	0.215
Am-243	0.217	0.226	0.280

As the data of Table 5 suggests, the fast reactor with natural-lead coolant practically does not differ from the reactor with sodium coolant relative to MA incineration. The use of Pb-208 as a coolant in the fast reactor results in increasing incineration of MA from 18 to 26 % in comparison with a usual fast reactor. For maximum hardening the neutron spectrum, the heavy lead isotope as a coolant is necessary.

III. FISPACT-3 CODE SIMULATION

Calculation of induced radioactivity in lead coolant was performed using the FISPACT-3 inventory code /6/, activation cross-section library FENDL-2/A, and decay data library FENDL-2/D /7/. The results include total induced radioactivity and dose rate for initial material composition and selected long-lived radionuclides. The analysis is carried out in the following conditions:

- the neutron spectrum is taken as the one for central zone of the fast BOR-60 reactor and shown in Fig.1;
- the flux of fission neutrons is equal to $5 \cdot 10^{15}$ n/cm^2·/s;
- the mass of material is equal to 1 kg;
- irradiation time is 30 years and corresponding neutron fluence is equal to $4.8 \cdot 10^{24}$ n/cm^2;
-the decay time interval is of 10^{-8} to 10^3 years after shutdown.

One of the important results of performed calculation is a strong dependence of the activity and dose rate induced in natural lead on the irradiation time. It is shown in Fig.2 and Fig.3. One can see that for reaching a remote level of recycling, a cooling time of 50 years is necessary after 30 years irradiation time in the BOR-60 spectrum while a very short time is required for the same after 1 year irradiation. The difference reason is connected with bismuth isotopes accumulation in lead during long time irradiation. The stable bismuth isotope, Bi-209, is generated from natural lead due to radiative neutron capture by Pb-208 and fast beta decay of Pb-209 ($T_{1/2}$=3.25 h). If bismuth removing off is not envisaged, a concentration of stable bismuth will increase year by year and as a result of nuclear reactions, long-lived toxic radionuclides, Bi-207 and Bi-208, will be accumulated in lead. In Fig.4 and Fig.5 time dependent activity and dose rate for Bi-207 and Bi-208 induced in natural lead after 30 years irradiation is given. Comparing these decay curves with the ones given in Fig.2 and Fig.3, it may be concluded that Bi-207 and Bi-208 make the most contribution to the total activity and dose rate for Pb-nat at cooling time above 1 year. Total dose rates of coolants consisted of 100 percent of Pb-208, 207, 206 and 204 are given in Fig.6. These calculations show that the coolant consisting of lead isotope, Pb-206 or Pb-207, can be considered as the low-activation one because it does not practically contain long-lived toxic radionuclides. The use of Pb-206 as a coolant seems to be the most attractive, its dose rate runs into the remote recycling level a month after shutdown, and it may be completely released from a regulatory control in an year. The use of Pb-206 as a coolant permits it to decrease accumulation of alpha-active radionuclides, Po-210 and Pb-210, that is demonstrated in Fig.7 and Fig.8.

IV. SNT CODE SIMULATION.

Calculation for lead activation in the hard proton-neutron ADS spectrum was performed using SNT code /8/. In Fig. 9 time dependent activities of Bi-207 produced in Pb-nat and Pb-206 after irradiation during one year with a proton beam having energy 0.8 GeV and current 30 mA are given. It can be seen that activity of Bi-207 is decreased by 4 orders of magnitudes in going from natural lead to lead isotope, Pb-206, as a coolant for ADS targets.

Accordingly, activities of the other heavy hazardous nuclides such as Pb-210, Bi-208, Po-210 can be suppressed essentially when Pb-206 is used instead of Pb-nat in ADS targets. As an example, in Fig. 10 activities of Po-210 produced in Pb-nat and Pb-206 is represented. It is clear that production of such radiotoxic nuclide as Po-210 can be practically excluded.

REFERENCES

1. V.Mikhailov, E.Adamov. The next step for nuclear power development – a need for revised reactor and fuel cycle concept. – In. Intern. Conf. "40 Years of United Nations", Russia, Minatom (1997).

2. G.L.Khorasanov, A.P. Ivanov, A.I.Blokhin et al. Lead and tin targets for reducing polonium waste. Paper #Tu-O-E8 presented at the Third Intern. Conf. On Accelerator Driven Transmutation Technologies and Applications ADTTA'99, Praha, Czech Republic, June 7-11, 1999.
3. G.L.Khorasanov, A.P. Ivanov, A.I.Blokhin et al. Low activation materials with isotopic tailoring for future NPPs. Paper #345 presented at the Intern. Conf. on Future Nuclear Systems GLOBAL'99, Jakson Hole, Wyoming, USA, August 29 – September 3, 1999.
4. JEF Report 14. Table of Simple Integral Cross Section Data from JEF -2.2, ENDF/B-VI, JENDL-3.2, BROND-2 and CENDL-2, Paris, NEA (1994).
5. L.B. Kazakova, O.B. Kamaeva, L.B. Korobeinikova, V.V. Korobeinikov, and V.B. Polevoy. In: Proceedings of the 7th All-Union Meeting on Monte-Carlo Methods in Computer Mathematics and Mathematical Physics, Novosibirsk, Siberian Branch of the USSR Academy of Science (1985).
6. R.A.Forrest and J.Ch.Sublet."FISPACT-3 user manuel".Report AEA/FUS/227 (1993).
7. A.B.Pashchenko. "Summary report on the IAEA advisory group meeting on completion of FENDL-1 and start of FENDL-2". Report IAEA/INDC(NDS)-352 (1996).
8. G.Gherardi, A.Konobeyev, Yu.Korovin et al. Study of neutron multiplication in accelerator driven reactor system. Paper # Tu-O-E9 presented at the Third Intern. Conf. On Accelerator Driven Transmutation Technologies and Applications. ADTTA'99, Praha, Czech Republic, June 7-11, 1999.

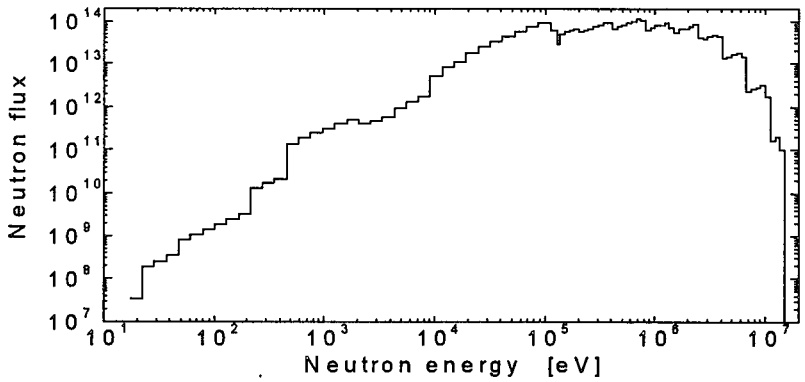

Fig 1. Neutron spectrum in n/cm^2/s units for the BOR-60 reactor.

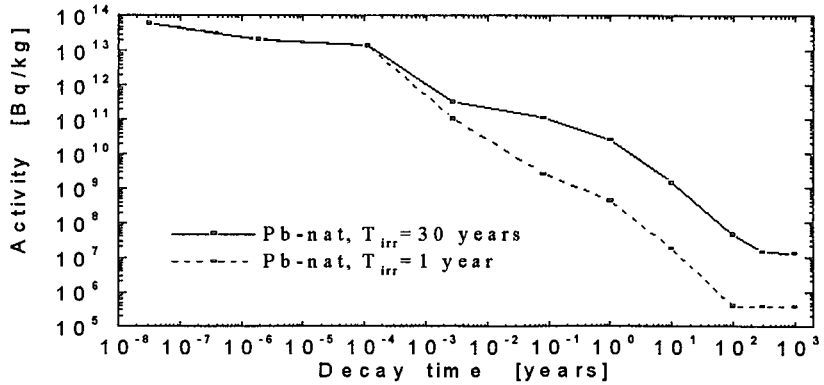

Fig.2. The total activity of Pb-nat for irradiation time 1 y and 30 y (BOR-60).

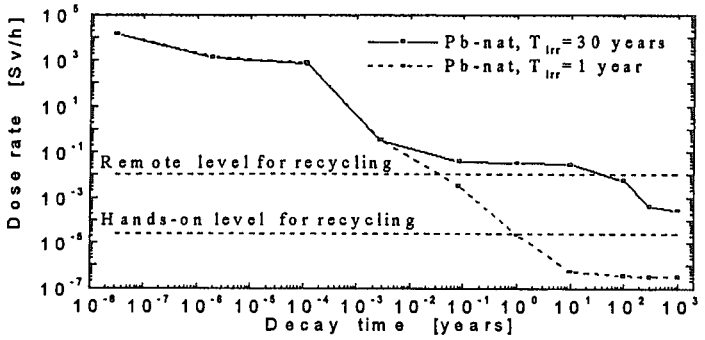

Fig 3. The total dose rate of Pb-nat for irradiation time 1 y and 30 y (BOR-60).

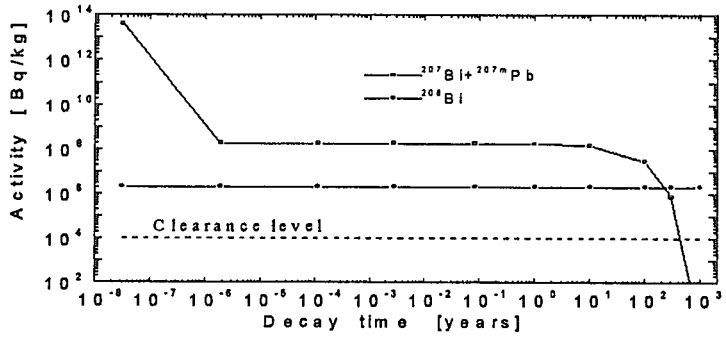

Fig.4. The activity of Bi-207 and Bi-208 produced in Pb-nat (BOR-60).

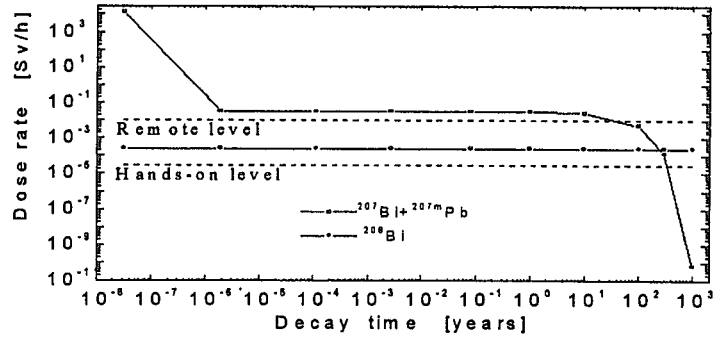

Fig5. The dose rate of Bi-207 and Bi-208 produced in Pb-nat (BOR-60).

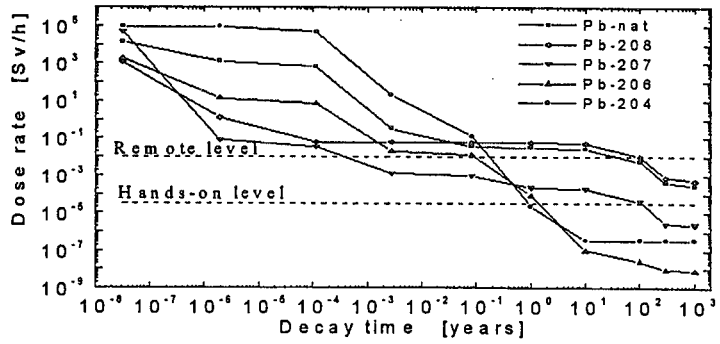

Fig.6. The dose rate for Pb-nat, Pb-208, Pb-207, Pb-206 and Pb-204 (BOR-60).

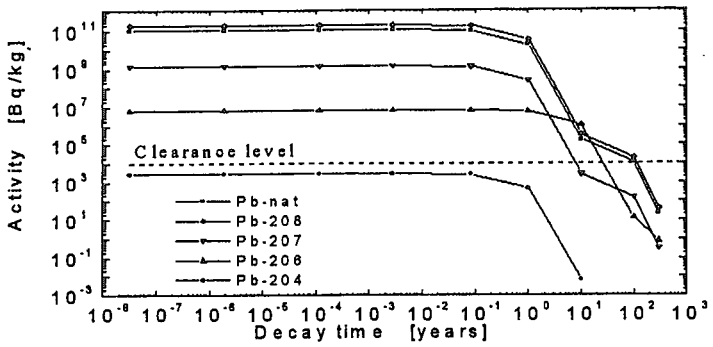

Fig.7. The activity of Po-210 produced in Pb-nat, Pb-208, Pb-207, Pb-206, Pb-204 (BOR-60).

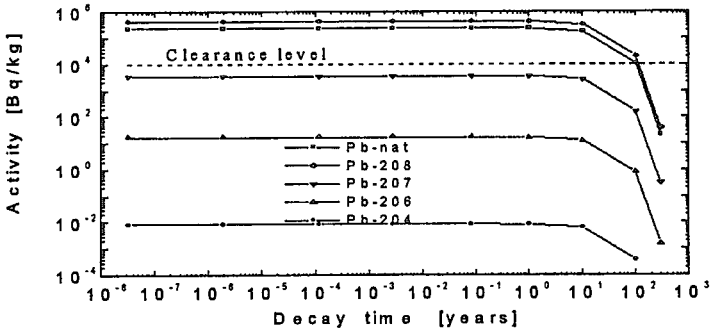

Fig.8. The activity of Pb-210 produced in Pb-nat, Pb-208, Pb-207, Pb-206, Pb-204 (BOR-60).

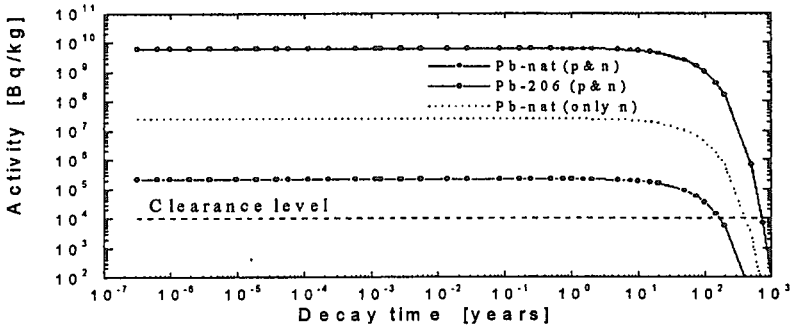

Fig.9. The activity of Bi-207 produced in Pb-nat and Pb-206 after irradiation with proton beam E_p=0.8 GeV, I_p=30 mA, and T_{irr}=1 year.

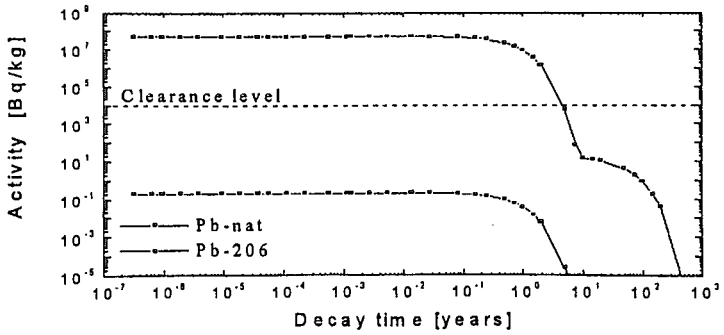

Fig.10. The activity of Po-210 produced in Pb-nat and Pb-206 after irradiation with proton beam E_p=0.8 GeV, I_p=30 mA, and T_{irr}=1 year.

3.39 Current Status of Pohang Neutron Facility

G. N. Kim, Y. S. Lee, M. H. Cho, I. S. Ko, W. Namkung
Pohang Accelerator Laboratory, POSTECH
San 31, Hyoja-dong, Nam-gu, Pohang 790-784, Korea

D. W. Lee, H. D. Kim
Physics Department, Pusan National University,
30 Changjeon-dong, Keumjeong-ku, Pusan 609-735, Korea

S. Ko, K. H. Kim, S. H. Park
Physics Department, Ulsan University,
San 29, Muge 2-dong, Nam-gu, Ulsan 680-749, Korea

D. S. Kim, J. H. Lee
Department of Physics Education, Taegu University,
Kyungsan, Kyungbuk 712-714, Korea

T. Ro, Y. K. Min
Physics Department, Donga University,
840 Hadan-dong, Saha-gu, Pusan 604-714, Korea

We present the current status of Pohang Neutron Facility, which is the pulsed neutron facility, based on the 70-MeV electron linear accelerator completed on Dec.1997. We have prepared the 15-m time-of-flight path, a Ta-target system, and the Data Acquisition System. Meanwhile we have measured the total cross-sections of Dy and Hf samples at the Research Reactor Institute, Kyoto University and the neutron capture cross-sections of ^{164}Dy isotope at Research Laboratory for Nuclear Reactors, Tokyo Institute of Technology both in Japan. We also were participated the experiment at the 122-m flight path of the IBR-30 pulsed neutron source of Joint Institute of Nuclear Research in Dubna, Russia.

1. Introduction

In order to support the active nuclear power development program and the nuclear R&D application, the Korea Atomic Energy Research Institute (KAERI) decides to establish the nuclear data project [1]. Its main goals are to establish a nuclear data system, to construct the infrastructure for the nuclear data productions and evaluations, and to develop a highly reliable nuclear data system. To build the infrastructure for the nuclear data production, KAERI wants to build an intense pulsed neutron source by utilizing accelerator facility, technology and men- power at the Pohang Accelerator Laboratory (PAL). We proposed the Pohang Neutron Facility (PNF), which consists of a 100-MeV electron linac, a water-cooled Ta target, and at least three different time-of-flight (TOF) paths [2]. The 100-MeV electron linac was designed and constructed based on experiences obtained from construction and operation of the 2-GeV linac at PAL.

We present the status of the pulsed neutron facility, and activities on the nuclear data production.

2. The Status of Pohang Neutron Facility

2.1. Construction of electron linac

We have constructed an electron linac for the various R&D activities of the neutron facility by utilizing the existing components and infrastructures at PAL on December 1997 [3]. The linac consists of a thermionic RF-gun, an alpha magnet, four quadrupole magnets, two SLAC-type accelerating sections, a quadrupole triplet, and a beam-analyzing magnet as shown in Fig. 1. We have used a thermionic RF-gun

instead of a triode gun, which is different from the 100-MeV linac for the neutron facility. The RF-gun is a one-cell cavity with a 6-mm-diameter tungsten dispenser cathode. The RF-gun produces electron beams with average current of 300 mA, a pulse length of 6-μs, and about 1-MeV energy [4]. The alpha magnet is used to match the longitudinal acceptance from the gun to the first accelerating section. An electron moves along an 'α'-shaped trajectory in the alpha magnet, and the bend angle is 278.6°. A high-energy electron has a longer path length than a low-energy electron; thus, the length of the electron beam is neither lengthened nor shortened in the beam transport line from the gun to the first accelerating section. Four quadrupole magnets are used to focus the electron beams in the beam transport line from the gun to the first accelerating section. The quadrupole triplet installed in between the first and the second accelerating sections is used to focus the electron beams during the transport to the experimental beam line at the end of the linac. Three beam-current transformers (BCT) and three beam-profile monitors are installed to monitor the beam quality during the beam operation. The beam-analyzing magnet at the end of the linac has a bending angle of 30 degree and a zero pole-face rotation.

The electron linac is located inside a tunnel beside the PLS 2-GeV linac. The building has three levels: the tunnel in 6 m below ground level, the klystron gallery is on the ground floor, and utilities, including the air-condition and the air handling units, are on the second floor. There is 3-m-thick concrete shield between the tunnel ceiling and the klystron gallery.

After the RF-conditioning of the accelerating structures and the wave-guide network, we performed the beam acceleration test [5]. The maximum RF power from a SLAC 5045 klystron was reached to 45 MW. The RF power fed to the RF-gun was 3 MW. The beam acceleration experiment was performed after any breakdown had disappeared through the RF structures. The bunched electron beam at the alpha magnet was accelerated in the accelerating sections and transported to the end of the linac. The maximum energy is 75 MeV up to now which is still lower than the target value. The measured beam currents at the entrance of the first accelerating structure and at the end of linac are 100 mA and 40 mA, respectively. The length of electron beam pulse is 1.8 μs and the pulse repetition rate is 12 Hz. The measured energy spread is ±1% at minimum. The energy spread was reduced when optimizing the RF phase of the RF-gun and the magnetic field strength of the alpha magnet.

2.2. TOF Facility

The design of the target system is done using the MC simulation codes, EGS4 and MCNP4. The target system, 4.9-cm in diameter and 7.4-cm in length, is composed of ten sheets of Ta plate, and there is 0.15-cm water gap between them, in order to cool the target effectively as shown in Fig. 2 [6]. The estimated flow rate of the cooling water is about 5 liters per minute in order to maintain below 45 °C. The housing of the target is made of titanium. The conversion ratio obtained from MCNP4 code from a 100-MeV electron to neutrons is 0.032 as seen in Fig. 3. From the Fig. 3, we can see the neutron yield per kW beam power at the target is 2.0×10^{12} n/sec, which is about 2.5% lower than the calculated value based on the Swanson's formula [7].

The pulsed neutron facility based on the electron linac is a useful tool for high-resolution measurement of microscopic neutron cross sections with the TOF method. In the TOF method, the energy resolution of neutrons depends on the TOF path length. Since we have to utilize the space and the infrastructures in the laboratory, TOF paths and experimental halls are placed perpendicular to the electron linac. We constructed a 15-m long TOF path perpendicular to the electron linac as shown in Fig. 4. With this, the test of the Ta-target system and a data acquisition system will be performed.

3. Activities on Nuclear Data Production

Since there was no nuclear data production facility in Korea, there was no activity until the nuclear data project was launched in 1997. Since then, the collaboration group for nuclear data production was organized from several universities in Korea and joined some experiments in the various neutron facilities in the world. We have measured the capture cross-sections [8] and the total cross-sections [9] of natural Dy and Hf samples in the energy region from 0.003 eV to 50 keV (100 keV) by using the neutron TOF method at the 46 MeV electron linear accelerator of the Research Reactor Institute, Kyoto University. We also have measured the capture cross sections for ^{232}Th [10] at the 122-m flight path of the IBR-30 pulsed neutron source of Joint Institute of Nuclear Research (JINR) in Dubna, Russia. The capture cross-

sections of ^{164}Dy isotope [11] was measured by using pulsed neutrons provided from the 3.2 MV Pelletron Accelerator of the Research Laboratory for Nuclear Reactors at the Tokyo Institute of Technology. We have planed to measure the capture cross sections for ^{162}Dy and ^{164}Dy isotope samples at KURRI in this year. There is also a discussion with Prof. M. Baba to join an experiment at the Tohoku University 4.5 MV Dynamitron facility in this year in order to get experiences.

As explained on the previous section, they have completed to construct a 15-m TOF facility at PAL. After checking the radiation level around the TOF facility and the linac, they would like to measure the angular distributions and energy spectra of photoneutrons from Ta-target system with the activation method and the TOF method. From the next year, they would like to measure total cross-sections for the well-known samples with TOF method.

4. Summary and Discussion

The nuclear data project was launched by KAERI from 1996 in order to support nuclear R&D activities, medical and industrial applications. We have constructed and tested a test-linac for the pulsed neutron facility by utilizing the existing components and infrastructures at PAL. The characteristics of accelerated electron beams are about 75 MeV of energy, 12 Hz of repetition rate, 1.8 μs of pulse width and about 40 mA of peak current. We made a 15-m TOF path perpendicular to the test-linac in order to test a Ta-target system and a data acquisition system.

We have joined two facilities to get experiences for cross section measurements at KURRI in Japan and at JINR in Russia. In these facilities, we have measured the capture and the transmission cross sections for various samples. There are also several activities for data evaluations at KAERI with international collaborators.

The workshop for nuclear data production and evaluation was held on August 7 and 8, 1998 and Aug. 19 and 20, 1999 at PAL. The aim of the workshop was to review recent progress, exchange ideas and search future directions in the nuclear data production and evaluation. During these workshops, we discussed various subjects on the nuclear data production and evaluation.

References

[1] Ministry of Science and Technology of Korea (1997), "1997 Request for Project on Long- Term Nuclear R&D Program."

[2] G. N. Kim, *et al.*, "Proposed Neutron Facility using 100-MeV electron linac at Pohang Accelerator Laboratory," Proceedings of International Conference on Nuclear Data for Science and Technology (May 19-24, 1997, Trieste, Italy), 556 (1997).

[3] G. N. Kim, *et al.*, J. Accel. Plasma Res. **3** (1998) 9.

[4] H. S. Kang, G. N. Kim, M. H. Cho, W. Namkung, and K. H. Chung, IEEE Trans. Nucl. Sci. **44**, 1639 (1997).

[5] H. S. Kang *et al.*, "Beam Acceleration Result of Test Linac," Proceedings of the First Asian Particle Accelerator Conference (Mar. 23-27, 1998, Tsukuba, Japan), 743 (1998).

[6] W. Y. Baek *et al.*, "Design of the Photoneutron Target for Pulsed Neutron Sources at PAL," Proceedings of Workshop for Nuclear Data Production and Evaluation (Aug. 7-8, 1998, Pohang, Korea) (1998).

[7] W. P. Swanson, "Radiological Safety Aspects of the Operation of Electron Linear Accelerators," IAEA Technical Reports No. 188 (1979).

[8] H. J. Cho *et al.*, J. of Korean Physical Society, **34** (1999) 333.

[9] H. J. Cho *et al.*, "Measurement of Neutron Total Cross-Sections for Dy and Hf in the Energy Region from 0.003 eV to 0.1 MeV," to be presented in this Symposium.

[10] W. Y. Baek, *et al.*, "Investigation of γ-multiplicity Spectra and Neutron Capture Cross Sections of ^{232}Th in the energy region 21.5 eV-215 eV," Proceedings of Workshop on Nuclear Data Production and Evaluation, August 7-8, 1998, Pohang, Korea.

[11] H. D. Kim *et al.*, "Measurement of Capture Cross-Sections and Capture γ-ray Spectra of ^{164}Dy," to be submitted for Korean Physical Society Meeting (Oct. 15-19, 1999, Bukyung Univ., Korea) (1999).

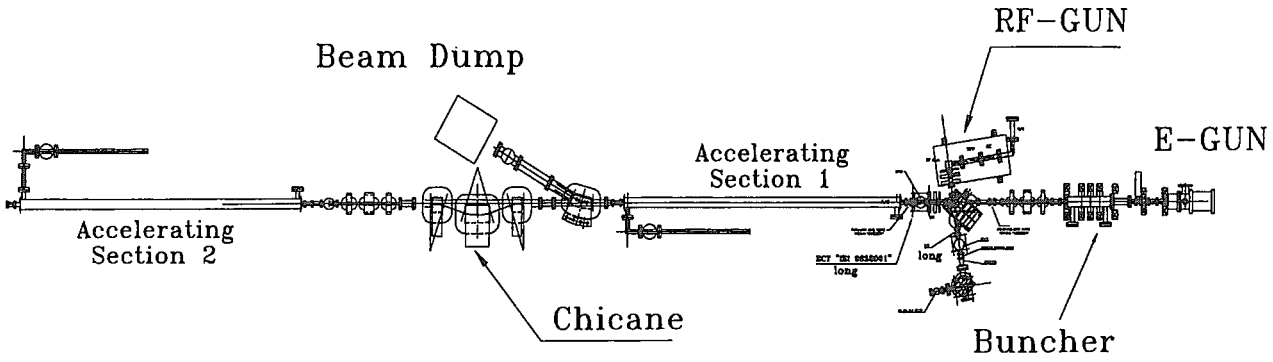

(a)

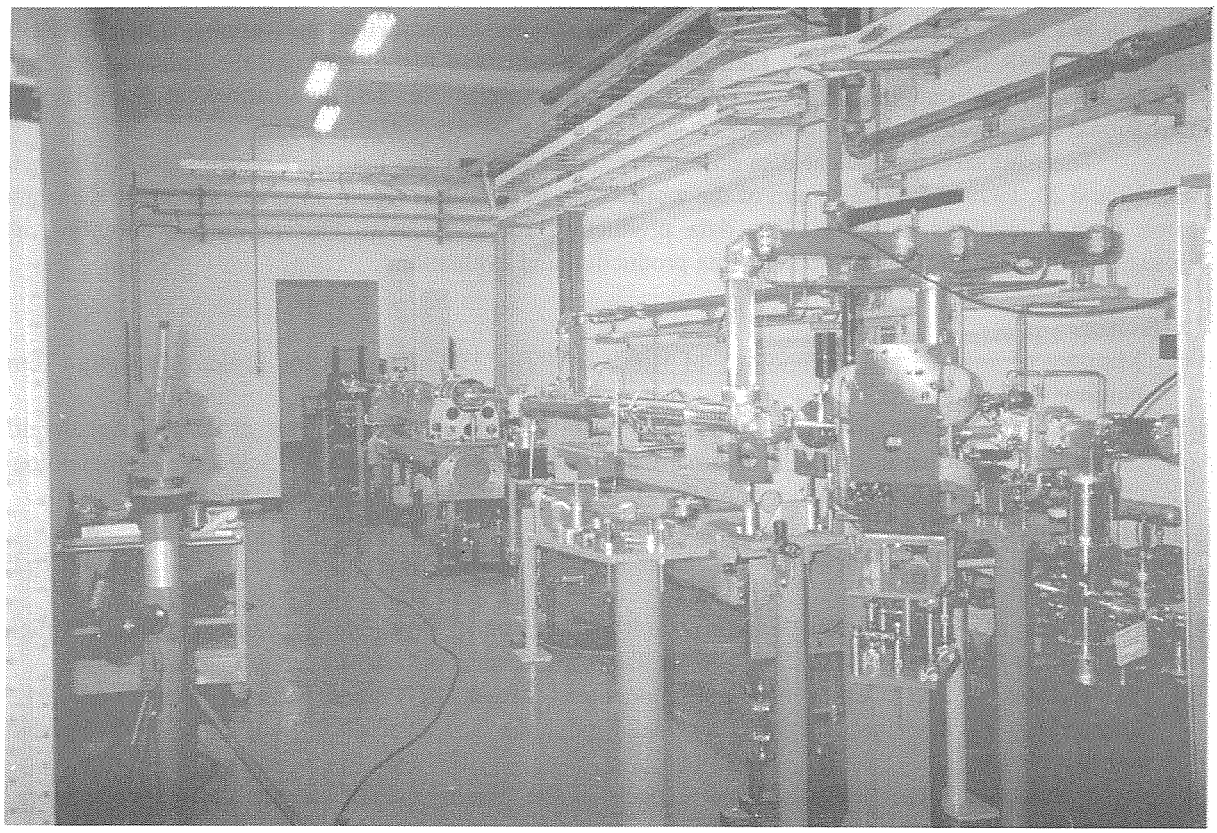

(b)

Fig. 1. (a) Design of the electron acceleractor, (b) Picture of constructed electron acceleractor

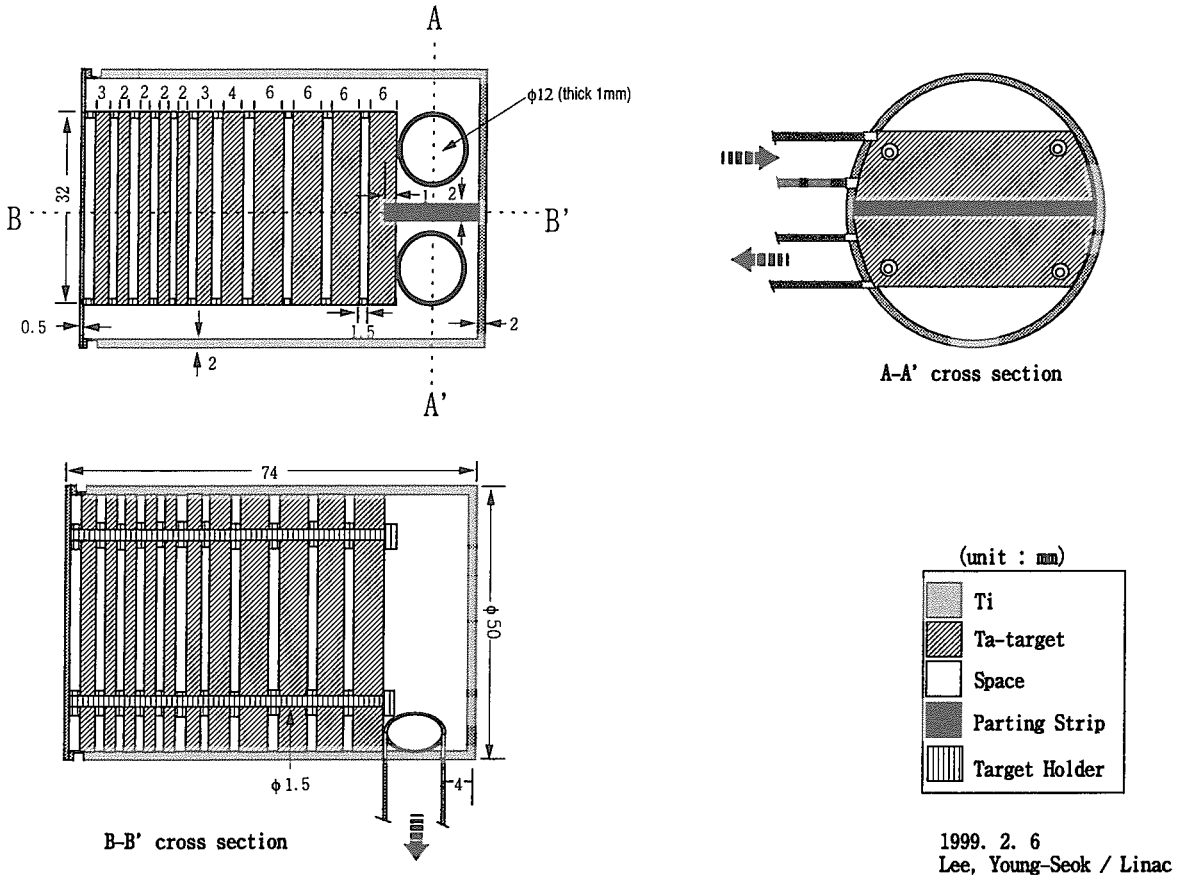

(a)

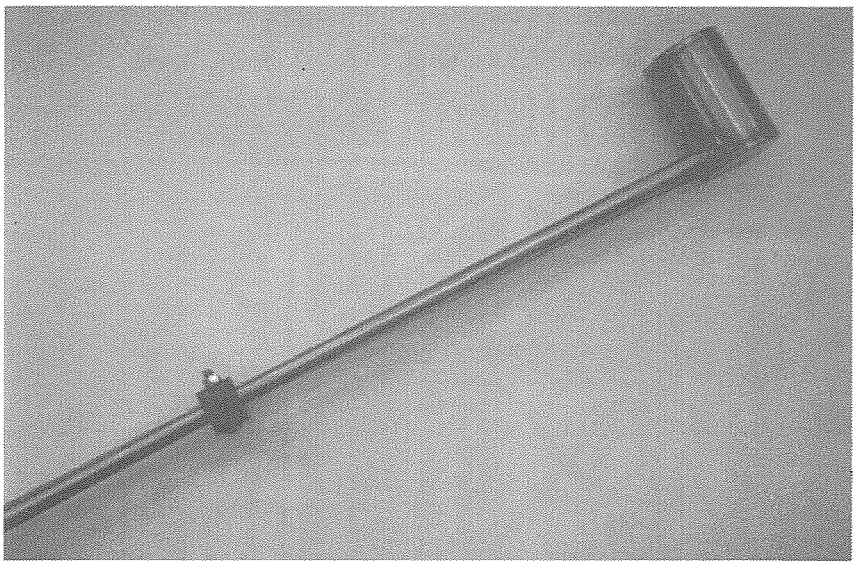

(b)

Fig. 2. (a) Design of Ta-target system, (b) Picture of constructed Ta-target system

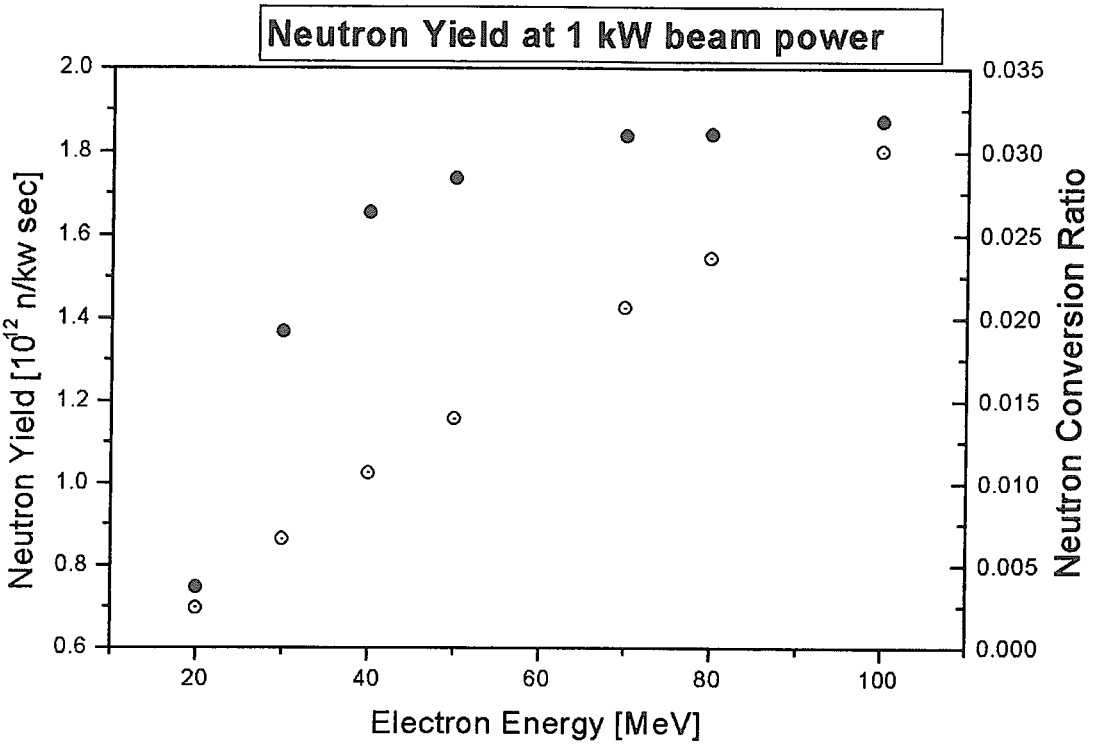

Fig. 3. Calculated neutron yield at 1 kW beam power and the conversion ratio from one electron to neutrons as a function of electron energy.

Fig. 4. Picture of constructed TOF facility

3.40

A FACILITY FOR LOW ENERGY CHARGED PARTICLE INDUCED REACTION STUDIES

T. Vilaithong, S. Singkarat, L.D. Yu, S. Intarasiri and U. Tippawan
Fast Neutron Research Facility, Department of Physics, Faculty of Science,
Chiang Mai University, Chiang Mai 50200, Thailand
e-mail: fnrf@loxinfo.co.th

Abstract

In Chiang Mai, a highly stable low energy ion accelerator ($0 - 350$ kV) facility is being established. A subnano-second pulsing system will be incorporated into the beam transport line. The detecting system will consist of a time-of-flight charged particle spectrometer and a high resolution gamma-ray system. The new facility will be used in the studies of low energy heavy ion backscattering and charged particle induced cross section measurement in the interests of material characterization and nucleosynthesis.

1 INTRODUCTION

In order to develop ion beam analysis techniques in the laboratory by giving further play to the potential of present research facilities instead of generous investing and installing new facilities, we introduce the time-of-flight (TOF) analyzing technique but using backscattering of low-energy ion beams [1]. The technique is considered to be a new ion beam analysis technique, different from using conventional high or medium energy ion beams, specially benefiting compositional and depth-profiling analysis of thin films, ion-implanted layers and deposited thin coatings. The basics of the technique is Rutherford Backscattering Spectrometry (RBS) [2], however, the traditional detection is revolutionized to be the time-of-flight method, which then provides an unprecedented resolution of energy or mass. The techniques to be applied in the composite facility include the pulsed beam TOF-RBS, low-medium-energy RBS, (p,γ) & $(p,\alpha\gamma)$ reaction, and E & ΔE spectrometry.

2 FEATURES OF LOW-ENERGY-ION-BEAM RBS ANALYSIS

2.1 Ion Beam Conditions Currently Available at FNRF

Figure 1 shows the present 150-kV accelerator-based neutron generator [3], which is to be modified for the purpose of low energy charged particle induced reaction studies.
The ion beam conditions available at the facility are listed below.

Ion:	H^+, D^+, He^+, He^{2+}
Accelerating voltage:	200 kV (maximum)
Mass-analysis bending angle:	90°
Beam pulse:	1.5 ns
Target chamber vacuum:	$10^{-6} - 10^{-5}$ Torr

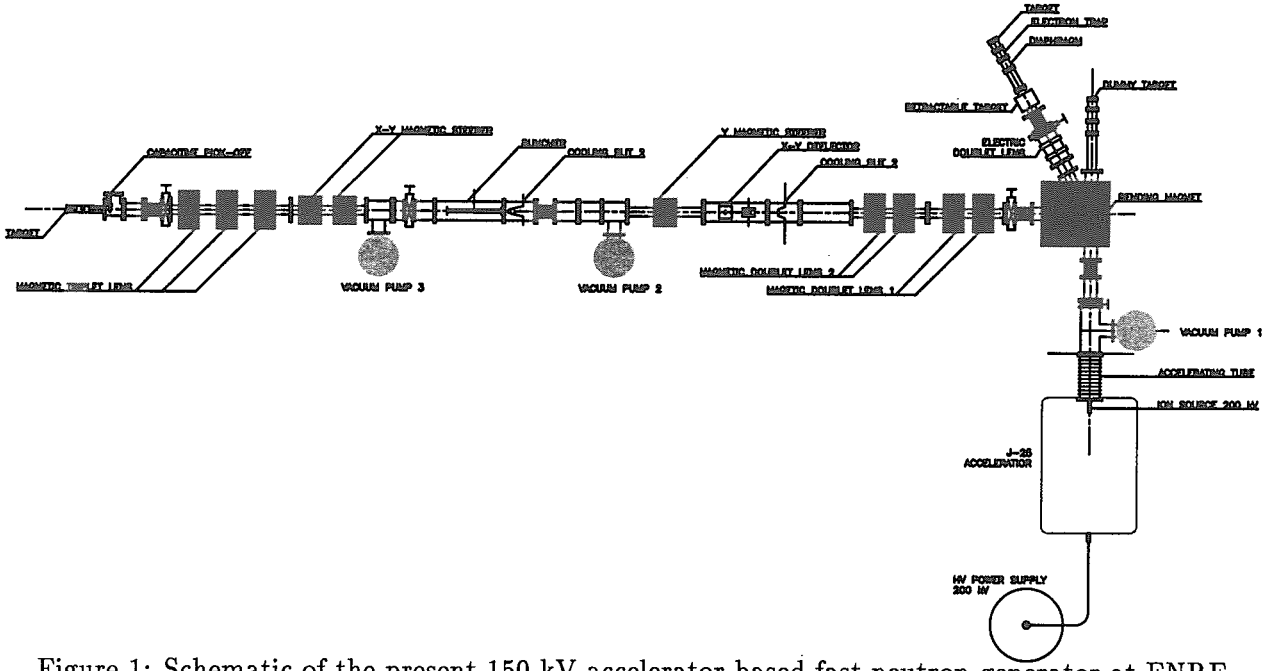

Figure 1: Schematic of the present 150-kV accelerator-based fast neutron generator at FNRF.

2.2 Features of Low-Energy RBS

Table 1 lists the calculated/estimated results for H^+, D^+, He^+ and He^{2+} ions accelerated by 150 kV (the actual energy of He^{2+}-ion is then 300 keV) analyzing (a) Si and (b) Fe with 0°-incident-angle and 150°-scattering-angle [4,5,6,2,7]. The resolvable mass difference from the target-mass is based on a 5-keV energy resolution of a silicon surface barrier detector. For comparisons, the results from 2-MeV H^+ and He^+ ions and 600-keV He^{2+} ion are also listed. In the case of 2 MeV, the energy resolution is used as 15 keV; in the case of 600 keV, the energy resolution is taken as 8 keV. σ: Scattering cross section; R: Projected range; K: Kinematic factor; d_a: Maximum analyzing depth; r_m: Mass resolution; ΔM_2: Resolvable mass difference from the target-atom mass M_2. D^+ is emphasized as it is primarily considered as the standard ion beam.

Table 1. Features of Low-Energy RBS.

(a) Target: Si

Ion	H^+	H^+(2MeV)	D^+	He^+	He^+(2MeV)	He^{2+}	He^{2+}(0.6MeV)
$\sigma(10^{-10}\mathrm{nm}^2)$	12.9	0.07	**12.8**	50	0.28	12.4	3.1
R(nm)	1,238	46,300	**990**	840	6,800	1,300	2,120
K	0.8752	0.8752	**0.7658**	0.5845	0.5845	0.5845	0.5845
d_a(nm)	400	20,000	**370**	350	2,500	400	800
$r_m(\frac{\Delta E_1}{\Delta M_2})$	0.71	9.5	**1.43**	2.85	38	5.7	11.4
ΔM_2	7	1.6	**3.5**	2	0.4	1	0.7

(b) Target: Fe

Ion	H^+	H^+(2MeV)	D^+	He^+	He^+(2MeV)	He^{2+}	He^{2+}(0.6MeV)
$\sigma(10^{-10}\mathrm{nm}^2)$	44.7	0.25	**44.8**	173	1.0	44.3	11.0
R(nm)	624	18,400	**500**	436	3,260	700	1,146
K	0.9355	0.9355	**0.8752**	0.7656	0.7656	0.7656	0.7656
d_a(nm)	200	8,000	**180**	170	1,300	300	480
$r_m(\frac{\Delta E_1}{\Delta M_2})$	0.18	2.5	**0.36**	0.73	10	1.46	3.0
ΔM_2	28	6	14	7	1.5	3.5	2.7

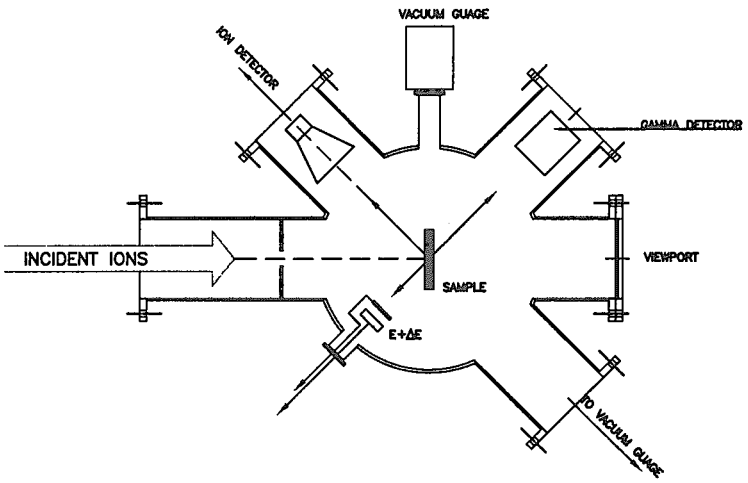

Figure 2: Schematic of the fully-designed 90°-chamber.

3 FEATURES OF THE NEW COMPOSITE FACILITY

Based on the theoretical analysis of the low-energy ion beam RBS, it has been considered that appropriate designing of the new facility is feasible to satisfy the application requirements. The new installations include three parts, an accelerating system and two application chambers. The current 150-kV accelerating capability is to be upgraded to 350 kV. A multiple-purpose chamber containing detecting systems which consist of a time-of-flight charged particle spectrometer and a high resolution gamma-ray system is to replace the old target chamber at the 90°-beam-line terminal, as shown in Figure 2. A TOF-RBS chamber is to be built at the 30°-beam-line terminal, as shown in Figure 3. At the first stage the 90°-chamber is designed only for the pulsed low-energy D-ion beam TOF+RBS analysis, as shown in Figure 4. The new facility to be finally completed is shown in Figure 5.

4 RESOLUTION ANALYSIS

4.1 TOF Method Able to Achieve a Super-High Energy/Mass Resolution

Since the energy, E, of a flying particle (its mass: m) is

$$E = \frac{1}{2}m(\frac{L}{t})^2, \tag{1}$$

where L is the flight path length and t is the flight time from the target to the detector (Figure 4). If Δt is the timing resolution of the spectrometer, then the corresponding energy resolution is

$$\Delta E = \frac{mL^2}{2}[\frac{1}{(t-\Delta t)^2} - \frac{1}{(t+\Delta t)^2}] = \frac{2mL^2 t\Delta t}{[t^2-(\Delta t)^2]^2}. \tag{2}$$

It is noted that $t^2 = \frac{mL^2}{2E}$ and generally $t >> \Delta t$, so the denominator of the above expression can be simplified as t^4. Thus, the final expression for the energy resolution converted from the timing resolution is

$$\Delta E = \frac{4\sqrt{2/m}E^{3/2}}{L}\Delta t. \tag{3}$$

If $m = (1.673+1.675)\times 10^{-27}$ kg (the mass of deuteron), $E = 150$ keV, $L = 0.3$ m, and $\Delta t = 10^2$ ps, the energy resolution calculated from the above formula then becomes around 1 keV. This is just about 1/10 of the energy resolution of conventional RBS. When this resolution is applied to the data in the table above, the resolvable mass difference will be satisfactorily reduced to around 1.

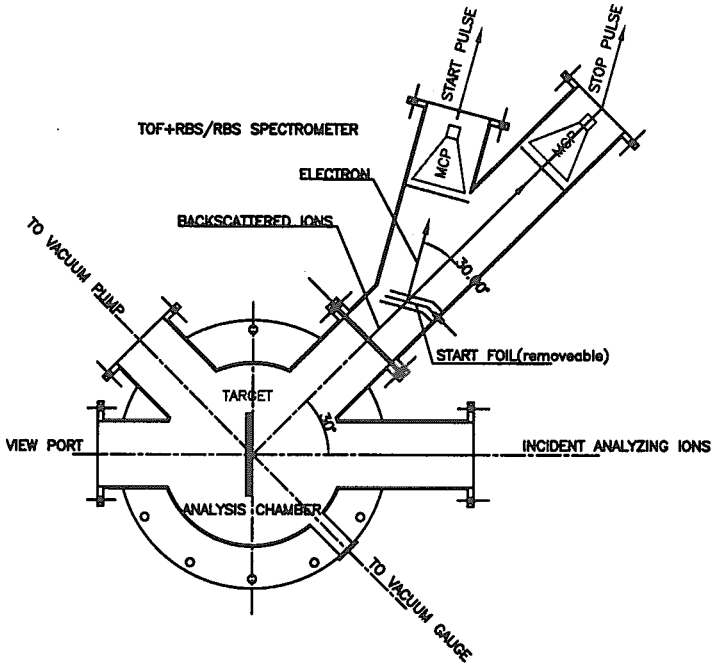

Figure 3: Schematic of the 30°-terminal chamber for the medium-energy ion beam TOF+RBS/RBS analysis.

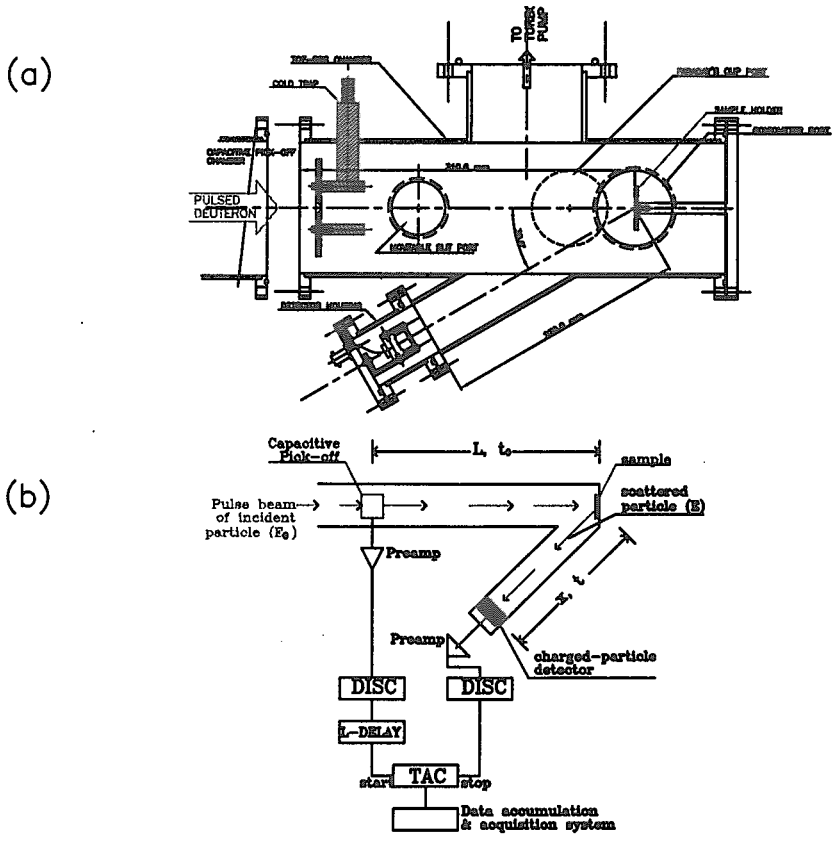

Figure 4: Designing of the pulsed low-energy D-ion beam TOF+RBS analysis. (a) Schematic of the 90°-terminal chamber, (b) the principle of the technique (DISC: discriminator, L-DELAY: logic delay, TAC: time-to-amplitude convertor).

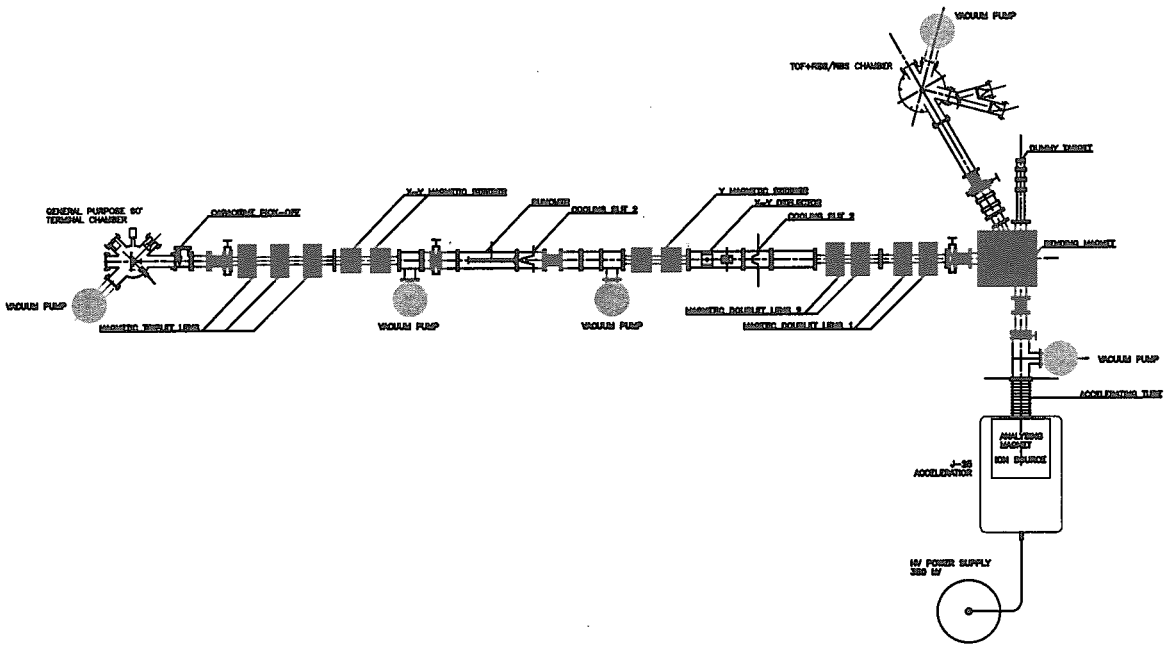

Figure 5: Schematic of the new facility.

4.2 Total System Energy Resolution Analysis (for the low-energy beam line)

The final energy of a backscattered particle detected is

$$\begin{aligned} E_1 &= \frac{m}{2}\frac{L_b^2}{t_b^2} \\ &= \frac{m}{2}\frac{L_b^2}{(t_f - t_c - \Delta t_t)^2}, \end{aligned} \tag{4}$$

where

$$t_c = \sqrt{\frac{m}{2E_0}} L_c, \tag{5}$$

and

$$\begin{aligned} \Delta t_t &= \sqrt{\frac{m}{2E_0}}(l_{in} + \frac{l_{out}}{K^{1/2}}) \\ &= \sqrt{\frac{m}{2E_0}} l_{in}(1 + \frac{1}{K^{1/2}\cos\theta}), \end{aligned} \tag{6}$$

where l_{in} and l_{out} are the path lengths of the analyzing particle travelling-in and travelling-out in the target, respectively, K is the kinematic factor, and θ is the scattering angle.
As discussed before, Δt_t is negligible, then E_1 is simplified as

$$E_1 = \frac{m}{2}\frac{L_b^2}{(t_f - t_c)^2}. \tag{7}$$

The total energy resolution is then approximately

$$\Delta E_1 = \sqrt{(\frac{\partial E_1}{\partial L_b}\Delta L_b)^2 + (\frac{\partial E_1}{\partial t_f}\Delta t_f)^2 + (\frac{\partial E_1}{\partial t_c}\Delta t_c)^2}$$
$$= 2E_1\sqrt{(\frac{\Delta L_b}{L_b})^2 + (\frac{\Delta t_f}{t_f - t_c})^2 + (\frac{\Delta t_c}{t_f - t_c})^2}. \quad (8)$$

As $t_c = \sqrt{\frac{m}{2E_0}}L_c$, which is the actual way t_c is measured, its variance is then

$$(\Delta t_c)^2 = (\frac{\partial t_c}{\partial L_c}\Delta L_c)^2 + (\frac{\partial t_c}{\partial E_0}\Delta E_0)^2$$
$$= (t_c)^2[(\frac{\Delta L_c}{L_c})^2 + \frac{1}{4L_c}(\frac{\Delta E_0}{E_0})^2], \quad (9)$$

where ΔL_c is the uncertainty of the measurement of L_c, and ΔE_0 is the uncertainty of the incident energy, which is dominated by the ripple of the high-voltage generator and the pulse-generation induced energy deviation.
Generally, the uncertainties of the measurements of L_b and L_c are fairly small compared with themselves, i.e. $\Delta L_b/L_b$ and $\Delta L_c/L_c$ are negligible. For ΔE_0, although the ripple of the accelerating voltage is fairly small compared with the high voltage itself, the bunching of the beam to form the pulses causes a 0.2% uncertainty, i.e. $\Delta E_0/E_0 \simeq 2 \times 10^{-3}$. Therefore, besides by Δt_c, the total energy resolution is dominated by Δt_f, which can be expressed by

$$\Delta t_f = \sqrt{(\Delta t_{start})^2 + (\Delta t_{stop})^2 + (\Delta(\Delta t_t))^2}, \quad (10)$$

where Δt_{start} and Δt_{stop} are the uncertainties of measuring the start pulse and the stop pulse, respectively, and $\Delta(\Delta t_t)$ is the timing uncertainty due to the energy straggling of the particle traveling in the target.
The uncertainties of measuring the start pulse and the stop pulse are composed of two factors, which are the uncertainty of the pulse generation and the timing resolution of the detector. So, as the detector only detects the stop pulse,

$$\Delta t_{start} = \sqrt{(\Delta t_{s-pulse})^2} \quad (11)$$

and

$$\Delta t_{stop} = \sqrt{(\Delta t_{s-pulse})^2 + (\Delta t_{s-timing})^2}, \quad (12)$$

where $\Delta t_{s-pulse}$ is the uncertainty of the pulse generation, which is the same for both start pulse and stop pulse, and $\Delta t_{s-timing}$ is the timing resolution of the detector detecting the stop pulse. The uncertainty of the pulse generation is supposed to be proportional to the pulse length, i.e. $\Delta t_{s-pulse} = \alpha l_{pulse}$, where α is the proportional factor and l_{pulse} is the pulse length.
As estimated before, Δt_t is at the order of 10^{-15} s., $\Delta(\Delta t_t)$ is then further smaller, while the timing resolution of a MCP detector is generally at an order of 0.1 ns, or 10^{-10} s., $\Delta(\Delta t_t)$ is neglected. Therefore, basically,

$$\Delta t_f = \sqrt{2(\Delta t_{s-pulse})^2 + (\Delta t_{s-timing})^2}. \quad (13)$$

And now

$$\begin{aligned}\Delta E_1 &\simeq \frac{2E_1}{t_b}\sqrt{(\Delta t_f)^2+(\Delta t_c)^2} \\ &\simeq \frac{2E_1}{t_b}\sqrt{2(\Delta t_{s-pulse})^2+(\Delta t_{s-timing})^2+(\Delta t_c)^2},\end{aligned} \tag{14}$$

where $t_b \simeq t_f - t_c$. Due to $t_b = \sqrt{\frac{m}{2E_1}}L_b$, the above expression then becomes

$$\Delta E_1 = \frac{4E_1^{3/2}}{\sqrt{2m}L_b}\sqrt{2(\Delta t_{s-pulse})^2+(\Delta t_{s-timing})^2+(\Delta t_c)^2}. \tag{15}$$

For example, detection of a backscattered D^+ ($m = (1.673 + 1.675) \times 10^{-27}$ kg) at an energy of 100 keV ($E_1 = 100 \times 10^3 \times 1.6 \times 10^{-19}$ J) at a distance of 0.3 m ($L_b = 0.3$ m) from the target surface using a pulse with the pulse length of 1 ns but a proportional factor α of the uncertainty about 10% and a MCP detector with a timing resolution about 200 ps will have the total energy resolution at about 1.3 keV.

5 CONCLUSION

A low-energy ion accelerator facility (0-350 kV) has been proposed and is being established at Chiang Mai University for high-resolution TOF+RBS analysis, charged particle induced γ-ray and charged particle emission measurement.

ACKNOWLEDGEMENTS

The work is supported by the International Atomic Energy Agency, Vienna, project No. THA/1/009 and the Thailand Research Fund.

References

[1] M.H. Mendenhall and R.A. Weller, Nucl. Instr. and Meth. B47(1990)193.

[2] W-K. Chu, J.W. Mayer and M-A. Nicolet, Backscattering Spectrometry, Academic Press, New York, 1978.

[3] T. Vilaithong, S. Singkarat, W. Pairsuwan, JF. Kral, D. Boonyawan, D. Suwannakachorn, S. Konklong, P. Kanjanarat, and G.G. Hoyes, Int. Cong. on Nuclear Data for Science and Technology, May 13-17, 1991, Julich, Germany, pp.483-486.

[4] J.F. Ziegler, Helium Stopping Powers and Ranges in All Element Matter, Pergamon Press, New York, 1977.

[5] H.H. Andersen and J.F. Ziegler, Hydrogen Stopping Powers and Ranges in All Elements, Pergamon Press, New York, 1980.

[6] J.F. Ziegler, Handbook of Stopping Cross-Sections for Energetic Ions in All Elements, Pergamon Press, New York, 1980.

[7] Yu Liangdeng, Diffusion of Ions Implanted in Solids, Ph.D. Series 1992-02, University of Copenhagen, ISSN 0906-0286 (1992).

3.41 Nuclear Reaction Database on Meme Media

Yosihide OHBAYASI [a], Shigeyoshi AOYAMA [b], Hiroshi MASUI [a],
Kiyoshi KATÔ [c] and Masaki CHIBA [d]

a) Meme Media Laboratory, Hokkaido University, Sapporo, Hokkaido 060-8628

b) Information Processing Center, Kitami Institute of Technology, Kitami, Hokkaido 090-8507

c) Division of Physics, Graduate School of Science, Hokkaido University, Sapporo, Hokkaido 060-0810

d) Division of Social Information, Sapporo Gakuin University, Ebetsu, Hokkaido 069-8555

Email: dbadmin@nrdf.meme.hokudai.ac.jp

We have developed the system of charged particle nuclear reaction data (CPND) on the IntelligentPad architecture. We called the system CONTIP, which is an abbreviation of "Creative, Cooperative and Cultural Objects for Nuclear data and Tools". NRDF (Nuclear Reaction Data File), which is a kind of CPND compilation, is applied as an application example. Although CONTIP is currently applied to NRDF, the framework can be generalized to use the other nuclear database. We will develop CONTIP to give the framework for effective utilization of nuclear data.

1. Introduction

Nuclear data compilation is one of the most important bases for the application of atomic nuclei to science and technology. There are various nuclear data compilations in the world [1]. As a consequence of continuous activities in such compilations, the utilization of nuclear data is expanding from nuclear engineering and nuclear physics to the other related fields. For every data compilation, the amount of data becomes larger year by year, and the contents of data will be more complex. Therefore, development of utility systems for compiled data is an important subject. In recent years, development of computer technologies, infrastructures and software architectures enables us to support and expand utilization of the nuclear data. Indeed, the real issue is how to organize the system which extends our research activities.

We show a new type of nuclear data retrieval system, in which NRDF (Nuclear Reaction Data File), a kind of charged particle nuclear data (CPND) compilation in Japan [2-4], is applied as an example. To get benefits from recent computer and network technologies, we adopt the IntelligentPad architecture [5] as a framework of the present system. This software architecture has many useful features for handling multimedia, media-based system construction, and graphical user interface.

We call the present system CONTIP, which is an abbreviation of "Creative, Cooperative and Cultural Objects for Nuclear data and Tools on IntelligentPad". A prototype of the system was built by one of the authors (M.C.) on a UNIX workstation in 1995[6]. For the practical use, development of the system is now pursued [7]. The purposes of this paper are i) presentation of the feature of CONTIP, ii) discussion of the functions and the elements to be essentially possessed by CONTIP, from the viewpoint of effective utilization of nuclear data.

2. NRDF –A charged particle nuclear reaction data compilation –

For the purpose of international exchange of experimental nuclear reaction data, EXFOR compilation is used as a de facto standard [8]. EXFOR was designed to accumulate mainly the neutron nuclear reaction data (NND). Therefore, the data description format of EXFOR was not necessarily suitable for CPND. For this historical background, The Japan Charged Particle Reaction data Group (JCPRG) designed NRDF, as a study of database, to accumulate scientific information of CPND from experiments of nuclear reactions. Using the own data description rule in NRDF, which is different from EXFOR, the contents are taken from published papers associated with nuclear experimental physics. The detail of the data structure of NRDF is shown in Ref. [2,9].

JCPRG has compiled CPND on NRDF (Nuclear Reaction Data File) for more than 20 years. NRDF consists of over 20,000 of data what are mainly produced in Japanese experimental facilities. Due to the large variety of particles and physical quantities, CPND has a large number of reaction types in contrast to NND. Furthermore, measured reaction types are evolved with the development of the experimental techniques. In addition, motivation of experiment and considering aspects are changed along with the progress of research. Therefore, in order to utilize the data in the future, each data of NRDF is encoded maximum information of CPND from the published papers.

Whereas JCPRG compiles CPND produced in Japanese experimental facilities, parts of NRDF data is transported as CPND in EXFOR. Thus, JCPRG contributes as a member of nuclear reaction data centers (NRDC) coordinated by the IAEA NDS [10,11].

3. IntelligentPad - Meme media architecture -

The IntelligentPad architecture has been proposed and developed at Hokkaido University since 1987 [5]. The development was started as making somewhat object-oriented system construction toolkit that is based on the graphical user interface (GUI). A pad in the IntelligentPad can be treated as an object of GUI, like a view of "real paper pad", and each pad has functions such as data control programs, input/output devices between other pads, and so on. On this environment, intuitively pasting and peeling off operation with pads can carry out programming of tools. In addition, through the research and the development of the IntelligentPad, fundamental prospect and directivity of this architecture is being clarified: IntelligentPad is not only a specific software package, but also the fundamental environment architecture to support the effective utilization of computerized resources. It is called Meme media architecture [5,12].

As shown in Ref. [12], Meme media is the environment that shares and re-uses the resources of all over the world connected to the Internet. In order to develop and enlighten this architecture, more than 60 Japanese and other foreign companies organize the IntelligentPad Consortium (IPC) [13]. Furthermore, in the future, the kernel system of the IntelligentPad will be distributed freely to all users. Recently, the IntelligentPad system is available as some commercial software packages on personal computers [14,15].

4. Features of current trial system.

We have constructed this CONTIP client on MS-Windows95,98/NT-based Intelligent-Pad[14]. On this system, each utility component is constructed as a composition of primitive pads. For example, database proxy pad is used for the connection to the database server. As shown in previous papers [6,7], Major features of this system are: i) 2-dimensional intuitive data navigation (Figure 1.), ii) interactive data visualization and comparison (Figure 2.). Although CONTIP is currently applied to NRDF, the framework of CONTIP can be generalized to use the other nuclear database.

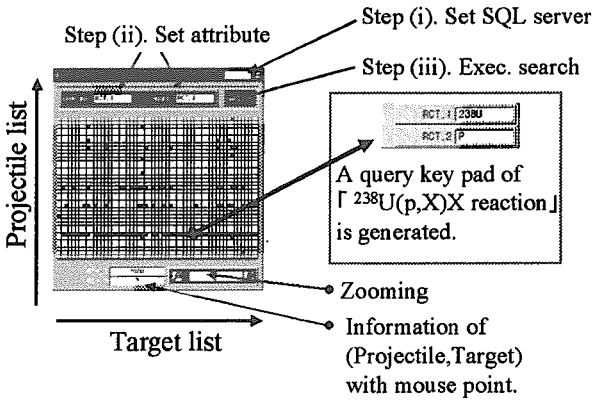

Figure 1 Data navigation pad.

For effective utilization of nuclear data, seamless linkages between measured experimental data and its application should be important. Considering these linkages, it is essential to link accumulation, evaluation and circulation on the same system. Furthermore, there are interdependences among them: evaluation of accumulated data, circulation of evaluated data, and re-accumulation evaluated data. Therefore, we should consider constructing the framework so as to achieve this continuous cycle. In addition, we should consider integrating the different databases which have different compilation policy or evaluation policy. Using the integrated database, we can retrieve and utilize the various resources concerned with nuclear data.

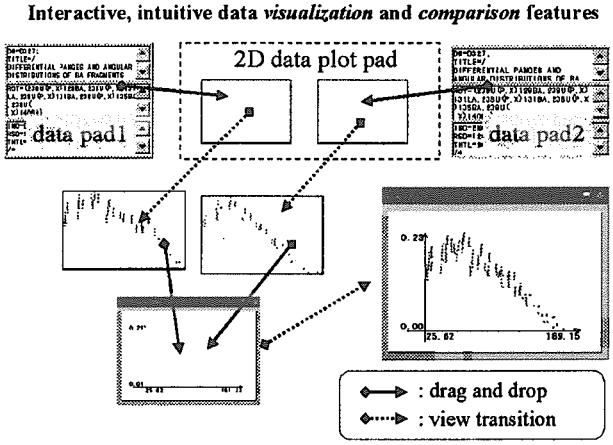

Figure 2 Interactive data visualization and comparison.

With the above background and motivation, we discuss the aim of the framework of CONTIP for nuclear reaction data with future computer facilities.

4.1. Re-production, Re-edit, Re-use

On the IntelligentPad, composite pads can be decomposed to more primitive pads. As shown in Figure 3, composition of the data pad with the text-browsing pad or 2D plot pad gives each specific function. Resources are encapsulated in the primitive pads, and linkages among them are standardized. Thus, we can customize the function of pad by adding other functional pads, and/or by replacing to other implemented pads.

For the further development, construction of utility pads, which, e.g., interpolates experimental data, or compares the data with theoretical calculations, supports to lead us to a kind of interactive analysis. Such a synthetic feature of the IntelligentPad would be achieved by many users' cooperative activities of "Re-produce, -edit, -use" of both nuclear data and useful tools.

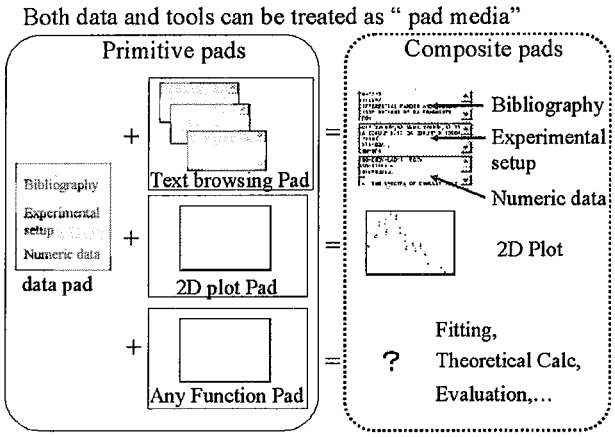

Figure 3 Synthetic features of pads.

4.2. Circulation, Coordination and Evolution

The IntelligentPad architecture supports cooperative fundamentals through the network. Once we construct a server to distribute and circulate not only data but also tools, it already gives a basis of the circular system of nuclear data as integrated intellectual resources. Figure 4 shows a schematic figure for the circular system of nuclear data and tools as the pad media by using PIAZZA [16], which is a software technology to enable to circulate pads through the network. Using PIAZZA, many users can retrieve many tools and data as the pad media. Ultimately, although any resources are scattered all over the world, we can circulate them as pad media on the IntelligentPad architecture (Figure 5).

4.3. Knowledge discovery

The amount of nuclear reaction data is getting huge and increasing day by day. In addition, variety of the data will also be more complex. Hence, as the amount of data increases, it will be more difficult to get essential information from huge databases. The data navigation pad of CONTIP is one of our answers for this issue. The data navigation pad enables us to investigate the correlation among the attributes of experimental data. Generally, experimental data has many attributes, hence the utility, which supports to show the correlation among them, would be helpful. Consequently, development of these kind of utility pads realizes easier navigation to needed data, and would support a new discovery of knowledge concerned with nuclear data.

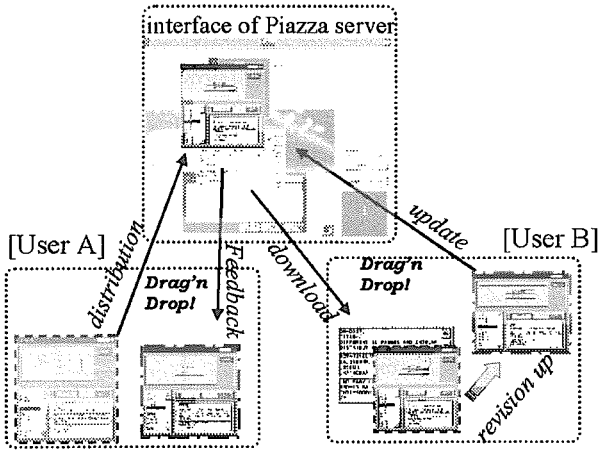

Figure 4 *PIAZZA*: circulation and coordination are supported by using these architectures.

5. Summary and future extension

Development of CONTIP is reported where NRDF is applied as an example. The current trial system has mainly two features: i) interactive data visualization and comparison and ii) 2D intuitive data navigation. Although the present system is constructed only for NRDF, the framework of the system can be generalized for utilization of the other nuclear data resources. As discussed in Section 4, we attempt to extract the important elements for effective utilization of nuclear data. Consequently, we conclude the system should be provided with the following three features: i) Re-production, Re-edit, and Re-use, ii) Circulation, Coordination, and Evolution, iii) Knowledge discovery.

We have developed the system using the IntelligentPad software package. The IntelligentPad is not only a programming package but also media architecture to share the knowledge of our research activities. Although, now we use the Microsoft Visual C++ [17] to develop primitive pads, there are several projects to develop the IntelligentPad software packages on the other programming languages. Ultimately, once the standardization of application programming interfaces among other programming languages achieved, this architecture proceeds to be independent of the programming languages.

Although it is easy to "distribute" the nuclear data and tools programmed by the other competing software architectures, e.g., Java and Active-X control, through the networks, it is still impossible to "re-edit" the objects on the client and also impossible for Java to "re-circulate" them from the clients. The IntelligentPad is currently the only one to have ability to "re-edit" the objects as pads and to "re-circulate" them through the network. Therefore, the concept of the IntelligentPad seems to be one of the prospects for effective utilization of nuclear data. We will improve the utilities of CONTIP, which will be used by a huge number of users and which would be supported to share and to evolve the knowledge of all users.

As the future extensions, inclusion of EXFOR [8] to CONTIP provides more comprehensive retrieval system for the nuclear reaction data. We are planning to distribute the system to researchers and to blush-up the trial system with feedback. Furthermore, through our development, we aim at giving the framework of the ideal environment for nuclear data like as displayed in Figure 5.

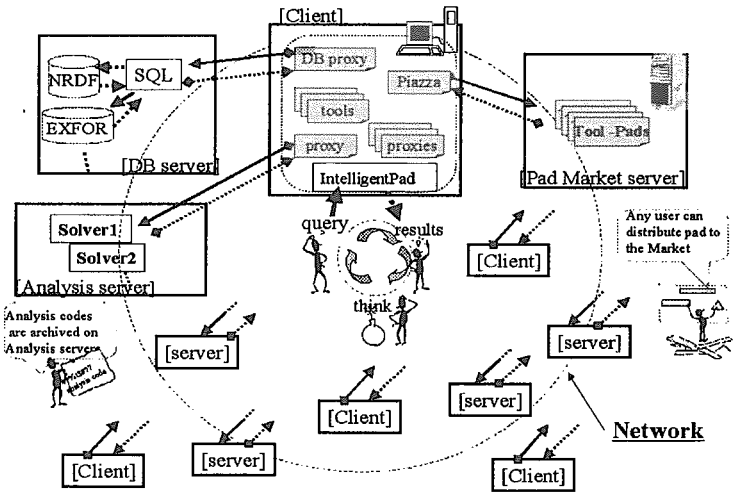

Figure 5 An schematic image of the ideal system for nuclear data.

Acknowledgment

This work is supported by Meme Media Laboratory, Hokkaido University. The authors would like to express their thanks to Prof. Y. Tanaka for helpful discussions and suggestions. To develop the system, some pad modules are constructed by C'sLab. LTD.

References

[1] For example, the list of major compilation is shown on the web page, http://www-nds.iaea.org/.

[2] M. Togashi and H. Tanaka, An information system for charged particle nuclear reaction data, Journal of Information Science 4 (1982) 213.

[3] S. Aoyama, et al., Development of utility system of charged particle nuclear reaction data on unified interface, JAERI-Conf 99-002,222(1999).

[4] NRDF web page: http://nrdf .meme.hokudai.ac.jp/

[5] Y. Tanaka, IntelligentPad as Meme media and its application to multimedia databases, Information and Software Technology 38(3) (1996) 201.

[6] M Chiba, "An IntelligentPad system for the reuse of nuclear reaction data", Conference proceedings Vol.59: Nuclear data for science and Technology, SIF, Bologna (1997) 1057.

[7] Y. Ohbayasi, et al, Development of Charged Particle Nuclear Reaction Data Retrieval System on IntelligentPad, JAERI-Conf 99-002 (1999) 228.

[8] http://www-nds.iaea.org/exfor/.

[9] K. Katô, Charged particle nuclear reaction database NRDF – Present status and its usage –, Genshikaku Kenkyu 39 (1995, in Japanese) 63.

[10] For example, see INDC (NDS)-401. this document is available via http://www-nds.iaea.org/.

[11] M.Chiba, T. Katayama and H. Tanaka, A database translator of nuclear reaction data for international data exchange, Journal of Information Science 12 (1986) 153.

[12] Y. Tanaka, Meme Media and a World-Wide Meme Pool, The fourth ACM International Multimedia Conference, November, Boston (1996) 175.

[13] IntelligentPad Consortium, http://www.pads.or.jp/.

[14] Microsoft Windows version, http:/www.fujitsu.co.jp/hypertext/softinfo/product/use/ipad/.

[15] Apple Macintosh version, http://www.hitachi-sk.co.jp/Products/IntelligentPad/HomePage.html.

[16] PIAZZA project is developed under the initiative of IntelligentPad Consortium.

[17] http://www.microsoft.com/.

3.42 Development of a Search System of NRDF on WWW

Hiroshi MASUI, Yoshihide OHBAYASI, Shigeyoshi AOYAMA*,
Aakira OHINISHI**, Kiyoshi KATŌ** and Masaki CHIBA***

Meme Media Laboratory, Hokkaido University, Sapporo 060-8628, Japan
**Information Processing Center, Kitami Institute of Technology, Kitami 090-8507, Japan*
***Graduate School of Science,Hokkaido University, Sapporo 060-0810, Japan*
**** Faculty of Social Information, Sapporo Gakuin University, Ebetsu 069-8555, Japan*
Email: masui@nucl.sci.hokudai.ac.jp

We develop a data search system and a data entry system for the Nuclear Reaction Data File (NRDF), which is one of the charged-particle reaction database compiled by Japan Charged Particle Reaction Group (JCPRG). Using a WWW browser, we can easily search, retrieve and utilize the data of NRDF.

1 Introduction

For twenty-five years, Japan Charged Particle Reaction Group (JCPRG) has been accumulated charged-particle nuclear reaction data mainly form the papers concerned with domestic experimental facilities and authors [1]. The accumulated data are compiled to the original database of nuclear data, NRDF (Nuclear Reaction Data File). The data format of NRDF has flexibility for a variety of data type of nuclear reactions. Hence, the data contains not only the bibliographical data and the experimental results but also almost all of information about the experiment. Therefore, NRDF can be a kind of "scientific" database, which has an ability to utilize the data for both scientific and practical use (e.g. for a medical use). Data of NRDF are also transported to the data of the EXFOR (EXchange FORmat) for a sake of our international contribution in nuclear data [2].

In the beginning of NRDF compilation, the data was opened on a mainframe, hence the user was restricted to the member who had an account on the mainframe [3]. Moreover, the retrieved data was the NRDF data cord itself, then the user has to know the meanings of words in the cord and the structure of NRDF data format. On such the situation, from 1996, we experimentally started a WWW data retrieval system on our web server [4]. Using this system, we can easily retrieve the NRDF data on a WWW browser, same as a usual data search page. However, it still remained some difficulties in utilization of the retrieved data. First, the view of

retrieved data was the NRDF cord itself, then we also has to know the meanings of the words and the structure. Second, the numerical data of experiments were graphically displayed, but the attributes of x- and y-axes were not shown explicitly.

In this work, we develop a new WWW data search system in order to overcome the difficulties as mentioned above. On the new developed system, we need not know any words of NRDF data cord and the structure of data format. The numerical data of experiments is graphically visualized with information of the attributes of x- and y-axes. Now, our activities of development of utility systems extend for several ways: WinNRDF [5] and WinNRDF2 [6], which are another data retrieval systems works with/without the network, CONTIP [7,8,9], which is a new types of data utility system using IntelligentPad [10]. And more, we start to develop a data entry system on WWW.

2 Data Search System

The new data search system is opened on the following address:

http://nrdf.meme.hokudai.ac.jp/tools/nrdf_search.html

Features of this system are: (1) easy operations using "friendly" inter face of a WWW browser, (2) graphically data visualization with information about the experiment and x- and y-axes, (3) simpleness in the development of the system, and (4) platform-free for users.

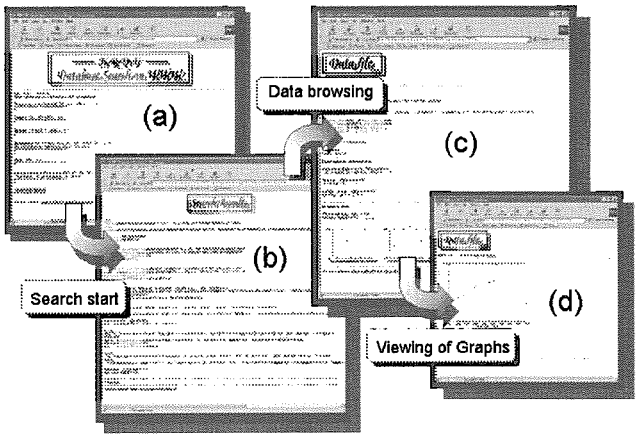

Figure 1: Sequence of data search on the new WWW search system.

A sequence of data retrieve is on following steps (see Fig. 1). First, to list up data to be retrieved, we input search keywords in the first data-search page as marked (a). Search results are listed up in the search-result page as marked (b). We can choose the data to be retrieved with some information, the title of the article, the authors, the reference and the reaction types of the experiments. The retrieved data is precisely shown in the data-browsing page as marked (c). The information of the experiment is shown, and thumbnail-pictures of graphs are displayed in the bottom of the page. We can see each graph data precisely in the graph-display page as marked (d).

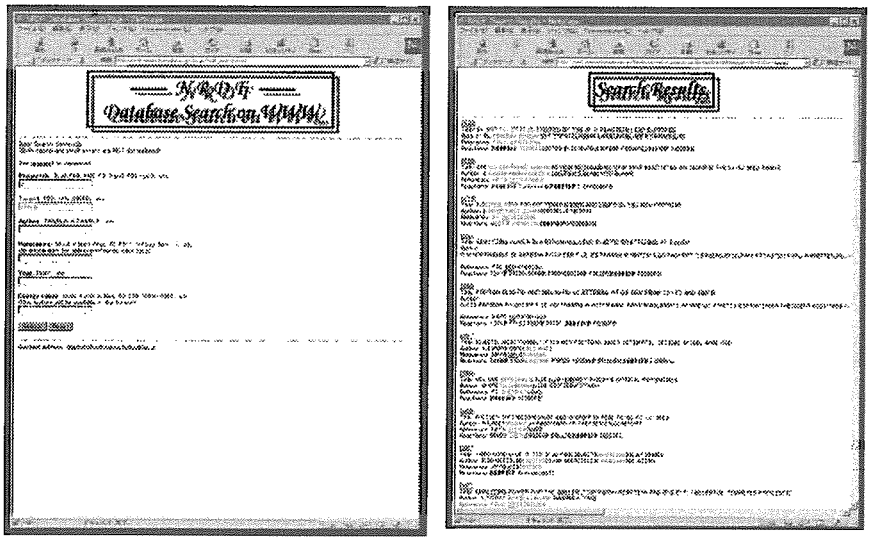

Figure 2: (a) First data-search page of the system, and (b) the result.

Here, we show functions and features of this system in each page. We start a data search with some search keywords with the first data-search page shown in Fig. 2. Similarly to almost all other WWW data search systems, this data-search page works as keyword-matching search system. We input some search keywords of a projectile, a target, an author, a reference article and the published year of the reference, (in Fig. 2a). The search results are listed up in the search-results page, and search keywords are emphasized by bold-face font, see Fig. 2b. We can choose a data to be retrieved in the list with information, say, the title, the authors, the reference and its volume, and reaction types of the experiments.

The data-browsing page has some remarkable features (see Fig. 3). The most improved function is that we can easily to see the title, the authors, and the relation between the figures

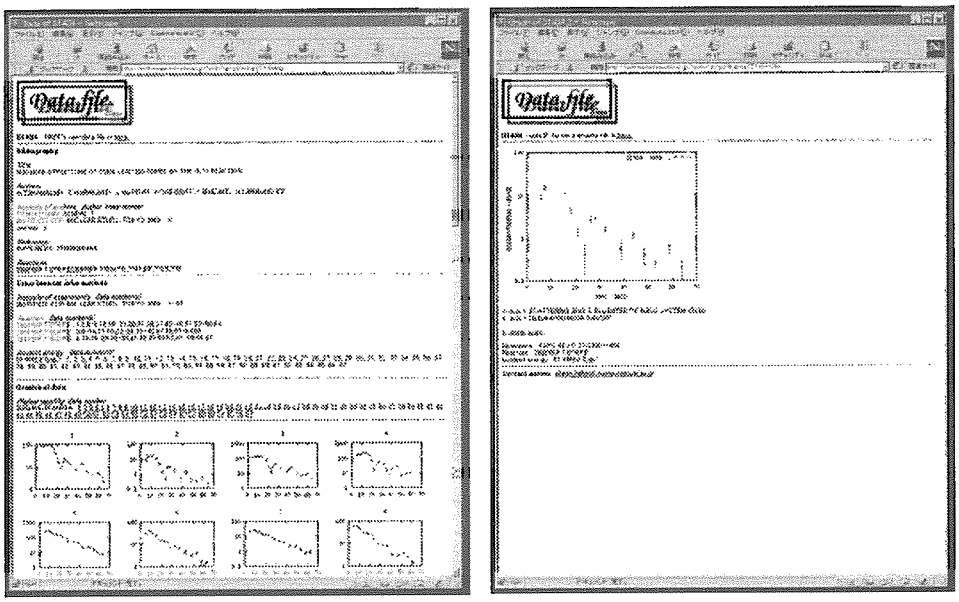

Figure 3: (a) The data-browsing page, and (b) graph-display page.

and the information of the experiments. Each word in the NRDF cord is translated with appropriate NRDF-words dictionary file. Hence we can obtain information of the experiment as if we read the original article, shown in Fig. 3a. The original NRDF formatted cord is also available in the upper part of the page where the link for the original cord is set up. To overlook all of figures of the numerical data of the experiments, the data-browsing page has a function to create "thumbnail-pictures" of the figures. Each thumbnail has a link for a graph-display page, see Fig. 3b. The graph-display page shows the figure of the numerical data and the information of the experiment, reaction type, incident energy, and the reference. The numerical data itself can be obtained in the upper part of the page, same as the data-browsing page.

The present data search system is constructed by using Perl script. Perl script is suitable to develop this kind of system and has a portability to other servers, which support a CGI of the Perl script.

3 Trial of Data Entry System

At present stage, we have been accumulating charged-particle nuclear reaction data form published papers and compilation has been done by reading the papers. However, such a process of

the compilation may cause some mistakes due to misreading of the compiler. Therefore, we just start to develop a WWW data entry system on our Web server.

Here, we introduce a "trial" data entry system. First of all, the title, the authors and the purpose of the experiment are to be input as a free text, shown in Fig. 4a. Next, to avoid careless mistakes, the reference and the institute of the experiments are chosen from each pull-down menu, since these words are to be translated into the NRDF cord. Finally, we count the number of graphs to be compiled and input it.

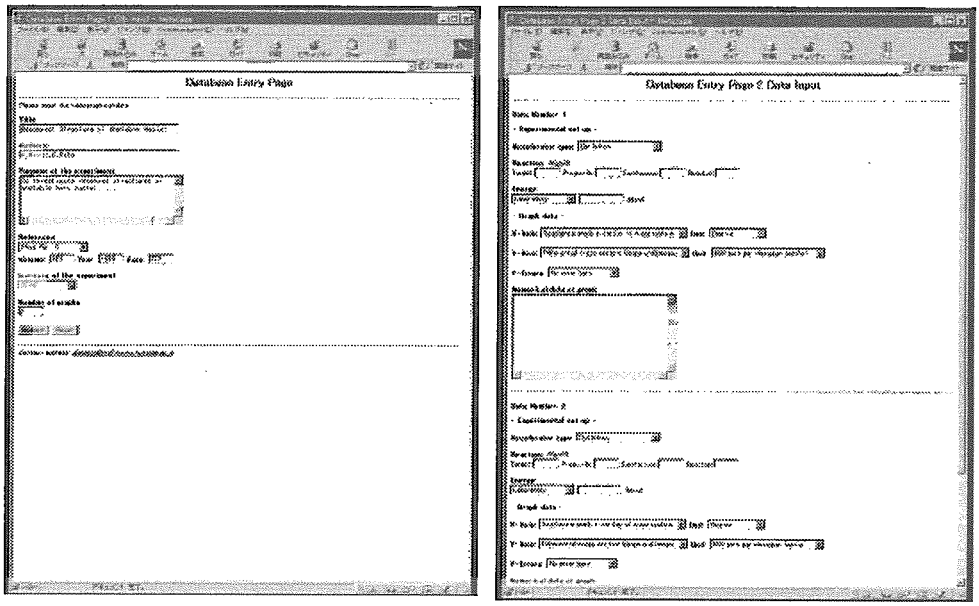

Figure 4: (a) The bibliographical data input page, and (b) graph-data input page.

According to the input number of graphs, the graph-data input page will be provided, as shown in Fig. 4b. In this page, we input the information of the experiment, i.e. an accelerator type, a reaction type, an incident energy, attributes of x- and y-axes, and numerical values of the graph, using pull-down menus and free text-boxes.

The NRDF formatted cord is automatically generated, and the input data is linked to the data-browsing page, hence we can see and confirm the input data with graphical views.

4 Conclusions

We developed a WWW data-search system. Almost all difficulties and inconveniences of old system, i.e. on the the mainframe-system and the old WWW search system, are avoided. And now we develop a data-entry system, which enables us to input nuclear reaction data without any knowledge of the NRDF cord. Both systems are constructed by using the Perl script, hence the systems can work on any servers, which supports a CGI of the Perl script. We propose that the combination of these two systems provides an "individual nuclear data management system" for us. That is because, once we input the data with the data-entry system, we can store the data as a NRDF cord, and the data can always be retrieved using the data-search system on the local server, independently of the original NRDF data server. Moreover, the data is not restricted to the experimental data, the theoretical calculated data can also be stored on the local server. Therefore, nuclear physicists can utilize nuclear reaction data both on the local and original NRDF servers, according to a purpose of a investigation. This concept can be realized in more sophisticated way on CONTIP as shown in Refs. [7,8,9].

Acknowledgement

This work is supported by Meme Media Laboratory at Hokkaido university. The authors thank to Prof. Y. Takaka for an encouragement.

References

[1] Katō K.: "Charged particle nuclear reaction database NRDF -present status and its usage-", Genshikaku Kenkyu, **39** 63 (1995, in Japanese).

[2] Chiba M., Katayama T. and Tanaka H.: Journal of Information Science, **12**, 153 (1986)

[3] Togashi M. and Tanaka H.: Journal of Information Science, **4**, 213 (1982).

[4] Old NRDF WWW search page: http://nucl.sci.hokudai.ac.jp/~nrdf

[5] Aoyama S. et al.: JAERI-Conf. **99-002**, 222 (1999).

[6] Aoyama S. et al: "Development of a Utility System for Charged Particle Nuclear Reaction Data by using IntelligentPad", JAERI-Conf. (this conference).

[7] Ohbayasi Y. et al.: JAERI-Conf. **99-002**, 228 (1999).

[8] Ohbayasi Y. et al: "Nuclear Reaction Database on Meme Media", JAERI-Conf. (this conference).

[9] Ohbayasi Y. et al: Journal of Information Science, **26**, 1 (2000), in publish.

[10] IntelligentPad Consortium (WWW address): http://www.pads.or.jp/

3.43 Development of a Utility System for Charged Particle Nuclear Reaction Data by using IntelligentPad

Shigeyoshi AOYAMA
Yosihide OHBAYASI, Hiroshi MASUI [a)]
Kiyoshi KATO [b)] and Masaki CHIBA [c)]

Information Processing Center, Kitami Institute of Technology, Kitami 090, JAPAN
a) Meme Media Laboratory, Hokkaido University, Sapporo 060, JAPAN
b) Graduate School of Science, Hokkaido University, Sapporo 060, JAPAN
c) Faculty of Social Information, Sapporo Gakuin University, Ebetsu 069, JAPAN
e-mail: dbadmin@nrdf.meme.hokudai.ac.jp

Abstract

We have developed a utility system, WinNRDF2, for a nuclear charged particle reaction data of NRDF (Nuclear Reaction Data File) on the IntelligentPad architecture. By using the system, we can search the experimental data of a charged particle reaction of NRDF. Furthermore, we also see the experimental data by using graphic pads which was made through the CONTIP project.

1. Introduction

NRDF (Nuclear Reaction Data File) has been accumulated by JCPRG (Japan Charged Particle Reaction Group). NRDF contains the experimental data of the nuclear charged particle reaction in Japan. The number of accumulated data files is several ten thousands, which may be almost all data in Japan. However, the utility system for searching data is very poor, which was made more than ten years ago on the main frame of the computer center in Hokkaido University [1]. Furthermore, it is almost impossible to modify the old system to accept new applications because of the old architecture. On the other hand, recently, PC (Personal Computer) has been widely spread all over the world. The EXFOR (EXchange FORmat) database which is an international standard is determined to support it on the PC (Windows) interface and WWW (World Wide Web). Then, it is meaningful to develop the utility system of NRDF on the Windows interface and WWW.

On such a situation, we have three projects of the development of new data searching and utility systems for NRDF; i) A data search and utility system with Windows interface on the local PC. ii) A data search system on the network circumstance such as WWW. iii) A data search and utility system by Intelligent Pad (IP) architecture [2] (see a paper by Ohbayasi *et al.* in this proceeding). As far as

i) and iii) are concerned, we reported two systems i) WinNRDF [3] and iii) CONTIP [4] on the 1998 symposium on nuclear data. However, WinNRDF for the local PC circumstance is made by using a programming language (c++) on the normal Windows95/NT architecture. Then, we mentioned that WinNRDF would be made on the IP architecture in the future. The purpose of the present paper is to show such the development of WinNRDF as WinNRDF2 on the IntelligentPad architecture.

In this paper, first, we explain the IP in brief, because the details and the advantages of using it for the nuclear reaction database is discussed by Ohbayasi [4]. Next, we describe an overview of the present system, WinNRDF2, for the local PC and explain the practical system of WinNRDF2. Finally, summary and future problems are given.

2. IntelligentPad

In this section, we describe the IP architecture. This architecture is proposed in 1989 by Yuzuru Tanaka at Hokkaido University[2]. In the IP system, every object is represented as a media object called a "pad". The "pad" can be treated as an object of the graphical user interface, like a sheet of paper or a card on the computer display (Fig. 1). By using this pad, users, even if he is a beginner, can record, store, distribute, share, edit, etc, various kinds of information in an integrated manner on computers. The "pad" also represents varieties of intellectual resources such as multimedia documents, system utilities and applications. We can easily compose tools or software (editor, database, graphic representation tool, etc.) by directly pasting some pads on another pads. In Fig.1, we display a text pad and a command pad on a mount pad.

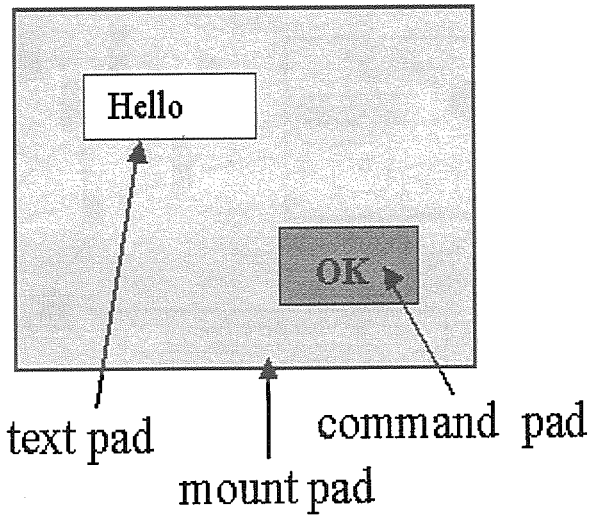

Fig.1 text pad and command pad on mount pad

In the IP, each pad has several connection jacks called slots. One of them is called a primary slot. Each pad has a single pin-plug to connect itself to one of the slots of another pad. The pad architecture and the standard linkage facility are provided by a kernel of the IP system. However, in practical uses, we do not have to worry about them because it is handled by the system. The application linkage interface of a pad is defined by a list of slots. Each slot is accessed either by a 'set' message: 'set <*slot_name*> *value*' or by 'gimme' message: 'gimme <*slot_name*>'. Each of these two messages invokes the respective procedure attached to the slot. Slots and attached procedures of each pad define the internal mechanism of the pad. The slots and the procedures are defined by a developer of the pad.

3. System design of WinNRDF2

We describe the system design of WinNRDF2 for a local PC in brief. In Fig. 2, we show the overview of the system design. CONTIP is designd for the nuclear database on the internet circumstance with the IP architecture, whose details are given by Ohbayasi [4,5]. Present WinNRDF2 is a package of CONTIP for the local PC. The using interface of WinNRDF2 is IP one and the database of NRDF is constructed on the Microsoft Access 97. We can search the charged particle nuclear reaction data when we query the data to the database on the pad. If we have other databases on the local PC, we can also easily use it by the IP system with simple procedure such as a pasting or a slot connection.

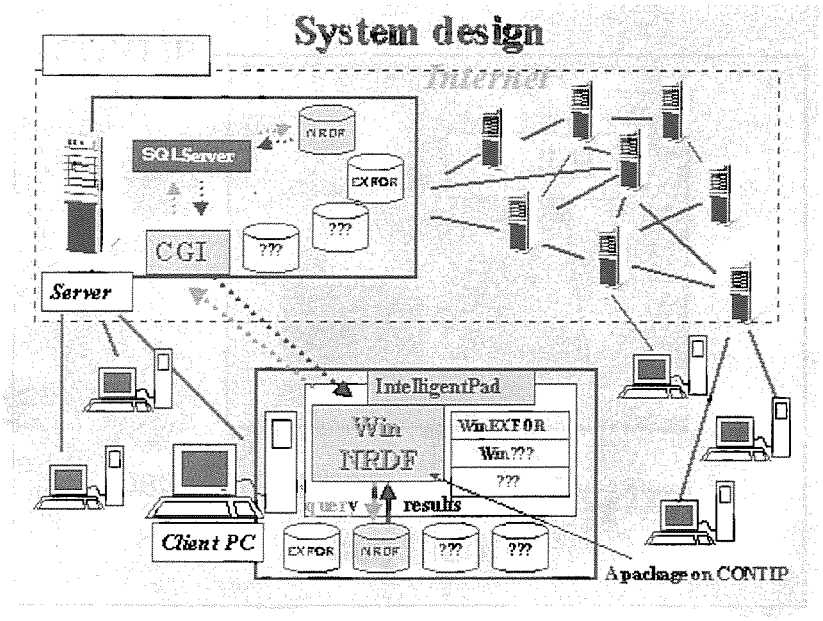

Fig. 2 System design

4. Pads in WinNRDF2

In this section, we explain pads in WinNRDF2. We input some codes (keywords) to the input boxes in the main query pad in WinNRDF2 (Fig. 3). In the case of pushing the "Search" button, we can see the list of the so called D-number, which is an identification number of the data file basically corresponding to an article, and several information in NRDF (Fig. 4). If we select one of the D-numbers and push the "Open File" button in the list window, then we get the data file with the D-numbers.

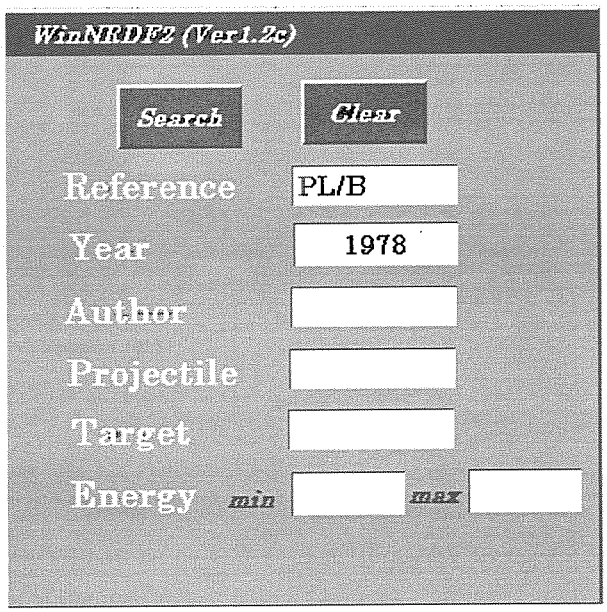

Fig. 3 Query pad

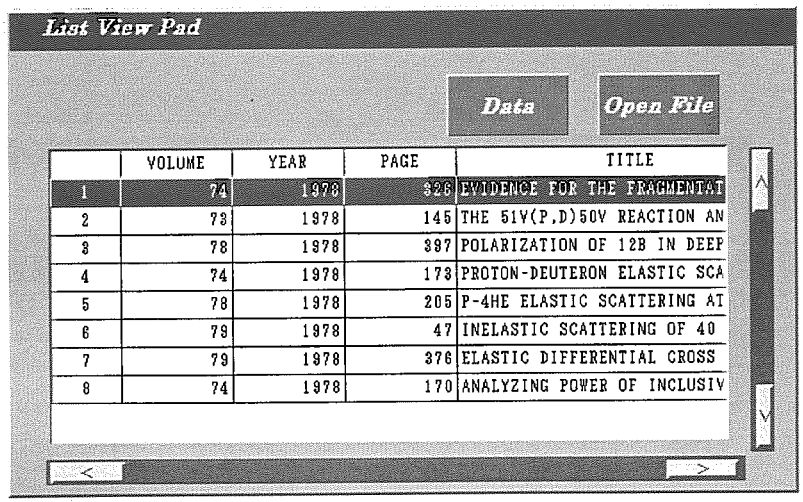

	VOLUME	YEAR	PAGE	TITLE
1	74	1978	326	EVIDENCE FOR THE FRAGMENTAT
2	78	1978	145	THE 51V(P,D)50V REACTION AN
3	78	1978	397	POLARIZATION OF 12B IN DEEP
4	74	1978	173	PROTON-DEUTERON ELASTIC SCA
5	78	1978	205	P-4HE ELASTIC SCATTERING AT
6	79	1978	47	INELASTIC SCATTERING OF 40
7	79	1978	376	ELASTIC DIFFERENTIAL CROSS
8	74	1978	170	ANALYZING POWER OF INCLUSIV

Fig. 4 List view pad

These pads are also constructed by using several basic pads. For example, query pad is decomposed to text pads, edit pads and so on as seen from Fig.5. As shown in Fig.5, these pads are connected to slots of a SQL generating pad. When the "Search" button is pushed, a query with generating SQL is performed to the database of NRDF.

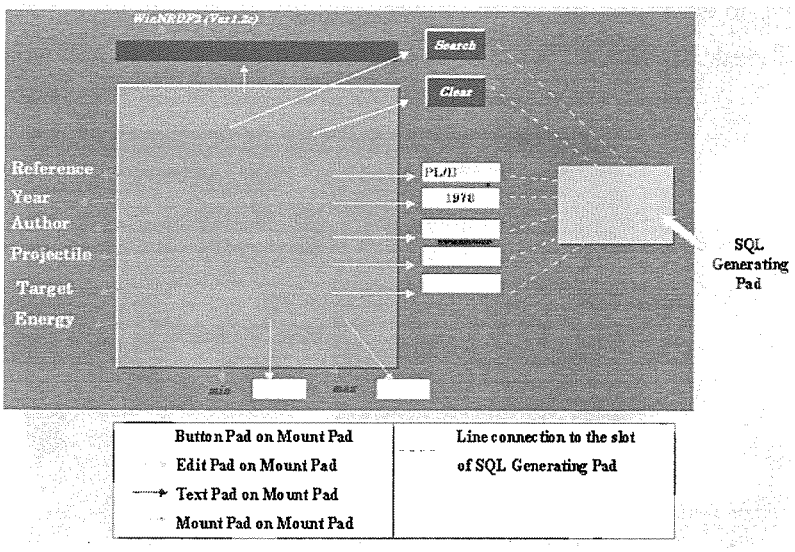

Fig. 5 Decomposition of the query

The obtained data is represented as a data pad which has experimental information. When the data pad is pasted on a graph pad, we can see graphically the experimental data. Graph pads correspond to other experimental data can be compared by using a graph base pad as seen form Fig.6. We will also compare the theoretical one, if we have the calculation code on the IntelligentPad system.

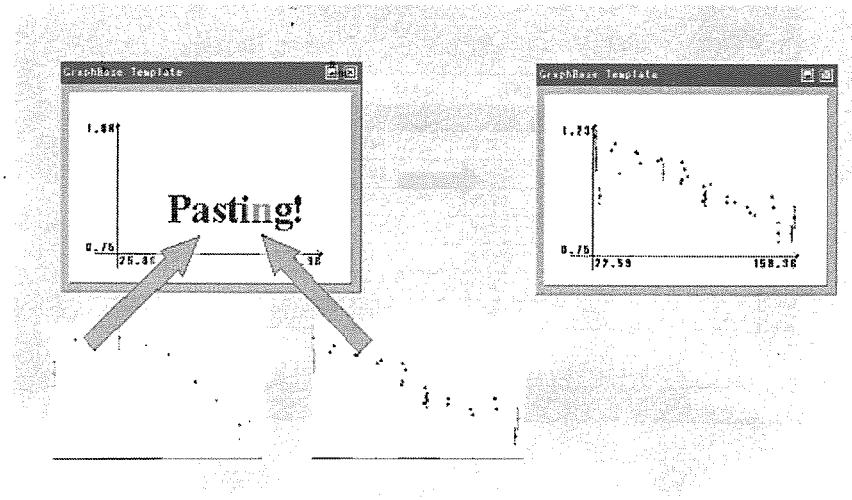

Fig. 6 Comparison between experimental data

5. Summary and future problem

In this paper, we have described a new utility system, WinNRDF2, for a nuclear charged particle reaction data of NRDF (Nuclear Reaction Data File) with the IP architecture. By using the system, we can search the experimental data of charged particle reactions in NRDF and see the graphic data on GUI. In the future, we will want to apply to the EXFOR database.

Acknowledgment

The authors thank to Professor Y. Tanaka for variable supports and encouragement.

References

[1] M. Togashi and H. Tanaka, Jour. Inf. Sci. **Vol.4**, No.5(1982), 213.

[2] Y. Tanaka, Inf. and Sof. Tec. **38** (1996), 201.

[3] S. Aoyama, Y. Ohbayasi, H. Masui, K. Kato, M. Chiba and A. Ohnishi, Proc. of 1998 Symp. on Nuclear Data, JAERI, TOKAI, JAPAN, 222.

[4] Y. Ohbayasi, S. Aoyama, H. Masui, K. Kato and M. Chiba, Proc. of 1998 Symp. on Nuclear Data, JAERI, TOKAI, JAPAN, 228.

[5] Y. Ohbayasi, S. Aoyama, H. Masui, K. Kato and M. Chiba, Proc. of 1999 Symp. on Nuclear Data, JAERI, TOKAI, JAPAN, to be given somewhere in this volume.

3.44 New Formulas for TKE Release in Nuclear Fission Process

Y. L. Zhao, H. Nakahara, K. Sueki
Graduate School of Science, Tokyo Metropolitan University
Y. Nagame, and I. Nishinaka,
Advanced Science Research Center, Japan Atomic Energy Research Institute
zhao-yuliang@c.metro-u.ac.jp

New TKE formulas that will replace the previous existing ones are obtained. Recently, three types of the final deformation of fissioning nuclei were found for actinides out off which only one was observed. The final deformations of the fissioning nuclei was found to be constant and independent of the mass and temperature of the fissioning system. These hence allow to deduce a new formula for the TKE release in nuclear fission process based on the invariance of scission deformations of fissioning nuclei. They yield, TKE(sym) = $0.1173\times(Z_f^2/A_f^{1/3})+7.5$ MeV for the symmetric fission and TKE(asym) = $0.1217\times(Z_f^2/A_f^{1/3})+3.5$ MeV for the asymmetric fission. Details for the new formulas and their comparison with the experimental data are given.

1. Introduction

Mass yield and a kinetic energy of a fission product in fission process of an atomic nucleus are important observable quantities not only for physically understanding fission mechanism but also for practical application in various aspects of nuclear industry. To establish databases for various fission properties is of significant interest and active efforts have been making by the researchers in the nuclear data field. Fission of light elements producing a single symmetric mass yield curve is known, as a nuclide becomes heavy and close to such an element as Ra, the fission yield curve of fragments becomes complicated at low energy and gives a triple humped shape, then a further increase of the mass of a fissioning nucleus leads to an appearance of a double humped mass yield curve. Thus, it was considered that fission of nuclides over the periodic table should show gradually and systematically predictable changes of such properties as mass-yield distribution, total kinetic energy (TKE), etc. But later, as heavy elements were studied, their fission properties always introduced some unexpected results. One of them is the bimodal fission which is characterized by two distinct fission modes for the same symmetric mass division [1]. Also in the spontaneous fission of Fm isotopes, fission properties show dramatic changes [2,3]. They produce very narrow mass yield curves with a very large TKE release which deviate from the prediction of the existing TKE-systematics [4,5] reproducing well the fission observations in a wide region of the relatively lighter nuclides.

In this paper, we report new formulas for the TKE release in nuclear fission processes, which are derived from the scission deformations [6] of fissioning nuclei. Better reproduction of the experimental data by the new TKE formulas than the previously existing ones is indicated.

2. New Formulas for the TKE Release in Nuclear Fission Process

2. 1 TKE formula for the symmetric fission process

For the mass split leading to the average mass of the symmetric fission: $A_1=A_2=A_f/2$, the TKE depends primarily on their mutual Coulomb repulsion of the nascent fragments at scission:

$$TKE_{sym}=e^2\times\rho^2\times(A_f/2)^2/D_{sym}. \quad (1)$$

Where, ρ is the charge density of the fission fragment and given by the UCD model, i.e. $\rho=Z_f/A_f$, Z_f and A_f being the charge and mass of the fissioning nucleus. The ambiguity brought into the final results by the use of the UCD assumption is less than 1% which has been confirmed via a comparison of the results obtained via UCD charges and via experimental measured charges, respectively[6]. The D_{sym} is the distance between two charge centers of the paired fragments at scission and given by $D_{sym}=\beta_{sym}\times D_0$, β_{sym} is the shape elongation of a nucleus at scission configuration and D_0 is radius of a spherical nucleus. Then the TKE_{sym} is written as,

$$TKE_{sym}=e^2\times(Z_f/A_f)^2\times(A_f/2)^2/[\beta_{sym}\times 2\times r_0\times(A_f/2)^{1/3}] \quad (2)$$

It is further expressed in terms of the conventionally used parameter, $Z_f^2/A_f^{1/3}$,

$$TKE_{sym}=e^2\times[8\times r_0\times(1/2)^{1/3}\times\beta_{sym}]^{-1}\times(Z_f^2/A_f^{1/3}) \quad (3)$$

Where the term of $e^2\times[8\times r_0\times(1/2)^{1/3}\times\beta_{sym}]^{-1}$ gives a constant of 0.1173 because the β_{sym} is 1.65 for nuclei undergoing the ordinary symmetric fission dominated by the liquid drop like property of the nucleus, and the β_{sym} value is identical and independent from the mass of the fissioning nucleus and its temperature[6]. By applying this functional form, $TKE_{sym}=0.1173\times(Z_f^2/A_f^{1/3})+b$, to the experimental data, the constant b is determined to be 7.5 MeV. Then, the TKE release in the mass-symmetric fission process is hence obtained.

$$TKE_{sym}=0.1173\times(Z_f^2/A_f^{1/3})+7.5\ \text{MeV} \quad (4)$$

In Fig. 1, comparison of the present TKE-function with the available experimental data is shown. Symbols include the experimental data of the present work, the low-energy symmetric fission and the high-energy heavy-ion induced symmetric fission. The experimental data of literature are taken from Refs.[2,4,7-22] and references therein. The result of the presently derived TKE-function is shown by a bold line. The systematics of Viola et al. [4] is displayed by a thin line. The dashed line is the theoretical results from the dynamical calculations by Nix, Davies and Sierk [7,23]. In the calculations, the effects of surface-plus-window dissipation on the dynamical evolution of the fissioning nucleus beyond its fission saddle point was taken into account. In the figure, that the present TKE formula well reproduces the experimental data is seen.

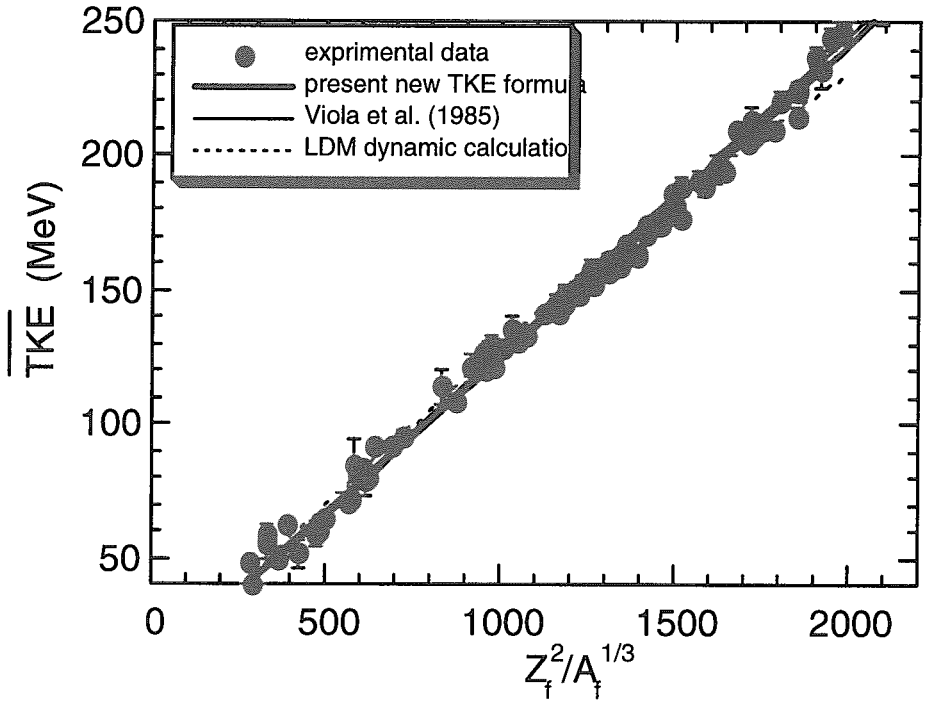

Fig. 1, A comparison of the new TKE formula with experimental data (symbols). The total kinetic energy release in the symmetric fission process is plotted as a function of Coulomb parameter, $Z_f^2/A_f^{1/3}$. Bold line represents the results of the equation (4). The theoretical results by dynamical calculations of liquid drop model are indicated using a dashed line.

2.2 *TKE formula for the asymmetric fission process*

The mass split leading to the average mass of the asymmetric fission is considered. As being known for several decades that the mean mass for the heavier products of the asymmetric fission is mostly at A_H=140 [24-26]. Hence, the average total kinetic energy can be expressed by,

$$TKE_{asym}=e^2\times\rho^2\times 140\times(A_f-140)/D_{asym}. \quad (5)$$

From the UCD assumption and $D_{asym}=\beta_{asym}\times D_0$, it is rewritten as a form of,

$$TKE_{asym}=e^2\times(Z_f/A_f)^2\times 140\times(A_f-140)/[\beta_{asy}\times r_0\times(140^{1/3}+(A_f-140)^{1/3})] \quad (6)$$

The term of $(140^{1/3}+(A_f-140)^{1/3})$ for all of nuclei from A_f=227~259 which covers most of the nuclides fissioning asymmetrically can be approximately replaced by $1.587\times A_f^{1/3}$. The term of $140\times(A_f-140)/A_f^2$ is approximately equal to a constant of 0.24 for nuclei in the above asymmetric fission region if the uncertainty of ~4% is allowed. Then one obtains,

$$TKE_{asym}=0.1816\times\beta^{-1}_{asym}\times(Z_f^2/A_f^{1/3}) \quad (7)$$

The asymmetric shape elongation, β_{asym} was obtained and reported in Ref.[6]. It is a constant value of 1.53 and independent from the fissioning mass, A_f. This gives the coefficient of 0.1217 for equation (7). Thus one obtains the function for the TKE release in the asymmetric fission,

$$TKE_{asym}=0.1217\times(Z_f^2/A_f^{1/3})+3.5\ \text{MeV} \quad (8)$$

The constant term of 3.5 MeV was obtained from the fitting to the experimental data by applying equation (7) to experimental data measured accurately by the double velocity time-of-flight spectrometers [27-30]. In Fig. 2, the experimental data of the average TKE measured from asymmetric fission reactions are plotted as a function of the parameter $Z_f^2/A_f^{1/3}$. The data indicated by solid circles are from the present measurements in which the observed TKE were decomposed into the independent ones for the symmetric and asymmetric fission [27-30], respectively. The experimental data shown by open squares are taken from Ref. [3] and modified to study very the asymmetric process. The mass-yield curves corresponding to the open squares are all very asymmetric with the peak-to-valley ratios of several tens or even several hundreds. The dashed line is the linear fit by the TKE systematics of Unik et al. [5], the thin line shows the TKE systematic formula of Viola et al. The present TKE function indicated by a bold line very well reproduces the experimental data.

The TKE formula of Viola et al. was first proposed in 1963 [31], then modified in 1966 [20] and further revised in 1985 [4] as the experimental data in a wider range of fissioning nuclei became available. The newest Viola's expression is $0.1187\times(Z_f^2/A_f^{1/3})+7.3$ MeV [4]. From a comparison with the new TKE formulas of equations (4) and (8), it is found that the Viola's TKE function gives values in between the present two functions but closer to equation (4) which is derived from the shape elongation of the symmetric fission. This is a not too surprising result because Viola's formula was obtained from a least-square fitting to the experimental TKE data from fission of nuclides over the chart of the nuclides, most of them fission symmetrically.

3. Conclusion

New formulas for the TKE release in nuclear fission processes were derived. Three types of the final deformation of fissioning nuclei were found for actinides outoff which only one exists. The results indicated that the final deformations of the fissioning nuclei showed to be constant and independent of the mass and temperature of the fissioning system. The identical value of final deformations of fissioning nuclei hence allows one to obtain new empirical TKE formulas: $TKE(sym) = 0.1173\times(Z_f^2/ A_f^{1/3})+7.5$ MeV for the symmetric fission and $TKE(asym) = 0.1217\times(Z_f^2/ A_f^{1/3})+3.5$ MeV for the asymmetric fission. The present TKE functions show very well reproduction of the experimental data and also provide answers to question why the previous existing TKE systematics couldn't reproduce the experimental data observed from the asymmetric fission of heavy elements.

Acknowledgments

We thank Drs. K. Tsukada, S. Ichikawa (JAERI) and Y. Oura (TMU) for their help. Fruitful discussions with Dr. Ikezoe (JAERI) are gratefully acknowledged.

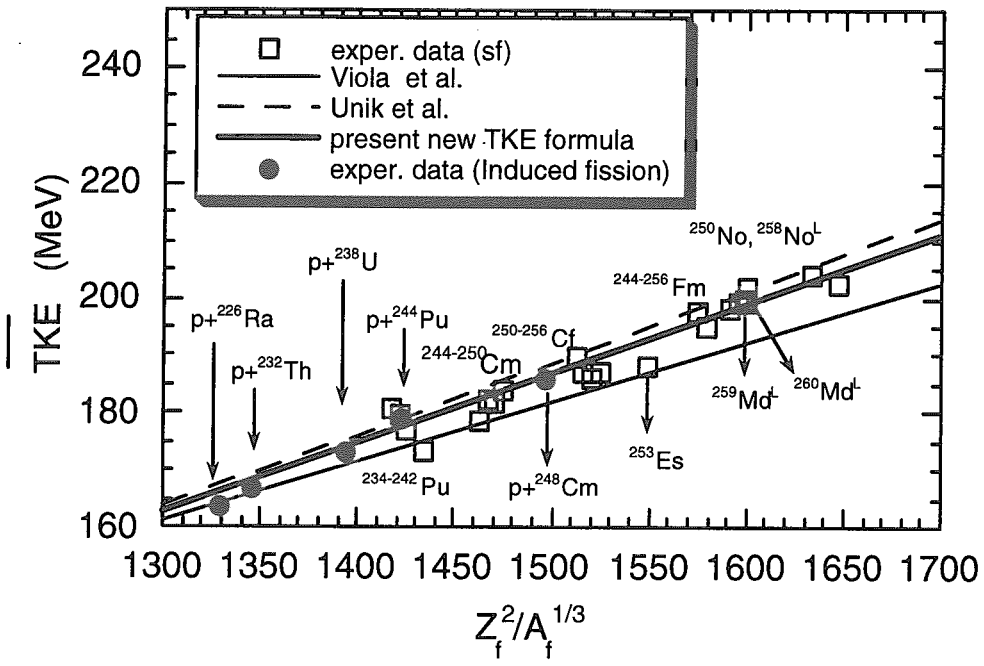

Fig. 2, A comparison of the new TKE formula with experimental data (Symbols). The total kinetic energy release in the asymmetric fission process is plotted as a function of Coulomb parameter, $Z_f^2/A_f^{1/3}$. Bold line shows the results of equation (8). The thin and dashed lines are the results of the previous TKE systematics proposed by Viola and Unik et al., respectively. The fissioning nuclei or systems corresponding to data points are indicated by the names close to data points or far away to the symbols but with arrows.

References

[1] E.K. Hulet, J.F. Wild, R.J. Dougan, R.W. Lougheed, J.H. Landrum, A.D. Dougan, M. Schadel, R.L. Hahn, P.A. Baisden, C.M. Henderson, R.J. Dupzyk, K.Summerer, and G.R.Bethune, Phys. Rev. Lett., 56, 313 (1986); Phys. Rev., C 40, 770 (1989).

[2] D. C. Hoffman, J. B. Wilhelmy, J. Weber, and W. R. Daniels, E. K. Hulet, R. W. Lougheed, J. H. Landrum, J. F. Wild, and R. J. Dupzyk, Phys. Rev., C 21, 972 (1980).

[3] D. C. Hoffman, and M. R. Lane, Radiochim. Acta, 70/71, 135 (1995).

[4] V.E. Viola, K. Kwiatkowski, and M. Walker, Phys. Rev., C 31, 1550 (1985).

[5] J. P. Unik, J. E. Gindler, L. E. Glendenin, K. F. Flynn, A. Gorski, R. K. Sjoblom, *in Proceedings of the 3rd IAEA Symposium on Physics and Chemistry of Fission,* Rochester, 1973, Vol.2, p.19, (IAEA, Viena, 1974).

[6] Y. L. Zhao, I. Nishinaka, Y. Nagame, M. Tanikawa, K. Tsukada, S. Ichikawa, K. Sueki, Oura, H. Ikezoe, S. Mitsuoka, H. Kudo, and H. Nakahara, Phys. Rev. Lett. , 82, 3408 (1999).

[7] J. R. Nix, and A. J. Sierk, Nucl. Phys., A428, 161c (1984).

[8] M. R. Lane, K. E. Gregorich, D. M. Lee, M. F. Mohar, M. Hsu, C. D. Kacher, M. P. Neu, N. J. Stoyer, E. R. Sylwester, J. C. Yang, and D. C. Hoffman, Phys. Rev., C 53, 2893 (1996).

[9] E. Konecny, and H. W. Schmitt, Phys. Rev., 172, 1213 (1968).

[10] H.C. Britt, H.E. Wegner and J.C. Gursky, Phys. Rev., 129, 2239 (1963).

[11] S. D. Beizin, S. V. Zhdanov, M. G. Itkis, V. N. Okolovich, G. N. Smirenkin, and M. I. Subbotin, Yad. Fiz. 50, 626 (1989); Sov. J. Nucl. Phys., 50, 386 (1989).

[12] H. C. Britt, and S. L. Whetstone, Jr., Phys. Rev., 133, B603 (1964).

[13] D. C. Hoffman, D. Lee, A. Ghiorso, M. Nurmia, K. Aleklett, Phys. Rev., C 22,1581 (1980).

[14] J. E. Gindler, K. F. Flynn, L. E. Glendenin, and R. K. Sjoblom, Phys. Rev., C 16, 1483 (1977).

[15] C. E. Bemis, R. L. Ferguson, F. Plasil, R. J. Silva, F. Pleasonton, and R. L. Hahn, Phys. Rev., C 15, 705 (1977).

[16] H. W. Schmitt, J. H. Neiler, and F. J. Walter, Phys. Rev., 141, 1146 (1966).

[17] F. Plasil, D. B. Burnett, H. C. Britt, and S. G. Thompson, Phys. Rev., 142, 696 (1966).

[18] S. D. Beizin, G. N. Smirenkin, M. G. Itkis, S. V. Zhdanov, and M. I. Subbotin, V. N. Okolovich, Yad. Fiz. 53, 656 (1991). Sov. J. Nucl. Phys., 53(3), 411 (1991).

[19] D. G. Perry, and A. W. Fairhall, Phys. Rev., C 4, 977 (1971).

[20] V. E. Viola, Nucl. Data Tables, A 1, 391 (1966).

[21] M. G. Itkis, V. Okolovich, A. Rusanov, and G. N. Smirenkin, Z. Phys, A 320, 433 (1985).

[22] I. Nishinaka, Y. Nagame, K. Tsukada, H. Ikezoe, K. Sueki, H. Nakahara, M. Tanikawa, and T. Ohtsuki, Phys. Rev., C 56, 891 (1997).

[23] K. T. R. Davies, A. J. Sierk, and J. R. Nix, Phys. Rev., C 28, 679(1983).

[24] R. Vandenbosch and J.R. Huizenga, *Nuclear Fission*, Academic Press, 1973.

[25] H. Nakahara, and T. Ohtsuki, J. Radioanal. and Nucl. Chem., Articles, 142, 231 (1990).

[26] Y. L. Zhao, M. Tanikawa, K. Sueki, I. Nishinaka, K. Tsukada,Y. Oura, Y. Nagame, and H. Nakahara, Radiochim. Acta, in press. (Dec., 1999).

[27] Y. Nagame, I. Nishinaka, K. Tsukada, Y. Oura, S. Ichikawa, H. Ikezoe, Y.L. Zhao, K. Sueki, H. Nakahara, M. Tanikawa, T. Ohtsuki, H. Kudo, Y. Hamajima, K. Takamiya, Y.H. Chung, Phys. Lett., B 387, 26 (1996).

[28] Y. L. Zhao, T. Otuski, Y. Nagame, I. Nishinaka, K.Tsukada, S. Ichikawa, H. Ikezoe, Y. Hatuskawa, K. Hata, M. Tanikawa, Z. Qin, K. Sueki, Y. Oura, H. Kudo, H. Nakahara, J. Radiochem. Nucl. Chem., 239, 113 (1999).

[29] Y. L. Zhao, I. Nishinaka, Y. Nagame, K.Tsukada, M. Tanikawa, K. Sueki, Y. Oura, S. Ichikawa, H. Ikezoe, T. Otsuki, S. Goto, H. Kudo, H. Nakahara, J. Alloys and Compounds (Elsevier), 271, 327 (1998).

[30] Y. Nagame, I. Nishinaka, Y. L. Zhao, K.Tsukada, S. Ichikawa, Z. Qin, H. Ikezoe, Y. Oura, K. Sueki, H. Nakahara, M. Tanikawa, T. Otuski, S. Goto, H. Kudo, Y. Hamajima, K. Takamiya, K. Nakanishi, H. Baba, J. Radiochem. Nucl. Chem., 239, 97 (1999).

[31] V. E. Viola, and T. Sikkeland, Phys. Rev., 130, 2044 (1963).

3.45 TCA UO_2 / MOX Core Analyses

Yoshihisa Tahara
Reactor Core Engineering & Safety Engineering Department Mitsubishi Heavy Industries, Ltd.
3-1,Minatomirai 3-chome Nishi-ku Yokohama 220-8401
e-mail: tahara@atom.hq.mhi.co.jp

Hideyuki Noda
Engineering Department Reactor Analysis Group Engineering Development Co., Ltd.
3-1,Minatomirai 3-chome Nishi-ku Yokohama 220-8401
e-mail: noda@atom.hq.mhi.co.jp

In order to examine the adequacy of nuclear data, the TCA UO_2 and MOX core experiments were analyzed with MVP using the libraries based on ENDF/B-VI Mod.3 and JENDL-3.2. The ENDF/B-VI data underpredict k_{eff} values. The replacement of ^{238}U data with the JENDL-3.2 data and the adjustment of $^{235}\nu$-value raise the k_{eff} values by 0.3% for UO_2 cores, but still underpredict k_{eff} values. On the other hand, the nuclear data of JENDL-3.2 for H, O, Al, ^{238}U and ^{235}U of ENDF/B-VI whose $^{235}\nu$-value in thermal energy region is adjusted to the average value of JENDL-3.2 give a good prediction of k_{eff}.

1. Introduction UO_2 and MOX core experiments carried out using TCA of JAERI have been analyzed with the continuous energy Monte Carlo code MVP using the libraries based on ENDF/B-VI Mod.3 and JENDL-3.2 to examine the adequacy of the nuclear data. The effect on k_{eff} with fuel burnup was also evaluated with 2-D transport depletion calculation code PHOENIX-P using a 70-group library based on ENDF/B-VI.

2. Analyses and discussions MVP calculations are performed in three-dimensional core configuration shown in Fig.1. The cores whose moderator to fuel volume ratios are 1.5 ～3.0 for UO_2 and 2.42～5.55 for MOX are analyzed. The three libraries are examined here : ENDF/B-VI; ENDF/B-VI whose ^{238}U data are replaced with that of JENDL3.2; JENDL3.2. The results are shown in Table-1.

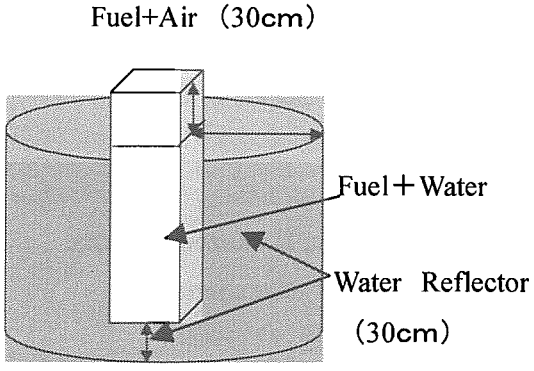

Fig.1 Core Configuration

The followings can be found from the table :

① ENDF/B-VI gives lower k_{eff} by about 0.5% $\Delta k/k$ for UO_2 cores and about 0.25% $\Delta k/k$ for MOX cores,

② ^{238}U of JENDL-3.2 raises k_{eff} by 0.2% $\Delta k/k$ for UO_2 cores and 0.1% $\Delta k/k$ for MOX cores,

③ JENDL3.2 gives higher k_{eff} by 0.2 to 0.4% $\Delta k/k$ for UO_2 cores and 0.1 to 0.2% $\Delta k/k$ for MOX cores.

Table-1 k_{eff} calculated with MVP for TCA U/MOX Cores

Core Name	Fuel rods array	EN/B-VI*	EN/B-VI+ J3.2 ^{238}U	JENDL3.2
1.50U	24X24	0.99508±0.0251%	0.99738±0.0243%	1.00419±0.0232%
1.83U	22X22	0.99448±0.0250%	0.99661±0.0237%	1.00290±0.0244%
2.48U	20X20	0.99448±0.0245%	0.99614±0.0240%	1.00251±0.0243%
3.00U	19X19	0.99444±0.0246%	0.99658±0.0232%	1.00206±0.0230%
2.42Pu	22X22	0.99735±0.0236%	0.99843±0.0235%	1.00095±0.0240%
2.98Pu	21X21	0.99782±0.0239%	0.99882±0.0234%	1.00197±0.0232%
4.24Pu	20X20	0.99788±0.0232%	0.99878±0.0229%	1.00135±0.0224%
5.55Pu	21X21	0.99729±0.0216%	0.99825±0.0215%	1.00187±0.0218%

* A cross-section library based on the ENDF/B-VI Mod.3 is used

The results are also shown in Fig.2 and Fig.3.

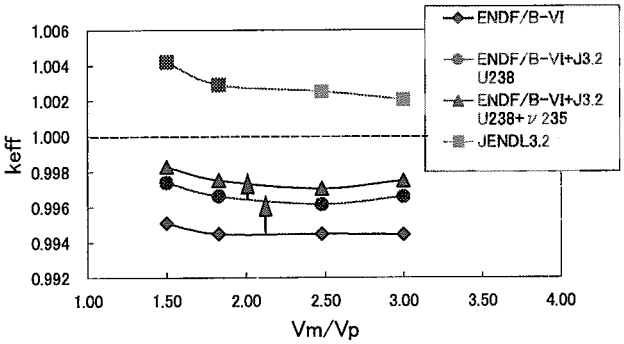

Fig.2 keff of TCA UO2 Core

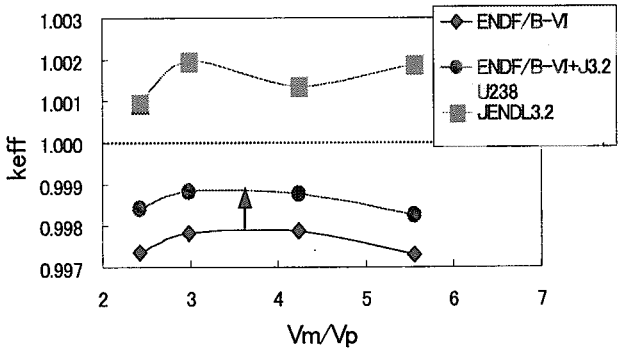

Fig.3 keff of TCA MOX Core

The reason why ENDF/B-VI data underpredict k_{eff} values was investigated. According to H.Takano, the k_{eff} values calculated with ENDF/B-VI are underpredicted and the harder neutron spectrum due to the inelastic scattering of ^{238}U and the ν-value of ^{235}U are the cause of the underprediction[1]. Therefore, we did the check calculations to confirm the effects.

First, we processed inelastic cross-sections and scattering matrices of ^{238}U of ENDF/B-VI and JENDL-3.2 with NJOY. The results are shown in Fig.4 and Fig.5.

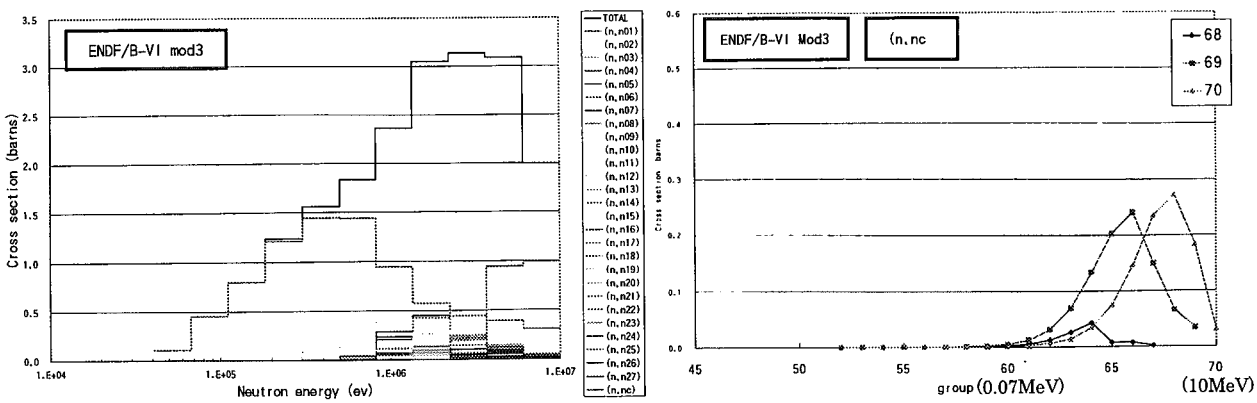

Fig.4 In-elastic Scattering Cross-sections and Matrix of ENDF/B-VI

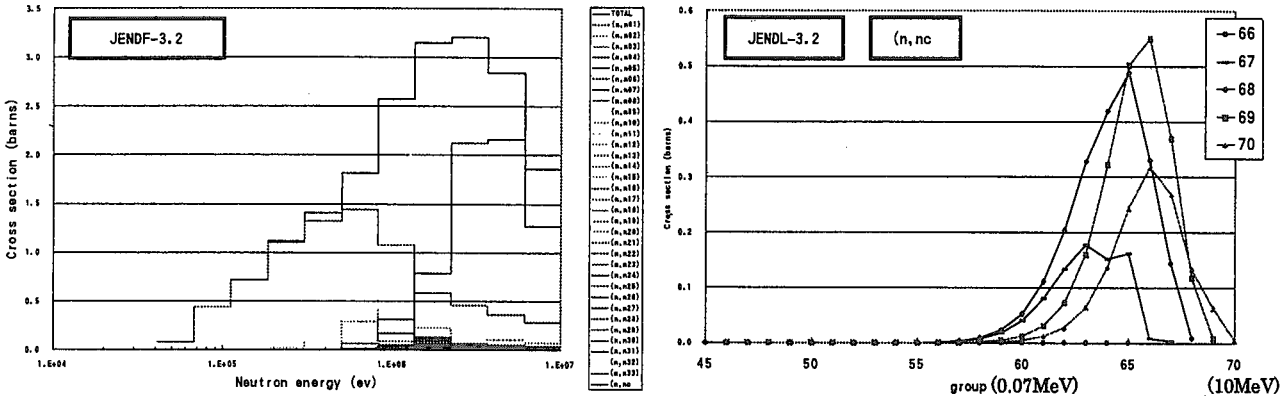

Fig.5 In-elastic Scattering Cross-sections and Matrix of JENDL-3.2

It is obvious from the figures that the continuum scattering matrix of ENDF/B-VI is smaller than that of JENDL-3.2 and gives harder neutron spectrum, and hence more neutron leakage.

In order to confirm that the cause of the underprediction of k_{eff} for the TCA critical experiments is the neutron leakage from the core, the k_{inf} values of MVP were compared for an infinite array of the PWR standard cell shown in Fig.6. As can be seen from Table 2, the replacement of ^{238}U nuclear data gives little effect on k_{inf} of the infinite array system. So, it is clear that the difference of inelastic scattering matrix, especially that of the continuum, affects strongly k_{eff} prediction of experimental cores through the change in neutron leakage from the cores.

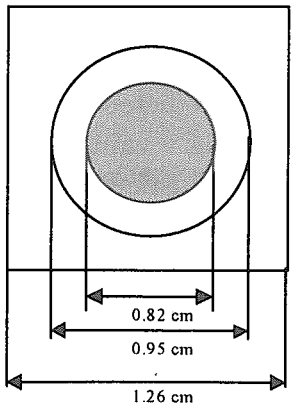

Fig.6 PWR standard cell

Table 2 Effect of ^{238}U on infinite lattice

	k_{inf}
ENDF/B-VI ^{238}U	1.38273±0.0153%
JENDL-3.2 ^{238}U	1.38254±0.0153%

Secondly, the fission-reaction rate ($\sigma_f \phi$) averaged ν-value of JENDL3.2 in the thermal energy range below 2.1 eV was calculated and then ν-value of ^{235}U of JENDL-3.2 was found to be bigger than that of ENDF/B-VI by 0.14% and the adjustment to ν-value of ^{235}U of ENDF/B-VI increase multiplication factor by 0.09% Δ k/k.

$$\bar{\nu}_f^{JENDL3.2} = \frac{\int \nu\sigma\phi E}{\int \sigma\,\phi\, dE} = 2.4372, \quad \bar{\nu}_f^{ENDF/B-VI} = 2.4338, \quad f = \frac{\bar{\nu}_f^{JENDL3.2}}{\bar{\nu}_f^{ENDF/B-VI}} = 1.0014.$$

Energy dependence of $^{235}\nu$-values is presented in Fig.7.

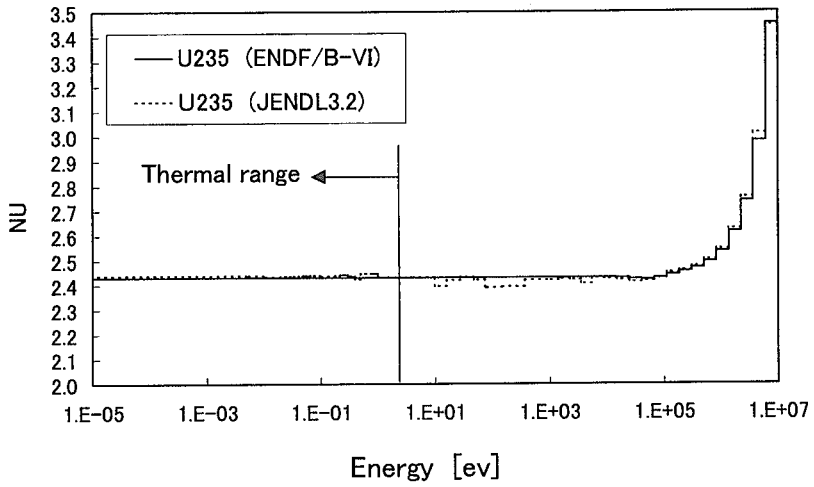

Fig.7 Number of neutrons per fission

The effect of the replacement of ^{238}U is 0.2% Δk/k and the adjustment of $^{235}\nu$ is 0.1% Δk/k. Finally, summing up those effects, we can explain 0.3% difference totally in 0.4～0.5% difference found in Table 1. It is shown in Fig.2 and Fig.3 that the modified library taken into account of them gives almost the same calculation accuracy of k_{eff} for both UO_2 and MOX cores.

The effect on k_{eff} due to the change in ^{238}U and $^{235}\nu$ data with fuel burnup have been also evaluated with 2-D transport depletion calculation code PHOENIX-P. Nuclear data of both libraries were processed and 70 energy-group libraries were generated with NJOY for this purpose. A 17×17 PWR standard assembly was used for the evaluation. The result is shown in Fig.8. It can be found from the figure that the total effect on k_{eff} is 0.1% Δk/k at 0 MWd/t and -0.07% Δk/k at 60 GWd/t for a PWR 17×17 standard assembly with 4.1 w/o enriched UO_2 rods.

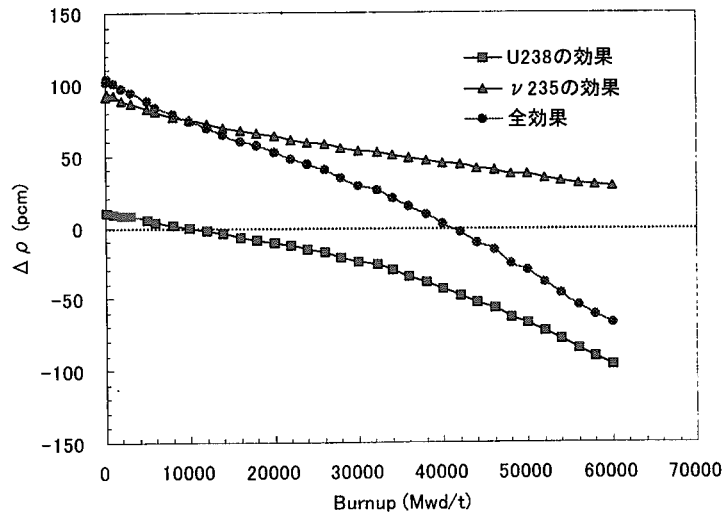

Fig.8 Change in keff with Burnup

The effect of the difference of nuclear data between JENDL-3.2 and ENDF/B-VI on k_{eff} value was investigated for the TCA 15×15 UO_2 core with fuel rods of 2.6w/o ^{235}U. The results are shown in the Table 3 where, e.g., in the case of "JENDL-3.2 base", the reference k_{eff} value is based on all the JENDL-3.2 data and the nuclear data of a nuclide is replaced with the corresponding data of ENDF/B-VI. Considering the result obtained previously with regard to $^{235}\nu$, it can be concluded that the use of the JENDL-3.2 data with ^{235}U of ENDF/B-VI whose $^{235}\nu$ in thermal range is adjusted to the average value of JENDL-3.2 gives good criticality : keff=0.99916+0.0009=1.00006.

Table 3 k_{eff} values calculated with MVP for the TCA 15×15 core

JENDL3.2 Base

Cross-section Library	MVP	
	Keff	Δρ(%)
①J3.2 (H,O,Al,U235,U238)	1.00293±0.0236	0.000
②J3.2 (O,Al,U235,U238) ENDF/B-VI(H)	1.00258±0.0232	-0.035
③J3.2 (H,Al,U235,U238) ENDF/B-VI(O)	1.00275±0.0239	-0.018
④J3.2 (H,O,U235,U238) ENDF/B-VI(Al)	1.00172±0.0239	-0.120
⑤J3.2 (H,O,Al,U238) ENDF/B-VI(U235)	0.99916±0.0239	-0.376
⑥J3.2 (H,O,Al,U235) ENDF/B-VI(U238)	0.99995±0.0238	-0.297
⑦ENDF/B-VI(H,O,Al,U235,U238)	0.99487±0.0234	-0.808

H is the cross-section of H_2O.

ENDF/B-VI Base

Cross-section Library	MVP	
	Keff	Δρ(%)
①ENDF/B-VI (H,O,Al,U235,U238)	0.99487±0.0234	0.000
②ENDF/B-VI (O,Al,U235,U238) J3.2 (H)	0.99593±0.0239	0.107
③ENDF/B-VI (H,Al,U235,U238) J3.2 (O)	0.99626±0.0248	0.140
④ENDF/B-VI (H,O,U235,U238) J3.2 (Al)	0.99607±0.0240	0.121
⑤ENDF/B-VI (H,O,Al,U238) J3.2 (U235)	0.99873±0.0244	0.388
⑥ENDF/B-VI (H,O,Al,U235) J3.2 (U238)	0.99726±0.0243	0.241
⑦J3.2(H,O,Al,U235,U238)	1.00293±0.0236	0.808

H is the cross-section of H_2O.

3. Conclusions UO_2 and MOX core experiments of TCA have been analyzed with MVP using the libraries based on ENDF/B-VI and JENDL-3.2. It has been found that the replacement of ^{238}U data with the JENDL-3.2 data and the adjustment of $^{235}\nu$-value raise the k_{eff} values obtained using ENDF/B-VI based library by 0.3% for UO_2 cores, but still underpredict k_{eff} values. On the other hand, the use of a combined library of JENDL-3.2 for H, O, Al, ^{238}U and ENDF/B-VI for ^{235}U whose $^{235}\nu$ in thermal energy region is adjusted to the average value of JENDL-3.2 seems to give a good prediction of k_{eff}, while the adequacy should be examined from other points of view, e.g., reaction rate ratio measurements, PIE data etc.

Acknowledgements

The authors express their thanks to Mr. Yasunori Nagaya of JAERI, who supplied them with the MVP library based on ENDF/B-VI Mod.3.

Reference

[1] Takano, H., et al: "Reactor Benchmark Testing for JENDL3.2,JEF-2.2,and ENDF/B-VI-2," Int. Conf. Phys. of Nucl. Sci. Technol. (1998).

3.46 Simple estimate of fission rate during JCO criticality accident

Kazuhiro Oyamatsu
Faculty of Studies on Contemporary Society, Aichi Shukutoku University
9 Katahira, Nagakute, Nagakute-cho, Aichi-gun, Aichi, 480-1197, Japan
e-mail : oyak@asu.aasa.ac.jp

The fission rate during JCO criticality accident is estimated from fission-product (FP) radioactivities in a uranium solution sample taken from the preparation basin 20 days after the accident. The FP radioactivity data are taken from a report by JAERI released in the Accident Investigation Committee. The total fission number is found quite dependent on the FP radioactivities and estimated to be about 4×10^{16} per liter, or 2×10^{18} per 16kgU (assuming uranium concentration 278.9 g/liter). On the contrary, the time dependence of the fission rate is rather insensitive to the FP radioactivities. Hence, it is difficult to determine the fission number in the initial burst from the radioactivity data.

1. Introduction

The power history (or the fission rate) in JCO criticality accident is the key parameter to evaluate the exposure dose and doses from released radioactive materials for workers and general public. In principle, the time dependence of the fission rate can be evaluated from the populations of the Fission Products (FP) after the accident. In this paper, we perform a semi-quantitative analysis of the fission rate using FP radioactivity data in a uranium solution sample taken from the preparation basin 20 days after the accident. The data are taken from a report by JAERI [1] released in the Accident Investigation Committee. The report gives the radioactivities of 7 FP nuclides obtained from two different measurements. In this paper, we only use the results of one measurement (group A data) because the author could obtain only the group A data when this study was reported in the symposium. However, we have confirmed that, even if we include the remaining group B data, the conclusion of this study does not change in the present semi-quantitative analysis.

2. Assumption

It is somewhat unclear whether the uranium sample contains the average concentrations of the FP's in the preparation basis. Furthermore, there is no way to evaluate the FP releases from the preparation basin, either.

Therefore, we postulate that no more than two parameters of the fission rate can be obtained from the FP radioactivity data. For simplicity, we assume that the fission reactions continued for 17 hours at a constant rate after the initial burst as shown in Fig. 1. The two parameters to be estimated are the number of fissions in the initial burst (F_b) and in the following 17 hours (F_c).

3. Method of analysis

The population of an FP nuclide can be calculated in the summation method at any cooling time. The fission yield and decay data required for the calculations are taken from JNDC version 2 [2]. We assume that all the fission reactions are induced by thermal neutrons. In this study, the numerical calculations are performed with a handy computer code [3].

To start with, let us denote N_b (N_c) as the populations of an FP nuclide from a pulse fission (fissions for 17 hours at constant fission rate 1 fission/s). Then, the total population of the FP, N, is given by

$$N = F_b N_b + F_c N_c / (17 \times 60 \times 60). \quad (1)$$

Here, N_b and N_c are calculated in the summation method while the total population N can be obtained from the FP radioactivity (λN) in Table I.

Equation (1) gives a line in the (F_c, F_b) plane for each FP nuclide. Then, we have 7 lines for the 7 FP nuclides. Ideally, the lines should have a single intersection that gives the values of F_b and F_c.

It is also possible to obtain the values of F_b and F_c from the linear simultaneous equations (Eq. (1)) in the least squares method. However, we do not adopt the least squares but confine ourselves to the graphical method because the uncertainties of the FP radioactivity data are not clear.

4. Results

Figure 2 shows the 7 lines (Eq. (1)) for the 7 FP nuclides. Unfortunately, it is very hard to identify a single plausible intersection in the figure. Hence, from the present radioactivity data alone, it is very difficult to determine the reliable the (F_c, F_b) values.

When the fission number becomes smaller, a lines in Fig. 2 goes to the lower left side because the total fission number F is given by the straight line $F=F_b+F_c$. From this viewpoint, the lines for ^{95}Zr, ^{131}I and ^{137}Cs seem to imply

that portions of these FP's were lost or released from the uranium solution. Actually, a portion of ^{95}Zr was reported to have been be lost in the preparation process before the radioactivity measurement [1]. Furthermore, ^{131}I was detected outside the JCO site although the quantity was quite small.

In spite of these uncertainties, the total fission number may be known well from Fig. 2. We note that the intersections with the axes show the number of fissions in extreme cases with F_c=0 or F_b=0. These values agree so well that the total number of fissions can be estimated to be about 4×10^{16} fission/liter from the FP radioactivity data.

5. Discussions

The assumption of the fission rate model in Fig. 1 is rather crude. However, it should be noted that the total fission number does not vary much in the two extreme cases. This suggests that the FP radioactivity data give good information to estimate the total fission number independently of the detailed time dependence.

Let us turn to the time scale of the initial burst. Even if the initial burst continued for 10 minutes, this time scale is quite small compared with the total duration of the accident; 10 minutes / 17 hours = 1%. Hence, F_b could include the fission numbers in the possible 2nd and 3rd bursts in the order of 10 minutes after the onset of the accident.

It is also noted that the FP radioactivities were measured after a quite long cooling time compared with the duration of the criticality accident; 17 hours / 20 days = 3.5 %. This is the major reason for the difficulty in evaluating the time dependence of the fission rate from the FP radioactivity data.

6. Conclusions

The fission rate during JCO criticality accident is estimated assuming simple time dependence using the FP radioactivity data taken from preparation basin 20 days after the accident. The total number of fissions is found quite dependent on the FP radioactivities and estimated to be about 4×10^{16} per liter, or 2×10^{18} per 16kgU (assuming uranium concentration 278.9 g/liter). On the contrary, the time dependence of the fission rate is rather insensitive to the FP radioactivities. Hence, it is difficult to determine the fission number in the initial burst from the radioactivity data.

References

[1] "Analysis of a uranium solution sample" by JAERI (October 27, 1999) released during the forth Accident Investigation Committee (October 29, 1999) in Japanese.
[2] K. Tasaka, et al., JNDC Nuclear Data Library of Fission Products - 2nd Version, JAERI-1320 (1988).
[3] K. Oyamatsu, Easy-to-use Application Programs to Calculate Aggregate Fission-Product Properties on Personal Computers, Proc. 1998 Sympo. on Nucl. Data, JAERI-Conf 99-002, pp. 234-239, 1999.

Table I. The FP radioactivity data analyzed from a uranium solution sample taken from the preparation basin 20 days after the accident [1].

nuclide	half life (s)	radioactivity (Bq/ml)
^{95}Zr	5.53×10^{6}	2.15×10^{5}
^{99}Mo	2.38×10^{5}	4.34×10^{4}
^{103}Ru	3.41×10^{6}	1.77×10^{5}
^{144}Ce	2.46×10^{7}	6.91×10^{4}
^{131}I	6.95×10^{5}	1.89×10^{5}
^{137}Cs	9.52×10^{8}	1.48×10^{3}
^{140}Ba	1.10×10^{6}	5.31×10^{5}

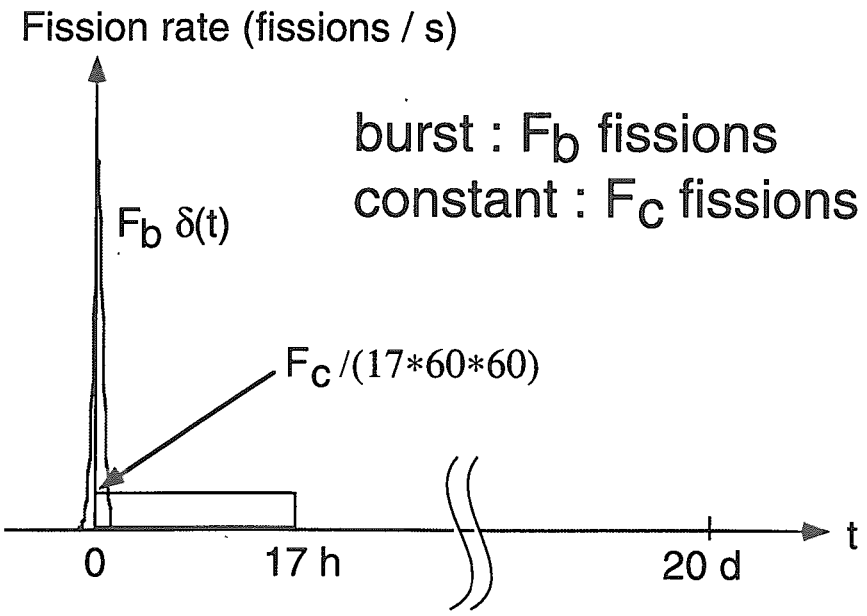

Fig. 1. Fission rate model. The time t=0 corresponds to the beginning of the accident.

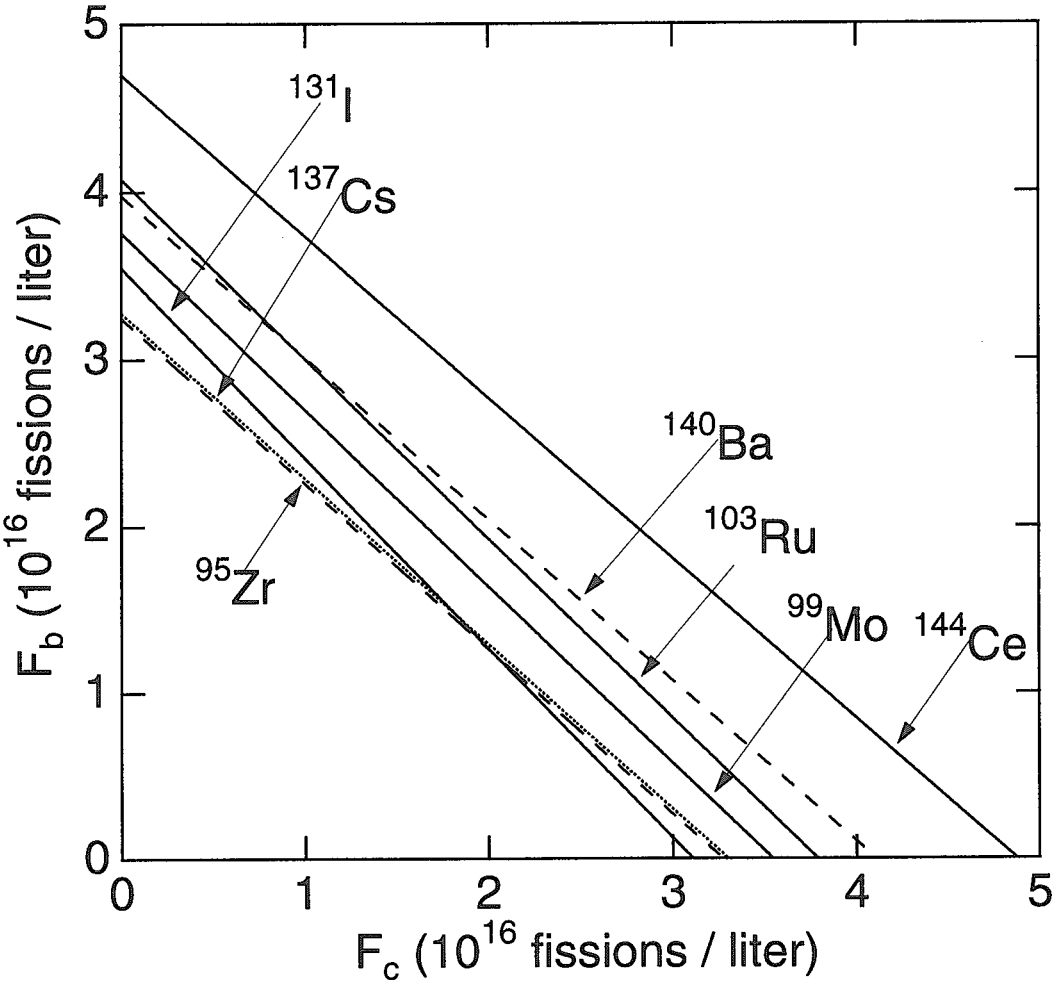

Fig. 2. Fission number in the (F_c, F_b) plane. The values of F_c and F_b are shown as the concentrations in the uranium solution sample.

This is a blank page.

Appendix: Participant List

Vladimir, Barchevtsev	Tokyo Inst. of Tech.
Jonghwa Chang	KAERI
Edward T. Cheng	TSI
Hyun-Je Cho	Kyoto Univ.
Harun-Ar-Rashid A.K.	Tokyo Inst. of Tech.
Guinyun Kim	PAL/POSTECH
Sam Yol Lee	Tokyo Inst. of Tech.
Young-Ouk Lee	KAERI
Manokhin, V	IPPE
Nurul Islam Molla	Director General, AERE
Sun Weili	Kyushu Univ.
Vuong Huu Tan	Vice-Chairman, VAEC
Thiraphat Vilaithong	Chiang Mai Univ.
Yican Wu	ASIPP
Y.L. Zhao	Tokyo Metropolitan Univ.
Youxiang Zhuang	CIAE
Aoki, M.	Osaka Univ.
Aoki, Takao	Tohoku Univ.
Aoki, Tamotsu	Fuji Electric Co., Ltd.
Aoyama, Sigeyoshi	Kitami Inst. of Tech.
Aoyama, Takafumi	JNC
Akino, Fujiyoshi	IRM
Asai, Masato	JAERI
Aruga, Takeo	JAERI
Ando, Yoshihira	JAERI
Iimura, Hideki	JAERI
Igashira, Masayuki	Tokyo Inst. of Tech.
Igarasi, Sin-iti	
Ikezoe, Hiroshi	JAERI
Ikeda, Yujiro	JAERI
Ishii, Kimiya	Osaka Univ.
Ishii, T.	JAERI
Ibaraki, Masanobu	Tohoku Univ.
Imai, Kazuhiko	JAERI
Iwamoto, Osamu	JAERI
Iwamoto, Yousuke	Kyushu Univ.
Uchiyama, T.	JAERI
Oigawa, Hiroyuki	JAERI
Ohkawachi, Yasushi	JNC
Ohkubo, Makio	SOHONRR
Ohsaki, Toshiro	Tokyo Inst. of Tech.
Ohsawa, Takaaki	Kinki Univ.
Ohbayasi, Yosihide	Hokkaido Univ.
Okajima, Shigeaki	JAERI
Okamoto, Koichi	Nihon Univ.
Okuno, Hiroshi	JAERI
Odano, Naoteru	JAERI
Ono, Mikinori	MES
Oyamatsu, Kazuhiro	Aichi Shukutoku Univ.
Kai, Tetsuya	JAERI
Kaise, Yoitiro	ARTECH
Katakura, Jun-ichi	JAERI
Kawai, Masayoshi	KEK
Kawade, Kiyoshi	Nagoya Univ.
Kawano, Toshihiko	Kyushu Univ.
Kitazawa, Hideo	NDA
Kitsuki, Hirohiko	Kyushu Univ.
Kimura, Itsuro	INSS
Kugo, Teruhiko	JAERI
Kurosawa, Tadahiro	Tohoku Univ.
Koura, Hiroyuki	Waseda Univ.
Koori, Norihiko	Tokushima Univ.
Kosako, Kazuaki	SAE
Goto, S.	JAERI
Kobayashi, Katsuhei	Kyoto Univ.
Komuro, Y.	JAERI
Kondo, Tetsuo	Osaka Univ.
Sakata, Hideaki	JAERI
Sakane, Hitoshi	Nagoya Univ.
Sakama, Minoru	JAERI
Sakurai, Takeshi	JAERI
Sakurai, Hiroyoshi	RIKEN
Sasa, Toshinobu	JAERI
Sasaki, Kenji	JNC
Sasahara, Akihiro	CRIEPI
Sato, Daisuke	Osaka Univ.
Sato, Tatsuhiko	Kyoto Univ.
Sato, Hisaki	Tohoku Univ.
Sawamura, Hidenori	CSD
Shigyo, Nobuhiro	Kyushu Univ.
Shinohara, Nobuo	JAERI
Shibata, Keiichi	JAERI
Shibata, Kei-ichiro	JAERI
Shimakawa, Satoshi	JAERI
Shono, Akira	JNC
Sugi, Teruo	JAERI
Sugino, Kazuteru	JNC
Zukeran, Atsushi	HEC
Suyama, Kenya	JAERI
Seki, Yasushi	JAERI
Senga, T.	Nagoya Univ.
Sengoku, M.	JAERI
Takao, Yoshiyuki	Kyushu Univ.
Takagi, Hiroyuki	Osaka Univ.
Taji, Y.	RIST
Tachibana, Takahiro	Waseda Univ.
Tahara, Yoshihisa	MHI
Tabuchi, Shiro	JNC
Tamura, Tsutomu	RIST
Tsukada, Kazuaki	JAERI
Tsujimoto, Kazufumi	JAERI
Tsubosaka, Akira	JAERI
Nakagawa, Tsuneo	JAERI
Nakagawa, Masayuki	JAERI Director
Nakazawa, Masaharu	Univ. of Tokyo
Nakashima, Hiroshi	JAERI

Nakasima, Ryuzo	Hosei Univ.
Nakane, Yoshihiro	JAERI
Nakamura, Shoji	JNC
Nakamura, Takashi	Tohoku Univ.
Nakamura, Takeshi	KCC
Nakamura, Masahiro	JNC
Nagame, Y.	JAERI
Nagaya, Yasunobu	JAERI
Niita, Koji	RIST
Nishio, Katsuhisa	JAERI
Nishio, Takashi	Osaka Univ.
Nishinaka. Ichiro	JAERI
Nishihara, Kenji	JAERI
Noda, Hideyuki	MHI
Hasegawa, Akira	JAERI
Haba, Hiromitsu	JAERI
Baba, Mamoru	Tohoku Univ.
Harada, Hideo	JNC
Harada, Masahide	JAERI
Hirasawa, Yoshitaka	Tohoku Univ.
Hiroishi, Tsutomu	Tohoku Univ.
Furutaka, Kazuyoshi	JNC
Maekawa, Hiroshi	JAERI
Maekawa, Fujio	JAERI
Maeda, Shigetaka	JNC
Maki, Koichi	Hitachi Ltd.
Masui, Hiroshi	Hokkaido Univ.
Matsuoka, Yasuaki	Kyusyu Univ.
Matsunobu, Hiroyuki	DEI
Miura, Takako	Tohoku Univ.
Mizumoto, Motoharu	JAERI
Mitsuoka, S.	JAERI
Miyoshi, Yoshinori	JAERI
Munakata, Kenzo	Kyushu Univ.
Murata, Isao	Osaka Univ.
Murata, Toru	AITEL
Meigo, Shin-ichiro	JAERI
Morimoto, Yuuichi	Hitachi Ltd.
Morotomi, Ryutaro	Osaka Univ.
Yashima, Hiroshi	Tohoku Univ.
Yamano, Naoki	SAE
Yoshizawa, Nobuaki	MRI
Yoshida, Shiro	Tohoku Univ.
Yoshida, Tadashi	Musashi Inst. of Tech.
Yonezawa, Chushiro	JAERI
Wada, Hiroaki	JNC
Watanabe, Takashi	KHI
Watanabe, Yukinobu	Kyushu Univ.

国際単位系 (SI) と換算表

表 1　SI基本単位および補助単位

量	名称	記号
長さ	メートル	m
質量	キログラム	kg
時間	秒	s
電流	アンペア	A
熱力学温度	ケルビン	K
物質量	モル	mol
光度	カンデラ	cd
平面角	ラジアン	rad
立体角	ステラジアン	sr

表 2　SIと併用される単位

名称	記号
分，時，日	min，h，d
度，分，秒	°，′，″
リットル	l，L
トン	t
電子ボルト	eV
原子質量単位	u

1 eV = 1.60218 × 10^{-19} J

1 u = 1.66054 × 10^{-27} kg

表 5　SI接頭語

倍数	接頭語	記号
10^{18}	エクサ	E
10^{15}	ペタ	P
10^{12}	テラ	T
10^{9}	ギガ	G
10^{6}	メガ	M
10^{3}	キロ	k
10^{2}	ヘクト	h
10^{1}	デカ	da
10^{-1}	デシ	d
10^{-2}	センチ	c
10^{-3}	ミリ	m
10^{-6}	マイクロ	μ
10^{-9}	ナノ	n
10^{-12}	ピコ	p
10^{-15}	フェムト	f
10^{-18}	アト	a

表 3　固有の名称をもつSI組立単位

量	名称	記号	他のSI単位による表現
周波数	ヘルツ	Hz	s^{-1}
力	ニュートン	N	m·kg/s^2
圧力，応力	パスカル	Pa	N/m^2
エネルギー，仕事，熱量	ジュール	J	N·m
工率，放射束	ワット	W	J/s
電気量，電荷	クーロン	C	A·s
電位，電圧，起電力	ボルト	V	W/A
静電容量	ファラド	F	C/V
電気抵抗	オーム	Ω	V/A
コンダクタンス	ジーメンス	S	A/V
磁束	ウェーバ	Wb	V·s
磁束密度	テスラ	T	Wb/m^2
インダクタンス	ヘンリー	H	Wb/A
セルシウス温度	セルシウス度	℃	
光束	ルーメン	lm	cd·sr
照度	ルクス	lx	lm/m^2
放射能	ベクレル	Bq	s^{-1}
吸収線量	グレイ	Gy	J/kg
線量当量	シーベルト	Sv	J/kg

表 4　SIと共に暫定的に維持される単位

名称	記号
オングストローム	Å
バーン	b
バール	bar
ガル	Gal
キュリー	Ci
レントゲン	R
ラド	rad
レム	rem

1 Å = 0.1 nm = 10^{-10} m

1 b = 100 fm^2 = 10^{-28} m^2

1 bar = 0.1 MPa = 10^5 Pa

1 Gal = 1 cm/s^2 = 10^{-2} m/s^2

1 Ci = 3.7 × 10^{10} Bq

1 R = 2.58 × 10^{-4} C/kg

1 rad = 1 cGy = 10^{-2} Gy

1 rem = 1 cSv = 10^{-2} Sv

（注）

1. 表1－5は「国際単位系」第5版，国際度量衡局 1985年刊行による。ただし，1 eVおよび1 uの値はCODATAの1986年推奨値によった。
2. 表4には海里，ノット，アール，ヘクタールも含まれているが日常の単位なのでここでは省略した。
3. barは，JISでは流体の圧力を表わす場合に限り表2のカテゴリーに分類されている。
4. EC閣僚理事会指令ではbar，barnおよび「血圧の単位」mmHgを表2のカテゴリーに入れている。

換算表

力	N(=10^5 dyn)	kgf	lbf
	1	0.101972	0.224809
	9.80665	1	2.20462
	4.44822	0.453592	1

粘度　1 Pa·s(N·s/m^2) = 10 P(ポアズ)(g/(cm·s))

動粘度　1 m^2/s = 10^4 St(ストークス)(cm^2/s)

圧力	MPa(=10 bar)	kgf/cm^2	atm	mmHg(Torr)	lbf/in^2(psi)
	1	10.1972	9.86923	7.50062 × 10^3	145.038
	0.0980665	1	0.967841	735.559	14.2233
	0.101325	1.03323	1	760	14.6959
	1.33322 × 10^{-4}	1.35951 × 10^{-3}	1.31579 × 10^{-3}	1	1.93368 × 10^{-2}
	6.89476 × 10^{-3}	7.03070 × 10^{-2}	6.80460 × 10^{-2}	51.7149	1

エネルギー・仕事・熱量	J(=10^7 erg)	kgf·m	kW·h	cal(計量法)	Btu	ft·lbf	eV
	1	0.101972	2.77778 × 10^{-7}	0.238889	9.47813 × 10^{-4}	0.737562	6.24150 × 10^{18}
	9.80665	1	2.72407 × 10^{-6}	2.34270	9.29487 × 10^{-3}	7.23301	6.12082 × 10^{19}
	3.6 × 10^6	3.67098 × 10^5	1	8.59999 × 10^5	3412.13	2.65522 × 10^6	2.24694 × 10^{25}
	4.18605	0.426858	1.16279 × 10^{-6}	1	3.96759 × 10^{-3}	3.08747	2.61272 × 10^{19}
	1055.06	107.586	2.93072 × 10^{-4}	252.042	1	778.172	6.58515 × 10^{21}
	1.35582	0.138255	3.76616 × 10^{-7}	0.323890	1.28506 × 10^{-3}	1	8.46233 × 10^{18}
	1.60218 × 10^{-19}	1.63377 × 10^{-20}	4.45050 × 10^{-26}	3.82743 × 10^{-20}	1.51857 × 10^{-22}	1.18171 × 10^{-19}	1

1 cal = 4.18605 J（計量法）

= 4.184 J （熱化学）

= 4.1855 J （15 °C）

= 4.1868 J（国際蒸気表）

仕事率　1 PS（仏馬力）

= 75 kgf·m/s

= 735.499 W

放射能	Bq	Ci
	1	2.70270 × 10^{-11}
	3.7 × 10^{10}	1

吸収線量	Gy	rad
	1	100
	0.01	1

照射線量	C/kg	R
	1	3876
	2.58 × 10^{-4}	1

線量当量	Sv	rem
	1	100
	0.01	1

（86年12月26日現在）